

# Light Sterile Neutrinos: A White Paper

K. N. Abazajian<sup>a,1</sup> M. A. Acero,<sup>2</sup> S. K. Agarwalla,<sup>3</sup> A. A. Aguilar-Arevalo,<sup>2</sup> C. H. Albright,<sup>4,5</sup> S. Antusch,<sup>6</sup> C. A. Argüelles,<sup>7</sup> A. B. Balantekin,<sup>8</sup> G. Barenboim<sup>a,3</sup> V. Barger,<sup>8</sup> P. Bernardini,<sup>9</sup> F. Bezrukov,<sup>10</sup> O. E. Bjaelde,<sup>11</sup> S. A. Bogacz,<sup>12</sup> N. S. Bowden,<sup>13</sup> A. Boyarsky,<sup>14</sup> A. Bravar,<sup>15</sup> D. Bravo Berguño,<sup>16</sup> S. J. Brice,<sup>5</sup> A. D. Bross,<sup>5</sup> B. Caccianiga,<sup>17</sup> F. Cavanna,<sup>18,19</sup> E. J. Chun,<sup>20</sup> B. T. Cleveland,<sup>21</sup> A. P. Collin,<sup>22</sup> P. Coloma,<sup>16</sup> J. M. Conrad,<sup>23</sup> M. Cribier,<sup>22</sup> A. S. Cucoanes,<sup>24</sup> J. C. D'Olivo,<sup>2</sup> S. Das,<sup>25</sup> A. de Gouvêa,<sup>26</sup> A. V. Derbin,<sup>27</sup> R. Dharmapalan,<sup>28</sup> J. S. Diaz,<sup>29</sup> X. J. Ding,<sup>16</sup> Z. Djuric,<sup>30</sup> A. Donini,<sup>31,3</sup> D. Duchesneau,<sup>32</sup> H. Ejiri,<sup>33</sup> S. R. Elliott,<sup>34</sup> D. J. Ernst,<sup>35</sup> A. Esmaili,<sup>36</sup> J. J. Evans,<sup>37,38</sup> E. Fernandez-Martinez,<sup>39</sup> E. Figueroa-Feliciano,<sup>23</sup> B. T. Fleming<sup>a,18</sup> J. A. Formaggio<sup>a,23</sup> D. Franco,<sup>40</sup> J. Gaffiot,<sup>22</sup> R. Gandhi,<sup>41</sup> Y. Gao,<sup>42</sup> G. T. Garvey,<sup>34</sup> V. N. Gavrin,<sup>43</sup> P. Ghoshal,<sup>41</sup> D. Gibin,<sup>44</sup> C. Giunti,<sup>45</sup> S. N. Gninenko,<sup>43</sup> V. V. Gorbachev,<sup>43</sup> D. S. Gorbunov,<sup>43</sup> R. Guenette,<sup>18</sup> A. Guglielmi,<sup>44</sup> F. Halzen,<sup>46,8</sup> J. Hamann,<sup>11</sup> S. Hannestad,<sup>11</sup> W. Haxton,<sup>47,48</sup> K. M. Heeger,<sup>8</sup> R. Henning,<sup>49,50</sup> P. Hernandez,<sup>3</sup> P. Huber<sup>b,16</sup> W. Huelsnitz,<sup>34,51</sup> A. Ianni,<sup>52</sup> T. V. Ibragimova,<sup>43</sup> Y. Karadzhev,<sup>15</sup> G. Karagiorgi,<sup>53</sup> G. Keefer,<sup>13</sup> Y. D. Kim,<sup>54</sup> J. Kopp<sup>a,5</sup> V. N. Kornoukhov,<sup>55</sup> A. Kusenko,<sup>56,57</sup> P. Kyberd,<sup>58</sup> P. Langacker,<sup>59</sup> Th. Lasserre<sup>a,22,40</sup> M. Laveder,<sup>60</sup> A. Letourneau,<sup>22</sup> D. Lhuillier,<sup>22</sup> Y. F. Li,<sup>61</sup> M. Lindner,<sup>62</sup> J. M. Link<sup>b,16</sup> B. L. Littlejohn,<sup>8</sup> P. Lombardi,<sup>17</sup> K. Long,<sup>63</sup> J. Lopez-Pavon,<sup>64</sup> W. C. Louis<sup>a,34</sup> L. Ludhova,<sup>17</sup> J. D. Lykken,<sup>5</sup> P. A. N. Machado,<sup>65,66</sup> M. Maltoni,<sup>31</sup> W. A. Mann,<sup>67</sup> D. Marfatia,<sup>68</sup> C. Mariani,<sup>53,16</sup> V. A. Matveev,<sup>43,69</sup> N. E. Mavromatos,<sup>70,39</sup> A. Melchiorri,<sup>71</sup> D. Meloni,<sup>72</sup> O. Mena,<sup>3</sup> G. Mention,<sup>22</sup> A. Merle,<sup>73</sup> E. Meroni,<sup>17</sup> M. Mezzetto,<sup>44</sup> G. B. Mills,<sup>34</sup> D. Minic,<sup>16</sup> L. Miramonti,<sup>17</sup> D. Mohapatra,<sup>16</sup> R. N. Mohapatra,<sup>51</sup> C. Montanari,<sup>74</sup> Y. Mori,<sup>75</sup> Th. A. Mueller,<sup>76</sup> H. P. Mumm,<sup>77</sup> V. Muratova,<sup>27</sup> A. E. Nelson,<sup>78</sup> J. S. Nico,<sup>77</sup> E. Noah,<sup>15</sup> J. Nowak,<sup>79</sup> O. Yu. Smirnov,<sup>69</sup> M. Obolensky,<sup>40</sup> S. Pakvasa,<sup>80</sup> O. Palamara,<sup>18,52</sup> M. Pallavicini,<sup>81</sup> S. Pascoli,<sup>82</sup> L. Patrizii,<sup>83</sup> Z. Pavlovic,<sup>34</sup> O. L. G. Peres,<sup>36</sup> H. Pessard,<sup>32</sup> F. Pietropaolo,<sup>44</sup> M. L. Pitt,<sup>16</sup> M. Popovic,<sup>5</sup> J. Pradler,<sup>84</sup> G. Ranucci,<sup>17</sup> H. Ray,<sup>85</sup> S. Razzaque,<sup>86</sup> B. Rebel,<sup>5</sup> R. G. H. Robertson,<sup>87,78</sup> W. Rodejohann<sup>a,62</sup> S. D. Rountree,<sup>16</sup> C. Rubbia,<sup>39,52</sup> O. Ruchayskiy,<sup>39</sup> P. R. Sala,<sup>17</sup> K. Scholberg,<sup>88</sup> T. Schwetz<sup>a,62</sup> M. H. Shaevitz,<sup>53</sup> M. Shaposhnikov,<sup>89</sup> R. Shrock,<sup>90</sup> S. Simone,<sup>91</sup> M. Skorokhvatov,<sup>92</sup> M. Sorel,<sup>3</sup> A. Sousa,<sup>93</sup> D. N. Spergel,<sup>94</sup> J. Spitz,<sup>23</sup> L. Stanco,<sup>44</sup> I. Stancu,<sup>28</sup> A. Suzuki,<sup>95</sup> T. Takeuchi,<sup>16</sup> I. Tamborra,<sup>96</sup> J. Tang,<sup>97,98</sup> G. Testera,<sup>81</sup> X. C. Tian,<sup>99</sup> A. Tonazzo,<sup>40</sup> C. D. Tunnell,<sup>100</sup> R. G. Van de Water,<sup>34</sup> L. Verde,<sup>101</sup> E. P. Veretenkin,<sup>43</sup> C. Vignoli,<sup>52</sup> M. Vivier,<sup>22</sup> R. B. Vogelaar,<sup>16</sup> M. O. Wascko,<sup>63</sup> J. F. Wilkerson,<sup>49,102</sup> W. Winter,<sup>97</sup> Y. Y. Y. Wong<sup>a,25</sup> T. T. Yanagida,<sup>57</sup> O. Yasuda,<sup>103</sup> M. Yeh,<sup>104</sup> F. Yermia,<sup>24</sup> Z. W. Yokley,<sup>16</sup> G. P. Zeller,<sup>5</sup> L. Zhan,<sup>61</sup> and H. Zhang<sup>62</sup>

<sup>1</sup>*University of California, Irvine*

<sup>2</sup>*Instituto de Ciencias Nucleares, Universidad Nacional Autónoma de México*

<sup>3</sup>*Instituto de Física Corpuscular, CSIC and Universidad de Valencia*

<sup>4</sup>*Northern Illinois University*

<sup>5</sup>*Fermi National Accelerator Laboratory*

<sup>6</sup>*University of Basel*

<sup>a</sup>Section editor

<sup>b</sup>Editor and corresponding author (pahuber@vt.edu and jmlink@vt.edu)

- <sup>7</sup>*Pontificia Universidad Católica del Perú*
- <sup>8</sup>*University of Wisconsin, Madison*
- <sup>9</sup>*Università del Salento and INFN*
- <sup>10</sup>*Arnold Sommerfeld Center for Theoretical Physics, Ludwig-Maximilians-Universität*
- <sup>11</sup>*Aarhus University*
- <sup>12</sup>*Jefferson Laboratory*
- <sup>13</sup>*Lawrence Livermore National Laboratory*
- <sup>14</sup>*Leiden University and BITP, Kiev*
- <sup>15</sup>*University of Geneva*
- <sup>16</sup>*Center for Neutrino Physics, Virginia Tech*
- <sup>17</sup>*Università di Milano and INFN Milano*
- <sup>18</sup>*Yale University*
- <sup>19</sup>*University of L'Aquila*
- <sup>20</sup>*Korea Institute for Advanced Study*
- <sup>21</sup>*SNOLAB*
- <sup>22</sup>*Commissariat à l'Énergie Atomique et aux Énergies Alternatives - Irfu*
- <sup>23</sup>*Massachusetts Institute of Technology*
- <sup>24</sup>*SUBATECH, CNRS/IN2P3, Université de Nantes, Ecole des Mines de Nantes*
- <sup>25</sup>*Institut für Theoretische Teilchenphysik und Kosmologie, RWTH Aachen*
- <sup>26</sup>*Northwestern University*
- <sup>27</sup>*Petersburg Nuclear Physics Institute*
- <sup>28</sup>*The University of Alabama, Tuscaloosa*
- <sup>29</sup>*Indiana University*
- <sup>30</sup>*Argonne National Laboratory*
- <sup>31</sup>*Instituto de Física Teórica UAM CSIC*
- <sup>32</sup>*LAPP, Université de Savoie, CNRS/IN2P3*
- <sup>33</sup>*RCNP, Osaka University*
- <sup>34</sup>*Los Alamos National Laboratory*
- <sup>35</sup>*Vanderbilt University*
- <sup>36</sup>*Instituto de Física Gleb Wataghin/UNICAMP*

- <sup>37</sup>*University of Manchester*
- <sup>38</sup>*University College London*
- <sup>39</sup>*CERN*
- <sup>40</sup>*Astroparticule et Cosmologie APC*
- <sup>41</sup>*Harish Chandra Research Institute*
- <sup>42</sup>*University of Oregon*
- <sup>43</sup>*Institute for Nuclear Research of the Russian Academy of Sciences*
- <sup>44</sup>*INFN, Sezione di Padova*
- <sup>45</sup>*INFN, Sezione di Torino*
- <sup>46</sup>*Wisconsin IceCube Particle Astrophysics Center*
- <sup>47</sup>*Lawrence Berkeley National Laboratory*
- <sup>48</sup>*University of California, Berkeley*
- <sup>49</sup>*University of North Carolina, Chapel Hill*
- <sup>50</sup>*Triangle Universities Nuclear Laboratory*
- <sup>51</sup>*University of Maryland, College Park*
- <sup>52</sup>*INFN, Laboratori Nazionali del Gran Sasso*
- <sup>53</sup>*Columbia University*
- <sup>54</sup>*Sejong University*
- <sup>55</sup>*ITEP*
- <sup>56</sup>*University of California, Los Angeles*
- <sup>57</sup>*IPMU, University of Tokyo*
- <sup>58</sup>*Brunel University*
- <sup>59</sup>*Institute for Advanced Study*
- <sup>60</sup>*University of Padua and INFN, Padua*
- <sup>61</sup>*Institute of High Energy Physics, Chinese Academy of Sciences,*
- <sup>62</sup>*Max-Planck-Institut fuer Kernphysik, Heidelberg*
- <sup>63</sup>*Imperial College London*
- <sup>64</sup>*University of Durham*
- <sup>65</sup>*Instituto de Física, Universidade de São Paulo*
- <sup>66</sup>*Institut de Physique Théorique, CEA-Saclay*

<sup>67</sup>*Tufts University*

<sup>68</sup>*University of Kansas*

<sup>69</sup>*Joint Institute for Nuclear Research, Dubna*

<sup>70</sup>*King's College London*

<sup>71</sup>*University of Rome and INFN Sezione di Roma I*

<sup>72</sup>*Universit degli Studi Roma Tre*

<sup>73</sup>*KTH Royal Institute of Technology*

<sup>74</sup>*INFN, Sezione di Pavia*

<sup>75</sup>*Kyoto University*

<sup>76</sup>*Ecole Polytechnique, IN2P3-CNRS, Laboratoire Leprince-Ringuet*

<sup>77</sup>*National Institute of Standards and Technology*

<sup>78</sup>*University of Washington*

<sup>79</sup>*University of Minnesota*

<sup>80</sup>*University of Hawaii*

<sup>81</sup>*Università di Genova and INFN Genova*

<sup>82</sup>*IPPP, Durham University*

<sup>83</sup>*INFN Bologna*

<sup>84</sup>*Perimeter Institute for Theoretical Physics*

<sup>85</sup>*University of Florida*

<sup>86</sup>*George Mason University*

<sup>87</sup>*Center for Experimental Nuclear Physics and Astrophysics*

<sup>88</sup>*Duke University*

<sup>89</sup>*Institute of Theoretical Physics, Ecole Polytechnique Federale de Lausanne*

<sup>90</sup>*C. N. Yang Institute for Theoretical Physics*

<sup>91</sup>*University of Bari and INFN*

<sup>92</sup>*National Research Center Kurchatov Institute, Moscow*

<sup>93</sup>*Harvard University*

<sup>94</sup>*Princeton University*

<sup>95</sup>*KEK, High Energy Accelerator Research Organization*

<sup>96</sup>*Max Planck Institute for Physics, Munich*

<sup>97</sup>*Institut für theoretische Physik und Astrophysik, Universität Würzburg*

<sup>98</sup>*Centre for Particle Physics, University of Alberta*

<sup>99</sup>*Univeristy of South Carolina*

<sup>100</sup>*John Adams Institute, University of Oxford*

<sup>101</sup>*ICREA and Instituto de Ciencias del Cosmos Universitat de Barcelona*

<sup>102</sup>*Oak Ridge National Laboraory*

<sup>103</sup>*Tokyo Metropolitan University*

<sup>104</sup>*Brookhaven National Laboratory*

(Dated: November 27, 2024)

*In memoriam*  
Ramaswami “Raju” S. Raghavan  
1937 – 2011

# CONTENTS

Executive summary	1
I. Theory and Motivation	3
A. Introduction: What is a Sterile Neutrino?	3
B. Theoretical Motivations and Symmetries Behind the Existence of Light Sterile Neutrinos	9
Sterile neutrinos in “standard approaches”	9
Sterile neutrinos in “non-standard approaches”	14
C. The Low-Energy Seesaw and Minimal Models	16
General Aspects	16
eV-scale Seesaw	18
The $\nu$ MSM	22
D. Sterile Neutrino Dark Matter	23
Dark matter in the $\nu$ MSM	26
Neutrinos in gauge multiplets – thermal production of DM neutrinos	27
Primordial generation of DM neutrinos	28
Other models	29
E. Light Sterile Neutrinos as Messengers of New Physics	29
F. Non-Standard Neutrino Interactions (NSI)	30
CC-like NSI	31
NC-like NSI	31
Models to evade charged lepton NSI	32
Summary of the present status on NSI	34
G. Extra Forces	34
H. Lorentz Violation	35
Violation of Lorentz invariance in the standard model	36
Lorentz-violating neutrinos	37
Global models using Lorentz violation	37
Some types of Lorentz violation: CPT violation, non-standard interactions, and lepton-number-violating oscillations	39

I. CPT Violation in Neutrino Oscillations and the Early Universe as an Alternative to Sterile Neutrinos	39
II. Astrophysical Evidence	45
A. Cosmology	45
Sterile neutrino thermalization	46
Big Bang Nucleosynthesis	47
Cosmic microwave background and large-scale structure	49
B. Core Collapse Supernovae	55
III. Evidence from Oscillation Experiments	60
A. The LSND Signal	60
Description of the Experiment	60
Event Selection	63
Neutrino Oscillation Signal and Background Reactions	65
LSND Oscillation Results	66
B. The KARMEN Constraint	69
Description of the Experiment	69
Event Selection	71
Neutrino Oscillation Signal and Background Reactions	71
KARMEN Neutrino Oscillation Results	72
C. Joint Analysis of LSND and KARMEN Data	72
D. Sterile Neutrino Analysis of Super-K	73
Comparison of $\nu_\mu \rightarrow \nu_\tau$ and $\nu_\mu \rightarrow \nu_s$ Oscillations	73
An Admixture Model	79
E. The MiniBooNE $\nu_e$ and $\bar{\nu}_e$ Appearance Searches	80
Description of the Experiment	80
Neutrino Oscillation Event Selection	80
Neutrino Oscillation Signal and Background Reactions	81
MiniBooNE Neutrino Oscillation Results	81
MiniBooNE Antineutrino Oscillation Results	85
F. Disappearance Results from Accelerator Experiments	86



$\nu_\mu$ Disappearance from MiniBooNE and SciBooNE	86
$\nu_\mu$ Disappearance Results from CDHSW	93
$\nu_\mu$ and $\bar{\nu}_\mu$ Disappearance Results from CCFR	93
G. The Gallium Anomaly	94
H. The Reactor Antineutrino Anomaly	98
Antineutrinos from Reactors	98
Reference antineutrino spectra	99
New Reference Antineutrino Spectra	100
Off equilibrium effects	106
$^{238}\text{U}$ reference spectrum	106
Summary of the new reactor antineutrino flux prediction	108
New Predicted Cross Section per Fission	108
Impact on past experimental results	111
The fourth neutrino hypothesis (3+1 scenario)	114
Combination of the Reactor and the Gallium Anomalies	117
Summary of the reactor antineutrino anomaly	117
I. Limit on Disappearance Derived from KARMEN and LSND $\nu_e$ -Carbon Cross Sections	118
J. Constraints from the MINOS Long-Baseline Experiment	121
K. Conclusion	124
IV. Global Picture	125
A. 3+1 Global Fit of Short-Baseline Neutrino Oscillation Data	125
B. 3+1 and 3+2 Fits of Short-Baseline Experiments	128
Short-baseline reactor experiments	128
Global analysis of SBL data	130
C. Discussion of the LSND and MiniBooNE Results	135
(3+1) Oscillations	136
(3+2) Oscillations	136
D. Impact of Sterile Neutrinos for Absolute Neutrino Mass Measurements	137
Impact for $\beta$ -Decay and Neutrinoless $\beta\beta$ -Decay	137

On Neutrinoless double- $\beta$ decay with Sterile Neutrinos	142
E. Sterile Neutrinos and IceCube	145
F. Sterile Neutrinos and Dark Matter Searches	147
Sterile neutrinos and indirect dark matter search in IceCube	148
Sterile neutrinos and direct dark matter searches	150
G. Brief Summary	153
V. Requirements for Future Measurements	155
A. Historical Precedent	155
B. Requirements for a Future Sterile Program	156
A. Future Experiments	159
1. LENS-Sterile	160
LENS Technology	160
MCi Neutrino Source	161
LENS-Sterile Measurement	161
2. RICOCHET: Coherent Scattering and Oscillometry Measurements with Low-temperature Bolometers	163
The Source	164
The Detector	164
Sensitivity and Outlook	167
3. Very Short Baseline $\nu_e \rightarrow \nu_x$ Oscillation Search with a Dual Metallic Ga Target at Baksan and a $^{51}\text{Cr}$ Neutrino Source	170
4. Proposed search of sterile neutrinos with the Borexino detector using neutrino and antineutrino sources	176
5. Ce-LAND: A proposed search for a fourth neutrino with a PBq antineutrino source	180
Experimental Concept	180
Limitations of $\nu_e$ Sources	181
Choice and Production of $\bar{\nu}_e$ Sources	182
The $\bar{\nu}_e$ source and its signal	183
Backgrounds	184
Sensitivity	185
6. Search for Sterile Neutrinos with a Radioactive Source at Daya Bay	188

7. SNO+Cr	192
8. Reactors with a small core	195
9. SCRAAM: A reactor experiment to rapidly probe the Reactor Antineutrino Anomaly	196
10. Nucifer: a Small Detector for Short-Distance Reactor Electron Antineutrino Studies	200
Introduction	200
Description	200
Background	201
Short baseline oscillation study	202
Conclusions	203
11. Stereo Experiment	204
Principle	204
Inner Detector	205
Backgrounds	205
Performances	207
Sensitivity	208
12. A Very Short-Baseline Study of Reactor Antineutrinos at the National Institute of Standards and Technology Center for Neutron Research	211
13. OscSNS: A Precision Neutrino Oscillation Experiment at the SNS	214
14. LSND Reloaded	218
15. Kaon Decay-at-Rest for a Sterile Neutrino Search	220
Experimental description	220
Flux, nuclear effects, background and detector resolution	220
Sensitivity	222
16. The MINOS+ Project	224
17. The BooNE Proposal	225
18. Search for anomalies with muon spectrometers and large LArTPC imaging detectors at CERN	227
The new SPS neutrino facility	228
Expected sensitivities to neutrino oscillations	229
19. Liquid Argon Time Projection Chambers	232

MicroBooNE	232
Two LAr-detector experiment at FNAL	233
20. Very-Low Energy Neutrino Factory (VLENF)	236
Physics Reach	238
Detector Considerations	239
Conclusions	239
21. Probing active-sterile oscillations with the atmospheric neutrino signal in large iron/liquid argon detectors	241
Exclusion limits with a combined $\nu_\mu, \bar{\nu}_\mu$ analysis	242
Testing LSND and Miniboone results with sterile oscillations in the $\bar{\nu}$ sector	243
Summary	244
References	246

# EXECUTIVE SUMMARY

This white paper addresses the hypothesis of sterile neutrinos based on recent anomalies observed in neutrino experiments. It is by no means certain that sterile neutrinos are responsible for the set of anomalies which have triggered the current effort, but the extraordinary consequence of such a possibility justifies a detailed assessment of status of the field. Decades of experimentation have produced a vast number of results in neutrino physics and astrophysics, some of which are in perfect agreement with only three active<sup>1</sup> neutrinos, while a small subset calls for physics beyond the standard model<sup>2</sup>. The first, and individually still most significant, piece pointing towards new physics is the LSND result, where electron antineutrinos were observed in a pure muon antineutrino beam. The most straightforward interpretation of the LSND result is antineutrino oscillation with a mass squared difference,  $\Delta m^2$ , of about  $1 \text{ eV}^2$ . Given that solar neutrino oscillations correspond to  $\Delta m_{\text{sol}}^2 \simeq 7 \times 10^{-5} \text{ eV}^2$  and atmospheric neutrino oscillations correspond to  $\Delta m_{\text{atm}}^2 \simeq 2.3 \times 10^{-3} \text{ eV}^2$ , the LSND  $\Delta m^2$  requires a fourth neutrino. However, the results from the Large Electron Positron collider (LEP) at CERN on the invisible decay width of the  $Z$  boson show that there are only three neutrinos with a mass below one half of the mass of the  $Z$  boson, which couple to the  $Z$  boson, and therefore the fourth neutrino, if it indeed exists, can not couple to the  $Z$  boson and hence is a sterile neutrino, *i.e.* a Standard Model gauge singlet.

A new anomaly supporting the sterile neutrino hypothesis emerges from the recent re-evaluations of reactor antineutrino fluxes, which find a 3% increased flux of antineutrinos relative to the previous calculations. At the same time, the experimental value for the neutron lifetime became significantly smaller, which in turn implies a larger inverse  $\beta$ -decay cross section. In combination with the previously-neglected effects from long-lived isotopes which do not reach equilibrium in a nuclear reactor, the overall expectation value for antineutrino events from nuclear reactors increased by roughly 6%. As a result, more than 30 years of data from reactor neutrino experiments, which formerly agreed well with the flux prediction, have become the observation of an apparent 6% deficit of electron antineutrinos. This is known as the reactor antineutrino anomaly and is compatible with sterile neutrinos having a  $\Delta m_{\text{sterile}}^2 > 1 \text{ eV}^2$ .

Another hint consistent with sterile neutrinos comes from the source calibrations performed for radio-chemical solar neutrino experiments based on gallium. In these calibrations very intense sources of  $^{51}\text{Cr}$  and  $^{37}\text{Ar}$ , which both decay via electron capture and emit mono-energetic electron neutrinos, were placed in proximity to the detector and the resulting event rate were measured. Both the source strength and reaction cross section are known with some precision and a 5-20% deficit of the measured to expected count rate was observed. Again, this result would find a natural explanation by a sterile neutrino with  $\Delta m_{\text{sterile}}^2 > 1 \text{ eV}^2$ , which would allow some of the electron neutrinos from the source to “disappear” before they can interact. This anomaly persists even if one used the minimum cross section compatible with the precisely known  $^{71}\text{Ga}$  lifetime.

The aforementioned results suggesting a sterile neutrino with a mass around 1 eV have to be contrasted with a number of results which clearly disfavor this interpretation. The strongest constraints derive from the non-observation of muon neutrino disappearance by accelerator experiments like CDHSW or MINOS. Bounds on the disappearance of electron neutrinos are obtained from KAR-MEN and LSND, as well. The MiniBooNE neutrino result, a non-observation of electron neutrino appearance in a muon neutrino beam, is incompatible with the LSND appearance result, if CP is

<sup>1</sup>Active neutrinos are those which couple to  $Z$  and  $W$  bosons.

<sup>2</sup>Here, the standard model is to be understood to include massive neutrinos.

conserved. On the other hand, the antineutrino result from the same experiment is fully compatible with the LSND result. A further difficulty in interpreting experimental evidence in support of a light sterile neutrino is that the effects are purely in count rates. The energy and distance-dependent characteristic of the oscillation phenomena associated with sterile neutrinos remains to be observed.

The existing data from oscillation experiments, both for and against the sterile neutrino hypothesis, are summarized in Section III of this report, while Section IV discusses the compatibility of and tensions between the various oscillation data sets.

Cosmological data, mainly from observations of the cosmic microwave background and large scale structure favor the existence of a fourth light degree-of-freedom which could be a sterile neutrino. At the same time the standard cosmological evolution model prefers this neutrino to be lighter than 1 eV. The relevant cosmological and astrophysical evidence is discussed in Section II.

From a theoretical point of view (see Section I) the existence of sterile neutrinos is a rather natural consequence of neutrinos having a non-zero mass. Sterile neutrinos are gauge singlets and as a result no *a priori* scale for their mass is set. Once neutrino mass generation via the seesaw mechanism is put into the wider context of grand unification and leptogenesis, light sterile neutrinos are slightly less natural. However, in this context, expectations for the mass of sterile neutrinos are ultimately based on an attempt to predict the eigenvalues of a  $6 \times 6$  matrix in which we do not know any entries and therefore, having one or several sterile neutrinos in the 1 eV mass range is certainly far from being a surprise. The same is true for keV sterile neutrinos, which are warm dark matter candidates.

In summary, there are a number of experimental results that appear anomalous in the context of the standard 3 neutrino framework, and can be explained by a sterile neutrino with mass around 1 eV. At the same time, there are a number of results which are in conflict with this interpretation. The data collected to date present an incomplete, perhaps even contradictory picture, where 2-3  $\sigma$  agreement *in favor of* and *in contradiction to* the existence of sterile neutrinos is present. The need thus arises to provide a more ardent and complete test of the sterile neutrino hypothesis, which will unambiguously confirm or refute the interpretation of past experimental results. This white paper documents the currently available evidence for and against sterile neutrinos, it highlights the theoretical implications of their existence and provides an overview of possible future experiments (see the appendix) to test the LSND result and the sterile neutrino hypothesis. The overriding goal is to provide the motivation for a new round of measurements so that the questions laid out here can be definitively answered.

# I. THEORY AND MOTIVATION

In this Chapter we provide an overview of the theoretical background of sterile neutrinos. We will set the stage by defining the term “sterile neutrino”, and will present model building aspects of these entities. Sterile neutrinos are naturally present in many theories beyond the standard model, in particular in several manifestations of the seesaw mechanism. We will be often interested in directly observable sterile neutrinos, and will categorize different possibilities for naturally accommodating them. More concretely, the so-called low energy seesaw will be analyzed in some detail. Particle physics aspects of keV scale neutrinos as warm dark matter candidates will be focussed on as well. Finally, for the sake of completeness, other non-standard neutrino physics fields, often connected to sterile neutrinos or used as an alternative explanation to some of the current experimental hints, are summarized.

## A. Introduction: What is a Sterile Neutrino?

A sterile neutrino is a neutral lepton with no ordinary weak interactions except those induced by mixing. They are present in most extensions of the standard model, and in principle can have any mass. Very heavy sterile neutrinos are utilized in the minimal type I seesaw model [1–5] and play a pivotal role in leptogenesis [6, 7]. However, here we are especially concerned with relatively light sterile neutrinos that mix significantly with ordinary neutrinos and those that are relevant to neutrino oscillation experiments, astrophysics, dark matter, etc. We first introduce the necessary terminology and formalism to discuss sterile neutrinos and their possible mixing with ordinary neutrinos, following the notation of [8].

A massless fermion can be described by a Weyl spinor, which necessarily has two components of opposite chirality related (up to Dirac indices) by Hermitian conjugation. Chirality coincides with helicity for a massless particle and is associated with the chiral projections  $P_{L,R} = \frac{1}{2}(1 \mp \gamma^5)$ . Thus, a left-chiral Weyl spinor  $\psi_L = P_L \psi_L$ , which annihilates a left-chiral particle, is related to its right-chiral CP conjugate  $\psi_R^c = P_R \psi_R^c$ , which annihilates a right-chiral antiparticle, by

$$\psi_R^c = C\gamma^{0T}\psi_L^*. \quad (1)$$

In (1)  $C$  is the charge conjugation matrix<sup>3</sup> and  $\psi_{L\alpha}^* \equiv (\psi_{L\alpha})^\dagger$ .  $\psi_R^c$  exists even if CP is not conserved. One can just as well define a right-chiral Weyl spinor  $\psi'_R$  and its associated left-chiral anti-spinor  $\psi_L^c$ . It is a matter of convention which is called the particle and which the antiparticle.

A Weyl neutrino is said to be active (or ordinary or doublet) if it participates in the conventional charged and neutral current weak interactions. This means that it transforms as a member of a doublet together with a charged lepton partner under the weak  $SU(2)$  gauge group of the standard model. There are three light active neutrinos in nature,  $\nu_{eL}$ ,  $\nu_{\mu L}$ , and  $\nu_{\tau L}$ , which are associated respectively with  $e_L^-$ ,  $\mu_L^-$ , and  $\tau_L^-$  in charged current transitions. Their CP conjugates,  $\nu_{\alpha R}^c$ ,  $\alpha = e, \mu, \tau$ , are the weak partners of the  $\alpha_R^+$ . Including small neutrino masses, the  $\nu_{\alpha L}$  (and  $\nu_{\alpha R}^c$ ) are linear combinations of the mass eigenstates. The observed  $Z$ -boson decay width implies that any additional active neutrinos are quite heavy,  $m_\nu \gtrsim M_Z/2$ .

<sup>3</sup> $C = i\gamma^2\gamma^0$  in the Pauli-Dirac representation.

A sterile (or singlet or right-handed) neutrino is an  $SU(2)$  singlet which does not take part in weak interactions except those induced by mixing with active neutrinos. It may participate in Yukawa interactions involving the Higgs boson or in interactions involving new physics. Many extensions of the standard model introduce a right-chiral sterile  $\nu_R$ , which has a left-chiral CP conjugate  $\nu_L^c$ .

Chirality can be a conserved quantum number for massless fermions, depending on the nature of their interactions. However, fermion mass terms violate chirality and also break its equivalence to helicity (which is not a Lorentz invariant quantity). For example, a weak transition involving, *e.g.*, a massive but relativistic  $\nu_L$ , may produce the “wrong helicity” state, with amplitude  $\propto m_\nu/E_\nu$ . The chirality violation is due to the fact that a fermion mass term describes a transition between right and left chiral Weyl spinors:

$$-\mathcal{L} = m(\bar{\psi}_L\psi_R + \bar{\psi}_R\psi_L), \quad (2)$$

where we have taken  $m$  to be real and non-negative by choosing an appropriate relative  $\psi_{L,R}$  phase. There are two important types of fermion mass terms, Dirac and Majorana, depending on whether or not  $\psi_R$  is distinct from  $\psi_R^c$ , the CP conjugate of  $\psi_L$ .

A Dirac neutrino mass term relates two distinct Weyl spinors:

$$-\mathcal{L}_D = m_D(\bar{\nu}_L\nu_R + \bar{\nu}_R\nu_L) = m_D\bar{\nu}_D\nu_D, \quad (3)$$

where, in the second form,  $\nu_D \equiv \nu_L + \nu_R$  is the Dirac field.  $\nu_D$  (and its conjugate  $\nu_D^c = \nu_R^c + \nu_L^c$ ) have four components,  $\nu_L, \nu_R, \nu_R^c$ , and  $\nu_L^c$ . One can define a global lepton number ( $L = 1$  for  $\nu_D$  and  $L = -1$  for  $\nu_D^c$ ), which is conserved by  $\mathcal{L}_D$ . In most theories  $\nu_L$  and  $\nu_R$  in a Dirac mass term are respectively active and sterile. In this case,  $\mathcal{L}_D$  violates the third component of weak isospin by  $\Delta t_L^3 = \pm\frac{1}{2}$ .  $m_D$  can be generated by the vacuum expectation value (VEV) of the neutral component  $\phi^0$  of a Higgs doublet, as illustrated in Figure 1, yielding

$$m_D = y\langle\phi^0\rangle = yv/\sqrt{2}, \quad (4)$$

where  $y$  is the Yukawa coupling and  $v \simeq 246$  GeV is the weak scale. This is analogous to the generation of quark and charged lepton masses in the standard model. In order to accommodate the observed neutrino masses,  $y$  must be extremely small, *e.g.*  $y \sim 10^{-12}$  for  $m_D \sim 0.1$  eV, as compared to  $y_e \sim 3 \times 10^{-6}$  for the electron. These small Dirac neutrino masses are often considered unnatural, or as evidence that some more subtle underlying mechanism is at play. For example, one may interpret the tiny neutrino Yukawa couplings as evidence that the elementary Yukawa couplings  $y$  are required to vanish by some new discrete, global, or gauge symmetry. A small effective Yukawa coupling can then be generated by higher-dimension operators [9, 10] or by non-perturbative effects such as string instantons [11, 12]. Another possibility is that a small Dirac coupling is due to wave function overlaps between  $\nu_L$  and  $\nu_R$  in theories involving large and/or warped extra dimensions [13, 14].

A Majorana mass term requires only one Weyl spinor. Majorana masses are forbidden by color and electromagnetic gauge invariance for quarks and charged leptons, but are possible for both active (after electroweak symmetry breaking) and sterile neutrinos if there is no conserved lepton number. For an active neutrino  $\nu_L$ ,

$$-\mathcal{L}_T = \frac{m_L}{2}(\bar{\nu}_L\nu_R^c + \bar{\nu}_R^c\nu_L) = \frac{m_L}{2}(\bar{\nu}_L C\bar{\nu}_L^T + \nu_L^T C\nu_L) = \frac{m_L}{2}\bar{\nu}_M\nu_M, \quad (5)$$

where  $\nu_M \equiv \nu_L + \nu_R^c = \nu_M^c$  is a (self-conjugate) two-component Majorana field.  $\mathcal{L}_T$  violates lepton number by two units,  $\Delta L = \pm 2$ , and weak isospin by one unit,  $\Delta t_L^3 = \pm 1$  (hence one sometimes



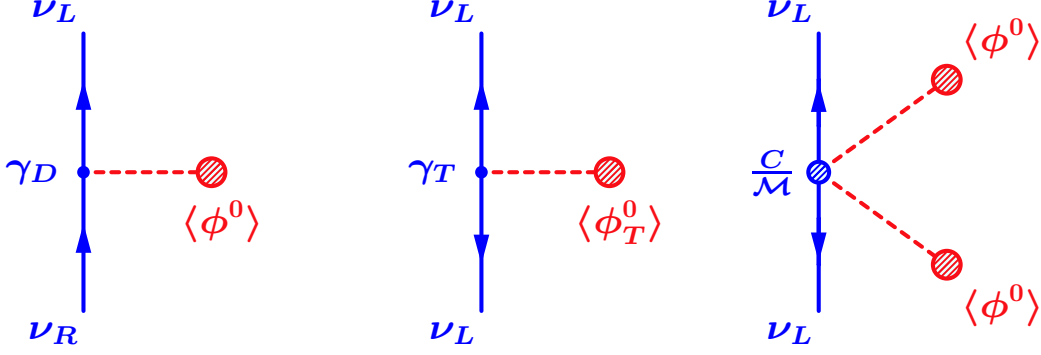


Figure 1. Left: Dirac mass term generated by a Higgs doublet. Center: Majorana mass term generated by a Higgs triplet. Right: Majorana mass term generated by a higher-dimensional operator.

writes  $m_L$  as  $m_T$ , with  $T$  for triplet).  $m_L$  can be generated by a Higgs triplet, with a small Yukawa coupling  $\gamma_T$  and/or a small VEV  $\langle\phi_T^0\rangle$ , as illustrated in Figure 1. It could instead be associated with a higher-dimensional operator (the Weinberg operator [15]) involving two Higgs doublets, with a coefficient  $C/\mathcal{M}$ . The scale  $\mathcal{M}$  represents some heavy new physics which has been integrated out, such as the exchange of a very heavy Majorana sterile neutrino (the type I seesaw) [1–5], a heavy scalar triplet (the type II seesaw) [16], a fermion triplet (the type III seesaw) [17], or new degrees of freedom in a string theory [18]. The second form in (5) emphasizes that  $\mathcal{L}_T$  also describes the creation or annihilation of two neutrinos. A sterile neutrinos  $\nu_R$  can also have a Majorana mass term,

$$-\mathcal{L}_S = \frac{M_R}{2} (\bar{\nu}_L^c \nu_R + \bar{\nu}_R \nu_L^c) = \frac{M_R}{2} (\bar{\nu}_L^c C \bar{\nu}_L^{cT} + \nu_L^c C \nu_L^c) = \frac{M_R}{2} \bar{\nu}_{M_S} \nu_{M_S}, \quad (6)$$

where  $\nu_{M_S} \equiv \nu_L^c + \nu_R = \nu_{M_S}^c$  is a Majorana field.  $\mathcal{L}_S$  also violates lepton number by  $\Delta L = \pm 2$ , but does not violate weak isospin ( $S$  denotes singlet, one often writes  $M_R$  as  $m_S$ ) and can in principle occur as a bare mass term. However, in some models a bare mass for the right-handed neutrinos is forbidden by new physics, and  $M_R$  is instead generated by the VEV of, say, a SM Higgs singlet field  $S$ , or by a higher-dimension operator.

When Dirac and Majorana mass terms are both present, one must diagonalize the resulting mass matrix in order to identify the mass-eigenstates, which will, in general, be linear combinations of  $\nu_L$  and  $\nu_R^c$ . For one active neutrino  $\nu_L^0 \xrightarrow{CP} \nu_R^{0c}$  and one sterile neutrino  $\nu_R^0 \xrightarrow{CP} \nu_L^{0c}$  (the superscripts imply weak eigenstates)

$$-\mathcal{L} = \frac{1}{2} \begin{pmatrix} \bar{\nu}_L^0 & \bar{\nu}_L^{0c} \end{pmatrix} \begin{pmatrix} m_L & m_D \\ m_D & M_R \end{pmatrix} \begin{pmatrix} \nu_R^{0c} \\ \nu_R^0 \end{pmatrix} + h.c. \quad (7)$$

The mass matrix can be diagonalized by a unitary matrix  $\mathcal{U}$ ,

$$\mathcal{U}^\dagger \begin{pmatrix} m_L & m_D \\ m_D & M_R \end{pmatrix} \mathcal{U}^* = \begin{pmatrix} m_1 & 0 \\ 0 & m_2 \end{pmatrix}, \quad (8)$$

because the matrix is symmetric. The mass eigenvalues  $m_{1,2}$  can be taken to be real and positive by appropriate phase choices. The corresponding eigenvectors represent two Majorana mass eigenstates,  $\nu_{iM} = \nu_{iL} + \nu_{iR}^c = \nu_{iM}^c$ ,  $i = 1, 2$ , where

$$\begin{pmatrix} \nu_{1L} \\ \nu_{2L} \end{pmatrix} = \mathcal{U}^\dagger \begin{pmatrix} \nu_L^0 \\ \nu_L^{0c} \end{pmatrix}, \quad \begin{pmatrix} \nu_{1R}^c \\ \nu_{2R}^c \end{pmatrix} = \mathcal{U}^T \begin{pmatrix} \nu_R^{0c} \\ \nu_R^0 \end{pmatrix}. \quad (9)$$

There are a number of important special cases and limits of (7):

- (a) The pure Majorana case,  $m_D = 0$ . There is no mixing between the active and sterile states, and the sterile neutrino decouples (unless there are new interactions);
- (b) The pure Dirac case,  $m_L = M_R = 0$ . This leads to two degenerate Majorana neutrinos which can be combined to form a Dirac neutrino with a conserved lepton number;
- (c) The seesaw limit,  $M_R \gg m_{D,T}$ . There is one, mainly sterile, state with  $m_2 \simeq M_R$ , which decouples at low energy, and one light, mainly active, state, with mass  $m_1 \simeq m_L - m_D^2/M_R$ . For  $m_L = 0$ , this yields an elegant explanation for why  $|m_1| \ll m_D$ . The sterile state may be integrated out, leading to an effective higher-dimensional operator for the active Majorana mass with  $\mathcal{M}/C = \langle \phi^0 \rangle^2 M_R/m_D^2$ ;
- (d) The pseudo-Dirac limit,  $m_D \gg m_L, M_R$ , which leads to a small shift in the mass eigenvalues  $|m_{1,2}| = m_D \pm (m_L + M_R)/2$  (we are taking the masses here to be real and positive for simplicity). Another possibility for the pseudo-Dirac limit occurs when  $m_L \simeq M_R$ ;
- (e) The active-sterile mixed case, in which  $m_D$  is comparable to  $M_R$  and/or  $m_L$ . The mass eigenstates contain significant admixtures of active and sterile.

The mass matrix in (7) can be generalized to 3 active and  $n_R$  sterile neutrinos, where  $n_R$  need not be 3. In case (a), and in cases (b) and (c) with  $n = 3$ , the observable spectrum consists of three active or essentially active neutrinos. The left-chiral components  $\nu_{iL}$  are related to the weak eigenstate fields  $\nu_{\alpha L}$ ,  $\alpha = e, \mu, \tau$ , by  $\nu_{\alpha L} = \sum_{i=1}^3 U_{\alpha i} \nu_{iL}$ , where  $U$  is the unitary PMNS matrix [19, 20], and similarly for their CP conjugates  $\nu_{iR}^c$ .

In the case of  $n_R$  singlet neutrinos, the full neutral fermion mass matrix takes the form

$$\mathcal{M}_\nu = \begin{pmatrix} m_L & m_D \\ m_D^T & M_R \end{pmatrix}, \quad (10)$$

where  $M_R$  can, without loss of generality, be made diagonal  $M_R = \text{Diag}(M_1, M_2, \dots)$ , while  $m_D$  is a generic  $3 \times n_R$  complex matrix. This matrix is diagonalized by a unitary  $(3 + n_R) \times (3 + n_R)$  matrix  $\mathcal{U}$ . From now on we will neglect  $m_L$ , unless otherwise noted. This scenario is the result of the most general renormalizable Lagrangian consistent with the standard model augmented by gauge-singlet (right-handed neutrino) fermion fields  $N_i$ , written as

$$\mathcal{L}_\nu \supset -\frac{M_{Rij}}{2} N_i N_j - y^{ai} L_\alpha N_i H + h.c. \quad (11)$$

For sterile neutrinos to be relevant to neutrino oscillations, as suggested by LSND and Mini-BooNE, or for most astrophysical and cosmological implications, there has to be non-negligible mixing between active and sterile states of the same chirality. That does not occur in the pure Majorana, pure Dirac, or very high energy seesaw limits, but only for the pseudo-Dirac and active-sterile cases (of course, hybrid possibilities can occur for three families and  $n_R > 1$ ). In fact, the pseudo-Dirac case is essentially excluded unless  $m_L, M_R \lesssim 10^{-9}$  eV. Otherwise, there would be significant oscillations of solar neutrinos into sterile states, contrary to observations [21] (mass-squared differences as small as  $10^{-18}$  eV<sup>2</sup> could be probed with neutrino telescopes [22]). An

elegant method to parameterize  $\mathcal{U}$  for pseudo-Dirac neutrinos can be found in [23]. Therefore, significant active-sterile mixing requires that at least some Dirac masses ( $m_D$ ) and some Majorana masses ( $M_R$  and/or  $m_L$ ) are simultaneously very small but non-zero<sup>4</sup>, presenting an interesting challenge to theory. One possibility is that some new symmetry forbids all of the mass terms at the perturbative level, but allows, *e.g.*  $M_R \sim 1$  eV and  $m_D \sim 0.1$  eV due to higher-dimensional operators (as in the mini-seesaw). A list of models and some of the general aspects associated with building them will be discussed below.

In the case  $M_R \gg m_D$ , the so-called seesaw limit, which is an excellent approximation for  $M_R \in [1 \text{ eV}, 10^{15} \text{ GeV}]$ , it is instructive to express  $\mathcal{U}$  in terms of 4 submatrices,

$$\mathcal{U} = \begin{pmatrix} U & \Theta \\ \Theta'^T & V_s \end{pmatrix}, \quad (12)$$

where  $U$  is a  $3 \times 3$  matrix,  $V_s$  is an  $n_R \times n_R$  matrix,  $\Theta, \Theta'$  are  $3 \times n_R$  matrices, and we will refer to  $\Theta$  as the ‘‘active–sterile’’ mixing matrix. In the case of interest, the elements of  $U$  are very similar to those of the standard neutrino mixing matrix, which are measured with different degrees of precision [25]. The elements of  $\Theta$  are parametrically smaller than those of  $U$ . In the seesaw limit,  $U$  is approximately unitary:  $UU^\dagger \sim \mathbb{1}_{3 \times 3}$ . In the absence of interactions beyond those in Eq. (11),  $V_s$  is not physical, while the elements of  $\Theta'$  are proportional to those of  $\Theta$ . For more details on how to parameterize  $\mathcal{U}$  in the case at hand see, for example, [26–29].

Eq. (10) is expressed in the so-called flavor basis:  $\nu_e, \nu_\mu, \nu_\tau, \nu_{s_1}, \dots, \nu_{s_n}$ . This is related to the neutrino mass basis –  $\nu_1, \nu_2, \dots, \nu_{3+n}$  – via the  $(3+n) \times (3+n)$  neutrino unitary mixing matrix  $U$ :

$$\nu_\alpha = \mathcal{U}_{\alpha i} \nu_i, \quad \mathcal{U}\mathcal{U}^\dagger = \mathcal{U}^\dagger\mathcal{U} = \mathbb{1}, \quad (13)$$

$\alpha = e, \mu, \tau, s_1, \dots, s_n, i = 1, 2, \dots, n_R + 3$  such that

$$\mathcal{M}_\nu = \begin{pmatrix} 0 & m_D \\ m_D^T & M_R \end{pmatrix} = \mathcal{U}^* \begin{pmatrix} m_1 & & & \\ & m_2 & & \\ & & \ddots & \\ & & & m_{3+n_R} \end{pmatrix} \mathcal{U}^\dagger, \quad (14)$$

where  $m_1, m_2, \dots, m_{3+n_R}$  are the neutrino masses.

In the seesaw limit, there are 3 light, mostly active neutrinos with mass matrix  $m_\nu = -m_D M_R^{-1} m_D^T$  and  $n_R$  heavy, mostly sterile, neutrinos with mass matrix  $M_R$ . The distribution of masses is parametrically bimodal:  $m_{1,2,3} \ll m_{4,5,\dots} \sim M_R$ . It is easy to show (see, for example, [30]) that

$$\Theta^2 \sim \frac{m_{1,2,3}}{m_{4,5,\dots}} \sim \frac{m_D^2}{M_R^2}. \quad (15)$$

Our ability to observe the mostly sterile states is proportional to  $\Theta^2$ . Given  $m_{1,2,3} \lesssim 10^{-1}$  eV, the mostly sterile states are very weakly coupled unless  $m_{4,5,\dots} \lesssim 10$  eV and  $\Theta^2 \gtrsim 10^{-2}$ . This generic behavior of the active–sterile mixing angles is also depicted in Fig. 2. In general, in a theory with

<sup>4</sup>More accurately, two distinct types of neutrino masses must be simultaneously small but non-zero. For example, there could be simultaneous Dirac mass terms between active and sterile neutrinos, as well as between sterile left and right-chiral neutrinos, as occurs in some extra-dimensional theories. See, *e.g.* [24].

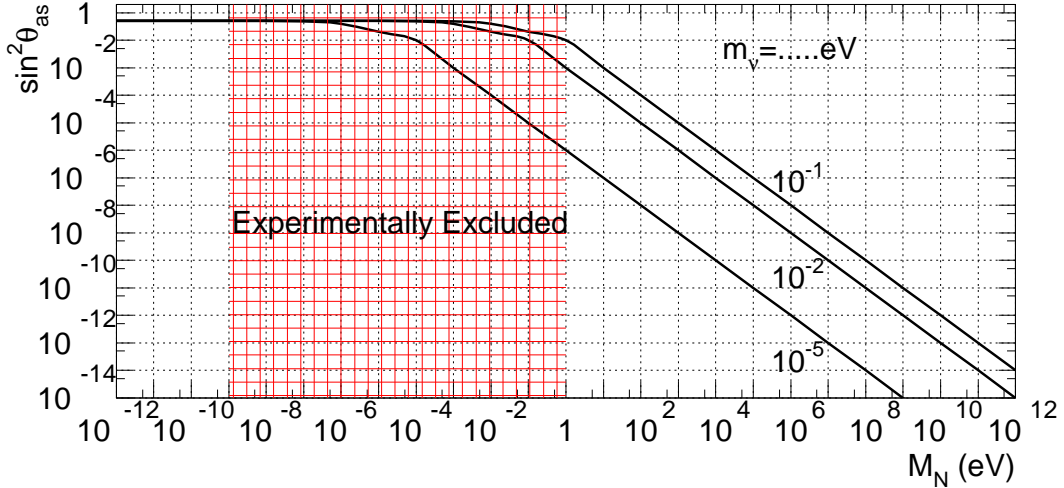


Figure 2. Estimate of the magnitude of the mixing between active and sterile neutrinos  $\sin^2 \theta_{as}$  as a function of the right-handed neutrino mass  $M_R$ , for different values of the mostly active neutrino masses,  $m_\nu = 10^{-1}$ ,  $10^{-2}$ , and  $10^{-5}$  eV. The hatched region qualitatively indicates the values of  $M_R$  that are currently excluded by the world's particle physics data. From [21].

sterile neutrinos, the leptonic neutral current is non-diagonal in mass eigenstates [5, 31]. This is a special case of a theorem [31] that the necessary and sufficient condition that the leptonic neutral current is diagonal in mass eigenstates is that all leptons of the same chirality and charge must have the same weak total and third component isospin. This condition is violated in a theory with sterile neutrinos.

In the context of the sterile neutrino parameters we are dealing with in this paper, there are two important statements one can make from Eq. (15): if there is a sterile neutrino of mass around eV and mixing around 0.1, then its contribution to the active neutrino masses is of order  $m_D^2/M_R \sim \Theta^2 M_R \sim 0.1$  eV, and can lead to interesting effects, see *e.g.* [32] for a detailed analysis. In case a sterile neutrino with mass around keV and mixing around  $10^{-4}$  exists, then its contribution to the active neutrino masses is of order  $m_D^2/M_R \sim \Theta^2 M_R \sim 10^{-5}$  eV, and completely negligible. This also implies that there is a massless active neutrinos in this case.

An example of a theory with sterile neutrinos and the seesaw mechanism is the  $SO(10)$  grand unified theory (GUT), in which a sterile neutrino is the  $SU(5)$ -singlet member of the 16-dimensional spinor representation for each SM generation, which has  $SU(5)$  decomposition  $16_L = 10_L + \bar{5}_L + 1_L$ . In the original  $SO(10)$  GUT, the number of sterile neutrinos,  $n_R$ , is thus equal to the number  $N_{gen} = 3$  of SM fermion generations, although in other models,  $n_R$  may differ from  $N_{gen}$  (there have been, and continue to be searches for quarks and leptons in a possible fourth SM generation, but since these are negative so far, we take  $N_{gen} = 3$ ). In an analogous manner, sterile neutrinos appear naturally as the spinor component of the corresponding chiral superfields in supersymmetric  $SO(10)$  GUTs. At the simplest level, in the  $SO(10)$  theory, SM fermion mass terms involve the bilinear  $16 \times 16$ , with the Clebsch-Gordon decomposition  $16 \times 16 = 10_s + 120_a + 126_s$  and arise from Yukawa couplings to corresponding Higgs fields transforming as 10, 120, and 126 dimensional representations. Dirac masses arise from terms transforming according to each of these representations, while Majorana mass terms for the sterile neutrinos occur in the terms transforming according to the 126-dimensional representation. Obviously, another aspect of the seesaw mechanism which makes it even more appealing is the remarkable fact that the decays of the right-

handed neutrinos in the early Universe can provide an explanation of the baryon asymmetry of the Universe, in the leptogenesis mechanism [6].

## B. Theoretical Motivations and Symmetries Behind the Existence of Light Sterile Neutrinos

In this Section the theoretical aspects entering models of sterile neutrinos will be discussed. It is important to stress that none of these imply that light sterile neutrinos must exist, and none specify the sterile neutrino mass scale. Most models allow for the possibility of light, mostly sterile states, and can accommodate a subset of the short-baseline anomalies and/or provide a (warm) dark matter candidate. This does not imply, of course, that sterile neutrinos do not exist. Recall that large mixing in the lepton sector, now a well established fact, was not predicted by theorists.

### Sterile neutrinos in “standard approaches”

We have seen that sterile neutrinos are a natural ingredient of the most popular and appealing mechanism to generate neutrino masses, the conventional or type I seesaw mechanism. No equally appealing alternative has emerged in the thirty years since it was discovered. In what follows, we will attempt to give a flavor of the required model building ingredients that can be introduced in order to generate or accommodate (light) sterile neutrinos in the mass range of eV or keV. Note that these scales are not far away from each other, and the same techniques apply for both cases.

- **The split seesaw mechanism**

The split seesaw model [33] consists of the Standard Model with three right-handed neutrinos and a spontaneously broken  $U(1)_{B-L}$  gauge symmetry. It is also assumed that space-time is a five-dimensional space compactified to four dimensions at some scale  $M_c = 1/l \sim 10^{16}$  GeV. If one of the right-handed neutrinos is localized on a brane separated from the standard-model brane by a distance  $l$ , then the wave function overlap between this right-handed neutrino and the other fields is very small. This leads to a suppression of both the Yukawa coupling and the sterile neutrino mass in the low-energy effective four-dimensional theory, but the successful seesaw formula is preserved. This opens a possibility for one of the right-handed, or sterile, neutrinos to serve as the dark-matter particle, and the observed abundance can be achieved for some values of parameters.

More specifically, in this model, one can express the effective mass  $M_s$  and the Yukawa coupling  $y$  of the sterile neutrino in terms of the fundamental (5-dimensional) Planck mass  $M$ , the distance  $l$  between the branes, and the right-handed neutrino bulk mass  $\tilde{m}$ :

$$M_s = \kappa_i v_{B-L} \frac{2\tilde{m}}{M(e^{2\tilde{m}l} - 1)}, \quad y = \tilde{\lambda} \sqrt{\frac{2\tilde{m}}{M(e^{2\tilde{m}l} - 1)}}, \quad (16)$$

where  $\tilde{\lambda}$  and  $\kappa$  are couplings in the underlying five-dimensional theory. Clearly, the exponential suppression in  $M_s$  is the square of the term which appears in  $y$ , so the ratio  $y^2/M_s$  is unchanged, while both the Yukawa coupling and the mass are much smaller than  $M$  or  $v_{B-L}$ . The idea has been extended with an  $A_4$  flavor symmetry in [34].

The split seesaw makes vastly different scales equally likely, because a small difference in the bulk masses or a small change in the distance  $l$  between the two branes can lead to exponentially different results for the sterile neutrino mass.<sup>5</sup> This provides a strong motivation for considering the sterile neutrino as a dark matter candidate. Indeed, the split seesaw model provides at least two ways of generating the correct dark-matter abundance [33]. Furthermore, each of these production scenarios generates dark matter that is substantially colder than the warm dark matter produced in neutrino oscillations [37–39]. The reason this dark matter is cold enough to agree with the structure formation constraints is simple: sterile neutrinos produced out of equilibrium at temperatures above the electroweak scale suffer redshifting when the standard model degrees of freedom go out of equilibrium and entropy is produced [40].

The emergence of a sterile neutrino as a dark-matter particle gives a new meaning to the fact that the standard model has three generations of fermions. Three generations of fermions allow for CP violation in the Cabibbo-Kobayashi-Maskawa matrix, but, quantitatively, this CP violation is too small to play any role in generating the matter-antimatter asymmetry of the Universe. In the context of leptogenesis, CP violation in the neutrino mass matrix would have been possible even with two generations, thanks to the Majorana phase. Hence, the existence of three families of leptons, apparently, has no purpose in the standard model, except for anomaly cancellation. However, if the lightest sterile neutrino is the dark-matter particle (responsible for the formation of galaxies from primordial fluctuations), while the two heavier sterile neutrinos are responsible for generating the matter-antimatter asymmetry via leptogenesis, the existence of three lepton families acquires a new, significant meaning.

- **Symmetries leading to a vanishing mass**

An appealing way to have a strong hierarchy in the neutrino masses is to introduce a symmetry that implies one vanishing sterile neutrino mass. A slight breaking of this symmetry will lead to a naturally small mass compared to those allowed by the symmetry. A very popular Ansatz is the flavor symmetry  $L_e - L_\mu - L_\tau$  [41].

The first suggestion to apply the  $L_e - L_\mu - L_\tau$  symmetry in the context of keV sterile neutrinos was made in [42], and a concrete model was presented later on in Ref. [43]. The basic idea is the following: the  $L_e - L_\mu - L_\tau$  symmetry leads to a very characteristic mass pattern for active neutrinos, namely to one neutrino being exactly massless, while the other two are exactly degenerate, denoted by  $(0, m, m)$ . Applying the symmetry to three right-handed neutrinos, results in an analogous pattern  $(0, M, M)$  for the heavy neutrino masses.

The flavor symmetry must be broken, which can be conveniently parameterized by *soft breaking terms* of the order of a new mass scale  $S$ . Any explicit or spontaneous symmetry breaking will result in terms of that form, and their general effect is to lift the degeneracies and to make the massless state massive,  $(0, M, M) \rightarrow (\mathcal{O}(S), M - \mathcal{O}(S), M + \mathcal{O}(S))$ , cf. left panel of Fig. 3. A similar effect is observed for the light neutrinos. Since the symmetry breaking scale  $S$  must be smaller than the symmetry preserving scale  $M$  (we would not speak of a symmetry otherwise), this mechanism gives a motivation for  $S \sim \text{keV}$  or eV, while  $M \gtrsim \mathcal{O}(\text{GeV})$  or heavier. Note, however, that  $L_e - L_\mu - L_\tau$  symmetry tends to predict bimaximal mixing, which is incompatible with data [44]. This problem can be circumvented by taking into account the mixing from the charged lepton sector [43, 45]. In this

---

<sup>5</sup>It is also possible to have multiple light sterile neutrinos because small changes in the bulk masses can result in big changes in  $y$  and  $M$ . In particular, it is possible to reproduce the mass spectrum of the model  $\nu\text{MSM}$  [35, 36], in which the lightest dark-matter sterile neutrino is accompanied by two GeV sterile neutrinos which are nearly degenerate in mass.

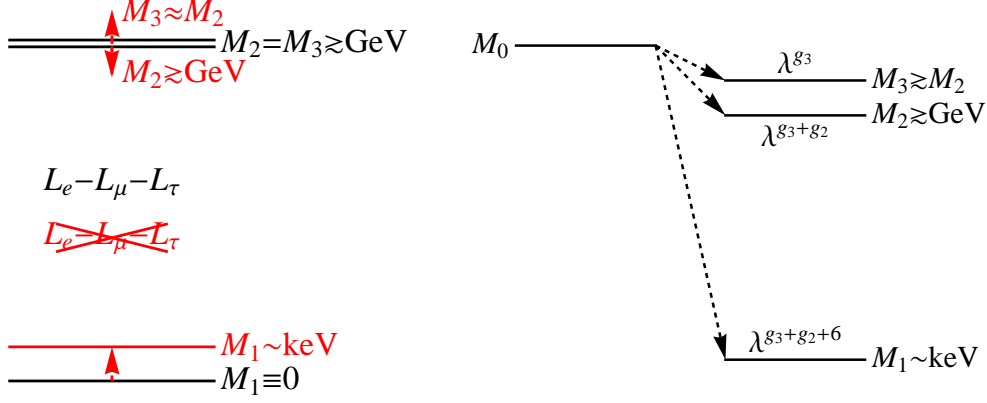


Figure 3. The mass shifting schemes for the  $L_e - L_\mu - L_\tau$  and the Froggatt-Nielsen models (figures taken from Ref. [49]).

case, an additional bonus is the prediction of a non-zero value of the small mixing angle  $\theta_{13}$ , in accordance with recent experimental indications [46–48].

The potential of  $L_e - L_\mu - L_\tau$  to accommodate eV-scale neutrinos within the type I seesaw was noted earlier in [50]. Suppose we have a symmetry in the theory that leads to  $\det M_R = 0$  with only one of the eigenvalues zero. If the same symmetry also guarantees that  $\det M_D = 0$ , then one can “take out” the zero mass eigenstates from both  $M_R$  and  $M_D$  and then use the seesaw formula for the  $2 \times 2$  sub-system.<sup>6</sup> The spectrum will consist of two light Majorana neutrinos (predominantly left-handed), two heavy right-handed Majorana neutrinos; one massless right-handed neutrino, which will play the role of the sterile neutrino of the model, and a massless left-handed neutrino. Breaking the symmetry very weakly either by loop effects or by higher dimensional operators can lead to a nonzero mass for the light sterile neutrino as well as its mixing with the  $\nu_{e,\mu}$ , so that one can have oscillations between sterile and active states. The simplest realization makes use of an  $L_e - L_\mu - L_\tau$  times a  $Z_2$  symmetry for the right-handed sector, and yields [50]

$$M_R = \begin{pmatrix} 0 & M & M \\ M & 0 & 0 \\ M & 0 & 0 \end{pmatrix}, \quad m_D = \begin{pmatrix} m_{11} & 0 & 0 \\ 0 & m_{22} & m_{22} \\ 0 & m_{32} & m_{32} \end{pmatrix} \quad (17)$$

It is easy to see that in this case the two massless neutrino states are:  $(\nu_\mu - \nu_\tau)/\sqrt{2}$  and  $(N_\mu - N_\tau)/\sqrt{2}$ , where we are using the symbol  $N$  for the SM singlet RH neutrino states. The second of the above states is a sterile state and can be identified as  $\nu_s$ . Excluding these two modes, the mass matrix reduces to a  $2 \times 2$  seesaw form and one gets an inverted mass hierarchy for the active neutrino with  $(\nu_\mu - \nu_\tau)/\sqrt{2}$  being the lightest active state. Note that a similar method for generating a suitable mass pattern is to use discrete instead of continuous symmetries, which do not automatically suffer from problems with Goldstone bosons. One example from the literature is [58], where the authors have used a  $Q_6$  symmetry to forbid a leading order mass for one of the sterile neutrinos.

- **The Froggatt-Nielsen mechanism**

<sup>6</sup>The case of vanishing determinant of  $M_R$  is called singular seesaw [51], and leads to two light, two intermediate and two heavy masses [52–57].

Another idea to associate small right-handed neutrino masses to ultra-high new physics scales is to use the Froggatt-Nielsen (FN) mechanism [59]. The FN mechanism introduces an implicit high-energy sector of scalars and fermions, which are all suitably charged under a new global  $U(1)_{FN}$  symmetry. Although this has the drawback of lacking an explicit UV-completion [60], it has the big advantage of leading to a very strong (exponential) generation-dependent suppression of mass eigenvalues, and thus to strong hierarchies, cf. right panel of Fig. 3. This is the reason why this mechanism is so popular when it comes to explaining the pattern of quark masses and mixing, and it is equally well applicable to the problem of generating a keV or eV scale for right-handed neutrinos.

Recent applications of the FN mechanism to sterile states were presented in [49, 61, 62], the latter work combining it with an explicit flavor symmetry in order to generate (close-to) tri-bimaximal mixing for the neutrinos. Effects of the leading and next-to-leading order breaking terms have been carefully analyzed and it was shown that, *e.g.* the strong constraints on the active-sterile mixing as well as a non-zero mixing angle  $\theta_{13}$  are consistent with the model. Corrections to the leading order seesaw formula [63, 64] have also been addressed. In addition, many constraints arising from different requirements, such as anomaly cancellation, embedding into Grand Unified Theories, or bounds on lepton flavor violation have been taken into account [49]. The combination of all of these requirements may render the FN models predictive: For example, they would be incompatible with the left-right symmetry used for keV neutrino DM production in [65]. Finally, in [62] the FN charges of all 3 right-handed neutrinos were varied such that several different results could be achieved: two super heavy neutrinos for leptogenesis and one for keV warm dark matter; one eV-scale neutrino for the reactor anomaly/LSND and one for warm dark matter, etc.

Similar to the split seesaw case, the FN models presented accommodate only slightly modified versions of the high scale seesaw mechanism, even though keV or eV scale right-handed neutrinos are involved. The reason for this is that the charges of the right-handed neutrinos under any global  $U(1)$  – be lepton number or the  $U(1)_{FN}$  – drop out of the seesaw formula: if a right-handed neutrino has charge  $F_1$  under the  $U(1)_{FN}$ , then its mass is suppressed by  $\lambda^{2F_1}$ , where  $\lambda = \langle \Theta \rangle / \Lambda$  is the ratio of the FN field VEV and the cutoff scale of the theory. The respective column of  $m_D$  is suppressed by  $\lambda^{F_1}$ , hence the seesaw formula is constant.

- **Extended seesaw mechanisms**

Other approaches to the problem extend the seesaw mechanism. One possibility is similar to the “take out zero mass eigenstates” idea discussed above, and was put forward in [66]. Considering the gauge group  $SU(2)_L \times U(1)_{I_{3R}} \times U(1)_{B-L}$  and various new weak singlets leads to an extended (inverse) seesaw mass matrix [67, 68]

$$\mathcal{M}_{\nu NS} = \begin{pmatrix} 0 & m_D & 0 \\ m_D^T & 0 & M \\ 0 & M^T & \mu \end{pmatrix}, \quad (18)$$

where

$$m_D = \begin{pmatrix} m_{11} & m_{12} & m_{12} \\ m_{21} & m_{22} & m_{22} \\ m_{21} & m_{22} & m_{22} \end{pmatrix}, \quad M = \begin{pmatrix} M_{11} & M_{12} & M_{13} \\ M_{21} & M_{22} & M_{23} \\ M_{21} & M_{22} & M_{23} \end{pmatrix} \quad (19)$$



The matrix  $\mu$  has an arbitrary (symmetric) form. Decoupling first the fields associated with  $\mu$  gives

$$\mathcal{M}_{\nu NS} = \begin{pmatrix} 0 & m_D \\ m_D^T & M\mu^{-1}M^T \end{pmatrix} \quad (20)$$

The determinant of the  $(N_e, N_\mu, N_\tau)$  mass matrix  $M_R = M\mu^{-1}M^T$  vanishes and the zero mass eigenstate is given by  $\frac{1}{\sqrt{2}}(N_\mu - N_\tau)$ . We “take out” this state and the remaining right-handed neutrino mass matrix is  $2 \times 2$  involving only the states  $(N_e, \frac{1}{\sqrt{2}}(N_\mu + N_\tau))$ . Similar to the discussion above, the seesaw matrix is now a two generation matrix yielding two light Majorana neutrino states. The other active neutrino state is massless, together with  $\nu_s \equiv \frac{1}{\sqrt{2}}(N_\mu - N_\tau)$ .

Another model is given in Ref. [69], where an attempt was made to understand the tiny Majorana mass required in the inverse seesaw mechanism from warped extra-dimensional models. Parity anomaly cancellation requires the total number of bulk fermions that couple to gauge and gravity fields to be even, thus a fourth singlet fermion was needed. Three of the singlet fields pair up with the three right-handed Majorana neutrino fields to make the three pseudo-Dirac fermions of inverse seesaw, and the remaining singlet in the end becomes the sterile neutrino with mass in the eV range.

A related approach, first discussed in [70] and studied in detail in [71], introduces in addition to the three generations of left-handed active neutrinos  $\nu_{Li}$  and three generations of right-handed sterile neutrinos  $N_{Rj}$ , another singlet right-handed field  $S_R$ . This field carries a non-trivial charge under a new discrete  $A_4 \times Z_4$  auxiliary symmetry, different from the charges of the  $N_{Rj}$ . The effect of these chirality and charge assignments is to forbid any direct Dirac or Majorana masses for the field  $S$ , which only obtains a mass by coupling to one generation of ordinary right-handed neutrinos, resulting in a mixed mass term of size  $M_S$ . The full mass matrix is

$$M_v^{7 \times 7} = \begin{pmatrix} 0 & m_D & 0 \\ m_D^T & M_R & M_S^T \\ 0 & M_S & 0 \end{pmatrix}. \quad (21)$$

With  $M_R \gg M_S$  and  $M_S \gg m_D$ , one block-diagonalizes this matrix and finds active neutrinos roughly of order  $m_D^2/M_R$  and a sterile neutrino of order  $M_S^2/M_R$ . In such a framework, both active and sterile neutrino masses are suppressed via the seesaw mechanism, and thus an eV scale sterile neutrino together with sizable active-sterile mixing is accommodated without the need of inserting small mass scales or Yukawa couplings.

Very often the  $4 \times 4$  mass matrix for the active plus sterile neutrinos obeys an approximate  $\mu$ - $\tau$  symmetry, which naturally generates small  $\theta_{13}$  and close-to maximal  $\theta_{23}$ . For instance [66],

$$M_\nu = \begin{pmatrix} m_{11} & m_{12} & m_{12} & f_1 \\ m_{12} & m_{22} & m_{22} & f_2 \\ m_{12} & m_{22} & m_{22} & f_2 \\ f_1 & f_2 & f_2 & f_4 \end{pmatrix}. \quad (22)$$

Due to small mixing with the active states the  $f_i$  are typically smaller than the  $m_{ij}$ , and one can diagonalize the mass matrix with

$$U \simeq \begin{pmatrix} c & s & 0 & \delta_1 \\ \frac{-s}{\sqrt{2}} & \frac{c}{\sqrt{2}} & \frac{1}{\sqrt{2}} & \delta_2 \\ \frac{-s}{\sqrt{2}} & \frac{c}{\sqrt{2}} & \frac{-1}{\sqrt{2}} & \delta_2 \\ -\delta_1 c + \sqrt{2}\delta_2 s & -\delta_1 s - \sqrt{2}\delta_2 c & 0 & 1 \end{pmatrix} \quad (23)$$

where  $\delta_1 \simeq \frac{f_1}{f_4}$  and  $\delta_2 \simeq \frac{f_2}{f_4}$ .

There are other related approaches capable of “explaining” or at least accommodating light sterile neutrinos. For example, a general effective approach is possible: in many flavor symmetry models to generate the unusual lepton mixing scheme (see Refs. [72, 73] for recent reviews) the mass terms are effective. Simply adding a sterile state to the particle content, and making it a singlet under the flavor symmetry group as well as the SM group, does the job [61]. Other models which accommodate light sterile neutrinos include [9, 58, 74–86].

### Sterile neutrinos in “non-standard approaches”

A variety of other ways to explain light sterile neutrinos exists, for instance **mirror models**. Starting from the famous Lee and Yang parity violation paper [87] attempts were made to generalize the concepts of mirror symmetry and parity by assuming the existence of mirror images of our particles. According to [87], these mirror particles were supposed to have strong and electromagnetic interactions with our particles. For a few years it seemed plausible that the role of these mirror particles is played by anti-particles of ordinary matter and that the true mirror symmetry is the CP symmetry. But in 1964 violation of CP symmetry was discovered. Then Kobzarev, Okun and Pomeranchuk [88] returned to the idea of mirror particles, which are different from the ordinary matter, and came to the conclusion that mirror particles cannot have strong and electromagnetic interaction with ordinary matter and hence could appear as dark matter. This “dark matter mirror model” was discussed by many authors, for instance [89–94]. For a review of some two hundred papers see [95].

Mirror model were invoked to understand neutrino puzzles in [74, 96, 97] after the LSND results were announced. In this picture, the mirror sector of the model has three new neutrinos which do not couple to the  $Z$ -boson and would therefore not have been seen at LEP, even if these are light. We will refer to the  $\nu'_i$  as sterile neutrinos of which we now have three. The lightness of  $\nu'_i$  is dictated by the mirror  $B' - L'$  symmetry in a manner parallel to what happens in the standard model. The masses of the mirror (sterile) neutrinos could arise for example from a mirror analog of the seesaw mechanism.

The two “Universes” communicate only via gravity or other forces that are very weakly coupled or associated to very heavy intermediate states. This leads to a mixing between the neutrinos of the two Universes and can cause neutrino oscillation between, say, the  $\nu_e$  of our Universe to the  $\nu'_e$  of the parallel one in order to explain the LSND results without disturbing the three neutrino oscillation picture that explains the solar and the atmospheric data.

Such a picture appears quite natural in superstring theories which lead to  $E_8 \times E'_8$  gauge theories below the Planck scale, where both  $E_8$ 's living on two separate branes are connected by gravity.

There are two classes of mirror models: (i) after symmetry breaking, the breaking scales in the visible sector are different from those in the mirror sector (this is called asymmetric mirror model); or (ii) all the scales are the same (symmetric mirror model). If all scales in both sectors are identical and the neutrinos mix, this scenario is a priori in contradiction with solar and atmospheric data since it leads to maximal mixing between active and sterile neutrinos. In the asymmetric mirror model, one can either have different weak scales or different seesaw scales or both. Either way, these would yield different neutrino spectra in the two sectors, along with different mixing between the two sectors.

As far as neutrino masses and mixings go, they can arise from a seesaw mechanism, with the mixings between sterile and active neutrinos given by higher dimensional operators of the form  $(LH)(L'H')/M$  after both electroweak symmetries are broken. The mixing between the two sectors could arise from a mixing between RH neutrinos in the two sectors *i.e.*, operators of the form  $N^T \sigma_2 N' + h.c.$  In this case the active-sterile neutrino mixing angles are of order  $v/v'$  implying that if this is the dominant mechanism for neutrino masses, the mirror weak scale should be within a factor 10-30 of the known weak scale. In this case, all charged fermion masses would be scaled up by a common factor of  $v'/v$ .

Regarding warm dark matter, in the mirror model there is no need to use oscillation to generate dark matter keV steriles. Here the inflaton reheating produces primordial sterile neutrinos. However, due to asymmetric inflation, the density of the keV steriles is down by a factor  $(T'_R/T_R)^3$ , where  $T_R$  ( $T'_R$ ) is the reheating temperature of our (the mirror) sector. One has

$$\Omega_m h^2 \sim 108 \left( \frac{T'_R}{T_R} \right)^3 \frac{m_{\nu_s}}{10 \text{ keV}}. \quad (24)$$

To get  $\Omega_m h^2 \sim 0.12$ , with  $(T'_R/T_R)^3 \sim 10^{-3}$ , one needs  $m_{\nu_s} \sim 10 \text{ keV}$ . Note that this is regardless of whether the active and sterile neutrinos mix at all. Since the X-ray constraints depend on the active-sterile mixing angles, the mirror model for warm dark matter need not be seriously constrained by X-ray data. In this picture, one of the two other  $\nu$ 's could be in the eV range to explain LSND if needed.

The bottom line here is that in this case, there are three sterile neutrinos with arbitrary masses and mixings. For example, one could accommodate a 3+2 solution to the LSND puzzle as well as a keV warm dark matter.

A completely different sterile “neutrino” candidate is the **axino**. It has been argued that this particle, arising from the supersymmetric version of the axion solution to the strong CP problem, is a natural candidate for a sterile neutrino in the framework of gauge mediated supersymmetry breaking.

A long-standing puzzle in the standard model is the smallness of the QCD vacuum angle  $\bar{\theta}$  which appears in the Lagrangian

$$\mathcal{L}_{QCD} = \frac{\bar{\theta}}{32\pi^2} G_{\mu\nu}^a \tilde{G}_{\mu\nu}^a, \quad (25)$$

where  $G_{\mu\nu}^a$  is the QCD gauge field strength. The current upper limits of the neutron electric dipole moment severely constrain  $|\bar{\theta}| \lesssim 10^{-11}$ , which is a priori a free parameter. The apparently arbitrary “smallness” of  $\bar{\theta}$  is referred to as the strong CP problem [98]. An elegant solution is to promote

the parameter  $\bar{\theta}$  to a dynamical degree of freedom, the axion  $a$ , which is a pseudo-Goldstone boson of the Peccei-Quinn (PQ) symmetry. The QCD potential of the axion sets its vacuum expectation value to zero;  $\bar{\theta} = \langle a \rangle / f_{PQ} = 0$ , and thus the strong CP problem is solved dynamically. Here  $f_{PQ}$  is the scale of the PQ symmetry breaking which is constrained to be  $10^{10} \text{ GeV} \lesssim f_{PQ} \lesssim 10^{12} \text{ GeV}$  [98].

In supersymmetric theories, the axion is accompanied by its fermionic partner, the axino  $\tilde{a}$ , which can remain very light due to its quasi Goldstone fermion character [70]. In the following we argue that the axino can naturally be a sterile neutrino in gauge mediated supersymmetry breaking models [99, 100] implementing the PQ symmetry through the Kim-Nilles mechanism [101, 102].

We first discuss how the axino can be as light as  $O(\text{eV})$ . As the superpartner of a Goldstone boson, the axino is massless as long as supersymmetry is unbroken. When the supersymmetry breaking scale is higher than the PQ symmetry breaking scale as in gravity-mediated supersymmetry breaking, the axino is expected to have generically a supersymmetry breaking mass, that is the gravitino mass  $m_{3/2}$  [103, 104]:

$$m_{\tilde{a}} \sim m_{3/2}. \quad (26)$$

However, if the PQ symmetry breaking occurs before supersymmetry breaking as in gauge mediated supersymmetry breaking, the axino mass is suppressed by the high PQ scale and thus can remain very light even after supersymmetry breaking. In the effective Lagrangian below the PQ scale, the axion (axino) appears in combination of  $a/f_{PQ}$  ( $\tilde{a}/f_{PQ}$ ) due to its Goldstone nature. This implies that the axino would get a mass of order

$$m_{\tilde{a}} \sim \frac{m_{SUSY}^3}{f_{PQ}^2}, \quad (27)$$

where  $m_{SUSY}$  is a supersymmetry breaking scale [99]. In the framework of gauge mediated supersymmetry breaking [105], a hidden sector field breaking supersymmetry can be charged under the PQ symmetry. In this case,  $m_{SUSY}$  is the hidden sector supersymmetry breaking scale. Taking roughly  $m_{SUSY} \gtrsim 10^5 \text{ GeV}$ , one gets  $m_{\tilde{a}} \gtrsim 1 \text{ eV}$  for  $f_{PQ} \lesssim 10^{12} \text{ GeV}$ . Otherwise, the axino mass would get a generic contribution from the supersymmetry breaking scale  $m_{SUSY} \sim 10^3 \text{ GeV}$  of the Supersymmetric Standard Model (SSM) sector:  $m_{\tilde{a}} \lesssim 10^{-2} \text{ eV}$  for  $f_{PQ} \gtrsim 10^{10} \text{ GeV}$ . There exists also a supergravity contribution

$$m_{\tilde{a}} \sim m_{3/2} \sim 1 \text{ eV} \quad (28)$$

where  $m_{3/2} \sim m_{SUSY}^2 / \bar{M}_{Pl}$  with  $m_{SUSY} \sim 10^5 \text{ GeV}$  and  $\bar{M}_{Pl} = 2.4 \times 10^{18} \text{ GeV}$ . This will be the main contribution to the axino mass in the scenario [100]. If the axino is light enough, appropriate mixing with active neutrinos and flavor structure can be constructed [106] and hence the supersymmetric axion solution to the strong CP problem can provide a candidate of a sterile neutrino.

## C. The Low-Energy Seesaw and Minimal Models

### General Aspects

Let us focus in more detail on the low energy seesaw. Recall the most general renormalizable Lagrangian

$$\mathcal{L}_\nu \supset \mathcal{L}_{old} - \frac{M_{Rij}}{2} N_i N_j - y^{\alpha i} L_\alpha N_i H + h.c., \quad (29)$$

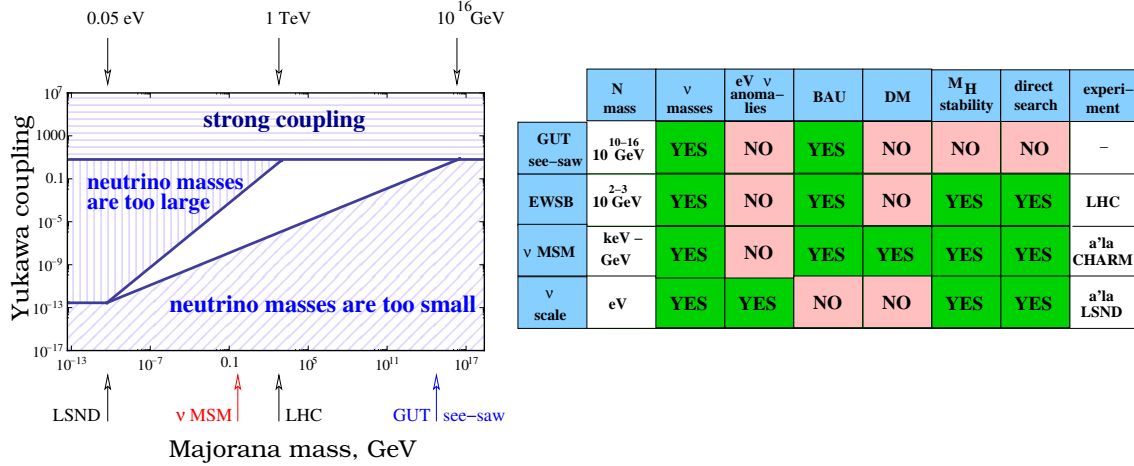


Figure 4. Left: possible values of the Yukawa couplings and Majorana masses of the sterile neutrinos in seesaw models. Right: the table shows whether the corresponding choice of the mass for Majorana fermions may explain neutrino masses and oscillations, accommodate eV neutrino anomalies, lead to baryogenesis, provide the dark matter candidate, ensure the stability of the Higgs mass against radiative corrections, and be directly searched at some experiments.

where  $\mathcal{L}_{old}$  is the standard model Lagrangian in the absence of gauge singlet fermions,  $y^{ai}$  are the neutrino Yukawa couplings, and  $M$  are the right-handed neutrino Majorana mass parameters. Eq. (29) is expressed in the weak basis where the Majorana mass matrix for the right-handed neutrinos is diagonal.

The seesaw formula allows the mass of singlet neutrinos to be a free parameter: Multiplying  $m_D$  by any number  $x$  and  $M_R$  by  $x^2$  does not change the right-hand side of the formula. Therefore, *the choice of  $M_R$  is a matter of theoretical prejudice* that cannot be fixed by active-neutrino experiments alone. A possible approach is to choose these parameters so that they explain certain phenomena and aspects beyond-the-standard model, for example, provide a dark matter candidate or a mechanism of baryogenesis. The most often considered standard approach takes Yukawa couplings  $y_{ai} \sim 1$  and the Majorana masses in the range  $M_N \sim 10^{10} - 10^{15}$  GeV. Models with this choice of parameters give rise to baryogenesis through leptogenesis [6]. For a review of the GUT-scale seesaw and the thermal leptogenesis scenario associated with it see *e.g.* [7]. Here we would like to focus on variants at lower energy scales.

Figure 4 summarizes various choices of combination of mass/Yukawa couplings of sterile neutrinos in seesaw models. The right panel summarizes properties of resulting seesaw models, their ability to solve various beyond-the-SM problems and anomalies, and their testability.

The main generic prediction of Eq. (29) is the existence of  $3 + n_R$  Majorana neutrinos, most of them massive. All of these “contain” the three active neutrino flavors and hence can, in principle, be observed experimentally. One exception is the case  $M_R = 0$ . In this case, the massive Majorana neutrinos “pair up” into at most three massive Dirac fermions.<sup>7</sup> The neutrino data can determine all physically observable values of  $y\nu = m_D$  – the neutrino masses and the elements of the neutrino mixing matrix, three angles and one CP-odd Dirac phase. Qualitatively, the neutrino data require  $m_D \sim 10^{-3}$  eV to  $\sim 10^{-1}$  eV. The case  $M \ll m_D$ , as far as observations are concerned, is similar

<sup>7</sup>In the case  $n_R = 2$ , there are two massive Dirac neutrinos and one massless neutrino. In the case  $n_R > 3$ , there are three massive Dirac neutrinos and  $n_R - 3$  massless gauge singlet, *bona fide* sterile, neutrinos that do not mix with any of the active states and are completely unobservable.

to the Dirac neutrino case. Here the neutrinos are Majorana fermions but they still “pair up” into pseudo-Dirac fermions. These can be distinguished from Dirac fermions if one is sensitive to the tiny mass splitting between the components of the pseudo-Dirac pair, which are proportional to  $M$ . Solar neutrino data require  $M \lesssim 10^{-9}$  eV [21], see also [107].

One can also deduce an upper bound for  $M$ . Theoretical considerations allow one to rule out  $M \gtrsim 10^{15}$  GeV [108], while a simple interpretation of the gauge hierarchy problem leads one to favor  $M \lesssim 10^7$  GeV, assuming there are no other new states at or above the electroweak symmetry breaking scale [109]. Naturalness is not a good guide when it comes to picking a value for  $M$  – all values for  $M$  are technically natural in the sense that in the limit where all  $M$  vanish the non-anomalous global symmetries of Eq. (11) are augmented by  $U(1)_{B-L}$ , global baryon number minus lepton number (see, for example, [30]). Finally, direct experimental probes of Eq. (11) are possible for  $M$  values below the TeV scale – the reach of collider experiments. We argue, however, that Eq. (29) can only be unambiguously tested for  $M$  values less than, very roughly, 10 eV, mostly via searches for the effects of light sterile neutrinos in neutrino oscillations.

A few important points are worthy of note. Eq. (15), describing the mixing between active and sterile states, can be severely violated and much larger values of  $\Theta$  are possible (see, for example, [110]). These are, however, not generic and require special choices for the entries in the neutrino mass matrix. This implies that, under extraordinary circumstances, one may be able to observe not-so-light seesaw sterile neutrinos for, say,  $M \sim 1$  MeV or 1 GeV, but it is not possible to falsify Eq. (29) if all  $M$  are much larger than 10 eV. On the flip side, the structure of the active–sterile mixing matrix is not generic. This means that Eq. (29) can be ruled out (or ruled “in”) if enough information concerning hypothetical sterile neutrinos is experimentally collected. For all the details see [111].

### eV-scale Seesaw

Here we will focus on the case that the seesaw scale corresponds to the scale of light sterile neutrinos responsible for various short baseline anomalies.

These light sterile neutrinos should be observable in short-baseline neutrino oscillation experiments sensitive to disappearance at the few percent level or appearance at the  $10^{-4}$  level [111]. It is interesting that these can also accommodate  $3+1$  and  $3+2$  solutions (see, for example, [112, 113]) to the so-called short baseline neutrino anomalies from LSND [114], MiniBooNE [115–117] and reactor data [118]. If that is indeed the case, Eq. (11) further predicts that  $\nu_\mu \rightarrow \nu_\tau$  appearance at short baselines is just beyond the current experimental upper bounds [111].

Non-oscillation experiments sensitive to the low energy seesaw include searches for double-beta decay [30, 119], precision measurements of the  $\beta$ -ray spectrum in nuclear  $\beta$ -decay [30, 119, 120], and cosmological bounds on the number of relativistic particle species in the early Universe and bounds on the fraction of hot dark matter [30, 119, 121, 122]. An interesting consequence of the low-energy seesaw (all masses well below 100 MeV) is that while the neutrinos are Majorana fermions, the rate for neutrinoless double-beta decay and all other potentially observable searches for lepton-number violation, vanishes [30, 119]. It is also possible that there is partial cancellation: this means that the contribution to neutrinoless double-beta decay of a light sterile neutrino, which generates an active neutrino via seesaw, cancels the contribution to double-beta decay from this active state [62]. The observation of a finite lifetime for neutrinoless double-beta decay would rule out Eq. (29) unless at least one of the right-handed neutrino mass parameters  $M$  is above a few tens

$n_R$	$L_i$	# zero modes	# masses	# angles	# CP phases
1	-	2	2	2	0
	+1	2	1	2	0
2	-	1	4	4	3
	(+1,+1)	1	2	3	1
	(+1,-1)	3	1	3	1
3	-	0	6	6	6
	(+1,+1,+1)	0	3	3	1
	(+1,-1,+1)	2	2	6	4
	(+1,-1,-1)	4	1	4	1

Table I. Spectrum and number of independent angles and phases for the models with  $n_R = 1, 2$  without and with global lepton number symmetries. The second column shows the lepton number charge assignments of the extra singlets,  $L_i$ .

of MeV. A recent re-analysis of sterile neutrino effects in double beta decay can be found in [123]. This is assuming that no other mechanisms [124] that can lead to double beta decay is realized in nature.

If a global symmetry (*e.g.* lepton number) is imposed on the Lagrangian (29), the general matrices  $y^{ai}$ , as well as the in general non-diagonal  $M_R$  have a more constrained structure which depends on how the different fields transform under the global symmetry. It is clear that the complexity of these models increases very fast with the number of extra Weyl fermions,  $n_R$ . This number is often taken to be the same as the number of families, but there is no fundamental reason why this should be the case. In Table I we summarize the neutrino mass spectrum and the number of leptonic mixing parameters as a function of  $n_R$ , with and without an exact global lepton number symmetry. Note that various lepton charge assignments are possible.

A first step towards a systematic exploration of the phenomenology of such models, in increasing order of complexity, in order to quantify the constraints imposed by data, was presented in [107], see also [29, 125]. For previous work on the subject, see also [21, 30, 119].

The requirement that two distinct mass splittings exist implies that the second, fifth and last entries on the table are excluded by neutrino oscillation data. The fourth and seventh entries correspond to two and three massive Dirac neutrinos, *i.e.*, to the standard three neutrino scenario. Here we consider the remaining cases for  $n_R = 1, 2$ . The addition of just one additional singlet Weyl fermion,  $n_R = 1$ , has in principle enough free parameters (two mixing angles and two mass differences) to fit the solar and atmospheric oscillation data. The next-to-minimal choice requires two Weyl fermions,  $n_R = 2$ . Such a possibility is, of course, well known to give a good fit to the data, in the limits  $M_R \rightarrow 0$  and  $M_R \rightarrow \infty$ , where the standard three neutrino scenario is recovered. In both cases, the physics spectrum contains one massless neutrino and two massive ones. The main goal will now be the exploration of the parameter space in between these two limits, in search for other viable solutions that could accommodate at least the solar and atmospheric oscillation, and maybe explain some of the outliers (*e.g.* LSND).

In the literature, several authors have devoted a lot of effort to study the implications of neutrino oscillation data on models with extra sterile neutrinos (some recent analyses are [112, 126–128]), usually referred to as  $3+1, 3+2, \dots, 3+N_s$ . Most of these studies have been done with the motivation

of trying to accommodate LSND [114], and MiniBooNE data [116, 117]. It is important to stress that these phenomenological models usually correspond to a generic model with  $3+N_s$  mass eigenstates, but *do not* correspond in general to a model with  $N_s$  extra Weyl fermions. The number of free parameters for  $N_s = n_R$  is typically much larger than what is shown in Table I, either because the number of Weyl fermions involved is larger (*e.g.*  $3+1$  Dirac fermions correspond in our context to  $n_R = 5$  and not to  $n_R = 1$ ) or because couplings that are forbidden by gauge invariance in our model, such as Majorana mass entries for the active neutrinos, are included, *effectively*, in the phenomenological models. Models for any  $n_R$  can be parameterized as the phenomenological models with  $N_s = n_R$ , but in that case there are generically correlations between parameters (*e.g.* between mixings and masses). The analyses performed in the context of the phenomenological models do not take such correlations into account, and usually restrict the number of parameters by assuming instead some hierarchies between neutrino masses that could accommodate LSND. In order to distinguish the  $3 + N_s$  phenomenological models from those in Eq. (29), we refer from now on to the latter as  $3 + n_R$  *minimal* models.

There are many possible parametrizations of the mass matrix. A good choice will usually be one that satisfies two properties: 1) it contains all independent parameters and no more, 2) it is convenient for imposing existing constraints. Without loss of generality, we can choose a basis where the mass matrix  $M_R$  takes a diagonal form, while  $m_D$  is a generic  $3 \times n_R$  complex matrix. In the case when  $m_D \ll M_N$ , a convenient parametrization is the one first introduced by Casas-Ibarra [129], which exploits the approximate decoupling of the light and heavy sectors, using as parameters the light masses and mixings that have already been measured. When this condition is not satisfied, we will use the following parametrization for the  $n_R = 1, 2$  cases:

$$\begin{aligned}
n_R = 1 \quad m_D &= U^*(\theta_{13}, \theta_{23}) \begin{pmatrix} 0 \\ 0 \\ m_D \end{pmatrix}, \\
n_R = 2 \quad m_D &= U^*(\theta_{12}, \theta_{13}, \theta_{23}, \delta) \begin{pmatrix} 0 & 0 \\ m_{D^-} & 0 \\ 0 & m_{D^+} \end{pmatrix} V^\dagger(\theta_{45}, \alpha_1, \alpha_2), \tag{30}
\end{aligned}$$

where  $U$  is a  $3 \times 3$  unitary matrix, with the same structure as the PMNS matrix, while  $V$  is a  $2 \times 2$  unitary matrix, depending on two phases and one angle. In the degenerate limit for  $n_R = 2$ , *i.e.*, when  $M_1 = M_2 = M$ , the matrix  $V$  becomes unphysical and  $U$  coincides with the PMNS matrix in the two limiting cases  $M \rightarrow 0, \infty$ .

It turns out that the  $3 + 1$  is excluded [107], even though in principle it has sufficient parameters to fit two mass splittings and two mixing angles. Thus, the most minimal working model is the  $3+2$  model, which contains one massless neutrino, four massive states, four angles and 2 CP phases. As a first simplification, the degenerate case in the CP conserving limit was explored, where the two eigenvalues of  $M_R$  were assumed to be the degenerate,  $M_1 = M_2 = M$  and no phases. The number of extra parameters with respect to the standard three-neutrino scenario is just one extra mass, the common Majorana mass,  $M$ . As mentioned above, this model in fact reduces to the standard three neutrino scenario in the two limits:  $M \rightarrow 0$ , when the four eigenstates degenerate into two Dirac pairs, and the opposite  $M \rightarrow \infty$ , when the two heavier states decouple. It is clear therefore that the fit to neutrino data will be good for  $M$  below the quasi-Dirac limit,  $M \leq M_{QD}$  ( $M_{QD}$  being the scale where the two massive neutrinos become Pseudo-Dirac particles) and also for  $M$  above the seesaw limit  $M \geq M_{SS}$  ( $M_{SS}$  being the scale where the mass of the active neutrinos is given by the seesaw



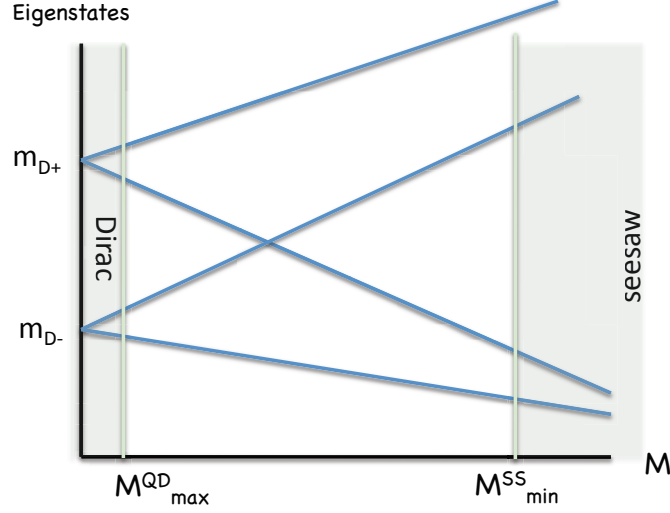


Figure 5. Spectrum in the 3 + 2 minimal model in the degenerate limit as a function of  $M$ .

formula), see Fig. 5. As it turns out, only the expected region  $M \leq M_{QD}$  and  $M \geq M_{SS}$  survive the fits to oscillation data. The value of  $M_{QD}$  is essentially fixed by solar data to be very small. The seesaw limit is mostly determined by long-baseline data.

Above and near the seesaw limit  $M \sim M_{SS}$ , the spectrum has two almost degenerate states with mass  $\mathcal{O}(\text{eV})$ . The heavy-light mixings in the minimal model with degenerate Majorana masses are completely fixed in terms of the parameters measured in oscillations and  $M$  ( $m_{D^\pm}$  are fixed in terms of  $M$  and the atmospheric/solar mass splittings):

$$(U_{mix})_{e4} = -s_{13} \frac{m_{D^+}}{M}, \quad (U_{mix})_{e5} = c_{13} s_{12} \frac{m_{D^-}}{M},$$

$$(U_{mix})_{\mu 4} = -c_{13} s_{23} \frac{m_{D^+}}{M}, \quad (U_{mix})_{\mu 5} = (c_{12} c_{23} - s_{12} s_{13} s_{23}) \frac{m_{D^-}}{M}.$$

Interestingly, for the inverse hierarchy, these mixings are in the right ballpark as indicated by the phenomenological 3 + 1 and 3 + 2 fits of all oscillation data. However, due to a strong cancellation of the probabilities related to the existence of two almost degenerate heavy states, a more detailed analysis shows that the degenerate case does not provide a better fit to the anomalies than the standard three neutrino scenario. A different situation is found away from the degenerate limit. In this case the heavy-light mixings depend on the light masses and mixings, but also on the two heavy masses, and on a new complex angle.

Varying the free parameters (*i.e.*,  $\theta_{13}$ ,  $\delta$ ,  $M_1$ ,  $M_2$  and the extra complex angle) to match the best-fit heavy-light mixings and splittings found in the 3 + 2 phenomenological fit of [112, 128] we find that there are regions of parameter space where the two minimal and phenomenological models are rather close. The oscillation probabilities relevant for MiniBooNE are compared in Fig. 6.

Although it looks like the 3 + 2 minimal model could be as efficient as the 3 + 2 phenomenological model in fitting all oscillation data, while being much more predictive, a definite conclusion regarding this point requires a detailed fit of this more constrained model. In particular, if this model were to explain the LSND/MiniBooNE anomaly, it would do so only for relatively large

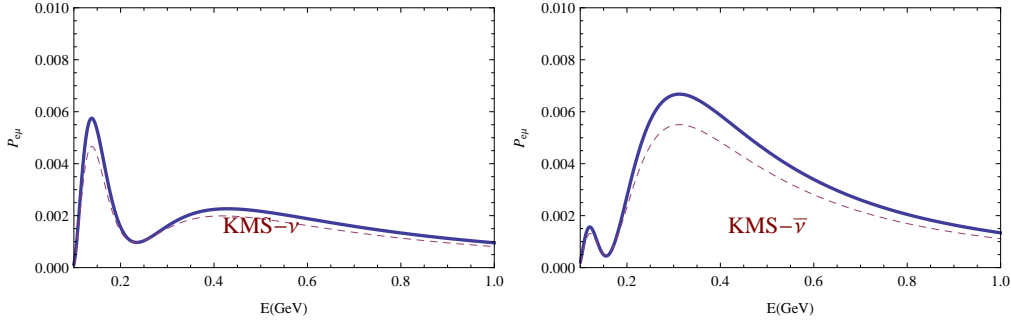


Figure 6. Oscillation probabilities relevant for MiniBooNE setup for the 3 + 2 best fit of [112] and the minimal 3 + 2 model for some choice of the parameters  $\theta_{13}$ ,  $\delta$  and the free complex angle.

value of  $\theta_{13}$  and particular values of the CP phase  $\delta$ .

### The $\nu$ MSM

One can choose masses of sterile neutrinos of the order of masses of other leptons in the standard model, in keV–GeV range. It turns out that with this choice of parameters it is possible to explain simultaneously the data on neutrino oscillations, the dark matter in the Universe and generate the correct matter-antimatter asymmetry of the Universe without introducing any new physics above the electro-weak scale [35, 36, 130]. Of course, there is still no explanation for the various parameters (masses, mixing parameters, couplings) of the extended SM. This model is called *the  $\nu$ MSM* – Neutrino Minimal Standard Model [35, 130].<sup>8</sup> The  $\nu$ MSM provides a new approach to the “physics beyond the standard model”, concentrating on its observational problems (see discussion in [36, 134]).

*The  $\nu$ MSM is testable already with existing experimental means*, as the masses of all new particles are within the laboratory-accessible range, including bounds on neutrinoless double beta-decay [135], and possibilities to see the heavier non-DM neutrinos in rare decay experiments [136]. The most direct experimental verification of the  $\nu$ MSM would be a discovery of two heavier sterile neutrinos, responsible for baryogenesis and generation of lepton asymmetry for resonant production of sterile neutrino dark matter [136]. The current experimental bounds on parameters of these particles are shown in Fig. 7. Future experiments (for example, NA62 in CERN<sup>9</sup>, LBNE experiment in FNAL<sup>10</sup> or the LHCb experiment) are capable of entering into cosmologically interesting regions of parameters of the  $\nu$ MSM which might lead to the discovery of light neutral leptons (see *e.g.* [137]). If the LHC experiment will not find any particles other than Higgs boson, these searches may provide the only way to learn about the origin of neutrino masses and of mechanism of baryogenesis.

The final test of the  $\nu$ MSM would be to find in astrophysical X-ray observation clear signatures of DM decay line (potentially distinguishable from any signal of astrophysical origin [138–140]), with parameters consistent with those of two heavier neutrinos.

<sup>8</sup>This theory can accommodate inflation, if one considers non-minimal coupling between the Higgs boson and gravity [131]. Finally, a scale-invariant extension of the model [132, 133] that includes unimodular gravity may solve the problem of stability of the Higgs mass against radiative corrections, even if the Planck scale is included, and could lead to an explanation of dark energy and of the absence of the cosmological constant.

<sup>9</sup><http://na62.web.cern.ch/NA62>

<sup>10</sup><http://lbne.fnal.gov>

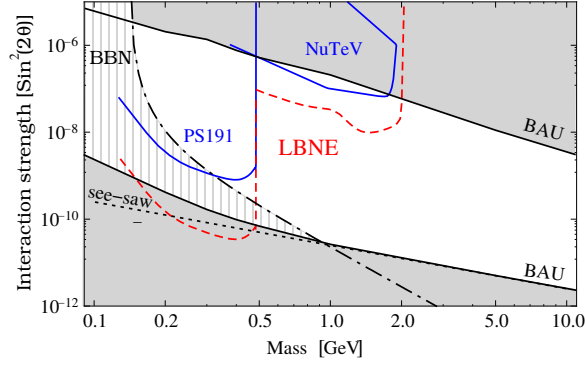


Figure 7. The allowed region of parameters of two sterile neutrinos in the  $\nu$ MSM, responsible for neutrino oscillations (region above dotted line “seesaw”) and for baryo/leptogenesis (region between two black solid lines). The hatched region “BBN” is excluded from primordial nucleosynthesis [141, 142]. Accelerator experiments, searching for heavy neutral leptons exclude regions above blue solid lines (see [143] for up-to-date details). Prospects for sterile neutrino searches with the LBNE experiment are showed in red dashed line [137].

## D. Sterile Neutrino Dark Matter

The nature of Dark Matter (DM) is among the most intriguing questions of modern physics. Its resolution will have a profound impact on the development of particle physics. Indeed, massive neutrinos of the Standard Model were among the first dark matter candidates. However, it was understood that in a Universe filled with such *hot* dark matter particles, large scale structure would be incompatible with observations [144]. Standard model neutrinos turned out to be too light to be viable dark matter candidate. As a result, the DM particle hypothesis necessarily implies an extension of the standard model. Candidate DM particles in such hypothetical standard model extensions differ drastically in their properties (such as mass, interaction strength, clustering properties) and therefore in their observational signatures.

Sterile neutrinos (that have very weak interaction with the ordinary matter, exactly as DM does) are attractive dark matter candidates *if* the model provides

**Sufficient stability.:** This originates from the requirement that the dark matter candidate lives at least as long as the age of the Universe and, what is perhaps more important, from astrophysical X-ray bounds. This requirement poses strict bound on the sterile neutrino Yukawa couplings and on interactions beyond those of the SM (if any are present).

**Production mechanism.:** This may be the most complicated problem with the sterile neutrino DM. Depending on the model, this may give further requirements on the DM neutrino Yukawa couplings, and constrain properties of other particles (for example other sterile neutrinos).

**Specific mass scale.:** The mass scale of the DM neutrino is bounded from several considerations. A lower bound is provided by the structure formation in the Universe, in a way that is dependent on the neutrino momentum distribution, which itself depends on the production mechanism. In specific models, different additional requirements may appear for the masses of the non-DM sterile neutrinos.

The generation of the mass scale has been discussed before, below we review the other points. The masses of the sterile neutrinos can vary in a wide range. On the one hand, sterile neutrinos, as any fermionic dark matter, should satisfy the Tremaine-Gunn bound [145], meaning that their masses should be above roughly 400 eV [146, 147]. On the other hand, because their decay width is proportional to  $M_N^5$  [148] (at least in the models without extra light particles, *e.g.* Majorons), high mass neutrinos require very small Yukawa couplings to warrant their stability. The considerations of stability over the lifetime of the Universe favor relatively light (keV scale) neutrinos. More stringent constraints are imposed on the combination of the masses and mixing angles of the sterile neutrino dark matter by the non-observation of a dark matter decay line in X-ray spectra of DM-dominated objects [149, 150]. The search for such a *decaying dark matter* is very promising [139, 140]. First of all, a positive result would be conclusive, as the DM origin of any “suspicious” line can be unambiguously checked. Indeed, the decay signal is proportional to the *column density* — the integral of DM distribution along the line of sight ( $\int \rho_{DM}(r)dr$ ) and not to the  $\int \rho_{DM}^2(r)dr$  (as it is the case for annihilating DM). As a result a vast variety of astrophysical objects of different nature would produce a comparable decay signal (cf. [138, 151, 152]). Therefore (i) one has the freedom of choosing the observational targets, avoiding complicated astrophysical backgrounds; and (ii) if a candidate line is found, its surface brightness profile may be measured (as it does not decay quickly away from the centers of the objects), distinguished from astrophysical lines (which usually decay in outskirts) and compared among several objects with the same expected signal. This allows one to distinguish the decaying DM line from any possible astrophysical background rendering astrophysical searches for the decaying DM *another type of a direct detection experiment* [149, 150].

If the sterile neutrino dark matter interacts with other particles so that it enters into thermal equilibrium in the early Universe and then freezes out while relativistic (so called “*thermal relic DM*” [153]), then the contribution  $\Omega_N$  of a thermal relic of mass  $M_N$  to the energy balance of the Universe is

$$\frac{\Omega_N}{\Omega_{DM}} \simeq \frac{1}{S} \left( \frac{10.75}{g_{*f}} \right) \left( \frac{M_N}{1 \text{ keV}} \right) \times 100, \quad (31)$$

where  $\Omega_{DM} = 0.105h^{-2}$  is the observed DM density,  $g_{*f}$  is the effective number of degrees of freedom at freeze-out, and  $S$  is the additional entropy release after the sterile neutrino DM freezes out. One can see that in order to obtain the proper amount of DM one either needs to have significant entropy release, or prevent the DM neutrino from entering thermal equilibrium at all.<sup>11</sup> Three main possibilities of sterile neutrino dark matter production will be reviewed below:

1. Production from mixing with SM neutrinos,
2. Thermal production with subsequent dilution,
3. Non-thermal production from additional beyond-SM physics.

Some details on general aspects of relic abundance formation are displayed in Fig. 8. The first mechanism (weak reactions like  $\ell\ell \rightarrow N\nu qq' \rightarrow N\nu$  with interaction strength proportional to  $G_F \times \sin^2(2\theta)$ ) is always effective if the sterile neutrino mixes with active ones [37–39, 154–158]. Some amount of sterile neutrinos is *always* produced via this mixing in the early Universe (the so-called *non-resonant production of sterile neutrinos*, NRP [37, 154–157, 159]), and allows one to

<sup>11</sup>Reducing the mass of the thermal relic leads to Hot DM, in contradiction with data on large-scale structure formation.

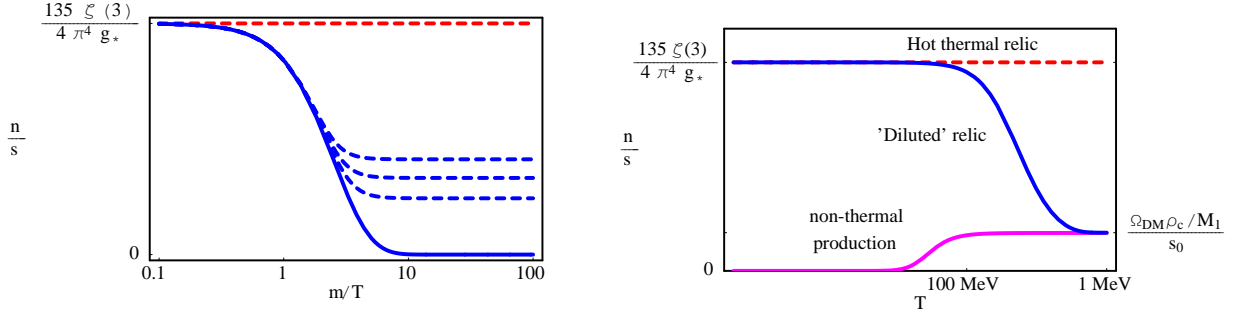


Figure 8. Schematic evolution of the relic abundance in the Universe. Left plot depicts the standard non-relativistic freeze-out mechanism, where the abundance is controlled by the decoupling moment (several dashed curves). Right plot illustrates various non-thermal mechanisms. The dashed line is a thermal relic decoupled while being relativistic (hot thermal relic), leading to the over closure of the Universe. The blue decreasing line is the same hot thermal relic, but with the abundance diluted by rapid expansion of the Universe (entropy production), leading to correct DM abundance. The lowest (magenta) line depicts the evolution of the non-thermally produced particle with zero primordial abundance.

set a rather robust upper bound on the mixing angle (from the requirement that sterile neutrinos do not overclose the Universe). This production is peaked at temperatures  $T \gtrsim 150 \text{ MeV} (M_N/\text{keV})^{1/3}$  and the resulting momentum distribution function of DM particles is a rescaled Fermi-Dirac distribution [150, 157]. As a result, keV-scale sterile neutrinos are *created relativistic* and become non-relativistic deeply in the radiation dominated epoch.

Such dark matter particles may have a significant free streaming horizon (see [160] for discussion), which influences structure formation. These DM models (often called *Warm Dark Matter*, WDM as opposed to non-relativistic “cold” dark matter) are as compatible with the data on CMB and large scale structure as the  $\Lambda$ CDM “concordance” model [160]. The difference between cold and warm DM particles would show up at approximately galactic (sub-Mpc) scales and only very recently such small scale effects are starting to be resolved both theoretically and experimentally. There are several reasons for that. First of all, dark matter-only simulations of structure formation require, in the case of WDM, significantly larger number of particles to achieve a resolution comparable with the CDM case (see *e.g.* [161–163]). Additionally, at scales of interest, the baryonic physics can hide (or mimic) the WDM suppression of power (see *e.g.* [164]).

Experimentally, the effects of suppression of the matter power spectrum are probed with the Lyman- $\alpha$  forest method. This method was successfully applied to “warm” thermal relics and to non-resonantly produced sterile neutrinos (*e.g.* [160, 165–170]). The resulting Lyman- $\alpha$  restrictions are strong enough that free-streaming would affect only structures at scales considerably less than galactic (see *e.g.* [171–174]).

The Lyman- $\alpha$  method was also extended in [160] to a more realistic, particle physics motivated class of “cold+warm DM models” (CWDM). In this case, the Lyman- $\alpha$  constraints allow a significant fraction of very warm DM particles [160]. Sterile neutrino dark matter, produced via *resonant oscillations* in the presence of a significant lepton asymmetry in the plasma [38, 39, 158] (resonant production, RP) resembles CWDM models at scales probed by the Lyman- $\alpha$  method [175]. RP DM particles can easily evade Lyman- $\alpha$  constraints and light (1–2 keV) sterile neutrinos remain viable dark matter candidates [175], consistent with all astrophysical and cosmological data down to galactic scales.

Recent results [163] demonstrate that these DM models modify the amount of substructure in Galaxy-sized halo along with their properties. The discrepancy between the number of observed substructures with small masses and those predicted by  $\Lambda$ CDM models [176, 177] can simply mean that these substructures did not confine gas and are therefore completely dark (see *e.g.* [178, 179]). This is not true for larger objects. In particular, CDM numerical simulations invariably predict several satellites “too big” to be masked by galaxy formation processes, in contradiction with observations [176, 177, 180, 181]. Resonantly produced sterile neutrino DM turns out to be “warm enough” to amend these issues [163] and “cold enough” to be in agreement with Lyman- $\alpha$  bounds [175].

Along with the Lyman- $\alpha$  forest method, weak gravitational lensing can be used to probe primordial velocities of dark matter particles (see *e.g.* [164, 182, 183]), as the next generation of weak lensing surveys (such as *e.g.* KiDS, LSST, WFIRST, Euclid) will be able to measure the matter power spectrum at scales down to 1 – 10 h/Mpc with a few percent accuracy (see *e.g.* [184]). As in the case of the Lyman- $\alpha$  forest method, the main challenge is to properly take into account the baryonic effects on the matter power spectrum [164].

### Dark matter in the $\nu$ MSM

The lightest sterile neutrino in the  $\nu$ MSM can be coupled to the rest of the matter weakly enough to provide a viable DM candidate. In the  $\nu$ MSM sterile neutrino dark matter particles can be produced *only* via oscillations with active neutrinos [39, 156–158]. Their abundance must correctly reproduce the measured density of DM. The allowed region lies between the two black thick lines in Fig. 9(a). The shaded (red) upper right corner corresponds to a region excluded by searches for the DM decay line from X-ray observations [138, 149, 150, 185–194] neutrinos [195]. Finally, a lower limit on the mass of DM sterile neutrino  $M_{DM} \gtrsim 1$  keV comes from the analysis of the phase-space density of the Milky way’s dwarf spheroidal galaxies [146]. For non-resonantly produced sterile neutrinos the Lyman- $\alpha$  method provides a *lower bound* on the mass  $M_{DM} \gtrsim 8$  keV (assuming that baryonic feedback on matter distribution, discussed *e.g.* in [164] do not affect this result significantly). This result is in tension with the combination of the X-ray limits, that put an *upper bound*  $M_{DM} \lesssim 3 - 4$  keV (see *e.g.* [160, 168, 189]).

However, in the  $\nu$ MSM there is an allowed region with the masses as low as 1 – 2 keV in which *sterile neutrinos, produced resonantly, remain a viable DM candidate* [175]. The required large lepton asymmetry is generated by two other sterile neutrinos of the  $\nu$ MSM, also responsible for baryogenesis and neutrino oscillations. We stress that the resonant production of sterile neutrino DM requires the presence of large,  $\Delta L/L > 2 \times 10^{-3}$  lepton asymmetry at temperature  $T \sim 100$  MeV and it can only be produced in the  $\nu$ MSM [158] (the GUT, electro-weak, or eV scale seesaw cannot provide it).<sup>12</sup> The thin colored curves between thick black lines in Fig. 9(a) represent production curves for different values of lepton asymmetry,  $L_6 \equiv 10^6(n_{\nu_e} - n_{\bar{\nu}_e})/s$  (where  $s$  – entropy density). The resulting parameter space of the  $\nu$ MSM is bounded, with the highest possible DM mass  $M_{DM} \lesssim 50$  keV [192]. Therefore, in the  $\nu$ MSM the properties of dark matter particles are tightly related to the mechanism of baryogenesis and properties of two other sterile neutrinos.

<sup>12</sup>See however [196] where a possibility of cancellation between lepton asymmetries stored in different flavours was discussed.

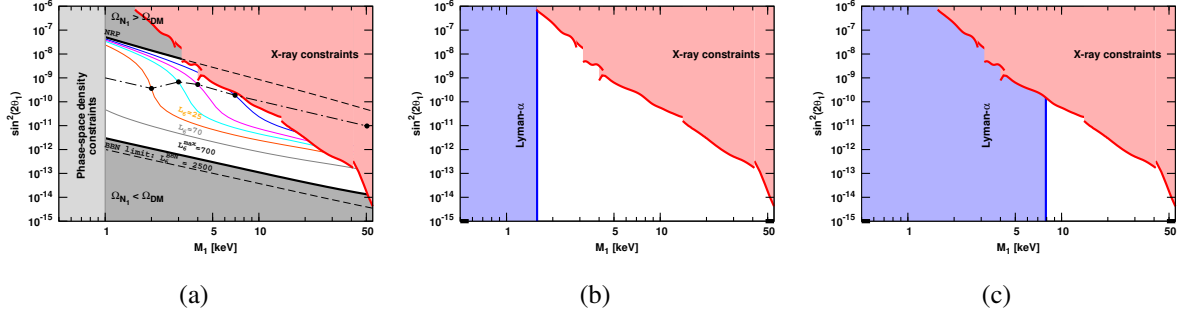


Figure 9. Bounds on the mass  $M_1$  and the mixing angle  $\theta_1$  of the sterile neutrino dark matter for the models, discussed in Section ID: DM in the  $\nu$ MSM (Panel a, see text for details); DM produced in the model with entropy dilution (Panel b); and DM produced in the light singlet Higgs decays (Panel c).

### Neutrinos in gauge multiplets – thermal production of DM neutrinos

In this model sterile neutrinos are charged under some beyond the SM gauge group [65]. A natural candidate are here left-right symmetric theories, in which the sterile neutrinos are sterile only under the SM  $SU(2)_L$  gauge group, but are active with respect to an additional  $SU(2)_R$ , under which the left-handed SM particles are sterile. The steriles couple in particular to a new gauge boson  $W_R$ , which belongs to  $SU(2)_R$ . One of the sterile neutrinos  $N_1$  is light and plays the role of dark matter, entering in thermal equilibrium before freeze-out. Other sterile neutrinos  $N_{2,3}$  should dilute its abundance up to the correct amount via out-of-equilibrium decays. This entropy production happens if there are heavy particles with long lifetimes, which first decouple while still relativistic and then decay when already non-relativistic [197]. The proper DM abundance is controlled by the properties of this long-lived particle through the entropy dilution factor  $S \simeq 0.76 \frac{g_*^{-1/4} M_2}{g_* f \sqrt{\Gamma} M_{Pl}}$ , where  $g_*$  is an averaged number of d.o.f. during entropy generation, and  $M_2$  is the mass of the sterile neutrino, responsible for the dilution. The X-ray constraint here bounds the mixing angle  $\theta_1$  of the DM neutrino in the same way as for the  $\nu$ MSM. The mixing between new and SM gauge bosons is also severely constrained. The structure formation from the Lyman- $\alpha$  analysis constraints the DM neutrino mass:  $M_1 > 1.6$  keV, because its velocity distribution is that of the cooled thermal relic [65, 160]. At the same time, this implies that the DM in this model is cold (CDM).

All other constraints in this scenario apply to the heavier sterile neutrinos and to the new gauge sector. The correct abundance of the CDM sterile neutrino requires entropy dilution. To properly provide the entropy dilution,  $N_2$  should decouple while relativistic and has a decay width

$$\Gamma \simeq 0.50 \times 10^{-6} \frac{g_N^2 g_{*f}^2}{4 g_*^2} \bar{g}_*^{1/2} \frac{M_2^2}{M_{Pl}} \left( \frac{1 \text{ keV}}{M_1} \right)^2. \quad (32)$$

At the same time, the heavy neutrino  $N_2$  should decay before BBN, which bounds its lifetime to be shorter than approximately  $0.1 \div 2$  s. Then, the proper entropy can be generated only if its mass is larger than

$$M_2 > \left( \frac{M_1}{1 \text{ keV}} \right) (1.7 \div 10) \text{ GeV}. \quad (33)$$

The entropy is effectively generated by out-of-equilibrium decays if the particle decoupled while still relativistic. The bound on the decoupling temperature leads to a bound on the new gauge

boson mass

$$M > \frac{1}{g_{*f}^{1/8}} \left( \frac{M_2}{1 \text{ GeV}} \right)^{3/4} (10 \div 16) \text{ TeV}. \quad (34)$$

An alternative way of fighting the overproduction in a model with sterile neutrinos charged under some gauge symmetry is analyzed in [33], where the mass of the corresponding gauge boson is heavy, of the order of  $10^{15}$  GeV. In this case, if the reheating temperature is also lower than the GUT scale, the additional gauge interactions do not fully thermalize the SM sterile neutrinos but still allow the generation of the required DM abundance.

Note here that in most models with additional physics responsible for the properties of sterile neutrinos, similar analyses should be performed, since new sterile neutrino interactions may lead to an increase in its decay width or bring it into thermal equilibrium.

### Primordial generation of DM neutrinos

Finally, the DM neutrinos may be produced by some other mechanism related to interactions beyond the SM which do not lead to thermal equilibration of the DM sterile neutrino. An example is provided by models with an additional scalar  $\phi$ , which provides Majorana masses to the sterile neutrinos when it acquires a vacuum expectation value

$$\mathcal{L} = \sum_i f_i \phi \bar{N}_i^c N_i.$$

Here, the neutrinos will get masses  $m_i = f_i \langle \phi \rangle$ . At the same time, this interaction leads to the decay of the scalar  $\phi$  into sterile neutrinos. This decay can be made responsible for the generation of the DM.

A scenario where the scalar  $\phi$  is also responsible for inflation in the early Universe was analyzed in [198–200]. In this setup the inflaton decays during reheating mostly into SM particles, but some fraction of decays are directly into DM neutrino. In this case, the production is not connected with  $\theta_1$ , and the only bounds present for the DM neutrino properties are the X-ray bound and the Lyman- $\alpha$  bound. The DM neutrino in this model is produced with nearly thermal spectrum [198] (“thermal relic” case of [160]), so its mass should be  $M_1 > 8$  keV. In this scenario, the mass of the DM sterile neutrino can be related to the mass of the inflaton, which is quite light and can be searched for in B-meson decays [200].

Note that it is also possible that a keV mass sterile DM neutrino (if produced from non-thermal decay) can belong to a thermalized hidden sector which is not in thermal equilibrium with SM. One particular example [201] is a lower limit of 1.5 keV (from free-streaming and phase space density) set on hidden sector warm dark matter which might be at a different temperature than the SM.

Another setup, where the additional scalar is produced itself from its interaction with the Higgs boson is described in [40, 202]. The laboratory consequences for it in sterile neutrino decays are discussed in [203].

Alternatively, one can also produce DM neutrinos from higher dimensional operators appearing in the model. This was analyzed in the context of the  $\nu$ MSM and Higgs-inflationary models [204,



205]. In this mechanism it is possible to produce only neutrinos with higher masses, of the order  $10^4$  keV.

The generation of DM sterile neutrinos is also possible in inflationary model with  $R^2$  modification of gravity [206]. In such a model an additional degree of freedom, the scalaron, effectively appears from the higher order operator  $R^2$ , and serves as the inflaton. At a subsequent reheating, the scalaron decays into all non-conformal fields, with the main decay products being the SM particles (via the Higgs decay). The right-handed neutrinos are also produced, because their Majorana mass terms are not conformal, and can provide for DM. The required mass in this case is of the order  $10^7$  GeV, making it CDM.

### Other models

Several other papers attempt to provide an explanation for the specific mass patterns of the sterile neutrinos with a keV DM neutrino and heavier sterile neutrinos (see *e.g.* [43, 49, 62, 85, 207]). However, further research is needed in order to explicitly verify whether the sterile neutrino dark matter in these models is produced in the correct amount and does not contradict existing astrophysical and cosmological bounds.

## E. Light Sterile Neutrinos as Messengers of New Physics

Before discussing alternative scenarios to non-standard neutrino physics, which can be invoked to explain hints usually interpreted in terms of sterile neutrinos, let us set the stage with an overview.

It is often said that, because neutrinos have only weak interactions, neutrino experiments can be sensitive to small new physics effects that would not otherwise be manifest. Indeed, the interferometric nature of neutrino oscillations and their tiny masses make them excellent candidates to search for new physics. As will be seen in the next subsection, however, any new physics affecting neutrinos must also affect at some level the properties of charged leptons, since neutrinos and charged leptons are related by  $SU(2)$  gauge symmetry. For instance, neutrino non-standard interactions (NSI) from  $d = 6$  effective operators, which in principle could affect neutrino production, detection, and matter effects in propagation, are already strongly constrained by charged lepton data. Instead of higher dimension effective operators, one can introduce new light force carriers that couple to neutrinos; the resulting flavor-dependent Long-Range Interactions (LRI) then affect neutrino flavor oscillations, in a way that will appear as a non-standard matter effect if sufficiently short-range, or as a non-standard vacuum oscillation if sufficiently long-range. However here again such flavor-dependent interactions are already highly constrained by charged lepton data (and, for sufficiently long-range forces, by tests of the equivalence principle) [208, 209]. To put it mildly, it is a challenge to theorists to formulate UV-complete scenarios of new physics that satisfy existing bounds from the charged lepton and quark sectors while making dramatic predictions for the neutrino sector.

The prospects for observing exotic physics in the neutrino sector brighten considerably in scenarios with light steriles. Now one has the possibility of combining new interactions with active-sterile mixing, such that the combined effects are less constrained by charged lepton data while still detectable in present or future neutrino oscillation experiments. Let us mention a few examples

illustrating this synergy<sup>13</sup>.

In the analysis of Ref. [127, 211], a single light sterile neutrino is combined with NSI in an attempt to reconcile LSND with MiniBooNE short-baseline antineutrino data. The NSI couplings are taken to be of the order of  $10^{-2}$ , and to affect both neutrino production and detection. In the presence of NSI, the neutrino transition probabilities exhibit CP violation even in the one-mass-scale-dominance limit relevant to the short-baseline experiments; this allows to reconcile the antineutrino data in a (3+1) oscillation scheme.

The analyses in Refs. [212, 213] posit a light sterile neutrino in combination with a new light gauge boson that couples to  $B - L$ . In the absence of the sterile neutrino the new force would have no effect on neutrino flavor oscillations, since all three active neutrino flavors have the same  $B - L$  charge. In the presence of active-sterile mixing, the light gauge boson produces a non-standard matter effect in neutrino propagation that effectively violates CPT and is energy dependent. For a coupling  $< 10^{-5}$  and gauge boson mass on the order of tens of keV, this new physics can reconcile LSND and MiniBooNE data. A lighter gauge boson could instead produce an apparent CPT asymmetry in MINOS long baseline muon-neutrino oscillations.

In the event that genuine CPT-violating mass differences are discovered in the neutrino sector, it would be difficult not only to produce a plausible model for such an effect, but also to reconcile CPT violation in the neutrino sector with the very strong upper bounds on CPT-violating physics for quarks and charged leptons [214]. These problems were addressed in Ref. [215], which exhibited an explicit model for neutrinos with a CPT-asymmetric mass spectrum. In this framework the active neutrinos are conventional Dirac fermions, while there is one or more species of exotic sterile neutrinos. The steriles are nonlocal and respect CPT, but the implementation of CPT differs from that for Dirac fermions. When the actives and steriles mix, the mismatch between CPT operators induces a CPT asymmetry in the mass eigenstates.

Light sterile fermions, through mixing with the active neutrino flavors, could be the messengers of one or more varieties of exotic physics. As we see from these examples, in such scenarios the leakage of the exotic physics into phenomena with charged leptons is reduced, both because the steriles are standard model singlets, and because they can differ in other respects from the active neutrinos.

## F. Non-Standard Neutrino Interactions (NSI)

Non-standard neutrino interactions (NSI) are a very widespread and convenient way of parameterizing the effects of new physics in neutrino oscillations [216, 217]. NSI can lead to non-diagonal neutral currents. Heavy SM-singlet (*i.e.* sterile) neutrinos, for instance, induce certain types of NSI, as will be discussed in subsection IF. Recall that in the presence of sterile neutrinos the leptonic neutral current is in general non-diagonal in mass eigenstates, and therefore also in flavor eigenstates [5, 31]. The formalism, however, is model-independent. Even though present data constrain NSI to be a subleading effect in neutrino oscillation experiments, the possibility of their eventual detection and interference with standard neutrino oscillation measurements has triggered a considerable interest in the community. Here we review the present bounds on NSI and discuss the possibility of saturating them in particular standard model (SM) extensions.

---

<sup>13</sup>An aspect of sterile neutrinos which is similar to a non-standard neutrino physics aspect is a “zero-distance” effect [210], which denotes the property that in case of a non-unitary mixing matrix the oscillation probabilities have the property  $P(\nu_\alpha \rightarrow \nu_\beta) \neq \delta_{\alpha\beta}$  in the limit  $L \rightarrow 0$ . In case sterile neutrinos are present, the averaged out oscillation corresponding to its large mass-squared difference mimics this effect.

## CC-like NSI

In this section we discuss NSI for source and detector charged-current processes, we will refer to these as charged-current-like NSI. Leptonic NSI are given by the effective Lagrangian density <sup>14</sup>.

$$\mathcal{L}_{\text{NSI}}^\ell = -2\sqrt{2}G_F\varepsilon_{\gamma\delta}^{\alpha\beta P}[\bar{\ell}_\alpha\gamma^\mu P\ell_\beta][\bar{\nu}_\gamma\gamma_\mu P_L\nu_\delta], \quad (35)$$

where  $G_F$  is the Fermi constant and  $P$  is either  $P_L$  or  $P_R$  and, due to Hermiticity,  $\varepsilon_{\gamma\delta}^{\alpha\beta P} = \varepsilon_{\delta\gamma}^{\beta\alpha P*}$ . For NSI at neutrino production via muon decay  $\alpha = \mu$  and  $\beta = e$ . Note that  $\alpha = \beta = e$  would instead correspond to NSI with electrons in matter.

In a similar fashion, the charged-current-like NSI with quarks are given by

$$\mathcal{L}_{\text{NSI}}^q = -2\sqrt{2}G_F\varepsilon_{\alpha\beta}^{qq'P}V_{qq'}[\bar{q}\gamma^\mu Pq'][\bar{\ell}_\alpha\gamma_\mu P_L\nu_\beta] + h.c., \quad (36)$$

where  $q$  is an up-type and  $q'$  is a down-type quark. Only  $q = u$  and  $q' = d$  are of practical interest for neutrino oscillations, due to their contributions to charged-current interactions with pions and nuclei. In Ref. [218] bounds on these production and detection NSI were derived from constraints on the comparison of different measurements of  $G_F$ : through  $\mu$  decay (affected by leptonic NSI of Eq. (35)),  $\beta$  decays (affected by quark NSI of Eq. (36)) and the kinematic measurements of the masses of the gauge bosons  $M_Z$  and  $M_W$  (not affected by neutrino NSI). Universality tests of  $G_F$  from  $\pi$  and  $\tau$  decays as well as short baseline neutrino oscillation experiments such as KARMEN or NOMAD, were also considered. Note that in order to derive those bounds only one NSI parameter was switched on at a time in order to avoid the relaxation of the bounds through cancellations among different parameters. Here we present a summary of the most stringent bounds derived:

$$|\varepsilon_{\alpha\beta}^{\mu e}| < \begin{pmatrix} 0.025 & 0.030 & 0.030 \\ 0.025 & 0.030 & 0.030 \\ 0.025 & 0.030 & 0.030 \end{pmatrix}, \quad |\varepsilon_{\alpha\beta}^{ud}| < \begin{pmatrix} 0.041 & 0.025 & 0.041 \\ 1.8 \cdot 10^{-6} & 0.078 & 0.013 \\ 0.026 & 0.013 & 0.13 \\ 0.087 & 0.013 & 0.13 \\ 0.12 & 0.018 & 0.13 \end{pmatrix}.$$

Whenever two values are quoted, the upper value refers to left-handed NSI and the lower to right-handed NSI. These bounds stem from the direct effect of the corresponding effective operator and are rather weak. However, Eqs. (35) and (36) are not gauge invariant and can be related to flavour changing processes involving charged leptons when promoting the neutrino fields to full lepton doublets which would lead to much tighter constraints. In Sect. IF we will discuss possible ways to evade these stronger constraints.

## NC-like NSI

We next review the current status of the bounds on NSI matter effects, or neutral-current-like NSI defined as

$$\mathcal{L}_{\text{NSI}}^M = -2\sqrt{2}G_F\varepsilon_{\alpha\beta}^{fP}[\bar{f}\gamma^\mu Pf][\bar{\nu}_\alpha\gamma_\mu P_L\nu_\beta], \quad (37)$$

<sup>14</sup>Note that for simplicity only vector couplings are assumed, neglecting the possibility of scalar, pseudoscalar, axial vector or tensor terms.

where  $f = e, u, d$ . This type of NSI is the most extensively studied in the literature, since the constraints on the charged-current-like NSI are generally stronger. Indeed, the bounds from Refs [219–222], but discarding the loop constraints on  $\varepsilon_{e\mu}^{fP}$  given the discussion in [223], result in the following  $O(10^{-1})$  constraints:

$$|\varepsilon_{\alpha\beta}^e| < \begin{pmatrix} 0.06 & 0.10 & 0.4 \\ 0.14 & 0.10 & 0.27 \\ 0.10 & 0.03 & 0.10 \\ 0.4 & 0.10 & 0.16 \\ 0.27 & 0.10 & 0.4 \end{pmatrix}, |\varepsilon_{\alpha\beta}^u| < \begin{pmatrix} 1.0 & 0.05 & 0.5 \\ 0.7 & 0.05 & 0.5 \\ 0.05 & 0.003 & 0.05 \\ 0.008 & 0.008 & 0.05 \\ 0.5 & 0.05 & 1.4 \\ & & 3 \end{pmatrix}, |\varepsilon_{\alpha\beta}^d| < \begin{pmatrix} 0.3 & 0.05 & 0.5 \\ 0.6 & 0.05 & 0.5 \\ 0.05 & 0.003 & 0.05 \\ 0.015 & 0.015 & 0.05 \\ 0.5 & 0.05 & 1.1 \\ & & 6 \end{pmatrix}.$$

Again, the operator in Eq. (37) is not gauge invariant.

### Models to evade charged lepton NSI

In Refs. [224, 225] extensions of the SM leading to neutrino NSI but avoiding their charged current counterparts were studied both through  $d = 6$  and  $d = 8$  operators. Only two examples of SM extensions giving rise to matter NSI but avoiding their charged lepton counterpart exist at  $d = 6$ . The most direct one involves an antisymmetric 4-lepton operator, generated from the exchange of virtual singly charged scalar fields. In the second possibility NSI are induced through the dimension 6 operator modifying the neutrino kinetic terms, generated by the exchange of virtual fermionic singlets. The latter operator generates the NSI in an indirect way, *i.e.*, after canonical normalization of the neutrino kinetic terms.

In the first case, NSI with electrons in matter appear through the operator [226–228]

$$\mathcal{L}_{NSI}^{d=6,as} = c_{\alpha\beta\gamma\delta}^{d=6,as} (\bar{L}_\alpha^c i\sigma_2 L_\beta) (\bar{L}_\gamma i\sigma_2 L_\delta^c), \quad (38)$$

which is generated after integrating out a charged scalar  $SU(2)$  singlet coupling to the SM lepton doublets:

$$\mathcal{L}_{int}^S = -\lambda_{\alpha\beta}^i \bar{L}_\alpha^c i\sigma_2 L_\beta S_i = \lambda_{\alpha\beta}^i S_i (\bar{\ell}_\alpha^c P_L \nu_\beta - \bar{\ell}_\beta^c P_L \nu_\alpha) \quad (39)$$

Integrating out the heavy scalars  $S_i$  generates the dimension 6 operator of Eq. (38) at tree level. We find that, given the antisymmetric flavour coupling of Eq. (39), the only NSI induced are those between  $\nu_\mu$  and  $\nu_\tau$  with electrons in matter. Bounds on these NSI can be derived from  $\mu$  and  $\tau$  decays:

$$|\varepsilon_{\mu\mu}^{m,eL}| < 8.2 \cdot 10^{-4}, |\varepsilon_{\tau\tau}^{m,eL}| < 8.4 \cdot 10^{-3}, |\varepsilon_{\mu\tau}^{m,eL}| < 1.9 \cdot 10^{-3}. \quad (40)$$

NSI in production and detection are also induced with similar strengths.

The second realization of NSI at  $d = 6$  is via the dimension 6 operator

$$\mathcal{L}_{kin}^{d=6} = -c_{\alpha\beta}^{d=6,kin} (\bar{L}_\alpha \cdot H^\dagger) i\not{\partial} (H \cdot L_\beta), \quad (41)$$

which induces non-canonical neutrino kinetic terms [229–231] though the vev of the Higgs field. After diagonalizing and normalizing the neutrino kinetic terms, a non-unitary lepton mixing matrix

is produced from this operator and hence non-standard matter interactions as well as related non-standard interactions at the source and detector are induced. The tree level generation of this operator, avoiding a similar contribution to charged leptons that would lead to flavour changing neutral currents, requires the introduction of SM-singlet fermions which couple to the Higgs and lepton doublets via the Yukawa couplings (see *e.g.* [232]). Electroweak decays set the following bounds on the operator of Eq. (41) due to the effects a deviation from unitarity of the mixing matrix would imply [224, 231, 233]:

$$\frac{v^2}{2} |c_{\alpha\beta}^{d=6,kin}| < \begin{pmatrix} 4.0 \cdot 10^{-3} & 1.2 \cdot 10^{-4} & 3.2 \cdot 10^{-3} \\ 1.2 \cdot 10^{-4} & 1.6 \cdot 10^{-3} & 2.1 \cdot 10^{-3} \\ 3.2 \cdot 10^{-3} & 2.1 \cdot 10^{-3} & 5.3 \cdot 10^{-3} \end{pmatrix}. \quad (42)$$

These bounds can be translated to constraints in the matter NSI that would be induced by a non-unitary mixing:

$$|\varepsilon_{\alpha\beta}| < \frac{v^2}{4} \left| \frac{n_n}{n_e} - \delta_{ae} - \delta_{e\beta} \right| c_{\alpha\beta}^{d=6,kin}. \quad (43)$$

Since the ratio of the neutron to electron density  $\frac{n_n}{n_e}$  is in general close to 1, this implies that the bounds on  $|\varepsilon_{e\mu}|$  and  $|\varepsilon_{e\tau}|$  are significantly stronger than the bounds on the individual  $\varepsilon_{\alpha\beta}$ . For the main constituents of the Earth's crust and mantle the factor  $\frac{n_n}{n_e} - 1$  means an additional suppression of two orders of magnitude of the NSI coefficient [224]. Thus, even if two  $d = 6$  possibilities exist to induce neutrino NSI while avoiding the corresponding charged lepton NSI, they cannot saturate the mild direct bounds from Eqs. (37) and (38) and stronger  $\mathcal{O}(10^{-3})$  bounds apply.

In Refs. [224, 225] the generation of matter NSI avoiding similar operators involving charged leptons was also studied through  $d = 8$  operators. In [224] the analysis was restricted to new physics realizations that did not involve cancellations between diagrams involving different messenger particles and, under those conditions, the bounds derived for the  $d = 6$  realizations can be translated also to the  $d = 8$  operators and, even if charged fermion NSI are avoided, no large neutrino NSI are obtained. In [225] it was shown that, allowing cancellation between diagrams involving different messengers, large neutrino NSI could be obtained by tuning away all other dangerous contributions to the charged lepton sector. However, this cancellation is only exact at zero momentum transfer, therefore constraints can be derived when probing larger energies at colliders, as studied in Ref. [234], and strong constraints  $\varepsilon < 10^{-2} - 10^{-3}$  are again recovered through LEP2 data.

Finally, the analyses of Refs. [224, 225] were limited to tree level effective operators. Therefore, they do not cover the possibility of loop-induced NSI or lighter mediators that cannot be integrated out of the theory. These can thus be ways out of the stringent constraints derived and potential sources of large NSI. Unfortunately, neither the loop generation nor lighter mediators seem to provide ways in which to evade gauge invariance and avoid the more stringent bounds leaking from the charged lepton sector. The generation of NSI via loop processes was studied in detail in Ref. [235] and applied in particular to the MSSM contributions. It was found that charged lepton flavor-violating processes constrain the induced NSI to the  $\sim 10^{-3}$  level, as with the other alternatives explored. Concerning lighter mediators, this is a way out of the effective theory treatment presented in [224, 225], but gauge invariance still poses strong constraints and, indeed, flavor-conserving interactions, much more weakly constrained in the charged lepton sector than the flavor-violating counterparts, are usually considered instead.

## Summary of the present status on NSI

The present model independent bounds on NSI were reviewed, which state that the production and detection NSI are bounded to be  $< \mathcal{O}(10^{-2})$ . Conversely the bounds on matter NSI are around one order of magnitude weaker. Saturating these mild direct bounds could lead to large observable signals at neutrino experiments. Matter NSI are however related to production and detection NSI and to flavour changing operators for charged leptons through gauge invariance. Exploring gauge invariant realizations one finds that gauge invariant NSI are constraint to be  $\mathcal{O}(10^{-3})$  making them very challenging, but not impossible, to probe at present [236, 237] facilities with dedicated new detectors or future neutrino oscillation facilities such as the Neutrino Factory [238–243]. Furthermore, the stringent constraints from gauge invariance mainly apply to flavor-violating processes, thus, fully  $SU(2)$  invariant operators can be considered with  $\mathcal{O}(10^{-2})$  entries in some of the diagonal elements, see, *e.g.* Ref. [244].

## G. Extra Forces

The term “sterile neutrino” may be misleading, and covers an extremely broad range of theoretical possibilities. The states which could be discovered in a sterile neutrino search may have little to do with the standard neutrinos from a fundamental theory point of view, and need not be “sterile” when non-standard interactions are concerned. Consider that 96% of the energy density of our Universe today resides in mysterious dark matter and dark energy, neither of which are comprised of standard model particles. From a fundamental theory point of view, there is no reason to exclude additional “sectors”, *i.e.*, a field or set of fields which have not yet been discovered due to the extreme feebleness of their interactions with the fields of the standard model. Such sectors are ubiquitous in string-based constructions and theories with extra dimensions, and it is possible that the answer to the dark matter and/or dark energy puzzles resides in a hidden sector, which contains one or more light fermions that manifests as a sterile neutrino or neutrinos that can mix with the neutrinos of the standard model. If such a hidden sector also contains at least one light boson which couples to the sterile neutrinos, sterile neutrino cosmology can be altered as well, in some cases alleviating the cosmological tension [121, 245] between more than one additional ultralight states or reconciling a large neutrino mass with cosmology [246], or even contributing to dark matter [247] or dark energy [248, 249].

The wealth of theoretical possibilities may at first seem overwhelming when one is trying to design experiments to search for hidden sectors, but effective field theory and dimensional analysis provides a useful guideline for focussing the search. At low energy, one may write a generic interaction between the standard model and a hidden sector as

$$\frac{C}{\Lambda^n} \mathcal{O}_H \mathcal{O}_{SM}, \quad (44)$$

where  $C$  is a dimensionless number,  $\Lambda$  is a scale (typically large) associated with particles that can readily interact with both sectors,  $\mathcal{O}_H$  is a hidden sector operator,  $\mathcal{O}_{SM}$  is a gauge invariant operator in the standard model, and  $n = \dim \mathcal{O}_{SM} + \dim \mathcal{O}_H - 4$ . Dimensional analysis tells us to focus on operators of low dimension in both sectors, as these are likely to be the most important.

Neutrinos offer a uniquely sensitive window into hidden sectors, because neutrinos do not carry any electric or color charge, because their masses are so small, and because the operator  $LH$  is the lowest dimension gauge invariant operator involving standard model fermions (here  $L$  refers to any

of the lepton doublets and  $H$  to the Higgs doublet). For instance, if the hidden sector contains a composite fermion  $N$  which can be created by a dimension  $5/2$  operator  $\mathcal{O}_H$ , the operator

$$\frac{C}{\Lambda} \mathcal{O}_H L H \quad (45)$$

gives an effective Dirac-type mass term connecting the standard and hidden sectors. If the compositeness scale in the hidden sector is  $f$ , the size of the resulting mass term  $m_D$  is of order  $C \frac{f}{\Lambda} v$ , where  $v$  is the Higgs vev. For instance,  $C \sim 1$ ,  $f \sim 10$  eV, and  $\Lambda \sim 10^4$  GeV would give  $m_D \sim 10^{-1}$  eV. If there were no other mass terms in the theory, such a term could be the origin of the neutrino mass, which would be of the Dirac type. In the presence of a Majorana mass term for the hidden fermion, this term could give rise to neutrino masses via a seesaw type mechanism, and provide mixing between active and sterile neutrinos [9]. Depending on the size of the Majorana and Dirac-type mass terms, the seesaw could be of the “mini” type, with sufficiently light sterile neutrinos to show up in neutrino oscillation experiments [125]. Another possibility is that the hidden fermion has a Dirac-type mass of its own, of size  $M$ , in which case the mixing between neutrinos and hidden fermions would have a mixing angle of order  $m_D/M$ , unconnected with the size of the neutrino mass. The visible neutrino masses would then have to arise via an additional term, which could be via the conventional seesaw or could be a small, Majorana-type mass in the hidden sector (this latter type possibility is known as the “inverse seesaw”). Such mixing with a heavy neutral fermion could show up as a non-unitary mixing matrix in the neutrino sector, potentially allowing for interesting observable effects such as CP violation in neutrino oscillations even with effective 2 flavor mixing [238, 250].

Mixing between neutrinos and hidden fermions provides a unique mechanism for the neutrinos to interact with any new dark forces that may be present. Such forces could be responsible for an anomalous dependence of neutrino oscillation parameters on their environment, which could reconcile otherwise conflicting discoveries [246, 251, 252].

## H. Lorentz Violation

Lorentz invariance is a fundamental ingredient in the standard model (SM) and General Relativity (GR). The discovery of the breakdown of such a fundamental symmetry that underlies our successful descriptions of nature would definitely impact our notions of space-time. The fact that we do not observe Lorentz violation in our current experiments indicate that if real, this violation should be small. Nonetheless, effects of Lorentz violation could be sizable and remain undetected because of couplings with suppressed effects, such as weak gravitational fields [253].

The various anomalous experimental results described elsewhere in this White Paper put challenges to the model of three active neutrinos. This has led to explore Lorentz violation as a possible explanation, despite the fact that sterile neutrinos are a more popular solution. One point in which Lorentz violation as a possible solution of neutrino anomalies can overtake the sterile neutrino interpretation is the preservation of the number of neutrino states to three active flavors. Additionally, the global models to be described attempt to be alternatives to the massive model instead of extensions of it. Moreover, these global models take advantage of the unconventional energy dependence in the effective Hamiltonian to minimize the number of necessary parameters.

## Violation of Lorentz invariance in the standard model

One of the most common reasons to accept Lorentz invariance as an exact symmetry of nature is the large number of tests that relativity has passed. Nevertheless, these dozens of tests have explored just a tiny fraction of the possible observable signals that could appear in the presence of Lorentz violation. Another reason is the misleading idea that Lorentz violation implies observer dependence. Physical laws are independent of any coordinate system; therefore, an observer (characterized by a set of coordinates) cannot be privileged to determine the physics of a system respect to another. This statement is sometimes confused with Lorentz invariance, despite the fact that Lorentz invariance is the symmetry of a theory under Lorentz transformations acting on the fields of the theory (this transformation is called *particle Lorentz transformation*) rather than on the coordinates used to describe the system (this transformation is called *observer Lorentz transformation*) [254].

In order to guarantee coordinate independence, the construction of a general theory would require SM operators coupled to general tensor fields. The space-time structure of these tensor fields would make them functions in a given frame, acting as background fields filling the Universe. When properties such as spin and momentum of the fields in the theory are boosted or rotated (particle Lorentz transformation) the background fields remain unaffected, making the coupling between them and the particle properties change under this type of transformation. In other words, the physics of a theory of this type is not invariant under *particle Lorentz transformations*; we say that Lorentz invariance is broken. When a Lorentz transformation is applied on the observer rather than particle properties, this is a boost or rotation of the coordinate system, both background fields and properties of the particles in the theory transform inversely, leaving the coupling invariant under coordinate changes. We say that the theory is invariant under *observer Lorentz transformations*; therefore, coordinate independent.

In 1989, Kostelecký and Samuel discovered that background fields like the ones described above could arise as vacuum expectation values of dynamic tensor fields string theory, in which Lorentz symmetry is spontaneously broken [255, 256]. Various developments led to a theoretical robust framework describing Lorentz violation for all the particles in the SM known as the Standard-Model Extension (SME) [254, 257]. The background fields, called coefficients for Lorentz violation, appear coupled to conventional SM operators of the form  $\mathcal{L}_{LV} \supset a_\alpha \bar{\psi} \gamma^\alpha \psi$ , where this term from the fermion sector exhibits coordinate invariance via the properly contracted form of the space-time indices of the coefficient for Lorentz violation  $a_\alpha$  and the SM operator. Since SM operators with odd number of free space-time indices reverse sign under CPT, the SME contains all possible terms that break CPT, which are a subset of the terms that break Lorentz symmetry [258]. For this reason, the SME is a general framework to study Lorentz and CPT violation in field theory.

SME preserves the  $SU(3) \times SU(2) \times U(1)$  gauge structure of the SM. The spontaneous  $SU(2) \times U(1)$  symmetry breaking is also maintained. Since space-time translations lie outside the Lorentz group, the violation of particle Lorentz invariance leaves unaffected the conservation of energy and momentum [257]. Moreover, since the SME was created from a Lagrangian its physics is not limited to phenomenologically-driven constructions or modified dispersion relations. In fact, any possible description that breaks Lorentz and CPT symmetry in a realistic field theory is a subset of the SME. For instance, in 1998 Coleman and Glashow [259] presented a popular framework for possible tests of Lorentz invariance at high energies that corresponds to an isotropic limit of the SME. There are also alternative approaches that violate Lorentz symmetry lying outside local quantum field theory, see, *e.g.* Refs. [260, 261].



The development of the SME triggered theoretical developments and also boosted the experimental front because for a given experiment the SME serves a guide for the key observable signatures that would appear if Lorentz invariance is broken. The results are summarized in the annually-updated *Data tables for Lorentz and CPT violation* [262]. Review articles on experimental and theoretical approaches to Lorentz and CPT violation can be found in Ref. [263, 264].

### Lorentz-violating neutrinos

The renormalizable neutrino sector of the SME is the starting point to study oscillations in the presence of Lorentz violation. The propagation of three left-handed neutrinos is described by a  $3 \times 3$  effective Hamiltonian of the form [265]

$$(h_{\text{eff}})_{ab} = E\delta_{ab} + \frac{m_{ab}^2}{2E} + (a_L)_{ab}^{\alpha}\hat{p}_{\alpha} - (c_L)_{ab}^{\alpha\beta}\hat{p}_{\alpha}\hat{p}_{\beta}E, \quad (46)$$

where the indices take the values  $a, b = e, \mu, \tau$ . The first two terms correspond to the conventional massive description of neutrino propagation, where the constant mass matrix appears with the standard  $1/E$  energy dependence. The third term breaks both Lorentz and CPT symmetry and exhibits no energy dependence. Finally, the last term grows linearly with energy and breaks only Lorentz invariance. The fact that space-time indices are properly contracted with the neutrino direction of propagation  $\hat{p}_{\alpha} = (1; -\hat{p})$  manifests coordinate invariance. The explicit dependence of the effective Hamiltonian on neutrino direction of propagation reveals the loss of invariance under particle rotations. The corresponding Hamiltonian for antineutrinos is obtained by reversing the sign of the real part of  $(a_L)_{ab}^{\alpha}$  and the imaginary part of  $(c_L)_{ab}^{\alpha\beta}$ . Notice that these coefficients also have flavor indices, meaning that these coefficients are  $3 \times 3$  matrices in flavor space. The effective Hamiltonian (46) has been used to develop formalisms for generic searches of observable signals of Lorentz violation [266, 267]. Using these formalisms, LSND [268], MINOS [269–271], IceCube [272], and MiniBooNE [273] collaborations have performed searches of this type [262].

### Global models using Lorentz violation

The variety of observable effects introduced by the Lorentz-violating terms in the effective Hamiltonian (46) is very rich. Ref. [265] presents a general classification of the key signals of Lorentz violation in neutrinos. Characterized by unconventional energy dependence, spectral anomalies are among the generic signals that arise due to the presence of non-negative powers of the energy in the effective Hamiltonian (46). Even though the most popular solution for neutrino anomalies is the incorporation of  $N$  sterile neutrino states that allow  $2 + N$  mass-square differences in a  $(3 + N) \times (3 + N)$  effective Hamiltonian for neutrinos, we can alternatively keep the three active neutrino states by using (46) and its unconventional energy dependence. Since the oscillation length is proportional to the difference of the Hamiltonian eigenvalues, positive powers of the energy can reduce the oscillation length as the energy increases and possibly produce oscillation signals in short-baseline experiments.

One of the interesting features of the effective Hamiltonian (46) is that neutrinos can oscillate even in the absence of masses. This idea was explored [274] in the construction of a simple two-parameter description known as the *bicycle* model, in which neutrinos are massless. One of the challenges of a model with non-negative powers of the energy is the description of atmospheric

neutrinos observed in Super-Kamiokande (SK) [275], which shows an excellent agreement with an oscillation length that grows linearly with energy. In the bicycle model, the elements of the effective Hamiltonian have a mixed energy dependence, specifically the non-vanishing coefficients  $\hat{a}$  and  $\hat{c}E$  in the effective Hamiltonian combine at high energy to form the dimensionless oscillation phase  $\hat{a}^2L/\hat{c}E$ . This Lorentz-violating seesaw mechanism [265, 274] makes the ratio  $\hat{a}^2/\hat{c}$  mimic the effect of a neutrino mass-squared difference, leading to the conventional  $L/E$  oscillatory signature observed in SK. In 2007 it was proved that the combination of recent long-baseline accelerator, atmospheric, and reactor data excludes this direction-dependent model [276]. Even though the use of new experimental data allows its exclusion, the bicycle model served to show that simple descriptions of neutrino oscillations are possible in the SME and that neutrino masses might be irrelevant at high energies. Recently Ref. [277] studied general isotropic textures based on the bicycle model. They conclude that massless models can easily describe atmospheric data but a tension appears between new solar and KamLAND data.

In 2006, the structure of the bicycle model motivated [278] to construct the so-called *tandem* model, a hybrid three-parameter model that involves neutrino masses at low energies and isotropic Lorentz violation that leads to a seesaw at high energies. This model is consistent with long-baseline accelerator, atmospheric, reactor, and solar data. Additionally, the tandem model is consistent with the puzzling LSND signal and the null result in KARMEN. As an extra feature, the tandem model predicted an oscillation signal at low energies in MiniBooNE one year before its observation.

Until 2011, all studies of Lorentz-violating neutrinos only considered the minimal SME, which means only renormalizable terms. Following the general ideas of the tandem model, the so-called *puma* model was proposed [279, 280]. This isotropic three-parameter model incorporates non-renormalizable terms that appear in the SME [281–283]. The breaking of Lorentz invariance is manifest by the different powers of the energy that control neutrino oscillations at high energies. A Lorentz-violating seesaw mechanism produces not only the appropriate  $L/E$  oscillatory signature but also leads to maximal  $\nu_\mu \rightarrow \nu_\tau$  mixing consistent with SK and accelerator experiments. A mass term controls oscillations at low energies, in perfect agreement with solar data and producing the  $L/E$  signature observed by KamLAND [284, 285]. The description that the puma model provides of neutrino data at low and high energies is very similar to the massive model; nonetheless, due to the unconventional energy dependence of the effective Hamiltonian, the puma differs drastically from the massive model in the mid-energy range. In particular, for the oscillation channel  $\nu_\mu \rightarrow \nu_e$  the oscillation phase grows very rapidly with energy producing an oscillation signal in MiniBooNE. While the oscillation phase gets larger with neutrino energy, the seesaw mechanism suppresses the oscillation phase at energies above 500 MeV, resulting in an oscillation signal in MiniBooNE only at low energies, in perfect agreement with the data. For the same reason, the model is consistent with null results in short-baseline high-energy experiments. An enhanced version of the puma model also produces a signal in LSND that preserves all the features mentioned above. The different features of this model make it a simple and effective alternative to the massive model and consistent with all established data and some anomalous results using less parameters. A list of many other models that make use of the effective Hamiltonian (46) is presented in Refs. [213, 286–294].

## Some types of Lorentz violation: CPT violation, non-standard interactions, and lepton-number-violating oscillations

One of the important features of the study of Lorentz violation is its connection with CPT violation, that corresponds to a subset of the terms in the SME that break Lorentz invariance. Note, however, that there are no terms that break CPT preserving Lorentz symmetry [258]. Additionally, note that as mentioned earlier, CPT-odd operators have an odd number of space-time indices (properly contracted with a coefficient with the same number of space-time indices to preserve coordinate invariance); therefore, in the SME particles and anti-particles have exactly the same masses, even in the presence of CPT violation.

Another interesting property of the study of Lorentz violation in neutrinos is the connection to another popular approach to describe neutrino oscillations, non-standard neutrino interactions (NSI) [295], discussed in Section I F. Independent of its origin, the effect of NSI in neutrino oscillations is a constant contribution to the effective Hamiltonian, producing energy-dependent mixing similar to neutrino oscillations in matter. This constant contribution is usually parameterized by a matrix  $\varepsilon_{ab}$  in flavor space. We emphasize that the resulting effective Hamiltonian is indistinguishable from (46) with nonzero  $(a_L)_{ab}^T$ . This means that analyses using NSI are studying the time component of the CPT-odd coefficient for Lorentz violation  $(a_L)_{ab}^\alpha$ .

Another important remark is that Lorentz-violating terms can also produce neutrino-antineutrino oscillations [265, 267]. The Hamiltonian (46) corresponds to the  $3 \times 3$  diagonal block of a  $6 \times 6$  Hamiltonian. A similar  $3 \times 3$  block parameterizes antineutrinos that is related to (46) by a CP transformation. When Lorentz symmetry is broken there is, however, a  $3 \times 3$  off-diagonal block that mixes neutrinos and antineutrinos given by [265]

$$h_{a\bar{b}} = i\sqrt{2}(\epsilon_+)_{\alpha}\tilde{H}_{a\bar{b}}^{\alpha} - i\sqrt{2}(\epsilon_+)_{\alpha}\hat{p}_{\beta}\tilde{g}_{a\bar{b}}^{\alpha\beta}E, \quad (47)$$

where  $(\epsilon_+)_{\alpha}$  is a complex 4-vector representing the helicity state, and the flavor indices span  $a = e, \mu, \tau$ ;  $\bar{b} = \bar{e}, \bar{\mu}, \bar{\tau}$ . Notice that the two terms in (47) are direction dependent, which exhibits explicitly that Lorentz symmetry is broken through the loss of invariance under rotations. The size of this breaking is parameterized by the coefficients for Lorentz violation  $\tilde{H}_{a\bar{b}}^{\alpha}$  and  $\tilde{g}_{a\bar{b}}^{\alpha\beta}$ . The second term in (47) also breaks CPT. The comments on unconventional energy dependence described for (46) also apply for (47). These coefficients cause lepton-number violating oscillations ( $\nu \leftrightarrow \bar{\nu}$ ). These terms also produce lepton-number preserving oscillations as a second-order effect. Details about the effects of these coefficients and their application to different experiments can be found in Ref. [267]. These lepton-number-violating oscillations have been studied as an alternative to explain the LSND and MiniBooNE anomalies [296].

## I. CPT Violation in Neutrino Oscillations and the Early Universe as an Alternative to Sterile Neutrinos

One of the most important questions of fundamental physics, that is still unanswered today, is the reason for our existence, namely why the Universe is made up mostly of matter. To put it in more microscopic terms, the important unanswered question relates to a theoretical understanding of the magnitude of the observed Baryon Asymmetry in the Universe (BAU). According to the Big Bang theory, matter and antimatter have been created at equal amounts in the early Universe. The observed charge-parity (CP) violation in particle physics [297], prompted Sakharov [298] to

conjecture that non-equilibrium physics in the early Universe produce Baryon number (B), charge (C) and charge-parity (CP) violating, but CPT *conserving*, interactions/decays of anti-particles in the early Universe, resulting in the observed baryon–anti-baryon ( $n_B - n_{\bar{B}}$ ) asymmetry. In fact there are two types of non-equilibrium processes in the early Universe that could produce this asymmetry: the first type concerns processes generating asymmetries between leptons and anti-leptons (*Leptogenesis*), while the second produce asymmetries between baryons and anti-baryons (*Baryogenesis*).

The almost 100% observed asymmetry today, is estimated in the Big Bang theory [299] to be of order:

$$\Delta n(T \sim 1 \text{ GeV}) = \frac{n_B - n_{\bar{B}}}{n_B + n_{\bar{B}}} \sim \frac{n_B - n_{\bar{B}}}{s} = (8.4 - 8.9) \times 10^{-11} \quad (48)$$

at the early stages of the expansion, *e.g.* for times  $t < 10^{-6}$  s and temperatures  $T > 1$  GeV. In the above formula  $n_B$  ( $n_{\bar{B}}$ ) denotes the (anti-)baryon density in the Universe, and  $s$  is the entropy density. Unfortunately, the observed CP violation within the standard model cannot reproduce (48) [300].

A basic assumption in all current models employing sterile neutrinos is that the *CPT symmetry* holds in the early Universe, and this produces matter and antimatter in equal amounts initially. It is then, the CP violating decays of the sterile neutrinos that produce the observed BAU, as mentioned above. Such CPT invariance is a cornerstone of all known *local effective relativistic* field theories without gravity, which current particle physics phenomenology is based upon. An interesting idea, though, is that during the Big Bang, one or more of the assumptions for the CPT theorem (Lorentz Invariance, unitarity and/or locality of interactions) break down (*e.g.* due to quantum gravity influences, that may be strong at such early times). This may result in *CPT Violation* (CPTV) and a naturally induced matter-antimatter asymmetry, without the need for extra sources of CP violation, such as sterile neutrinos [301].

What we examine below is whether such ideas are viable, in the sense that they can be realized in concrete models, in a way consistent with the known particle physics and cosmology today. The simplest possibility [302] for inducing such CPT violations in the early Universe is through particle–anti-particle mass differences  $m \neq \bar{m}$ . These would affect the (anti) particle phase-space distribution functions

$$f(E, \mu) = [\exp(E - \mu)/T \pm 1]^{-1}, \quad E^2 = p^2 + m^2 \quad (49)$$

and similarly for anti-matter, upon the replacements  $m \rightarrow \bar{m}$ ,  $\mu \rightarrow \bar{\mu}$  (from now on, overlined quantities refers to anti-particles). Mass differences between particles and anti-particles,  $\bar{m} \neq m$ , generate a matter anti-matter asymmetry in the relevant densities

$$n - \bar{n} = g_{d.o.f.} \int \frac{d^3p}{(2\pi)^3} [f(E, \mu) - f(\bar{E}, \mu)], \quad (50)$$

where  $g_{d.o.f.}$  denotes the number of degrees of freedom of the particle species under study.

Upon making the quite reasonable assumption [302] that the dominant contributions to baryon asymmetry come from quark–anti-quark mass differences, and that their masses are increasing, say, linearly with the temperature  $m \sim gT$  (with  $g$  the QCD coupling constant), one can provide estimates for the induced baryon asymmetry by the fact that the maximum quark–anti-quark mass difference is bounded by the current experimental bound on proton–anti-proton mass difference,



Figure 10. A generic CPT-violating neutrino spectrum that can explain MINOS results.

$\delta m_p = |m_p - \bar{m}_p|$ , which is known to be less than  $\delta m_p < 2 \cdot 10^{-9}$  GeV. This leads to the following estimate for the baryon( $n_B$ )-to-photon( $n_\gamma$ )-density ratio in the Universe, at temperature  $T$  [302]:

$$\beta_T = \frac{n_B}{n_\gamma} = 8.4 \times 10^{-3} \frac{m_u \delta m_u + 15 m_d \delta m_d}{T^2}, \quad \delta m_q = |m_q - \bar{m}_q|. \quad (51)$$

Unfortunately, for  $n_\gamma \sim 0.24 T^3$ , which is the photon equilibrium density at temperature  $T$ , this produces too small BAU compared to the observed one. To reproduce the observed  $\beta_{T=0} \sim 6 \cdot 10^{-10}$  one would need  $\delta m_q(T = 100 \text{ GeV}) \sim 10^{-5} - 10^{-6} \text{ GeV} \gg \delta m_p(T = 0)$ , which is rather unnatural, although admittedly such a scenario cannot be excluded on theoretical grounds.

However, active (*light*) neutrino–antineutrino mass differences alone may reproduce BAU; some phenomenological models in this direction have been discussed in [260], considering, for instance, particle–anti-particle mass differences for active neutrinos compatible with current oscillation data. This leads to the result

$$n_B = n_\nu - n_{\bar{\nu}} \simeq \frac{\mu_\nu T^2}{6} \quad (52)$$

yielding  $n_B/s \sim \frac{\mu_\nu}{T} \sim 10^{-11}$  at  $T \sim 100 \text{ GeV}$ , in agreement with the observed BAU. Above,  $s$  denotes the entropy density, and  $n_\nu, \mu_\nu$  are the neutrino densities and chemical potential respectively.

It should also be noticed that CPT violating spectra can not only accommodate the established oscillation experiments but also provide distinguishing features to be observed in future ones. A CPT violation of the kind represented in Fig. 10, can accommodate the intriguing results of the MINOS data, indicating possible differences between the neutrino and antineutrino oscillation parameters. The CPT-violating features in this case are encapsulated basically in the atmospheric channel :

$$\Delta \bar{m}_{atm}^2 \approx 0.0030 \text{ eV}^2, \quad \sin^2 2\bar{\theta}_{23} \approx 0.8, \quad (53)$$

and

$$\Delta \bar{m}_{atm}^2 \approx 0.0025 \text{ eV}^2, \quad \sin^2 2\theta_{23} \approx 1. \quad (54)$$

Notice however that no CPT-violating spectra can easily accommodate LSND without conflicting with other existing experiments.

But particle–anti-particle mass differences may not be the only way by which CPT is violated. As discussed in [303, 304], quantum gravity fluctuations in the structure of space-time, that may be strong in the early Universe, may act as an *environment* inducing decoherence for the (anti-)neutrinos, but with couplings between the particles and the environment that are different between

the neutrino and antineutrino sectors. Once there is decoherence for a low-energy (compared to the Planck scale  $M_{Pl} \simeq 10^{19}$  GeV) observer, the effective CPT symmetry generator may be *ill-defined* as a quantum mechanical operator, according to a theorem by Wald [305], leading to an intrinsic violation of CPT symmetry. This type of violation may characterize models of quantum gravity with stochastic space-time fluctuations due, for instance, to gravitational space-time defects, as is the case of certain brane models [306–308]. In such a case, there may be a slight mismatch in the strength of the stochastic space-time fluctuations between particle and anti-particle sectors, leading to different decoherence parameters to describe the interaction of the gravitational environment with matter.

In [303, 304], simple models of Lindblad decoherence [309], conjectured to characterize also quantum-gravity-induced CPT violating decoherent situations [310, 311], have been considered for neutrinos [312], assuming, though, non-trivial decoherence parameters *only* in the anti-particle sector, consistently with the lack of any experimental evidence to date [313–315] for vacuum decoherence in the particle sector. The antineutrino decoherence parameters (with dimension of energy) had a mixed energy dependence. Some of the eight coefficients (necessary to parameterize, in a minimal way, a diagonal Lindblad decoherence matrix for three-generation neutrinos, assumed for simplicity in [303, 304]) were proportional to the antineutrino energy

$$\bar{\gamma}_i = \frac{T}{M_P} E, \quad i = 1, 2, 4, 5 \quad (55)$$

while the remaining ones (sub-dominant) were inversely proportional to it

$$\bar{\gamma}_j = 10^{-24} \frac{1}{E}, \quad j = 3, 6, 7, 8, \quad (56)$$

in the notation of [303, 304]. The model is phenomenological and its choice was originally motivated by fitting the LSND “anomalous data” in the antineutrino sector [114] with the rest of the neutrino data (in fact, for such a purpose, the coefficient  $T/M_P$  in  $\bar{\gamma}_i$ ,  $i = 1, \dots, 5$  was assumed to get a value  $T/M_P \sim 10^{-18}$ , *i.e.*, “frozen” at the Temperature range of Electroweak Symmetry Breaking (EWSB) in the Universe). However, the model may be disentangled from this issue and presented as a candidate model entailing CPT violation that can lead to phenomenologically acceptable estimates for the BAU today.

In this context, one can derive [303, 304] an active (light)  $\nu - \bar{\nu}$  asymmetry of order

$$\mathcal{A} = \frac{n_\nu - n_{\bar{\nu}}}{n_\nu + n_{\bar{\nu}}} = \frac{\bar{\gamma}_1}{\sqrt{\Delta m^2}} = \frac{T}{M_P} \cdot \frac{E}{\sqrt{\Delta m^2}}, \quad (57)$$

where  $\Delta m^2$  denotes the (atmospheric) neutrino mass squared difference, which plays the role of a characteristic low mass scale in the problem (analogous to the difference in widths  $\Delta\Gamma$  between nearly mass generate Kaon states, entering the final expression for the dimensionless decoherence parameters  $(\alpha, \beta, \gamma)/\Delta\Gamma$  in the notation of the CPT violating decoherence models of [310, 311], which physical processes depend upon). This lepton number violation is communicated to the baryon sector by means of baryon plus lepton ( $B + L$ ) number conserving sphaleron processes. The so-induced Baryon number in the Universe today may be estimated as [303]

$$B = \frac{n_\nu - n_{\bar{\nu}}}{s} \sim \mathcal{A} \frac{n_\nu}{g^* n_\gamma}, \quad (58)$$

with  $n_\gamma$  the photon number density and  $g^*$  the effective number of degrees of freedom (at the temperature where the asymmetry is developed, in the model of [303] this is the EWSB temperature),

which depends on the matter content of the model (with a typical range  $g^* \in [10^2 - 10^3]$ ). Taking into account that in the model considered in [303]  $\mathcal{A} \sim 10^{-6}$  at the EWSB Temperature range, one can therefore see that the observed BAU may be reproduced in this case without the need for extra sources of CP violation and thus sterile neutrinos.

Unfortunately, at present such models lack microscopic understanding, although progress in this direction is currently being made. One issue that arises with such models concerns the preferential role of neutrinos on being involved in this early Universe quantum-gravity-decoherence-induced CPT violation in contrast to other particles in the standard model (SM). Within some microscopic models of space-time foam, involving populations of point-like brane defects (D-particles) puncturing three(or higher)-spatial dimension brane worlds [306–308], such a preferred role may be justified by electric charge conservation: the representation of SM particles as open strings, with their ends attached to the brane worlds, prevents capture and splitting of open strings carrying electric fluxes by the D-particles. This is due to the fact that the latter are electrically neutral and thus electric charge would not have been conserved if such processes had taken place. Hence, the D-particle foam is transparent to charged excitations of the SM, leaving neutral particles, in particular neutrinos, to be vulnerable to the foam effects. Of course to construct realistic cosmologies from such models is still an open issue.

Before closing, we would like to discuss one more scenario [316–319] of neutrino–antineutrino CPT violation, induced by local curvature effects in geometries of the early Universe, and its connection to leptogenesis/baryogenesis. The scenario is based on the well-known fact that fermions in curved space times exhibit a coupling of their spin to the curvature of the background space time. In fact, the Dirac Lagrangian density of a fermion can be re-written as (the analysis can also be adapted to incorporate Majorana neutrinos, with similar results):

$$\mathcal{L} = \sqrt{-g} \bar{\psi} (i\gamma^a \partial_a - m + \gamma^a \gamma^5 B_a) \psi, \quad B^d = \epsilon^{abcd} e_{b\lambda} (\partial_a e_c^\lambda + \Gamma_{\nu\mu}^\lambda e_c^\nu e_a^\mu), \quad (59)$$

in a standard notation, where  $e_a^\mu$  are the vielbeins,  $\Gamma_{\alpha\beta}^\mu$  is the Christoffel connection and Latin (Greek) letters denote tangent space (curved space-time) indices. The space-time curvature background has, therefore, the effect of inducing an “axial” background field  $B_a$  which can be non trivial in certain axisymmetric (in general anisotropic) space time geometries, such as certain Bianchi-type Cosmologies, that may characterize epochs of the early Universe, according to the assumptions of [316–319]. If the background axial field  $B_a$  is constant in some local frame, this breaks CPT symmetry, and the dispersion relation of neutrinos in such backgrounds differs from that of antineutrinos:

$$E = \sqrt{(\vec{p} - \vec{B})^2 + m^2} + B_0, \quad \bar{E} = \sqrt{(\vec{p} + \vec{B})^2 + m^2} - B_0. \quad (60)$$

The relevant neutrino asymmetry is then generated through the same steps (cf. (49), (50)) as in the case where CPT is violated through particle–anti-particle mass differences, leading to the following neutrino-antineutrino density differences in, say, Bianchi II Cosmologies [316–319]:

$$\Delta n_\nu \equiv n_\nu - n_{\bar{\nu}} \sim g^* T^3 \left( \frac{B_0}{T} \right), \quad (61)$$

with  $g^*$  the number of degrees of freedom for the (relativistic) neutrino. At temperatures  $T < T_d$ , with  $T_d$  the decoupling temperature of the lepton-number violating processes, the ratio of the net lepton number  $\Delta L$  (neutrino asymmetry) to entropy density (which scales as  $T^3$ ) remains constant,

$$\Delta L(T < T_d) = \frac{\Delta n_\nu}{s} \sim \frac{B_0}{T_d} \quad (62)$$

which, for  $T_d \sim 10^{15}$  GeV and  $B_0 \sim 10^5$  GeV, implies a lepton asymmetry (leptogenesis) of order  $\Delta L \sim 10^{-10}$ , in agreement with observations. The latter can then be communicated to the baryon sector to produce the observed BAU (baryogenesis), either by a  $B - L$  conserving symmetry in the context of Grand Unified Theories (GUT), or via  $(B + L)$ -conserving sphaleron processes, as in the decoherence-induced CPT violating case of [303, 304], mentioned previously.

From the above analysis, we therefore conclude that it is plausible to have CPT violation in the early Universe, due to a variety of reasons. These range from (exotic) quantum-gravity stochastic space-time fluctuations, inducing decoherence on low-energy matter of different strength between particle and anti-particle sectors, to standard general relativity background effects due to anisotropic space-time geometries that may characterize such early epochs of the Universe. Such CPT violating scenarios may generate differences between neutrino and antineutrino populations that can in turn reproduce, via subsequent sphaleron processes or  $B - L$  conserving GUT symmetries, the observable BAU without the presence of sterile neutrinos, unlike the standard CPT violating scenario involving only particle–anti-particle mass differences. The cosmology and particle-physics phenomenology of such scenarios are of course at their infancy, but we believe they are worth pursuing.



## II. ASTROPHYSICAL EVIDENCE

### A. Cosmology

In the early universe, neutrinos of left-handed chirality are held in a state of thermal equilibrium with other standard model particles by weak interactions. As the universe expands and the thermal plasma cools, interactions become increasingly infrequent. When the plasma cools to a temperature of order 1 MeV, the interaction rate per neutrino drops below the universal expansion rate; the neutrinos therefore “decouple” from the thermal plasma. Because neutrino decoupling happens while the neutrinos are ultra-relativistic, they retain their relativistic Fermi-Dirac phase space distribution parametrized by a temperature, and possibly a nonzero chemical potential.

Shortly after neutrino decoupling is the event of electron-positron annihilation at  $T \sim 0.2$  MeV. The energy released in this process “reheats” the photon population, but this reheating is not felt by the neutrinos because they have already decoupled. The net effect is that the neutrinos emerge from the event a little colder than the photons. Using entropy conservation arguments and assuming instantaneous neutrino decoupling, one can show that

$$T_\nu = \left(\frac{4}{11}\right)^{1/3} T_\gamma, \quad (63)$$

where  $T_\nu$  and  $T_\gamma$  are the neutrino and the photon temperatures, respectively, after  $e^+e^-$  annihilation.

In current usage, the relation (63) is generally taken to *define* the standard neutrino temperature after  $e^+e^-$  annihilation, in spite of finite temperature QED effects and non-instantaneous decoupling which render the actual neutrino energy density and number density a little higher than is implied by this relation. The extra energy density is commonly absorbed into the definition of the *effective number of neutrino families*  $N_{eff}$  via

$$\rho_\nu = N_{eff} \frac{7\pi^2}{120} T_\nu^4. \quad (64)$$

Here,  $\rho_\nu$  is the total neutrino energy density deep in the radiation domination era (but after  $e^+e^-$  annihilation) when the neutrinos are ultra-relativistic, the factor  $(7\pi^2/120)T_\nu^4$  denotes the energy density in one family of relativistic neutrinos with temperature  $T_\nu$ , as defined in equation (63), and  $N_{eff} = 3.046$  in the standard model with three generations of fermions [320]. Note that because the parameter  $N_{eff}$  is defined in relation to the neutrino energy density in an epoch when the neutrinos are ultra-relativistic, there is no ambiguity in the definition (64) even if the neutrinos should become nonrelativistic at a later time because of their nonzero masses (provided they do not exceed the eV-mass scale).

Cosmology is sensitive to the effective number of neutrino families  $N_{eff}$  primarily because energy density in relativistic particles affects directly the universe’s expansion rate during the radiation domination era. In the epoch immediately after  $e^+e^-$  annihilation, the expansion rate  $H(t)$  is given by

$$H^2(t) \simeq \frac{8\pi G}{3}(\rho_\gamma + \rho_\nu). \quad (65)$$

With the photon energy density  $\rho_\gamma$  being extremely well determined from measurements of the cosmic microwave background (CMB) temperature, constraints on  $H(t)$  in the early universe can

be interpreted as bounds on  $\rho_\nu$  and hence  $N_{eff}$ . From the particle physics perspective, a thermal population of light sterile neutrinos is one possible cause of a non-standard  $N_{eff}$ . However, it is important to emphasize that, as far as  $H(t)$  is concerned, any thermal background of light particles such as axions and axion-like particles, hidden sector photons, majorons, or even gravitons will contribute to the relativistic energy density. Likewise, any process that alters the thermal abundance of neutrinos (*e.g.*, a low reheating temperature) or affects directly the expansion rate itself (*e.g.*, a time-dependent Newton’s constant  $G$ ) can mimic a non-standard  $N_{eff}$  value.

In the following, we describe first the production of a thermal light sterile neutrino population in the early universe. We then discuss the various signatures of light sterile neutrinos in cosmological observables such as the light elemental abundances from big bang nucleosynthesis (BBN), the CMB anisotropies and the large-scale structure (LSS) distribution, as well as the strength of evidence for sterile neutrinos from the current generation of observations.

### **Sterile neutrino thermalization**

A sterile neutrino that mixes with an active neutrino can augment the relativistic energy density in the early universe through oscillation-based thermal production in the early universe, leading to an  $N_{eff} > 3.046$ . The primary thermalization process is collisional production from active neutrinos that oscillate into sterile neutrinos, with collisions “forcing” the evolved neutrino back into a flavor state. The oscillation production is enhanced with a larger mixing amplitude  $\sin^2 2\theta$  and more rapid (shorter wavelength) oscillations due to a larger  $\Delta m^2$ . This effect and the region of parameter space leading to thermalization of the sterile neutrino was found by the early work of [321]. If sterile neutrinos do become thermalized, then we expect them to have the same temperature as the active neutrinos.

Most analyses so far have focused exclusively on two-neutrino mixing solutions of sterile neutrino thermalization, although multiple flavor effects were studied in references [322, 323], and in [324, 325] using the momentum-averaged approximation. The conclusions of these works were that the LSND neutrino mixing parameters would inevitably lead to thermalization of the two or more sterile neutrinos associated with the signal. We emphasize however that a full thermalization calculation involving momentum-dependent density matrices for 3 active and  $N_s$  sterile flavors has never been performed, though studies of the range of physical effects have been done [326].

Thermalization of the sterile neutrino can be suppressed by the presence of a large lepton asymmetry ( $L \sim 10^{-5}$ ). Such an asymmetry alters the matter potential of the active-sterile system, thereby suppressing the effective mixing angle and reducing or stopping the thermal production of the sterile neutrinos [327]. The required lepton asymmetry may be pre-existing, or, interestingly, dynamically generated by the multi-flavored active-sterile system [328]. The multi-flavored effects of lepton-number generation, the conversion of this lepton number into other flavors, and thermalization was studied in detail in reference [326]. However, as discussed above, a full multi-flavor density matrix calculation has not been performed. The main conclusions of the work performed so far is that the sterile neutrino or neutrinos associated with the LSND oscillation interpretation would be thermalized except for limited cases of inherent lepton number generation or in the presence of a pre-existing lepton number.

## Big Bang Nucleosynthesis

### Sterile neutrino and primordial elemental abundances

The formation of light elements from protons and neutrons commences at a temperature of order 0.1 MeV with the synthesis of deuterium, which subsequently fuels a number of nuclear reactions, thereby enabling the production of heavier nuclei. Because of its large binding energy, almost all of the initially available neutrons end up bound in  ${}^4\text{He}$  nuclei, resulting in a helium-4 mass fraction

$$Y_p \equiv \frac{4n_{\text{He}4}}{n_n + n_p} \quad (66)$$

of order 0.25, where  $n_{\text{He}4}$ ,  $n_n$ , and  $n_p$  are the number densities of  ${}^4\text{He}$ , neutron and proton respectively. After freeze-out of the nuclear processes and decay of unstable isotopes, small amounts of deuterium and  ${}^3\text{He}$  ( $\text{D}/\text{H} \sim {}^3\text{He}/\text{H} \sim \mathcal{O}(10^{-5})$ ), as well as traces of  ${}^6\text{Li}$  and  ${}^7\text{Li}$  remain in addition. In standard BBN, barring experimental uncertainties in the nuclear reaction rates and the free neutron lifetime, the baryon-to-photon ratio  $\eta$  alone determines the elemental abundances.

Neutrinos are important in this picture for two reasons. Firstly, electron neutrinos participate directly in the charged current weak interactions that determine the neutron-to-proton ratio,

$$\begin{aligned} \nu_e + n &\leftrightarrow p + e^-, \\ \bar{\nu}_e + p &\leftrightarrow n + e^+. \end{aligned} \quad (67)$$

Secondly, neutrinos of all flavors influence the expansion rate of the universe prior to and during BBN via equation (65). Changing this expansion rate alters the neutron-to-proton ratio at the onset of BBN and hence the light element abundances, most notably the abundance of  ${}^4\text{He}$ .

The presence of sterile neutrinos therefore has the potential to change BBN in two ways: distorting the  $\nu_e$  phase space distribution via flavor oscillations, and enhancing the Hubble expansion rate by contributing to  $N_{eff}$ . For sterile neutrinos with mixing parameters currently favored by terrestrial experiments, however, only the second effect is at play. This is because the large mass-square difference  $\Delta m^2 \sim 1 \text{ eV}^2$  and mixing  $\sin^2 2\theta \sim 10^{-3}$  between the sterile and the active (standard model) neutrino states essentially guarantee full thermalization of the sterile species prior to the decoupling of the active neutrinos. Therefore, the phase space distribution of the sterile states follows closely those of the active neutrinos, namely, a relativistic Fermi-Dirac distribution, thereby contributing  $\Delta N_{eff} = 1$  per sterile species. This also means that active-sterile flavor oscillations after decoupling will not cause the  $\nu_e$  phase space distribution to deviate from a relativistic Fermi-Dirac distribution.<sup>15</sup> Thus, under this approximation, the standard BBN scenario need only be extended with one extra parameter, namely,  $N_{eff}$ , to incorporate the effects of sterile neutrinos.

### Current observational constraints

The limiting factor in using BBN to constrain cosmology is the presence of significant systematic uncertainties in the astrophysical measurements of all primordial abundances. These uncertainties

---

<sup>15</sup>In the general case with arbitrary  $\Delta m^2$  and  $\sin^2 2\theta$ , it is necessary to solve the quantum kinetic equations through BBN in order to establish both the total neutrino energy density *and* the exact form of the  $\nu_e$  phase space distribution.

Table II. Current constraints on  $N_{eff}$  from BBN, with 68% (95%) uncertainties. Different results for the same nominal data set are due to different measurements of  $Y_p$ .

Model	Data	$N_{eff}$	Ref.	
$\eta+N_{eff}$	$\eta_{CMB}+Y_p+D/H$	$3.8^{(+0.8)}_{(-0.7)}$	[331]	
	$\eta_{CMB}+Y_p+D/H < (4.05)$		[332]	
	$Y_p+D/H$	}	$3.85 \pm 0.26$	[333]
			$3.82 \pm 0.35$	[333]
$3.13 \pm 0.21$			[333]	
$\eta+N_{eff}, (\Delta N_{eff} \equiv N_{eff} - 3.046 \geq 0)$	$\eta_{CMB}+D/H$	$3.8 \pm 0.6$	[122]	
	$\eta_{CMB}+Y_p$	$3.90^{+0.21}_{-0.58}$	[122]	
	$Y_p+D/H$	$3.91^{+0.22}_{-0.55}$	[122]	

essentially preclude the use of  $^3\text{He}$  and  $\text{Li}$  abundance measurements for precision cosmology, leaving us with the helium-4 mass fraction  $Y_p$  and the deuterium abundance  $D/H$  as the only reasonable probes (see, *e.g.*, [329] and [330] for a discussion of progress in the determination of these two abundances).

Generally,  $Y_p$  is regarded as the most sensitive probe of  $N_{eff}$ . This can be understood in the following way: increasing the radiation energy density leads to a higher expansion rate, which means that the reactions (67) freeze-out at an earlier time, thus enhancing the neutron-to-proton ratio at the onset of BBN. Because almost all neutrons eventually wind up bound in  $^4\text{He}$  nuclei, the resulting  $Y_p$  will be larger. The deuterium abundance  $D/H$ , on the other hand, is mainly sensitive to  $\eta$ . Combination of the two therefore constrains the two free parameters of the standard BBN+sterile neutrino scenario.

Optionally, under the assumption that  $\eta$  remains constant between the epochs of BBN and of photon decoupling, the primordial abundance data can be complemented by the very precise CMB constraint on the baryon-to-photon ratio  $\eta_{CMB}$  (which is obtained by combining the measurement of the photon energy density  $\omega_\gamma$  via the CMB energy spectrum, and the baryon energy density  $\omega_b$  inferred from the CMB anisotropy angular power spectra).

Current estimates suggest that  $N_{eff} \sim 3\text{--}4$  is compatible with observations, with perhaps a slight preference for higher-than-standard values [122, 331–333] (see table II). Within the minimal BBN scenario, models with more than one fully thermalized extra species seem at odds with current BBN data. These results hold even after folding the uncertainties in the nuclear reaction rates and the free neutron lifetime into the analysis [122, 333]. If a higher value turns out to be required by late time observables such as the CMB anisotropies and the large-scale structure distribution, its explanation will presumably require additional non-standard physics such as the decay of massive particles after BBN.

Finally, we stress that the picture in which the sterile sector can be described by just one parameter  $N_{eff}$  may not hold in more complicated scenarios, such as models with a non-zero lepton asymmetry (see *e.g.* [326, 334, 335]).

## Cosmic microwave background and large-scale structure

Unlike BBN, probes of the universe's late-time inhomogeneities such as the CMB anisotropies and the large-scale structure distribution are not sensitive to the flavor content of the neutrino sector, only to its contribution to the stress-energy tensor. If neutrinos are massless, then the  $N_{eff}$  parameter as defined in equation (64) alone characterizes their effects on the universe's evolution. If neutrinos are massive, then in principle it is necessary to know the exact form of the neutrino phase space distribution in order to solve the evolution equations for the inhomogeneities exactly. However, the current generation of late-time cosmological probes are not sensitive to deviations of the neutrino phase space distribution from the relativistic Fermi-Dirac distribution [336, 337]. Therefore, it suffices to discuss the neutrino sector only in terms of the neutrino masses  $m_{\nu_i}$  and the  $N_{eff}$  parameter.

### Signatures of light sterile neutrinos in the CMB

Additional relativistic energy density due to a thermal population of light particles affects the CMB anisotropies mainly through its effect on the epoch around matter-radiation equality. If the particle has a rest mass substantially below the temperature of the thermal population around matter-radiation equality (a rough estimate for neutrinos might be  $m_{\nu_i} \ll 0.1$  eV), then it alters the equality redshift  $z_{eq}$  according to

$$1 + z_{eq} = \frac{\omega_m}{\omega_\gamma} \frac{1}{1 + 0.227N_{eff}}, \quad (68)$$

where  $\omega_m$  and  $\omega_\gamma$  are the present-day matter and photon energy densities respectively. Because observations of the CMB temperature anisotropies strongly constrain  $z_{eq}$  through the ratio of the first and the third acoustic peaks [338], measuring  $z_{eq}$  essentially fixes the ratio of the energy density in matter to the energy density in radiation. However, equation (68) also implies that  $N_{eff}$  and the physical matter density  $\omega_m$  are strongly degenerate parameters.

If the particle's rest mass is such that the thermal population transits from an ultra-relativistic to a non-relativistic distribution around matter-radiation equality (a crude estimate for neutrinos is  $m_{\nu_i} \sim 0.1\text{--}1$  eV), then  $z_{eq}$  depends also somewhat on the particle's mass to temperature ratio. In other words, we expect some degeneracy of  $N_{eff}$  with the particle's rest mass. Heavier and/or colder particle populations (*e.g.*,  $m_{\nu_i} \gg 10$  eV) that have already become fully non-relativistic before matter-radiation equality is a non-relativistic matter component in the context of CMB and LSS. For this reason, the  $N_{eff}$  parameter does not encompass keV-mass sterile neutrinos in CMB and LSS studies.

A non-standard  $N_{eff}$  also affects the sound horizon  $r_s$  at the time of CMB decoupling  $\tau_*$ ,

$$\begin{aligned} r_s &= \int_0^{\tau_*} d\tau' c_s(\tau') \\ &\simeq \frac{1}{H_0} \sqrt{\frac{4}{3} \frac{a_{eq}}{\Omega_m R(z_{eq})}} \ln \left[ \frac{\sqrt{1 + R(z_*)} + \sqrt{R(z_*) + R(z_{eq})}}{1 + \sqrt{R(z_{eq})}} \right], \end{aligned} \quad (69)$$

where  $R(z) \equiv (3/4)(\rho_b/\rho_\gamma) = (3/4)(\omega_b/\omega_\gamma)a$ , and  $H_0 = 100 h \text{ km s}^{-1} \text{ Mpc}^{-1}$  is the present-day Hubble parameter. The sound horizon in turn affects the angular position of the acoustic peaks via

$$\theta_s = \frac{r_s}{D_A}, \quad (70)$$

where  $D_A$  is the angular diameter distance to the last scattering surface.

Since both  $z_{\text{eq}}$  and  $\omega_b$ —and hence  $R(z_{\text{eq}})$  and  $R(z_*)$ —are well-constrained parameters<sup>16</sup> ( $\omega_b$  is constrained via the ratio of the odd to the even acoustic peaks), equations (69) and (70) imply that  $\omega_m = \Omega_m h^2$ —and hence  $N_{\text{eff}}$  through  $z_{\text{eq}}$ —is exactly degenerate with those parameters governing the angular diameter distance  $D_A$  in its effects on  $\theta_s$ . In the simplest  $\Lambda$ CDM model<sup>17</sup> extended with a freely varying  $N_{\text{eff}}$  parameter, holding  $\omega_b$  and  $z_{\text{eq}}$  fixed we find from equations (69), and (70) that

$$\theta_s \propto \frac{\Omega_m^{-1/2}}{\int_{a_*}^1 \frac{da}{a^2 \sqrt{\Omega_m a^{-3} + (1 - \Omega_m)}}}. \quad (71)$$

This relation implies that while  $\theta_s$  constrains the parameter combination  $\Omega_m = \omega_m/h^2$ , it does not constrain  $\omega_m$  and  $h$  individually. Hence, a strong correlation can be expected between  $N_{\text{eff}}$  and the present-day Hubble parameter  $H_0$ . In more complex models, degeneracies of  $N_{\text{eff}}$  with the spatial curvature  $\Omega_k$  and the dark energy equation of state are also possible.

Because of the strong  $N_{\text{eff}}-\omega_m$  and  $N_{\text{eff}}-H_0$  degeneracies, measurements of the CMB acoustic peaks alone generally do not completely constrain  $N_{\text{eff}}$ . However, non-interacting, free-streaming relativistic particles such as neutrinos leave another important imprint on the CMB anisotropies through their anisotropic stress [339]. This anisotropic stress suppresses the amplitude of higher harmonics in the temperature anisotropy spectrum ( $\ell > 200$ ) [340] and is phenomenologically somewhat degenerate with the effects of changing the primordial fluctuation amplitude. However, because anisotropic stress also shifts slightly the higher acoustic peak positions [340], it has been possible since the measurement of the third acoustic peak by WMAP after 5 years of observations to constrain  $N_{\text{eff}}$  from below using WMAP data alone, with  $N_{\text{eff}} = 0$  excluded at better than 99.5% confidence in a  $\Lambda$ CDM+ $N_{\text{eff}}$  fit [338, 341]. An upper limit on  $N_{\text{eff}}$  is however not yet possible with WMAP data alone.

More recently, measurements of the CMB damping tail ( $\ell \gtrsim 1000$ ) by ACT and SPT has provided us with an additional handle on  $N_{\text{eff}}$  through the effect of  $z_{\text{eq}}$  on diffusion damping (or Silk damping). The diffusion damping scale  $r_d$  can be approximated as [342]

$$\begin{aligned} r_d^2 &\simeq (2\pi)^2 \int_0^{a_*} \frac{da}{a^3 \sigma_T n_e H} \left[ \frac{R^2 + (16/15)(1+R)}{6(1+R)^2} \right] \\ &\simeq \frac{(2\pi)^2}{H_0 \sqrt{\Omega_m}} \int_0^{a_*} \frac{da}{a \sqrt{a + a_{\text{eq}}} \sigma_T n_e} \left[ \frac{R^2 + (16/15)(1+R)}{6(1+R)^2} \right] \end{aligned} \quad (72)$$

where  $\sigma_T$  is the Thomson scattering cross-section, and  $n_e$  is the free electron number density. As with  $\theta_s$ , it is the angular diffusion scale  $\theta_d = r_d/D_A$  that we measure. Thus, assuming fixed values

<sup>16</sup>The decoupling redshift  $z_*$  also depends logarithmically on the Hubble parameter  $h$ . We ignore this dependence here for our crude estimates.

<sup>17</sup>The vanilla  $\Lambda$ CDM model assumes (i) a flat spatial geometry, (ii) an energy content of cold dark matter, baryons, dark energy due to a cosmological constant, and massless neutrinos, and (iii) adiabatic, scalar-only primordial perturbations described by a nearly scale-invariant power spectrum.

of  $z_{eq}$ ,  $\omega_b$ ,  $a_*$ , and  $n_e$ , and using the definition of  $\theta_s$  in equation (70), we can show that

$$\theta_d \propto (\Omega_m H_0^2)^{1/4} \theta_s. \quad (73)$$

In other words, once  $\theta_s$  has been established by large angular-scale CMB experiments such as WMAP, measurement of  $\theta_d$  in the CMB damping tail allows us to pin down the physical matter density  $\omega_m$  and hence  $N_{eff}$  through the  $N_{eff}$ – $\omega_m$  degeneracy independently of the details of  $D_A$  (e.g., spatial curvature, dark energy equation of state, etc.). The measurement of  $\theta_d$  by ACT and SPT has allowed us to place constraints on  $N_{eff}$  also from above using CMB data alone [342–344].

In deriving equation (73) we have had to assume fixed values of  $a_*$  and  $n_e$ . These quantities can in principle be changed, while keeping the baryon density  $\omega_b$  constant, by altering the helium-4 mass fraction  $Y_p$ . Therefore, we expect a degeneracy between  $N_{eff}$  and  $Y_p$ . At present, this degeneracy can be overcome by either assuming a fixed value of  $Y_p = 0.24$ , or by implementing a BBN consistency relation linking each pair of  $\{\omega_b, N_{eff}\}$  to a specific value of  $Y_p$  [345].

### Signatures of light sterile neutrinos in the LSS

Two quantities determine the general shape of the present-day LSS matter power spectrum  $P(k)$ : the comoving wavenumber

$$\begin{aligned} k_{eq} &\equiv a_{eq} H(a_{eq}) \\ &\simeq 4.7 \times 10^{-4} \sqrt{\Omega_m (1 + z_{eq})} \text{ hMpc}^{-1} \end{aligned} \quad (74)$$

at matter-radiation equality, and the baryon-to-matter fraction

$$f_b \equiv \frac{\omega_b}{\omega_m}. \quad (75)$$

The former determines the position of the “turning point” of  $P(k)$ , while the latter controls the power suppression due to baryon acoustic oscillations at  $k > k_{eq}$ . If some of the neutrinos are massive and non-relativistic today, then a third parameter

$$f_\nu \equiv \frac{\omega_\nu}{\omega_m} = \frac{\sum_i m_{\nu,i}/94 \text{ eV}}{\omega_m} \quad (76)$$

controls power suppression at  $k > k_{eq}$  due to the neutrinos’ thermal velocity dispersion.

If there are extra neutrino species and all neutrino species are still relativistic today, then consistency with the CMB-determined  $z_{eq}$  and  $\Omega_m$  implies that  $k_{eq}$  is unaffected (recall that  $k$  is measured in units of  $\text{hMpc}^{-1}$ ). However, because the physical matter density  $\omega_m$  is now higher while  $\omega_b$  remains unchanged, the baryon fraction  $f_b$  decreases. This leads to a higher matter fluctuation amplitude today at  $k > k_b$ , where  $k_b$  corresponds roughly to the comoving Hubble rate at the baryon drag epoch (i.e., when baryons decouple from photons). Thus, measurements of the LSS matter power spectrum can be used to break the strong  $N_{eff}$ – $\omega_m$  degeneracy in the CMB data.

On the other hand, if some of the neutrinos—sterile or standard model—are massive enough to be non-relativistic today, then they will contribute to the expansion rate of the universe but not cluster on small scales. This leads to a  $f_\nu$ -dependent suppression of the matter fluctuation amplitude at  $k > k_\nu$ , where  $k_\nu$  is the neutrino free-streaming scale at the time neutrinos become nonrelativistic, which in turn obviates some of the enhancement due to the extra relativistic energy density near CMB decoupling. For this reason, some degeneracy persists between  $N_{eff}$ – $f_\nu$  in combined analyses of CMB and LSS data.

## Other cosmological observations

Low redshift measurements of the expansion rate and of the distance versus relation are not directly sensitive to the presence of light sterile neutrinos: if these sterile neutrinos are still relativistic today, then their energy density is completely negligible; if they are non-relativistic, then they simply act like a matter component indistinguishable from cold dark matter as far as the low-redshift expansion history is concerned. However, because of the strong correlation between  $N_{eff}$  and  $H_0$  from WMAP data alone, direct measurements of  $H_0$  and  $H(z)$  at low redshifts can be a very effective means to break this degeneracy and to constrain  $N_{eff}$  [346]. In more complex models where the spatial curvature and/or the dark energy equation of state are also allowed to vary, geometric constraints from baryon acoustic oscillations (BAO) and type Ia supernovae (SN) can be used to further break degeneracies.

## Present constraints on light sterile neutrinos

Table III shows a selection of recent constraints on the relativistic energy density  $N_{eff}$ . The salient features can be summarized as follows:

1. Precision cosmological data since the WMAP 5-year data release have consistently shown a mild preference for an excess of relativistic energy density. With one exception, all combinations of data find a  $> 68\%$  preference for  $N_{eff} > 3$ , although whether  $N_{eff} = 3.046$  falls inside or outside the 95% credible region depend on the exact data sets used.
2. The only set of observations that tend to prefer a more “standard”  $N_{eff}$  is the cluster catalog from the ROSAT All-Sky Survey/Chandra X-ray Observatory combined with WMAP-5+CMB+BAO+ $H_0$ . Here, the preferred value is  $N_{eff} = 3.4_{-0.5}^{+0.6}$  [349].
3. Measurement of the CMB damping tail by ACT has disfavored for the first time the standard value of  $N_{eff} = 3.046$  at more than 95% confidence within the  $\Lambda$ CDM+ $N_{eff}$  class of models, when ACT data are analyzed together with WMAP-7+BAO+ $H_0$  [342, 343]. A similar measurement by SPT also finds a preference for a large  $N_{eff} = 3.85 \pm 0.42$  from WMAP-7+SPT+BAO+ $H_0$ , albeit with a smaller statistical significance [344].
4. Some earlier analyses have also reported a  $> 95\%$  significant deviation from  $N_{eff} = 3.046$  without using either ACT or SPT data [352, 353]. This result can be traced to the fact that the massive neutrino fraction  $f_\nu$  was also allowed to vary in these analysis. Because of the  $N_{eff}-f_\nu$  degeneracy discussed earlier, a non-zero  $f_\nu$  tends to drag up the preferred values of  $N_{eff}$  after marginalization.
5. The evidence for  $N_{eff} > 3$  does not appear to be strongly dependent on the complexity of the cosmological model. As discussed in the previous point, non-zero neutrino masses in fact tend to push up the preferred  $N_{eff}$ . Including other parameters degenerate with  $N_{eff}$  such as spatial curvature  $\Omega_k$  or a dark energy equation of state  $w \neq 1$  also does not remove the data’s preference for a large  $N_{eff}$ . Fitting WMAP-7+ACT+SPT+BAO+ $H_0$ , for example, the analysis of [351] finds that  $N_{eff} = 3.046$  remains disfavored at  $> 95\%$  confidence in the  $\Lambda$ CDM+ $N_{eff}$ + $\Omega_k$  model.



Table III. A selection of recent constraints on  $N_{eff}$ , with 68% (95%) uncertainties. W-5 and W-7 stand for WMAP 5-year and 7-year data respectively,  $H_0$  refers to the constraint  $H_0 = 74.2 \pm 3.6 \text{ km s}^{-1}$  from [347], LRG the halo power spectrum determined from the luminous red galaxy sample of the SDSS data release 7 [348], while CMB denotes a combination of small-scale CMB experiments such as ACBAR, BICEP and QUaD.

Model	Data	$N_{eff}$	Ref.
$N_{eff}$	W-5+BAO+SN+ $H_0$	$4.13^{+0.87(+1.76)}_{-0.85(-1.63)}$	[346]
	W-5+LRG+ $H_0$	$4.16^{+0.76(+1.60)}_{-0.77(-1.43)}$	[346]
	W-5+CMB+BAO+XLF+ $f_{gas}$ + $H_0$	$3.4^{+0.6}_{-0.5}$	[349]
	W-5+LRG+maxBCG+ $H_0$	$3.77^{+0.67(+1.37)}_{-0.67(-1.24)}$	[346]
	W-7+BAO+ $H_0$	$4.34^{+0.86}_{-0.88}$	[338]
	W-7+LRG+ $H_0$	$4.25^{+0.76}_{-0.80}$	[338]
	W-7+ACT	$5.3 \pm 1.3$	[343]
	W-7+ACT+BAO+ $H_0$	$4.56 \pm 0.75$	[343]
	W-7+SPT	$3.85 \pm 0.62$	[344]
	W-7+SPT+BAO+ $H_0$	$3.85 \pm 0.42$	[344]
	W-7+ACT+SPT+LRG+ $H_0$	$4.08^{(+0.71)}_{(-0.68)}$	[350]
	W-7+ACT+SPT+BAO+ $H_0$	$3.89 \pm 0.41$	[351]
$N_{eff}+f_\nu$	W-7+CMB+BAO+ $H_0$	$4.47^{(+1.82)}_{(-1.74)}$	[352]
	W-7+CMB+LRG+ $H_0$	$4.87^{(+1.86)}_{(-1.75)}$	[352]
$N_{eff}+\Omega_k$	W-7+BAO+ $H_0$	$4.61 \pm 0.96$	[351]
	W-7+ACT+SPT+BAO+ $H_0$	$4.03 \pm 0.45$	[352]
$N_{eff}+\Omega_k+f_\nu$	W-7+ACT+SPT+BAO+ $H_0$	$4.00 \pm 0.43$	[351]
$N_{eff}+f_\nu+w$	W-7+CMB+BAO+ $H_0$	$3.68^{(+1.90)}_{(-1.84)}$	[352]
	W-7+CMB+LRG+ $H_0$	$4.87^{(+2.02)}_{(-2.02)}$	[352]
$N_{eff}+\Omega_k+f_\nu+w$	W-7+CMB+BAO+SN+ $H_0$	$4.2^{+1.10(+2.00)}_{-0.61(-1.14)}$	[353]
	W-7+CMB+LRG+SN+ $H_0$	$4.3^{+1.40(+2.30)}_{-0.54(-1.09)}$	[353]

Because most constraints listed in table III have been obtained using Bayesian statistics, concern has been raised over their sensitivity to the choice of priors on the model parameters [354, 355]. However, fitting a  $\Lambda$ CDM+ $N_{eff}$  model to WMAP-7+ACT, the analysis of [355] finds no significant difference ( $< 0.1\sigma$ ) in the  $N_{eff}$  constraints between using a uniform prior on  $H_0$ ,  $\Omega_\Lambda$ , or on  $\theta_s$ . The difference becomes even smaller when  $H_0$  data are also included in the analysis. Similarly, while prior-independent ‘‘frequentist’’ constraints obtained from profile likelihood ratios tend to prefer smaller values of  $N_{eff}$  [354, 355], the shift is only marginal: in the case of WMAP-7+ACT, roughly  $0.4\sigma$ – $0.6\sigma$ , while for WMAP-7+ACT+ $H_0$ ,  $< 0.3\sigma$  [355].<sup>18</sup> As future data become even more constraining, we expect the Bayesian and the frequentist credible/confidence intervals to converge completely [346, 356]. Thus, we conclude that while the current data do not yet imply a

<sup>18</sup>The mapping between the profile likelihood ratios  $\mathcal{L}/\mathcal{L}_{max} \leq \exp(-1/2)$  and  $\mathcal{L}/\mathcal{L}_{max} \leq \exp(-4/2)$  and the frequentist  $1\sigma$  and  $2\sigma$  confidence intervals is valid only in the limit Wilks’ theorem is satisfied, *i.e.*, the profile likelihood approaches a Gaussian distribution. If a mapping cannot be established, then the profile likelihood ratios have no statistical interpretation.

definitive detection of  $N_{eff} > 3$ , the preference for  $N_{eff} > 3$  is not an artifact driven by the choice of priors.

### Connection to terrestrial neutrino oscillation experiments

An important issue now is, if the excess relativistic energy density is interpreted as a thermal population of light sterile neutrinos, do these sterile neutrino have anything to do with the sterile neutrino(s) required to explain the anomalies observed in the LSND, MiniBooNE, and reactor neutrino oscillation experiments?

As we saw earlier, active-sterile neutrino oscillations with mixing parameters required to explain the terrestrial anomalies inevitably lead to sterile neutrino thermalization and hence a non-standard  $N_{eff}$ , unless some new physics is introduced to suppress their production. However, the fact that the anomalies point to a mass-square splitting of  $\Delta m^2 \sim 1 \text{ eV}^2$  implies that the sterile neutrino must have a minimum mass of  $\sim 1 \text{ eV}$ , which could potentially come into conflict with cosmological neutrino mass bounds. Indeed, if we extend the  $\Lambda$ CDM model with one species of thermalized sterile neutrino of some arbitrary mass  $m_s$ , then WMAP-7+LRG+ $H_0$  impose a 95% constraint on  $m_s$  of [121, 357]

$$m_s < 0.45 \text{ eV}. \quad (77)$$

A similar constraint on  $m_s$  exists also in the case of two sterile neutrino species each with mass  $m_s$  [121, 357]. Thus, the sterile neutrino oscillation interpretation of the neutrino oscillation anomalies appear at first glance to be incompatible with precision cosmology.

However, if we are willing to make further modifications to the  $\Lambda$ CDM model, it is possible to circumvent these constraints to some extent by exploiting parameter degeneracies. One well-known solution is to endow the dark energy component with an equation of state parameter  $w$  that is more negative than  $-1$  [122, 358]. Another is to allow for a non-flat geometry [351, 353, 358] Yet another is to exploit the  $N_{eff}-f_\nu$  degeneracy and allow for even more massless degrees of freedom [122]. In all three cases, one species of sterile neutrinos with  $m_s = 1 \text{ eV}$  can be reasonably accommodated by precision cosmological data. However, two species with  $m_s = 1 \text{ eV}$  each, or one species with  $m_s = 2 \text{ eV}$  is still strongly disfavored.

### Future cosmological probes

As discussed above, because of the multitude of parameter degeneracies, no single cosmological observation at present is able to constrain  $N_{eff}$  on its own. The ongoing Planck mission, however, will be able to do so, with a projected 68% sensitivity to  $N_{eff}$  at the 0.2–0.25 level [340, 359]. With this level of sensitivity, Planck will be able to conclusively confirm or exclude the presence of a fully thermalized light sterile neutrino. Combining Planck data with ongoing ground-based small-scale polarization experiments and future, high precision CMB measurements, a sensitivity to  $N_{eff}$  of 0.05 may be possible [360]. A comparable precision may also be achieved by combining Planck data with future weak lensing (cosmic shear) measurements by facilities such as LSST or EUCLID [359].

Because the effect of a non-zero neutrino mass is important for the CMB anisotropies only if the mass is comparable to the temperature of CMB decoupling ( $T \sim 0.3 \text{ MeV}$ ), Planck on its own is not expected to improve on the upper bound on the sterile (or active) neutrino mass (77). However,

since even very small neutrino masses are important for the subsequent evolution of the large-scale structure distribution, a non-zero neutrino mass could well be detected through weak lensing of the CMB signal. Naturally, cosmic shear measurements at low redshifts have an even greater potential for probing the mass of light sterile neutrinos. Combining Planck data with cosmic shear data from LSST or EUCLID, a 68% sensitivity to  $m_s$  of 0.05 eV may be possible [357, 359]. Future galaxy cluster surveys combined with Planck data might also reach a similar level of sensitivity to  $m_s$  [361].

## B. Core Collapse Supernovae

The progenitors of core collapse supernovae are massive stars which evolve in a few millions of years to the endpoint of their evolution. Progenitor stars with masses in excess of about  $12 M_\odot$  will evolve through a series of nuclear burning stages, slowly and modestly neutronizing, and continually losing entropy through weak interactions and neutrino emission, ultimately forming a core composed of iron peak material and supported by electron degeneracy pressure. The relativistic electron degeneracy means that the cores of these stars are trembling on the verge of instability, and one or all of general relativity, electron capture, or nuclear statistical equilibrium shifts will lead to collapse. Lower progenitor star masses, roughly in the range of  $9 M_\odot$  to  $12 M_\odot$ , will give rise to cores that suffer this instability before they have burned all the way to iron, in fact while still composed of O-Ne-Mg. In either case, since the pressure support in these cores is coming mostly from relativistically degenerate electrons, they will have roughly the Chandrasekhar mass,  $\sim 1.4 M_\odot$ . These cores will collapse in  $\sim 1$  s to nuclear density where the collapse will be violently halted by nucleon pressure, and a shock wave and proto-neutron star will be formed. The shock wave will move out and, though initially very energetic, will have its energy sapped by nuclear photo-dissociation, eventually ( $\sim 100$  ms) forming a standing accretion shock  $\sim 100$  km from the neutron star center.

The shock wave is probably re-energized by neutrinos emitted from the neutron star surface (neutrino-sphere) capturing on nucleons nearer the shock front. In turn, this process is augmented by hydrodynamic motion, *e.g.*, in the Standing Accretion Shock Instability (SASI) [362]. Sufficiently re-energized, the shock moves out and blows up the star, removing the bulk of the envelope. Subsequently, the still-hot, neutrino emitting proto-neutron star can drive a neutrino-heated wind which is a candidate site for the production of heavy *r*-process elements [363]. Neutrinos play a dominant role in every one of these aspects of the supernova.

### Sterile neutrino oscillations in supernovae

When the core collapses to a neutron star configuration, initially with a radius  $\sim 40$  km, but within a few seconds shrinking down to  $\sim 10$  km, ultimately some  $10^{53}$  ergs of gravitational binding energy (10% of the core's rest mass) will be radiated as active neutrinos and antineutrinos of all flavors. During the in-fall phase of the collapse, neutrino mean free paths become smaller than the size of the collapsing core once the central density reaches about one percent of nuclear matter density. The proto-neutron star harbors trapped seas of neutrinos of all types. These random-walk, with a diffusion timescale of seconds, to the neutron star surface where they decouple and more or less freely stream away.

As in other astrophysical systems (*e.g.*, the Sun), this free-streaming stage of the neutrinos' evolution is influenced by matter effects due to coherent forward scattering of the neutrinos on the ambient matter (electrons and nucleons). In a supernova, however, one must consider in addition forward scattering on the neutrinos themselves. Such neutrino-neutrino interactions turn out to play a crucial role in the flavor evolution of both neutrinos and antineutrinos, inducing large flavor conversions depending on the ratio among the neutrino fluxes of different flavors and the mass hierarchy (see [364] for a recent review and references therein). Self-induced neutrino oscillations dominate the neutrino propagation at a radius much deeper than the conventional matter-induced MSW effect among active flavors and impact on  $r$ -process nucleosynthesis [365, 366]. For sterile neutrinos, however, the location of the active-sterile MSW resonance varies according to the sterile neutrino mass, possibly coupling active-sterile MSW conversion with collective oscillations among the active states.

Neutrino oscillations in a supernova are treated in terms of the usual matrices of neutrino densities  $\rho_E$  for each neutrino mode with energy  $E$ , where the diagonal elements are neutrino densities, and the off-diagonal elements encode phase information caused by flavor oscillations. The radial flavor variation of the quasi-stationary neutrino flux is given by the ‘‘Schrödinger equation’’

$$i\partial_r \rho_E = [H_E, \rho_E] \quad \text{and} \quad i\partial_r \bar{\rho}_E = [\bar{H}_E, \bar{\rho}_E], \quad (78)$$

where an overbar refers to antineutrinos, and sans-serif letters denote matrices in flavor space. The Hamiltonian matrix contains vacuum, matter, and neutrino–neutrino terms

$$H_E = H_E^{\text{vac}} + H_E^{\text{m}} + H_E^{\nu\nu}, \quad (79)$$

and  $\bar{H}_E^{\text{vac}} = H_E^{\text{vac}}$ ,  $\bar{H}_E^{\text{m}} = -H_E^{\text{m}}$ , and  $\bar{H}_E^{\nu\nu} = -H_E^{\nu\nu}$ . In the flavor basis, the vacuum term is

$$H_E^{\text{vac}} = U \frac{M^2}{2E} U^\dagger, \quad (80)$$

where  $M^2$  is a diagonal matrix containing the squared mass differences between the mass eigenstates, and  $U$  is a unitary matrix containing the mixing angles that encode the transformation between the mass and the weak interaction bases. In a supernova environment  $\nu_\mu$  and  $\nu_\tau$  are indistinguishable. Therefore, we can define  $\nu_x$  as a linear combination of  $\nu_\mu$  and  $\nu_\tau$ , so that the matter term  $H_E^{\text{m}}$  in the flavor basis spanned by  $(\nu_e, \nu_x, \nu_s)$  is

$$H^{\text{m}} = \sqrt{2}G_{\text{F}} \text{diag}(N_e - \frac{N_n}{2}, -\frac{N_n}{2}, 0), \quad (81)$$

where  $N_e$  is the net electron number density (electrons minus positrons), and  $N_n$  the neutron number density. Note that  $H_E^{\text{m}}$  here contains both charged-current (CC) and neutral-current (NC) contributions.

In all neutral media,  $Y_e = Y_p$  and  $Y_n = 1 - Y_e$ , where  $Y_j$  is the number density of particle species  $j$  relative to the baryon number density  $N_b$ . Therefore, we can rewrite the local electron fraction as

$$Y_e(r) = \frac{N_e(r)}{N_e(r) + N_n(r)}, \quad (82)$$

so that the matter Hamiltonian becomes

$$H^{\text{m}} = \sqrt{2}G_{\text{F}}N_b \text{diag}\left(\frac{3}{2}Y_e - \frac{1}{2}, \frac{1}{2}Y_e - \frac{1}{2}, 0\right), \quad (83)$$

with  $N_b = N_e + N_n$ . Note that, in presence of sterile neutrinos, the matter potential can be positive or negative depending on the size of  $Y_e$ . For  $Y_e > 1/3$ , it is  $\nu_e$  that can undergo an active-sterile MSW resonance, whereas for  $Y_e < 1/3$  it is  $\bar{\nu}_e$ .

The last term in the Hamiltonian (79),  $H_E^{\nu\nu}$ , corresponding to neutrino-neutrino interactions vanishes for all elements involving the sterile neutrino flavor eigenstate [367], *i.e.*,  $H_{es}^{\nu\nu} = H_{xs}^{\nu\nu} = H_{ss}^{\nu\nu} = 0$ ; only the block involving the active flavors is non-zero. In particular, the only non-vanishing off-diagonal elements are the ones involving only active species.

## Electron abundance evolution

The material in a fluid element moving away from the supernova core will experience three stages of nuclear evolution. Near the surface of the neutron star, the material is typically very hot, and essentially all of the baryons are in the form of free nucleons. As the material flows away from the neutron star, it cools. When the temperature drops below  $\sim 1$  MeV,  $\alpha$ -particles begin to assemble. As the fluid flows farther out and cools even more, heavier nuclei begin to form. Around half of the nuclei with mass numbers  $A > 100$  are supposed to be created via the  $r$ -process.

Activation of the  $r$ -process requires a neutron-rich environment, *i.e.*, an electron fraction per baryon  $Y_e < 0.5$ , sufficiently large entropy to favor a high ratio of free neutrons, and sufficiently fast timescales to lower the efficacy of  $\alpha$ -particle conversion to heavier nuclei. The electron abundance  $Y_e$  in the neutrino-heated material flowing away from the neutron star is set by a competition between the rates of, predominantly, the reactions



and their associated reverse processes. Because of the slow time variations of the outflow conditions during the cooling phase, a near steady-state situation applies, and the  $Y_e$  rate-of-change within an outflowing mass element may be written as [368]

$$\frac{dY_e}{dt} = v(r) \frac{dY_e}{dr} \simeq (\lambda_{\nu_e} + \lambda_{e^+}) Y_n^f - (\lambda_{\bar{\nu}_e} + \lambda_{e^-}) Y_p^f , \quad (86)$$

where  $v(r)$  is the velocity of the outflowing mass element,  $Y_n^f$  and  $Y_p^f$  are the abundances of free nucleons, and  $\lambda$  are the rates of the neutrino capture processes (84) and (85) and their reverse processes. The forward rates (neutrino capture on free nucleons) are given by

$$\lambda_{\nu_e} \propto \frac{L_{\nu_e}}{\langle E_{\nu_e} \rangle} \langle \sigma_{\nu_e n}(r) \rangle , \quad (87)$$

$$\lambda_{\bar{\nu}_e} \propto \frac{L_{\bar{\nu}_e}}{4\pi r^2 \langle E_{\bar{\nu}_e} \rangle} \langle \sigma_{\bar{\nu}_e p}(r) \rangle , \quad (88)$$

with  $L_{\nu_e}$  ( $L_{\bar{\nu}_e}$ ) the  $\nu_e$  ( $\bar{\nu}_e$ ) luminosity, and  $\langle E_{\nu_e} \rangle$  ( $\langle E_{\bar{\nu}_e} \rangle$ ) the  $\nu_e$  ( $\bar{\nu}_e$ ) mean energy. The rates for the reverse processes (electron and positron capture on free nucleons) are functions of the relativistic electron chemical potential  $\mu_e$  and the electron temperature  $T_e$ . The details are generally quite complex, but  $Y_e$  at small radii is determined mainly by the  $e^-$  and  $e^+$  capture rates, whereas at larger radii the neutrino-capture reactions dominate.

The values of  $Y_e$  found in standard (*i.e.*, no flavor oscillations) supernova simulations are generally too high to enable a successful  $r$ -process. However, as it is clear from equation (86) that a variation of neutrino fluxes due to flavor oscillations can affect the evolution of  $Y_e$ , one possible solution to the high  $Y_e$  problem is to remove the  $\nu_e$  flux by way of active-sterile oscillations [369–375]. On the other hand, a variation of  $Y_e$  changes the matter potential felt by the neutrinos according to equation (83), and can significantly alter the flavor evolution especially if  $Y_e$  is driven to below 1/3 (see discussion immediately after equation (83)). This can have important consequences for key aspects of energy transport in the proto-neutron star core. We discuss these possibilities below.

### Light sterile neutrinos in supernovae

If the sterile neutrino rest mass is in the range  $\sim 0.1$  eV to few eV, *i.e.*, overlapping with the preferred mass range of the MiniBooNE/LSND and the reactor-anomalies, two MSW resonances are expected to occur close to the neutrino-sphere, one for neutrinos and one for antineutrinos. However, because the matter potential is very steep as a result of a rapidly changing  $Y_e$  at small radii, these resonances are not adiabatic. At larger radii, a second and more adiabatic resonance occurs in the neutrino sector only. The net effect, therefore, is that a large fraction of  $\nu_e$  is converted to  $\nu_s$  while the  $\bar{\nu}_e$  flux is only partially converted to  $\bar{\nu}_s$ . The equilibrium of the neutrino capture processes (84) and (85) and their reverse processes then drives down the electron abundance  $Y_e$  as a consequence, thereby creating a neutron-rich environment that enables the formation of elements via the  $r$ -process. However, recent studies have shown that collective oscillations in the active sector due to neutrino-neutrino interactions become dominant especially in the late cooling phase. They act to repopulate the  $\nu_e$  flux so that the resulting  $Y_e$  is always lower than in the case with no active-sterile oscillations, but not always as low as in the “naive” case without considerations of the neutrino-neutrino matter effects [376]. Therefore, the presence of light sterile neutrinos can alter the conditions for element formation, although active-sterile oscillations alone probably cannot activate the  $r$ -process.

Observations of ultra-metal poor halo stars with  $r$ -process excesses reveal the curious feature that the nuclear mass 130 and 195 abundance peaks have similar overall abundances, suggesting that fission cycling in the  $r$ -process may be operating, essentially tying the abundances in these two peaks together in steady state equilibrium. Such an equilibrium would require very large neutron excesses and, so far, the only models that can stimulate such an excess in neutrino-heated ejecta are those that invoke active-sterile neutrino flavor conversion in the wind as outlined above. Although the actual site of  $r$ -process nucleosynthesis remains an open question, however, many neutron-rich environments, like those associated with neutron star mergers and accretion disks, also may have large neutrino fluxes and so be subject to some form of the alpha effect. In any case, the connection between BBN and  $r$ -process nucleosynthesis on the one hand, and active-sterile neutrino conversion physics on the other, is tantalizing.

### Heavy sterile neutrinos in supernovae

Sterile neutrinos with rest masses in the keV region and mixing angles with active species that make them dark matter candidates can also affect key aspects of energy transport in the proto-neutron star core. In fact, the high matter density (essentially nuclear matter density) and large electron lepton number in the core and typical active neutrino energies of order 10 MeV mean

that keV-mass sterile neutrinos can be resonant [159]. If flavor evolution through the resonance is sufficiently adiabatic, then the  $\nu_e$  will be turned into a sterile neutrino and this neutrino likely will stream out of the core at near light speed—unless it encounters another MSW resonance further out that re-converts it to an active neutrino. In fact, the dependence of the potential on  $Y_e$  can engineer just such an effect: at first as the core collapses  $\nu_e$ 's are converted, and unbalanced electron capture lowers  $Y_e$ , eventually driving it below  $\frac{1}{3}$  so that the matter potential becomes negative as per equation (83), thereby causing the conversion of  $\bar{\nu}_e$ 's to sterile species. This will bring the potential back up if the collapse/expansion rate of the material in the core is slow enough, engineering a double resonance scenario where  $\nu_e$ 's are regenerated from the sterile neutrinos but closer to the neutrino-sphere [374, 377]. The result of such a scenario is that the effective transport time for  $\nu_e$ 's can be dramatically reduced, bringing up the  $\nu_e$  luminosity at the neutrino-sphere, and thereby affecting nearly every aspect of downstream supernova evolution, for example increasing the material heating rate behind the shock.

Moreover, active-to-sterile conversion has been considered as a way to produce large space motions of pulsar/neutron star remnants following core collapse [378–380]. Even heavier sterile neutrinos, with rest masses in the  $\sim 100 \text{ MeV}$  range, could aid supernova shock re-heating [381], although these may run afoul of cosmological constraints on nucleosynthesis or measurements of  $N_{eff}$  derived from the cosmic microwave background anisotropies [142, 382–384].

Invoking  $\sim \text{keV}$  rest mass sterile neutrinos and active-to-sterile neutrino flavor conversion to engineer shock re-heating is a dangerous gambit, however, because energy can be lost from the core. Ultimately, this could prove to be in conflict with what we know about neutrinos from the SN 1987A neutrino burst observations [385]. But there is plenty of cushion here. The total kinetic energy of bulk motion plus optical energy in a core collapse supernova explosion is only  $10^{51} \text{ ergs}$ , some 1% of the energy resident in the active neutrino energy in the core. Therefore, much energy could be “thrown away” in sterile states escaping from the core and still there will be plenty of active neutrino energy to power an explosion, especially if the transport of this energy to the shock is augmented by efficient hydrodynamic motion, as in SASI-like scenarios.

### III. EVIDENCE FROM OSCILLATION EXPERIMENTS

While the standard three-flavor framework of neutrino oscillations is by now well established, there are a number of oscillation experiments whose results cannot be explained in this framework, but, should they stand up to further scrutiny, might require the introduction of extra, sterile, neutrino species. The first piece of evidence in favor of oscillations beyond the three-flavor framework came from the LSND experiment, which performed a sensitive search for neutrino oscillations and obtained  $> 3\sigma$  evidence for  $\bar{\nu}_\mu \rightarrow \bar{\nu}_e$  oscillations with  $\Delta m^2 > 0.2 \text{ eV}^2$  [114]. The MiniBooNE experiment, which was designed to test LSND, has reported oscillation results in both neutrino mode and antineutrino mode. Whereas the results obtained in neutrino mode disfavor most of the parameter space preferred by LSND, the MiniBooNE antineutrino data, though not yet conclusive, are consistent with the LSND signal and consistent with oscillations at a  $\Delta m^2 \sim 1 \text{ eV}^2$ . Moreover, MiniBooNE reports an excess of events at low energy, outside the energy range where LSND-like oscillations are expected. Further hints and evidence for the existence of sterile neutrinos come from measurements of the neutrino flux from intense radioactive sources, and from short-baseline reactor experiments. In particular, a recent re-evaluation of the expected antineutrino flux from nuclear reactor indicates that the measured flux is about 3% below the prediction, with a significance above  $3\sigma$ .

On the other hand, there are a number of experiments that do not support this body of evidence for sterile neutrinos. The KARMEN experiment, which is very similar to LSND, observed no such evidence. (But a joint analysis of the two experiments [386] shows that their data sets are compatible with oscillations occurring either in a band from 0.2 to 1  $\text{eV}^2$  or in a region around 7  $\text{eV}^2$ .) Also, a number of  $\nu_\mu$  disappearance searches in the relevant mass range, as well as a MINOS search for disappearance of active neutrinos in neutral current events, produced negative results.

In this section, we will discuss the evidence for sterile neutrinos from LSND, MiniBooNE, the radiocative source experiments and the reactor experiments, and also the null results from KARMEN and MINOS. A combined global analysis of these datasets (and others) will be presented in sec. IV.

#### A. The LSND Signal

##### Description of the Experiment

The LSND experiment [387] was designed to search for  $\bar{\nu}_\mu \rightarrow \bar{\nu}_e$  oscillations with high sensitivity and to measure  $\nu C$  cross sections. A photograph of the inside of the detector tank is shown in Fig. 11. The main characteristics of the LSND experiment are given in Table IV. LSND had the advantage of a very high proton intensity, a large detector mass, and good particle identification. Also shown in Table IV are the main characteristics of the KARMEN experiment, which had a lower duty factor than LSND and excellent energy resolution. An important difference between the experiments is that in LSND the distance travelled by the neutrinos was 30 m, compared to 17.7 m for KARMEN, so that a combined analysis provides a more sensitive search for neutrino oscillations over a wider range of  $\Delta m^2$  values. Both experiments made use of a high-intensity, 800 MeV proton beam that interacted in an absorber to produce a large number of pions. Most of the pions produced are  $\pi^+$ , which almost all decay. The  $\pi^-$  are mainly absorbed and only a small



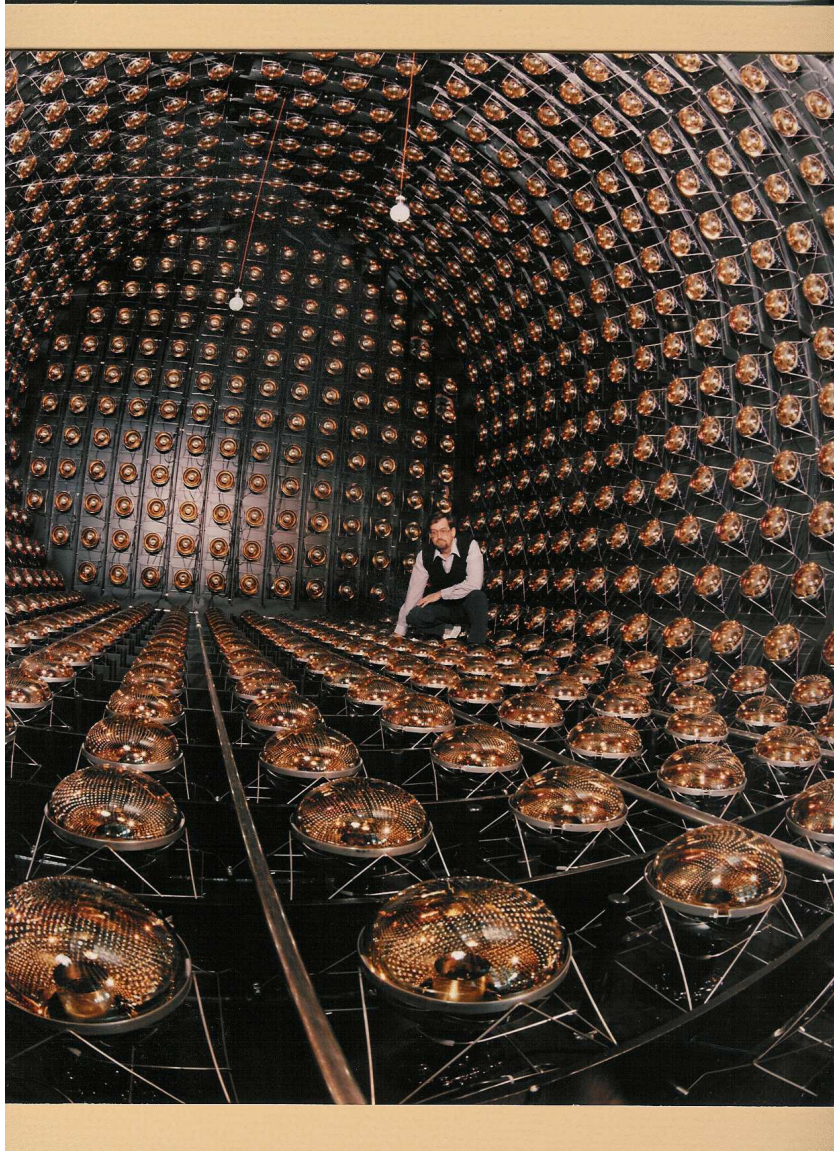


Figure 11. A photograph of the inside of the LSND detector tank.

fraction decay to  $\mu^-$ , which in turn are largely captured. Therefore, almost all of the neutrinos produced arise from  $\pi^+ \rightarrow \mu^+ \nu_\mu$  and  $\mu^+ \rightarrow e^+ \bar{\nu}_\mu \nu_e$  decays, where most of the decays ( $> 95\%$ ) are at rest and only a small fraction ( $< 5\%$ ) are in flight.

LSND made use of the LAMPF accelerator, which was an intense source of low energy neutrinos produced with a proton current of 1 mA at 798 MeV kinetic energy. For the 1993–1995 running period the production target consisted of a 30 cm long water target (20 cm in 1993) followed by a water-cooled Cu beam dump, while for the 1996–1998 running period the production target was reconfigured with the water target replaced by a close-packed, high-Z target. The resulting DAR neutrino fluxes are well understood because almost all detectable neutrinos arise from  $\pi^+$  or  $\mu^+$  decay;  $\pi^-$  and  $\mu^-$  that stop are readily captured in the Fe of the shielding and Cu of the beam stop [388]. The production of kaons or heavier mesons is negligible at these proton energies. The  $\bar{\nu}_e$  flux is calculated to be only  $\sim 8 \times 10^{-4}$  times as large as the  $\bar{\nu}_\mu$  flux in the  $20 < E_\nu < 52.8$  MeV energy range, so that the observation of a  $\bar{\nu}_e$  event rate significantly above the calculated background would be evidence for  $\bar{\nu}_\mu \rightarrow \bar{\nu}_e$  oscillations. Fig. 12 shows the neutrino energy spectra

Property	LSND	KARMEN
Proton Energy	798 MeV	800 MeV
Proton Intensity	1000 $\mu$ A	200 $\mu$ A
Protons on Target	28,896 C	9425 C
Duty Factor	$6 \times 10^{-2}$	$1 \times 10^{-5}$
Total Mass	167 t	56 t
Neutrino Distance	30 m	17.7 m
Particle Identification	YES	NO
Energy Resolution at 50 MeV	6.6%	1.6%
Events for 100% $\bar{\nu}_\mu \rightarrow \bar{\nu}_e$ Transmutation	33,300	14,000

Table IV. The main characteristics of the LSND and KARMEN experiments.

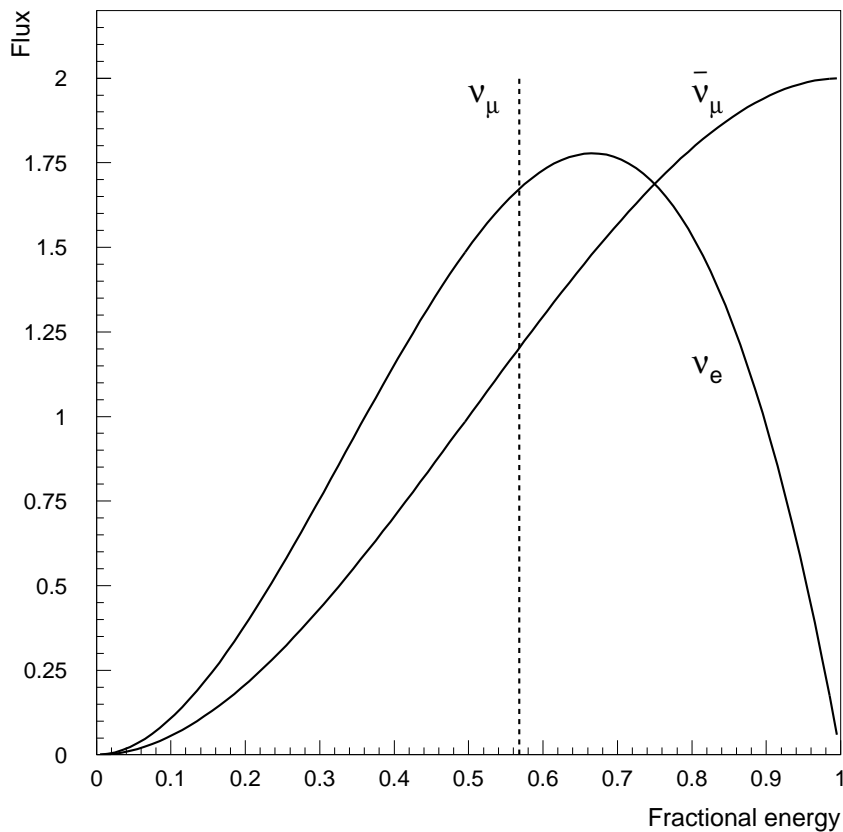


Figure 12. The neutrino energy spectra from  $\pi^+$  and  $\mu^+$  DAR.

from  $\pi^+$  and  $\mu^+$  DAR.

The LSND detector [387] consisted of an approximately cylindrical tank 8.3 m long by 5.7 m in diameter. A schematic drawing of the detector is shown in Fig. 13. The center of the detector was located 30 m from the neutrino source. On the inside surface of the tank, 1220 8-inch Hamamatsu PMTs covered 25% of the area with photocathode. The tank was filled with 167 t of liquid

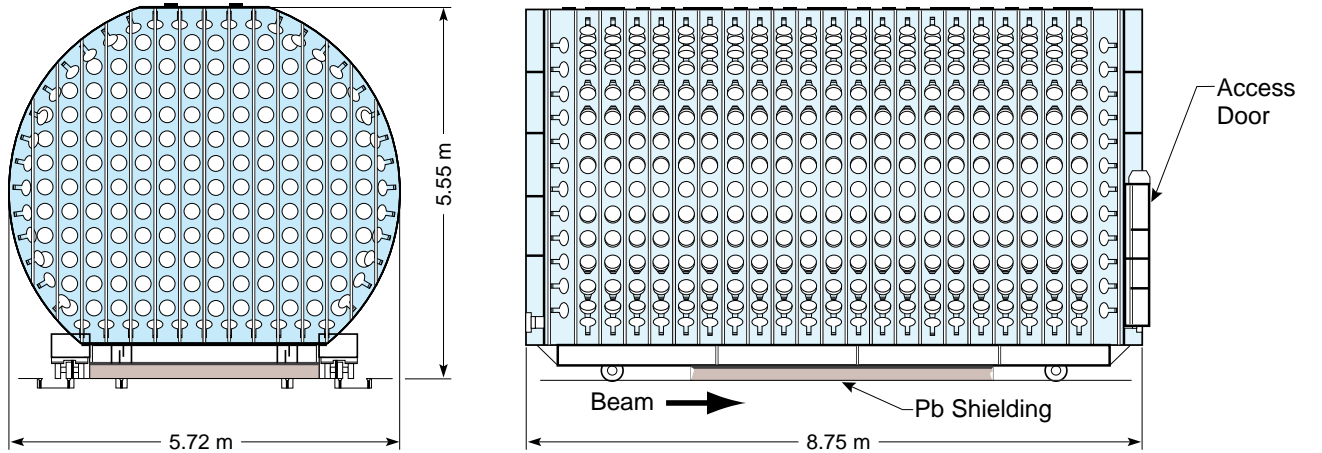


Figure 13. A schematic drawing of the LSND detector.

scintillator consisting of mineral oil and 0.031 g/l of b-PBD. This low scintillator concentration allows the detection of both Cherenkov light and scintillation light and yields an attenuation length of more than 20 m for wavelengths greater than 400 nm [389]. A typical 45 MeV electron created in the detector produced a total of  $\sim 1500$  photoelectrons, of which  $\sim 280$  photoelectrons were in the Cherenkov cone. PMT time and pulse-height signals were used to reconstruct the track with an average RMS position resolution of  $\sim 14$  cm, an angular resolution of  $\sim 12^\circ$ , and an energy resolution of  $\sim 7\%$  at the Michel endpoint of 52.8 MeV. The Cherenkov cone for relativistic particles and the time distribution of the light, which is broader for non-relativistic particles [387], gave excellent separation between electrons and particles below Cherenkov threshold. Identification of neutrons was accomplished through the detection of the 2.2 MeV photon from neutron capture on a free proton. The veto shield enclosed the detector on all sides except the bottom. Additional counters were placed below the veto shield after the 1993 run to reduce cosmic-ray background entering through the bottom support structure. The main veto shield [390] consisted of a 15 cm layer of liquid scintillator in an external tank and 15 cm of lead shot in an internal tank. This combination of active and passive shielding tagged cosmic-ray muons that stopped in the lead shot. A veto inefficiency  $< 10^{-5}$  was achieved for incident charged particles.

### Event Selection

The goal of the event selection is to reduce the cosmic-ray background to as low a level as possible, while retaining a high efficiency for neutrino-induced electron events. The selection criteria and corresponding efficiencies are shown in Table V. The energy range  $20 < E < 200$  MeV is chosen so as to accept both decay-at rest (DAR)  $\bar{\nu}_\mu \rightarrow \bar{\nu}_e$  and decay-in-flight (DIF)  $\nu_\mu \rightarrow \nu_e$  oscillation candidates. The energy region  $20 < E_e < 60$  MeV is required for the  $\bar{\nu}_\mu \rightarrow \bar{\nu}_e$  oscillation search and  $60 < E_e < 200$  MeV for the  $\nu_\mu \rightarrow \nu_e$  oscillation search. Below 20 MeV there are large backgrounds from the  $\beta$  decay of  $^{12}\text{B}$  created by the capture of stopped cosmic-ray  $\mu^-$  on  $^{12}\text{C}$ . Above 200 MeV the beam-related backgrounds from  $\pi^+ \rightarrow e^+\nu_e$  are large compared to any likely oscillation signal. Events with a previous activity within  $12 \mu\text{s}$ , a future activity within  $8 \mu\text{s}$ , or a bottom veto counter hit are rejected in order to eliminate cosmic-ray muon events. To further minimize cosmic-ray background, a tight electron particle identification is applied,  $-1.5 < \chi'_{tot} <$

Criteria	Efficiency
Electron Reduction	
Veto Hits < 4	$0.98 \pm 0.01$
Loose Electron PID	$0.96 \pm 0.01$
Cosmic Muon Cut	$0.92 \pm 0.01$
Electron Selection	
$\Delta t_{past} > 12\mu s$	$0.96 \pm 0.01$
$\Delta t_{future} > 8\mu s$	$0.99 \pm 0.01$
$-1.5 < \chi'_{tot} < 0.5$	$0.84 \pm 0.01$
$0.3 < \chi_{tot}^{old} < 0.65$ (1993 only)	$0.98 \pm 0.01$
$\Delta t_{veto}^{best} > 30ns$	$0.97 \pm 0.01$
$D > 35$ cm	$0.88 \pm 0.02$
$N_\gamma < 1, E > 60$	1.00
$N_\gamma < 2, E < 60$	1.00
Deadtime	
DAQ & Tape Deadtime	$0.96 \pm 0.02$
Veto Deadtime	$0.76 \pm 0.02$
Total	$0.42 \pm 0.03$

Table V. The LSND average efficiencies for electrons in the fiducial volume with energies in the range  $20 < E_e < 60$  MeV.

0.5, where the allowed range is chosen by maximizing the selection efficiency divided by the square root of the beam-off background with a correlated neutron. The  $\chi'_{tot}$  parameter depends on the product of the  $\chi$  parameters defined in reference [387]. Briefly,  $\chi_r$  and  $\chi_a$  are the quantities minimized for the determination of the event position and direction, and  $\chi_t$  is the fraction of PMT hits that occur more than 12 ns after the fitted event time. The dependence of the  $\chi$  parameters on energy and position for Michel electrons was studied, and a correction was developed that made  $\chi'_{tot}$  independent of energy or position. Additionally, no veto hit is allowed within 30 ns of the trigger time and the reconstructed electron vertex is required to be inside a volume 35 cm from the faces of the photomultiplier tubes. Finally, the number of associated  $\gamma$ s with  $R_\gamma > 10$  ( $R_\gamma$  is discussed below) is required to be  $< 2$  ( $< 1$ ) for events  $< 60$  ( $> 60$ ) MeV in order to reject neutron-induced events, which tend to have many associated  $\gamma$ s. In addition to the electron reduction and selection efficiencies, Table V also shows the efficiencies due to the data acquisition (DAQ) and veto deadtime. The total efficiency for electrons in the fiducial volume with energies in the range  $20 < E_e < 60$  MeV is  $0.42 \pm 0.03$ .

Correlated 2.2 MeV  $\gamma$  from neutron capture are distinguished from accidental  $\gamma$  from radioactivity by use of the likelihood ratio,  $R_\gamma$ , which is defined to be the likelihood that the  $\gamma$  is correlated divided by the likelihood that the  $\gamma$  is accidental.  $R_\gamma$  depends on three quantities: the number of hit PMTs associated with the  $\gamma$  (the multiplicity is proportional to the  $\gamma$  energy), the distance between the reconstructed  $\gamma$  position and positron position, and the time interval between the  $\gamma$  and positron (neutrons have a capture time in mineral oil of  $186 \mu s$ , while the accidental  $\gamma$  are uniform in time). Fig. 14 shows these distributions, which are obtained from fits to the data, for both correlated 2.2 MeV  $\gamma$  (solid curves) and accidental  $\gamma$  (dashed curves). To determine  $R_\gamma$ , the product of prob-

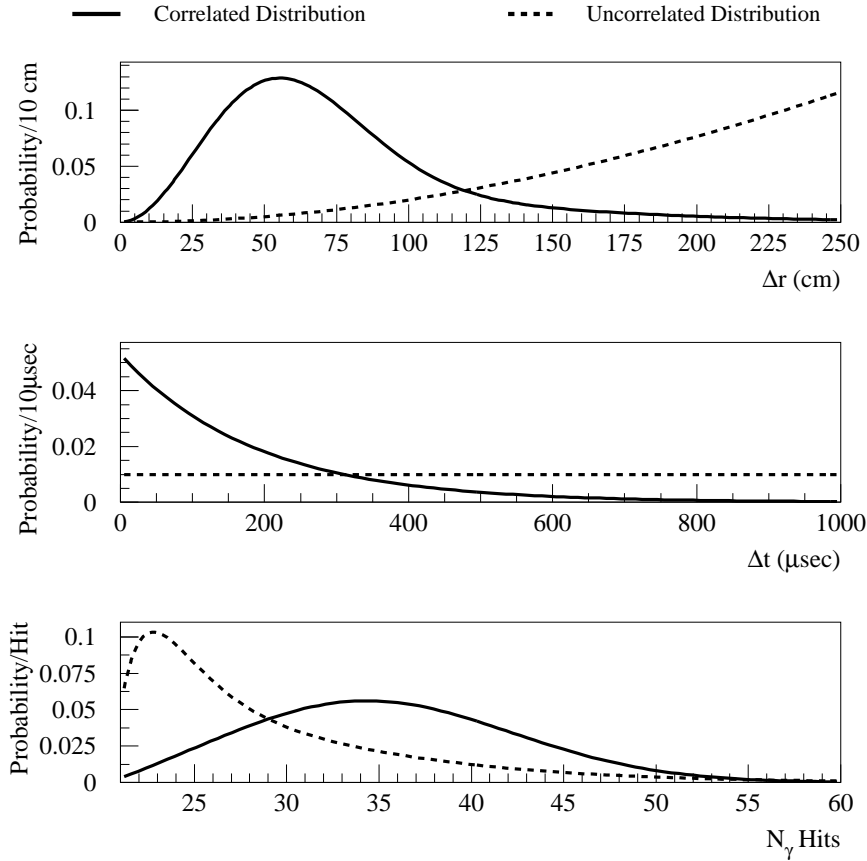


Figure 14. Distributions of correlated 2.2 MeV  $\gamma$  (solid curves) and accidental  $\gamma$  (dashed curves) from LSND. The top plot shows the distance between the reconstructed  $\gamma$  position and positron position,  $\Delta r$ , the middle plot shows the time interval between the  $\gamma$  and positron,  $\Delta t$ , and the bottom plot shows the number of hit PMTs associated with the  $\gamma$ ,  $N_{hits}$ .

abilities for the correlated distributions is formed and divided by the product of probabilities for the uncorrelated distributions. The accidental  $\gamma$  efficiencies are measured from the laser-induced calibration events, while the correlated  $\gamma$  efficiencies are determined from the MC simulation of the experiment. Similar results for the correlated  $\gamma$  efficiencies are obtained from the cosmic-ray neutron events, whose high energy gives them a slightly broader position distribution. The systematic uncertainty of these efficiencies is estimated to be  $\pm 7\%$  of their values. For  $R_{\gamma} > 10$ , the correlated and accidental efficiencies are 0.39 and 0.003, respectively.

## Neutrino Oscillation Signal and Background Reactions

The primary oscillation search in LSND is for  $\bar{\nu}_{\mu} \rightarrow \bar{\nu}_e$  oscillations, where the  $\bar{\nu}_{\mu}$  arise from  $\mu^+$  DAR in the beam stop and the  $\bar{\nu}_e$  are identified through the reaction  $\bar{\nu}_e p \rightarrow e^+ n$ . This reaction allows a two-fold signature of a positron with a 52.8 MeV endpoint and a correlated 2.2 MeV  $\gamma$  from neutron capture on a free proton. There are only two significant neutrino backgrounds with a positron/electron and a correlated neutron. The first background is from  $\mu^-$  DAR in the beam stop followed by  $\bar{\nu}_e p \rightarrow e^+ n$  scattering in the detector. As mentioned earlier, this background is highly

Neutrino Source	Reaction	Number of Events
$\mu^+$ DAR	100% $\bar{\nu}_\mu \rightarrow \bar{\nu}_e$	$33300 \pm 3300$
$\mu^-$ DAR	$\bar{\nu}_e p \rightarrow e^+ n$	$19.5 \pm 3.9$
$\pi^-$ DIF	$\bar{\nu}_\mu p \rightarrow \mu^+ n$	$10.5 \pm 4.6$

Table VI. The LSND estimated number of events in the  $20 < E_e < 60$  MeV energy range due to 100%  $\bar{\nu}_\mu \rightarrow \bar{\nu}_e$  transmutation and to the two beam-related backgrounds with neutrons,  $\mu^-$  DAR in the beam stop followed by  $\bar{\nu}_e p \rightarrow e^+ n$  scattering in the detector and  $\pi^-$  DIF in the beam stop followed by  $\bar{\nu}_\mu p \rightarrow \mu^+ n$  scattering. The events must satisfy the electron selection criteria, but no correlated  $\gamma$  requirement is imposed.

Selection	Beam-On Events	Beam-Off Background	$\nu$ Background	Event Excess
$R_\gamma > 1$	205	$106.8 \pm 2.5$	$39.2 \pm 3.1$	$59.0 \pm 14.5 \pm 3.1$
$R_\gamma > 10$	86	$36.9 \pm 1.5$	$16.9 \pm 2.3$	$32.2 \pm 9.4 \pm 2.3$
$R_\gamma > 100$	27	$8.3 \pm 0.7$	$5.4 \pm 1.0$	$13.3 \pm 5.2 \pm 1.0$

Table VII. Numbers of LSND beam-on events that satisfy the selection criteria for the primary  $\bar{\nu}_\mu \rightarrow \bar{\nu}_e$  oscillation search with  $R_\gamma > 1$ ,  $R_\gamma > 10$ , and  $R_\gamma > 100$ . Also shown are the beam-off background, the estimated neutrino background, and the excess of events that is consistent with neutrino oscillations.

suppressed due to the requirements that a  $\pi^-$  be produced, the  $\pi^-$  DIF, and the  $\mu^-$  DAR prior to capture. The second background is from  $\pi^-$  DIF in the beam stop followed by  $\bar{\nu}_\mu p \rightarrow \mu^+ n$  scattering in the detector. (Additional contributions are from  $\bar{\nu}_\mu C \rightarrow \mu^+ nX$  and  $\nu_\mu C \rightarrow \mu^- nX$  scattering.) This background will mimic the oscillation reaction if the  $\mu^+$  is sufficiently low in energy that it is below the threshold of 18 hit PMTs, corresponding to  $E_\mu < 4$  MeV. Table VI shows the estimated number of events in the  $20 < E_e < 60$  MeV energy range satisfying the electron selection criteria for 100%  $\bar{\nu}_\mu \rightarrow \bar{\nu}_e$  transmutation and for the two beam-related backgrounds with neutrons.

## LSND Oscillation Results

Table VII shows the LSND statistics for events that satisfy the selection criteria for the primary  $\bar{\nu}_\mu \rightarrow \bar{\nu}_e$  oscillation search. An excess of events is observed over that expected from beam-off and neutrino background that is consistent with neutrino oscillations. A  $\chi^2$  fit to the  $R_\gamma$  distribution, as shown in Fig. 15, gives  $f_c = 0.0567 \pm 0.0108$  ( $\chi^2 = 10.7/9$  DOF), which leads to a beam on–off excess of  $117.9 \pm 22.4$  events with a correlated neutron. Subtracting the neutrino background from  $\mu^-$  DAR followed by  $\bar{\nu}_e p \rightarrow e^+ n$  scattering ( $19.5 \pm 3.9$  events) and  $\pi^-$  DIF followed by  $\bar{\nu}_\mu p \rightarrow \mu^+ n$  scattering ( $10.5 \pm 4.6$  events)<sup>19</sup> leads to a total excess of  $87.9 \pm 22.4 \pm 6.0$  events. This excess corresponds to an oscillation probability of  $(0.264 \pm 0.067 \pm 0.045)\%$ , where the first error is statistical and the second error is the systematic error arising from uncertainties in the backgrounds, neutrino flux (7%),  $e^+$  efficiency (7%), and  $\gamma$  efficiency (7%).

A clean sample of oscillation candidate events can be obtained by requiring  $R_\gamma > 10$ , where as shown in Table VII, the beam on–off excess is  $49.1 \pm 9.4$  events while the estimated neutrino background is only  $16.9 \pm 2.3$  events. Fig. 16 displays the energy distribution of events with  $R_\gamma > 10$ .

<sup>19</sup>This background also includes contributions from  $\bar{\nu}_\mu C \rightarrow \mu^+ nX$  and  $\nu_\mu C \rightarrow \mu^- nX$ .

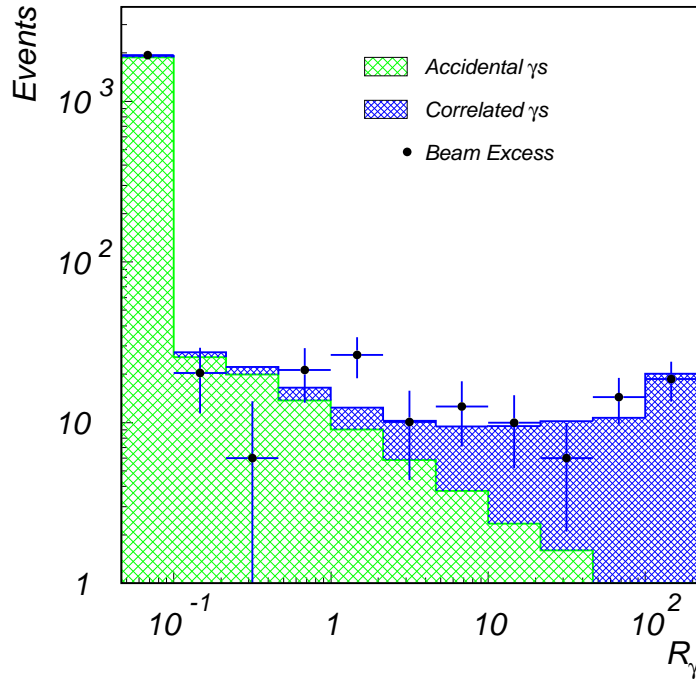


Figure 15. The LSND  $R_\gamma$  distribution for events that satisfy the selection criteria for the primary  $\bar{\nu}_\mu \rightarrow \bar{\nu}_e$  oscillation search.

The shaded regions show the combination of neutrino background plus neutrino oscillations at low  $\Delta m^2$ . The data agree well with the oscillation hypothesis. Fig. 17 shows the spatial distribution for events with  $R_\gamma > 10$  and  $20 < E_e < 60$  MeV, where  $z$  is along the axis of the tank (and approximately along the beam direction),  $y$  is vertical, and  $x$  is transverse. The shaded region shows the expected distribution from a combination of neutrino background plus neutrino oscillations. Finally, Fig. 18 shows the  $L_\nu/E_\nu$  distribution for events with  $R_\gamma > 10$  and  $20 < E_e < 60$  MeV, where  $L_\nu$  is the distance travelled by the neutrino in meters and  $E_\nu$  is the neutrino energy in MeV determined from the measured positron energy and angle with respect to the neutrino beam. The data agree well with the expectation from neutrino background plus neutrino oscillations at low  $\Delta m^2$  ( $\chi^2/\text{dof} = 4.9/8$ ) or high  $\Delta m^2$  ( $\chi^2/\text{dof} = 5.8/8$ ).

The  $(\sin^2 2\theta, \Delta m^2)$  likelihood ( $\mathcal{L}$ ) fitter is applied to beam-on events in the final oscillation sample and calculates a likelihood in the  $(\sin^2 2\theta, \Delta m^2)$  plane in order to extract the favored oscillation parameters. The  $\mathcal{L}$  product in the  $(\sin^2 2\theta, \Delta m^2)$  plane is formed over the individual beam-on events that pass the oscillation cuts. This three-dimensional contour is sliced to arrive finally at the LSND allowed oscillation region. The beam-related backgrounds are determined from Monte Carlo (MC) event samples for each individual background contribution. The MC contains the trigger simulation and generally very well reproduces the tank response to all particles of interest. Agreement between the data and MC is excellent.

The  $(\sin^2 2\theta, \Delta m^2)$  oscillation parameter fit for the entire data sample,  $20 < E_e < 200$  MeV, is shown in Fig. 19. The fit includes both  $\bar{\nu}_\mu \rightarrow \bar{\nu}_e$  and  $\nu_\mu \rightarrow \nu_e$  oscillations, as well as all known neutrino backgrounds. The inner and outer regions correspond to 90% and 99% CL allowed regions, while the curves are 90% CL limits from the Bugey reactor experiment [391] and the KARMEN experiment at ISIS [392] (see below). The most favored allowed region is the band

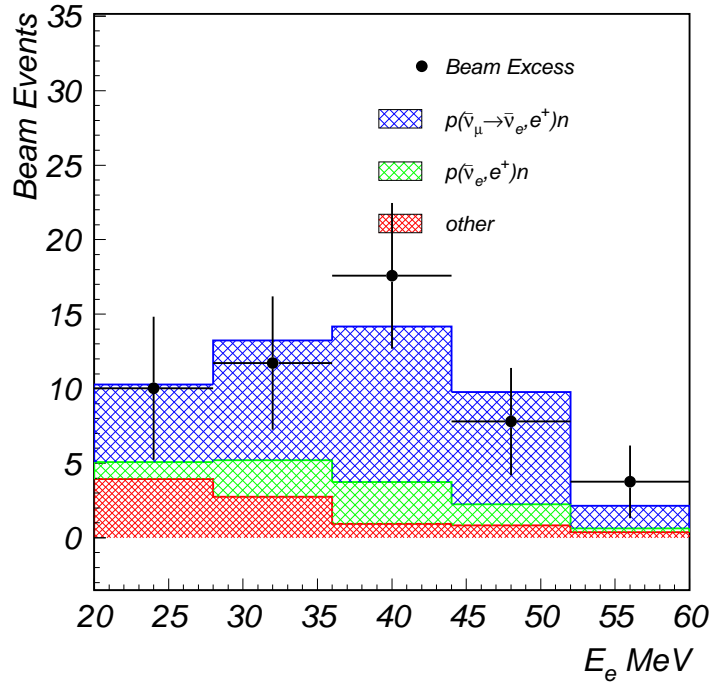


Figure 16. The LSND energy distribution for events with  $R_\gamma > 10$ . The shaded region shows the expected distribution from a combination of neutrino background plus neutrino oscillations at low  $\Delta m^2$ .

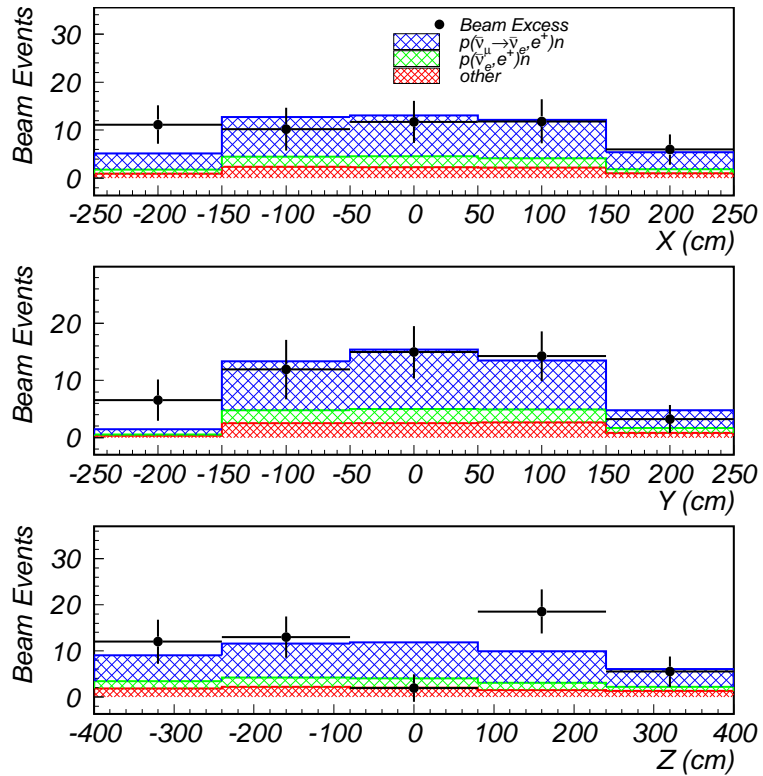


Figure 17. The LSND spatial distributions for events with  $R_\gamma > 10$  and  $20 < E_e < 60$  MeV. The shaded region shows the expected distribution from a combination of neutrino background plus neutrino oscillations at low  $\Delta m^2$ .



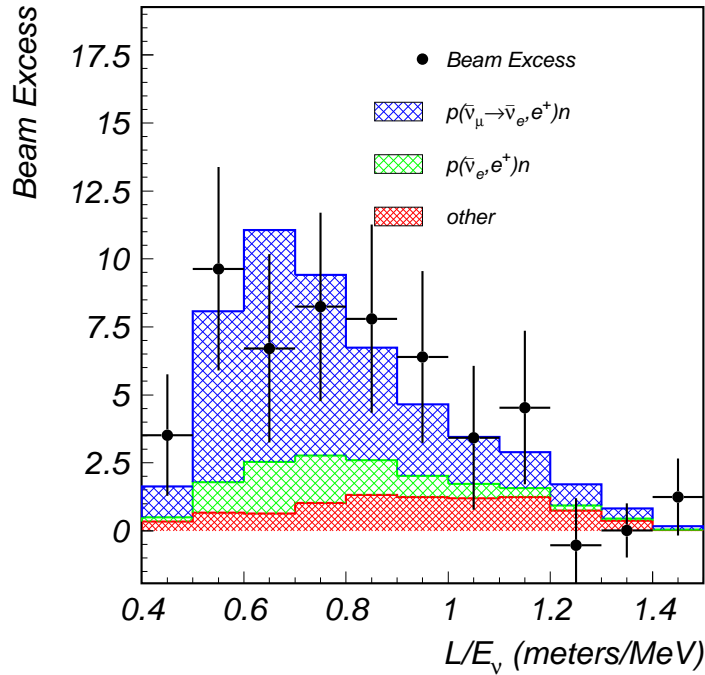


Figure 18. The LSND  $L_\nu/E_\nu$  distribution for events with  $R_\gamma > 10$  and  $20 < E_e < 60$  MeV, where  $L_\nu$  is the distance travelled by the neutrino in meters and  $E_\nu$  is the neutrino energy in MeV. The data agree well with the expectation from neutrino background and neutrino oscillations at low  $\Delta m^2$ .

from  $0.2 - 2.0 \text{ eV}^2$ , although a region around  $7 \text{ eV}^2$  is also possible.

## B. The KARMEN Constraint

### Description of the Experiment

The KARMEN experiment [393] made use of the ISIS rapid-cycling synchrotron, which accelerates protons up to 800 MeV at an intensity of  $200 \mu\text{A}$ . The protons are extracted from the synchrotron at a frequency of 50 Hz as a double pulse consisting of two 100 ns pulses separated by 325 ns. The two bursts, therefore, occur within 600 ns and lead to an overall duty factor of about  $10^{-5}$ . After extraction, the protons interact in a water-cooled Ta-D<sub>2</sub>O target, producing about  $(0.0448 \pm 0.0030) \pi^+$  per incident proton [388]. Due to the small duty factor,  $\nu_\mu$  from  $\pi^+$  decay can be clearly separated from the  $\bar{\nu}_\mu$  and  $\nu_e$  from  $\mu^+$  decay. The  $\bar{\nu}_e/\bar{\nu}_\mu$  background is estimated to be  $6.4 \times 10^{-4}$  [388], slightly smaller than for LSND.

The KARMEN detector, as shown in Fig. 20, is a segmented liquid scintillator calorimeter with 608 modules and a total mass of 56 t. The liquid scintillator is made of paraffin oil (75% vol.), pseudocumene (25% vol.), and PMP (2 g/l). The modules are read-out by pairs of 3-inch PMTs and are enclosed by a tank with outside dimensions  $3.53 \text{ m} \times 3.20 \text{ m} \times 5.96 \text{ m}$ . Excellent energy resolution is obtained for electrons produced inside the detector and can be parametrized by  $\sigma_E = 11.5\% / \sqrt{E/\text{MeV}}$ . Gadolinium-coated paper was inserted between the modules for the detection of thermal neutrons. The detector is enclosed by a multilayer active veto system and 7000 t of steel

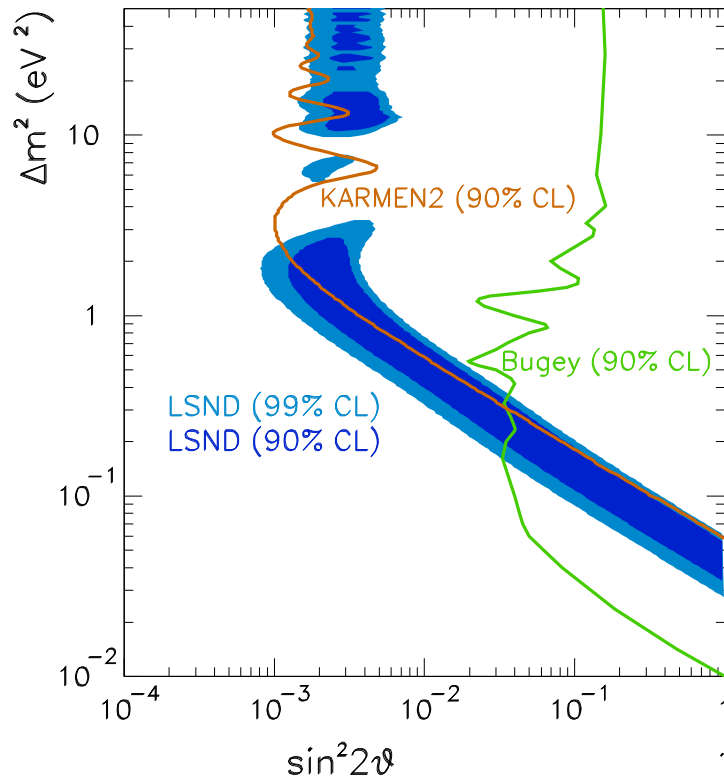


Figure 19. The  $(\sin^2 2\theta, \Delta m^2)$  oscillation parameter fit for the entire LSND data sample,  $20 < E_e < 200$  MeV. The inner and outer regions correspond to 90% and 99% CL allowed regions, while the curves are 90% CL limits from the Bugey reactor experiment and the KARMEN experiment at ISIS.

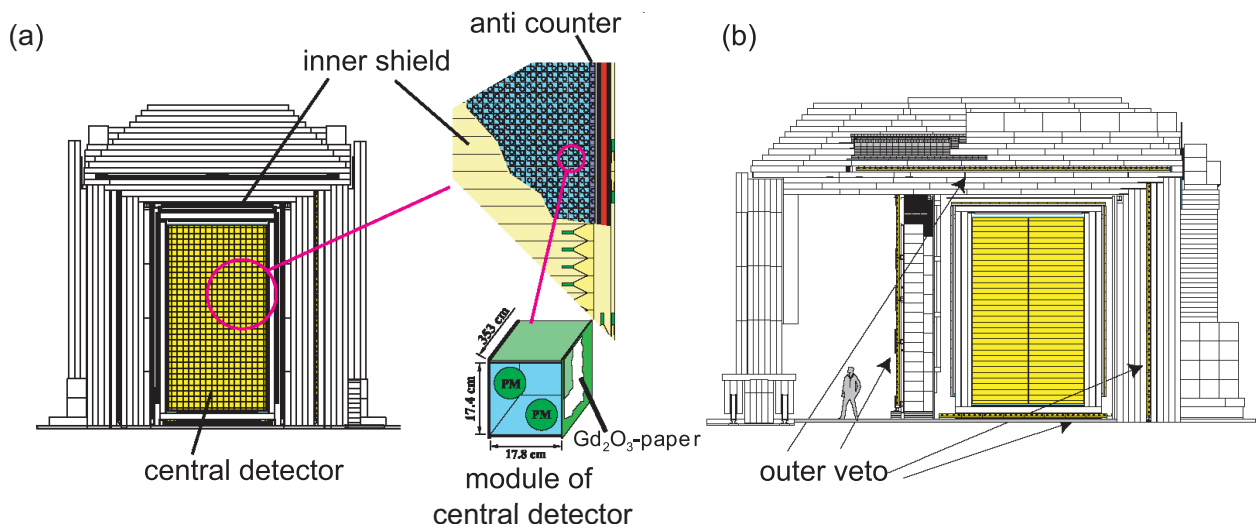


Figure 20. (a) Front view of the KARMEN detector showing details of the central detector region. (b) Side view of the detector.

shielding and is located 17.7 m from the neutrino source at an angle of  $100^\circ$  to the incident proton beam direction.

Event	Selection	Efficiency
$e^+$	no previous activity	0.709
$e^+$	$0.6 < t_{pr} < 300\mu s$	0.840
$e^+$	$16 < E_{pr} < 50 \text{ MeV}$	0.775
$(n, \gamma)$	$5 < \Delta t < 300\mu s$	
$(n, \gamma)$	$E_{del} < 8.0 \text{ MeV}$	0.416
$(n, \gamma)$	$V_c = 1.3m^3$	

Table VIII. The KARMEN event selection and corresponding efficiencies for the  $\bar{\nu}_\mu \rightarrow \bar{\nu}_e$  oscillation search.

Process	Number of Events
100% $\bar{\nu}_\mu \rightarrow \bar{\nu}_e$	$5826 \pm 534$
Cosmic-induced Background	$3.9 \pm 0.2$
Charged-current Coincidences	$5.1 \pm 0.2$
$\nu_e$ -induced Random Coincidences	$4.8 \pm 0.3$
Intrinsic $\bar{\nu}_e$ Background	$2.0 \pm 0.2$

Table IX. The KARMEN estimated number of events in the  $16 < E_e < 50 \text{ MeV}$  energy range due to 100%  $\bar{\nu}_\mu \rightarrow \bar{\nu}_e$  transmutation and to the four backgrounds with apparent neutrons.

## Event Selection

KARMEN searches for  $\bar{\nu}_\mu \rightarrow \bar{\nu}_e$  oscillations in the same way as in LSND by looking for the reaction  $\bar{\nu}_e p \rightarrow e^+ n$ , which gives a two-fold signature of a  $e^+$  followed by one or more  $\gamma$  from neutron capture. The neutrino oscillation event selection and corresponding efficiencies are summarized in Table VIII. For the  $e^+$  candidate it is required that there be no previous activity in the detector and veto, that the  $e^+$  occur from  $0.6 \mu s$  to  $10.6 \mu s$  after the beam spill, and that the  $e^+$  energy be in the range from 16 MeV to 50 MeV. For the  $\gamma$  candidate it is required that the  $\gamma$  occur from  $5 \mu s$  to  $300 \mu s$  after the  $e^+$ , that the  $\gamma$  have an energy less than 8.0 MeV, and that the  $\gamma$  be reconstructed within a coincidence volume of  $1.3 \text{ m}^3$ . The total efficiency for the two-fold signature is estimated to be  $0.192 \pm 0.0145$ .

## Neutrino Oscillation Signal and Background Reactions

Table IX shows the estimated number of events in the  $16 < E_e < 50 \text{ MeV}$  energy range for 100%  $\bar{\nu}_\mu \rightarrow \bar{\nu}_e$  transmutation. Also shown are the number of events for the four backgrounds with apparent neutrons. The first background is the cosmic-induced background, which is well measured from data collected with the beam off. The second background is due to  $\nu_e C \rightarrow e^- N_{gs}$ , where the  $N_{gs} \beta$  decay mimics the  $\gamma$  from neutron capture. The third background is due to normal  $\nu_e C \rightarrow e^- N^*$  inclusive interactions with an accidental  $\gamma$  coincidence. The final background is due to the intrinsic  $\bar{\nu}_e$  contamination in the beam from  $\mu^-$  DAR. The total background is estimated to be  $15.8 \pm 0.5$  events.

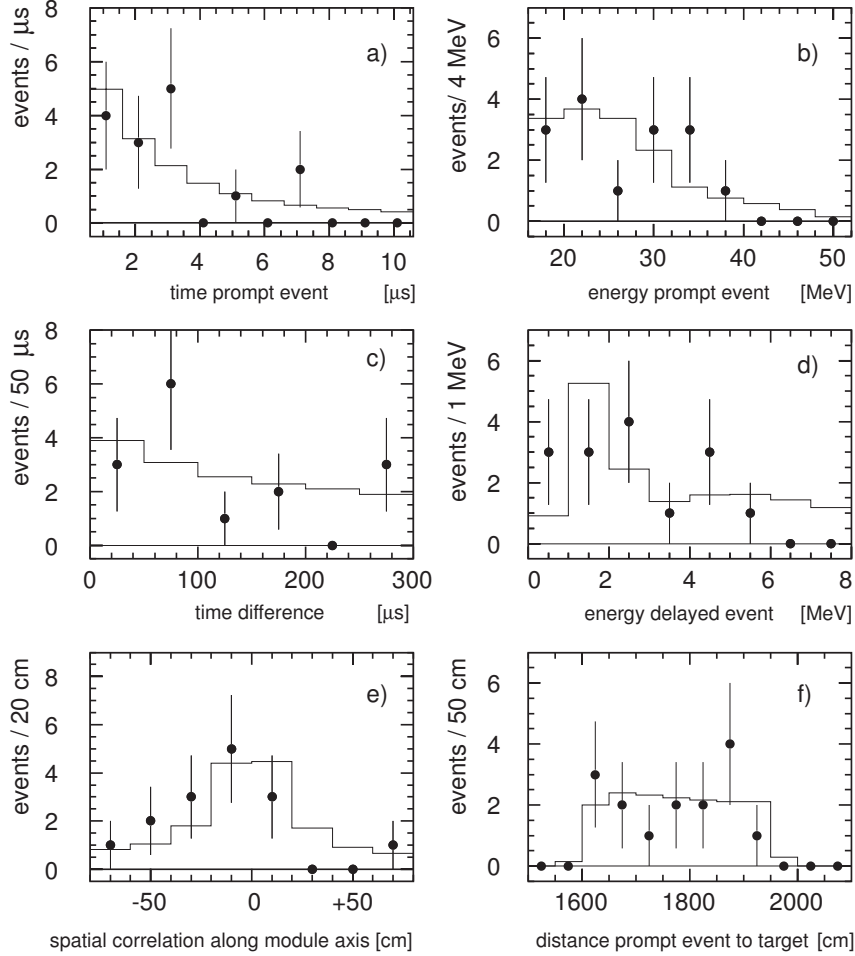


Figure 21. The energy, time, and spatial distributions for the events observed by the KARMEN experiment: (a) time of prompt events, (b) energy of prompt events, (c) time difference between prompt and delayed events, (d) energy of delayed events, (e) spatial correlation, and (f) distance to target of prompt events. The 15 oscillation candidate events are in good agreement with the background expectation of 15.8 events (solid line).

### KARMEN Neutrino Oscillation Results

KARMEN observes 15 events that pass the selection criteria discussed above, which is consistent with the estimated background of  $15.8 \pm 0.5$  events. The energy, time, and spatial distributions for the 15 events are shown in Fig. 21. Also shown are the shapes of the expected backgrounds, which are in good agreement with the data. A maximum likelihood fit to the data is performed [392] to obtain the 90% C.L. limits, as shown in Fig. 19. The LSND oscillation region with  $\Delta m^2 > 10 \text{ eV}^2$  is ruled-out by the KARMEN data; however, in the regions  $< 2 \text{ eV}^2$  and around  $7 \text{ eV}^2$  the KARMEN result is compatible with the LSND oscillation evidence.

### C. Joint Analysis of LSND and KARMEN Data

A joint analysis of the LSND and KARMEN experiments has been performed [386] that is based on a frequentist approach following the suggestions of reference [394]. For both experiments, the

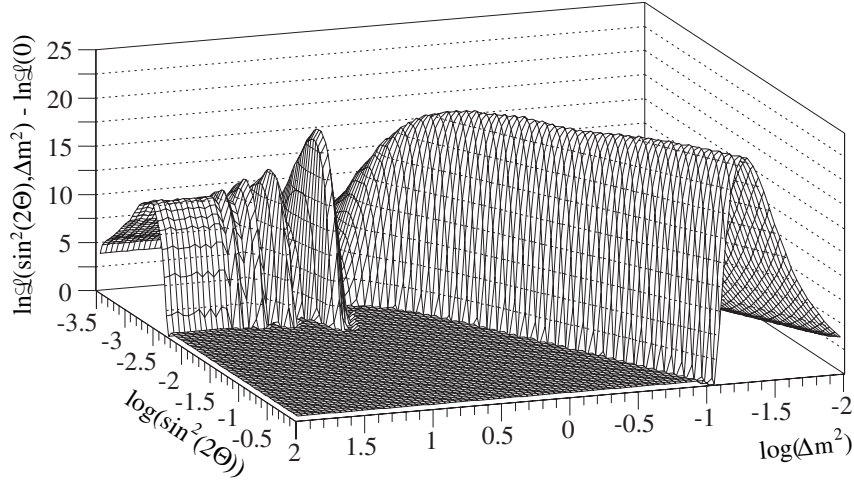


Figure 22. The combined LSND and KARMEN log-likelihood function in terms of  $\sin^2 2\theta$  and  $\Delta m^2$ .

data are analyzed with a maximum likelihood analysis followed by the extraction of confidence levels in a unified approach. The two experiments are found to be incompatible at a level of combined confidence of 36%. For the cases of statistical compatibility, Fig. 22 shows the combined LSND and KARMEN log-likelihood function in terms of  $\sin^2 2\theta$  and  $\Delta m^2$ . The maximum log-likelihood function occurs at  $\sin^2 2\theta = 1$  and  $\Delta m^2 = 0.05 \text{ eV}^2$ , which is 21.5 units of log-likelihood above the no oscillation hypothesis. Fig. 23 shows the confidence regions of the oscillation parameters for the combined likelihood analysis, assuming statistical compatibility of LSND and KARMEN. By combining the two experiments, the solutions with  $\Delta m^2 > 10 \text{ eV}^2$  are excluded, and there remain essentially two solutions: one with  $\Delta m^2 < 1 \text{ eV}^2$  and the other with  $\Delta m^2 \sim 7 \text{ eV}^2$ .

## D. Sterile Neutrino Analysis of Super-K

This section describes the sterile neutrino analysis done using the Super-K I and II atmospheric data. For detailed description of the Super-K experiment and the atmospheric neutrino data, one can refer to Ref. [395]. First there is a comparison of the results of the two oscillation models  $\nu_\mu \rightarrow \nu_\tau$  and  $\nu_\mu \rightarrow \nu_s$ . Then there is a study of how much sterile admixture can be allowed in the atmospheric neutrino oscillation based on a 2+2 model.

### Comparison of $\nu_\mu \rightarrow \nu_\tau$ and $\nu_\mu \rightarrow \nu_s$ Oscillations

#### Signatures of $\nu_\mu \rightarrow \nu_s$ oscillation

For the two competing models,  $\nu_\mu \rightarrow \nu_\tau$  and  $\nu_\mu \rightarrow \nu_s$ , though the second neutrino is not identified, there are some signatures which can be used to tell two oscillations apart. First, sterile neutrinos do not interact with matter at all so they do not even make any neutral current signals in the detector; and second, because the potentials experienced by  $\nu_\mu$  and  $\nu_s$  in matter are different, the matter effect modifies the survival probabilities of muon neutrinos.

To utilize the first signature, one must identify the neutral current events. For a water Cherenkov detector, neutral current events can be enriched by identifying the  $\pi^0$  particles which are produced

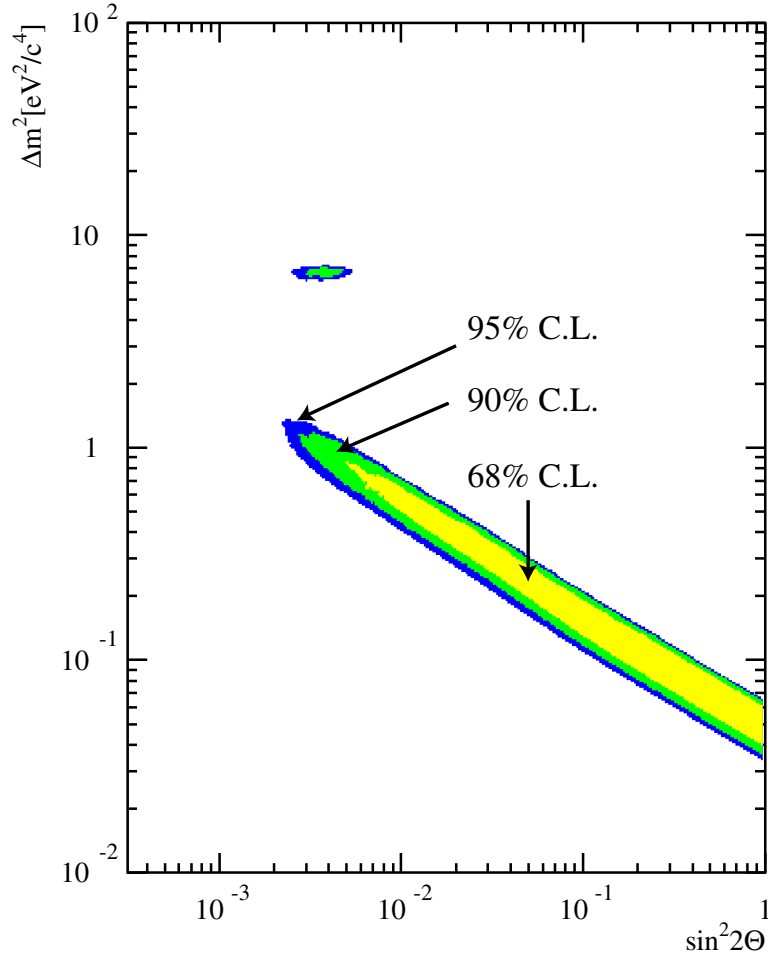


Figure 23. The confidence regions of the oscillation parameters for the combined likelihood analysis, assuming statistical compatibility of LSND and KARMEN.

in neutral current single-pion neutrino reactions [395]. Unlike in Ref. [395] tight cuts are not used in this analysis, in order to keep as many events as possible. As will be seen later, even without tight cuts, the neutral current enhanced selection defined below can be used to differentiate two models quite well. For sub-GeV events, the cuts used to enhance neutral current events are:

- Multi-ring events:  $\pi^0$  particles produced in neutral current reactions produce two  $e$ -like rings.
- The most energetic ring is  $e$ -like: this cut is chosen to get rid of CC  $\nu_\mu$  events.
- $400 \text{ MeV} < E_{vis} < 1330 \text{ MeV}$ : this cut is chosen to preserve the directional information of the parent neutrinos.

For the multi-GeV samples, the events rejected by the enhanced the charged current likelihood selection developed for the standard Super-K analysis are used. Ref. [396] provides detailed description on the charged and neutral current event enhancement method.

The zenith distributions of neutral current enhanced samples selected by these cuts are shown in Fig. 24. The hatched areas are neutral current events based on the Monte Carlo simulation. The percentages of neutral current events and charge current  $\nu_\mu$  contaminations are shown in Table X.

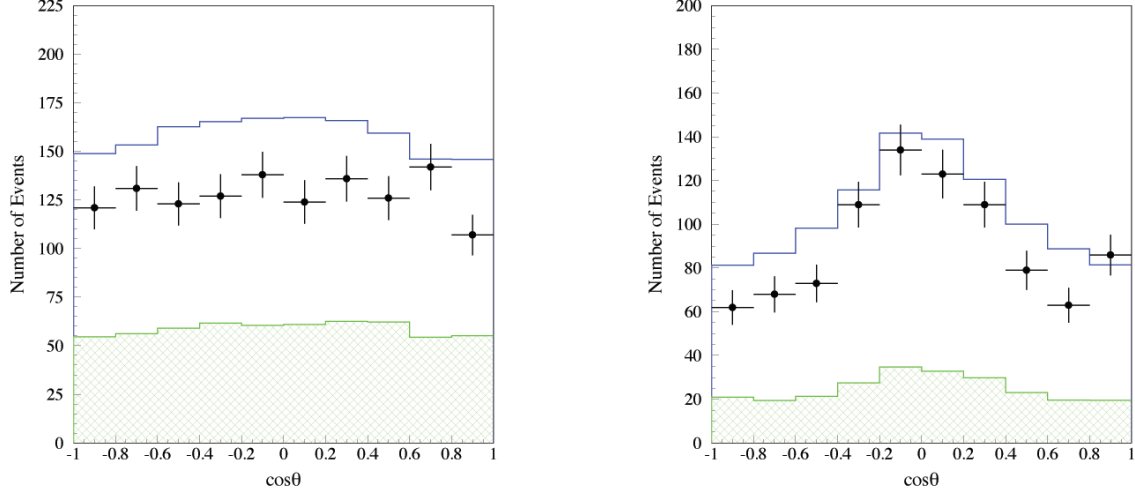


Figure 24. Zenith angle distributions of neutral current enhanced samples. Left: sub-GeV; right: multi-GeV

Table X. Portions of NC and CC events in the NC enhanced data samples

	NC events	CC $\nu_\mu$	CC $\nu_e$
Sub-GeV sample	37%	22%	41%
Multi-GeV sample	24%	35%	41%

The second signature of  $\nu_\mu \rightarrow \nu_s$  oscillation is the matter effect. It is known that in vacuum oscillation, the two-flavor survival probability is:  $P_{survival} = 1 - \sin^2 2\theta_{atm} \sin^2 1.27 \Delta m_{atm}^2 (eV^2) L(km) / E(GeV)$ . Where  $\sin^2 2\theta_{atm}$  is the mixing angle term and  $\Delta m_{atm}^2$  is the mass-squared difference between the two mass eigenstates. In matter with constant density, due to different forward scattering potentials between  $\nu_\mu / \bar{\nu}_\mu$  and  $\nu_s$ , the mixing angle and the mass-squared difference are replaced by the effective values in matter:

$$\begin{cases} \sin^2 2\theta_M = \frac{\sin^2 2\theta}{(\cos 2\theta - 2\zeta/\Delta m^2)^2 + \sin^2 2\theta} \\ \Delta m_M^2 = \Delta m^2 \sqrt{(\cos 2\theta - 2\zeta/\Delta m^2)^2 + \sin^2 2\theta} \end{cases} \quad (89)$$

Where  $\zeta = \mp \sqrt{2} G_F E N_n$  is the potential difference between  $\nu_\mu / \bar{\nu}_\mu$  and  $\nu_s$ .  $G_F$  is the Fermi constant,  $E$  is the neutrino (or antineutrino) energy, and  $N_n$  is the number density of neutrons in matter.

The density of the Earth is not a constant [397], so for atmospheric neutrinos crossing the Earth, the two-flavor survival probability with modifications due to the matter effect as shown in Eq. 89 is not valid any more. However, one can divide the Earth into different sections along the trajectories of neutrinos and approximate each section with a constant density. The final survival probability is calculated by diagonalizing the Hamiltonian of each small section, the method is described in Ref. [398]. Figure 25 shows the survival probabilities of neutrinos crossing the Earth with and without the matter effect using the density profile provided in Ref. [397]. As can be seen in Fig. 25, for atmospheric neutrinos, the oscillation probability is suppressed by the matter effect around and above 10 GeV.

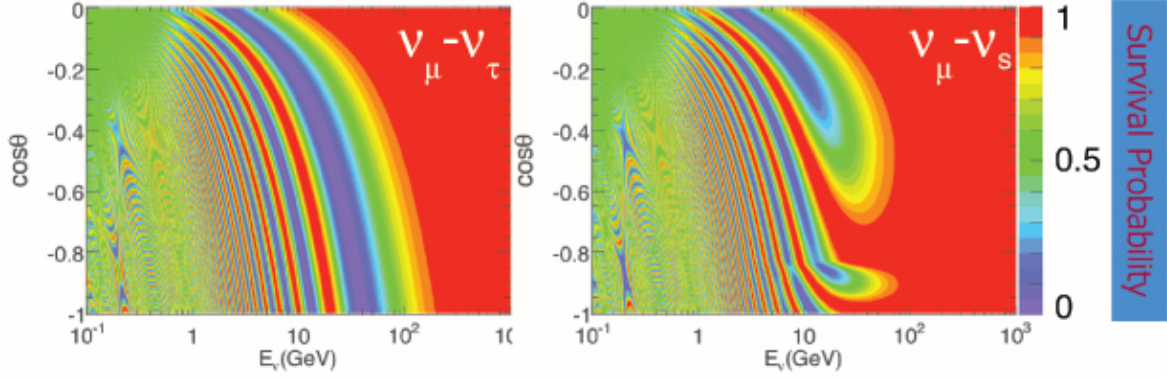


Figure 25. Survival probabilities of muon neutrinos crossing the Earth

### Best-fits of two models

These charged current and neutral current enhanced data samples can now be used to do the oscillation analysis. Considering that the uncertainty on the total number of multi-ring  $e$ -like events is relatively large, the neutral current enhanced sample is given an independent flux normalization, as was done for the charged current enhanced  $e$ -like events. The sub-GeV neutral current events are treated as one energy bin and the multi-GeV sample is divided into 4 energy bins based on  $\log E_{vis}$  values since the parent neutrinos have wider energy spread. Both samples are divided into 10 zenith angle bins based on the reconstructed event direction.

Using the least chi-square method, a  $\nu_\mu \rightarrow \nu_\tau$  oscillation fit using both CC and NC data samples is performed and the best-fit values for the mixing parameters are obtained. However, the goodness-of-fit is worse when compared to the results of a fit based on CC samples only. The minimum  $\chi^2/ndf$  is 971.2/853 with a probability of 7.3% as determined by toy Monte Carlo. Figure 26 (left) shows the  $\chi^2$  confidence contours. For the  $\nu_\mu \rightarrow \nu_s$  oscillation, maximal mixing is still preferred by  $\nu_\mu \rightarrow \nu_s$  oscillation as shown in Fig. 26 (right). However, the  $\Delta m^2$  value is driven up a bit,  $3.5 \times 10^{-3} \text{eV}^2$ . This is because, as was argued in the previous sub-section, the survival probabilities of  $\nu_\mu \rightarrow \nu_s$  oscillations are suppressed, thus, in order to fit the Super-K data, the best-fit value of  $\Delta m^2$  is increased to compensate for this suppression, which is also why the constraint on mixing angle is tighter than the  $\nu_\mu \rightarrow \nu_\tau$  case. The  $\chi^2/ndf$  value at the best-fit point is 1023.6/853, which is much worse than  $\nu_\mu \rightarrow \nu_\tau$  model. The  $\Delta\chi^2$  of 52.4 corresponds to a  $7.2\sigma$  exclusion level for the pure  $\nu_\mu \rightarrow \nu_s$  model.

Figure 27 shows the comparison of best-fit zenith angle distributions. For many bins of the data sample, the  $\nu_\mu \rightarrow \nu_s$  model reproduces SK observation as well as the  $\nu_\mu \rightarrow \nu_\tau$  model. However, for sub-GeV neutral current enhanced events, partially contained (PC) through-going events, upward  $\mu$  stopping events and non-showering  $\mu$  events, the  $\nu_\mu \rightarrow \nu_\tau$  model fits the data better than the  $\nu_\mu \rightarrow \nu_s$  model. Table XI shows the detailed  $\chi^2$  differences for the different categories of events. The  $\Delta\chi^2$  from data bins is 38.3. And Fig. 28 shows the comparison of the distributions of the pull terms. The pull term distribution of the  $\nu_\mu \rightarrow \nu_s$  oscillation is wider than the  $\nu_\mu \rightarrow \nu_\tau$  one, which is another sign that  $\nu_\mu \rightarrow \nu_\tau$  oscillation is a better model accounting for the atmospheric neutrino data. Pull terms contribute 14.1 to the  $\chi^2$  difference out of the total difference 52.4.

The  $\nu_\mu \rightarrow \nu_s$  model can not reproduce sub-GeV neutral current enhanced events as well as the  $\nu_\mu \rightarrow \nu_\tau$  model. The  $\nu_\mu \rightarrow \nu_\tau$  model expects the data fairly flat which is what is observed. However, for the  $\nu_\mu \rightarrow \nu_s$  model, the loss of neutral current events makes the expected distribution



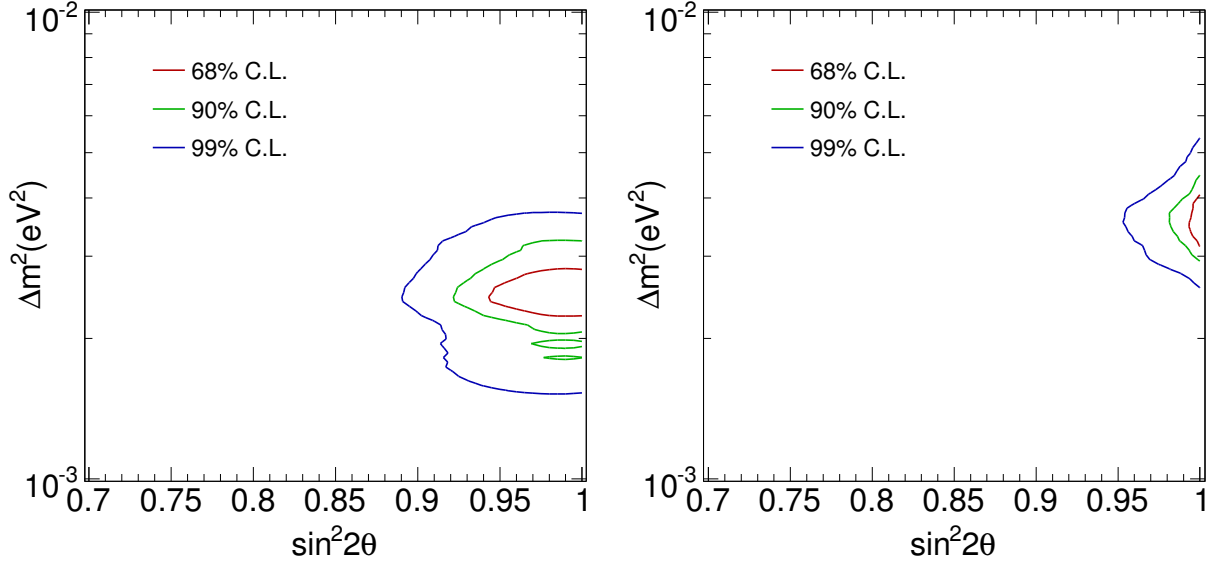


Figure 26.  $\chi^2$  contours of oscillations with NC enhanced samples for (left)  $\nu_\mu \rightarrow \nu_\tau$  (right)  $\nu_\mu \rightarrow \nu_s$

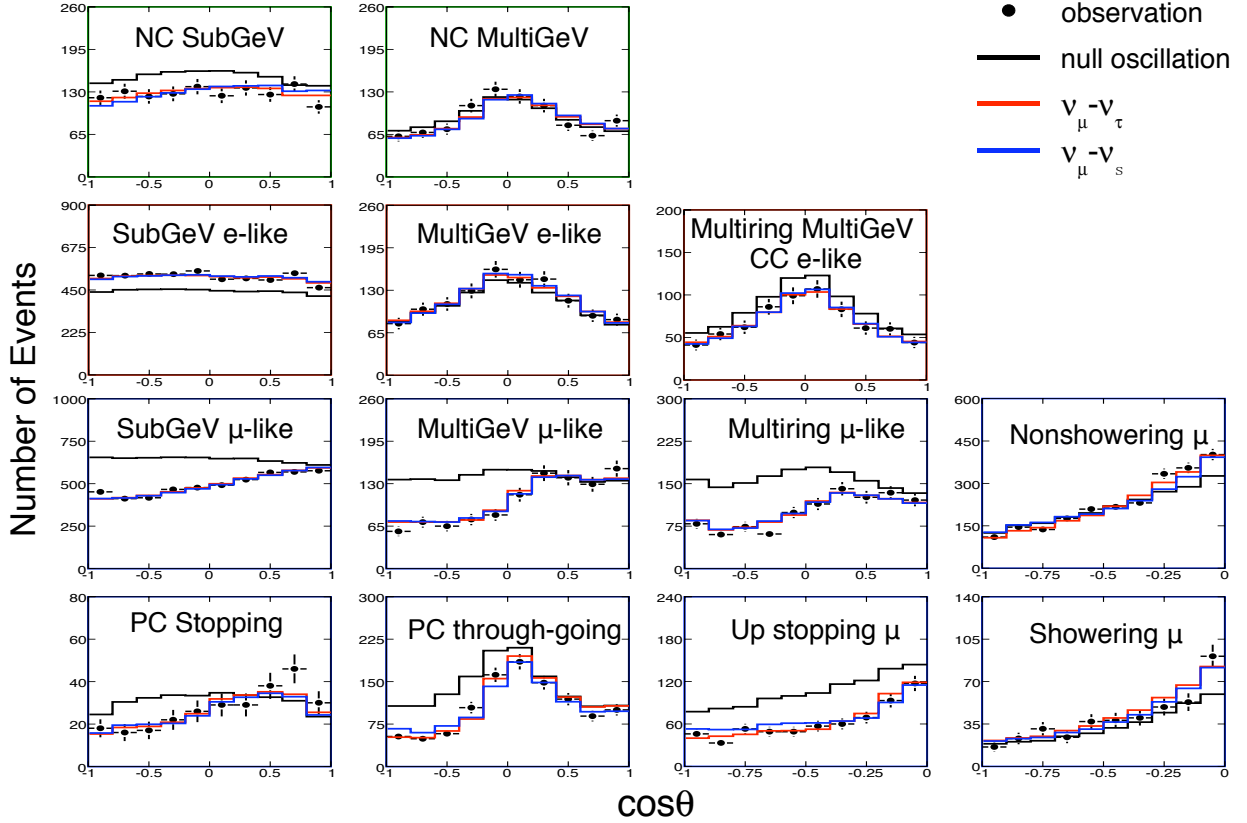


Figure 27. Comparison of the best-fit zenith angle distributions of  $\nu_\mu \rightarrow \nu_\tau$  and  $\nu_\mu \rightarrow \nu_s$  oscillations

tilted toward upward going bins where muon neutrinos oscillate into sterile ones.

As is shown in Fig. 25, around the atmospheric  $\Delta m^2$  scale, the strongest matter effect happen around 10 GeV. The typical energy of PC through-going events, Up $\mu$  stopping events and non-showering  $\mu$  events is around this scale, which is why these events can differentiate the two models

Table XI. Chi-square difference breakdown ( $\Delta\chi^2 = \chi_{\nu_\mu \rightarrow \nu_s}^2 - \chi_{\nu_\mu \rightarrow \nu_\tau}^2$ )

Data Samples	Bins (SK-I+SK-II)	$\chi_{\nu_\mu \rightarrow \nu_s}^2$	$\chi_{\nu_\mu \rightarrow \nu_\tau}^2$	$\Delta\chi^2$
Single ring sub-GeV $e$ -like	50+50	104.8	104.0	0.8
Single ring multi-GeV $e$ -like	50+50	108.6	110.7	-2.1
Multi-ring multi-GeV CC $e$ -like	50+50	86.6	85.8	0.8
Single ring sub-GeV $\mu$ -like	50+50	104.9	106.1	-1.2
Single ring multi-GeV $\mu$ -like	30+30	64.8	66.8	-2.0
Multi-ring $\mu$ -like	40+40	79.3	75.5	3.8
NC-enhanced sub-GeV events	10+10	19.5	14.5	5.0
NC-enhanced multi-GeV events	40+40	105.7	104.5	1.2
PC stopping $\mu$	40+40	128.7	125.8	2.9
PC through-going $\mu$	40+40	114.4	102.1	12.3
Upward stopping $\mu$	10+10	21.1	14.1	7.0
Upward non-showering $\mu$	10+10	28.1	16.9	11.2
Upward showering $\mu$	10+10	24.5	25.0	-1.5
TOTAL	430+430	991.1	952.8	38.3

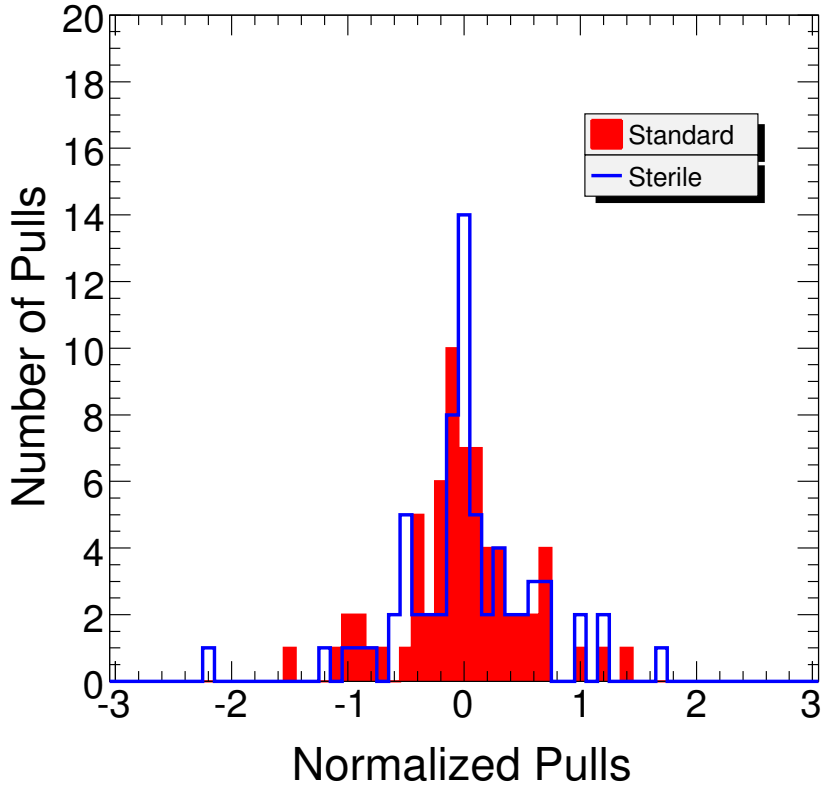


Figure 28. Distributions of the normalized pull terms of  $\nu_\mu \rightarrow \nu_\tau$  and  $\nu_\mu \rightarrow \nu_s$  oscillations

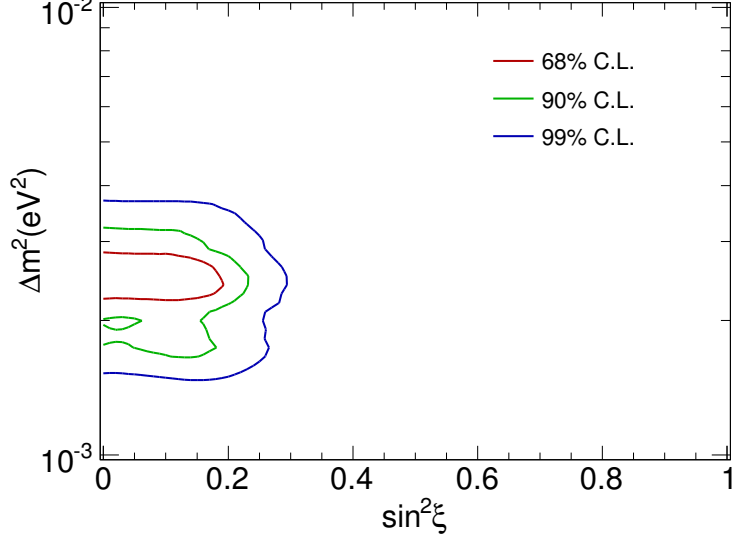


Figure 29. The  $\nu_s$  admixture allowance

better than other types of neutrino events. One can also see that though neutral current enhanced events help to tell two models apart, it is mainly the matter effect that distinguish two models due to the advantages such as long baselines, high energies and high matter densities that atmospheric neutrinos possess compared to long baseline experiments.

### An Admixture Model

Compared to  $\nu_\mu \rightarrow \nu_\tau$  oscillation, the fact that the  $\nu_\mu \rightarrow \nu_s$  oscillation is excluded at  $7.2\sigma$  level does not mean that there is no involvement of sterile neutrinos in Super-K atmospheric neutrino oscillations. It is still possible that a certain portion of muon neutrinos are oscillating into sterile neutrinos in addition to the dominant  $\nu_\mu \rightarrow \nu_\tau$  channel.

In the case of 2+2 mass hierarchy, according to G. L. Fogli *et. al.* [399], based on the current experimental results, the four flavor mixing can be transformed into two 2-flavor mixings by constructing two superposition states of  $\nu_\tau$  and  $\nu_s$  in the following way:

$$\begin{pmatrix} \nu_+ \\ \nu_- \end{pmatrix} = \begin{pmatrix} \cos \xi & \sin \xi \\ -\sin \xi & \cos \xi \end{pmatrix} \begin{pmatrix} \nu_\tau \\ \nu_s \end{pmatrix}.$$

For the atmospheric sector, the oscillation now is between  $\nu_\mu$  and  $\nu_+$  which is a superposition state:  $\cos \xi |\nu_\tau\rangle + \sin \xi |\nu_s\rangle$ . Thus, the portion of sterile neutrinos is  $\sin^2 \xi$ . Accordingly, the matter effect strength is weakened by a factor of  $\sin^2 \xi$ . Now, there are 3 parameters in this oscillation: the mixing angle between  $|\nu_{m_3}\rangle$  and  $|\nu_{m_4}\rangle$ ,  $\Delta m^2 = m_4^2 - m_3^2$  and the portion of sterile neutrinos  $\sin^2 \xi$ . Since the maximal mixing is a very strong constraint, it is assumed in this analysis, *i.e.*  $\sin^2 2\theta_{atm} = 1$ .

Using the same least chi-square framework, the best-fit is  $\sin^2 \xi = 0$  which means Super-K data prefer no sterile neutrino involvement, see Fig. 29. However, at 90% C.L., the data do allow a sterile admixture of 23%. Compared to the limit of 67% at 90% C.L. set by Fogli *et al* in Ref. [399] using the published Super-K data, this limit using the complete SK-I and SK-II data sets is much more stringent.

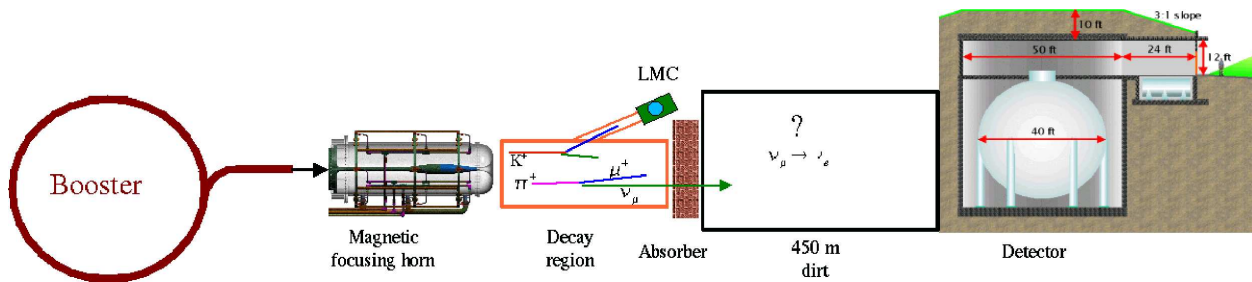


Figure 30. A schematic drawing of the MiniBooNE experiment.

## E. The MiniBooNE $\nu_e$ and $\bar{\nu}_e$ Appearance Searches

### Description of the Experiment

A schematic drawing of the MiniBooNE experiment at FNAL is shown in Fig. 30. The experiment is fed by protons with 8 GeV of kinetic energy from the Fermilab Booster, which interact in a 71 cm long Be target located at the upstream end of a magnetic focusing horn. The horn pulses with a current of 174 kA and, depending on the polarity, either focuses  $\pi^+$  and  $K^+$  and defocuses  $\pi^-$  and  $K^-$  to form a pure neutrino beam or focuses  $\pi^-$  and  $K^-$  and defocuses  $\pi^+$  and  $K^+$  to form a somewhat pure antineutrino beam. The produced pions and kaons decay in a 50 m long pipe, and a fraction of the neutrinos and antineutrinos [400] interact in the MiniBooNE detector, which is located 541 m downstream of the Be target. For the MiniBooNE results presented here, a total of  $6.5 \times 10^{20}$  POT (protons on target) were collected in neutrino mode and  $8.58 \times 10^{20}$  POT have been collected so far in antineutrino mode.

The MiniBooNE detector [401] consists of a spherical tank with a diameter of 12.2 m, filled with approximately 800 tons of mineral oil ( $CH_2$ ). A schematic drawing of the MiniBooNE detector is shown in Fig. 31. There are a total of 1280 8 inch detector phototubes (covering 10% of the surface area) and 240 veto phototubes. The fiducial volume has a 5 m radius and corresponds to approximately 450 tons. Only  $\sim 2\%$  of the phototube channels failed so far over the course of the run.

### Neutrino Oscillation Event Selection

MiniBooNE searches for  $\nu_\mu \rightarrow \nu_e$  oscillations by measuring the rate of  $\nu_e C \rightarrow e^- X$  (known as charged current quasi-elastic events or CCQE) and testing whether the measured rate is consistent with the estimated background rate. To select candidate  $\nu_e$  CCQE events, an initial selection is first applied:  $> 200$  tank hits,  $< 6$  veto hits, reconstructed time within the neutrino beam spill, reconstructed vertex radius  $< 500$  cm, and visible energy  $E_{vis} > 140$  MeV. It is then required that the event vertex reconstructed assuming an outgoing electron and the track endpoint reconstructed assuming an outgoing muon occur at radii  $< 500$  cm and  $< 488$  cm, respectively, to ensure good event reconstruction and efficiency for possible muon decay electrons. Particle identification (PID) cuts are then applied to reject muon and  $\pi^0$  events. Several improvements have been made to the neutrino oscillation data analysis since the initial data was published [116], including an improved background estimate, an additional fiducial volume cut that greatly reduces the background from events produced outside the tank (dirt events), and an increase in the data sample from  $5.579 \times 10^{20}$  POT to  $6.462 \times 10^{20}$  POT. A total of 89,200 neutrino events pass the initial selection, while

## MiniBooNE Detector

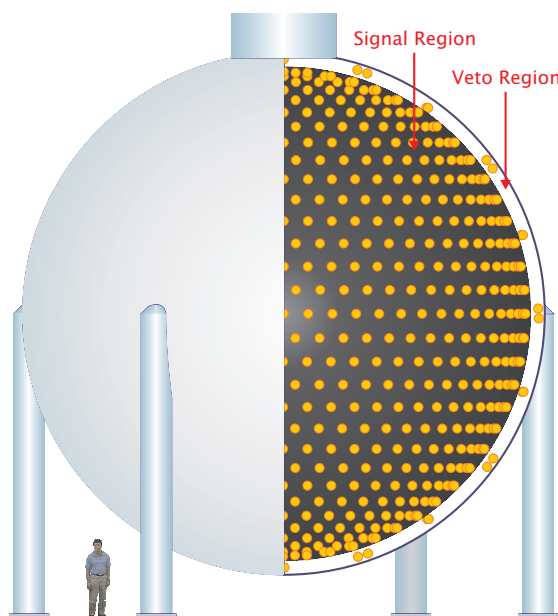


Figure 31. A schematic drawing of the MiniBooNE detector.

1069 events pass the complete event selection of the final analysis with  $E_\nu^{QE} > 200$  MeV, where  $E_\nu^{QE}$  is the reconstructed neutrino energy.

### Neutrino Oscillation Signal and Background Reactions

Table XII shows the expected number of candidate  $\nu_e$  CCQE background events with  $E_\nu^{QE}$  in the intervals 200–300 MeV, 300–475 MeV, and 475–1250 MeV, respectively, after the complete event selection of the final analysis. The background estimate includes antineutrino events, representing  $< 2\%$  of the total. The total expected backgrounds for the three energy regions are  $186.8 \pm 26.0$  events,  $228.3 \pm 24.5$  events, and  $385.9 \pm 35.7$  events, respectively. For  $\nu_\mu \rightarrow \nu_e$  oscillations at the best-fit LSND solution of  $\Delta m^2 = 1.2$  eV<sup>2</sup> and  $\sin^2 2\theta = 0.003$ , the expected number of  $\nu_e$  CCQE signal events for the three energy regions are 7 events, 37 events, and 135 events, respectively.

### MiniBooNE Neutrino Oscillation Results

Fig. 32 shows the reconstructed neutrino energy distribution for candidate  $\nu_e$  data events (points with error bars) compared to the MC simulation (histogram) [116], while Fig. 33 shows the event excess as a function of reconstructed neutrino energy. Good agreement between the data and the MC simulation is obtained for  $E_\nu^{QE} > 475$  MeV; however, an unexplained excess of electron-like events is observed for  $E_\nu^{QE} < 475$  MeV. As shown in Fig. 33, the magnitude of the excess is very similar to what is expected from neutrino oscillations based on the LSND signal. Although the shape of the excess is not consistent with simple two-neutrino oscillations, more complicated oscillation models with CP violation have shapes that may be consistent with the LSND signal.

Table XIII shows the number of data, background, and excess events for different  $E_\nu^{QE}$  ranges, together with the excess significance. For the final analysis, an excess of  $128.8 \pm 20.4 \pm 38.3$

Process	200 – 300 MeV	300 – 475 MeV	475 – 1250 MeV
$\nu_\mu$ CCQE	9.0	17.4	11.7
$\nu_\mu e \rightarrow \nu_\mu e$	6.1	4.3	6.4
NC $\pi^0$	103.5	77.8	71.2
NC $\Delta \rightarrow N\gamma$	19.5	47.5	19.4
Dirt Events	11.5	12.3	11.5
Other Events	18.4	7.3	16.8
$\nu_e$ from $\mu$ Decay	13.6	44.5	153.5
$\nu_e$ from $K^+$ Decay	3.6	13.8	81.9
$\nu_e$ from $K_L^0$ Decay	1.6	3.4	13.5
Total Background	$186.8 \pm 26.0$	$228.3 \pm 24.5$	$385.9 \pm 35.7$
LSND Best-Fit Solution	$7 \pm 1$	$37 \pm 4$	$135 \pm 12$

Table XII. The expected number of events in the  $200 < E_\nu^{QE} < 300$  MeV,  $300 < E_\nu^{QE} < 475$  MeV, and  $475 < E_\nu^{QE} < 1250$  MeV energy ranges from all of the significant backgrounds after the complete event selection of the final analysis. Also shown are the expected number of  $\nu_e$  CCQE signal events for two-neutrino oscillations at the LSND best-fit solution.

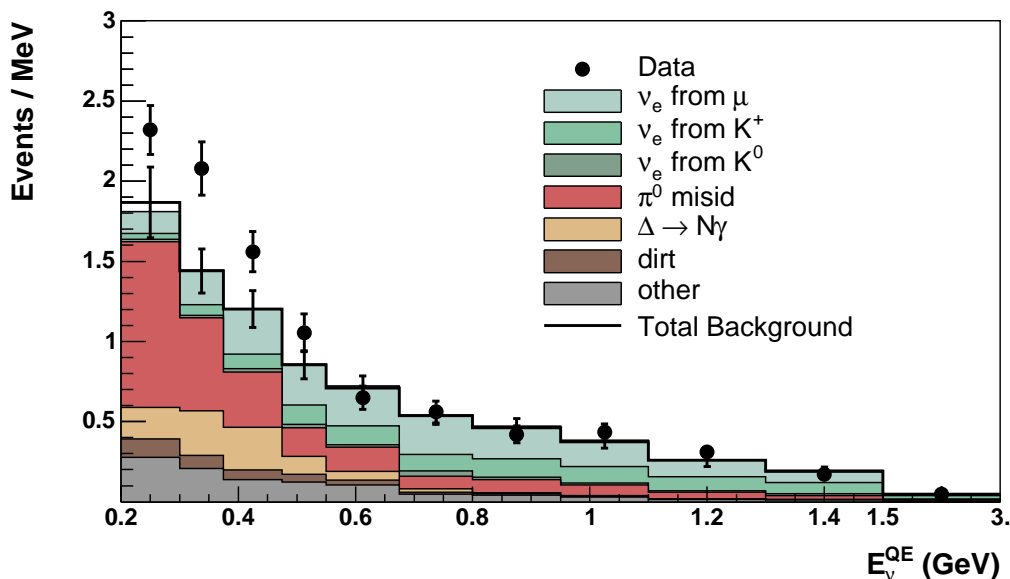


Figure 32. The MiniBooNE reconstructed neutrino energy distribution for candidate  $\nu_e$  data events (points with error bars) compared to the Monte Carlo simulation (histogram).

events is observed for  $200 < E_\nu^{QE} < 475$  MeV. For the entire  $200 < E_\nu^{QE} < 1250$  MeV energy region, the excess is  $151.0 \pm 28.3 \pm 50.7$  events. As shown in Fig. 34, the event excess occurs for  $E_{vis} < 400$  MeV, where  $E_{vis}$  is the visible energy.

Figs. 35 and 36 show the event excess as functions of  $Q^2$  and  $\cos(\theta)$  for events in the  $300 < E_\nu^{QE} < 475$  MeV range, where  $Q^2$  is determined from the energy and angle of the outgoing lepton and  $\theta$  is the angle between the beam direction and the reconstructed event direction. Also shown in the figures are the expected shapes from  $\nu_e C \rightarrow e^- X$  and  $\bar{\nu}_e C \rightarrow e^+ X$  charged-current (CC)

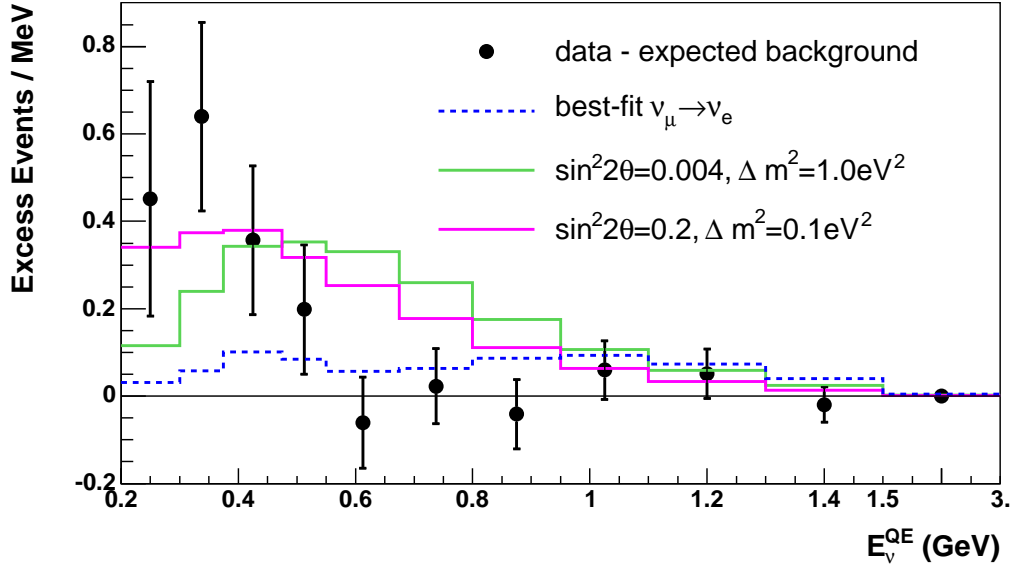


Figure 33. The excess of  $\nu_e$  candidate events observed by MiniBooNE in neutrino mode.

Event Sample	Final Analysis
200 – 300 MeV	
Data	232
Background	$186.8 \pm 13.7 \pm 22.1$
Excess	$45.2 \pm 13.7 \pm 22.1$
Significance	$1.7\sigma$
300 – 475 MeV	
Data	312
Background	$228.3 \pm 15.1 \pm 19.3$
Excess	$83.7 \pm 15.1 \pm 19.3$
Significance	$3.4\sigma$
200 – 475 MeV	
Data	544
Background	$415.2 \pm 20.4 \pm 38.3$
Excess	$128.8 \pm 20.4 \pm 38.3$
Significance	$3.0\sigma$
475 – 1250 MeV	
Data	408
Background	$385.9 \pm 19.6 \pm 29.8$
Excess	$22.1 \pm 19.6 \pm 29.8$
Significance	$0.6\sigma$

Table XIII. The number of data, background, and excess events for different  $E_\nu^{QE}$  ranges, together with the significance of the excesses in neutrino mode.

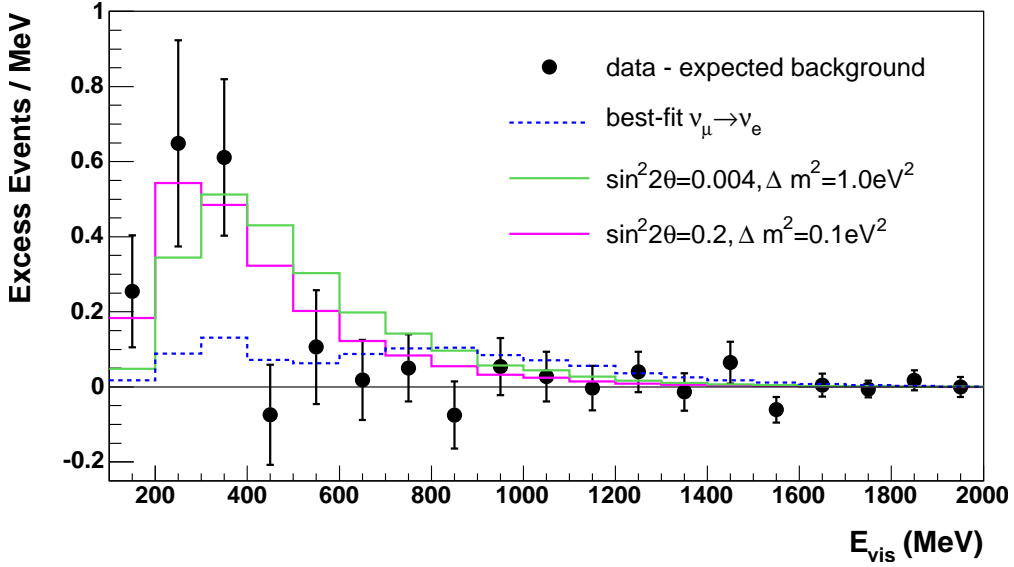


Figure 34. The neutrino event excess as a function of  $E_{vis}$  for  $E_{\nu}^{QE} > 200$  MeV. Also shown are the expectations from the best oscillation fit ( $\sin^2 2\theta = 0.0017$ ,  $\Delta m^2 = 3.14 \text{ eV}^2$ ) and from neutrino oscillation parameters in the LSND allowed region. The error bars include both statistical and systematic errors.

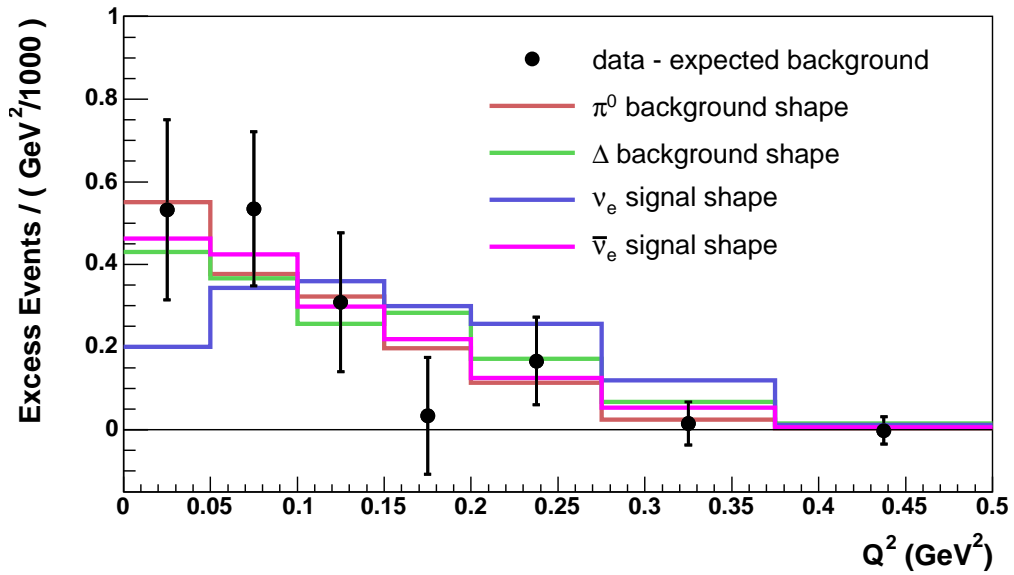


Figure 35. The neutrino event excess as a function of  $Q^2$  for  $300 < E_{\nu}^{QE} < 475$  MeV.

scattering and from the NC  $\pi^0$  and  $\Delta \rightarrow N\gamma$  reactions, which are representative of photon events produced by NC scattering. The NC scattering assumes the  $\nu_{\mu}$  energy spectrum, while the CC scattering assumes the transmutation of  $\nu_{\mu}$  into  $\nu_e$  and  $\bar{\nu}_e$ , respectively. As shown in Table XIV, the  $\chi^2$  values from comparisons of the event excess to the expected shapes are acceptable for all of the processes. However, any of the backgrounds in Table XIV would have to be increased by  $> 5\sigma$  to explain the low-energy excess.



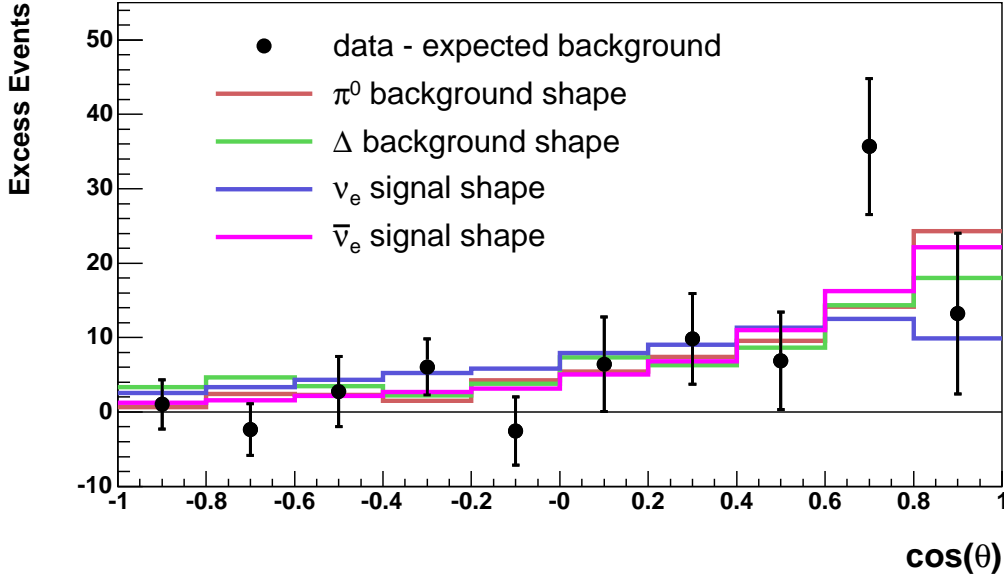


Figure 36. The neutrino event excess as a function of  $\cos(\theta)$  for  $300 < E_\nu^{QE} < 475$  MeV.

Process	$\chi^2(\cos\theta)/9$ DF	$\chi^2(Q^2)/6$ DF	Factor Increase
NC $\pi^0$	13.46	2.18	2.0 (6.8 $\sigma$ )
$\Delta \rightarrow N\gamma$	16.85	4.46	2.7 (18.4 $\sigma$ )
$\nu_e C \rightarrow e^- X$	14.58	8.72	2.4 (15.3 $\sigma$ )
$\bar{\nu}_e C \rightarrow e^+ X$	10.11	2.44	65.4 (41.0 $\sigma$ )

Table XIV. The  $\chi^2$  values from comparisons of the neutrino event excess  $Q^2$  and  $\cos(\theta)$  distributions for  $300 < E_\nu^{QE} < 475$  MeV to the expected shapes from various NC and CC reactions. Also shown is the factor increase necessary for the estimated background for each process to explain the low-energy excess and the corresponding number of sigma.

### MiniBooNE Antineutrino Oscillation Results

The same analysis that was used for the neutrino oscillation results is employed for the antineutrino oscillation results [117]. Fig. 37 shows the estimated neutrino fluxes for neutrino mode and antineutrino mode, respectively. The fluxes are fairly similar (the intrinsic electron-neutrino background is approximately 0.5% for both modes of running), although the wrong-sign contribution to the flux in antineutrino mode ( $\sim 18\%$ ) is much larger than in neutrino mode ( $\sim 6\%$ ). The average  $\nu_e$  plus  $\bar{\nu}_e$  energies are 0.96 GeV in neutrino mode and 0.77 GeV in antineutrino mode, while the average  $\nu_\mu$  plus  $\bar{\nu}_\mu$  energies are 0.79 GeV in neutrino mode and 0.66 GeV in antineutrino mode. Also, as shown in Fig. 38, the estimated backgrounds in the two modes are very similar, especially at low energy.

At present, with 8.58E20 POT in antineutrino mode, MiniBooNE observes an event excess,  $54.9 \pm 17.4 \pm 16.3$  events in the  $200 < E_\nu < 1250$  MeV energy range, which is consistent with the antineutrino oscillations suggested by the LSND data [114]. Fig. 39 shows the energy distributions of the MiniBooNE  $\bar{\nu}_e$  candidate events and the expected background, while Fig. 40 shows the excess of  $\bar{\nu}_e$  candidate events in antineutrino mode. Figs. 41 and 42 show that the MiniBooNE

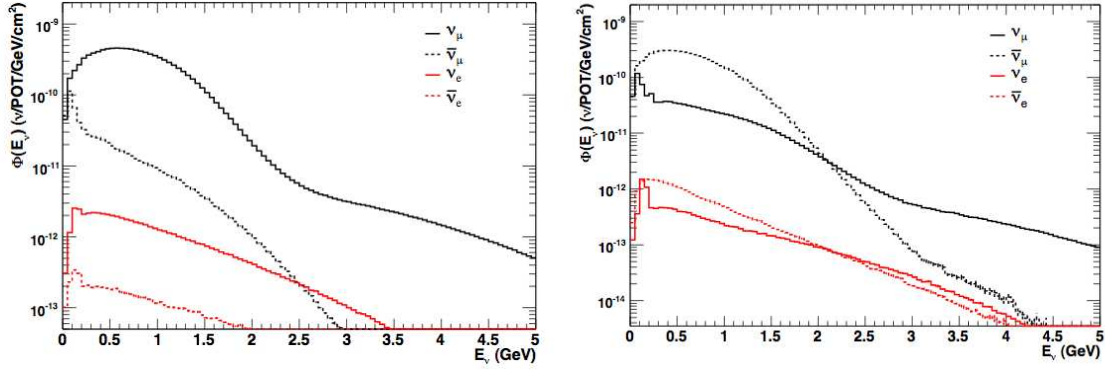


Figure 37. The estimated neutrino fluxes for neutrino mode (left plot) and antineutrino mode (right plot).

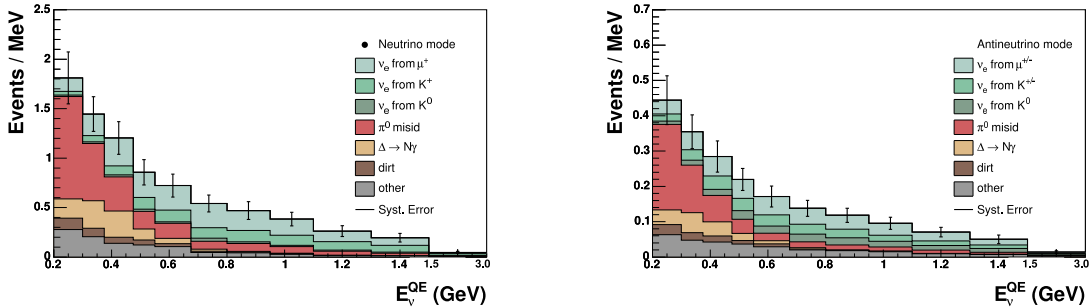


Figure 38. The estimated backgrounds for the neutrino oscillation search in neutrino mode (left plot) and antineutrino mode (right plot).

oscillation allowed region and  $L/E$  distribution agree well with LSND.

## F. Disappearance Results from Accelerator Experiments

### $\nu_\mu$ Disappearance from MiniBooNE and SciBooNE

MiniBooNE performed an initial search for  $\nu_\mu$  and  $\bar{\nu}_\mu$  disappearance in 2009 [402]. The search for  $\nu_\mu$  disappearance was revisited with the inclusion of data from the SciBooNE detector [403], which operated concurrently with MiniBooNE in the BNB for a period of time. So far, no evidence for  $\nu_\mu$  or  $\bar{\nu}_\mu$  disappearance due to short-baseline oscillations has been found. Limits have been placed on simple two neutrino mixing in the  $\Delta m^2$  region of interest for sterile neutrino models.

SciBooNE operated in the same beamline as MiniBooNE during 2007 and 2008, collecting data while the beam was operating in neutrino mode as well as antineutrino mode. SciBooNE was at a distance of 100 m from the target and consisted of three subdetectors. The first part is the SciBar detector [404], a finely segmented scintillation tracker that was relocated from the K2K neutrino beamline for cross section measurements at the neutrino energies available in the BNB. SciBar consists of 14,336 extruded polystyrene ( $C_8H_8$ ) scintillator strips arranged horizontally and vertically in a  $3 \times 3 \times 1.7$  m<sup>3</sup> volume. The 15 tons of the SciBar detector (10.6 tons fiducial volume) provides the primary interaction target for SciBooNE. The second sub-detector is an electron

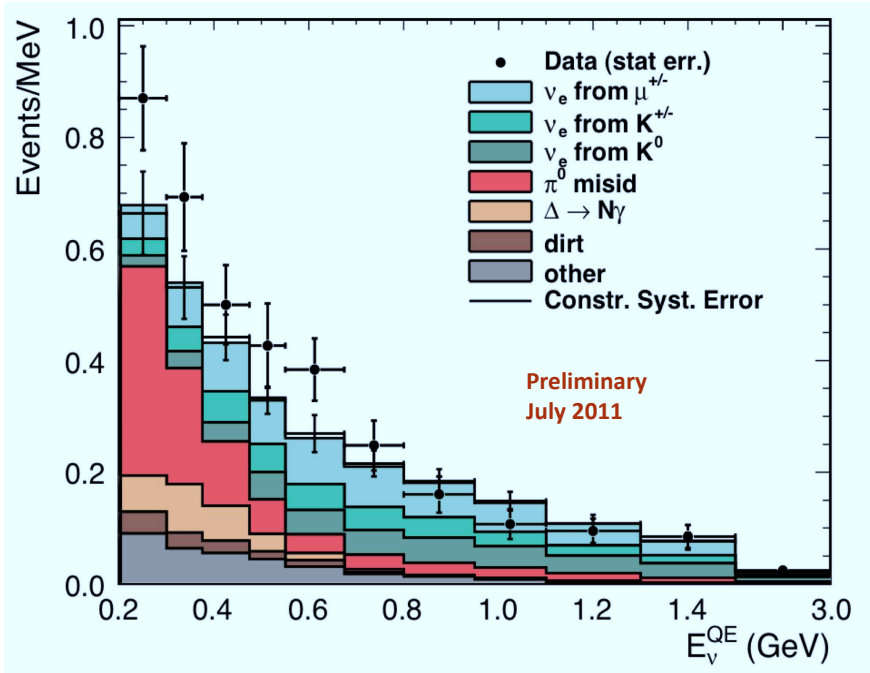


Figure 39. The energy distributions of the MiniBooNE  $\bar{\nu}_e$  candidate events and the expected background.

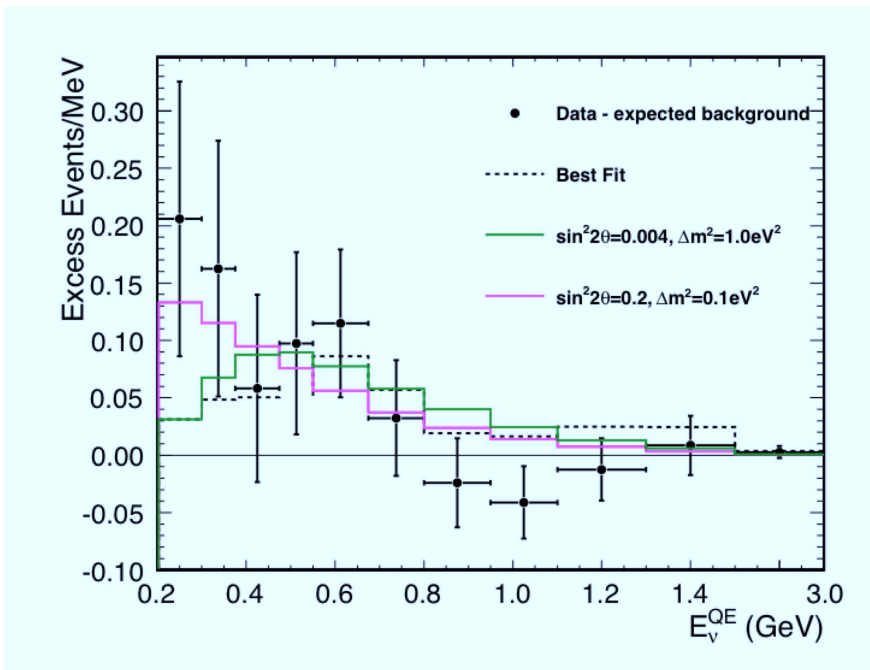


Figure 40. The excess of  $\bar{\nu}_e$  candidate events observed by MiniBooNE in antineutrino mode.

calorimeter (EC) constructed of 1 mm scintillating fibers embedded in lead foil and bundled into 64 modules. The third subdetector is a muon range detector (MRD). The MRD contains 12 iron plates sandwiched between scintillation counters, in alternating horizontal and vertical planes. The iron plates are 5 cm thick and the counters 6 mm thick. Photomultiplier tubes (PMTs) provide the readout for all three subdetectors.

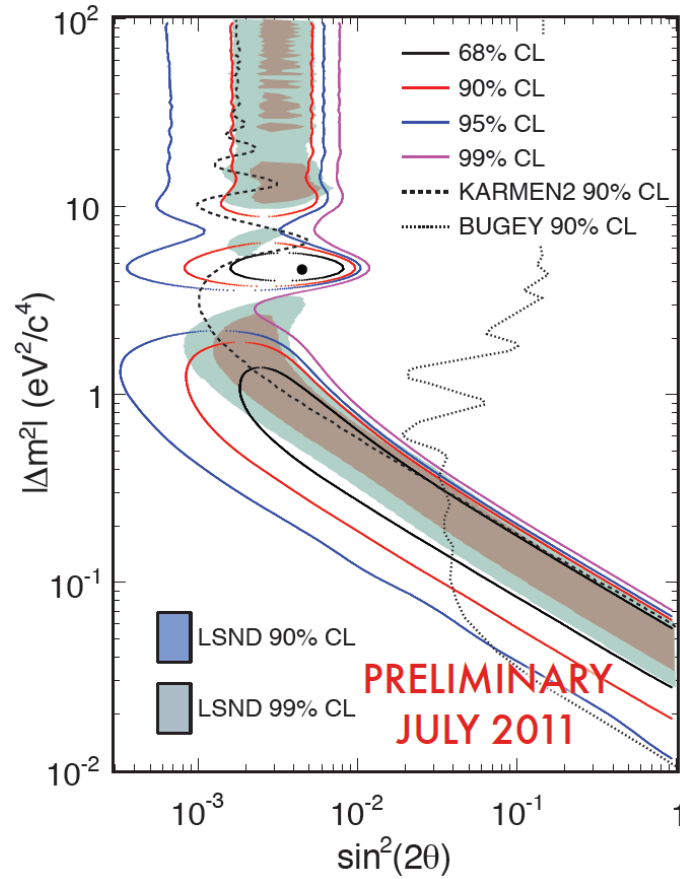


Figure 41. The MiniBooNE oscillation allowed region in antineutrino mode agrees well with LSND.

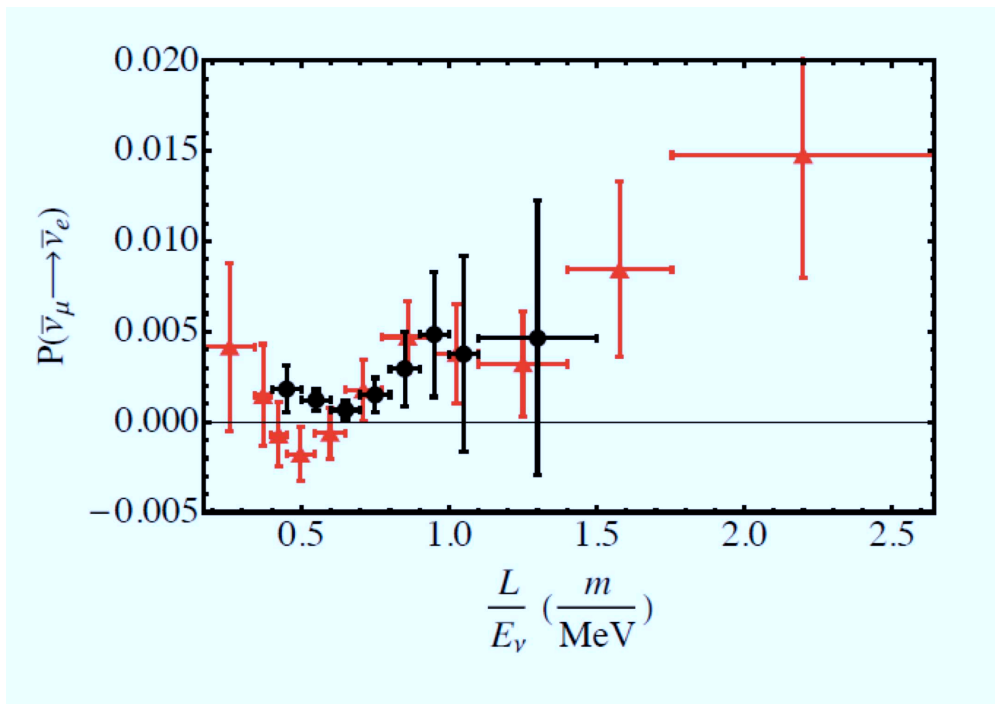


Figure 42. The MiniBooNE  $L/E$  distribution in antineutrino mode (red data points) agrees well with LSND (black data points).

## Neutrino Disappearance Event Selection

A CCQE event in MiniBooNE is selected by identifying a single muon track and the muon's decay electron. PMT timing information allows separating the neutrino interaction point from the decay electron. PMT timing and charge response data are used to reconstruct muon location, energy, and direction. The number of hits in the outer (veto) region, beam timing information, and number of hits within the fiducial volume, are used to reject cosmic ray muons. Particle ID cuts, based on event topology and reconstructions to alternate event hypotheses, are used to reject events that are not  $\nu_\mu$  or  $\bar{\nu}_\mu$  CCQE interactions.

Events that survive background rejection and particle ID cuts are binned in reconstructed neutrino energy,  $E_\nu^{QE}$ . The reconstructed neutrino energy is computed assuming that all events in the final sample are CCQE,  $\nu_l + N \rightarrow l + N'$ . This same assumption is applied to all events in data and Monte Carlo (MC), even though a sizeable fraction of the events are CC1 $\pi$  or multi-nucleon knockout events misidentified as CCQE events. 16 data bins from 0 to 1.9 GeV were used. The first bin was from 0 to 400 MeV and the remaining bins were 100 MeV wide each.

The MiniBooNE data set provided 190,454 events from  $5.58 \times 10^{20}$  protons on target (POT) collected prior to SciBooNE operation (MiniBooNE neutrino mode Run I). In addition, it included 29269 events from  $0.83 \times 10^{20}$  POT taken concurrently with the SciBooNE run (MiniBooNE neutrino mode Run II). In antineutrino mode, there were 27,053 events in MiniBooNE's final sample, from  $3.39 \times 10^{20}$  POT. The event rate as a function of POT is reduced by about a factor of five in antineutrino mode due to lower production and interaction rates.

SciBooNE collected neutrino mode data for  $0.99 \times 10^{20}$  POT.  $\nu_\mu(\bar{\nu}_\mu)$  CCQE interactions in SciBooNE are identified based on a single muon track [405]. The muon direction and energy is reconstructed based on the observed hits in each subdetector. Events are subdivided based on whether the muon stopped in the SciBar fiducial volume, within the MRD, or exited the MRD. Energy reconstruction was not possible for the MRD penetrated event sample. After event selection cuts and subtracting the prediction for cosmic ray events, the SciBar stopped sample contained 13589 events, the MRD stopped sample contained 20236 events, and the MRD penetrated sample contained 3544 events. Data were binned in 16 equally spaced bins from 300 MeV to 1.9 GeV.

## Disappearance Signal and Background Reactions

The MiniBooNE event samples were mostly  $\nu_\mu(\bar{\nu}_\mu)$  CCQE events, based on requiring two subevents (the initial interaction and the decay electron from the subsequent muon). The neutrino-mode sample had an estimated 74% CCQE purity, while the purity of the antineutrino mode sample was estimated at 70%. The antineutrino mode sample had roughly a 25%  $\nu_\mu$  content, while the  $\bar{\nu}_\mu$  content of the neutrino mode sample was negligible. The primary background was CC1 $\pi$  events where the outgoing pion is unobserved due to absorption in the nucleus.

SciBooNE's SciBar stopped sample was estimated to consist of 51% CCQE, 31% CC1 $\pi$ , and the remainder CC or neutral current (NC) multi-pion events. The MRD stopped sample had an estimated 52% CCQE content and 34% CC1 $\pi$  content and the MRD penetrated sample had an estimated 57% CCQE and 32% CC1 $\pi$  content.

Dominant uncertainties are the production of  $\pi^+$  in the target ( $\pi^+$  and  $\pi^-$  for antineutrino mode) and CCQE and CC1 $\pi$  cross sections for interactions in the detector. Detector related uncertainties

include light propagation and scattering in the mineral oil and PMT response. SciBooNE specific systematic uncertainties include muon energy loss in the scintillator and iron plates, light attenuation in the wavelength shifting fibers used for SciBar readout, and PMT response.

MiniBooNE (and SciBooNE) can not distinguish between  $\nu_\mu$  and  $\bar{\nu}_\mu$  events on an event-by-event basis. This is not a significant problem in neutrino mode, where the  $\bar{\nu}_\mu$  contamination is small. However, in antineutrino mode a sizeable fraction of the events are due to  $\nu_\mu$  interactions. In the oscillation analyses, neutrinos of the wrong sign (*i.e.* antineutrino in neutrino mode or neutrino in antineutrino mode) are assumed to not oscillate, unless otherwise stated.

A simple two neutrino oscillation model is used in the fits. MiniBooNE was at a distance of 541 m from the target and SciBooNE was at a distance of 100 m from the target. Mean neutrino flight distance, estimated from MC, was 76 m for SciBooNE events and 520 m for MiniBooNE events. Oscillations at the SciBooNE location are non-negligible for some of the physics parameter space of interest. Matter effects are assumed to be negligible.

### MiniBooNE $\nu_\mu$ and $\bar{\nu}_\mu$ Disappearance Results

The 2009 MiniBooNE-only oscillation search was a shape-only test. The MC prediction was normalized to data and the normalization uncertainty was removed from the error matrix. A Pearson's  $\chi^2$  test was used to determine confidence level (CL) boundaries. A  $16 \times 16$  error matrix accounted for bin-to-bin correlations in the uncertainties, which included flux, cross section, and detector systematic errors. The number of degrees of freedom (DOF) were determined with frequentist studies. The results of the analysis are shown in Fig. 43 (from Ref. [402]). Also shown are the results from CCFR [406, 407] ( $\nu_\mu$  and  $\bar{\nu}_\mu$ ) and CDHSW [408] ( $\nu_\mu$ ). More details on the CCFR and CDHSW results are provided below.

For the  $\nu_\mu$  disappearance analysis, the  $\chi^2$  for the null hypothesis (no disappearance) was 17.78. Based on 16 DOF, this implies a 34% probability. The best fit point was at  $\Delta m^2 = 17.5 \text{ eV}^2$  and  $\sin^2 2\theta = 0.16$ . With a  $\chi^2$  of 12.72 for 13 DOF, this has a 47% probability.

For the  $\bar{\nu}_\mu$  disappearance analysis, only the  $\bar{\nu}_\mu$  were assumed to oscillate in the fit. The  $\chi^2$  for the null hypothesis was 10.29 for 16 DOF, a probability of 85.1%. The best fit point was at  $\Delta m^2 = 31.32 \text{ eV}^2$  and  $\sin^2 2\theta = 0.96$ , with a  $\chi^2$  of 5.43 for 11 DOF, a 99.5% probability. When neutrinos and antineutrinos were allowed to oscillate in the fit, each with the same mixing parameters, the best fit point was at  $\Delta m^2 = 31.32 \text{ eV}^2$  and  $\sin^2 2\theta = 0.44$ , with a  $\chi^2$  of 7.90, a 99.2% probability.

### Joint MiniBooNE/SciBooNE $\nu_\mu$ Disappearance Results

Two complementary disappearance analyses were performed using the MiniBooNE and SciBooNE  $\nu_\mu$  CCQE event samples. In the simultaneous fit method, data from both detectors were fit simultaneously to a two neutrino oscillation model. In the spectrum fit method, SciBooNE data were used to determine energy dependent scale factors that were then applied to the MiniBooNE simulation. For both methods, a likelihood ratio test was used for the test statistic.

The simultaneous fit method used a total of 48 bins; 16 bins for the SciBar stopped data, 16 bins for the MRD stopped data, and 16 bins for the MiniBooNE data (either the Run I or the Run

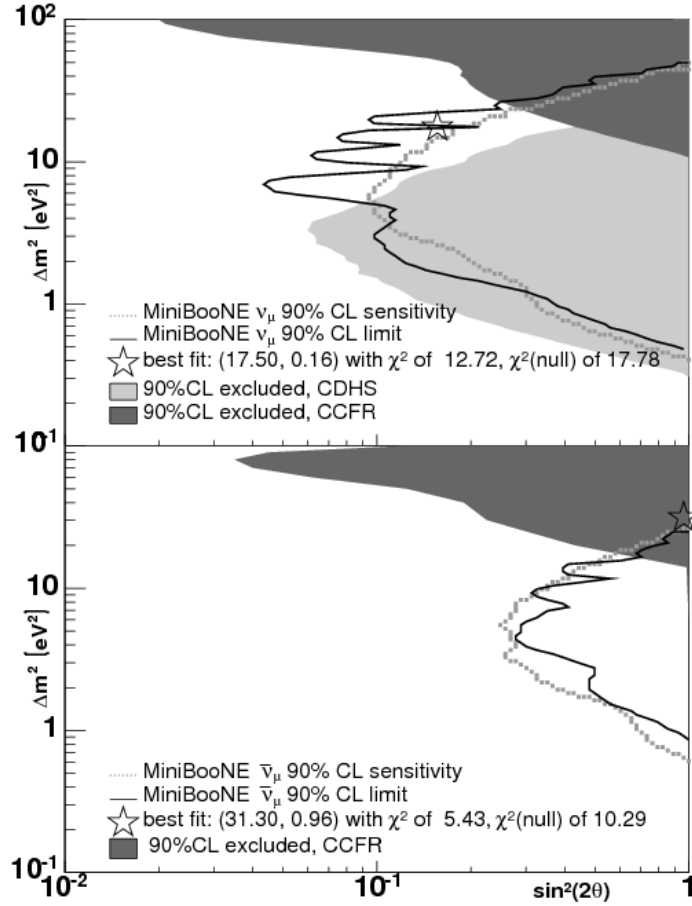


Figure 43. 90% CL sensitivity (dashed line) and limit (solid line) for MiniBooNE  $\nu_\mu$  disappearance analysis (top) and  $\bar{\nu}_\mu$  disappearance analysis (bottom). Previous limits from CCFR (dark gray) and CDHSW (light gray) are also shown.

II MiniBooNE data, which were handled separately). The prediction in each bin was normalized by the ratio of the total number of observed events in the MRD stopped and SciBar stopped data sets divided by the total number of predicted events for these data sets. The covariance matrix accounted for MiniBooNE uncertainties, SciBooNE uncertainties, as well as the correlations between the two detectors (a full 48 bin by 48 bin error matrix).

The spectrum fit method used a total of 32 bins; 16 bins for MiniBooNE Run I data, and 16 bins for MiniBooNE Run II data. The data in each bin were renormalized based on the data to MC ratio for the SciBooNE data, similar to the spectrum fit method. In addition, energy-dependent scale factors were applied to the MiniBooNE data. These scale factors were determined from SciBooNE data and constrained some of the neutrino flux and cross section uncertainties. Six scale factors, for six different true neutrino energy bins, were extracted by tuning the CC inclusive event predictions for all three SciBooNE event subsets. Uncertainties in these scale factors were incorporated in the MiniBooNE  $32 \times 32$  error matrix.

The results of this analysis can be seen in Fig. 44 (from Ref. [409]). Previous limits from CCFR [406, 407], CDHSW [408], MINOS [410], and MiniBooNE [402] are shown, for comparison. No evidence for  $\nu_\mu$  disappearance was found. However, limits on  $\sin^2 2\theta$  were improved, relative to previous results, in the region  $10 \rightarrow 30 \text{ eV}^2$ . Below  $\Delta m^2 = 5 \text{ eV}^2$ , the 90% CL limit excludes less parameter space than expected from the 90% CL sensitivity curve.

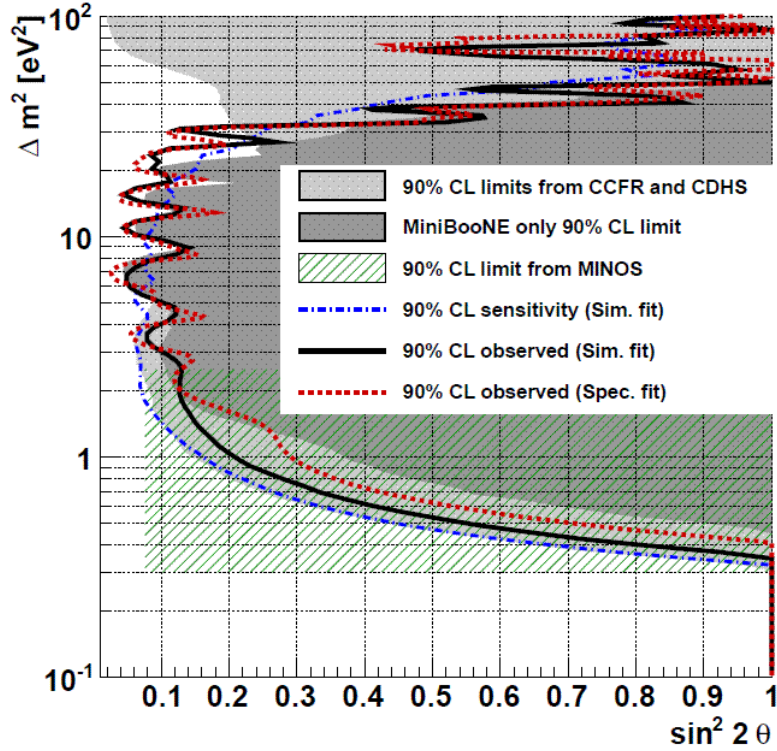


Figure 44. 90% CL sensitivity (dot-dash curve) and 90% CL limit (solid black curve) from simultaneous MiniBooNE/SciBooNE fit, and 90% CL limit from the spectrum fit method (red dashed curve). Previous limits from CCFR, CDHSW, MINOS, and MiniBooNE are also shown.

For the simultaneous fit, the  $\chi^2$  for the null hypothesis was 45.1 for a 59% probability (48 DOF). Using MiniBooNE Run I data, the best fit point was at  $\Delta m^2 = 43.7 \text{ eV}^2$ ,  $\sin^2 2\theta = 0.60$ , which had a  $\chi^2$  of 39.5. The best fit point using Run II data had a  $\chi^2$  of 41.5. Combining the two MiniBooNE data run periods provided negligible improvement relative to the Run I data alone. For the spectrum fit method, the  $\chi^2$  for the null hypothesis was 41.5 for a 12% probability (32 DOF). The best fit point was at  $\Delta m^2 = 41.7 \text{ eV}^2$ ,  $\sin^2 2\theta = 0.51$ , which had a  $\chi^2$  of 35.6. In Fig. 44, the 90% CL limit curve for the simultaneous fit is based on a  $\Delta\chi^2$  of 9.34. For the spectrum fit method, the  $\Delta\chi^2$  value for the 90% CL limit curve is 8.41.

A joint search for  $\bar{\nu}_\mu$  disappearance using data from MiniBooNE and SciBooNE is underway. This new analysis will take advantage of neutrino cross section measurements from neutrino mode data, as well as constraints on neutrino background in the antineutrino beam. In particular, the new analysis incorporates information learned from MiniBooNE's measurement of  $\nu_\mu$  CCQE cross sections and  $CC1\pi$  backgrounds in neutrino mode [411]. The normalization of the neutrino contamination in the antineutrino beam is adjusted based on direct measurements [412, 413]. A new  $K^+$  constraint from SciBooNE [414] reduces the MC estimate for  $K^+$  production in the beam and reduces its uncertainty.

The test statistic is a likelihood ratio for a two-neutrino oscillation fit. Normalization information is included (not a shape-only analysis). MiniBooNE's antineutrino mode data from  $7.4 \times 10^{20}$  POT and SciBooNE's antineutrino mode data from  $1.53 \times 10^{20}$  POT will be used. SciBooNE SciBar-stopped and MRD-stopped samples are combined.  $\nu_\mu$  are assumed to not oscillate, based on the results of the  $\nu_\mu$  disappearance analyses discussed above. MiniBooNE and SciBooNE CCQE event samples are in 21 bins, based on  $E_\nu^{QE}$  from 300 MeV to 1.9 GeV. Both histograms are simultane-



ously fit to MC predictions. A  $42 \times 42$  error matrix accounts for correlated systematic uncertainties.

The combination of improved constraints from MiniBooNE and SciBooNE, a MiniBooNE antineutrino dataset more than twice as large as that available for the 2009 disappearance analysis, and various changes in the analysis methodology, will significantly improve our sensitivity to muon antineutrino disappearance. Also planned is a joint MiniBooNE/SciBooNE analysis that will combine the neutrino mode and antineutrino mode data, further enhancing sensitivity to  $\nu_\mu$  ( $\bar{\nu}_\mu$ ) disappearance.

### $\nu_\mu$ Disappearance Results from CDHSW

The CDHSW (Cern Dortmund Heidelberg Saclay Warsaw) experiment performed a search for  $\nu_\mu$  disappearance [408]. 19.2 GeV protons struck a beryllium target, producing a shower of mesons that subsequently entered a 52 m long decay tunnel. The neutrino flux, produced by the decay of pions, kaons, and muons, peaked at about 1 GeV. The mean energy of accepted neutrino events was about 3 GeV. No magnetic focusing of the meson beam was employed. Two detectors operated simultaneously along the same beam line, enabling the reduction of systematic uncertainties in flux and cross sections.

The far detector, the original CDHSW detector, was located 885 m from the proton target. The near detector was located 130 m from the target. Each detector was made up of combinations of three different types of modules. The three module types consisted of layers of circular iron plates and scintillator hodoscopes sandwiched together, with PMTs for readout, but each module differed in the number of layers and the dimensions of the layers. The iron plates were not magnetized. The far detector was made up of a total of 21 of these modules and the near detector consisted of a total of six modules.

Timing and event selection cuts were used to eliminate most of the cosmic ray background and events from neutrino interactions that occurred outside the detector. Events were classified based on whether they originated in a module of type I or type II, and ratios of events in the near detector to events in the far detector were determined separately for the two module types. Events starting near the boundaries between modules were rejected.

Approximately 22,000 events passed selection cuts for the near detector, with a background contamination of 50 cosmic ray events. For the far detector, these numbers were 3300 and 290. Since the event range in the iron was a function of incident neutrino energy, events were binned according to this range projected onto the detector axis.

The far-to-near event ratios ( $R_{data}$ ) for each bin were corrected based on the square of the distance to the target and the detector masses. These ratios were also determined in MC that accounted for details of the beamline and the angular spread of the flux. The binned values of  $R_{data}/R_{MC}$  were then used in the disappearance analysis, based on two-neutrino mixing. Systematic uncertainty in the ratio of event rates was estimated at 2.5%. The data showed no significant signs of oscillations. The 90% CL result from CDHSW is shown in Figs. 43 and 44.

### $\nu_\mu$ and $\bar{\nu}_\mu$ Disappearance Results from CCFR

The CCFR experiment [406, 407] performed searches for  $\nu_\mu$  disappearance and  $\bar{\nu}_\mu$  disappearance as well as a combined analysis where the  $\nu_\mu$  and  $\bar{\nu}_\mu$  were assumed to have identical oscillation

parameters. Two detectors were operated at different distances along Fermilab’s narrow-band beam line. Five different  $\pi^+$  and  $K^+$  momentum settings were used: 100, 140, 165, 200, and 250 GeV/ $c$ . Mesons produced in the target were selected for sign and momentum by a series of dipole and quadrupole magnets. Subsequent neutrino energies ranged from 40 to 230 GeV. For the  $\bar{\nu}_\mu$  beam, a single momentum setting of 165 GeV/ $c$  was used.

The detectors were located at 715 and 1116 m from the midpoint of a 352 m long decay pipe. Each detector consisted of a calorimeter made up of steel plates instrumented with scintillation counters and spark chambers, followed by an iron toroidal muon spectrometer. The near detector calorimeter contained 108 tons of steel plates while the far detector calorimeter contained 4444 tons. Also, the near detector muon spectrometer had a single toroid while the far detector had three toroidal magnets. Muon neutrino and antineutrino CC interactions on iron produced a shower of hadrons measured by the iron calorimeter and a muon measured by the toroidal magnet(s). The neutrino energy was determined by summing the measured hadron and muon energies. For each beam setting, the events in each detector were divided into three energy bins.

Timing and event selection cuts were used to reduce background and to ensure that the same geometrical acceptance was realized for both detectors. After final event selection, the neutrino data consisted of 33,700 events in the near detector and 33,400 events in the far detector. For antineutrino data, the near detector sample contained 4960 events while the far detector sample contained 4600 events.

The oscillation analysis was based on the ratio of the number of events in each detector as a function of energy. The mean neutrino energy for each bin depended on the beam setting, and was determined from MC simulation. The ratios had to be corrected for differences between the detectors, including detector live times, veto counter dead times and reconstruction efficiencies. Additionally, MC was used to account for the effects of the finite size of the decay pipe. A likelihood ratio method was used to set 90% CL limits.

CCFR results can be seen in Figs. 43 and 44. For the  $\nu_\mu$  disappearance analysis, the  $\chi^2$  for the null hypothesis was 11.0 for 15 DOF. For the  $\bar{\nu}_\mu$  disappearance analysis, the  $\chi^2$  for the null hypothesis was 4.7 for 3 DOF. For the combined oscillation analysis (not shown)  $\nu_\mu$  and  $\bar{\nu}_\mu$  data were combined and assumed to have identical mixing parameters. In this case, the  $\chi^2$  for the null hypothesis was 15.7 for 18 DOF.

## G. The Gallium Anomaly

The GALLEX [415–417] and SAGE [418–421] solar neutrino detectors (see Refs. [422–430]) have been tested in so-called “Gallium radioactive source experiments” which consist in the detection of electron neutrinos produced by intense artificial  $^{51}\text{Cr}$  and  $^{37}\text{Ar}$  radioactive sources placed inside the detectors.

The radioactive nuclei  $^{51}\text{Cr}$  and  $^{37}\text{Ar}$  decay through electron capture,

$$e^- + {}^{51}\text{Cr} \rightarrow {}^{51}\text{V} + \nu_e, \quad (90)$$

$$e^- + {}^{37}\text{Ar} \rightarrow {}^{37}\text{Cl} + \nu_e, \quad (91)$$

emitting  $\nu_e$  lines with the energies and branching ratios listed in Tab. XV. The nuclear levels for the two processes are shown in Fig. 45. The two energy lines for each nuclear transition are due to electron capture from the K and L shells.

	$^{51}\text{Cr}$				$^{37}\text{Ar}$	
$E_\nu$ [keV]	747	752	427	432	811	813
B.R.	0.8163	0.0849	0.0895	0.0093	0.902	0.098
$\sigma$ [ $10^{-46}$ cm $^2$ ]	60.8	61.5	26.7	27.1	70.1	70.3

Table XV. Energies ( $E_\nu$ ), branching ratios (B.R.) and Gallium cross sections ( $\sigma$ ) of the  $\nu_e$  lines emitted in  $^{51}\text{Cr}$  and  $^{37}\text{Ar}$  decay through electron capture. The cross sections are interpolated from Tab. II of Ref. [432].

	GALLEX		SAGE	
k	G1	G2	S1	S2
source	$^{51}\text{Cr}$	$^{51}\text{Cr}$	$^{51}\text{Cr}$	$^{37}\text{Ar}$
$R_B^k$	$0.953 \pm 0.11$	$0.812^{+0.10}_{-0.11}$	$0.95 \pm 0.12$	$0.791 \pm^{+0.084}_{-0.078}$
$R_H^k$	$0.84^{+0.13}_{-0.12}$	$0.71^{+0.12}_{-0.11}$	$0.84^{+0.14}_{-0.13}$	$0.70 \pm^{+0.10}_{-0.09}$
radius [m]		1.9		0.7
height [m]		5.0		1.47
source height [m]	2.7	2.38		0.72

Table XVI. Experiment index  $k$ , source type and ratios  $R_B^k$  and  $R_H^k$  of measured and predicted  $^{71}\text{Ge}$  production rates in the GALLEX and SAGE radioactive source experiments. We give also the radii and heights of the GALLEX and SAGE cylindrical detectors and the heights from the base of the detectors at which the radioactive sources were placed along the axes of the detectors.

The neutrinos emitted by the radioactive sources have been detected through the same reaction used for the detection of solar neutrinos [431]:



which has the low neutrino energy threshold  $E_\nu^{\text{th}}({}^{71}\text{Ga}) = 0.233$  MeV. The cross sections of the  $\nu_e$  lines emitted in  $^{51}\text{Cr}$  and  $^{37}\text{Ar}$  decay interpolated from Tab. II of Ref. [432] are listed in Tab. XV.

The ratios  $R_B^k$  of measured and predicted  $^{71}\text{Ge}$  production rates in the GALLEX ( $k = \text{G1}, \text{G1}$ ) and SAGE ( $k = \text{S1}, \text{S1}$ ) radioactive source experiments are listed in Tab. XVI, together with the spatial characteristics of the experiments. The value of the average ratio is

$$R_B^{\text{Ga}} = 0.86 \pm 0.05. \quad (93)$$

Thus, the number of measured events is about  $2.8\sigma$  smaller than the prediction. This is the ‘‘Galium anomaly’’, which could be a manifestation of short-baseline neutrino oscillations [433–441].

As indicated by the ‘‘B’’ subscript, the ratios in Tab. XVI and Eq. (93) have been calculated with respect to the rate estimated using the best-fit values of the cross section of the detection process (92) calculated by Bahcall [432],

$$\sigma_B^{\text{bf}}({}^{51}\text{Cr}) = (58.1^{+2.1}_{-1.6}) \times 10^{-46} \text{ cm}^2, \quad (94)$$

$$\sigma_B^{\text{bf}}({}^{37}\text{Ar}) = (70.0^{+4.9}_{-2.1}) \times 10^{-46} \text{ cm}^2. \quad (95)$$

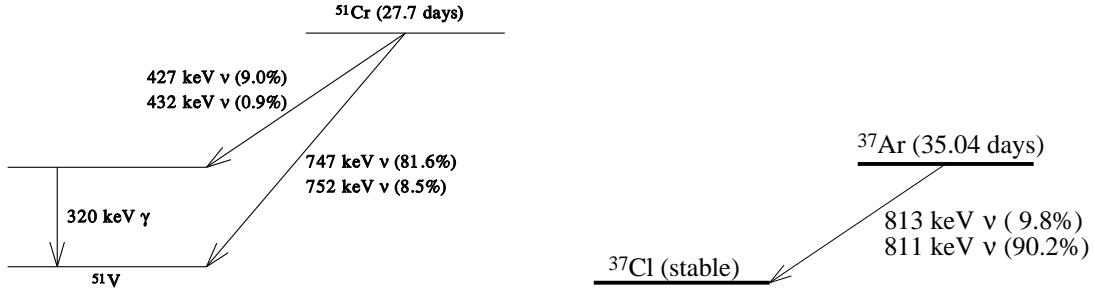


Figure 45. Nuclear levels for the electron capture processes in Eqs. (90) and (91). Figures from Ref. [419] and Ref. [420].

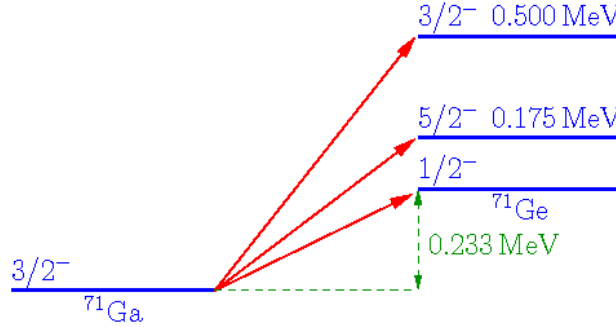


Figure 46. Nuclear levels for the Gallium detection process in Eq. (92).

The uncertainties of these cross sections are not taken into account in the ratios in Tab. XVI and Eq. (93). These uncertainties are large [432, 442, 443], because only the cross section of the transition from the ground state of  $^{71}\text{Ga}$  to the ground state of  $^{71}\text{Ge}$  is known with precision from the measured rate of electron capture decay of  $^{71}\text{Ge}$  to  $^{71}\text{Ga}$ . Electron neutrinos produced by  $^{51}\text{Cr}$  and  $^{37}\text{Ar}$  radioactive sources can be absorbed also through transitions from the ground state of  $^{71}\text{Ga}$  to two excited states of  $^{71}\text{Ge}$  at 175 keV and 500 keV (see Fig. 46), with cross sections which are inferred using a nuclear model from  $(p, n)$  measurements ( $p + ^{71}\text{Ga} \rightarrow ^{71}\text{Ge} + n$ ) [444].

Hence, at least part of the deficit of measured events with respect to the prediction could be explained by an overestimation of the transitions to the two excited states of  $^{71}\text{Ge}$  [420, 421, 445]. However, since the contribution of the transitions to the two excited states of  $^{71}\text{Ge}$  is only 5% [432], even the complete absence of such transitions would reduce the ratio of measured and predicted  $^{71}\text{Ge}$  event rates to about  $0.91 \pm 0.05$ , leaving an anomaly of about  $1.7\sigma$  [439].

The value and uncertainties of the detection cross section for the  $^{51}\text{Cr}$  source have been calculated in a reliable way by Haxton in Ref. [443] using the results of the  $(p, n)$  measurements [444] and nuclear shell-model calculations. His result is

$$\sigma_{\text{H}}(^{51}\text{Cr}) = (63.9 \pm 6.8) \times 10^{-46} \text{ cm}^2. \quad (96)$$

The mean value of this cross section is larger than the mean value of the Bahcall cross section in Eq. (94). This is due to a destructive interference between the spin and spin-tensor matrix elements in the  $(p, n)$  transition to the first excited states of  $^{71}\text{Ge}$  according to shell-model calculations. Therefore, the contribution of the transition to the first excited states of  $^{71}\text{Ge}$  in  $\nu_e$  detection is larger than that inferred from the  $(p, n)$  measurements, leading to a larger value for the total cross section.

The ratios  $R_{\text{H}}^k$  of measured and predicted  $^{71}\text{Ge}$  production rates in the GALLEX and SAGE

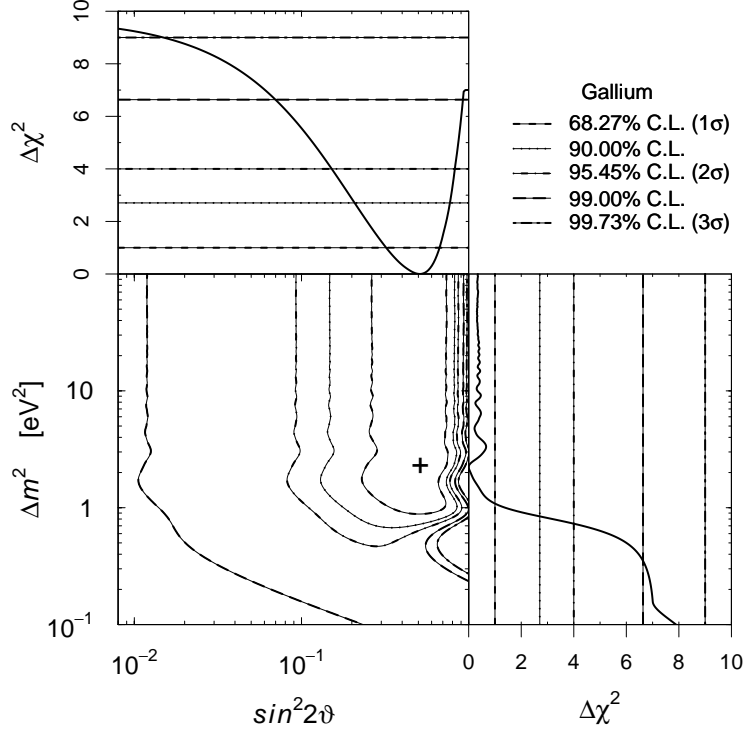


Figure 47. Allowed regions in the  $\sin^2 2\theta$ - $\Delta m^2$  plane and marginal  $\Delta\chi^2$ 's for  $\sin^2 2\theta$  and  $\Delta m^2$  obtained from the combined fit of the results of the two GALLEX  $^{51}\text{Cr}$  radioactive source experiments and the SAGE  $^{51}\text{Cr}$  and  $^{37}\text{Ar}$  radioactive source experiments [441]. The best-fit point corresponding to  $\chi^2_{\min}$  is indicated by a cross.

radioactive source experiments obtained with the Haxton detection cross section and uncertainties [441] are listed in Tab. XVI. The value of the average ratio is [441]

$$R_{\text{H}}^{\text{Ga}} = 0.76_{-0.08}^{+0.09}. \quad (97)$$

The mean value of  $R_{\text{H}}^{\text{Ga}}$  is smaller than that of  $R_{\text{B}}^{\text{Ga}}$ , but the uncertainties of  $R_{\text{H}}^{\text{Ga}}$  are rather large. Taking both effects into account, the statistical significance of the Gallium anomaly is about  $2.7\sigma$ , which is about equal to the  $2.8\sigma$  obtained with Eq. (93).

A natural explanation of the Gallium anomaly is electron neutrino disappearance due to short-baseline oscillations [433–441] (another explanation based on quantum decoherence in neutrino oscillations has been proposed in Ref. [446]).

Let us consider the electron neutrino survival probability

$$P_{\nu_e \rightarrow \nu_e}^{\text{SBL}}(L, E) = 1 - \sin^2 2\theta \sin^2\left(\frac{\Delta m^2 L}{4E}\right), \quad (98)$$

where  $\theta$  is the mixing angle,  $\Delta m^2$  is the squared-mass difference,  $L$  is the neutrino path length and  $E$  is the neutrino energy. This survival probability is effective in short-baseline (SBL) experiments in the framework of four-neutrino mixing schemes (see Refs. [424, 427, 429, 447]), which are the simplest extensions of three-neutrino mixing schemes which can accommodate the two measured small solar and atmospheric squared-mass differences  $\Delta m_{\text{SOL}}^2 \simeq 8 \times 10^{-5} \text{ eV}^2$  and  $\Delta m_{\text{ATM}}^2 \simeq 2 \times$

$10^{-3} \text{ eV}^2$  and one larger squared-mass difference for short-baseline neutrino oscillations,  $\Delta m^2 \gtrsim 0.1 \text{ eV}^2$ . The existence of a fourth massive neutrino corresponds, in the flavor basis, to the existence of a sterile neutrino  $\nu_s$ .

Figure 47 shows the allowed regions in the  $\sin^2 2\theta - \Delta m^2$  plane and the marginal  $\Delta\chi^2 = \chi^2 - \chi_{\min}^2$ 's for  $\sin^2 2\theta$  and  $\Delta m^2$ , from which one can infer the corresponding uncorrelated allowed intervals [441]. The best-fit values of the oscillation parameters are

$$\sin^2 2\theta_{\text{bf}} = 0.50, \quad \Delta m_{\text{bf}}^2 = 2.24 \text{ eV}^2. \quad (99)$$

The value of the likelihood ratio between the null hypothesis of no oscillations and the oscillation hypothesis,

$$\frac{\mathcal{L}_0}{\mathcal{L}(\sin^2 2\theta_{\text{bf}}, \Delta m_{\text{bf}}^2)} = 8 \times 10^{-3}, \quad (100)$$

is in favor of the oscillation hypothesis. It corresponds to  $\Delta\chi^2 = 9.7$ , which, with two degrees of freedom, disfavors the null hypothesis of no oscillations at 99.23% C.L. ( $2.7\sigma$ ).

In conclusion, the Gallium anomaly is statistically significant at a level of about  $2.7\sigma$ . The analysis of the data of the Gallium radioactive source experiments in terms of neutrino oscillations indicates values of the oscillation amplitude  $\sin^2 2\theta \gtrsim 0.07$  and squared-mass difference  $\Delta m^2 \gtrsim 0.35 \text{ eV}^2$  at 99% C.L..

## H. The Reactor Antineutrino Anomaly

### Antineutrinos from Reactors

Nuclear reactors are very intense sources of neutrinos that have been used all along the neutrino's history, from its discovery up to the most recent oscillation studies. With an average energy of about 200 MeV released per fission and 6 neutrinos produced along the  $\beta$ -decay chains of the fission products, one expects about  $2 \times 10^{20} \nu/s$  emitted in a  $4\pi$  solid angle from a 1 GW reactor (thermal power). Since unstable fission products are neutron-rich nuclei, all  $\beta$ -decays are of  $\beta^-$  type and the neutrino flux is actually pure electronic antineutrinos ( $\bar{\nu}_e$ ).

The neutrino oscillation search at a reactor is always based on a disappearance measurement, using the powerful inverse beta decay (IBD) detection process to discriminate the neutrino signal from backgrounds. The observed neutrino spectrum at a distance  $L$  from a reactor is compared to the expected spectrum. If a deficit is measured it can be interpreted in terms of the disappearance probability which, in the two neutrino mixing approximation, reduces to

$$P_{ee} = 1 - \sin^2 2\theta \sin^2 \left( \frac{\Delta m^2 L}{2E} \right) \quad (101)$$

with  $\Delta m^2$  the difference between the squared masses of the two neutrino states and  $\theta$  the mixing angle fixing the amplitude of the oscillation.

Here, we will especially consider reactor antineutrino detector at short distances below 100 m from the reactor core, in particular ILL-Grenoble, Goesgen, Rovno, Krasnoyarsk, Savannah River

and Bugey [391, 448–455]. These experiments have played an important role in the establishment of neutrino physics, and especially neutrino oscillations, over the last fifty years [25]. Unlike modern long baseline reactor experiments motivated by the measurement of the last unknown mixing angle  $\theta_{13}$  [456–458], which measure  $P_{ee}$  by comparing the event rate and spectrum in two detectors at different distances, the aforementioned short-baseline experiments can only employ one detector and therefore depend on an accurate theoretical prediction for the emitted  $\bar{\nu}_e$  flux and spectrum to measure  $P_{ee}$ .

Until late 2010, all data from reactor neutrino experiments appeared to be fully consistent with the mixing of  $\nu_e$ ,  $\nu_\mu$  and  $\nu_\tau$  with three mass eigenstates,  $\nu_1$ ,  $\nu_2$  and  $\nu_3$ , with the squared mass differences  $|\Delta m_{31}^2| \simeq 2.4 \cdot 10^{-3} \text{ eV}^2$  and  $\Delta m_{21}^2/|\Delta m_{31}^2| \simeq 0.032$ . The measured rate of  $\bar{\nu}_e$  was found to be in reasonable agreement with that predicted from the ‘old’ reactor antineutrino spectra [459–461], though slightly lower than expected, with the measured/expected ratio at  $0.980 \pm 0.024$ , including recent revisions of the neutron mean lifetime,  $\tau_n = 881.5 \text{ s}$ , in 2011 [25] (the cross section of the detection reaction of  $\bar{\nu}_e$  on free protons  $\bar{\nu}_e + p \rightarrow e^+ + n$  is inversely proportional to the neutron lifetime).

In preparation for the Double Chooz reactor experiment [47], the Saclay reactor neutrino group re-evaluated the specific reactor antineutrino flux for  $^{235}\text{U}$ ,  $^{239}\text{Pu}$ ,  $^{241}\text{Pu}$ , and  $^{238}\text{U}$ . In 2011, they reported their results [462], which correspond to a flux that is a few percent higher than the previous prediction. This also necessitates a reanalysis of the ratio of observed event rate to predicted rate for 19 published experiments at reactor–detector distances below 100 m.

### Reference antineutrino spectra

The distribution of the fission products of uranium or plutonium isotopes covers hundreds of nuclei, each of them contributing to  $S_k(E)$  through various  $\beta$ -decay chains. At the end the total antineutrino spectrum is a sum of thousands of  $\beta$ -branches weighted by the branching ratio of each transition and the fission yield of the parent nucleus. Despite the impressive amount of data available in nuclear databases the *ab initio* calculation of the emitted antineutrino spectrum is difficult. Moreover, when looking at the detected spectrum through the IBD process, the 1.78 MeV threshold and the quadratic energy dependence of the cross-section enhances the contribution of transitions with large end-points ( $E_0 > 4 \text{ MeV}$ ). Systematic errors of the nuclear data and the contribution of poorly known nuclei become a real limitation for the high energy part of the antineutrino spectrum. Uncertainties below the 10% level seem to be out of reach with the *ab initio* approach, preventing any accurate oscillation analysis.

In order to circumvent this issue, measurements of total  $\beta$ -spectra of fissile isotopes were performed in the 1980s at ILL [459–461], a high flux research reactor in Grenoble, France. Thin target foils of fissile isotopes  $^{235}\text{U}$ ,  $^{239}\text{Pu}$  and  $^{241}\text{Pu}$  were exposed to the intense thermal neutron flux of the reactor. A tiny part of the emitted electrons could exit the core through a straight vacuum pipe to be detected by the high resolution magnetic spectrometer BILL [463]. The electron rates were recorded by a pointwise measurement of the spectrum in magnetic field steps of 50 keV, providing an excellent determination of the shape of the electron spectrum with sub-percent statistical error. The published data were smoothed over 250 keV. Except for the highest energy bins with poor statistics, the dominant error was the absolute normalization, quoted around 3% (90% CL), with weak energy dependence.

In principle the conversion of a  $\beta$  spectrum into an antineutrino spectrum can be done using the

energy conservation between the two leptons

$$E_e + E_\nu = E_0 \quad (102)$$

with  $E_0$  the end-point of the  $\beta$  transition. However this approach requires to know the contribution of all single branches in the ILL spectra and this information is not accessible from the integral measurement. Therefore a specific conversion procedure was developed using a set of 30 ‘virtual’  $\beta$  branches, fitted on the data. The theoretical expression for the electron spectrum of a virtual branch was of the form

$$S_{\text{virtual}}(Z, A, E_e) = \underbrace{K}_{\text{Norm.}} \times \underbrace{\mathcal{F}(Z, A, E_e)}_{\text{Fermi function}} \times \underbrace{p_e E_e (E_e - E_0)^2}_{\text{Phase space}} \times \underbrace{(1 + \delta(Z, A, E_e))}_{\text{Correction}} \quad (103)$$

with  $Z$  and  $A$  the charge and atomic number of the parent nucleus and  $E_0$  the end-point of the transition. The origin of each term is described by the underbraces. The  $\delta$  term contains the corrections to the Fermi theory. In the ILL papers, it included the QED radiative corrections as calculated in [464]. The  $Z$  dependence comes from the Coulomb corrections. Since a virtual branch is not connected to any real nucleus the choice of the nuclear charge was described by the observed mean dependence of  $Z$  on  $E_0$  in the nuclear databases

$$Z(E_0) = 49.5 - 0.7E_0 - 0.09E_0^2, \quad Z \leq 34 \quad (104)$$

The  $A$  dependence is weaker and linked to the determination of  $Z$  through global nuclear fits.

Once the sum of the 30 virtual branches is fitted to the electron data, each of them is converted to an antineutrino branch by substituting  $E_e$  by  $E_0 - E_\nu$  in Eq. (103) and applying the correct radiative corrections. The predicted antineutrino spectrum is the sum of all converted branches. At the end of this procedure an extra correction term is implemented in an effective way as

$$\Delta S_{\text{branch}}(E_\nu) \simeq 0.65 (E_\nu - 4.00) \% \quad (105)$$

This term is an approximation of the global effect of weak magnetism correction and finite size Coulomb correction [465].

The final error of the conversion procedure was estimated to be 3–4% (90% CL), to be added in quadrature with the electron calibration error which directly propagates to the antineutrino prediction. Figure 48 shows the error stack for the case of  $^{235}\text{U}$ , representative of the other isotopes. From these reference spectra, the expected antineutrino spectrum detected at a reactor can be computed. All experiments performed at reactors since then relied on these reference spectra to compute their predicted antineutrino spectrum.

### New Reference Antineutrino Spectra

Triggered by the need for an accurate prediction of the reactor antineutrino flux for the first phase of the Double Chooz experiment, with a far detector only, the determination of antineutrino reference spectra has been revisited lately [462]. In a first attempt a compilation of the most recent nuclear



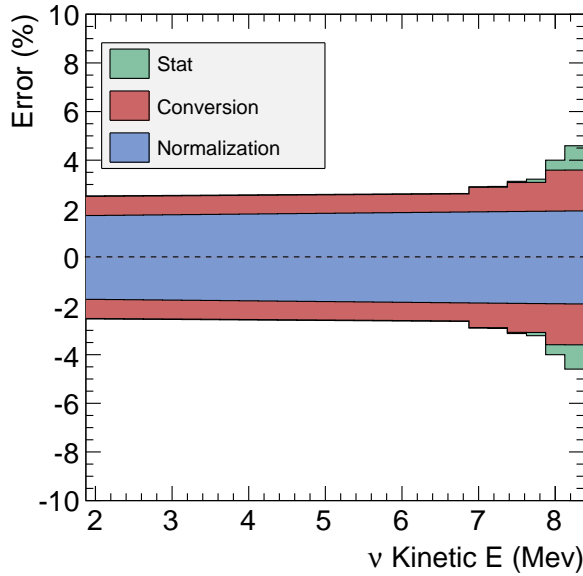


Figure 48. Stack of errors of the  $^{235}\text{U}$  antineutrino spectrum as predicted in [459]. Each new color is the quadratic sum of all previous contributions.

data was performed for an up to date *ab initio* calculation of the antineutrino fission spectra. The asset of this approach is the knowledge of each individual  $\beta$ -branch, providing a perfect control of the conversion between electron and antineutrino spectra. As a powerful cross-check, the sum of all the branches must match the very accurate electron spectra measured at ILL. Despite the tremendous amount of nuclear data available, this approach failed to meet the required accuracy of few % for two main reasons:

- The majority of the  $\beta$ -decays is measured using  $\beta$ - $\gamma$  coincidences, which are sensitive to the so-called pandemonium effect [466]. The net result is an experimental bias of the shape of the energy spectra, the high energy part being overestimated relative to the low energy part. New measurements are ongoing with dedicated experimental setups to correct for the pandemonium effect but in the case of the reference spectra many unstable nuclei have to be studied.
- As mentioned above, an important fraction of the detected neutrinos have a large energy ( $> 4$  MeV). The associated  $\beta$ -transitions mostly come from very unstable nuclei with a large energy gap between the parent ground state and the nuclear levels of the daughter nucleus. Their decay scheme is often poorly known or even not measured at all.

A reference data set was constituted based on all fission products indexed in the ENSDF database [467]. All nuclei measured separately to correct for the pandemonium effect were substituted when not in agreement with the ENSDF data (67 nuclei from [468] and 29 nuclei from [469]). A dedicated interface, BESTIOLE, reads the relevant information of this set of almost 10000  $\beta$ -branches and computes their energy spectrum based on Eq. (103). Then the total beta spectrum of one fissioning isotope is built as the sum of all fission fragment spectra weighted by their activity. These activities are determined using a simulation package called MCNP Utility for Reactor Evolution (MURE [470]). Following this procedure the predicted fission spectrum is about 90% of the reference ILL  $\beta$ -spectra, as illustrated in figure 2 for the  $^{235}\text{U}$  isotope. The missing contribution is the

image of all unmeasured decays as well as the remaining experimental biases of the measurements. To fill the gap one can invoke models of the decay scheme of missing fission products. Reaching a good agreement with the ILL electron data remains difficult with this approach.

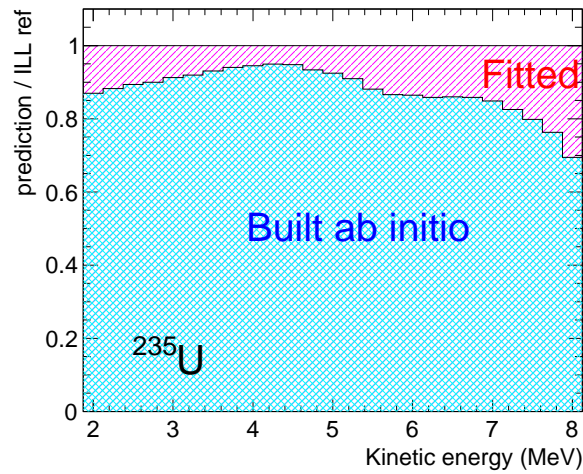


Figure 49. The blue hatched area shows the contribution of the ENSDF + pandemonium corrected nuclei relative to the ILL reference data. The missing contribution coming from unknown nuclei and remaining systematic effects of nuclear databases (red hatched area) is fitted using a set of 5 effective  $\beta$ -branches.

Another way to fill the gap is to fit the missing contribution in the electron spectrum with few virtual branches. The same ILL procedure can be used except that the virtual branches now rest on the base of physical transitions. This mixed approach combines the assets of *ab initio* and virtual branches methods:

- The prediction still matches accurately the reference electron data from the ILL measurements.
- 90% of the spectrum is built with measured  $\beta$ -transitions with ‘true’ distributions of endpoint, branching ratios, nuclear charges, etc. This suppresses the impact of the approximations associated with the use of virtual beta branches.
- All corrections to the Fermi theory are applied at the branch level, preserving the correspondence between the reference electron data and the predicted antineutrino spectrum.

The new predicted antineutrino spectra are found about 3% above the ILL spectra. This effect is comparable for the 3 isotopes ( $^{235}\text{U}$ ,  $^{239}\text{Pu}$ ,  $^{241}\text{Pu}$ ) with little energy dependence. The origin and the amplitude of this bias could be numerically studied in detail following a method initially developed in [471]. A ‘true’ electron spectrum is defined as the sum of all measured branches (blue area in figure 49). Since all the branches are known, the ‘true’ antineutrino spectrum is perfectly defined as well, with no uncertainty from the conversion. Applying the exact same conversion procedure than in the eighties on this new electron reference confirms the 3% shift between the converted antineutrino spectrum and the ‘true’ spectrum (see figure 50).

Further tests have shown that this global 3% shift is actually a combination of two effects. At high energy ( $E > 4$  MeV) the proper distribution of nuclear charges, provided by the dominant

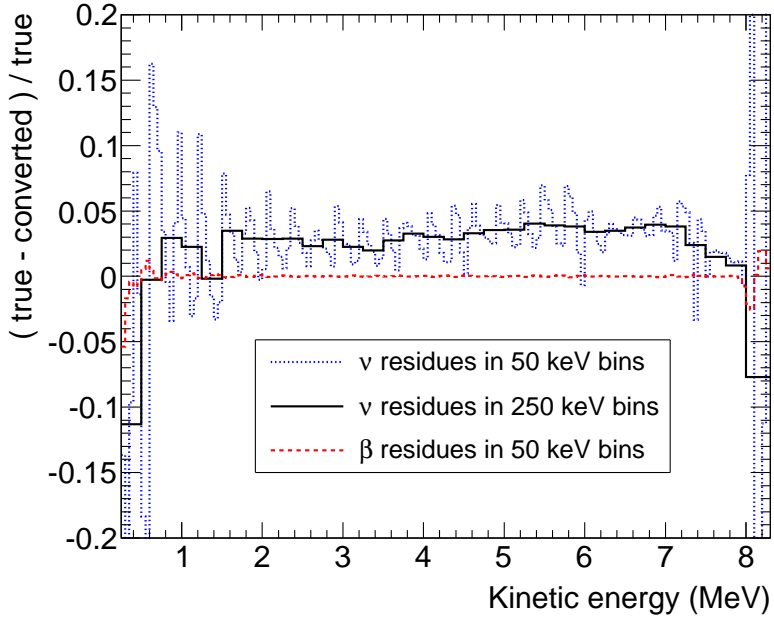


Figure 50. Independent cross-check of the new converted spectra based on known reference spectra (pure ENSDF database). Dashed red line: electron residuals after fitting with 30 virtual branches. Dotted blue line: relative difference between the reference antineutrino spectrum and the one converted according to the ILL procedure, in 50 keV bins. Smoothing out the residual oscillations in 250 keV bins (solid black line) exhibits a 3% normalization shift.

contribution of the physical  $\beta$ -branches, induces a 3% increase of the predicted antineutrino spectrum. On the low energy side it was shown that the effective linear correction of Eq. (105) was not accounting for the cancellations operating between the numerous physical branches when the correction is applied at the branch level (see figure 51).

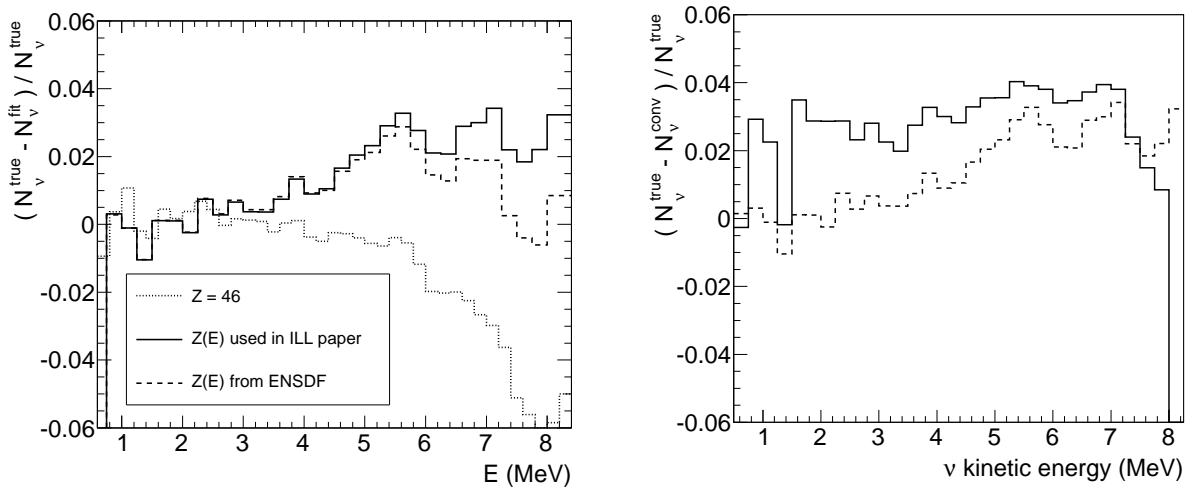


Figure 51. Numerical tests of the conversion-induced deviations from a ‘true’ spectrum built from a set of know branches (see text for details). Left: effect of various  $Z(E)$  polynomials used in the formula of the virtual branches. Right: deviation of converted spectra with the effective correction of Eq(105) (solid line), or with the correction applied at the branch level.

Beyond the correction of these above biases, the uncertainty of the new fission antineutrino spectra couldn't be reduced with respect to the initial predictions. The normalisation of the ILL electron data, a dominant source of error, is inherent to any conversion procedure using the electron reference. Then a drawback of the extensive use of measured  $\beta$ -branches in the mixed-approach is that it brings important constraints on the missing contribution to reach the electron data. In particular the induced missing shape can be difficult to fit with virtual branches, preventing a perfect match with the electron reference. These electron residuals are unfortunately amplified as spurious oscillations in the predicted antineutrino spectrum leading to comparable conversion uncertainties (see red curve in figure 53). Finally the correction of the weak magnetism effect is calculated in a quite crude way and the same approximations are used since the eighties.

In the light of the above results, the initial conversion procedure of the ILL data was revisited [472]. It was shown that a fit using only virtual branches with a judicious choice of the effective nuclear charge could provide results with minimum bias. A mean fit similar to Eq. (104) is still used but the nuclear charge of all known branches is now weighted by its contribution in the total spectrum, that is the associated fission yield. As shown in figure 52 the result is quite stable under various assumptions for the weighting of poorly known nuclei. The bias illustrated in the left plot of figure 51 is corrected.

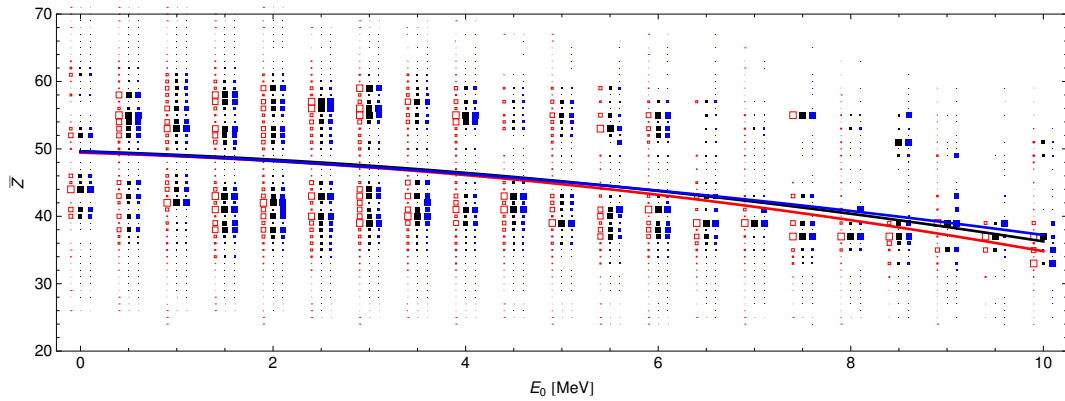


Figure 52. The effective nuclear charge  $\bar{Z}$  of the fission fragments of  $^{235}\text{U}$  as a function of  $E_0$ . The area of the each box is proportional to the contribution of that particular  $Z$  to the fission yield in that energy bin. The lines are fits of quadratic polynomials: black – ENSDF database, other colors illustrate the small sensitivity to different treatment of the missing isotopes.

The second bias (right plot of figure 51) is again corrected by implementing the corrections to the Fermi theory at the branch level rather than using effective corrections as in Eq. (105). Using the same expression of these corrections than in [462], the two independent new predictions are in very good agreement (figure 53) confirming the 3% global shift. Note that the spurious oscillations of the Mueller *et al.* spectra are flattened out by this new conversion because of the better zeroing of electron residuals.

A detailed review of all corrections to the Fermi theory is provided in [472] including finite size corrections, screening correction, radiative corrections and weak magnetism. To a good approximation they all appear as linear correction terms as illustrated in figure 54 in the case of a 10 MeV end-point energy. This refined study of all corrections leads to an extra increase of the predicted antineutrino spectra at high energy as illustrated by the blue curve in figure 53. The net effect is between 1.0 and 1.4% more detected antineutrinos depending on the isotope (see table XIX).

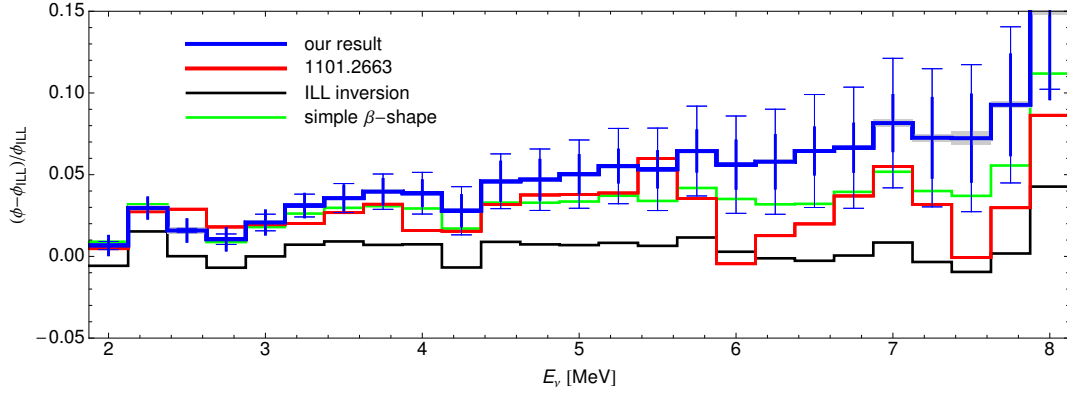


Figure 53. Comparison of different conversions of the ILL electron data for  $^{235}\text{U}$ . Black curve: cross-check of results from [459] following the same procedure. Red curve: results from [462]. Green curve: results from [472] using the same description of  $\beta$ -decay as in [462]. Blue curve: Update of the results from [462], including corrections to the Fermi theory as explained in the text. The thin error bars show the theory errors from the effective nuclear charge  $\bar{Z}$  and weak magnetism. The thick error bars are the statistical errors.

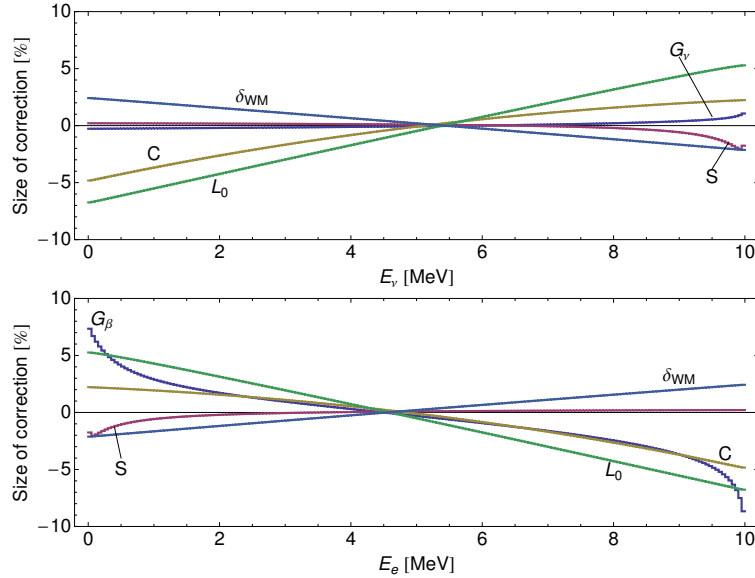


Figure 54. Shown is the relative size of the various corrections to the Fermi theory for a hypothetical  $\beta$ -decay with  $Z = 46$ ,  $A = 117$  and  $E_0 = 10$  MeV. The upper panel shows the effect on the antineutrino spectrum, whereas the lower panels shows the effect on the  $\beta$ -spectrum.  $\delta_{WM}$ : weak magnetism correction;  $L_0, C$ : Coulomb and weak interaction finite size corrections;  $S$  Screening correction;  $G_{\nu, \beta}$ : radiative corrections.

The corrections of figure 54 are known with a good relative accuracy except for the weak magnetism term. At the present time a universal slope factor of about 0.5% per MeV is assumed, neglecting any dependence on nuclear structure [465]. Accurate calculation for every fission product is out of reach. Using the conserved vector current hypothesis it is possible to infer the weak magnetism correction from the electromagnetic decay of isobaric analog states. Examples of the slope factors computed from the available data are shown in table I of [472]. While most examples are in reasonable agreement with the above universal slope, some nuclei with large value of  $\log ft$  have a very large slope factor. Moreover a review of the nuclear databases [473] shows

that  $\beta$ -transitions with  $\log ft > 7$  contribute between 15 and 30% to the total spectrum. Still the data on the weak magnetism slopes are scarce and none of them correspond to fission products. At this stage it is difficult to conclude if the uncertainty of the weak magnetism correction should be inflated or not. The prescription of the ILL analysis, 100%, corresponds to about 1% of the detected neutrino rate. The best constraints could actually come from shape analysis of the reactor neutrino data themselves. The Bugey and Rovno data are accurate although detailed information on the detector response might be missing for such a detailed shape analysis. The combination of the upcoming Daya Bay, Double Chooz and Reno data should soon set stringent limits on the global slope factor.

The error budget of the predicted spectra remains again comparable to the first ILL analysis. The normalization error of the electron data is a common contribution. The uncertainties of the conversion by virtual branches have been extensively studied and quantified based on the numerical approach illustrated in figure 50. The uncertainty induced by the weak magnetism corrections is, *faute de mieux*, evaluated with the same 100% relative error. The final central values and errors are summarized in table XVIII.

### Off equilibrium effects

For an accurate analysis of reactor antineutrino data, an extra correction to the reference fission spectra has to be applied. It comes from the fact that the ILL spectra were acquired after a relatively short irradiation time, between 12 hours and 1.8 days depending on the isotopes, whereas in a reactor experiment the typical time scale is several months. A non-negligible fraction of the fission products have a life-time of several days. Therefore the antineutrinos associated with their  $\beta$ -decay keep accumulating well after the ‘photograph at 1 day’ of the spectra taken at ILL. Very long-lived isotopes correspond to nuclei close to the bottom of the nuclear valley of stability. Hence one naively expects these  $\beta$ -transitions to contribute at low energy. For a quantitative estimate of this effect the same simulations developed in [462] for the *ab initio* calculation of antineutrino spectra were used. The sensitivity to the nuclear ingredients is suppressed because only the relative change between the ILL spectra and spectra of longer irradiations at commercial reactors were computed. The corrections to be applied are summarized in table XVII.

As expected they concern the low energy part of the detected spectrum and vanish beyond 3.5 MeV. The corrections are larger for the  $^{235}\text{U}$  spectrum because its irradiation time, 12 h, is shorter than the others. The uncertainty was estimated from the comparison between the results of MURE and FISPAC [474] codes as well as from the sensitivity to the simulated core geometry. A safe 30% relative error is recommended.

### $^{238}\text{U}$ reference spectrum

The  $^{238}\text{U}$  isotope is contributing about 8% of the total number of fissions in a standard commercial reactor. These fissions are induced by fast neutrons, therefore their associated  $\beta$  spectrum could not be measured in the purely thermal flux of ILL. A dedicated measurement in the fast neutron flux of the FRMII reactor in Munich has been completed and should be published in the coming months [475].

Meanwhile the *ab initio* calculation developed in [462] provides a useful prediction since the relatively small contribution of  $^{238}\text{U}$  can accommodate larger uncertainties in the predicted antineu-

$^{235}\text{U}$					
	2.0 MeV	2.5 MeV	3.0 MeV	3.5 MeV	4.0 MeV
36 h	3.1	2.2	0.8	0.6	0.1
100 d	4.5	3.2	1.1	0.7	0.1
1E7 s	4.6	3.3	1.1	0.7	0.1
300 d	5.3	4.0	1.3	0.7	0.1
450 d	5.7	4.4	1.5	0.7	0.1
$^{239}\text{Pu}$					
	2.0 MeV	2.5 MeV	3.0 MeV	3.5 MeV	4.0 MeV
100 d	1.2	0.7	0.2	< 0.1	< 0.1
1E7 s	1.3	0.7	0.2	< 0.1	< 0.1
300 d	1.8	1.4	0.4	< 0.1	< 0.1
450 d	2.1	1.7	0.5	< 0.1	< 0.1
$^{241}\text{Pu}$					
	2.0 MeV	2.5 MeV	3.0 MeV	3.5 MeV	4.0 MeV
100 d	1.0	0.5	0.2	< 0.1	< 0.1
1E7 s	1.0	0.6	0.3	< 0.1	< 0.1
300 d	1.6	1.1	0.4	< 0.1	< 0.1
450 d	1.9	1.5	0.5	< 0.1	< 0.1

Table XVII. Relative off-equilibrium correction (in %) to be applied to the reference antineutrino spectra for several energy bins and several irradiation times significantly longer than the reference times (12 h for  $^{235}\text{U}$ , 36 h for  $^{239}\text{Pu}$ , and 43 h for  $^{241}\text{Pu}$ ). Effects of neutron captures on fission products are included and computed using the simulation of a PWR fuel assembly with the MURE code.

trino spectrum. An optimal set of  $\beta$ -branches was tuned to match the ILL spectra of fissile isotopes as well as possible. The base of this data set consists of the ENSDF branches corrected for the pandemonium effect as described in the “New Reference Antineutrino Spectra” Section. Missing  $\beta$  emitters are taken from the JENDL nuclear database [476] where they are calculated using the gross-theory [477]. Finally the few remaining nuclei were described using a model based on fits of the distributions of the end-points and branching ratios in the ENSDF database, then extrapolated to the exotic nuclei.

The comparison of these various levels of ingredients with the reference  $^{235}\text{U}$  ILL data is shown in figure 55. With the most complete set of data one can see that the predicted spectrum agrees with the reference at the  $\pm 10\%$  level.

Then this optimal data set is used to predict a  $^{238}\text{U}$  spectrum. Again the activity of each fission product is calculated with the evolution code MURE. The case of an N4 commercial reactor operating for one year was simulated. After such a long irradiation time the antineutrino spectrum has reached the equilibrium. The results are summarized in table XVIII. The central values are about 10% higher than the previous prediction proposed in [478]. This discrepancy might be due to the larger amount of nuclei taken into account in the most recent work. Nevertheless both results are comparable within the uncertainty of the prediction, roughly estimated from the deviation with respect to the ILL data and the sensitivity to the chosen data set.

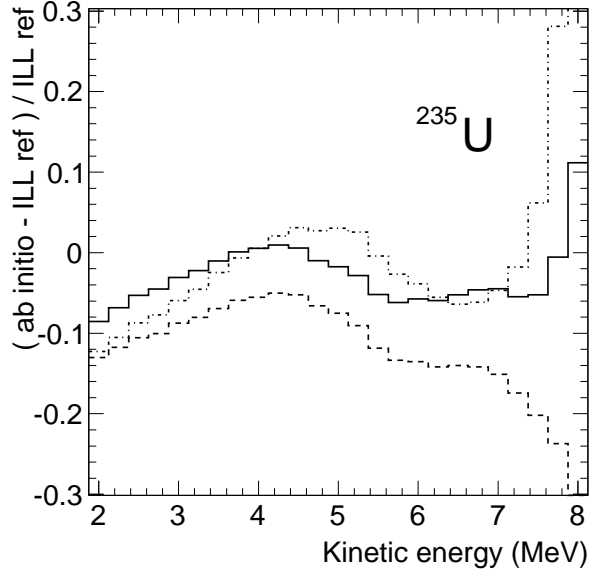


Figure 55. Relative difference between the *ab initio* calculation of the  $^{235}\text{U}$  spectrum and the ILL  $\beta$ -spectrum. Dashed-dotted curve: ENSDF data only; dashed curve: some ENSDF data replaced by pandemonium corrected data; solid curve: unmeasured  $\beta$  emitters are added on top of previous curve, using the gross-theory calculations of the JENDL nuclear database and few remaining exotic nuclei described by a simple model (see text).

### Summary of the new reactor antineutrino flux prediction

In summary, a re-evaluation of the reference antineutrino spectra associated to the fission of  $^{235}\text{U}$ ,  $^{239}\text{Pu}$  and  $^{241}\text{Pu}$  isotopes [462] has revealed some systematic biases in the previously published conversion of the ILL electron data [459–461]. The net result is a  $\simeq +3\%$  shift in the predicted emitted spectra. The origin of these biases were not in the principle of the conversion method but in the approximate treatment of nuclear data and corrections to the Fermi theory. A complementary work [472] confirmed the origin of the biases and showed that an extra correction term should be added increasing further the predicted antineutrino spectra at high energy. These most recent spectra are the new reference used for the analysis of the reactor anomaly in the next section. The prediction of the last isotope contributing to the neutrino flux of reactors,  $^{238}\text{U}$ , is also updated by *ab initio* calculations.

The new predicted spectra and their errors are presented in the summary table XVIII. The deviations with respect to the old reference spectra are given in table XIX

### New Predicted Cross Section per Fission

Fission reactors release about  $10^{20} \bar{\nu}_e \text{ GW}^{-1} \text{ s}^{-1}$ , which mainly come from the beta decays of the fission products of  $^{235}\text{U}$ ,  $^{238}\text{U}$ ,  $^{239}\text{Pu}$ , and  $^{241}\text{Pu}$ . The emitted antineutrino spectrum is then given by:  $S_{\text{tot}}(E_\nu) = \sum_k f_k S_k(E_\nu)$  where  $f_k$  refers to the contribution of the main fissile nuclei to the total number of fissions of the  $k^{\text{th}}$  branch, and  $S_k$  to their corresponding neutrino spectrum per fission. Antineutrino detection is achieved via the inverse beta-decay (IBD) reaction  $\bar{\nu}_e + {}^1\text{H} \rightarrow e^+ + \text{n}$ . Experiments at baselines below 100 m reported either the ratios (R) of the measured to predicted



$E_\nu$ (MeV)	$N_{\bar{\nu}}$ (fission <sup>-1</sup> MeV <sup>-1</sup> )				1 $\sigma$ errors (%)			
	<sup>235</sup> U	<sup>239</sup> Pu	<sup>241</sup> Pu	<sup>238</sup> U	<sup>235</sup> U	<sup>239</sup> Pu	<sup>241</sup> Pu	<sup>238</sup> U
2.	1.32	1.08	1.26	1.48	1.8	2.6	2.5	14
2.25	1.12	$9.2 \times 10^{-1}$	1.08	1.30	1.8	2.6	2.4	14
2.5	$9.15 \times 10^{-1}$	$7.19 \times 10^{-1}$	$8.94 \times 10^{-1}$	1.15	1.9	2.5	2.3	14
2.75	$7.70 \times 10^{-1}$	$6.20 \times 10^{-1}$	$7.77 \times 10^{-1}$	1.00	1.9	2.6	2.3	14
3.	$6.51 \times 10^{-1}$	$5.15 \times 10^{-1}$	$6.41 \times 10^{-1}$	$8.76 \times 10^{-1}$	1.9	2.9	2.4	14
3.25	$5.53 \times 10^{-1}$	$3.98 \times 10^{-1}$	$5.36 \times 10^{-1}$	$7.59 \times 10^{-1}$	2.0	3.1	2.5	14
3.5	$4.54 \times 10^{-1}$	$3.29 \times 10^{-1}$	$4.39 \times 10^{-1}$	$6.42 \times 10^{-1}$	2.0	3.3	2.5	14
3.75	$3.64 \times 10^{-1}$	$2.61 \times 10^{-1}$	$3.46 \times 10^{-1}$	$5.39 \times 10^{-1}$	2.1	3.3	+2.4 -2.5	14
4.	$2.94 \times 10^{-1}$	$1.95 \times 10^{-1}$	$2.82 \times 10^{-1}$	$4.51 \times 10^{-1}$	2.1	3.4	2.6	14
4.25	$2.30 \times 10^{-1}$	$1.57 \times 10^{-1}$	$2.20 \times 10^{-1}$	$3.67 \times 10^{-1}$	2.3	4.0	2.9	14
4.5	$1.79 \times 10^{-1}$	$1.13 \times 10^{-1}$	$1.66 \times 10^{-1}$	$2.93 \times 10^{-1}$	2.5	4.9	+3.3 -3.4	14
4.75	$1.38 \times 10^{-1}$	$8.33 \times 10^{-2}$	$1.25 \times 10^{-1}$	$2.32 \times 10^{-1}$	2.5	5.0	3.5	14
5.	$1.10 \times 10^{-1}$	$6.13 \times 10^{-2}$	$9.74 \times 10^{-2}$	$1.83 \times 10^{-1}$	2.6	4.7	+3.3 -3.4	14
5.25	$8.64 \times 10^{-2}$	$4.83 \times 10^{-2}$	$7.47 \times 10^{-2}$	$1.43 \times 10^{-1}$	2.6	5.1	+3.4 -3.5	14
5.5	$6.46 \times 10^{-2}$	$3.54 \times 10^{-2}$	$5.58 \times 10^{-2}$	$1.10 \times 10^{-1}$	+2.7 -2.8	5.7	+3.6 -3.8	18
5.75	$5.10 \times 10^{-2}$	$2.92 \times 10^{-2}$	$4.11 \times 10^{-2}$	$8.35 \times 10^{-2}$	+2.9 -3.0	6.4	+4.2 -4.3	18
6.	$3.89 \times 10^{-2}$	$1.92 \times 10^{-2}$	$3.05 \times 10^{-2}$	$6.21 \times 10^{-2}$	+3.1 -3.2	8.5	+4.9 -5.0	18
6.25	$2.87 \times 10^{-2}$	$1.28 \times 10^{-2}$	$1.98 \times 10^{-2}$	$4.70 \times 10^{-2}$	+3.3 -3.4	9.4	+5.3 -5.5	18
6.5	$2.17 \times 10^{-2}$	$9.98 \times 10^{-3}$	$1.54 \times 10^{-2}$	$3.58 \times 10^{-2}$	+3.3 -3.5	+9.7 -9.8	+5.4 -5.7	18
6.75	$1.61 \times 10^{-2}$	$7.54 \times 10^{-3}$	$1.09 \times 10^{-2}$	$2.71 \times 10^{-2}$	+3.4 -3.7	11.	+5.6 -5.9	18
7.	$1.14 \times 10^{-2}$	$4.48 \times 10^{-3}$	$7.75 \times 10^{-3}$	$1.95 \times 10^{-2}$	+3.6 -3.9	13.	+5.8 -6.1	22
7.25	$7.17 \times 10^{-3}$	$3.26 \times 10^{-3}$	$4.47 \times 10^{-3}$	$1.33 \times 10^{-2}$	+4.1 -4.5	18.	+7.2 -7.5	22
7.5	$4.64 \times 10^{-3}$	$1.95 \times 10^{-3}$	$2.90 \times 10^{-3}$	$8.65 \times 10^{-3}$	+4.3 -4.8	23.	+8.4 -8.8	> 22
7.75	$2.97 \times 10^{-3}$	$8.47 \times 10^{-4}$	$1.78 \times 10^{-3}$	$6.01 \times 10^{-3}$	+4.7 -5.2	27.	+9.1 -9.4	> 22
8.	$1.62 \times 10^{-3}$	$5.87 \times 10^{-4}$	$1.06 \times 10^{-3}$	$3.84 \times 10^{-3}$	+6.8 -7.2	29.	+12. -13.	> 22

Table XVIII. New reference spectra as predicted in [472] for the <sup>235</sup>U, <sup>239</sup>Pu and <sup>241</sup>Pu isotopes and their relative error. These spectra are converted from the ILL electron data hence they correspond to 12 h, 36 h and 43 h irradiation time respectively. Details on the error breakdown and related correlations can be found in [472]. The <sup>238</sup>U antineutrino spectra is taken from the *ab initio* calculation of [462]. A 10% normalization error has been added to the error budget of this spectrum.

cross section per fission, or the observed event rate to the predicted rate.

$(R_{new} - R_{ILL})/R_{ILL}$	$^{235}\text{U}$	$^{239}\text{Pu}$	$^{241}\text{Pu}$	$^{238}\text{U}$
values from [462]	2.5	3.1	3.7	9.8
values from [472]	3.7	4.2	4.7	-

Table XIX. Relative change of the new predicted events rates with respect to the ILL reference (in %). The relative change of the emitted flux is always close to 3%, dominated by the few first bins because the energy spectra are dropping fast.

The event rate at a detector is predicted based on the following formula

$$N_v^{Pred}(s^{-1}) = \frac{1}{4\pi L^2} N_p \frac{P_{th}}{\langle E_f \rangle} \sigma_f^{pred}, \quad (106)$$

where the first term stands for the mean solid angle and  $N_p$  is the number of target protons for the inverse beta-decay process of detection. These two detector-related quantities are usually known with very good accuracy. The last two terms come from the reactor side. The ratio of  $P_{th}$ , the thermal power of the reactor, over  $\langle E_f \rangle$ , the mean energy per fission, provides the mean number of fissions in the core.  $P_{th}$  can be known at the subpercent level in commercial reactors, somewhat less accurately at research reactors. The mean energy per fission is computed as the average over the four main fissioning isotopes, accounting for 99.5% of the fissions

$$\langle E_f \rangle = \sum_k \langle E_k \rangle, \quad k = ^{235}\text{U}, ^{238}\text{U}, ^{239}\text{Pu}, ^{241}\text{Pu} \quad (107)$$

It is accurately known from the nuclear databases and study of all decays and neutron captures subsequent to a fission [479]. Finally the dominant source of uncertainty and by far the most complex quantity to compute is the mean cross-section per fission defined as

$$\sigma_f^{pred} = \int_0^\infty S_{tot}(E_\nu) \sigma_{V-A}(E_\nu) dE_\nu = \sum_k f_k \sigma_{f,k}^{pred}, \quad (108)$$

where the  $\sigma_{f,k}^{pred}$  are the predicted cross sections for each fissile isotope,  $S_{tot}$  is the model dependent reactor neutrino spectrum for a given average fuel composition ( $f_k$ ) and  $\sigma_{V-A}$  is the theoretical cross section of the IBD reaction:

$$\sigma_{V-A}(E_e)[\text{cm}^2] = \frac{857 \times 10^{-43}}{\tau_n[\text{s}]} p_e[\text{MeV}] E_e[\text{MeV}] (1 + \delta_{rec} + \delta_{wm} + \delta_{rad}), \quad (109)$$

where  $\delta_{rec}$ ,  $\delta_{wm}$  and  $\delta_{rad}$  are respectively the nucleon recoil, weak magnetism and radiative corrections to the cross section (see [118, 462] for details). The fraction of fissions undergone by the  $k^{th}$  isotope,  $f_k$ , can be computed at the few percent level with reactor evolution codes (see for instance [480]), but their impact in the final error is well reduced by the sum rule of the total thermal power, accurately known from independent measurements

Accounting for new reactor antineutrino spectra [472] the normalization of predicted antineutrino rates,  $\sigma_{f,k}^{pred}$ , is shifted by +3.7%, +4.2%, +4.7%, +9.8% for  $k=^{235}\text{U}$ ,  $^{239}\text{Pu}$ ,  $^{241}\text{Pu}$ , and  $^{238}\text{U}$

	old [450]	Saclay/Huber [462, 472]
$\sigma_{f,^{235}\text{U}}^{\text{pred}}$	6.39±1.9%	6.69±2.11%
$\sigma_{f,^{239}\text{Pu}}^{\text{pred}}$	4.19±2.4%	4.40±2.45%
$\sigma_{f,^{238}\text{U}}^{\text{pred}}$	9.21±10%	10.10±8.15%
$\sigma_{f,^{241}\text{Pu}}^{\text{pred}}$	5.73±2.1%	6.03±2.15%

Table XX. Individual cross sections per fission per fissile isotope,  $\sigma_{f,k}^{\text{pred}}$  for the 'old' and the 'Saclay' predictions.

respectively. In the case of  $^{238}\text{U}$  the completeness of nuclear databases over the years largely explains the +9.8% shift from the reference computations [462].

The new predicted cross section for any fuel composition can be computed from Eq. (108). By default the new computation takes into account the so-called off-equilibrium correction [462] of the antineutrino fluxes (increase in fluxes caused by the decay of long-lived fission products). Individual cross sections per fission per fissile isotope,  $\sigma_{f,k}^{\text{pred}}$  are summarized in Table XX. These values are slightly different, by +1.25% for the averaged composition of Bugey-4 [450], with respect to the original publication of the reactor antineutrino anomaly [118] because of the slight upward shift of the antineutrino flux consecutive to the work of Ref. [472] (see the “New Reference Antineutrino Spectra” Section for details).

### Impact on past experimental results

In the eighties and nineties, experiments were performed with detectors located a few tens of meters from nuclear reactor cores at ILL, Goesgen, Rovno, Krasnoyarsk, Bugey (phases 3 and 4) and Savannah River [391, 448–455]. In the context of the search of  $O(\text{eV})$  sterile neutrinos, these experiments, with baselines below 100 m, have the advantage that they are not sensitive to a possible  $\theta_{13}$ -,  $\Delta m_{31}^2$ -driven oscillation effect (unlike the Palo Verde and CHOOZ experiments, for instance).

The ratios of observed event rates to predicted event rates (or cross section per fission),  $R = N_{\text{obs}}/N_{\text{pred}}$ , are summarized in Table XXI. The observed event rates and their associated errors are unchanged with respect to the publications, the predicted rates are reevaluated separately in each experimental case. One can observe a general systematic shift more or less significantly below unity. These reevaluations unveil a new *reactor antineutrino anomaly*<sup>20</sup> [118], clearly illustrated in Fig. 56 and in Fig. 57. In order to quantify the statistical significance of the anomaly, one can compute the weighted average of the ratios of expected over predicted rates, for all short baseline reactor neutrino experiments (including their possible correlations).

In doing so, the authors of [118] have considered the following experimental rate information: Bugey-4 and Rovno91, the three Bugey-3 experiments, the three Goesgen experiments and the ILL experiment, the three Krasnoyarsk experiments, the two Savannah River results (SRP), and the five Rovno88 experiments.  $\vec{R}$  is the corresponding vector of 19 ratios of observed to predicted event rates. A 2.0% systematic uncertainty was assumed, fully correlated among all 19 ratios,

<sup>20</sup>[http://irfu.cea.fr/en/Phocea/Vie\\_des\\_labos/Ast/ast-visu.php?id\\_ast=3045](http://irfu.cea.fr/en/Phocea/Vie_des_labos/Ast/ast-visu.php?id_ast=3045)

result	Det. type	$\tau_n$ (s)	$^{235}\text{U}$	$^{239}\text{Pu}$	$^{238}\text{U}$	$^{241}\text{Pu}$	old	new	err(%)	corr(%)	L(m)
Bugey-4	$^3\text{He}+\text{H}_2\text{O}$	888.7	0.538	0.328	0.078	0.056	0.987	0.926	3.0	3.0	15
ROVNO91	$^3\text{He}+\text{H}_2\text{O}$	888.6	0.614	0.274	0.074	0.038	0.985	0.924	3.9	3.0	18
Bugey-3-I	$^6\text{Li}-\text{LS}$	889	0.538	0.328	0.078	0.056	0.988	0.930	4.8	4.8	15
Bugey-3-II	$^6\text{Li}-\text{LS}$	889	0.538	0.328	0.078	0.056	0.994	0.936	4.9	4.8	40
Bugey-3-III	$^6\text{Li}-\text{LS}$	889	0.538	0.328	0.078	0.056	0.915	0.861	14.1	4.8	95
Goesgen-I	$^3\text{He}+\text{LS}$	897	0.620	0.274	0.074	0.042	1.018	0.949	6.5	6.0	38
Goesgen-II	$^3\text{He}+\text{LS}$	897	0.584	0.298	0.068	0.050	1.045	0.975	6.5	6.0	45
Goesgen-II	$^3\text{He}+\text{LS}$	897	0.543	0.329	0.070	0.058	0.975	0.909	7.6	6.0	65
ILL	$^3\text{He}+\text{LS}$	889	$\approx 1$	—	—	—	0.832	0.7882	9.5	6.0	9
Krasn. I	$^3\text{He}+\text{PE}$	899	$\approx 1$	—	—	—	1.013	0.920	5.8	4.9	33
Krasn. II	$^3\text{He}+\text{PE}$	899	$\approx 1$	—	—	—	1.031	0.937	20.3	4.9	92
Krasn. III	$^3\text{He}+\text{PE}$	899	$\approx 1$	—	—	—	0.989	0.931	4.9	4.9	57
SRP I	Gd-LS	887	$\approx 1$	—	—	—	0.987	0.936	3.7	3.7	18
SRP II	Gd-LS	887	$\approx 1$	—	—	—	1.055	1.001	3.8	3.7	24
ROVNO88-II	$^3\text{He}+\text{PE}$	898.8	0.607	0.277	0.074	0.042	0.969	0.901	6.9	6.9	18
ROVNO88-2I	$^3\text{He}+\text{PE}$	898.8	0.603	0.276	0.076	0.045	1.001	0.932	6.9	6.9	18
ROVNO88-1S	Gd-LS	898.8	0.606	0.277	0.074	0.043	1.026	0.955	7.8	7.2	18
ROVNO88-2S	Gd-LS	898.8	0.557	0.313	0.076	0.054	1.013	0.943	7.8	7.2	25
ROVNO88-3S	Gd-LS	898.8	0.606	0.274	0.074	0.046	0.990	0.922	7.2	7.2	18

Table XXI.  $N_{obs}/N_{pred}$  ratios based on old and new spectra. Off-equilibrium corrections have been applied when justified. The err column is the total error published by the collaborations including the error on  $S_{tot}$ , the corr column is the part of the error correlated among experiments (multiple-baseline or same detector).

resulting from the common normalization uncertainty of the beta-spectra measured in [459–461]. In order to account for the potential experimental correlations, the experimental errors of Bugey-4 and Rovno91, of the three Goesgen and the ILL experiments, the three Krasnoyarsk experiments, the five Rovno88 experiments, and the two SRP results were fully correlated. Also, the Rovno88 (II and 2I) results were fully correlated with Rovno91, and an arbitrary 50% correlation was added between the Rovno88 (II and 2I) and the Bugey-4 measurement. These latest correlations are motivated by the use of similar or identical integral detectors.

In order to account for the non-gaussianity of the ratios  $R$  a Monte Carlo simulation was developed to check this point, and it was found that the ratios distribution is almost Gaussian, but with slightly longer tails, which were taken into account in the calculations (in contours that appear later, error bars are enlarged). With the old antineutrino spectra the mean ratio is  $\mu=0.980\pm 0.024$ .

With the new antineutrino spectra, one obtains  $\mu=0.927\pm 0.023$ , and the fraction of simple Monte-Carlo experiments with  $r \geq 1$  is 0.3%, corresponding to a  $-2.9\sigma$  effect (while a simple calculation assuming normality would lead to  $-3.2\sigma$ ). Clearly the new spectra induce a statistically significant deviation from the expectation. This motivates the definition of an experimental cross section  $\sigma_f^{ano,2012} = 0.927 \times \sigma_f^{pred,new} 10^{-43} \text{ cm}^2/\text{fission}$ . With the new antineutrino spectra, the minimum  $\chi^2$  for the data sample is  $\chi_{min,data}^2 = 18.4$ . The fraction of simple Monte-Carlo experiments

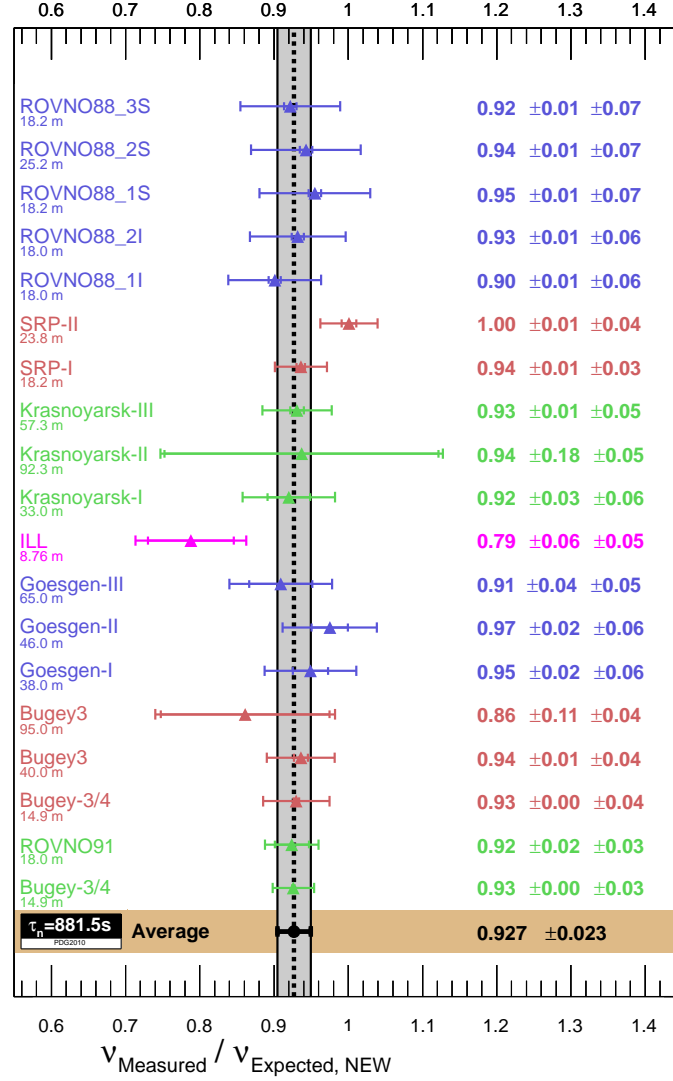


Figure 56. Weighted average (with correlations) of 19 measurements of reactor neutrino experiments operating at short baselines. A summary of experiment details is given in Table XXI.

with  $\chi^2_{min} < \chi^2_{min,data}$  is 50%, showing that the distribution of experimental ratios in  $\vec{R}$  around the mean value is representative given the correlations.

Assuming the correctness of  $\sigma_f^{pred,new}$  the anomaly could be explained by a common bias in all reactor neutrino experiments. The measurements used different detection techniques (scintillator counters and integral detectors). Neutrons were tagged either by their capture in metal-loaded scintillator, or in proportional counters, thus leading to two distinct systematics. As far as the neutron detection efficiency calibration is concerned, note that different types of radioactive sources emitting MeV or sub-MeV neutrons were used (Am-Be,  $^{252}\text{Cf}$ , Sb-Pu, Pu-Be). It should be mentioned that the Krasnoyarsk, ILL, and SRP experiments operated with nuclear fuel such that the difference between the real antineutrino spectrum and that of pure  $^{235}\text{U}$  was less than 1.5%. They reported similar deficits to those observed at other reactors operating with a mixed fuel. Hence the anomaly can be associated neither with a single fissile isotope nor with a single detection technique. All these elements argue against a trivial bias in the experiments, but a detailed analysis of the most

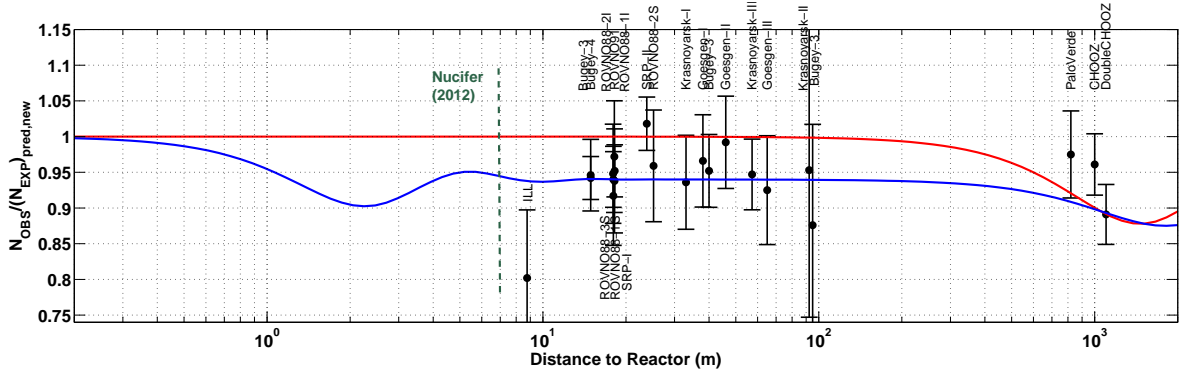


Figure 57. Short baseline reactor antineutrino anomaly. The experimental results are compared to the prediction without oscillation, taking into account the new antineutrino spectra, the corrections of the neutron mean lifetime, and the off-equilibrium effects. Published experimental errors and antineutrino spectra errors are added in quadrature. The mean averaged ratio including possible correlations is  $0.927 \pm 0.023$ . As an illustration, the red line shows a 3 active neutrino mixing solution fitting the data, with  $\sin^2(2\theta_{13}) = 0.15$ . The blue line displays a solution including a new neutrino mass state, such as  $|\Delta m_{new,R}^2| \gg 2 \text{ eV}^2$  and  $\sin^2(2\theta_{new,R}) = 0.12$ , as well as  $\sin^2(2\theta_{13}) = 0.085$ .

sensitive of them, involving experts, would certainly improve the quantification of the anomaly.

The other possible explanation of the anomaly is based on a real physical effect and is detailed in the next section. In that analysis, shape information from the Bugey-3 and ILL published data [391, 448] is used. From the analysis of the shape of their energy spectra at different source-detector distances [391, 449], the Goesgen and Bugey-3 measurements exclude oscillations with  $0.06 < \Delta m^2 < 1 \text{ eV}^2$  for  $\sin^2(2\theta) > 0.05$ . Bugey-3's 40 m/15 m ratio data from [391] is used as it provides the best limit. As already noted in Ref. [481], the data from ILL showed a spectral deformation compatible with an oscillation pattern in their ratio of measured over predicted events. It should be mentioned that the parameters best fitting the data reported by the authors of Ref. [481] were  $\Delta m^2 = 2.2 \text{ eV}^2$  and  $\sin^2(2\theta) = 0.3$ . A reanalysis of the data of Ref. [481] was carried out in order to include the ILL shape-only information in the analysis of the reactor antineutrino anomaly. The contour in Fig. 14 of Ref. [448] was reproduced for the shape-only analysis (while for the rate-only analysis discussed above, that of Ref. [481] was reproduced, excluding the no-oscillation hypothesis at  $2\sigma$ ).

## The fourth neutrino hypothesis (3+1 scenario)

### Reactor Rate-Only Analysis

The reactor antineutrino anomaly could be explained through the existence of a fourth non-standard neutrino, corresponding in the flavor basis to a sterile neutrino  $\nu_s$  (see [25] and references therein) with a large  $\Delta m_{new}^2$  value.

For simplicity the analysis presented here is restricted to the 3+1 four-neutrino scheme in which there is a group of three active neutrino masses separated from an isolated neutrino mass, such that  $|\Delta m_{new}^2| \gg 10^{-2} \text{ eV}^2$ . The latter would be responsible for very short baseline reactor neutrino oscillations. For energies above the IBD threshold and baselines below 100 m, the approximated

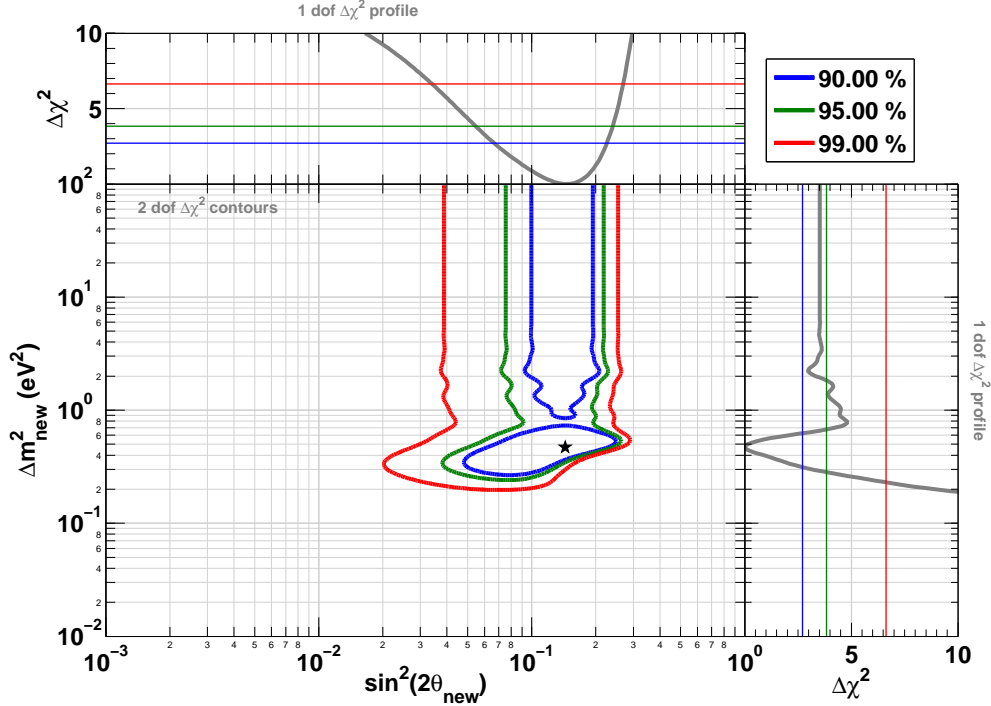


Figure 58. Allowed regions in the  $\sin^2(2\theta_{new}) - \Delta m_{new}^2$  plane obtained from the fit of the reactor neutrino data, without any energy spectra information, to the 3+1 neutrino hypothesis, with  $\sin^2(2\theta_{13}) = 0$ . The best-fit point is indicated by a star.

oscillation formula

$$P_{ee} = 1 - \sin^2(2\theta_{new}) \sin^2\left(\frac{\Delta m_{new}^2 L}{4E_{\bar{\nu}_e}}\right) \quad (110)$$

is adopted, where active neutrino oscillation effects are neglected at these short baselines. In such a framework the mixing angle is related to the  $U$  matrix element by the relation:

$$\sin^2(2\theta_{new}) = 4|U_{e4}|^2(1 - |U_{e4}|^2). \quad (111)$$

One can us now fit the sterile neutrino hypothesis to the data (baselines below 100 m) by minimizing the least-squares function

$$\left(P_{ee} - \vec{R}\right)^T W^{-1} \left(P_{ee} - \vec{R}\right), \quad (112)$$

assuming  $\sin^2(2\theta_{13}) = 0$ . Figure 58 provides the results of the fit in the  $\sin^2(2\theta_{new}) - \Delta m_{new}^2$  plane, including only the reactor experiment rate information. The fit to the data indicates that  $|\Delta m_{new,R}^2| > 0.2 \text{ eV}^2$  (99%) and  $\sin^2(2\theta_{new,R}) \sim 0.14$ . The best fit point is at  $|\Delta m_{new,R}^2| = 0.5 \text{ eV}^2$  and  $\sin^2(2\theta_{new,R}) \sim 0.14$ . The no-oscillation analysis is excluded at 99.8%, corresponding roughly to  $3\sigma$ .

### Reactor Rate+Shape Analysis

The ILL experiment may have seen a hint of oscillation in their measured positron energy spectrum [448, 481], but Bugey-3's results do not point to any significant spectral distortion more than

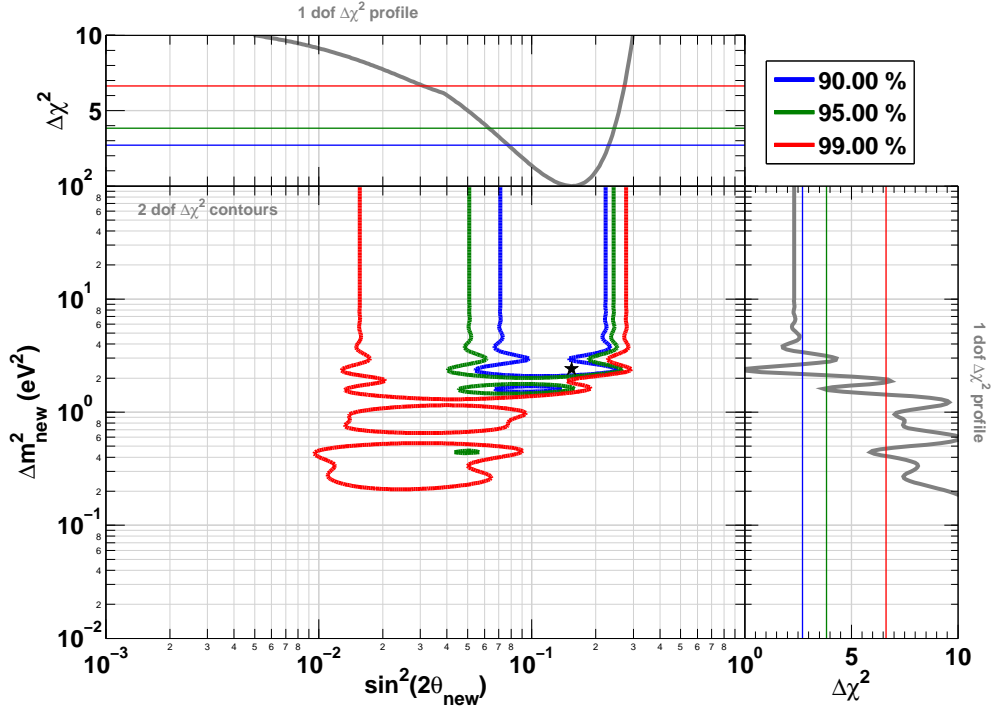


Figure 59. Allowed regions in the  $\sin^2(2\theta_{new}) - \Delta m_{new}^2$  plane obtained from the fit of the reactor neutrino data, without ILL-shape information, but with the stringent oscillation constraint of Bugey-3 based on the 40 m/15 m ratios to the 3+1 neutrino hypothesis, with  $\sin^2(2\theta_{13}) = 0$ . The best-fit point is indicated by a star.

15 m away from the antineutrino source. Hence, in a first approximation, hypothetical oscillations could be seen as an energy-independent suppression of the  $\bar{\nu}_e$  rate by a factor of  $\frac{1}{2} \sin^2(2\theta_{new,R})$ , thus leading to  $\Delta m_{new,R}^2 \gtrsim 1 \text{ eV}^2$  and accounting for the Bugey-3 and Goesgen shape analyses [391, 449]. Considering the weighted average of all reactor experiments one obtains an estimate of the mixing angle,  $\sin^2(2\theta_{new,R}) \sim 0.15$ . The ILL positron spectrum is thus in agreement with the oscillation parameters found independently in the re-analyses mainly based on rate information. Because of the differences in the systematic effects in the rate and shape analyses, this coincidence is in favor of a true physical effect rather than an experimental anomaly. Including the finite spatial extension of the nuclear reactors and the ILL and Bugey-3 detectors, it is found that the small dimensions of the ILL nuclear core lead to small corrections of the oscillation pattern imprinted on the positron spectrum. However the large extension of the Bugey nuclear core is sufficient to wash out most of the oscillation pattern at 15 m. This explains the absence of shape distortion in the Bugey-3 experiment. We now present results from a fit of the sterile neutrino hypothesis to the data including both Bugey-3 and ILL original results (no-oscillation reported). With respect to the rate only parameters, the solutions at lower  $|\Delta m_{new,R+S}^2|$  are now disfavored at large mixing angle because they would have imprinted a strong oscillation pattern in the energy spectra (or their ratio) measured at Bugey-3 and ILL. The best fit point is moved to  $|\Delta m_{new,R+S}^2| = 2.4 \text{ eV}^2$  whereas the mixing angle remains almost unchanged, at  $\sin^2(2\theta_{new,R+S}) \sim 0.14$ . The no-oscillation hypothesis is excluded at 99.6%, corresponding roughly to  $2.9\sigma$ . Figure 59 provides the results of the fit in the  $\sin^2(2\theta_{new}) - \Delta m_{new}^2$  plane, including both the reactor experiment rate and shape (Bugey-3 and ILL) data.



## Combination of the Reactor and the Gallium Anomalies

It is also possible to combine the results on the reactor antineutrino anomaly with the results on the gallium anomaly (see Section III G) [439]. The goal is to quantify the compatibility of the reactor and the gallium data.

For the reanalysis of the Gallex and Sage calibration runs with  $^{51}\text{Cr}$  and  $^{37}\text{Ar}$  radioactive sources emitting  $\sim 1$  MeV electron neutrinos [415–421], the methodology developed in Ref. [439, 441] is used. However, in the analysis shown here, possible correlations between these four measurements are included. Details are given in Ref. [118]. This has the effect of being slightly more conservative, with the no-oscillation hypothesis disfavored at 97.7% C.L., instead of 98% C.L. in Ref. [439]. Gallex and Sage observed an average deficit of  $R_G = 0.86 \pm 0.06$  ( $1\sigma$ ). The best fit point is at  $|\Delta m_{\text{gallium}}^2| = 2.4$  eV<sup>2</sup> (poorly defined) whereas the mixing angle is found to be  $\sin^2(2\theta_{\text{gallium}}) \sim 0.27 \pm 0.13$ . Note that the best fit values are very close to those obtained by the analysis of the rate+shape reactor data.

Combing both the reactor and the gallium data, The no-oscillation hypothesis is disfavored at 99.97% C.L (3.6  $\sigma$ ). Allowed regions in the  $\sin^2(2\theta_{\text{new}})-\Delta m_{\text{new}}^2$  plane are displayed in Fig. 60, together with the marginal  $\Delta\chi^2$  profiles for  $|\Delta m_{\text{new}}^2|$  and  $\sin^2(2\theta_{\text{new}})$ . The combined fit leads to the following constraints on oscillation parameters:  $|\Delta m_{\text{new}}^2| > 1.5$  eV<sup>2</sup> (99% C.L.) and  $\sin^2(2\theta_{\text{new}}) = 0.17 \pm 0.04$  ( $1\sigma$ ). The most probable  $|\Delta m_{\text{new}}^2|$  is now rather better defined with respect to what has been published in Ref. [118], at  $|\Delta m_{\text{new}}^2| = 2.3 \pm 0.1$  eV<sup>2</sup>.

### Summary of the reactor antineutrino anomaly

The impact of the new reactor antineutrino spectra has been extensively studied in Ref. [118]. The increase of the expected antineutrino rate by about 4.5% combined with revised values of the antineutrino cross section significantly decreased the normalized ratio of observed to expected event rates in all previous reactor experiments performed over the last 30 years at distances below 100 m [391, 448–455]. The new average ratio, updated early 2012, is now  $0.927 \pm 0.023$ , leading to an enhancement of reactor antineutrino anomaly, now significant at the  $3\sigma$  confidence level. The best fit point is at  $|\Delta m_{\text{new},R+S}^2| = 2.4$  eV<sup>2</sup> whereas the mixing angle is at  $\sin^2(2\theta_{\text{new},R+S}) \sim 0.14$ .

This deficit could still be due to some unknown in the reactor physics, but it can also be analyzed in terms of a suppression of the  $\bar{\nu}_e$  rate at short distance as could be expected from a sterile neutrino, beyond the standard model, with a large  $|\Delta m_{\text{new}}^2| \gg |\Delta m_{31}^2|$ . Note that hints of such results were already present at the ILL neutrino experiment in 1981 [481].

Considering the reactor  $\bar{\nu}_e$  anomaly and the gallium  $\nu_e$  source experiments [415–421, 439] together, it is interesting to note that in both cases (neutrinos and antineutrinos), comparable deficits are observed at a similar  $L/E$ . Furthermore it turns out that each experiment fitted separately leads to similar values of  $\sin^2(2\theta_{\text{new}})$  and similar lower bounds for  $|\Delta m_{\text{new}}^2|$ , but without a strong significance. A combined global fit of gallium data and of short-baseline reactor data, taking into account the reevaluation of the reactor results discussed here, as well as the existing correlations, leads to a solution for a new neutrino oscillation, such that  $|\Delta m_{\text{new}}^2| > 1.5$  eV<sup>2</sup> (99% C.L.) and  $\sin^2(2\theta_{\text{new}}) = 0.17 \pm 0.04$  ( $1\sigma$ ), disfavoring the no-oscillation case at 99.97% C.L (3.6  $\sigma$ ). The most probable  $|\Delta m_{\text{new}}^2|$  is now at  $|\Delta m_{\text{new}}^2| = 2.3 \pm 0.1$  eV<sup>2</sup>. This hypothesis should be checked against systematical effects, either in the prediction of the reactor antineutrino spectra or in the experimental results.

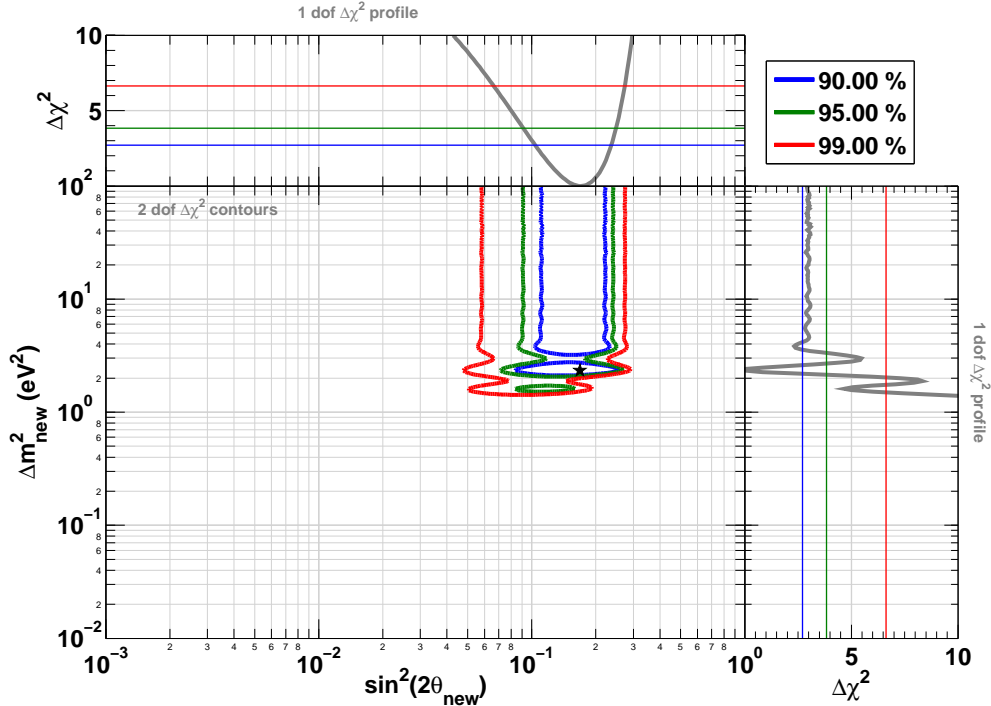


Figure 60. Allowed regions in the  $\sin^2(2\theta_{new})-\Delta m_{new}^2$  plane from the combination of reactor neutrino experiments, the Gallex and Sage calibration sources experiments, and the ILL and Bugey-3-energy spectra. The data are well fitted by the 3+1 neutrino hypothesis, while the no-oscillation hypothesis is disfavored at 99.97% C.L ( $3.6\sigma$ ).

## I. Limit on Disappearance Derived from KARMEN and LSND $\nu_e$ -Carbon Cross Sections

The  $\nu_e$ -carbon cross section data from the KARMEN [482, 483] and LSND [484] experiments have been interpreted within the context of electron neutrino oscillations at high  $\Delta m^2$ , leading to the most stringent limit on electron-flavor disappearance relevant to sterile neutrinos [485]. Both experiments measured the cross-section for the 2-body interaction  $\nu_e + {}^{12}\text{C} \rightarrow {}^{12}\text{N}_{gs} + e^-$ . The neutrino energy can be reconstructed by measuring the outgoing visible energy of the electron and accounting for the 17.3 MeV  $Q$ -value, allowing a measurement of the cross section versus neutrino energy. KARMEN and LSND were located at 17.7 m and 29.8 m respectively from the neutrino source. The neutrino flux normalization is known to 10% [388, 486]. Thus, the consistency of the two cross section measurements, as a function of antineutrino energy, sets strong limits on  $\nu_e$  oscillations.

Fig. 61 shows the KARMEN and LSND energy-dependent  $\nu_e + {}^{12}\text{C} \rightarrow {}^{12}\text{N}_{gs} + e^-$  cross sections [482–484]. Table XXII reports the corresponding flux-averaged cross sections measured by KARMEN, LSND and the LANL E225 experiment [487], which was located 9 m from a decay-at-rest source. Unfortunately, E225 did not publish energy-binned cross section measurements, and so is not included in this analysis. The agreement between all three experiments is excellent.

Predictions for the cross section, also shown in Fig. 61, come from Fukugita, *et al.* [488] and by Kolbe *et al.* [489]. Models follow a  $(E_\nu - Q)^2$  form, where  $Q = 17.3$  MeV because the interaction

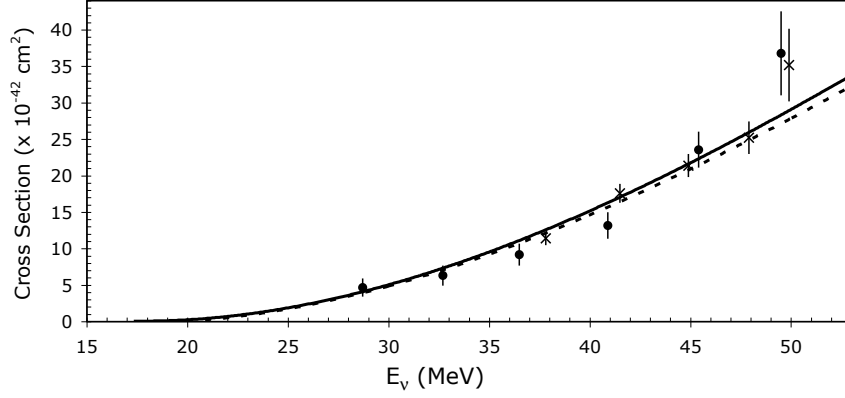


Figure 61. The KARMEN (points) and LSND (crosses) measured cross sections with statistical errors for  $\nu_e + {}^{12}\text{C} \rightarrow {}^{12}\text{N}_{gs} + e^-$  compared to the theoretical prediction of Fukugita [488] (solid line), based on the EPT model, and Kolbe [489] (dashed line), based on the CRPA model.

Experiment (Dist.)	Flux-Averaged Cross Section	Ref.
KARMEN (17.7 m)	$(9.1 \pm 0.5 \pm 0.8) \times 10^{-42} \text{ cm}^2$	[482, 483]
LSND (29.8 m)	$(8.9 \pm 0.3 \pm 0.9) \times 10^{-42} \text{ cm}^2$	[484]
E225 (9 .0 m)	$(1.05 \pm 0.10 \pm 0.10) \times 10^{-41} \text{ cm}^2$	[487]
Prediction	Flux-Averaged Cross Section	Ref.
Fukugita <i>et al.</i>	$9.2 \times 10^{-42} \text{ cm}^2$	[488]
Mintz <i>et al.</i>	$8.0 \times 10^{-42} \text{ cm}^2$	[491]
Donnelly	$9.4 \times 10^{-42} \text{ cm}^2$	[490]
Kolbe <i>et al.</i>	$8.9 \times 10^{-42} \text{ cm}^2$	[489]

Table XXII. Top: Flux-averaged  $\nu_e + {}^{12}\text{C} \rightarrow e^- + {}^{12}\text{N}_{gs}$  cross section measurements with statistical and systematic error. Bottom: Flux-averaged predictions from EPT (Fukugita, Mintz and Donnelly) and CRPA (Kolbe) models. Flux-average cross section values are equivalent to those for a neutrino of 35 MeV energy.

is an allowed transition ( $0^+ ({}^{12}\text{C}) \rightarrow 1^+ ({}^{12}\text{N})$ ). The calculations are approached in two models: the “elementary particle model” (EPT), with an associated 12% normalization uncertainty [488, 490, 491]; and the “continuum random phase approximation” (CRPA) approach [489]. Kolbe, Langanke, and Vogel have provided a discussion of the relative merits of EPT versus CRPA models for describing  $\nu_e + {}^{12}\text{C} \rightarrow {}^{12}\text{N}_{gs} + e^-$  [492]. However, from a strictly phenomenological point of view, both EPT and CRPA models fit the data well and serve as good predictions for tests of oscillations.

The analysis compares the LSND and KARMEN data with respect to the Fukugita and Kolbe predictions to set a limit on  $\nu_e \rightarrow \nu_s$  oscillations. For each set of oscillation parameters, ( $\Delta m^2$  and  $\sin^2 2\theta_{ee}$ ), one calculates a combined  $\chi^2$  for LSND and KARMEN with respect to the oscillation-modified prediction using the statistical error for each data point. Three pull terms incorporate systematic uncertainties:

1. The correlated normalization error. As noted in the KARMEN paper [482, 483], LSND and KARMEN have a common 7% systematic error on the neutrino flux normalization from the flux simulation [388, 486]. The pull term combines this in quadrature with the 12%

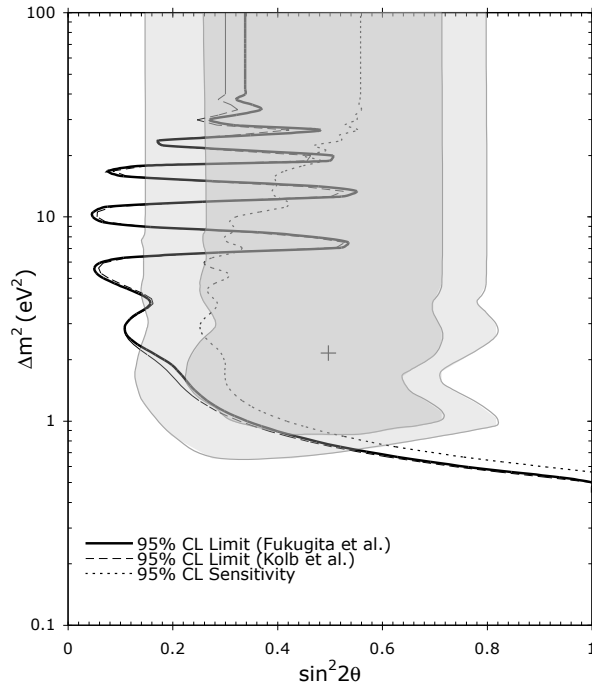


Figure 62. The 95%  $\nu_e$  disappearance limit from the Fukugita (EPT) fit (solid, black line) compared to the predicted sensitivity (dotted line). Also shown is the 68% (darker, shaded region) and 90% (lighter, shaded region) contours from the Gallium anomaly. The dashed line is the Kolbe (CRPA) fit.

systematic error on the normalization for the Fukugita prediction.

2. The uncorrelated LSND experimental uncertainty of 7% [484].
3. The uncorrelated KARMEN experimental uncertainty of 5% [482, 483].

To obtain the 90% CL allowed regions, one marginalizes over the three normalization pull parameters and use a  $\Delta\chi^2 > 4.61$  requirement for the two-degrees-of-freedom (associated with  $\Delta m^2$  and  $\sin^2 2\theta_{ee}$ ) excluded region.

The result is a 95% CL exclusion region, although the fit without oscillations has a  $\Delta\chi^2$  probability of 91.5% and is only excluded at the  $1.7\sigma$  level. The result is shown in Fig. 62. The best fit is at  $\Delta m^2 = 7.49 \pm 0.39 \text{ eV}^2$  and  $\sin^2 2\theta_{ee} = 0.290 \pm 0.115$ . This is true regardless of whether the Fukugita (EPT) and Kolbe (CRPA) predictions are used. Agreement between the results using these two predictions indicates that there is no substantial systematic effect from the underlying cross section model.

Fig. 62 compares this limit to the gallium anomaly described in Section III G, showing significant disagreement with this signal across substantial parameter space. CPT conservation requires that  $\nu_e$  and  $\bar{\nu}_e$  disappearance should occur at the same rate. Assuming that CPT is conserved allows comparison of this limit to the antineutrino reactor anomaly of Section III H, where it addresses a modest region of the allowed space.

## J. Constraints from the MINOS Long-Baseline Experiment

MINOS probes active to sterile neutrino mixing by measuring the rate of neutral-current (NC) events at two locations, over a baseline of 735 km. Because NC cross-sections are identical among the three active flavors, NC event rates are unaffected by standard neutrino mixing. However, oscillations into a sterile non-interacting neutrino flavor would result in an energy-dependent depletion of NC events at the far site. Furthermore, evidence of disappearance of charged-current (CC)  $\nu_\mu$  events at higher neutrino energies ( $> 10$  GeV), for which oscillations driven by  $\Delta m_{\text{atm}}^2$  oscillations are suppressed, could be an indication of oscillations into sterile neutrinos driven by a large mass-square difference  $\sim 1 \text{ eV}^2$ .

MINOS measures neutrinos from the NuMI beam using two detectors: the 980 ton (27 ton fiducial) Near Detector (ND), located 1.04 km downstream of the beam target at Fermilab; and the 5.4 kton (4.0 kton fiducial) Far Detector (FD), placed 735 km downstream of the target in the Soudan Underground Laboratory, in Minnesota [493]. The energy resolution function for neutrino-induced hadronic showers is approximately  $56\% / \sqrt{E}$ . The results reported were obtained using an exposure of  $7.07 \times 10^{20}$  protons on target taken exclusively with a beam configuration for which the peak neutrino event energy is 3.3 GeV. The NuMI beam includes a 1.3% ( $\nu_e + \bar{\nu}_e$ ) contamination arising from the decay of muons originating in kaon and pion decays.

In the MINOS detectors, NC interactions give rise to events with a short diffuse hadronic shower and either small or no tracks, whereas CC events typically display a long muon track accompanied by hadronic activity at the event vertex. The separation between NC and CC events proceeds through selection criteria based on topological variables: events crossing fewer than 47 planes for which no track is reconstructed are selected as NC; events crossing fewer than 47 planes that contain a track are classified as NC only if the track extends less than 6 planes beyond the shower. These selections result in an NC-selected sample with 89% efficiency and 61% purity. Highly inelastic  $\nu_\mu$  and  $\bar{\nu}_\mu$  CC events, where the muon track is not distinguishable from the hadronic shower, are the main source of background for the NC-selected spectrum. Furthermore, the analysis classifies 97% of  $\nu_e$ -induced CC events as NC, requiring the possibility of  $\nu_e$  appearance to be considered when extracting results. The predicted NC energy spectrum in the FD is obtained using the ND data. An estimate of the ratio of events in the FD and ND as a function of reconstructed energy,  $E_{\text{reco}}$ , is calculated from Monte Carlo simulations. The ratio is multiplied by the observed ND energy spectrum to produce the predicted FD spectrum. To avoid biases, the analysis selections and procedures were determined prior to examining the FD data, following the precepts of a blind analysis. Figures 63 and 64 show the reconstructed energy spectra in each detector. The events not selected as NC-like are fed to the kNN-based selection method used by the MINOS  $\nu_\mu$  CC disappearance analysis [494] and the predicted CC FD energy spectrum is obtained with the same extrapolation methodology used for the NC prediction.

The NC selection procedures identify 802 NC interaction candidates in the FD, with  $754 \pm 28(\text{stat}) \pm 37(\text{syst})$  events expected from standard three-flavor mixing (assuming  $\theta_{13} = 0^\circ$ ) [410]. The NC-like reconstructed energy spectrum is shown on Fig. 64.

The agreement between the observed and predicted NC spectra is quantified using the statistic  $R \equiv \frac{N_{\text{data}} - B_{\text{CC}}}{S_{\text{NC}}}$ , where  $N_{\text{data}}$  is the observed number of events,  $B_{\text{CC}}$  is the predicted CC background from all flavors, and  $S_{\text{NC}}$  is the expected number of NC interactions. The values of  $N_{\text{data}}$ ,  $S_{\text{NC}}$  and contributions to  $B_{\text{CC}}$  for various reconstructed energy ranges are shown in Table XXIII.

The values of  $R$  for each energy range show no evidence of a depletion in the NC rate at the FD,

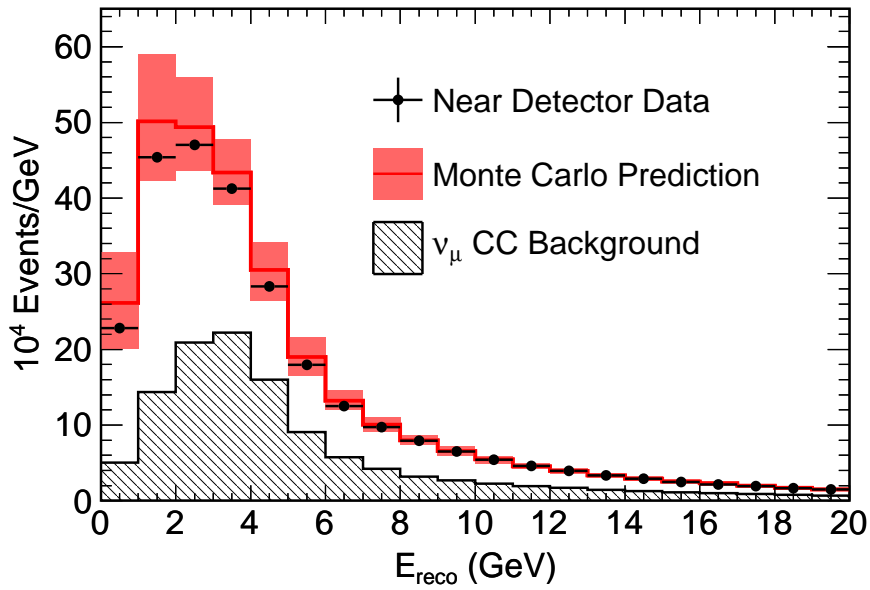


Figure 63. Reconstructed energy spectrum of NC-selected events in the ND compared to the Monte Carlo prediction shown with  $1\sigma$  systematic errors (shaded band). Also displayed is the simulation of the background from misidentified CC events (hatched histogram).

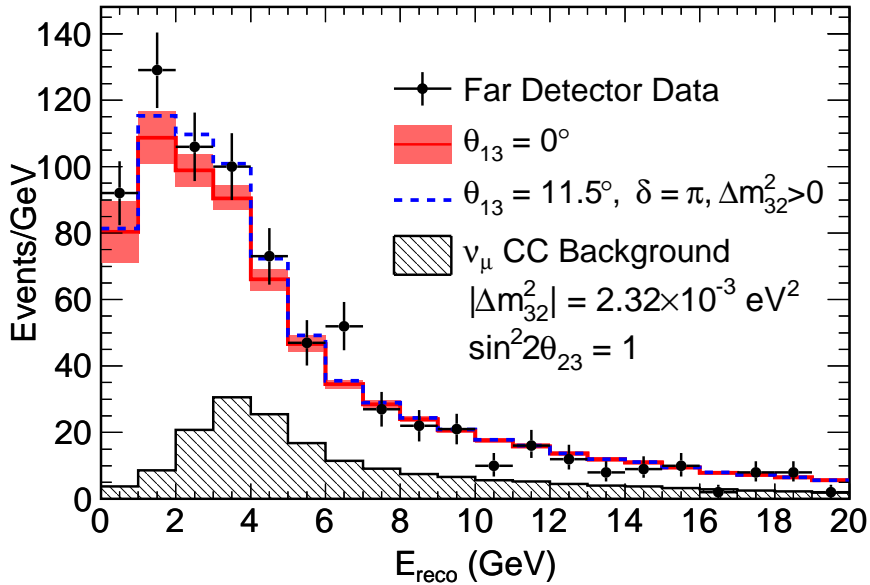


Figure 64. Reconstructed energy spectrum of NC-selected events in the FD compared with predictions for standard three-flavor mixing with and without  $\nu_e$  appearance at the MINOS 90% C.L. limit [495].

supporting the hypothesis that standard three-flavor oscillations explain the data.

The data are compared with a neutrino oscillation model that allows admixture with one sterile neutrino. In this model, an additional mass scale  $\Delta m^2_{43}$  with magnitude  $O(1\text{ eV}^2)$  is introduced,

$E_{\text{reco}}$ (GeV)	$N_{\text{Data}}$	$S_{\text{NC}}$	$B_{\text{CC}}^{\nu\mu}$	$B_{\text{CC}}^{\nu\tau}$	$B_{\text{CC}}^{\nu e}$
0 – 3	327	248.4	33.2	3.2	3.1 (21.5)
3 – 120	475	269.6	156.0	9.2	31.2 (53.8)
0 – 3	$R = 1.16 \pm 0.07 \pm 0.08 - 0.08(\nu_e)$				
3 – 120	$R = 1.02 \pm 0.08 \pm 0.06 - 0.08(\nu_e)$				
0 – 120	$R = 1.09 \pm 0.06 \pm 0.05 - 0.08(\nu_e)$				

Table XXIII. Values of the  $R$  statistic and its components for several reconstructed energy ranges. The numbers shown in parentheses include  $\nu_e$  appearance with  $\theta_{13} = 11.5^\circ$  and  $\delta_{CP} = \pi$ . The displayed uncertainties are statistical, systematic, and the uncertainty associated with  $\nu_e$  appearance.

along with the assumption that no oscillation-induced change of the neutrino event rate is measurable at the ND site, but rapid oscillations are predicted at the FD location. Based on the magnitude of the systematic uncertainties at the ND, this approximation is assumed to be valid for  $0.3 < \Delta m_{43}^2 < 2.5 \text{ eV}^2$ . A detailed description of this model is provided in Ref. [496] and references therein. Both the NC-selected energy spectrum shown in Fig. 64 and the CC-selected spectrum in the FD data are used in the fits to the oscillation models. Limits on the sterile mixing angles  $\theta_{34} < 26^\circ$  ( $37^\circ$ ) and  $\theta_{24} < 7^\circ$  ( $8^\circ$ ) are obtained at the 90% C.L.. The numbers in parentheses represent the limits extracted for maximal  $\nu_e$  appearance. The latter result is presently the most stringent constraint on  $\theta_{24}$  for  $\Delta m_{43}^2 \sim 1 \text{ eV}^2$ . A comparison of the MINOS result with other disappearance results is shown in Fig. 65.

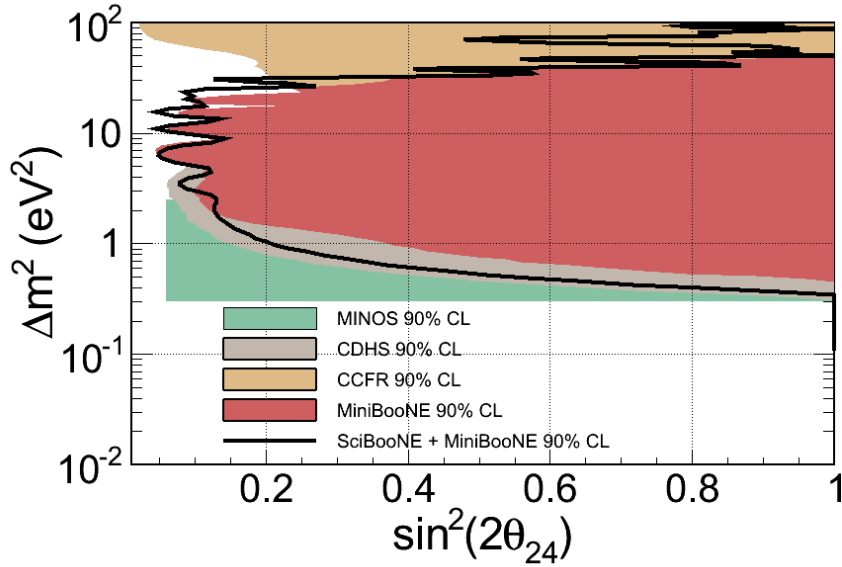


Figure 65. MINOS exclusion compared to MiniBooNE, CDHS, CCFR  $\nu_\mu$  disappearance results. The MINOS 90%CL excluded region is shown in green. Following the discussion in the text, the bound is assumed to be valid for  $0.3 < \Delta m_{43}^2 < 2.5 \text{ eV}^2$ .

The coupling between active and sterile neutrinos may also be quantified in terms of the fraction of disappearing  $\nu_\mu$  that oscillate into  $\nu_s$ ,  $f_s \equiv P_{\nu_\mu \rightarrow \nu_s} / (1 - P_{\nu_\mu \rightarrow \nu_\mu})$ , where the  $P_{\nu_\mu \rightarrow \nu_x}$  refer to

neutrino oscillation probabilities. MINOS places the most stringent constraint to date on this quantity,  $f_s < 0.22$  (0.40) at the 90% C.L., where the number in parentheses denotes the limit assuming  $\nu_e$  appearance.

A recent paper by Hernandez and Smirnov [497] analyzed the MINOS sterile neutrino search results in detail and points out that for large enough values of  $\Delta m_{43}^2$ , oscillations at the ND, even if not visible due to the size of systematic uncertainties on the ND energy spectrum, could affect the FD predicted spectrum and reduce the strength of the constraint on  $\theta_{24}$  for  $\Delta m_{43}^2 > 1 \text{ eV}^2$ . Moreover, in the same paper and also in a paper by Giunti and Laveder [498], it is pointed out that the combination of the MINOS bound on  $\theta_{24}$  with the Bugey bound on  $\theta_{14}$  largely rules out the LSND signal region for  $0.3 < \Delta m_{43}^2 < 1 \text{ eV}^2$ . Motivated by these remarks, MINOS is working on the inclusion of ND oscillations into the sterile mixing models and will update the analysis with reviewed results during 2012. These models are already being employed in the computation of sterile oscillation sensitivities for the MINOS+ project, as described in Appendix Section A 16. The results described above use exclusively NuMI data taken in neutrino running mode, which include a small 7% antineutrino contamination flatly distributed at higher neutrino energies. MINOS also plans to run the sterile neutrino analysis on the  $3.3 \times 10^{20}$  POT of antineutrino data already collected. The main challenges for this analysis arise from limited statistics and feed-down NC interactions from the higher energy neutrino component, which accounts for 58% of the beam composition when the NuMI horns focus  $\pi^-$  and  $K^-$ . Results of this analysis are also expected during 2012.

## K. Conclusion

The LSND and MiniBooNE antineutrino experiments observe excesses of events consistent with  $\bar{\nu}_\mu \rightarrow \bar{\nu}_e$  oscillations at a  $\Delta m^2 \sim 1 \text{ eV}^2$ . Although no excess is observed by the KARMEN experiment, which was very similar to LSND, a joint analysis of the two experiments still favors an allowed oscillation region with  $\Delta m^2 < 2 \text{ eV}^2$ . The MiniBooNE neutrino experiment observes an excess of events at low energy, which may be consistent with the antineutrino experiments with the inclusion of CP violation. A joint analysis of the MiniBooNE neutrino and antineutrino runs by the MiniBooNE collaboration is underway.

Further potential evidence for the existence of eV-scale sterile neutrinos comes from non-accelerator experiments. The Gallium anomaly—an event deficit observed in experiments with neutrinos from intense radioactive sources—has a statistical significance of  $2.7\sigma$ . The reactor antineutrino anomaly—a deficit of the measured reactor antineutrino flux compared to new and improved flux predictions—has a significance of  $3\sigma$ .

There are thus hints for the existence of sterile neutrinos from several different experiments, employing different neutrino sources and detector technologies, though none of them can claim a discovery. On the other hand, a number of other short-baseline oscillation searches have yielded null results, which, at least in the simplest sterile neutrino scenarios, are in some tension with the positive hints (see section IV for a discussion of global fits).



## IV. GLOBAL PICTURE

As we have seen in the previous sections, a number of (yet inconclusive) experimental results cannot be explained within the standard three-flavor framework and, when interpreted in terms of neutrino oscillations, seem to require at least an additional neutrino with a mass at the eV scale [114, 117, 118]. Such neutrinos cannot participate in the weak interactions due to collider constraints, and are therefore called “sterile” neutrinos. Apart from those hints for sterile neutrinos several data set exist which do not show any evidence for neutrino oscillations at the eV scale and the important question has to be addressed, whether a consistent description of all data is possible if sterile neutrinos are assumed, see [399, 499–514] for a list of early references. The following sections IV A, IV B, IV C review phenomenological studies and global fits taking into account all relevant data [112, 113, 127, 498, 515–519]. In Section IV D possible implications of sterile neutrinos for  $\beta$ -decay and neutrinoless double  $\beta$ -decay are discussed. A brief summary is given in Section IV G.

### A. 3+1 Global Fit of Short-Baseline Neutrino Oscillation Data

In this Section we review the results of the global fit of short-baseline neutrino oscillation data in the framework of 3+1 neutrino mixing presented in Refs. [113, 498, 515].

Short-baseline (SBL) neutrino oscillations are generated by a squared-mass difference  $\Delta m_{\text{SBL}}^2 \gtrsim 0.1 \text{ eV}^2$ , which is much larger than the two measured solar (SOL) and atmospheric (ATM) squared-mass differences  $\Delta m_{\text{SOL}}^2 = (7.6 \pm 0.2) \times 10^{-5} \text{ eV}^2$  [520] and  $\Delta m_{\text{ATM}}^2 = 2.32_{-0.08}^{+0.12} \times 10^{-3} \text{ eV}^2$  [494]. The minimal neutrino mixing schemes which can provide a third squared-mass difference for short-baseline neutrino oscillations require the introduction of a sterile neutrino  $\nu_s$  (see Refs. [424, 427, 429, 447]). Hierarchical 3+1 neutrino mixing is a perturbation of the standard three-neutrino mixing in which the three active neutrinos  $\nu_e, \nu_\mu, \nu_\tau$  are mainly composed of three massive neutrinos  $\nu_1, \nu_2, \nu_3$  with light masses  $m_1, m_2, m_3$ , such that  $\Delta m_{\text{SOL}}^2 = \Delta m_{21}^2$  and  $\Delta m_{\text{ATM}}^2 = |\Delta m_{31}^2| \simeq |\Delta m_{32}^2|$ , with the standard notation  $\Delta m_{kj}^2 \equiv m_k^2 - m_j^2$  (see Ref. [430]). The sterile neutrino is mainly composed of a heavy neutrino  $\nu_4$  with mass  $m_4$  such that  $\Delta m_{\text{SBL}}^2 = \Delta m_{41}^2$  and

$$m_1, m_2, m_3 \ll m_4 \quad \Rightarrow \quad m_4 \simeq \sqrt{\Delta m_{41}^2}. \quad (113)$$

Under these hypotheses, the effects of active-sterile neutrino mixing in solar [521, 522] and atmospheric [523–526] neutrino experiments are small, but should be revealed sooner or later.

In 3+1 neutrino mixing, the effective flavor transition and survival probabilities in short-baseline neutrino oscillation experiments are given by (see Refs. [424, 427, 429, 447])

$$P_{\nu_\alpha \rightarrow \nu_\beta}^{\text{SBL}(-)} = \sin^2 2\theta_{\alpha\beta} \sin^2 \left( \frac{\Delta m_{41}^2 L}{4E} \right) \quad (\alpha \neq \beta), \quad (114)$$

$$P_{\nu_\alpha \rightarrow \nu_\alpha}^{\text{SBL}(-)} = 1 - \sin^2 2\theta_{\alpha\alpha} \sin^2 \left( \frac{\Delta m_{41}^2 L}{4E} \right), \quad (115)$$

for  $\alpha, \beta = e, \mu, \tau, s$ , with the transition amplitudes

$$\sin^2 2\theta_{\alpha\beta} = 4|U_{\alpha 4}|^2 |U_{\beta 4}|^2, \quad (116)$$

$$\sin^2 2\theta_{\alpha\alpha} = 4|U_{\alpha 4}|^2 (1 - |U_{\alpha 4}|^2). \quad (117)$$

The hierarchical 3+1 scheme may be compatible with the results of standard cosmological  $\Lambda$ CDM analyses of the Cosmic Microwave Background and Large-Scale Structures data, which constrain the three light neutrino masses to be much smaller than 1 eV [346, 353, 527, 528] and indicate that one or two sterile neutrinos may have been thermalized in the early Universe [121, 122, 342, 350, 354, 355, 358, 529], with an upper limit of the order of 1 eV on their masses. Also Big-Bang Nucleosynthesis data [331, 530] are compatible with the existence of sterile neutrinos, with the indication however that the thermalization of more than one sterile neutrino is disfavored [122, 332].

We made a global fit of the following sets of data:

- The short-baseline  $\bar{\nu}_\mu \rightarrow \bar{\nu}_e$  data of the LSND [114], KARMEN [392], NOMAD [531] and MiniBooNE neutrino [116] and antineutrino [117, 532, 533] experiments.
- The short-baseline  $\bar{\nu}_e$  disappearance data of the Bugey-3 [391], Bugey-4 [450], ROVNO91 [534], Gosgen [449], ILL [535] and Krasnoyarsk [536] reactor antineutrino experiments, taking into account the new calculation of the reactor  $\bar{\nu}_e$  flux [462, 472] which indicates a small  $\bar{\nu}_e$  disappearance (the reactor antineutrino anomaly [118]), and the KamLAND [537] bound on  $|U_{e4}|^2$  (see Ref. [538]).
- The short-baseline  $\nu_\mu$  disappearance data of the CDHSW experiment [408], the constraints on  $|U_{\mu4}|^2$  obtained in Ref. [516] from the analysis of the data of atmospheric neutrino oscillation experiments, and the bound on  $|U_{\mu4}|^2$  obtained from MINOS neutral-current data [410] (see Refs. [497, 498]).
- The data of Gallium radioactive source experiments (GALLEX [415–417] and SAGE [418–421]) which indicate a  $\nu_e$  disappearance (the Gallium neutrino anomaly [118, 433–441]). We analyze the Gallium data according to Ref. [441].
- The  $\nu_e + {}^{12}\text{C} \rightarrow {}^{12}\text{N}_{\text{g.s.}} + e^-$  scattering data of the KARMEN [482, 483] and LSND [484] experiments, which constrain the short-baseline  $\nu_e$  disappearance [485].

Figure 66 shows the allowed regions in the  $\sin^2 2\theta_{e\mu} - \Delta m_{41}^2$ ,  $\sin^2 2\theta_{ee} - \Delta m_{41}^2$  and  $\sin^2 2\theta_{\mu\mu} - \Delta m_{41}^2$  planes obtained from the global analysis of short-baseline neutrino oscillation data. We considered values of  $\Delta m_{41}^2$  smaller than  $10 \text{ eV}^2$ , since larger values are strongly incompatible with the cosmological constraints on neutrino masses [121, 122, 342, 350, 354, 355, 358, 529]. We made two global analyses named GLO-LOW and GLO-HIG, respectively, with and without the three MiniBooNE electron neutrino and antineutrino bins with reconstructed neutrino energy smaller than 475 MeV, which have an excess of events called the "MiniBooNE low-energy anomaly". The best-fit values of the oscillation parameters are listed in Tab. XXIV.

Comparing the GLO-LOW and GLO-HIG parts of Fig. 66 and Tab. XXIV one can see that the inclusion of the fit of the MiniBooNE low-energy data favors small values of  $\Delta m_{41}^2$ . This fact has been noted and explained in Ref. [498]. Hence, the results of the GLO-LOW analysis are more attractive than those of the GLO-HIG in view of a better compatibility with cosmological constraints on the neutrino masses.

The results of both the GLO-LOW and GLO-HIG analyses confirm the well known tension between appearance and disappearance data [112, 113, 126, 127, 427, 498, 501, 506, 513, 516–519, 538]. In the GLO-LOW analysis the 0.008% parameter goodness-of-fit shows that the tension

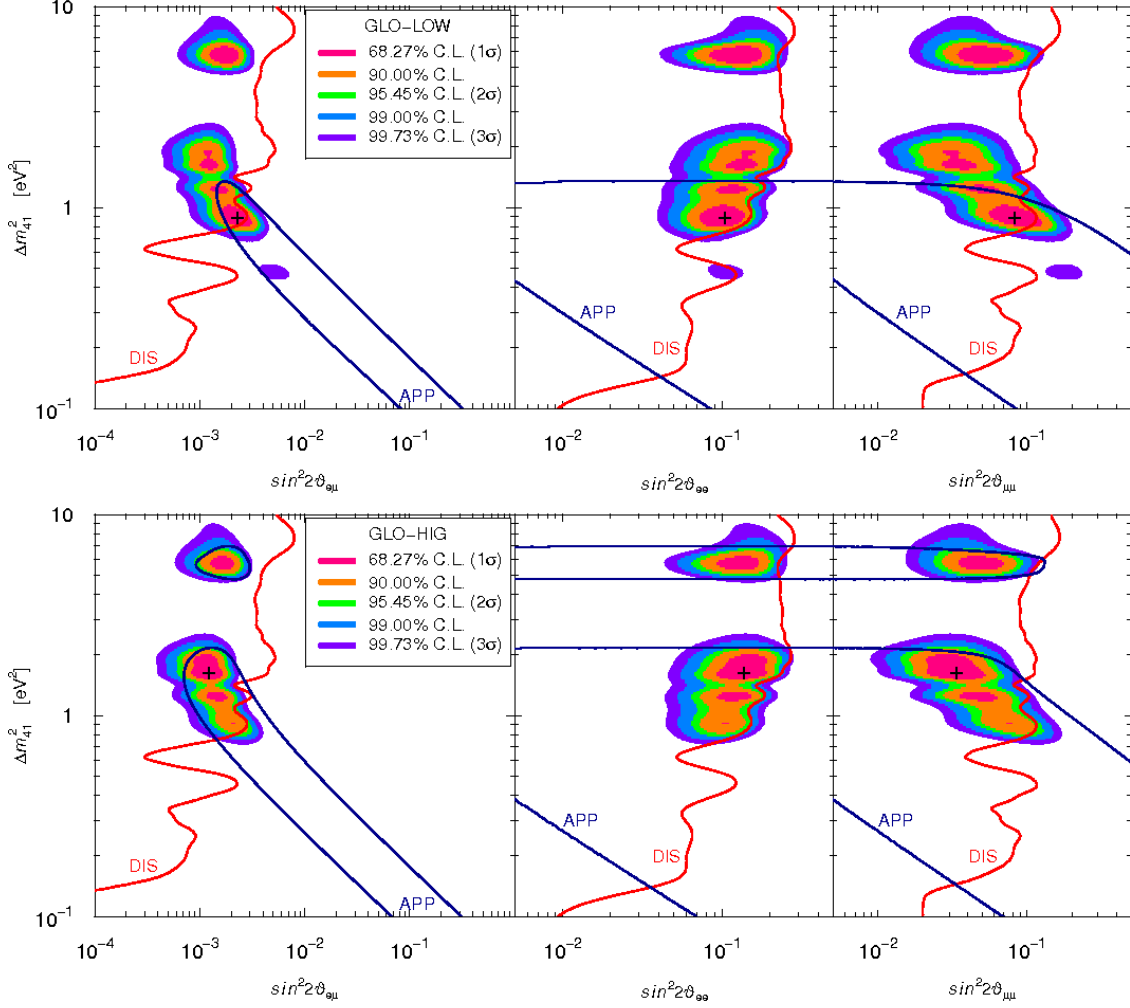


Figure 66. Allowed regions in the  $\sin^2 2\theta_{e\mu}-\Delta m_{41}^2$ ,  $\sin^2 2\theta_{ee}-\Delta m_{41}^2$  and  $\sin^2 2\theta_{\mu\mu}-\Delta m_{41}^2$  planes obtained [515] from the GLO-LOW and GLO-HIG global analyses of short-baseline neutrino oscillation data (see Tab XXIV). The best-fit points are indicated by crosses (see Table. XXIV). The thick solid blue lines with the label APP show the  $3\sigma$  allowed regions obtained from the analysis of  $\bar{\nu}_\mu \rightarrow \bar{\nu}_e$  appearance data. The thick solid red lines with the label DIS show the  $3\sigma$  allowed regions obtained from the analysis of disappearance data.

is very strong. Nevertheless, we do not fully discard this solution here, because we are not aware of an a-priori argument which allows to exclude from the analysis the MiniBooNE low-energy data. The exclusion a-posteriori motivated by the results of the fit may be hazardous, taking also into account the nice value of the global goodness-of-fit (30%) and the above-mentioned preference for small values of  $\Delta m_{41}^2$  in agreement with the same preference of the cosmological data. Considering the GLO-HIG analysis, the 0.3% appearance-disappearance parameter goodness-of-fit is not dramatically low and the fit cannot be rejected, also taking into account the pleasant 50% value of the global goodness-of-fit.

		GLO-LOW	GLO-HIG
No Osc.	$\chi^2_{\min}$	195.1	178.1
	NDF	147	141
	GoF	0.49%	1.9%
3+1	$\chi^2_{\min}$	152.4	137.5
	NDF	144	138
	GoF	30%	50%
	$\Delta m_{41}^2 [\text{eV}^2]$	0.9	1.6
	$ U_{e4} ^2$	0.027	0.036
	$ U_{\mu 4} ^2$	0.021	0.0084
	$\sin^2 2\theta_{e\mu}$	0.0023	0.0012
	$\sin^2 2\theta_{ee}$	0.10	0.14
	$\sin^2 2\theta_{\mu\mu}$	0.083	0.034
PG	$\Delta\chi^2_{\min}$	18.8	11.6
	NDF	2	2
	GoF	0.008%	0.3%

Table XXIV. Values of  $\chi^2$ , number of degrees of freedom (NDF), goodness-of-fit (GoF) and best-fit values of the 3+1 oscillation parameters obtained [515] from the global fit with (GLO-LOW) and without (GLO-HIG) the MiniBooNE electron neutrino and antineutrino data with reconstructed neutrino energy smaller than 475 MeV. The first three lines correspond to the case of no oscillations (No Osc.). The following nine lines correspond to the case of 3+1 mixing. The last three lines give the parameter goodness-of-fit (PG) [539].

## B. 3+1 and 3+2 Fits of Short-Baseline Experiments

Here we report the results on global fits assuming one or two sterile neutrinos obtained in Ref. [112], updated with the latest constraints on  $\nu_\mu$  mixing with eV states from MINOS NC data [410]. We first discuss the implications of the new reactor antineutrino fluxes (see section III and refs. [462, 472]) and later we present the fit results of the global data.

### Short-baseline reactor experiments

Following [118], we have analyzed data from several short baseline ( $L \lesssim 100$ ) reactor experiments. In particular, we include full spectral data from the Bugey3 detectors [391] at distances of 15, 40 and 95 m from the reactor core, and we take into account the total event rates measured at Bugey4 [450], ROVNO [534], Krasnoyarsk [540], ILL [448], and Gösgen [449] (see Table II of [118] for a summary of these measurements). We also include the Chooz [541] and Palo Verde [542] experiments at  $L \approx 1$  km. We use the neutrino fluxes from the isotopes  $^{235}\text{U}$ ,  $^{239}\text{Pu}$ ,  $^{238}\text{U}$ ,  $^{241}\text{Pu}$  obtained in [462] and we include the uncertainty on the integrated flux for each isotope given in Table I of [118], correlated between all experiments. For further technical details see [543].

Even though the 3+1 (3+2) framework has a large number of free parameters, SBL reactor

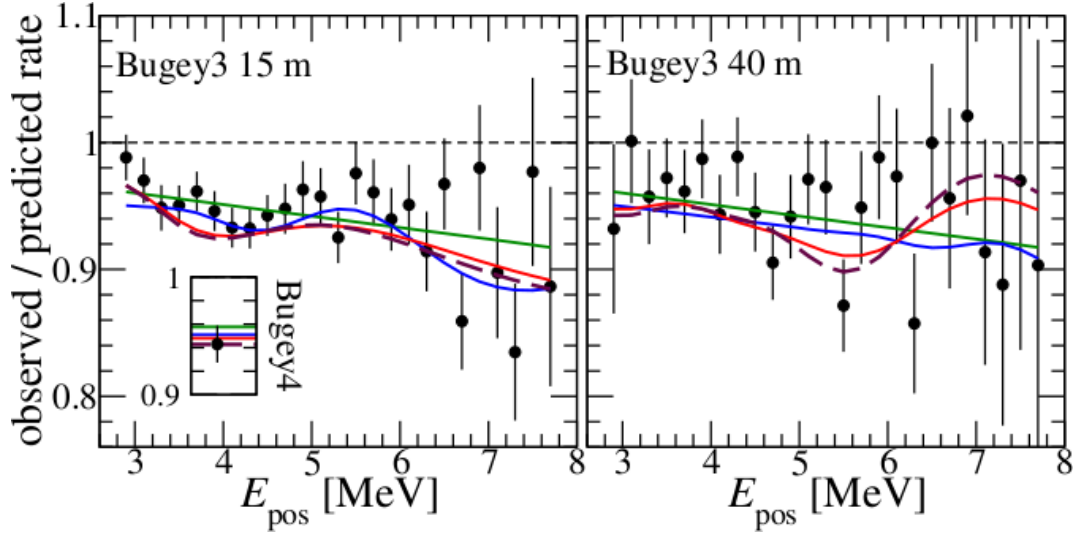


Figure 67. Comparison of sterile neutrino models to data from the Bugey reactor neutrino experiment. The data points show the ratio of the observed event spectra to the predicted ones in the absence of oscillations. The prediction is based on the new (higher) reactor antineutrino fluxes from [462]. The inset shows the ratio of the total rate measured in Bugey4 compared to the prediction. Bugey3 error bars are statistical only, whereas the error on the Bugey4 rate includes statistics and systematics and is dominated by the latter. The green solid curve shows the prediction for the no oscillation hypothesis, the blue solid and red solid curves correspond to the 3+1 and 3+2 best fit points for SBL reactor data (Table XXV), and the dashed curve corresponds to the 3+2 best fit point of global SBL data from Table II of [112].

experiments are only sensitive to two (four) independent parameters. These parameters are the mass-squared differences  $\Delta m_{41}^2$  and  $\Delta m_{51}^2$  between the eV-scale sterile neutrinos and the light neutrinos, and the elements  $|U_{e4}|$  and  $|U_{e5}|$  of the leptonic mixing matrix, which describe the mixing of the electron neutrino flavor with the heavy neutrino mass states  $\nu_4$  and  $\nu_5$ . Obviously, for the 3+1 case, only  $\nu_4$  is present. The best fit points for the two scenarios are summarized in Table XXV and illustrated in figure 67, which are both taken from ref. [112]. The lines in figure 67 show the best fit theoretical prediction for the no oscillation case (green) and for the 3+1 (blue) and 3+2 (red) models. Note that, even for no oscillations, the prediction may deviate from 1 due to nuisance parameters included in the fit to parametrize systematic uncertainties. The fit is dominated by Bugey3 spectral data at 15 m and 40 m and the precise rate measurement from Bugey4.

To study the sterile neutrino masses favored by short baseline reactor neutrino data, we show in the lower part of Fig. 68 the  $\chi^2$  of the SBL reactor fit as a function of  $\Delta m_{41}^2$ . We compare the 3+1 (blue) and 3+2 (red) models, and we also compare results obtained using the new (slod) and

	$\Delta m_{41}^2$ [eV <sup>2</sup> ]	$ U_{e4} $	$\Delta m_{51}^2$ [eV <sup>2</sup> ]	$ U_{e5} $	$\chi^2/\text{dof}$
3+1	1.78	0.151			50.1/67
3+2	0.46	0.108	0.89	0.124	46.5/65

Table XXV. Best fit points for the 3+1 and 3+2 scenarios from reactor antineutrino data alone. The total number of data points is 69 (Bugey3 spectra plus 9 SBL rate measurements; we have omitted data from Chooz and Palo Verde, which are not very sensitive to the model parameters, but would dilute the  $\chi^2$  by introducing 15 additional data points). For no oscillations we have  $\chi^2/\text{dof} = 59.0/69$ .

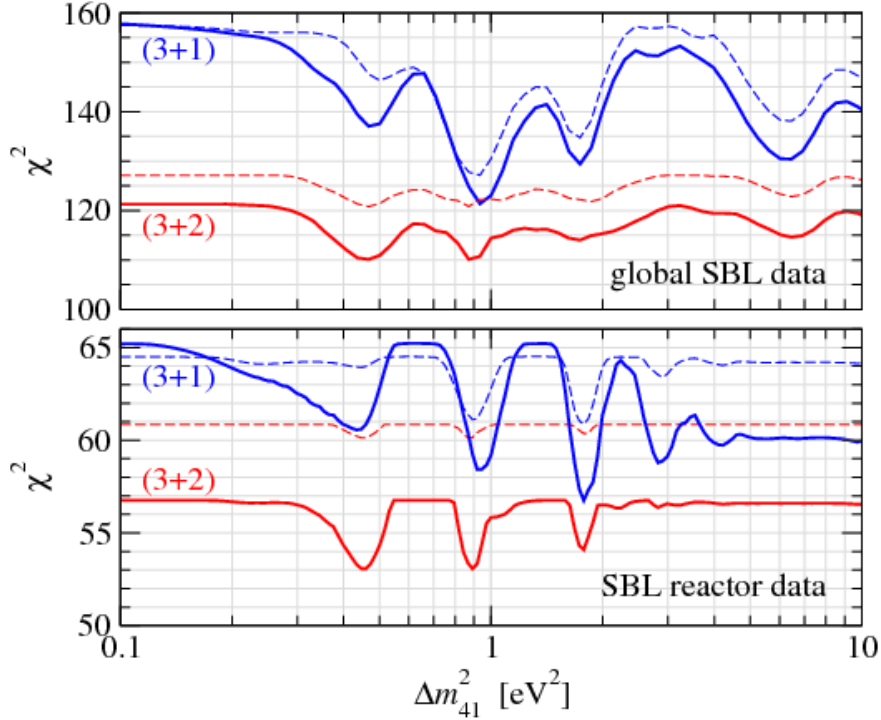


Figure 68.  $\chi^2$  from global SBL data (upper panel) and from SBL reactor data alone (lower panel) for the 3+1 (blue) and 3+2 (red) scenarios. Dashed (solid) curves were computed using the old [459] (new [462]) reactor  $\bar{\nu}_e$  flux prediction. All undisplayed parameters are minimized over. The total number of data points is 137 (84) for the global (reactor) analysis.

old (dashed) reactor flux predictions. Especially for the new fluxes, we find a clear preference for sterile neutrino oscillations: the  $\Delta\chi^2$  between the no oscillation hypothesis and the 3+1 best fit point is 8.5, which implies that the no oscillation case is disfavored at about 98.6% CL (2 dof). In the 3+2 case the no oscillation hypothesis is disfavored compared to the 3+2 best fit point with  $\Delta\chi^2 = 12.1$ , or 98.3% CL (4 dof). In contrast, with the old flux predictions the improvement of the fit is not significant, with a  $\Delta\chi^2$  between the best fit points and the no oscillation case of only 3.6 and 4.4 for the 3+1 and 3+2 hypotheses, respectively.

### Global analysis of SBL data

We now move on to a combined analysis of short-baseline reactor neutrino data together with other short-baseline data, including the LSND and MiniBooNE excesses. LSND has provided evidence for  $\bar{\nu}_\mu \rightarrow \bar{\nu}_e$  transitions [114], and MiniBooNE has reported an excess of events in the same channel, consistent with the LSND signal [117]. (In a new preliminary data release by the MiniBooNE collaboration [544], the significance of this excess has decreased, but it is still consistent with the LSND signal.) This hint for oscillations is however not confirmed by a MiniBooNE search in the  $\nu_\mu \rightarrow \nu_e$  channel [115], where the data in the energy range sensitive to oscillations is consistent with the background expectation. These results, together with the reactor antineutrino anomaly, seem to suggest an explanation involving CP violation in order to reconcile the differing results from neutrino and antineutrino searches.

An explanation of the LSND and MiniBooNE anomalies in terms of sterile neutrino oscilla-

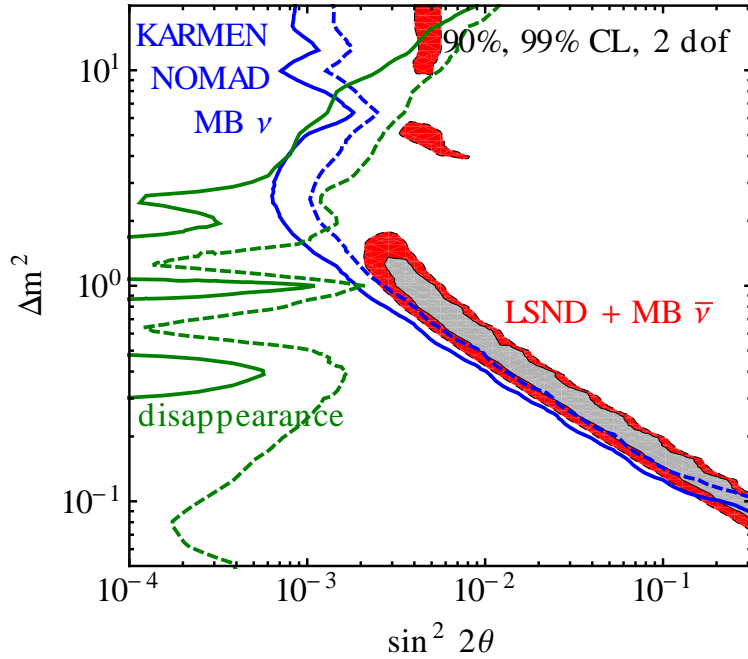


Figure 69. Global constraints on sterile neutrinos in the 3+1 model. We show the allowed regions at 90% and 99% CL from a combined analysis of the LSND [114] and MiniBooNE antineutrino [117] signals (filled regions), as well as the constraints from the null results of KARMEN [392], NOMAD [545] and MiniBooNE neutrino [115] appearance searches (blue contour). The limit from disappearance experiments (green contours) includes data from CDHS [408], atmospheric neutrinos, MINOS, and from the SBL reactor experiments. For the latter, we have used the new reactor flux predictions from [462], but we have checked that the results, especially regarding consistency with LSND and MiniBooNE  $\bar{\nu}_e$  data, are qualitatively unchanged when the old reactor fluxes are used [112].

tions requires mixing of the sterile neutrinos with both electron and muon neutrinos. Their mixing with electron neutrinos is probed also by reactor experiments, which lead to a tight constraint if the previous reactor flux prediction [459] is used. With the new reactor fluxes from [462], however, lead to a preference for active–sterile neutrino mixing at the 98% confidence level, hence the interesting question arises whether a consistent description of the global data on SBL oscillations (including LSND/MiniBooNE) becomes now possible. To answer this question we perform a fit by including, in addition to the reactor searches for  $\bar{\nu}_e$  disappearance, the LSND [114] and MiniBooNE [115, 117] results, as well as additional constraints from the appearance experiments KARMEN [392] and NOMAD [545], from the  $\nu_\mu$  disappearance search in CDHS [408], from atmospheric neutrinos, and from the MINOS search for active neutrino disappearance [410, 496]. Technical details of our analysis can be found in [127, 516] and references therein. For our MINOS simulation and for the combination of the different analyses, we have used the GLOBES package [546, 547]. For a recent discussion of MINOS data in the context of sterile neutrinos see also Ref. [548].

In the 3+1 scheme, short-baseline oscillations depend on the three parameters  $\Delta m_{41}^2$ ,  $|U_{e4}|$ , and  $|U_{\mu 4}|$ . Since short baseline oscillations in this case can be effectively reduced to a two-flavor problem in all experiments considered here, it is not possible to obtain CP violation. Therefore, oscillations involving one sterile neutrino are not capable of reconciling the different results for neutrino (MiniBooNE) and antineutrino (LSND and MiniBooNE) appearance searches. Fig. 69 compares

	$ \Delta m_{41}^2 $	$ U_{e4} $	$ U_{\mu 4} $	$ \Delta m_{51}^2 $	$ U_{e5} $	$ U_{\mu 5} $	$\delta/\pi$	$\chi^2/\text{dof}$
(3+1)	(0.48)	(0.14)	(0.23)					(255.5/252)
3+2	1.10	0.14	0.11	0.82	0.13	0.12	-0.31	245.2/247
1+3+1	0.48	0.13	0.12	0.90	0.15	0.15	0.62	241.6/247

Table XXVI. Parameter values and  $\chi^2$  at the global best fit points for 3+1, 3+2 and 1+3+1 oscillations. The mass squared differences are given in units of  $\text{eV}^2$ . Note that the 3+1 model, in spite of its seemingly unoffending  $\chi^2/\text{dof}$  value, does not provide a satisfactory fit to the data, as demonstrated by the parameter goodness of fit test (see text and Table XXVII). We therefore show the corresponding best fit point in parentheses.

the allowed regions from LSND and MiniBooNE antineutrino data to the constraints from the other experiments in the 3+1 model. Note that, even though reactor analyses using the new flux prediction prefer non-zero  $U_{e4}$ , no closed regions appear for the disappearance bound (solid curve), since  $\sin^2 2\theta_{\text{SBL}} = 4|U_{e4}|^2|U_{\mu 4}|^2$  can still become zero if  $U_{\mu 4} = 0$ . We find that the parameter region favored by LSND and MiniBooNE antineutrino data is ruled out by other experiments at the 99% confidence level. The strength of this exclusion is almost the same for the new [462] and old [459] reactor fluxes.<sup>21</sup>

Using the parameter goodness of fit test developed in [539], we find compatibility of the LSND+MiniBooNE( $\bar{\nu}$ ) signal with the rest of the data only at the level of  $\text{few} \times 10^{-6}$ , with  $\chi_{\text{PG}}^2 = 25.8(27.3)$  for new (old) reactor fluxes, see Table XXVII. Hence we conclude that the 3+1 scenario does not provide a satisfactory description of the data despite the new hint coming from reactors.

Moving on to the 3+2 model, we note that in this case, SBL experiments depend on the seven parameters listed in Table XXVI. In addition to the two mass-squared differences and the moduli of the mixing matrix elements, there is now also a physical complex phase,  $\delta \equiv \arg(U_{\mu 4}U_{e4}^*U_{\mu 5}^*U_{e5})$ . This phase leads to CP violation in SBL oscillations [516, 517], allowing to reconcile differing neutrino and antineutrino results from MiniBooNE, LSND, and short-baseline reactor experiments. Table XXVI shows the parameter values at the global best fit point and the corresponding  $\chi^2$  value. Changing from the previous to the new reactor flux calculations the  $\chi^2$  decreases by 10.5 units, indicating a significant improvement of the description of the data, see also upper panel of Fig. 68. From that figure follows also that going from 3+1 to 3+2 leads to a significant improvement of the fit with the new reactor fluxes, which was not the case with the old ones. The  $\chi^2$  improves by 10.3 units, which means that 3+1 is disfavored at the 96.4% CL (4 dof) with respect to 3+2, compared to  $\Delta\chi^2 = 5.5$  (76% CL) for the old fluxes.

In Fig. 67 we show the prediction for the Bugey spectra at the 3+2 global best fit point as dashed curves. Clearly they are very similar to the best fit of reactor data only. Fig. 70 shows the predicted spectra for MiniBooNE neutrino and antineutrino data, as well as the LSND  $\bar{\nu}_\mu \rightarrow \bar{\nu}_e$  transition probability. In this case some tension in the fit is apparent and the description of the data is clearly worse at the global best fit point than a fit to appearance data only (dashed histograms). The main difference to the results presented in [112] is the inclusion of MINOS NC

<sup>21</sup>Let us comment on the comparison of Fig. 69 based on [112] to the GLO-HIG analysis from [515] shown in the lower left panel of Fig. 66. The appearance region shown in Fig. 66 extends to lower values than the LSND+MB $\bar{\nu}$  region in Fig. 69, since it includes other appearance data (shown as blue curves in Fig. 69) which push the appearance region to lower values of  $\sin^2 2\theta$ . There are also differences in the limits from disappearance data, especially around  $\Delta m^2 \sim 1 \text{ eV}^2$ . Presumably the origin of those differences is related to a different treatment of spectral data from the Bugey reactor experiment.



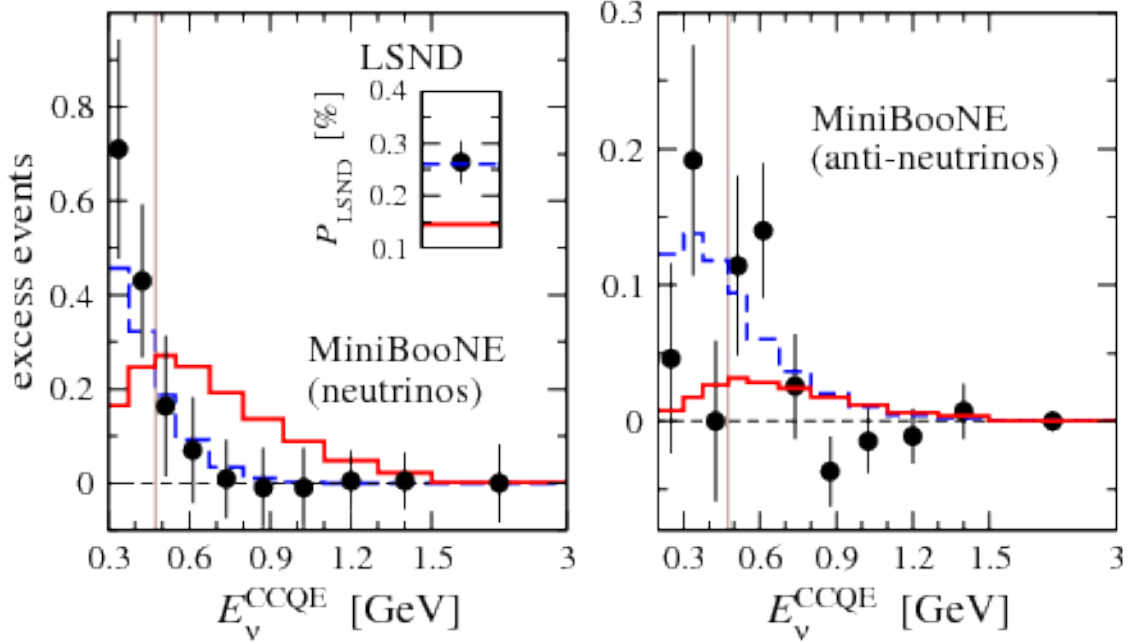


Figure 70. Predicted spectra for MiniBooNE data and the transition probability for LSND (inset). Solid histograms refer to the 3+2 global best fit point from Table. XXVI. Dashed histograms correspond to the best fit of appearance data only (LSND, MiniBooNE  $\nu/\bar{\nu}$ , KARMEN, NOMAD). For MiniBooNE we fit only data above 475 MeV.

results. Note that MiniBooNE observes an event excess in the lower part of the spectrum. This excess can be explained if only appearance data are considered, but not in the global analysis including disappearance searches [516]. Therefore, we follow [115] and assume an alternative explanation for this excess, *e.g.* [549].

In Table XXVII we show the compatibility of the LSND/MiniBooNE( $\bar{\nu}$ ) signal with the rest of the data, as well as the compatibility of appearance and disappearance searches using the PG test from [539]. Although the compatibility improves drastically when changing from old to new reactor fluxes, the PG is still well below 0.1% for 3+2. This indicates that some tension between data sets remains. The reason for the reduced PG values compared to the ones obtained in [112] comes from the inclusion of MINOS NC data. Note that within the 3+1 scenario there is an internal tension between LSND and MiniBooNE neutrino data worsening the fit of the appearance data set. This in turn can lead to an “improved” PG value in the comparison between appearance and disappearance data, since the tension in the fit is hidden in the appearance data set and does not contribute to the PG. Therefore the apparently better PG value for 3+1 compared to 3+2 has to be interpreted with care. We considered also a “1+3+1” scenario, in which one of the sterile mass eigenstates is lighter than the three active ones and the other is heavier [550]. As can be seen from Tables XXVI and XXVII the fit of 1+3+1 is slightly better than 3+2, with  $\Delta\chi^2 = 13.9$  between 3+1 and 1+3+1 (99.2% CL for 4 dof). However, due to the larger total mass in neutrinos, a 1+3+1 ordering might be in more tension with cosmology than a 3+2 scheme [121, 353, 529]. Fig. 71 shows the allowed regions for the two eV-scale mass-squared differences for the 3+2 and 1+3+1 schemes.

Let us comment briefly on other signatures of eV-scale sterile neutrinos. We have checked the fit of solar neutrino data and the KamLAND reactor experiment, and found excellent agreement. The effect of non-zero  $U_{e4}$  and  $U_{e5}$  for these data are similar to the one of  $U_{e3}$  in the standard three-

	LSND+MB( $\bar{\nu}$ ) vs rest		appearance vs disapp.	
	old	new	old	new
$\chi^2_{\text{PG},3+1}/\text{dof}$	27.3/2	25.8/2	15.7/2	14.2/2
PG <sub>3+1</sub>	$1.2 \times 10^{-6}$	$2.5 \times 10^{-6}$	$3.9 \times 10^{-4}$	$8.2 \times 10^{-4}$
$\chi^2_{\text{PG},3+2}/\text{dof}$	30.0/5	24.8/5	24.7/4	19.5/4
PG <sub>3+2</sub>	$1.5 \times 10^{-5}$	$1.5 \times 10^{-4}$	$5.7 \times 10^{-5}$	$6.1 \times 10^{-4}$
$\chi^2_{\text{PG},1+3+1}/\text{dof}$	24.9/5	21.2/5	19.6/4	10.7/4
PG <sub>1+3+1</sub>	$1.5 \times 10^{-4}$	$7.5 \times 10^{-4}$	$6.0 \times 10^{-3}$	$3.1 \times 10^{-2}$

Table XXVII. Compatibility of different data sets according to the parameter goodness of fit (PG) test [539] for the 3+1, 3+2 and 1+3+1 oscillation scenarios. Results are shown for both the old [459] and the new [462] reactor antineutrino flux predictions.

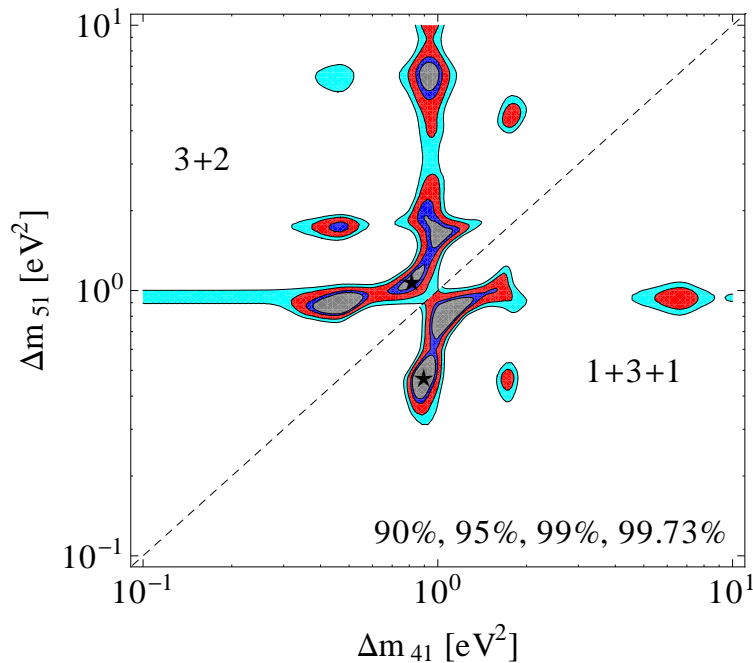


Figure 71. The globally preferred regions for the neutrino mass squared differences  $\Delta m_{41}^2$  and  $\Delta m_{51}^2$  in the 3+2 (upper left) and 1+3+1 (lower right) scenarios.

active neutrino case, and hence the 3+2 best fit point mimics a non-zero  $U_{e3}$  close to the preferred value of these data, see [543, 551, 552]. Our best-fit points also fall in the range of parameter values required to explain the Gallium anomaly, a small  $\nu_e$  deficit observed in the neutrino flux from intense radioactive sources by radiochemical neutrino detectors [437]. Finally, sterile neutrinos may manifest themselves in cosmology. Recent studies [121, 353, 529] indicate a slight preference for extra radiation content in the universe (mainly from CMB measurements), favoring the existence of light sterile neutrinos. On the other hand, Big-Bang nucleosynthesis constrains the number of extra neutrino species to be  $< 1.2$  at the 95% confidence level [332] and is therefore problematic in schemes with two or more sterile neutrinos. Moreover, global fits to cosmological data constrain the sum of the neutrino masses to be  $\leq 0.7$  to  $1.5$  eV at 95% CL [121, 353, 529], depending on the used data, whereas our 3+2 best fit point leads to  $\sum m_\nu \approx 1.7$  eV. Hence, sterile neutrino

explanations of short-baseline oscillation data are in tension with cosmology, or, if confirmed, would indicate a deviation from the standard cosmological picture. For instance, a mechanism that suppresses their production in the early universe may be required (see *e.g.* [553, 554]).

In conclusion, a global fit to short-baseline oscillation searches assuming two sterile neutrinos improves significantly when new predictions for the reactor neutrino flux are taken into account, although tension remains. We are thus facing an intriguing accumulation of hints for the existence of sterile neutrinos at the eV scale, and a confirmation of these hints in the future could certainly be considered a major discovery.

### C. Discussion of the LSND and MiniBooNE Results

At present, the evidence for oscillations at  $\Delta m_{41}^2 \sim 1 \text{ eV}^2$  and  $\sin^2 2\theta_{\mu e} \sim 0.005$  from the LSND experiment [114, 555, 556] remains the most significant hint for the existence of light sterile neutrinos, at  $3.8\sigma$ . The  $3.0\sigma$  excess of  $\nu_e$  observed by MiniBooNE, referred to as the “MiniBooNE low energy excess”, is only marginally consistent with a  $\nu_\mu \rightarrow \nu_e$  single sterile neutrino oscillation signature, and, under that interpretation, it corresponds to a significantly different  $L/E$  distribution than that suggested by the LSND excess [115, 116]. As a result, the MiniBooNE neutrino and LSND results have been shown to be significantly incompatible [516, 518] under the single sterile neutrino oscillation assumption.

Instead, past attempts to simultaneously interpret the MiniBooNE neutrino and LSND antineutrino excesses as signals induced by sterile neutrino oscillations lean on CP-violation [516, 518] and the assumption that more than one mostly-sterile mass eigenstates exist. This scenario will be discussed in Sec. IV C. Generally, one must resort to models which induce differences between neutrino and antineutrino oscillation probabilities and/or more complex  $L/E$  dependence in the observable oscillation probabilities. There are other scenarios besides CP-violating sterile neutrino oscillations which can induce such differences, and those include models with altered neutrino dispersion relations [557], extra dimensions [558], CPT-violation [264, 273, 280], and non-standard neutrino interactions [127, 212, 519, 559]. At the same! time, there have been several attempts to interpret the MiniBooNE low energy excess independently of oscillations. The possibility of mis-estimated background has been considered but has been ruled out by independent *in situ* measurements at MiniBooNE [116], in particular for the case of neutral-current single-photon production, which makes up the most dominant background to the MiniBooNE  $\nu_e$  appearance search at low energy. However, the possibility of a new background, such as that contributed by anomaly-mediated single-photon production [560], remains a viable interpretation for the MiniBooNE low energy excess. Viable theoretical interpretations include heavy sterile neutrino decay [561–566].

While it is unclear whether the MiniBooNE neutrino and LSND antineutrino excesses are a manifestation of the same underlying scenario, be it CP-violating light sterile neutrino oscillations, or some other physics, there are two independent measurements which are in direct agreement with LSND under the single sterile neutrino oscillation hypothesis. The first one is the appearance measurement performed by MiniBooNE during antineutrino running [117]. While the results of that measurement are statistics-limited, the small excess observed has an oscillations-like  $L/E$  dependence which agrees with that of LSND, and favors oscillations over the null hypothesis at the 91% CL [567].

The second measurement in support of the LSND single sterile neutrino oscillation interpretation comes from the electron antineutrino disappearance sector, and is what has been described

in previous sections as the “reactor antineutrino anomaly” [118]. This new finding has shed new light to light sterile neutrino oscillations. Until 2011, electron neutrino and antineutrino disappearance at  $\Delta m^2 \sim 1 \text{ eV}^2$  had been thought to be constrained to less than 10% by short-baseline reactor antineutrino experiments including Bugey [391] and CHOOZ [541]. This level of constraint on  $\bar{\nu}_e$  disappearance, when combined with equally stringent  $\nu_\mu$  disappearance limits from MiniBooNE/SciBooNE [409], CDHS [408], CCFR [406], MINOS [496], K2K and atmospheric neutrino experiments [427], reduces observable appearance to a level well below what is necessary to account for the LSND excess. Instead, the now anomalous measurements performed at ILL, Bugey, ROVNO, CHOOZ, and others [118], can be interpreted as—and are in support of—oscillations at a  $\Delta m^2$  consistent with that from LSND,  $\Delta m^2 \sim 1 \text{ eV}^2$ , and relatively small disappearance amplitude  $\sin^2 2\theta_{ee} \sim 0.1$ , consistent with a sterile neutrino hypothesis.

Finally, there has been a long-standing piece of evidence for much larger  $\nu_e$  disappearance at very short baselines from the Gallex and SAGE calibration source experiments. This evidence now seems excluded by a comparison of KARMEN and LSND  $\nu_e$  cross section measurements to theoretical predictions [485].

The following two sections present global oscillation fit results from the perspective of CPT-conserving light sterile neutrino oscillations. The conclusions are drawn from Refs. [112, 113, 519]. In summary, the present light sterile neutrino oscillation fits reveal that neutrino and antineutrino oscillation signatures which may be responsible for the LSND, MiniBooNE, and reactor antineutrino anomalies are incompatible with other, primarily neutrino, null results. The neutrino and antineutrino data sets show differences which cannot be explained away by just CP violation. That observation has prompted the consideration of even less standard scenarios, beyond the “reference picture” of CPT-conserving 3+N oscillations [568].

### (3+1) Oscillations

It has already been established that the MiniBooNE antineutrino and LSND excesses are highly compatible with each other under the single sterile neutrino oscillation scenario, referred to as the (3+1) scenario [516, 518]. It is, however, also necessary to consider how those excesses compare with other available data sets. This has been done by several authors in the past [516, 518, 519, 538], which find that the high compatibility persists even when one considers all other short-baseline *antineutrino* data sets, including the KARMEN  $\bar{\nu}_\mu \rightarrow \bar{\nu}_e$  appearance [392] and the Bugey and CHOOZ  $\bar{\nu}_e$  disappearance data sets, with a combined fit favoring oscillations at the  $> 99\%$  confidence level. The compatibility drops drastically, however, when one folds in constraints from  $\nu_\mu$  disappearance experiments, as well as additional  $\nu_e$  appearance constraints from NOMAD [531] and the MiniBooNE  $\nu_\mu \rightarrow \nu_e$  search. It should be noted that, under a CPT conserving (3+1) scenario, neutrino and antineutrino oscillations are identical, and therefore constraints from neutrino data sets are directly applicable to the global fits considered under this scenario. The compatibility found in a joint fit using most to all available experimental constraints is found to be at the  $\sim 1\%$  or less level [498, 518, 519], even after accounting for the reactor antineutrino anomaly.

### (3+2) Oscillations

The high compatibility seen in antineutrino-only fits in a (3+1) hypothesis is instructive, and the apparent differences seen among neutrino and antineutrino appearance signals make the (3+2) os-

cillation scenario interesting because of the offered possibility of CP violation. Combined analyses of most to all *appearance* data sets under the (3+2) scenario have been performed by several independent groups (see, *e.g.* [516, 518]), and consistently yield high compatibility when large CP violation is invoked. Furthermore, appearance-only fits yield oscillation parameters which predict excesses of low energy events at MiniBooNE in both neutrino and antineutrino running, which can account for the observed excesses. However, when disappearance data sets all included in the fits, the compatibility once again reduces significantly, and one finds tension among neutrino and antineutrino data sets. It is worth noting that the reactor anomaly is responsible for the significant reduction in tension found previously between neutrino and antineutrino data sets, or appearance and disappearance data sets; however, some tension remains, such that in order to make (3+2) CP-violating models viable, one or more experimental data sets other than those with antineutrino signals must be rejected [112, 113].

## D. Impact of Sterile Neutrinos for Absolute Neutrino Mass Measurements

### Impact for $\beta$ -Decay and Neutrinoless $\beta\beta$ -Decay

In this section we investigate possible signals of eV sterile neutrinos as indicated by the experiments discussed above in searches for the absolute neutrino mass in  $\beta$ -decay and neutrinoless double  $\beta$ -decay, based on the GLO-LOW and GLO-HIG analyses from section IV A of short-baseline neutrino oscillation data.

The effective electron neutrino mass  $m_\beta$  in  $\beta$ -decay experiments is given by [569–572] (other approaches are discussed in Refs. [573–575])

$$m_\beta^2 = \sum_k |U_{ek}|^2 m_k^2. \quad (118)$$

The most accurate measurements of  $m_\beta$  have been obtained in the Mainz [576] and Troitsk [577] experiments, whose combined upper bound is [439]

$$m_\beta \leq 1.8 \text{ eV} \quad (\text{Mainz+Troitsk, 95\% C.L.}). \quad (119)$$

In the hierarchical 3+1 scheme we have the lower bound

$$m_\beta \geq |U_{e4}| \sqrt{\Delta m_{41}^2} \equiv m_\beta^{(4)}. \quad (120)$$

Therefore, from the analysis of short-baseline neutrino oscillation data we can derive predictions for the possibility of observing a neutrino mass effect in the KATRIN experiment [578], which is under construction and scheduled to start in 2012, and in other possible future experiments.

Let us however note that the effective electron neutrino mass in Eq. (118) has been derived assuming that all the neutrino masses are smaller than the experimental energy resolution (see Ref. [430]). If  $m_4$  is of the order of 1 eV, the approximation is acceptable for the interpretation of the result of the Mainz and Troitsk experiments, which had, respectively, energy resolutions of 4.8 eV and 3.5 eV [579]. On the other hand, the energy resolution of the KATRIN experiment will be 0.93 eV near the end-point of the energy spectrum of the electron emitted in Tritium decay, at

	GLO-LOW	GLO-HIG
$m_4$	0.91 – 2.5	1.2 – 2.4
	0.88 – 2.5	0.91 – 2.5
	0.85 – 2.8	0.87 – 2.8
$ U_{e4} ^2$	0.02 – 0.04	0.03 – 0.05
	0.02 – 0.06	0.02 – 0.06
	0.01 – 0.07	0.01 – 0.07
$m_\beta^{(4)}$	0.14 – 0.49	0.21 – 0.45
	0.12 – 0.56	0.13 – 0.56
	0.10 – 0.65	0.11 – 0.63
$m_{\beta\beta}^{(4)}$	0.020 – 0.10	0.035 – 0.09
	0.015 – 0.13	0.018 – 0.12
	0.011 – 0.16	0.013 – 0.16

Table XXVIII. Allowed  $1\sigma$ ,  $2\sigma$  and  $3\sigma$  ranges of  $m_4 = \sqrt{\Delta m_{41}^2}$ ,  $|U_{e4}|^2$ ,  $m_\beta^{(4)} = |U_{e4}| \sqrt{\Delta m_{41}^2}$  and  $m_{\beta\beta}^{(4)} = |U_{e4}|^2 \sqrt{\Delta m_{41}^2}$  obtained [515] from the global fit with (GLO-LOW) and without (GLO-HIG) the MiniBooNE electron neutrino and antineutrino data with reconstructed neutrino energy smaller than 475 MeV. Masses are given in eV.

$T = Q$ , where  $T$  is the kinetic energy of the electron and  $Q = 18.574$  keV is the  $Q$ -value of the decay. If the value of  $m_4$  is larger than the energy resolution of the experiment, its effect on the measured electron spectrum cannot be summarized by one effective quantity, because the Kurie function  $K(T)$  is given by

$$\begin{aligned} \frac{K^2(T)}{Q-T} &= \sqrt{(Q-T)^2 - \tilde{m}_\beta^2} - |U_{e4}|^2(Q-T) \\ &+ |U_{e4}|^2 \sqrt{(Q-T)^2 - m_4^2} \theta(Q-T-m_4), \end{aligned} \quad (121)$$

where  $\tilde{m}_\beta^2 = \sum_{k=1}^3 |U_{ek}|^2 m_k^2$  is the contribution of the three neutrino masses much smaller than 1 eV and  $\theta$  is the Heaviside step function.

In the following we discuss the predictions obtained from the GLO-LOW and GLO-HIG analyses from section IV A of short-baseline neutrino oscillation data for both the contribution  $m_\beta^{(4)}$  to the effective mass in  $\beta$ -decay and the distortion of the Kurie function due to  $m_4$ . Figure 72 shows the marginal  $\Delta\chi^2 = \chi^2 - \chi_{\min}^2$  as a function of  $m_\beta^{(4)}$ , which gives the  $1\sigma$ ,  $2\sigma$  and  $3\sigma$  allowed ranges of  $m_4$ ,  $|U_{e4}|^2$  and  $m_\beta^{(4)}$  listed in Tab. XXVIII. As one can see from Fig. 72 and Tab. XXVIII, the results of both the GLO-LOW and GLO-HIG analyses favor values of  $m_\beta^{(4)}$  between about 0.1 and 0.7 eV. This is promising for the perspectives of future experiments.

In Figures 73 and 74 we show the relative deviation of the Kurie function from the massless case ( $K(T) = Q - T$ ) obtained in the GLO-LOW and GLO-HIG analyses, neglecting the contribution of  $\tilde{m}_\beta$  in Eq. (121). For  $T > Q - m_4$  the deviation is constant, because the Kurie function in Eq. (121) reduces to

$$K(T) = (Q - T) \sqrt{1 - |U_{e4}|^2}. \quad (122)$$

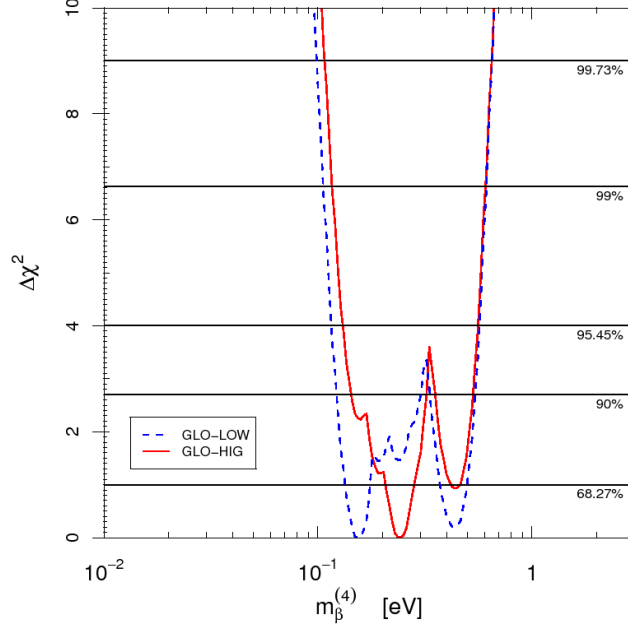


Figure 72. Marginal  $\Delta\chi^2 = \chi^2 - \chi_{\min}^2$  as a function of the contribution  $m_\beta^{(4)} = |U_{e4}|\sqrt{\Delta m_{41}^2}$  to the effective  $\beta$ -decay electron-neutrino mass  $m_\beta$  obtained [515] from the GLO-LOW and GLO-HIG global fits.

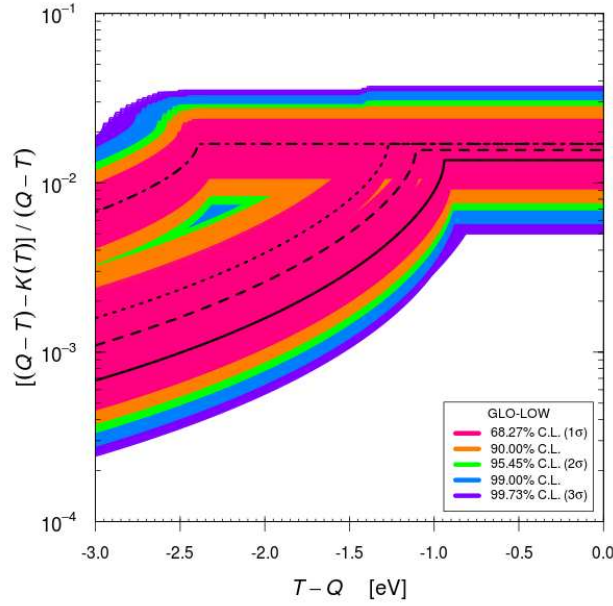


Figure 73. Bands of the relative deviation of the Kurie plot in  $\beta$ -decay corresponding to the allowed regions in the  $\sin^2 2\theta_{ee} - \Delta m_{41}^2$  plane in Fig. 66, obtained [515] from the GLO-LOW global analysis of short-baseline neutrino oscillation data (see Tab XXIV). The black solid line corresponds to the best-fit point ( $m_4 = 0.94$  eV and  $|U_{e4}|^2 = 0.027$ ). The dashed, dotted and dash-dotted lines correspond, respectively, to the local minima at ( $m_4 = 1.11$  eV,  $|U_{e4}|^2 = 0.03$ ), ( $m_4 = 1.27$  eV,  $|U_{e4}|^2 = 0.035$ ) and ( $m_4 = 2.40$  eV,  $|U_{e4}|^2 = 0.033$ ).

For  $T = Q - m_4$  there is a kink and for  $T < Q - m_4$  the Kurie function depends on both  $m_4$  and  $|U_{e4}|^2$ , as given by Eq. (121).

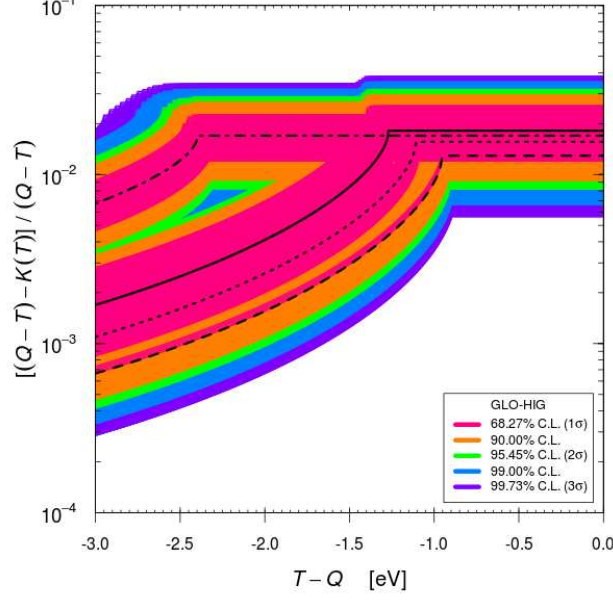


Figure 74. Bands of the relative deviation of the Kurie plot in  $\beta$ -decay corresponding to the allowed regions in the  $\sin^2 2\theta_{ee}-\Delta m_{41}^2$  plane in Fig. 66, obtained [515] from the GLO-HIG global analysis of short-baseline neutrino oscillation data (see Tab XXIV). The black solid line corresponds to the best-fit point ( $m_4 = 1.27$  eV and  $|U_{e4}|^2 = 0.036$ ). The dashed, dotted and dash-dotted lines correspond, respectively, to the local minima at ( $m_4 = 0.95$  eV,  $|U_{e4}|^2 = 0.027$ ), ( $m_4 = 1.11$  eV,  $|U_{e4}|^2 = 0.031$ ) and ( $m_4 = 2.40$  eV,  $|U_{e4}|^2 = 0.033$ ).

From Figs. 73 and 74 one can see that high precision will be needed in order to see the effect of  $m_4$  and measure  $|U_{e4}|^2$ , which is the only parameter which determines the deviation of  $K(T)$  from the massless Kurie function near the end point, for  $T > Q - m_4$ . If the mixing parameters are near the best-fit point of the GLO-LOW analysis, a precision of about one percent will be needed within 1 eV from the end-point of the spectrum. Finding the effect of  $m_4$  farther from the end-point, for  $T < Q - m_4$  is more difficult, because the relative deviation of the Kurie function can be as small as about  $10^{-3}$ . The GLO-HIG analysis prefers slightly larger values of  $m_4$ , but the discovery of an effect in  $\beta$ -decay will require a similar precision.

If massive neutrinos are Majorana particles, neutrinoless double- $\beta$  decay is possible, with a decay rate proportional to the effective Majorana mass (see Refs. [124, 430, 580–583])

$$m_{\beta\beta} = \left| \sum_k U_{ek}^2 m_k \right|. \quad (123)$$

The results of the analysis of short-baseline oscillation data allow us to calculate the contribution of the heaviest massive neutrino  $\nu_4$  to  $m_{\beta\beta}$ , which is given by

$$m_{\beta\beta}^{(4)} = |U_{e4}|^2 \sqrt{\Delta m_{41}^2}, \quad (124)$$

taking into account the mass hierarchy in Eq. (113). If there are no unlikely cancellations among the contributions of  $m_1$ ,  $m_2$ ,  $m_3$  and that of  $m_4$  [584] (possible cancellations are discussed in Refs.[585, 586]), the value of  $m_{\beta\beta}^{(4)}$  is a lower bound for the effective neutrino mass which could be observed in future neutrinoless double- $\beta$  decay experiments (see the review in Ref. [587]).



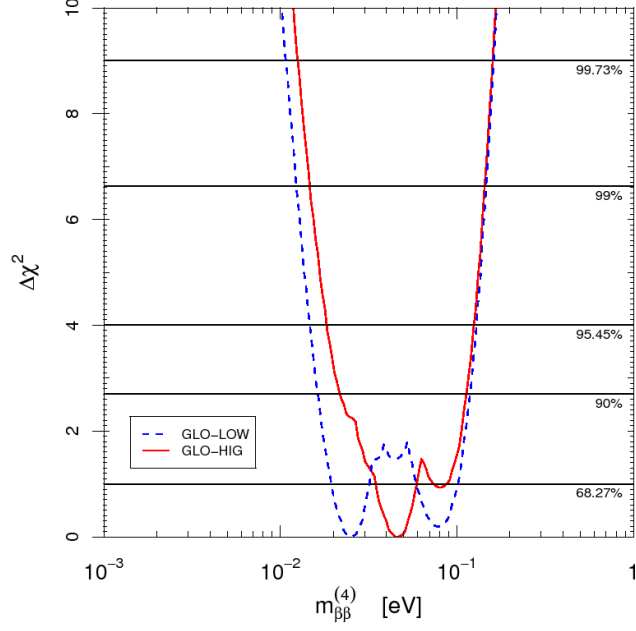


Figure 75. Marginal  $\Delta\chi^2 = \chi^2 - \chi_{\min}^2$  as a function of the contribution  $m_{\beta\beta}^{(4)} = |U_{e4}|^2 \sqrt{\Delta m_{41}^2}$  to the effective neutrinoless double- $\beta$  decay Majorana mass  $m_{\beta\beta}$  obtained [515] from the GLO-LOW and GLO-HIG global fits.

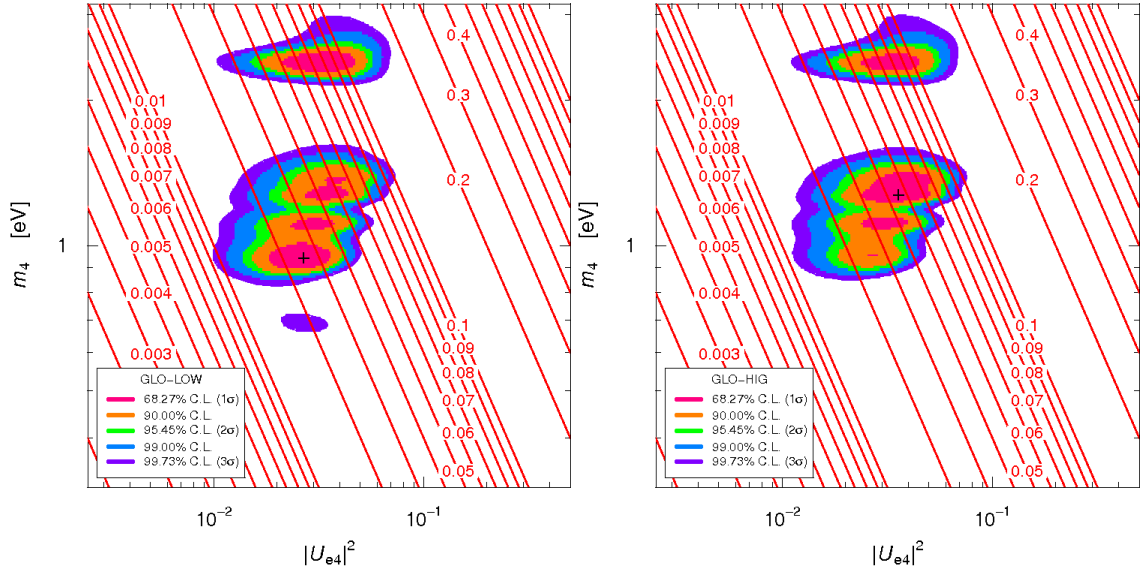


Figure 76. Allowed regions in the  $|U_{e4}|^2 - m_4$  plane obtained [515] from the GLO-LOW (left) and GLO-HIG (right) global analysis of short-baseline neutrino oscillation data (see Tab XXIV). The best-fit point is indicated by a cross (see Table. XXIV). The red lines have the indicated constant value of  $m_{\beta\beta}^{(4)} = |U_{e4}|^2 \sqrt{\Delta m_{41}^2}$ .

Figure 75 shows the marginal  $\Delta\chi^2$  as a function of  $m_{\beta\beta}^{(4)}$ , which gives the  $1\sigma$ ,  $2\sigma$  and  $3\sigma$  allowed ranges of  $m_{\beta\beta}^{(4)}$  listed in Tab. XXVIII. The predictions for  $m_{\beta\beta}^{(4)}$  obtained from global GLO-LOW and GLO-HIG agree in indicating a  $3\sigma$  allowed range between about 0.01 and 0.1 eV. The connection of the value of  $m_{\beta\beta}^{(4)}$  with the allowed regions for the oscillation parameters is clarified in Fig. 76,

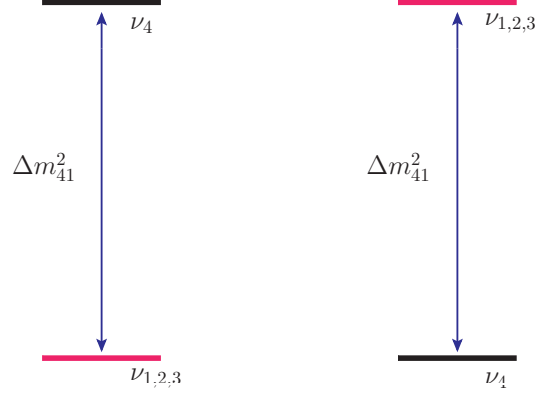


Figure 77. Description of the two possible mass orderings in the 3+1 case (left) and 1+3 case (right). Here  $\nu_{1,2,3}$  are the mostly active neutrinos whose mass splitting can be either normal or inverted.

where we show the allowed regions in the  $|U_{e4}|^2 - m_4$  plane obtained from the GLO-LOW and GLOW-HIG analyses, together with lines of constant  $m_{\beta\beta}^{(4)}$ . One can see that if the oscillation parameters are close to the best-fit point of the GLO-LOW analysis, at  $m_4 = 0.94$  eV, which is favored by cosmological data, the value of  $m_{\beta\beta}^{(4)}$  is about 0.02–0.03 eV. In order to have a large value of  $m_{\beta\beta}^{(4)}$ , around 0.1 eV, the oscillation parameters must lie in the large- $m_4$  region at  $m_4 \simeq 2.40$  eV, or on the large- $|U_{e4}|^2$  border of the allowed region at  $m_4 \simeq 1.27$  eV.

### On Neutrinoless double- $\beta$ decay with Sterile Neutrinos

Let us discuss in more detail how light sterile neutrinos may significantly affect neutrinoless double- $\beta$  decay. Needless to say, one needs to assume for the following discussion that neutrinos are Majorana particles, and that no other of the many proposed particle physics scenarios other than light neutrino exchange contribute to the process (see [124] for a recent review). The contributions of sterile neutrinos to the effective mass  $m_{\beta\beta}$  depend on the sterile neutrino masses, the active-sterile mixings and the neutrino mass ordering. In the presence of one sterile neutrino  $\nu_4$ , there are two typical mass orderings between active and sterile neutrinos, which are depicted in Fig. 77. The effective mass can be written as

$$m_{\beta\beta} = \underbrace{||U_{e1}|^2 m_1 + |U_{e2}|^2 m_2 e^{i\alpha} + |U_{e3}|^2 m_3 e^{i\beta}}_{m_{\beta\beta}^{(3)}} + \underbrace{|U_{e4}|^2 m_4 e^{i\gamma}}_{m_{\beta\beta}^{(4)}}, \quad (125)$$

where  $\gamma$  denotes the additional Majorana CP phase<sup>22</sup>, and  $m_{\beta\beta}^{(3)}$  is the active neutrino contribution to  $m_{\beta\beta}$ . Generalization to 2 or more sterile neutrinos is straightforward. We illustrate in Fig. 78 the allowed ranges of  $m_{\beta\beta}$  as a function of the lightest mass  $m_{\text{light}}$ , using data from Refs. [112, 543]. It is important to recall the standard three neutrino picture, namely that in the normal hierarchy ( $m_1 = 0$ )  $|m_{\beta\beta}^{(3,NH)}|$  can vanish and that in the inverted hierarchy ( $m_3 = 0$ )  $|m_{\beta\beta}^{(3,IH)}|$  cannot vanish, having a typical value of 0.02 eV. In the typically considered case of 3+1 ordering, let us take for

<sup>22</sup>In most parameterizations of scenarios with sterile neutrinos both Dirac and Majorana phases appear in the effective mass, and care has to be taken to introduce only the Majorana phases, see *e.g.* [588].

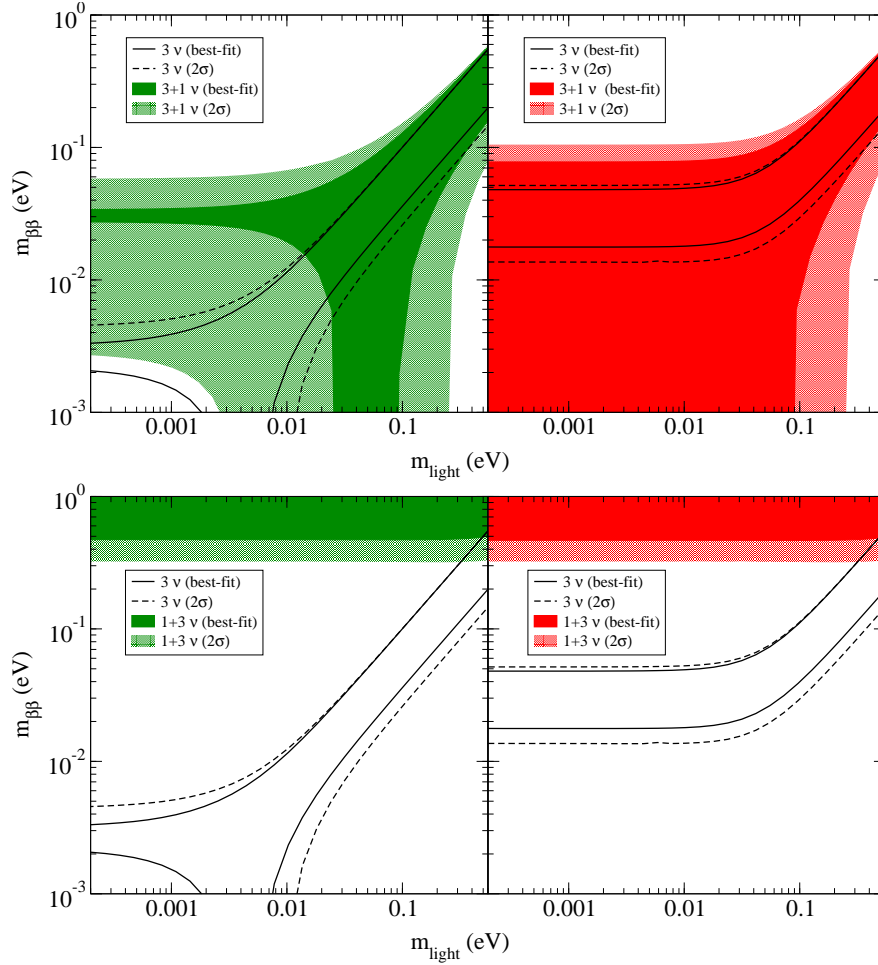


Figure 78. The allowed ranges in the  $m_{\beta\beta} - m_{light}$  parameter space, both in the standard three-neutrino picture (unshaded regions) and with one sterile neutrino (shaded regions), for the 3+1 (bottom) and 1+3 (top) cases.

illustration the parameters  $\Delta m_{41}^2 \simeq 1 \text{ eV}^2$  and  $|U_{e4}| \simeq 0.15$ . One finds with  $m_4 \simeq \sqrt{\Delta m_{41}^2} \gg m_{1,2,3}$  that

$$|m_{\beta\beta}^{(4)}| \simeq \sqrt{\Delta m_{41}^2} |U_{e4}|^2 \simeq 0.02 \text{ eV} \begin{cases} \gg |m_{\beta\beta}^{(3,NH)}| \\ \simeq |m_{\beta\beta}^{(3,IH)}| \end{cases} . \quad (126)$$

Therefore, if the active neutrinos are normally ordered, the effective mass *cannot* vanish anymore, whereas it *can* vanish when they are inversely ordered. Hence, the usual standard phenomenology has been completely turned around [61, 586]. The effective mass can also be zero in the regime where the active neutrinos are quasi-degenerate (lightest mass above 0.1 eV). This feature is of particular interest if future neutrinoless double- $\beta$  decay experiments measure a tiny effective mass smaller than the usual lower bound on the effective mass (cf. the solid and dashed lines in Fig. 78) and the neutrino mass hierarchy is confirmed to be inverted from long-baseline neutrino oscillations. In such a case one needs additional sources to cancel the active neutrino contributions to  $m_{\beta\beta}$ , and the sterile neutrino hypothesis would be an attractive explanation for this inconsistency.

If active neutrinos are heavier than the sterile one, *i.e.*, the 1+3 case (somewhat disfavored by cosmological bounds on the sum of neutrino masses) shown in Fig. 77, three active neutrinos are

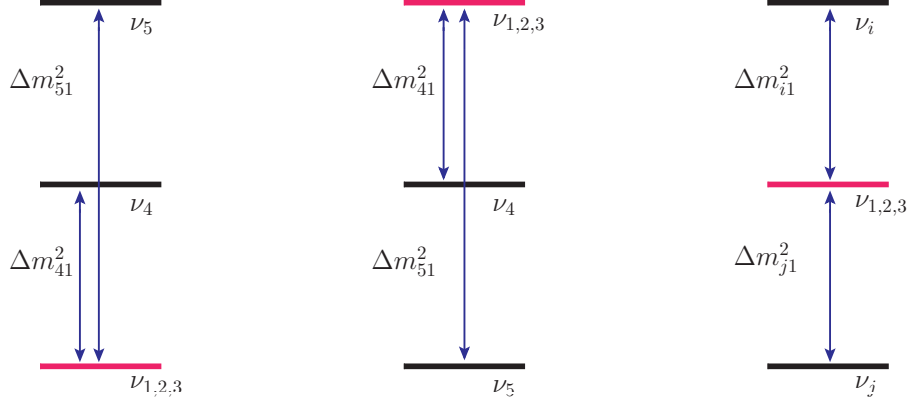


Figure 79. Description of three possible mass hierarchies in the 3+2 case (left), the 2+3 case (middle) and 1+3+1 case (right).

quasi-degenerate and the effective mass is approximately given by

$$m_{\beta\beta} \simeq \sqrt{\Delta m_{41}^2} \sqrt{1 - \sin^2 2\theta_{12} \sin^2 \alpha/2}, \quad (127)$$

no matter whether the active neutrino mass spectrum is normal ( $m_3 > m_2 > m_1$ ) or inverted ( $m_2 > m_1 > m_3$ ). For values of  $\Delta m_{41}^2$  around  $1 \text{ eV}^2$  this puts already constraints on the Majorana phase  $\alpha$ .

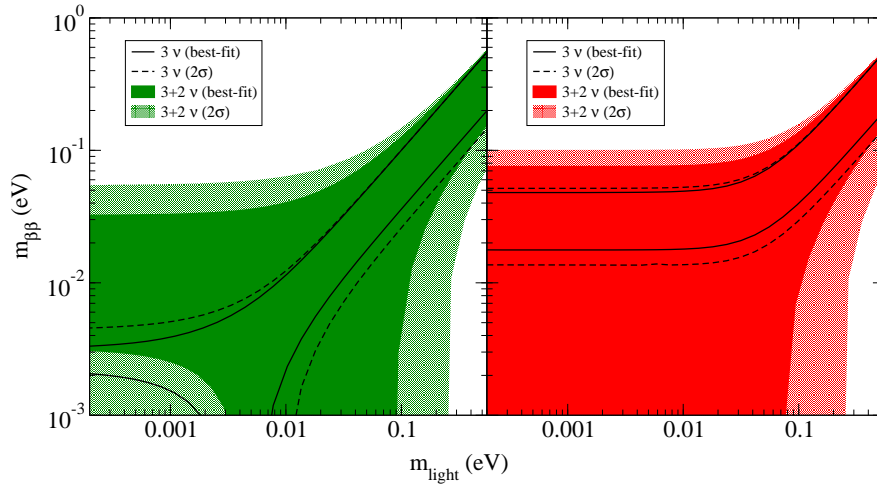


Figure 80. The allowed ranges of  $m_{\beta\beta} - m_{\text{light}}$  in the 3+2 case with normal mass ordering (left) and inverted mass ordering (right).

The situation is more complicated in the five neutrino case, since there are in principle three classes of neutrino mass spectra:  $m_5 > m_4 > m_{1,2,3}$  (3+2 case),  $m_{1,2,3} > m_4 > m_5$  (2+3 case), and  $m_i > m_{1,2,3} > m_j$  (1+3+1 case) [550], see Fig. 79. The latter two cases generally lead to a large sum of neutrino masses, because the active neutrinos are quasi-degenerate and there are in addition eV-scale sterile neutrinos. They induce more tension with cosmological constraints and we therefore only show in Fig. 80 the allowed ranges of  $m_{\beta\beta} - m_{\text{light}}$  in the interesting 3+2 case. Similar to the

above discussion for the 3+1 case above, the presence of two sterile neutrinos allows  $m_{\beta\beta}$  to take smaller values in the hierarchical region for the normal ordering, compared to the standard three neutrino case.

Let us remark here that for the other interesting sterile neutrino case discussed in the White Paper, keV-scale neutrinos with mixing of order  $10^{-4}$  with active neutrinos, the contribution to neutrinoless double- $\beta$  decay is negligible. In addition, if these keV-scale particles are part of the seesaw mechanism, they imply one essentially massless active neutrino, *i.e.*  $m_1 = 0$  or  $m_3 = 0$ .

## E. Sterile Neutrinos and IceCube

Neutrino experiments offer opportunities for new discoveries and, occasionally, total surprises. Examples of new physics include sterile neutrinos and additional degrees of freedom in the energy density of the Universe. Even though it is premature to motivate future facilities on the basis of present indications (which include some hints from short-baseline experiments [117] and reactor data [462]), recent developments underscore the possibility of unexpected discoveries, supporting the construction of neutrino facilities with the widest science reach. IceCube is such a facility [589]. IceCube measures the flux of atmospheric muons and neutrinos with high statistics in a high-energy range that has not been previously explored. The procedure is simply to compare data with expectations based on the extrapolation of lower-energy data. Any deviation observed is an opportunity for discovery in astrophysics or the physics of the neutrinos themselves.

The potential of IceCube to detect eV-mass sterile neutrinos has been recognized for some time [523, 590]. The problem has been revisited [112, 524, 526] with the measurement of the atmospheric neutrino flux in the energy range 100 GeV–400 TeV with unprecedented statistics, taken when IceCube was half complete [591]. The signature for sterile neutrinos is the disappearance of  $\nu_\mu(\bar{\nu}_\mu)$  resulting from the fact that they mix with the sterile neutrino during propagation between production and detection. Simply stated, some of the time they propagate in the sterile state with direct impact on matter effects when propagating through the Earth. As a result resonant oscillations occur in the atmospheric neutrino beam at characteristic zenith angles and energies in the TeV range for  $\delta m^2 \sim 1eV^2$ . Because the sterile neutrino acts as an intermediary between muon and electron neutrinos, an additional signature is the appearance of an excess of  $\nu_e(\bar{\nu}_e)$  with a characteristic energy and zenith dependence.

Given the high statistics, the focus is on the systematics of the experiment. The systematic issues are being studied with renewed emphasis; up to now, the priority has been the search for neutrino sources beyond the atmosphere, analyses where the simulation of the background is done using the data themselves.

**Zenith Distribution.** Figure 81 compares the predicted atmospheric  $\nu_\mu$  (plus  $\bar{\nu}_\mu$ ) flux with data taken while IceCube operated with 40 out of its final 86 strings. Since the uncertainty in the normalization is rather large [592], the shape of the zenith distribution will be more sensitive to the resonant oscillation. In Fig. 81, the predicted distribution, normalized to the event rate, is compared with the data. Uncertainties on the shape of the predicted flux are shown. These shape uncertainties reflect uncertainty in the relative ratio of pions to kaons produced by the cosmic ray flux, uncertainties in the spectral shape and composition of the cosmic ray flux, and uncertainties in the simulation of digital optical module sensitivity and ice properties [591, 592]. Some of

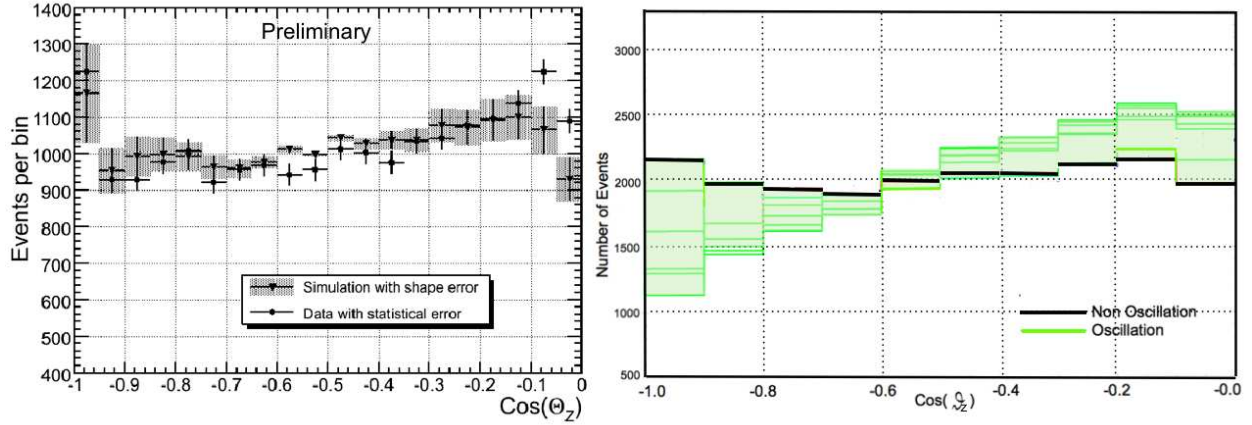


Figure 81. Zenith distribution  $\cos\theta_z$  of atmospheric neutrinos from [592]. *On the left*: Simulation has been normalized to the data. Error bars on the data are statistical only. Error bars on the simulation indicate the uncertainty in the shape of the predicted distribution only. *On the right*: Illustration of the impact of adding a sterile neutrino into the conventional 3-flavor scheme on the  $\cos\theta_z$  distribution. For this particular model (green lines),  $\Delta m_{41}^2 = 0.4 \text{ eV}^2$ ,  $\sin^2\theta_{24} = 0.1$ , and  $\sin^2\theta_{34}$  is varied from 0 to 0.5 in increments of 0.1. Green and black lines include standard atmospheric neutrino oscillations and detector acceptance. (credit: A. Esmaili, Universidade Estadual de Campinas, Brazil).

these will be reduced as the final detector and its irreducible systematic uncertainties are better understood.

Several possibilities have been explored to resolve the apparent mismatch between data and simulation in the near horizontal region, including the possibilities discussed in [592, 593]: regional and seasonal variations in atmospheric neutrino production, simulation of ice properties and photon propagation in the ice, and inadequate simulation of atmospheric muon backgrounds including various composition models of cosmic rays.

While these effects have some impact on the zenith distribution, we have found that an important change arose from improvements in the modeling of the rock layer below the detector and the ice/rock boundary, as well as the assignment of event weights according to model simulations. These event weights account for the probability of a simulated neutrino to survive propagation through the Earth and interact in or near the detector. Preliminary testing of improved simulation for the 59-string detector configuration indicates that these inadequacies in the modeling of the detector were a major contributor to the disagreement between the 40-string simulation and data in reference [592]. Atmospheric neutrino analyses and searches for a diffuse flux of astrophysical neutrinos, with data taken by the 59-string detector, are currently underway and are using this improved simulation.

**Energy Spectrum.** Figure 82 compares the results of a variety of atmospheric neutrino measurements in the GeV – 400 TeV energy range. For IceCube’s spectrum unfolding measurement [592], events in the  $90^\circ$  to  $97^\circ$  zenith region were not used. However, in Fig. 82, this result has been scaled to the flux for the entire hemisphere, to allow a more direct comparison to the other results. IceCube’s forward folding result from reference [591] is also shown. Both of these results are affected by the simulation issues discussed above. New analyses using improved simulation are underway using data taken while IceCube operated in the 59-string configuration.

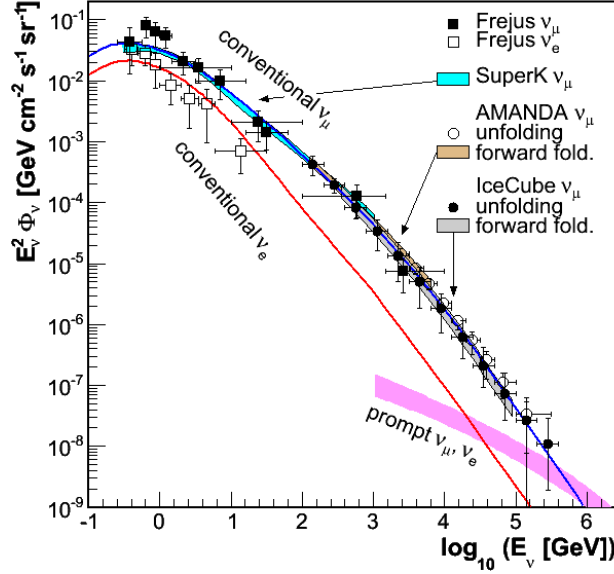


Figure 82. Measurements of the atmospheric neutrino energy spectrum; the Fréjus results [594], SuperK [595], AMANDA forward-folding analysis [596] and unfolding analysis [597], IceCube (40 strings) forward folding analysis [591] and unfolding analysis [592]. All measurements include the sum of neutrinos and antineutrinos. The expectations for conventional  $\nu_\mu$  and  $\nu_e$  flux are from [598]. The prompt flux is from [599].

**Conclusion.** IceCube has been stably operating with a completed detector since May 2011. Atmospheric neutrinos are collected at the rate of  $O(10^5)$  per year. Our ability to constrain a variety of sterile neutrino models is only limited by systematic uncertainties. The calibration of the detector in its final configuration will be superior to that of configurations operated during construction. A new generation of analysis tools are resulting in improved effective area and angular and energy resolution.

## F. Sterile Neutrinos and Dark Matter Searches

Recently, it has been noted that the existence of light sterile neutrinos would have important consequences for dark matter searches. On the one hand, as we will outline in section IV F, MSW-enhanced transitions between active and sterile neutrino flavors would have a substantial impact on searches for neutrinos from dark matter annihilation in the Sun [600, 601]. On the other hand, if sterile neutrinos possess, in addition to their mixing with the active neutrinos, also some new gauge interactions, they can lead to very interesting signals in direct dark matter searches, which can either be used to discover or constrain such sterile neutrino models, but may also be confused with dark matter signals [602–604]. We will discuss sterile neutrinos in direct dark matter detector in section IV F.

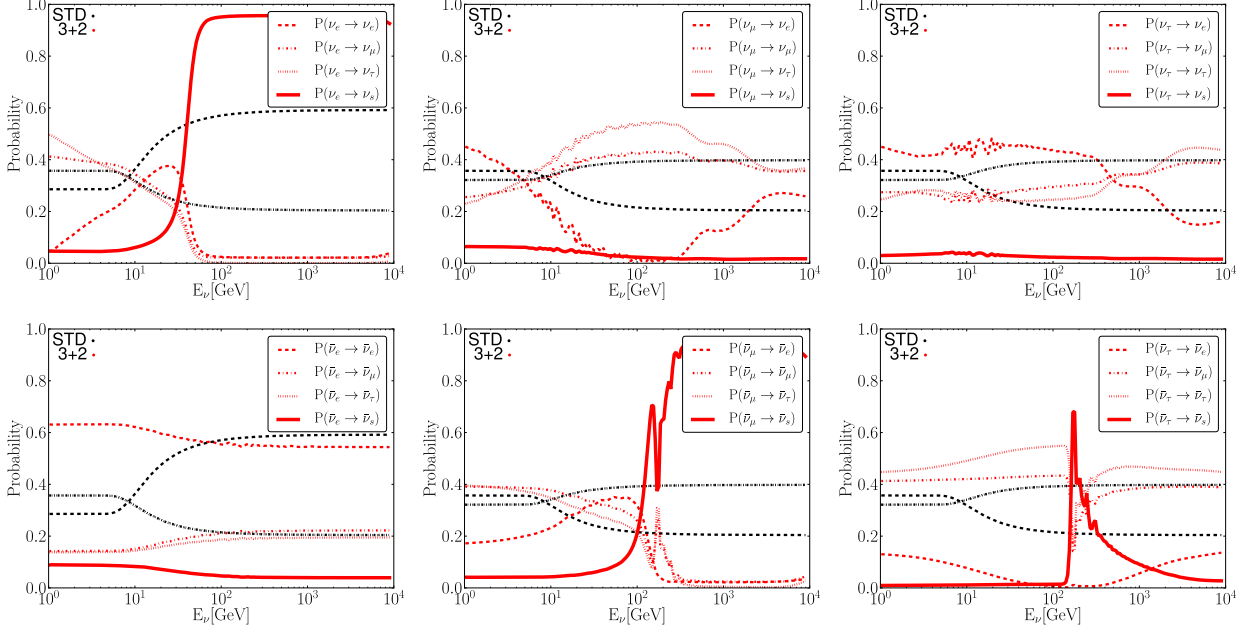


Figure 83. Flavor transition probabilities in the Sun as a function of the neutrino energy for an initial  $\nu_e$  (left), an initial  $\nu_\mu$  (center), and an initial  $\nu_\tau$  (right). The top plots are for neutrinos, the bottom ones are for antineutrinos. Black lines are for standard three-flavor oscillation, red lines are for a “3 + 2” model with two sterile neutrinos, and with mixing parameters determined from the global fit in section IV B. Absorption and  $\tau$  regeneration effects are neglected in these plots. Note that the black dotted lines ( $\nu_x \rightarrow \nu_\tau$  in the SM) and the black dot-dashed lines ( $\nu_x \rightarrow \nu_\mu$  in the SM) lie on top of each other since  $\nu_\mu$ - $\nu_\tau$  mixing is assumed to be maximal. Plots taken from ref. [601], see [600] for a similar study.

### Sterile neutrinos and indirect dark matter search in IceCube

In section IV E and ref. [524], it has been argued that transitions between high-energy active and sterile neutrinos can be enhanced by new MSW resonances. In refs. [600, 601], it was then pointed out that for high-energy ( $\gg$  GeV) neutrinos propagating out of the Sun, these resonances can lead to almost complete conversion of certain flavors into sterile states. This is particularly relevant for neutrinos produced when dark matter is captured by the Sun and annihilates into standard model particles at its center (see *e.g.* [605–607]). Such high-energy neutrinos from the Sun provide a unique opportunity to search for dark matter, and are actively exploited to that end by the IceCube and Super-Kamiokande collaborations [608–610]. If part of the high-energy neutrino flux from dark matter annihilation is converted into undetectable sterile neutrinos, these limits will be weakened. Moreover, if the existence of sterile neutrinos should be established in the future, but their parameters still remain uncertain, this uncertainty would constitute a significant systematic uncertainty for indirect dark matter searches using high-energy neutrinos from the Sun.

To illustrate the impact of active-to-sterile oscillations on neutrinos from dark matter annihilation, we show in fig. 83 the flavor transition probabilities in the Sun as a function of energy (thick red lines). Here, a scenario with two sterile neutrinos, and with mixing parameters determined from the global fit in section IV B has been assumed. We see that, for heavy dark matter whose annihilation leads to very hard neutrino spectra, almost all the  $\nu_e$ ,  $\bar{\nu}_\mu$ , and a significant fraction of  $\bar{\nu}_\tau$  could be converted into sterile states. Note that, for sterile neutrino models with different



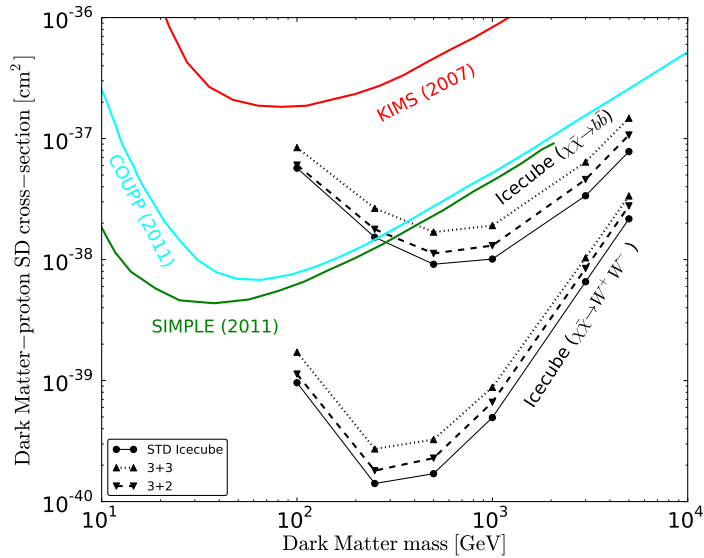


Figure 84. IceCube limits on spin-dependent dark matter–proton scattering [609, 611] in scenarios with (black dashed and dotted lines) and without (black solid lines) sterile neutrinos compared to data from direct detection experiments (colored lines) [612–614]. We see that for the 3 + 2 scenario which provides the best fit to short baseline neutrino oscillation data, the limits are only moderately weakened. A 3 + 3 toy model, on the other hand, illustrates that larger modifications are possible. Plot based on ref. [601].

parameter sets, the effects could be even larger.

To study how active–sterile flavor transitions would affect the actual limits that a neutrino telescope can set on the dark matter parameter space, it is useful to perform a complete simulation of neutrino propagation from the center of the Sun to a terrestrial detector, and to compute the ratios of expected signal events in a sterile neutrino model and in the standard oscillation framework. In doing so, it is important to include not only oscillations, but also neutrino absorption, scattering, and the generation of secondary neutrinos from  $\tau$  lepton decay (see [601] for details on the simulations used here).

Two illustrative examples are shown in fig. 84, where we compare the IceCube limit on the spin-dependent dark matter–nucleon scattering cross sections obtained under the assumption of standard 3-flavor oscillations to the limits that would be obtained if the best fit 3 + 2 model from section IV B is realized in nature (dashed black lines). We also show the results that would be obtained in a toy model with three sterile neutrinos, each of which mixes with only one of the active neutrinos, and with the corresponding mixing angles being equal (black dotted lines, see ref. [601] for details). We show results for two different dark matter annihilation channels, with  $b\bar{b}$  and  $W^+W^-$  final states, respectively. For comparison, we also show results from various direct dark matter searches. We observe that IceCube limits are weakened by an  $O(1)$  factor in the 3 + 2 model, and by roughly a factor 2 in the 3 + 3 model.

Another interesting annihilation channel for dark matter particles in the presence of sterile neutrinos is  $\chi\bar{\chi} \rightarrow \nu_s\bar{\nu}_s$ , which leads to monochromatic sterile neutrinos. For the low mass DM particles ( $m_\chi \lesssim 100$  GeV) this channel of annihilation is almost inaccessible to IceCube. However, thanks to the MSW resonant flavor conversion mentioned in this section, for the  $m_\chi \gtrsim 100$  GeV, the sterile neutrinos propagating to the surface of the Sun could convert to active neutrino which

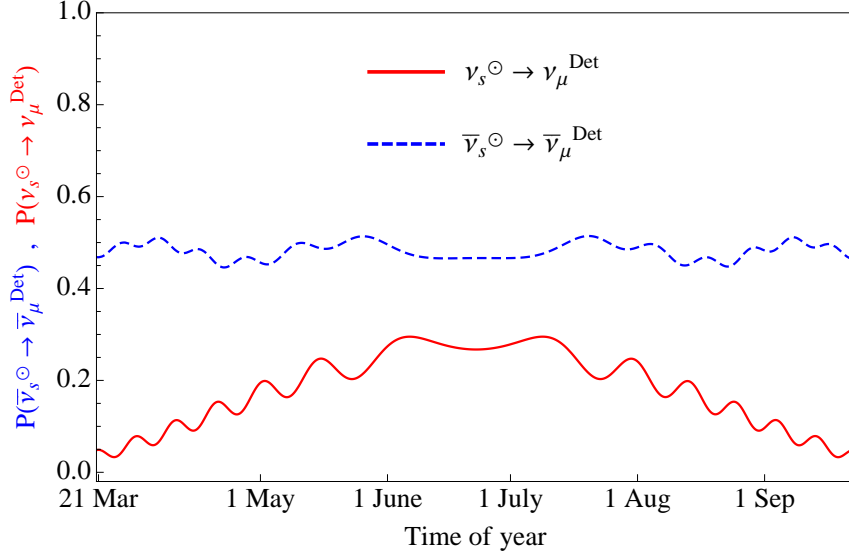


Figure 85. Seasonal variation of the oscillation probability for neutrinos from the dark matter annihilation channel  $\chi\bar{\chi} \rightarrow \nu_s\bar{\nu}_s$ . A neutrino energy of 400 GeV was assumed here and the sterile neutrino mixing parameters are  $\Delta m_{41}^2 = 1 \text{ eV}^2$ ,  $\sin^2 \theta_{14} = \sin^2 \theta_{24} = \sin^2 \theta_{34} = 0.008$ . Plot taken from [600].

can be detected in neutrino telescopes. Moreover, the annual variation of the Earth–Sun distance as well as MSW-enhanced oscillation effects inside the Earth can lead to a seasonal variation in the count rate [600, 615, 616]. As an illustrative example, Fig. 85 shows the oscillation probabilities  $\nu_s(\bar{\nu}_s) \rightarrow \nu_\mu(\bar{\nu}_\mu)$  from the production point in the center of Sun to the IceCube detector at the South Pole. As can be seen, the MSW induced conversion results in a nonzero, and time-dependent, oscillation probability.

### Sterile neutrinos and direct dark matter searches

It has been recognized for a long time that dark matter detectors sensitive to  $\mathcal{O}(\text{keV})$  electron recoils and nuclear recoils will become sensitive to solar neutrino interactions once they reach the ton scale [617]. In extensions of the standard model, low-energy neutrino interactions can be considerably enhanced by new physics, making dark matter detectors unique tools for probing such types of new physics [602–604].

Particularly appealing models involve light ( $\ll 1 \text{ MeV}$ ) sterile neutrinos, which are singlets under the standard model gauge group, but are charged under a new  $U(1)'$  gauge group. (Instead of introducing a new gauge group one could also postulate that neutrinos carry a large magnetic moment, see [603] for details on this possibility.) The  $U(1)'$  gauge boson  $A'$  is also assumed to be light ( $M_{A'} \ll 1 \text{ GeV}$ ) and very weakly coupled to standard model particles to avoid constraints. The new gauge group could, for instance, correspond to gauged baryon number [602–604] so that also standard model quarks are charged under it. This model would lead to sterile neutrino–nucleus scattering in a dark matter detector, whereas sterile neutrino–electron scattering would be absent at tree level. Alternatively, the coupling of standard model particles to the  $U(1)'$  gauge boson could be exclusively through a kinetic mixing term of the form  $-\frac{1}{2}\epsilon F_{\mu\nu}F'^{\mu\nu}$ , where  $F_{\mu\nu}$  and  $F'^{\mu\nu}$  are the field strength tensors of the photon and the  $A'$  boson, respectively. In this case, sterile neutrinos

can scatter both on electrons and on nuclei in a detector.

The differential  $A'$ -mediated sterile neutrino–electron scattering cross section is given by

$$\frac{d\sigma_{A'}(ve \rightarrow ve)}{dE_r} = \frac{g_{\nu_s}'^2 g_e'^2 m_e}{4\pi p_\nu^2 (M_{A'}^2 + 2E_r m_e)^2} [2E_\nu^2 + E_r^2 - 2E_r E_\nu - E_r m_e - m_\nu^2], \quad (128)$$

where  $g_e'$  and  $g_{\nu_s}'$  are the  $A'$  couplings to sterile neutrinos and electrons, respectively,  $E_\nu$ ,  $p_\nu$  and  $m_\nu$  are the neutrino energy, momentum and mass, respectively,  $E_r$  is the observed electron recoil energy, and  $m_e$  is the electron mass. We notice that, for small gauge boson mass  $A'$ , the denominator of the gauge boson propagator is dominated by the momentum transfer, so that the cross section for low- $E_r$  recoils drops as  $1/E_r^2$ . Thus, significant scattering rates can be obtained in low-threshold dark matter detectors, whereas dedicated neutrino experiments, which have energy thresholds of at least few hundred keV, would be insensitive (see refs. [602–604] for detailed studies of constraints on the models discussed here). Eq. (128) can be readily generalized to the case of sterile neutrino–nucleus scattering by replacing  $g_e'$  by the  $A'$  coupling to nucleons and  $m_e$  by the nuclear mass, and by including a coherence factor  $A^2$  (where  $A$  is the nucleon number of the target nucleus) and a nuclear form factor  $F^2(E_r)$ .

Sterile neutrinos can be produced by oscillations of solar neutrinos or, if they are too heavy to oscillate, by incoherent production of the heavy mass eigenstate due to its (mixing angle-suppressed) coupling to the  $W$ .

In fig. 86, we show examples of neutrino–electron and neutrino–nucleus scattering rates in models with light new gauge boson. The model parameters we have chosen for the different colored curves are still allowed by current bounds [603]. The black curves show the standard model rates, whereas in red we show the data from various dark matter experiments and from Borexino. Note that for electron recoils in Xenon-100, it is not entirely clear where the detection threshold is (electron recoils are not important for Xenon-100’s dark matter search except as a background), and this uncertainty is roughly indicated by a dashed line in fig. 86. The kinks in the solar neutrino event spectra shown in the plots arise from the kinematic edges of the various nuclear reactions contributing to the solar neutrino spectrum. We see that a substantial enhancement of the event rate compared to the standard model is easily possible, making present and future dark matter detectors very sensitive to models with sterile neutrinos and light new gauge bosons. We also see that it is even possible to *explain* some of the anomalous event excesses observed by some dark matter experiments (CoGeNT, CRESST) in terms of sterile neutrino interactions. On the other hand, there is also a danger that a sterile neutrino signal is misinterpreted as a dark matter signal.

One of the most robust signatures of dark matter in a low-threshold detector is an annual modulation of the nuclear recoil rate [622], which is induced by the varying velocity of the Earth with respect to the Milky Way’s dark matter halo throughout the year. Depending on the dark matter mass, the scattering rate is expected to peak either in early June or in early December. Indeed, the DAMA experiment reports a statistically significant annual modulation in the observed event rate peaking in summer [621, 623] (see, however, [624–628] for a discussion of systematic effects that could cause this modulation). In view of this, it is interesting to observe that the sterile neutrino scattering rate in the models introduced above can *also* show annual modulation.

There are several physical effects that can lead to this. First, the ellipticity of the Earth’s orbit around the Sun imply variations in the Earth–Sun distance, which in turn lead to a stronger geometric suppression of the flux in summer than in winter, with the extrema of the modulation occurring around January 3rd and July 4th, respectively. This phase differs by about one month from the one

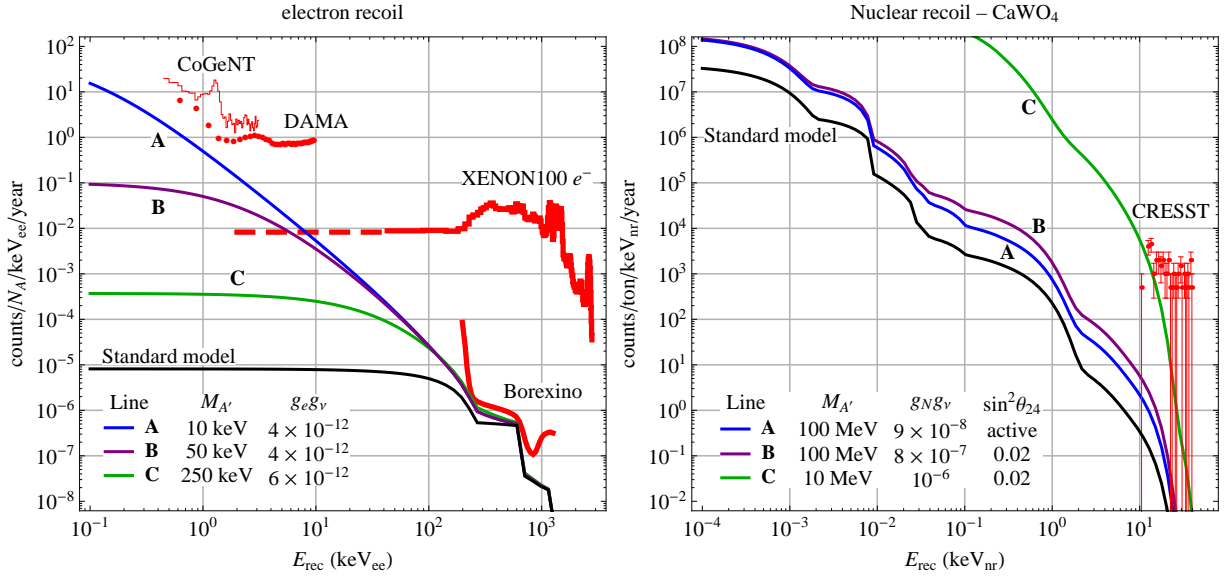


Figure 86. Expected event spectra in a dark matter detector from scattering of solar neutrinos on electrons (left) and on nuclei (right, for the specific case of a  $\text{CaWO}_4$  detector) mediated by a light new gauge boson with couplings  $g_e$  ( $g_N$ ) to electrons (nucleons) and  $g_\nu$  to neutrinos. The different colored curves correspond to different new physics models and parameter points: In the left-hand plot, a model with one sterile neutrino charged under a  $U(1)'$  gauge group was assumed, and the coupling of the  $A'$  boson to standard model particles was assumed to occur through kinetic mixing with the photon. In the right-hand plot, curve A is for a model with only active neutrinos and with scattering mediated by a  $U(1)_{B-L}$  (baryon number minus lepton number) boson, and curves B and C are for a model with gauged baryon number, and a sterile neutrino charged under it. The black curves shows the standard model rate, and the red curves and data points show the observed electron recoil rates in XENON-100 [618], Borexino [619], CoGeNT [620], and DAMA [621]. (Note that CoGeNT and DAMA cannot distinguish nuclear recoils from electron recoils, so their data can be interpreted as either.) Plots based on ref. [603].

expected from heavy dark matter, and by almost half a year from the phase observed in DAMA, which is consistent with light dark matter scattering.

The modulation of the sterile neutrino flux can be *reversed* if oscillations are taken into account [602–604]. Consider in particular scenarios where sterile neutrinos are produced through vacuum oscillations of active neutrinos, with an oscillation length somewhat smaller than one astronomical unit (this requires a  $\Delta m^2 \sim 10^{-10} \text{ eV}^2$  [603]). In this case, the oscillation probability can increase with increasing Earth–Sun distance, and this can overcompensate for the larger geometric suppression at larger distance. An illustration of such a scenario is shown in fig. 87, where the predicted residual sterile neutrino scattering rate in DAMA (after subtracting the time-averaged rate) in several energy bins is shown as a function of time and compared to the experimental data from [623]. We observe that the observed modulation amplitude can be well reproduced, whereas the phase differs from the observed one by about one month (on average roughly one time bin).

Another possible sources of modulation in the sterile neutrino flux are Earth matter effects [603]. The new gauge boson mediating the sterile neutrinos scattering can also lead to new MSW matter effects if ordinary matter carries some net  $U(1)'$  charge (as is the case, for instance, in the gauged baryon number model mentioned above). In this case, active–sterile oscillations in the Earth can

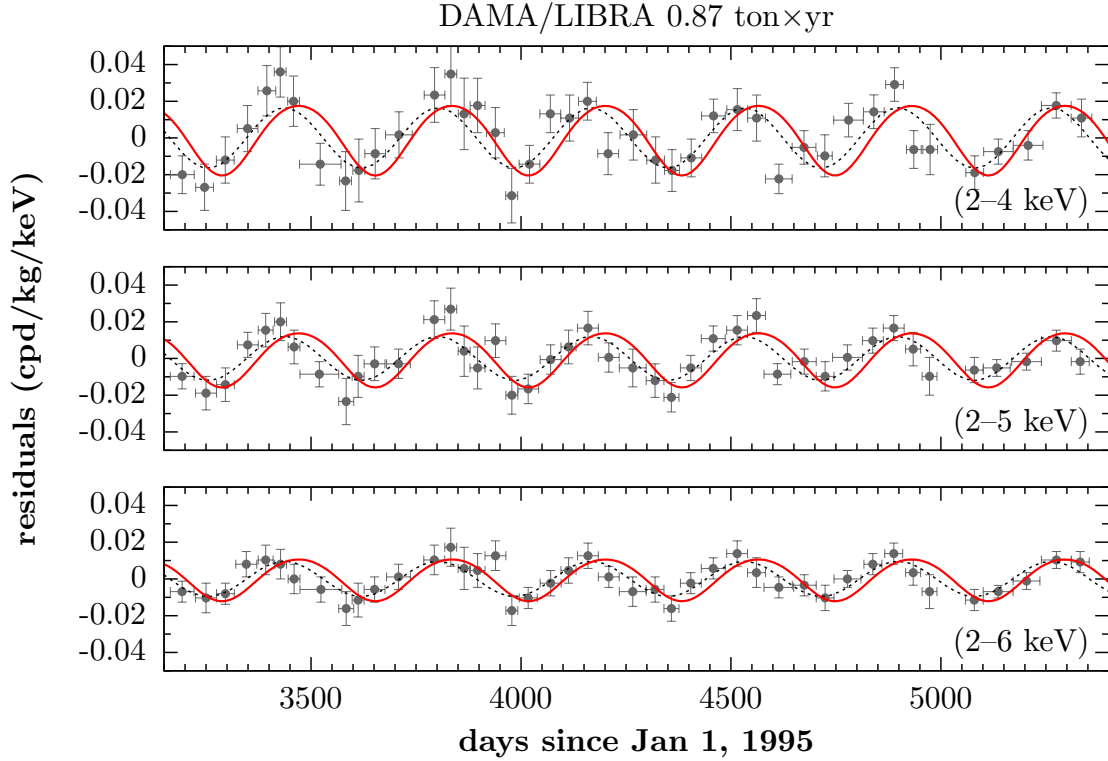


Figure 87. Comparison of DAMA/LIBRA data [623] (data points with error bars) to the predictions of a model with a sterile neutrino charged under gauge baryon number (solid red line). Also shown is a simple sinusoidal fit to the data, assuming a period of one year and a phase as expected from the scattering of light dark matter. Plot taken from ref. [604].

lead to a day–night asymmetry in the flux, and since nights are shorter in summer than in winter, this will also induce an annual modulation. If the new interaction of sterile neutrinos with matter is *very* strong, it is even imaginable that the Earth becomes partially opaque to sterile neutrinos.

In conclusion, if the “hidden sector” of particle physics contains at least one sterile neutrino *and* a new light gauge boson, coupled only weakly to standard model particles, an interesting and rich phenomenology arises in dark matter detectors. In particular, sterile neutrinos from the Sun can lead to strongly enhanced electron and/or nuclear recoil rates, and they can even lead to a temporal modulation of this signal not too different from what is expected from dark matter. Therefore, sterile neutrino recoils can on the one hand be used to detect or constrain such models, but they may also be problematic if they can be confused with a dark matter signal.

## G. Brief Summary

Several anomalies have been presented in Section III. In this Section we present studies coming to the conclusion that, even though the three neutrino scheme is unable to explain the data, augmenting the standard model by one (“3+1”) sterile neutrino with a mass at the eV scale is not sufficient to well describe all data (Sections IV A, IV B, IV C). Adding two eV-scale sterile neutrinos (“3+2”) is in better agreement with the data though severe tension remains even in this case.

We can summarize the situation in the following way:

- Three anomalies affect the oscillation data: LSND (about  $3.3 \sigma$ ), The Reactor Antineutrino Anomaly (about  $3 \sigma$ ), and the Gallium Anomaly (about  $2.5$  to  $3 \sigma$ ).
- Despite several hints pointing towards sterile neutrinos around the eV scale, no fully consistent picture has emerged so-far. New experimental data are mandatory to understand the origin of the anomalies.
- One important reason for the tension in the global data including the LSND evidence is the non-observation of  $\nu_\mu$  disappearance at the eV-scale, which is a generic prediction of an explanation of the LSND signal in terms of sterile neutrino oscillations.
- If the LSND signal is discarded the hints for sterile neutrinos from the reactor and Gallium anomalies remain. These hints are related to  $\bar{\nu}_e(\nu_e)$  disappearance and do not require  $\nu_\mu$  disappearance.
- The  $\Delta m^2$  values implied by global fits are in tension with constraints on the sum of neutrino masses from cosmology, assuming a standard cosmological scenario.
- The presence of additional neutrino mass states can affect the interpretation of beta decay and neutrinoless double beta decay experiments. This is studied in subsection IV D.
- The impact of an eV sterile neutrino on atmospheric neutrino data in Ice Cube is presented in subsection IV E.
- Finally, the existence of light sterile neutrinos can impact existing and future dark matter searches. This is discussed in subsection IV F.

## V. REQUIREMENTS FOR FUTURE MEASUREMENTS

### A. Historical Precedent

As the community proceeds forward in answering the question to the existence of sterile neutrinos (or equivalent mechanism which would be consistent with the observed phenomena), a natural question rises to the surface: *What criteria would need to be met for the community to be convinced of their existence?* Clearly, a mere statistically significant signal may not be sufficient, as even the present situation seems to suggest. Rather, a robust sequence of measurements, both testing the anomalies with as little model dependence as possible (re-doing the measurements but with definitive outcomes) and testing the anomalies in different ways (different L and E) to be able to best interpret the results.

Fortunately, we may draw on historical precedent to help guide us. Let us examine, for example, the acceptance of neutrino oscillations as the proper physical phenomenon behind solar neutrino measurements. Such a conclusion was not attained immediately by a single measurement, but was rather the culmination of almost thirty years of scientific investigation. Let us take the case of solar neutrinos as a concrete example. The progression over time suggests improvements not just in statistical accuracy, but in approach as well. Initial measurements with Ray David Jr. at Homestake indicated a discrepancy in the observed rate only. Follow-up experiments with SAGE, GALLEX and GNO, occurring at a slightly lower energy threshold and different targets, continued to confirm the discrepancy. However, all these experiments were confined to a single channel (charged current scattering), with little spectral information. In the advent of experiments such as Kamiokande and Super-Kamiokande, real-time measurements with an alternate channel (elastic scattering) provided stronger evidence of neutrino oscillations. With the appearance of the Sudbury Neutrino Observatory (SNO), one finally had multiple channels accessible within the same experiment (CC, ES, and NC), effectively making SNO both a disappearance *and* an appearance experiment. The last nail in the coffin came from an orthogonal confirmation using reactor neutrinos. KamLAND was able to confirm that the mechanism responsible for these observations was indeed neutrino oscillations, and further improve on the determination of the parameters. To date, neutrino oscillations are confirmed at the 13 sigma level. In truth neutrino oscillations and mass stand as the first and only definitive evidence in contradiction to the standard model of nuclear and particle physics, yet the neutrino oscillation model is now so well established that many view it as a part of a revised standard model.

If we now look at the sterile neutrino sector, we see a similar history unfolding. The LSND experiment stands perhaps as the first possible evidence, showing an excess  $\bar{\nu}_e$  signal indicative of the existence of one or more sterile neutrinos. The nature of the signal, however, is limited to rate (with some energy information). The MiniBooNE experiment does not see direct evidence in  $\nu_e$  appearance, though a low energy excess in their data could potentially accommodate the existence of sterile neutrinos. Their antineutrino data, though statistically limited, appears to show consistency with the original LSND signal. The latest results from a re-analysis of the neutrino reactor data, which reflects a rate dependence as well, appears consistent with the sterile oscillation picture. Finally, calibration data from Gallex and Sage also suggest a deficit which hints at the existence of sterile neutrinos.

To proceed forward with a program whose goal is to establish or refute the existence of sterile neutrinos, multiple and possibly orthogonal approaches in the same spirit as employed for neutrino oscillations is warranted. Current and future short-baseline experiments, such as MiniBooNE,

BooNE, MicroBooNE, and possible follow-ons to MicroBooNE, readily provide measurements of the energy and rate dependence using charged current reactions. There will also be in the near future an expansion of the reactor measurements to provide a charged current measurement of the length dependence of the oscillation formula.

New on the scene is the emergence of source-based measurements, whereby strong radioactive isotopes can be generated to provide a mono-chromatic neutrino source within a single detector. Such experiments provide a test of the *length* dependence of the oscillation formula. For large detectors, one can explore this for charged current and elastic scattering interactions. If one is able to push to very low thresholds, neutral current coherent scattering may also be accessible, providing the most direct test of sterile neutrino disappearance. More importantly, just as was done in the solar sector, multiple observations with several different channels will provide robustness to the sterile neutrino interpretation. Experiments in cosmology and direct neutrino mass measurements may finally provide the final orthogonal check on this physics.

Table XXIX. List of past experiments able to probe neutrino oscillations from the solar sector ( $\theta_{12}$ ). Experiments broken down in terms of incoming flux (solar or reactor), how they are sensitive to oscillations (total rate, energy spectrum, or both) and the reaction channel probed (either charged current (CC), neutral current (NC), or elastic scattering (ES)).

Experiment(s)	Source	Sensitivity to Oscillations	Channel
Homestake	Solar	Total Rate	CC
SAGE/GALLEX/GNO	Solar	Total Rate	CC
Kamiokande/Super-Kamiokande	Solar, Rate	Energy	ES
SNO	Solar	Energy, Rate	CC, ES, NC
KamLAND	Reactor	Energy, Rate	CC
Borexino	Solar	Energy, Rate	ES, CC

## B. Requirements for a Future Sterile Program

- ***Multiple Approaches:***

Given the potential implications of sterile neutrinos, it is important to confirm their existence in multiple (preferably orthogonal) approaches. A few of such approaches are already being sought by the experimental community, such as short/long baseline experiments, reactor experiments, neutrino source experiments, cosmology, and beta decay. Support on existing efforts should continue and new efforts should continue to be pursued. Both experiments which repeat existing experiments but with technologies that allow for definitive measurements, and experiments which assume an L/E model but vary L and E will be needed to identity and interpret the results.

- ***For Decay-at-Rest experiments: A stopped pion source***

A stopped pion neutrino source combined with a  $\nu_e$  detection via inverse  $\beta$ -decay at a distance of about 30 m is required. A key component will be to reduce both cosmogenic as well as beam-induced backgrounds. The reduction of cosmogenic backgrounds can be achieved by either a pulsed beam or sufficient overburden or a combination thereof. The reduction of



Table XXX. List of past and future planned experiments able to probe oscillations to sterile neutrinos. Experiments broken down in terms of type of experiment (decay-at-rest, short baseline, reactor, etc.) how they are sensitive to oscillations (total rate, energy spectrum, and/or length dependence) and the reaction channel probed (either charged current (CC), neutral current (NC), or elastic scattering (ES)). Past experiments are denoted by †.

Experiment(s)	Source	Type	Sensitivity to Oscillations	Channel
LSND <sup>†</sup>	Decay-at-rest	$\bar{\nu}_\mu \rightarrow \bar{\nu}_e$	Total Rate, Energy	CC
MiniBooNE <sup>†</sup>	Short baseline	$\bar{\nu}_\mu \rightarrow \bar{\nu}_e$	Total Rate, Energy	CC
Reactor measurements <sup>†</sup>	Reactor	$\bar{\nu}_e$ dis.	Total Rate	CC
Gallium Anomaly <sup>†</sup>	EC Source	$\nu_e$ dis.	Total Rate	CC
Future Decay-at-Rest ( <i>OscSNS, Super-K</i> )	Decay-at-rest	$\bar{\nu}_\mu \rightarrow \bar{\nu}_e$ $\nu$ dis.	Total Rate, Energy Total Rate	CC NC
Future Short Baseline ( <i><math>\mu</math>BooNE, BooNE, NESSiE, LArLAR</i> )	Short baseline	$\bar{\nu}_\mu^{(-)} \rightarrow \bar{\nu}_e^{(-)}$ $\bar{\nu}_\mu^{(-)}$ dis.	Total Rate, Energy Total Rate, Energy	CC CC
( <i>VLENF</i> )	Short baseline	$\bar{\nu}_e^{(-)} \rightarrow \bar{\nu}_\mu^{(-)}$ $\bar{\nu}_e^{(-)}, \bar{\nu}_\mu^{(-)}$ dis.	Total Rate, Energy Total Rate, Energy	CC CC, NC
Future Reactor Measurements ( <i>Nucifer, SCRAAM, Stereo</i> )	Reactor	$\bar{\nu}_e$ dis.	Total Rate, Length	CC
Future Source Experiments ( <i>Borexino, Ce-LAND, Daya Bay</i> )	$\beta^-$ Source	$\bar{\nu}_e$ dis.	Total Rate, Length	CC
( <i>Borexino, SNO+Cr</i> )	EC Source	$\nu_e$ dis.	Total Rate, Length	ES
( <i>LENS, Baksan</i> )	EC Source	$\nu_e$ dis.	Total Rate, Length	CC
( <i>RICOCHE</i> T)	EC Source	$\nu_e$ dis.	Total Rate, Length	NC

beam-induced backgrounds requires the detector to not be downstream of the target. This approach takes advantage of the philosophy of reducing model dependencies by repeating measurements but with an improved experimental setup.

- ***For Short Baseline Experiments: Two Detector Approach***

An experiment's sensitivity to sterile neutrinos depends highly on the ability to model the flux and cross-section for neutrinos on various targets and to definitively identify outgoing particles. Although improvements on understanding neutrino cross-sections is improving, it is likely not sufficient to definitely determine whether new physics may be at play. A two-detector approach, already adopted by a number of experiments, will significantly increase the sensitivity to sterile neutrinos and should be adopted by any future sterile neutrino search. An important feature of these new two detector approaches is to take advantage of precision detection techniques, such as Liquid Argon TPCs, in particular because of their ability to distinguish electrons from photons. This approach takes advantage of the philosophy of reducing model dependencies by repeating measurements but with an improved experimental setup.

- ***For Reactor Experiments: Emphasis on Short Baseline Measurements***

Recent re-analysis of reactor neutrino data indicates the possibility of an eV scale sterile neutrino at the  $3\sigma$  level. Given the energy involved in such experiments, any sterile neutrino search would benefit greatly from measurements at very short baselines. A program that constrains/measures the flux of neutrinos at very short (and possibly variable) baselines may provide further evidence and guidance for sterile neutrino oscillations.

- ***Source-Based Experiments: Development of Radioactive Sources***

Source-based initiatives add a complementary approach to the reactor and short baseline program both because of the purity of their source and because of their probe of the length dependence (as opposed to energy dependence) of their signal. As such, these programs are less susceptible to flux and cross-section uncertainties. However, the production of megacurie neutrino sources depends on reactor facilities for irradiation, and many, that have been used in the past, are no longer in operation. On the other hand, the kilocurie antineutrino sources come from fission fragments and can only be produced in countries with existing fuel reprocessing. Further, short half-lives and regulatory issues may make it difficult to transport these sources, especially across international borders. In regions like North America, where work on large scale source technology is just starting, a robust R&D program will be needed to mount such experiments. We strongly encourage the development of such sources ( $^{51}\text{Cr}$ ,  $^{37}\text{Ar}$ ,  $^{144}\text{Ce}$ , etc.) for use in sterile neutrino experiments.

- ***Source-Based Experiments: Multiple Channels***

Source-based initiatives also benefit from multiple channel approaches (elastic, neutral current, and charged current scattering). These channels may provide the necessary *orthogonal* measurement to positively claim the existence of sterile neutrinos. We strongly encourage that multiple channels for source-based initiatives be pursued.

- ***Theoretical Framework: Global Analysis Approach***

Given the complexity of data available, we encourage the development of a coordinated phenomenological approach in analyzing existing neutrino data (from both current and future experiments). Such an approach should not be limited to fitting for a possible signal, but also the backgrounds and systematic uncertainties associated with each measurement. Experiments should provide comprehensive information about their response function for use by the theoretical community. We also encourage that *all data*, including cosmological and beta decay measurements, also be incorporated in these fits.

## Appendix A: Future Experiments

This appendix contains a series of contributed descriptions of possible future experiments and experimental approaches that may be sensitive to sterile neutrino oscillations. The projects described are in various stages of development from under construction to conceptual.

- The first eight sections (A 1 to A 7) describe experiments using radioactive neutrino sources.
- Sections A 8 through A 12 describe experiments using nuclear reactors as their neutrino source.
- The experiments described in Sections A 13 and A 14 are using stopped pion beams to make a direct test of LSND.
- Section A 15 discusses the use of kaon decay at rest beams.
- Sections A 16 to A 20 cover experiments using decay in flight neutrino beams.
- And finally, Section A 21 describes the sensitivity of possible future atmospheric neutrino detectors.

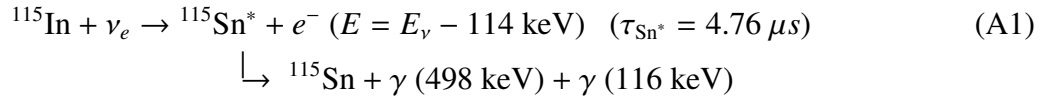
## 1. LENS-Sterile<sup>23</sup>

The LENS (for Low Energy Neutrino Spectroscopy) detector is intended to observe solar neutrinos in real time and as a function of energy. In particular, LENS is designed to study the lowest energy neutrino from proton-proton (pp) fusion. The unique capabilities of LENS not only open a definitive window on solar neutrinos, but also create opportunities for fundamental measurements of neutrino properties. In particular, LENS, when paired with a mono-energetic radioactive neutrino source, like  $^{51}\text{Cr}$ , could undertake a meaningful search for large  $\Delta m^2$  ( $O \sim 1\text{eV}^2$ ) sterile neutrinos [629].

The design of the typical neutrino oscillation experiment is greatly complicated by the long distance required for the oscillation probability to reach the first maximum. The relatively short baseline experiments LSND [114] and MiniBooNE [401] are most sensitive to  $\Delta m^2$  of about  $1\text{eV}^2$ . For LSND this was achieved with a mean neutrino energy of  $\sim 30\text{MeV}$  and a baseline of  $30\text{m}$ , while MiniBooNE used a mean neutrino energy of  $\sim 500\text{MeV}$  and a baseline of  $\sim 500\text{m}$ . It then follows that an oscillation search using neutrinos with energies in the few hundred keV range, typical of radioactive decays, would require a baseline of only a few tenths of a meter to cover the same  $\Delta m^2$  range. Such a compact experiment would, for the first time, allow for the possibility of fully reconstructing the oscillation pattern and could potentially observe oscillation minima and maxima beyond the first.

### LENS Technology

Making an energy spectrum measurement on low energy neutrinos requires a low threshold charged current process and the capability to reject the large background from radioactive decays. LENS uses the neutrino induced transition of  $^{115}\text{In}$  to an excited state of  $^{115}\text{Sn}$ :



to detect low energy neutrinos ( $E_\nu > 114\text{keV}$ ) and measure their energy. The primary interaction and secondary  $\gamma$  cascade make a triple coincidence, correlated in both time and space. The detection medium in LENS is liquid scintillator (LS), chemically doped with natural indium which is 95.7%  $^{115}\text{In}$ . To exploit the spatial correlation, the detector volume is segmented into 7.5 cm cubic cells by clear foils. The foils have a lower index of refraction than the LS and so the scintillation light produced in a cell is channeled, by internal reflection, in the directions of the 6 cell faces. The channeled light is read-out at the edge of the detector by photomultiplier tubes (PMTs). This segmentation, known as the scintillation lattice, allows the position of each event to be determined in three dimensions with the precision of an individual cell. The combination of the 4.76  $\mu\text{s}$  mean delay and the spatial correlation of the primary electron and the two de-excitation  $\gamma$ s of known energies provides a sharp tag for neutrino interactions. Radioactive backgrounds, including events from the  $\beta$ -decay of  $^{115}\text{In}$ , are rejected by a large factor ( $10^{11}$  in the pp solar neutrino energy range) with an efficiency for neutrino interactions of greater than 85% above 500 keV.

<sup>23</sup>Proposed by the LENS Collaboration

<http://www.phys.vt.edu/~kimballton/lens/public/collab/>

## MCi Neutrino Source

Radioactive neutrino sources (as opposed to antineutrino sources) involve either  $\beta^+$ -decay or electron capture. Electron capture decays produce mono-energetic neutrinos, a unique property in all of experimental neutrino physics. Mono-energetic neutrinos allow for a precise determination of  $L/E$  and provide the means for a sharp signal tag. Several electron capture sources have been proposed for the calibration of radiochemical solar neutrino experiments including  $^{65}\text{Zn}$  [630],  $^{51}\text{Cr}$  [631],  $^{152}\text{Eu}$  [632], and  $^{37}\text{Ar}$  [633]. Of the proposed source only  $^{51}\text{Cr}$  and  $^{37}\text{Ar}$  have ever been used. Production of an  $^{37}\text{Ar}$  source requires a large fast breeder reactor, the reactor used to make the only MCi-scale  $^{37}\text{Ar}$  source, is no longer running, that leaves  $^{51}\text{Cr}$  as the best source candidate.

$^{51}\text{Cr}$  has a half-life of 27.7 days. 90.1% of the time it decays to the ground state of  $^{51}\text{V}$  and emits a 751 keV neutrino while 9.9% of the time it decays to the first excited state of  $^{50}\text{V}$  and emits a 413 keV neutrino followed by 320 keV  $\gamma$ .  $^{50}\text{Cr}$  has a relatively high average thermal neutron capture cross section of 17.9 b which makes the large scale production of  $^{51}\text{Cr}$  straightforward. Natural Cr is primarily  $^{52}\text{Cr}$  (83.8%) and contains 4.35%  $^{50}\text{Cr}$ . The isotope  $^{53}\text{Cr}$ , which is present in natural chromium at 9.5%, has an average thermal neutron of 18.7 b, so when natural chromium is irradiated,  $^{53}\text{Cr}$  absorbs 2.5 neutrons to every one captured on  $^{50}\text{Cr}$ . This significantly reduces the  $^{51}\text{Cr}$  yield. Therefore enriched  $^{50}\text{Cr}$  must be used to eliminate  $^{53}\text{Cr}$  and to produce a compact target for irradiation. The chromium enrichment for both Sage and Gallex was done by gas centrifuge at the Kurchatov Institute [634] in Russia. The material used by Gallex was enriched to 38.6% in  $^{50}\text{Cr}$  while the Sage target was enriched to 92%. In both cases the remaining  $^{53}\text{Cr}$  content was less than 1%.

## LENS-Sterile Measurement

The LENS-Sterile concept calls for placing a multi-MCi source in the center of the LENS detector, and counting the source neutrino interactions as a function of distance from the source, or radius. By far the largest background under the 751 keV  $^{51}\text{Cr}$  peak comes from the  $^7\text{Be}$  solar neutrinos. Figure 88 shows the  $^{51}\text{Cr}$  signal superimposed on the solar background. The solar neutrino rate is down by two order of magnitude compared to the  $^{51}\text{Cr}$  signal. In addition, will be well measured in LENS from the extended source-free running. As our measurement is of a rate for a fixed energy, as a function of radius in a single detector, all other potential sources of systematic error generally cancel to first order. Therefore the sensitivity is limited by statistics and should improve with additional source running.

The sensitivity calculations are based on a 10 MCi initial source strength and assume 4 runs of 100 days each. This preliminary calculation uses no rate information, and depends only on the variation in neutrino interaction rate as a function of distance from the source <sup>24</sup>. Figure 89 shows the sensitivity of LENS-Sterile to  $\nu_e$  disappearance in the 0.1 to 10 eV<sup>2</sup> range, compared to the existing limit from the short baseline reactor neutrino experiment Bugey [391]. The LSND allowed region [114] and the MiniBooNE [115] limit are shown converted into  $\sin^2 \theta_{ee}$  by assuming equal overlap of the  $\nu_e$  and  $\nu_\mu$  flavor states with the fourth mass eigenstate.

<sup>24</sup>This is a conservative estimate of the sensitivity. On the one hand, absolute rate information can not be used, because the nuclear matrix element for the  $^{115}\text{In}$ - $^{115}\text{Sn}^*$  system is not known. On the other hand, the points of zero oscillation probability in the detector are known for a given  $\Delta m^2$  hypothesis, and the unoscillated interaction rate can be determined at these points. With this approach the  $^{51}\text{Cr}$  neutrino rate can be used to determine the  $^{115}\text{In}$ -neutrino matrix element to better than 5%, independent of possible oscillation, allowing a precision measurement of the absolute solar neutrino flux.

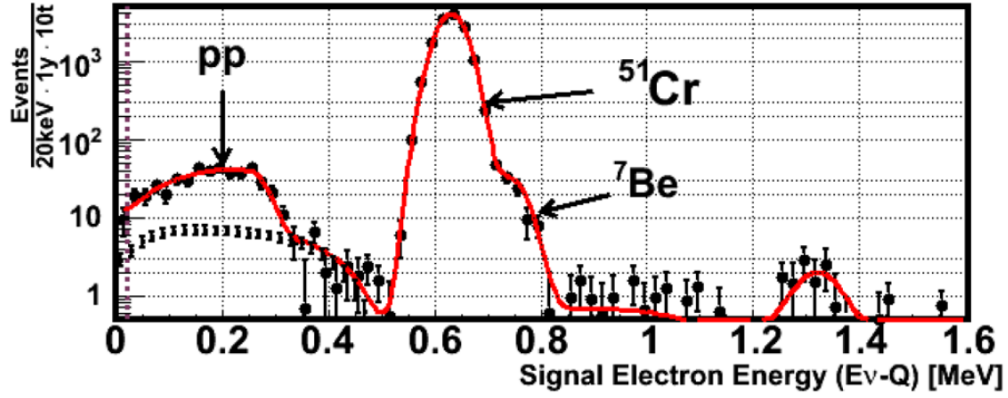


Figure 88. This log scale plot shows the 751 keV  $^{51}\text{Cr}$  neutrino peak superimposed on the solar neutrino spectrum. The  $^{51}\text{Cr}$  signal represents 4 runs of a 10 MCi source each lasting 100 days, while the solar rate corresponds to 400 days.

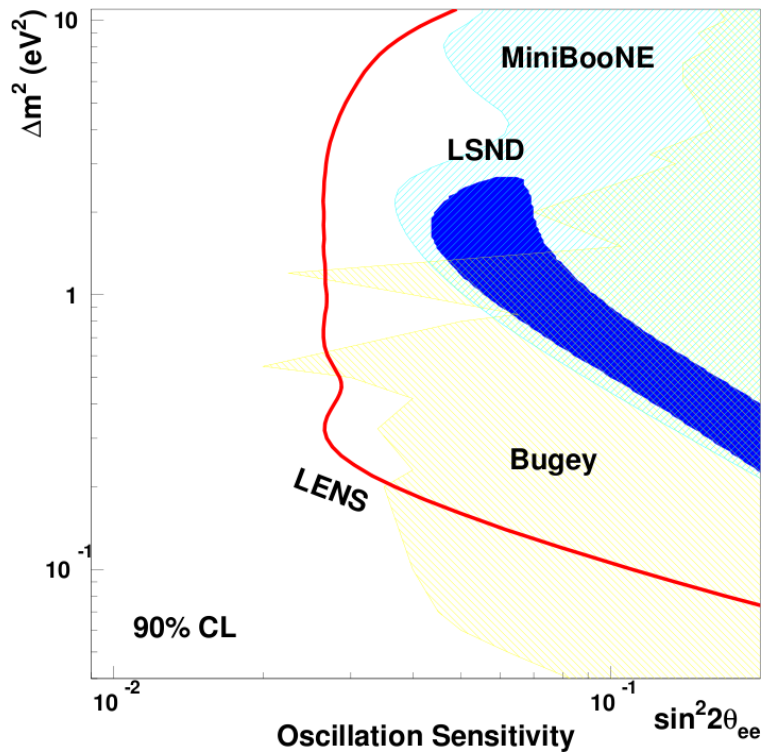


Figure 89. Sensitivity of the LENS  $\nu_e$  disappearance measurement with an exposure of  $4 \times 100$  days to a  $^{51}\text{Cr}$  source with an initial activity of 10 MCi. The LSND allowed region [114], the MiniBooNE appearance limit [115], and the  $\nu_e$  disappearance exclusion region from Bugey [391] are also shown. The LSND allowed region and MiniBooNE limit have been converted to  $\sin^2 2\theta_{ee}$  by assuming equal overlap of the  $\nu_e$  and  $\nu_\mu$  flavor states with the fourth mass eigenstate.

## 2. RICOCHET: Coherent Scattering and Oscillometry Measurements with Low-temperature Bolometers<sup>25</sup>

If the existence of sterile neutrinos is confirmed, the observation would be a clear manifestation of physics beyond the standard model. As such, the observation should be tested by making the least number of assumptions with regards to the underlying physics. Neutral current coherent scattering provides such a test, since it explicitly probes active-to-sterile neutrino oscillations. Such a role should be seen as complementary to other measurement programs, including charged current and elastic scattering channels currently being pursued.

Coherent scattering offers distinct advantages compared to other techniques in disentangling the signature of sterile neutrinos. First and foremost, coherent scattering off nuclei is a neutral current process. Thus, any observation of an oscillation structure would indicate mixing solely to non-active neutrinos. Other methods, such as neutrino-electron scattering, must disentangle the mixing to sterile neutrinos from mixing to active neutrinos. The technique becomes even more powerful when combined with low energy mono-energetic sources. Oscillations to neutrinos at the eV mass scale would manifest themselves over the length of a few meters (for  $\sim 1$  MeV neutrino energies). The signature would be quite difficult to mimic with typical backgrounds. Finally, the cross-section for the process is greatly enhanced thanks to the coherent nature of the reaction.

Neutrino-nucleus interactions which are coherent in character have the advantage of scaling as  $A^2$ , where  $A$  is the mass number of the target nucleus. For a target nucleus with atomic number  $Z$  and neutron number  $N$ , the cross-section as a function of recoil kinetic energy is given by the expression [635]:

$$\frac{d\sigma(\nu A \rightarrow \nu A)}{dT} = \frac{G_F^2}{4\pi} M_A Q_W^2 \left(1 - \frac{M_A T}{2E_\nu^2}\right) F(q^2)^2 \quad (\text{A2})$$

where  $G_F$  is the Fermi coupling constant,  $M_A$  is the mass of the nucleus,  $F(q^2)$  is the nuclear form factor, and  $Q_W$  is the weak charge, defined by the relation:

$$Q_W = N - Z(1 - 4 \sin^2 \theta_W) \quad (\text{A3})$$

In our study, we will mainly consider mono-energetic electron capture sources, all of which have neutrino energies below 1 MeV. The maximum momentum transfer for such sources is  $|q_{\max}| \leq 2E_\nu \ll 2$  MeV. Since the form factor  $F(q^2) \rightarrow 1$  for cases where the scale of the momentum probe is much larger than the size of the nucleus, we can safely ignore this correction factor for our analysis.

The maximum kinetic energy imparted on the nuclear recoil depends on the neutrino energy and the mass of the recoil target:

$$T_{\max} \leq \frac{E_\nu}{1 + \frac{M_A}{2E_\nu}} \quad (\text{A4})$$

---

<sup>25</sup>Proposed by K. Scholberg (Duke University), G. Karagiorgi, M. Shaevitz (Columbia University), M. Pyle (UC Berkeley), E. Figueroa-Feliciano, J. Formaggio, J. Conrad, K. Palladino, J. Spitz, L. Winslow, A. Anderson, N. Guerrero (MIT)

For a silicon target at 1 MeV, that implies a maximum kinetic energy of about 50 eV. For a germanium target the maximum kinetic energy would be around 20 eV. Such low kinetic energies are why detection of the process has been so elusive to date. Any detector hoping to detect such a signal with sufficient statistics must achieve as low a recoil threshold as possible.

## The Source

Oscillometry-based measurements benefit greatly from the use of mono-energetic neutrino sources, since it reduces the measurement to a pure flux-versus-distance analysis. Low energy electron capture sources provide the most effective and clean source of such neutrinos available to date [633]. Historically, two such high intensity source have been produced for neutrino studies: a  $^{51}\text{Cr}$  source, used by the SAGE and GALLEX experiments [415, 419], and an  $^{37}\text{Ar}$  gaseous source used in conjunction with the SAGE experiment [420].

The  $^{37}\text{Ar}$  source is perhaps the most ideal with respect to a future coherent-scattering measurement, for a number of reasons:

- $^{37}\text{Ar}$  produces a very high-energy, near mono-energetic neutrino (90.2% at 811 keV, 9.8% at 813 keV).
- With the exception of inner bremsstrahlung photons, almost all the energy is carried away by neutrinos, facilitating shielding and enabling the source to be extremely compact.
- Extremely high production yield per reactor target.

The SAGE collaboration successfully produced such a source with a total activity of about 400 kCi to be used in conjunction with their gallium solar neutrino detector. The source was also very compact, extending 14 cm in length and 8 cm in diameter, including shielding [636]. Further reduction in size might be possible, even with increased activity, making  $^{37}\text{Ar}$  an ideal portable neutrino source.

Despite its clear advantages as a source and its historical precedent, production of such sources is less than ideal. Far less complex to produce is  $^{51}\text{Cr}$ , which requires only thermal neutrons capturing on  $^{50}\text{Cr}$ . However, as a source, the high energy gamma produced from the decay of the excited state of  $^{51}\text{V}$  imposes more shielding requirements. As such, intense  $^{51}\text{Cr}$  may be less ideal for this investigation, but still worth considering given the advantages in producing the required activity.

## The Detector

The detector requirements for this experiment are extremely challenging. Due to the low energy of the neutrinos ( $\leq 1$  MeV), the recoil energy deposited in the target is in the order of tens of eV, while the minimum mass needed is hundreds of kilograms. Methods of determining the energy deposition from particle interactions in a target include measuring the ionization, the scintillation, and/or the phonon excitations in the material. For nuclear recoils of tens of eV, the fraction of the energy deposited by the scattering event that produces free or conduction band electrons (the quenching factor) is unknown at these energies, and is expected to be very low (could be zero for some materials). Thus any readout scheme involving ionization channels will be at a severe



disadvantage. Similar uncertainties hold for the scintillation yield from nuclear recoils at these energies. An additional problem for both ionization and scintillation readout is that the energy required to create a single electron, electron-hole pair, or scintillation photon from a nuclear recoil in most liquid or solid targets is a few eV for ionization and tens of eV for scintillation. Thus, even if any quanta were produced, Poisson statistics would make the measurement of the energy of any given recoil event fairly poor. We have therefore focused our attention to the measurement of phonons created in the interaction. With mean energies of the order of  $\mu\text{eV}$ , thermal phonons provide high statistics at 10 eV and sample the full energy of the recoil with no quenching effects.

The threshold for a bolometer is a function of its baseline energy resolution. A dimensionless measure of the sensitivity of a resistive thermometer at a temperature  $T$  and resistance  $R$  is the quantity  $\alpha$ , defined as  $\alpha \equiv \frac{T}{R} \frac{dR}{dT}$ . The energy resolution of a TES bolometer is approximately [637]

$$\Delta E_{\text{rms}} = \sigma_E \approx \sqrt{\frac{4k_B T^2 C_{\text{tot}}}{\alpha}} \sqrt{\frac{\beta + 1}{2}}, \quad (\text{A5})$$

where  $k_B$  is the Boltzmann constant,  $C_{\text{tot}}$  is the total heat capacity of the bolometer, and  $\beta$  is the exponent of the temperature dependence of the thermal conductivity between the bolometer and the refrigerator. To unambiguously detect events above the noise from the detector, we set the experimental threshold to  $7.5 \sigma_E$ . For a 10 eV threshold, we then need a detector with  $\sigma_E < 1.33$  eV, or expressed in terms of the full width at half maximum,  $\Delta E_{\text{FWHM}} = 2\sqrt{2 \ln 2} \sigma_E < 3.14$  eV.

Assuming a conduction path to the cold bath of the refrigerator dominated by Kapitza resistance,  $\beta = 4$ , and with a temperature  $T = 15$  mK, a 10 eV threshold could be attained with a heat capacity  $C_{\text{tot}} \leq 200$  pJ/K. However, this model is not complete, as it assumes a perfectly isothermal bolometer. In practice, the various internal heat capacity systems of the bolometer are decoupled from each other through internal conductances, and thermalization times of each separate heat capacity must also be taken into account. These internal decouplings introduce various sources of noise, degrading the energy resolution of the bolometer and consequently requiring a smaller heat capacity to attain the desired threshold.

For this study, we will assume the excess heat capacity is negligible, and optimize the heat capacity of the thermometer  $C_{\text{TES}}$ , the electron-phonon coupling  $G_{\text{ep}}$ , and the Si heat capacity  $C_{\text{Si}}$  to obtain the desired 10 eV threshold with the highest possible target mass. We make the following assumptions:

- Each detector is a Si cube ranging in mass from 20–100 g. The heat capacity is determined from Debye theory.
- The conductance between the Si and the cold bath,  $G_{\text{pb}}$ , can be engineered to give a desired value. The value is chosen to give a thermal impulse response time of 50 ms as measured by the thermometer readout.
- The thermometer is a Mo/Au TES bilayer with a superconducting transition engineered to a specific temperature between 10–100 mK. Mo/Au TES X-ray detectors have achieved resolutions of  $\Delta E_{\text{FWHM}} = 2$  eV [638].
- The TES heat capacity and electron-phonon coupling are taken from the literature and are a function of the chosen volume of the TES and the temperature.

Given these general assumptions, several combinations of detector mass and transition temperature were tested for both Si and Ge targets, scaling the TES volume to obtain the best energy resolution, following the theoretical framework of [639]. Due to practical limitations in refrigeration and considering the readout necessary for the size of the experiment, we focus on a transition temperature of 15 mK, with the refrigerator base temperature at 7.5 mK. At this temperature, a low-energy threshold of 10 eV can be obtained with bolometers with 50 g of Si or 20 g of Ge. A 50 g Si target sees about twice the rate of neutrino coherent recoil events as a 20 g Ge target when both have a 10 eV threshold.

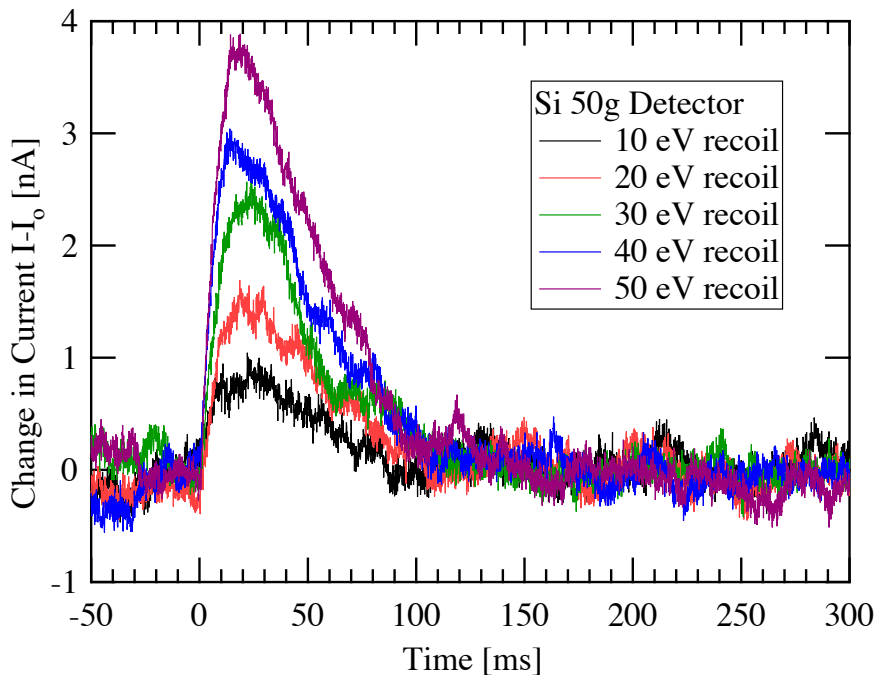


Figure 90. Simulated current readout for 10–50 eV recoils using the model parameters in this study. The current has been multiplied by -1 to make the pulses positive. Noise sources modeled are: the phonon noise between the target to the bath, the internal thermal fluctuation noise between the target and the TES thermometer, the Johnson noise from the TES and its bias resistor, and the electronics noise. The modeled 10 eV pulses are clearly separated from the noise.

Based on the performance of such low threshold detectors, it is possible envision constructing a highly modular coherent neutrino experiment with a total target mass of 500 kg. Multiplexing readout schemes for transition-edge sensors are now a mature technology being developed for many astronomical applications, for example [640], and 10,000 channel systems with time constants similar to this application are already in operation [641]. Schemes for even larger multiplexing gains are in development [642]. Given the slow time constants of this application, a 10,000 channel multiplexer design carries a fairly low risk and would allow 500 kg of Si to be instrumented.

A concept for a 500 kg payload is shown in Fig. 91. The 10,000 Si bolometers are arranged in a column of dimensions 0.42 (dia.)  $\times$  2.0 (length) meters inside a dilution refrigerator suspended from a vibration isolation mount. Passive or active shielding surrounds the refrigerator. A cylindrical bore, perhaps 10 cm or less in diameter, is removed from the shield and allows the  $^{37}\text{Ar}$  source, mounted on a radio-pure translation mechanism, to be moved to different positions along

the side of the array. Periodic movement of the source throughout the measurement sequence allows each detector to sample multiple baselines, enables cross-calibration among detectors, and aids in background subtraction.

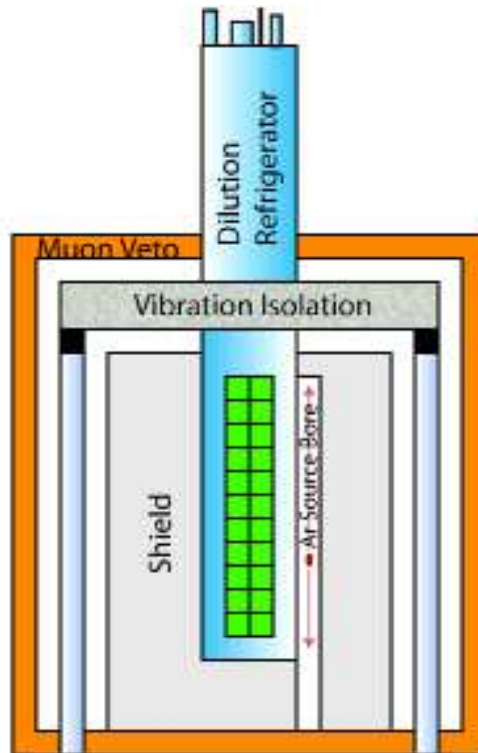


Figure 91. Conceptual schematic of the experimental setup for a bolometric measurement of coherent scattering from a high-intensity  $^{37}\text{Ar}$  neutrino source. An array of 10,000 Si bolometers is arranged in a column of dimensions 0.42 (dia.)  $\times$  2.0 (length) meters (shown in green) inside a dilution refrigerator suspended from a vibration isolation mount. Each Si bolometer has a mass of 50 g for a total active mass of 500 kg. Appropriate passive or active shielding surrounds the refrigerator. A cylindrical bore in the shield allows the  $^{37}\text{Ar}$  source, mounted on a translation mechanism, to be moved to different positions along the side of the array. Periodic movement of the source throughout the measurement sequence allows each detector to sample multiple baselines, enables cross-calibration among detectors, and aids in background subtraction. The minimum distance from the source to a bolometer is assumed to be  $\sim 10$  cm.

### Sensitivity and Outlook

For a monoenergetic source, the oscillation signal is all encoded within the spatial distribution of events. A deviation from the expected  $r^{-2}$  dependence could constitute a possible oscillation signal. We use simulated data from a mock experiment to determine the potential sensitivity to sterile neutrinos. We consider a compact 5 MCi  $^{37}\text{Ar}$  source to be used in conjunction with a 500 kg silicon array. We consider a total exposure of 300 days in order to extract both signal and background rates. Results for a 500 kg Si detector array are shown in Fig. 92(a). The distortion caused by a non-zero sterile mixing is statistically distinguishable in the measured distance profile. For the bulk of the region of  $\Delta m_s^2 = 1 - 10 \text{ eV}^2$  and  $\sin(2\theta_s)^2 \geq 0.08$ , typically preferred from the reactor data, is ruled out at the 90% C.L. If the best fit solution from the reactor anomaly is viable,

then the measurement should be detectable at the 99% C.L. (see Fig. 92(b)). It is possible to also conduct a shape-only analysis. Most of the sensitivity to sterile oscillations is retained for  $\Delta m_S^2$  masses below  $10 \text{ eV}^2$ .

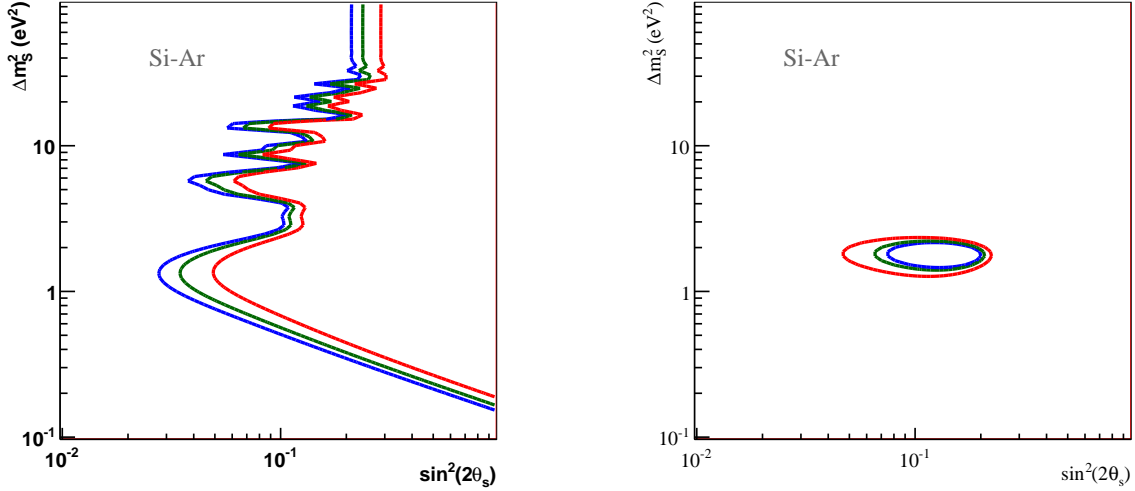


Figure 92. Left: Likelihood contours for a 300-day run on a 500 kg Si array exposed to a 5 MCi  $^{37}\text{Ar}$  source, using both shape and rate information. Confidence levels in all plots are shown at 90% (blue), 95% (green), and 99% (red). Statistical and systematic errors are included in the signal analysis. Right: Likelihood contour curves for a simulated neutrino oscillation signal ( $\Delta m_S^2 = 1.5 \text{ eV}^2$ ,  $\sin^2(2\theta_S) = 0.15$ ) after 300 days of data taking. Contour levels are shown at 90% (blue), 95% (green), and 99% (red).

We have outlined the possibility of probing the existence of sterile neutrinos using coherent scattering on a bolometric array. Such a method could provide the most direct test of oscillations to sterile neutrinos. With the advent of low threshold detectors and the use of intense neutrino sources, such an experiment appears feasible with our current technology. This program (known as RICOCHET) is also very complimentary to any existing dark matter search. Even in the absence of sterile neutrinos, the experiment as described in this letter can make other important measurements. Most prominently, such an experiment may constitute the first observation of coherent scattering. For a 500 kg detector, it should be able to make a  $\approx 5\%$  measurement on the overall cross-section, pending on the absolute calibration of the efficiency. For an isoscalar target, such as silicon, this provides a direct measurement of the weak mixing angle at momentum transfer as low as 1 MeV.

Sensitivity to the neutrino oscillation parameter space indicative of sterile neutrinos ( $\Delta m^2 \sim 1 \text{ eV}^2$ ) can also be provided with a dark matter style detector in combination with a decay-at-rest pion/muon source [643, 644]. Reference [644] calls for a germanium- or argon-based device placed within a few tens of meters of a DAE $\delta$ ALUS-style [645] cyclotron configured with two proton targets at different baselines from the single detector. The two targets allow the composition of the neutrino beam to be studied as a function of distance without the complication of having to move detectors or instrument multiple devices.

The disappearance of neutrinos interacting via the neutral current is a strict probe of active-to-sterile oscillations as there are no complicating contributions from active-to-active disappearance. That is, the disappearance of neutrinos via neutral current coherent neutrino-nucleus scattering

could definitively establish the existence of the sterile neutrino, especially when considered in combination with charged-current-based searches. Depending on the detector technology and run scenario, such an experiment could supply sensitivity to the LSND best-fit mass splitting at the  $3\text{-}5\sigma$  level and large regions of the LSND and reactor anomaly allowed regions. Furthermore, the configuration described could produce a first observation of the as-yet-unseen coherent scattering process as well as improve on non-standard neutrino interaction limits by over an order of magnitude in some cases [643].

### 3. Very Short Baseline $\nu_e \rightarrow \nu_x$ Oscillation Search with a Dual Metallic Ga Target at Baksan and a $^{51}\text{Cr}$ Neutrino Source <sup>26</sup>

There have been four experiments in which very intense neutrino-emitting radioactive sources, either  $^{51}\text{Cr}$  [417, 419] or  $^{37}\text{Ar}$  [420], have irradiated a Ga target. The weighted-average result of these experiments, expressed as the ratio  $R$  of the measured neutrino capture rate to the expected rate, based on the measured source intensity and the known neutrino capture cross section, is  $R = 0.87 \pm 0.05$  [421], considerably less than the expected value of unity.

If we assume that this unexpectedly low value of  $R$  is the result of transitions from active to sterile neutrinos, then the region of allowed oscillation parameters inferred from these Ga source experiments is shown in Fig. 93.

Sterile neutrinos are, however, not the only possible explanation for this lower than expected result. It could also be simply the result of a large statistical fluctuation, an effect that is unexpected, but which conceivably could have occurred. Another explanation, namely overestimation of the cross section for neutrino capture to the lowest two excited states in  $^{71}\text{Ge}$ , has been essentially ruled out by a recent experiment [646]. A final possible explanation could be an error in one of the efficiency factors that enters into the calculation of the rate, such as the extraction efficiency or the counting efficiency. As discussed in [421], however, many ancillary experiments have been performed which give us great confidence in these measured efficiencies.

The interpretation of the Ga source experiments in terms of oscillations to a sterile neutrino with  $\Delta m^2 \approx 1 \text{ eV}^2$ , as well as the agreement of these results with the reactor experiments Bugey, Chooz, and Gösgen and the accelerator experiments LSND and MiniBooNE is considered in detail in Ref. [435, 437–439].

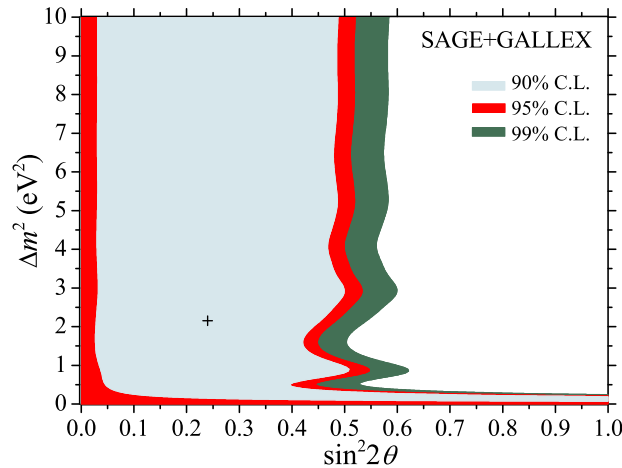


Figure 93. Region of allowed mixing parameters inferred from gallium source experiments assuming oscillations to a sterile neutrino. The plus sign at  $\Delta m^2 = 2.15 \text{ eV}^2$  and  $\sin^2 2\theta = 0.24$  indicates the best-fit point.

<sup>26</sup>Proposed by: B. T. Cleveland, R. G. H. Robertson (University of Washington), H. Ejiri (Osaka University), S. R. Elliott (Los Alamos National Laboratory), V. N. Gavrin, V. V. Gorbachev, D. S. Gorbunov, E. P. Veretenkin, A. V. Kalikhov, T. V. Ibragimova (Institute for Nuclear Research of the Russian Academy of Sciences), W. Haxton (University of California, Berkeley), R. Henning, J. F. Wilkerson (University of North Carolina, Chapel Hill), V. A. Matveev (Joint Institute for Nuclear Research, Dubna) J. S. Nico (National Institute of Standards and Technology) A. Suzuki (Tohoku University)

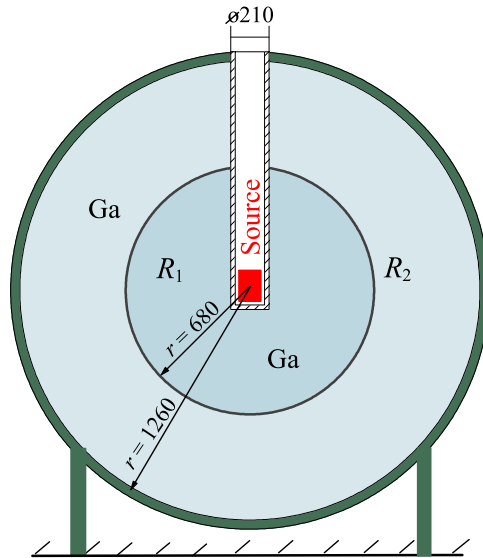


Figure 94. Schematic drawing of proposed neutrino source experiment.  $R_1$  and  $R_2$  are the ratios of measured capture rate to predicted rate in the absence of oscillations in the inner and outer zones, respectively. Outer radii  $r$  of the two zones and diameter  $\phi$  of source reentrant tube are given in mm.

To further investigate the sterile neutrino explanation for the Ga source experiments, we intend to pursue an improved version of these measurements which will now be described. In outline, our plan, as schematically pictured in Fig. 94, is to place a  $^{51}\text{Cr}$  source with initial activity of 3 MCi at the center of a 50-tonne target of liquid Ga metal that is divided into two concentric spherical zones, an inner 8-tonne zone and an outer 42-tonne zone. If oscillations to sterile neutrinos do not occur, then at the beginning of irradiation there is a mean of 65 atoms of  $^{71}\text{Ge}$  produced by the source per day in each zone. After an exposure period of a few days, the Ga in each zone is transferred to reaction vessels and the  $^{71}\text{Ge}$  atoms produced by neutrino capture are extracted. These steps are the same as were used in our prior source experiments [419, 420] and are well tested. Finally, the Ge atoms are placed in proportional counters and their number is determined by counting the Auger electrons released in the transition back to  $^{71}\text{Ge}$ , which occurs with a half life of 11.4 days. A series of exposures is made, each of a few days duration, with the  $^{71}\text{Ge}$  atoms from each zone measured in individual counters.

These extraction and counting procedures have been used in the SAGE experiment for the last 20 years [421] and are all very well understood. A Monte Carlo simulation of the entire experiment – ten extractions each with a 9-day exposure – that uses typical values of extraction efficiency, counter efficiency, counter background rates, and includes the known solar neutrino rate, indicates that the rate in each zone can be measured with a statistical uncertainty of  $\pm 3.7\%$ . From our prior experience in measurement of the solar neutrino flux we expect a systematic uncertainty of  $\pm 2.6\%$ , leading to a total uncertainty, statistical plus systematic, of  $\pm 4.5\%$ .

Some further details on various aspects of this experiment will now be given.

$^{51}\text{Cr}$  will be produced by the capture of thermal neutrons on the stable isotope  $^{50}\text{Cr}$ , whose content in natural Cr is 4.35%. To make the volume of the final source as small as possible, the first step in source production will be to use centrifuge technology to produce 3.5 kg of enriched  $^{50}\text{Cr}$  in the form of highly-purified chromium trioxide. Several facilities exist in Russia where this task can be carried out and enrichment in  $^{50}\text{Cr}$  up to 97% is achievable.

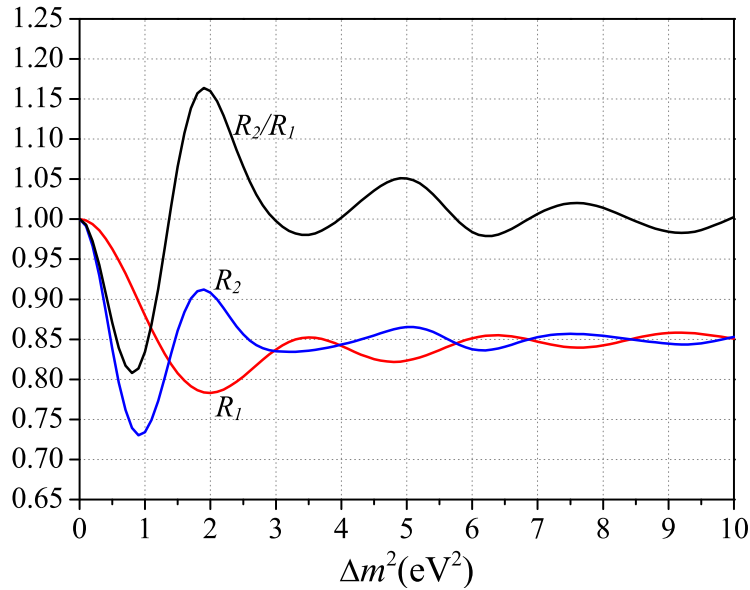


Figure 95. Ratio of measured capture rate to predicted rate in inner zone ( $R_1$ ), in outer zone ( $R_2$ ), and their ratio  $R_2/R_1$  as a function of  $\Delta m^2$  for the case of  $\sin^2 2\theta = 0.3$ . The outer shell of the outer zone is assumed to be a cylinder, not a sphere.

The isotopically enriched Cr will be converted to metal by electrolysis and pressed into 81 metallic Cr rods with diameter 8.5 mm and length 95 mm whose total mass is 3050 grams. These  $^{50}\text{Cr}$  rods will be placed in 27 cells in the central neutron trap of the research reactor SM-3 in Dimitrovgrad, where the flux is  $5.0 \times 10^{14}$  neutrons/( $\text{cm}^2\text{-sec}$ ), and irradiated for 54 effective days (63 calendar days). At the end of irradiation the reactor engineers calculate that the specific activity of the Cr will be 1003 Ci/g, and its total activity will be 3.06 MCi.

The Cr rods will be removed from the reactor and, in a hot cell, transferred to stainless steel tubes which are placed within a stainless steel can. The can is welded closed, put into a transport cask, and brought to the Baksan Neutrino Observatory in the northern Caucasus mountains of Russia. The gallium irradiation will take place in the SAGE laboratory where the overhead shielding is equivalent to 4700 m of water and the measured muon flux is  $(3.03 \pm 0.10) \times 10^{-9}/(\text{cm}^2\text{-s})$ .

The inner compartment of the vessel for irradiation of Ga will be made from Ti or from a thin inert plastic and the outer compartment will be plastic-lined steel. The distance that the neutrinos travel through the Ga in both the inner and outer zones is 55 cm. (To simplify construction, the outer shell of the outer zone will actually be a cylinder, not a sphere, but that has only a 2% effect on the neutrino capture rate and almost negligibly changes the sensitivity of the experiment to oscillations.)

We intend to follow the same experimental procedures as were used in the two previous SAGE source measurements [419, 420]. Each exposure of the Ga to the source will begin by placing the source at the center of the inner zone of Ga. After an exposure period of 9 days, the source will be removed from the tank and moved to a calorimeter, which will measure its intensity. During this time the Ga in each zone will be pumped to reaction vessels where the  $^{71}\text{Ge}$  atoms produced by neutrino capture will be extracted. When the extraction is completed, which requires about 12 hours, the Ga will be pumped back into the 2-zone vessel, the source will be again placed at its center, and the next irradiation will begin.



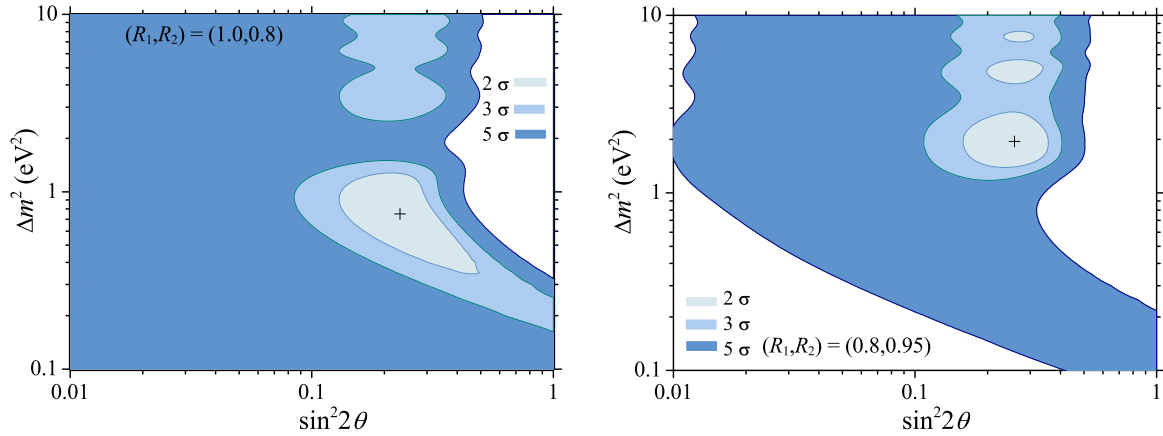


Figure 96. Regions of allowed mixing parameters for two possible outcomes of new two-zone Ga experiment.  $R_1$  and  $R_2$  are the ratios of measured rate to predicted rate in the absence of oscillations in the inner and outer zones, respectively. Plus sign indicates the best-fit point.

The activity of the source will be measured by calorimetry and other methods. Each  $^{51}\text{Cr}$  decay emits an average of 36 keV of thermal energy, *i.e.*, the energy that is not carried away by neutrinos. A 3-MCi source will thus emit about 650 W of heat. The source activity will be measured in a calorimeter several times while it decays and again, when all measurements are finished, the activity will be determined by measuring the amount of accumulated  $^{51}\text{V}$  – the product of  $^{51}\text{Cr}$  decay.

Because many isotopes have high neutron capture cross sections and their reaction products emit high-energy gamma rays great care will be taken during the production and handling of the Cr rods to minimize the introduction of chemical impurities. The source will be scanned with a semiconductor Ge detector to look for  $\gamma$ -emitting radioactive impurities, as was done in the first SAGE  $^{51}\text{Cr}$  experiment.

If oscillations to a sterile neutrino are occurring with mass-squared difference of  $\Delta m^2$  and mixing parameter  $\sin^2 2\theta$ , then the rates in the outer and inner zones of gallium will be different and their ratio, for the specific case of  $\sin^2 2\theta = 0.3$ , will be as shown in Fig. 95.

To see how our new 2-zone experiment may shed light on transitions to sterile neutrinos, let us consider several possible outcomes and the inferences therefrom:

- If the ratio of rates  $R$  in the two zones are statistically incompatible, such as  $R_1 = 1.00 \pm 0.05$  in the inner zone and  $R_2 = 0.80 \pm 0.04$  in the outer zone, or vice versa, then it can be evidence that transitions to sterile neutrinos are occurring. We show in Fig. 96 the allowed neutrino mixing parameters for two such possible outcomes of the experiment.
- If the ratio of rates  $R$  in both zones are statistically compatible, then the inferences will depend on what the average value may be. For example, average values of  $R$  much below 0.92 are also evidence of transitions to sterile neutrinos.

Figure 97 shows the region in  $\Delta m^2 - \sin^2 2\theta$  space to which the new 3 MCi  $^{51}\text{Cr}$  experiment will be sensitive. Our proposed experiment has several significant advantages over other methods of investigation of oscillations with parameters  $\Delta m^2 \approx 1 \text{ eV}^2$ :

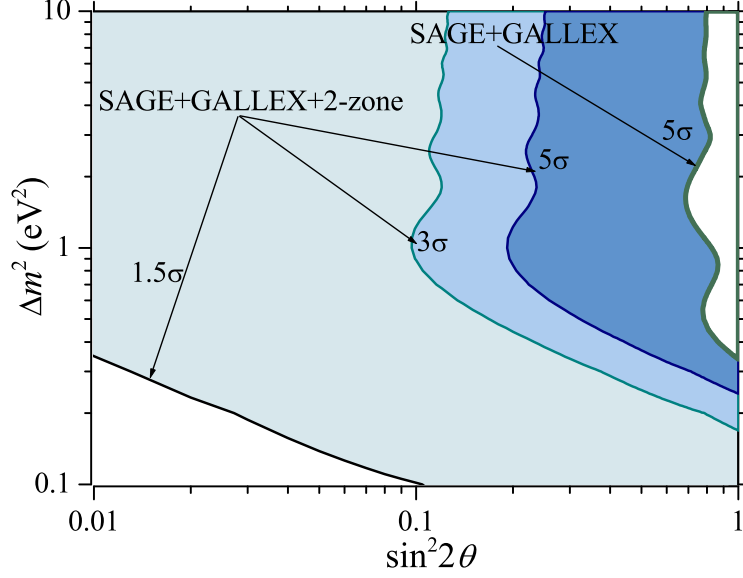


Figure 97. Region of mixing parameters to which proposed new  $^{51}\text{Cr}$  source experiment, in combination with previous source experiments, is sensitive with various levels of confidence. The white region in upper-right corner has been already excluded with  $5\sigma$  confidence by previous SAGE and GALLEX source experiments. As indicated, the new 2-zone experiment has the capability to greatly expand this exclusion region with high confidence.

- The neutrino spectrum is extremely well known. 90% of the decays of the  $^{51}\text{Cr}$  source give a neutrino with energy 750 keV and 10% an energy of 430 keV. This nearly-monochromatic energy is important for oscillation experiments because the energy occurs in the denominator of the transition probability  $P$  in the form

$$P(\nu_e \rightarrow \nu_e) = 1 - \sin^2(2\theta) \sin^2\left[1.27\Delta m^2(\text{eV}^2) \frac{L}{E_\nu}\right] \quad (\text{A6})$$

where  $\theta$  is the mixing angle,  $L$  is the distance in m from the point in the source where neutrino emission occurs to the point in the target where this neutrino is captured, and  $E_\nu$  is the neutrino energy in MeV. In the two-zone experiment the source is very compact, with typical linear dimension of 10 cm, and  $L$  is only about 1 m. As a result, the ripples of oscillation are strongly manifested and are not averaged out when  $\Delta m^2 \approx 1 \text{ eV}^2$ .

- The cross section for neutrino capture on  $^{71}\text{Ga}$  is  $5.5 \times 10^{-45} \text{ cm}^2$  and is known to an uncertainty of 2–3% [646]. Further, the density of gallium at its melting temperature of  $29.8^\circ\text{C}$  is  $6.095 \text{ g/cm}^3$ . These factors ensure that the neutrino capture rate will be very high and can be measured with good statistical accuracy.
- The main background will be from solar neutrinos, whose flux has been measured with the SAGE detector for many years and is now known to an uncertainty of 4.7% [421]. The extremely high intensity of the source,  $\sim 3 \text{ MCi}$ , should provide a production rate in the detector that will exceed the rate from the Sun by several factors of ten.
- The activity of the neutrino source can be measured in several ways leading to a total uncertainty on the source emission rate as low as 0.5% (see, *e.g.*, Ref. [420]).

- The statistical uncertainty can be reduced by re-irradiating the Cr and repeating the entire experiment.

In contrast, experiments with reactor and accelerator neutrinos suffer from several disadvantages. The neutrino energy  $E_\nu$  is distributed over a wide spectrum and the dimensions  $L$  of the sources and detectors are on the scale of several meters. Other disadvantages of a reactor or accelerator experiment are that the knowledge of the neutrino flux incident on the target is usually significantly worse than with a neutrino source and that, with some targets, there are appreciable uncertainties in the cross section for neutrino interaction.

To summarize, we propose a new experiment in which a very-intense  $^{51}\text{Cr}$  source irradiates a target of Ga metal that is divided into two zones and the neutrino capture rate in each zone is independently measured. If there is either a significant difference between the capture rates in the two zones, or the average rate in both zones is considerably below the expected rate, then there is evidence of nonstandard neutrino properties.

The proposed experiment has the potential to test neutrino oscillation transitions with mass-squared difference  $\Delta m^2 > 0.5 \text{ eV}^2$  and mixing angle  $\theta$  such that  $\sin^2 2\theta > 0.1$ . This capability exists because the experiment uses a compact nearly-monochromatic neutrino source with well-known activity, the dense target of Ga metal provides a high interaction rate, and the special target geometry makes it possible to study the dependence of the rate on the distance to the source.

#### 4. Proposed search of sterile neutrinos with the Borexino detector using neutrino and antineutrino sources<sup>27</sup>

The solar neutrino detector Borexino is perfectly suited to host a source experiment able to shed light on the many intriguing experimental hints, accumulated so far, pointing to the possible existence of a sterile neutrino at the few  $\text{eV}^2$  mass scale. The extreme radiopurity achieved in the liquid scintillator acting as detection medium, witnessed by the successful precise  ${}^7\text{Be}$  solar neutrino detection [619], and the thorough understanding of the detector performances gained throughout almost five years of data taking (and several calibration campaigns), make specifically Borexino the ideal choice for the sterile neutrino experimental investigation. Preliminary studies indicate, in particular, that Borexino could be a well suited location both for an external neutrino source experiment (with an ultimate background of about 50  $\text{eV}/\text{day}$  mainly due to the irreducible contribution of solar neutrinos) and for an internal antineutrino source test (in which case a virtually zero background can be achieved, *e.g.* 10  $\text{cpy}/100$  tons [647], due to reactor and geophysical antineutrinos).

Neutrino source experiments have been part of the Borexino program since the very beginning of the project. In the 1991 Borexino proposal [648], source experiments were explicitly mentioned, at that time mainly to perform neutrino magnetic moment search and for calibration purposes. During the detector construction, a small tunnel was built right below the water tank, providing a location as close as 8.25 m to the scintillator inner vessel center. This tunnel was maintained clean and sealed, as other parts of the Hall C, during the underground maintenance works done in 2004-2005, so it is ready to be used.

This location, together with other possible locations inside the detector which have been also investigated, is very appropriate for a sterile neutrino search with the current Borexino set-up. The distance between the source and the detector, and the size of the detector itself, are of the order of few meters, thus comparable with the expected oscillation length, that at the mass scale of  $\Delta m^2 = 1 \text{ eV}^2$  is also of this magnitude: therefore a possible striking signature of the occurrence of the oscillation involving the putative sterile neutrino would be the development across the detector of a clearly visible “spatial wave of detected neutrino events.

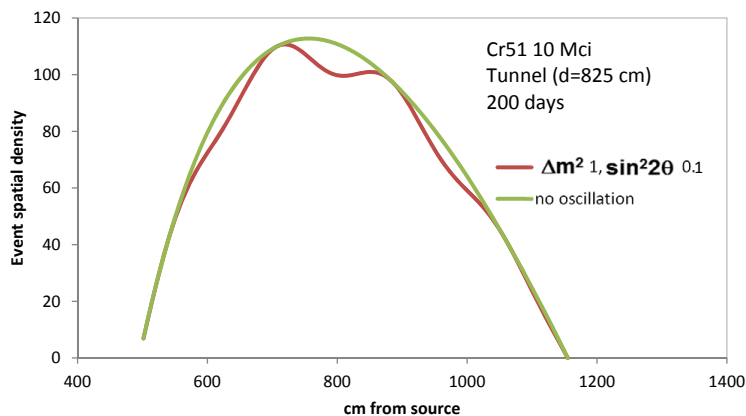


Figure 98. Distribution of the events as a function of the distance from the external  ${}^{51}\text{Cr}$  monochromatic neutrino, obtained with  $\Delta m^2 = 1 \text{ eV}^2$  and  $\sin^2(2\theta) = 0.1$ .

<sup>27</sup>Proposed by the Borexino Collaboration  
(<http://borex.lngs.infn.it>).

Actually, evidence of neutrino oscillations might be obtained in Borexino by exploiting jointly the standard disappearance technique, in which the total number of expected events without oscillations is compared with the observed rate, and the observation of the spatial waves in the distribution of the registered events. An example of these spatial waves is shown in Fig. 98 for the case of a source located externally to the detector. The position of each event in Borexino can be reconstructed with a precision of about 12 cm at 1 MeV energy, and it scales as  $1/\sqrt{E}$ . For monochromatic sources, like  $^{51}\text{Cr}$ , this automatically ensures a good sensitivity; in case of a continuous energy anti- $\nu$  source, like  $^{90}\text{Sr}$ - $^{90}\text{Y}$ , the complication of the non-monochromaticity is counterbalanced by the zero-background characteristic of the measurement and by the higher cross section: both features taken together ensure even superior performances for the anti- $\nu$  source. Preliminary evaluations show that in the T. V. Ibragimova range above 0.02-0.1 eV<sup>2</sup> in  $\Delta m^2$  (depending upon the energy of the emitted neutrinos) and for  $\sin^2(2\theta) \geq 0.04$  the sensitivity to oscillations into a sterile neutrino should be good with a reasonable neutrino or antineutrino source, also thanks to the additional handle of the search of the spatial waves.

Fig. 99 (left) shows the exclusion plots that might be obtained at 95% C.L., with a 10 MCi  $^{51}\text{Cr}$  source located externally at 8.25 m from the centre of the detector. The red line is the curve stemming from the rate-only analysis, while the blue contour is obtained through the more complete analysis involving also the spatial information; from the comparison of the two it can be appreciated clearly the boost to the sensitivity implied by the wave analysis, in the region where the spatial waves would be characterized by oscillation lengths well matched to the size of the detector.

In order to highlight the physics reach of a test accomplished with an external source, the figure displays also the 95% contour resulting from the joint analysis of the Gallium and reactor anomalies: though not conclusive, an external test performed with a sufficiently strong neutrino source will be extremely significant, since it will start to address a sizable portion of the oscillation parameter region of interest.

Fig. 99 (right) shows the sensitivity for the other scenario being considered, *i.e.* an antineutrino source deployed in the center of the detector. As anticipated above, several characteristics denote the antineutrino source as a most powerful choice with respect to the neutrino option: the correlated nature of the event detection (a positron-neutron correlation), which makes the background irrelevant and allows the possibility to deploy the source directly in the scintillator; furthermore, the higher energy spectrum with respect to that of  $^{51}\text{Cr}$  implies an higher cross section, and thus for the same number of events a lower source intensity, that hence in this respect can be more manageable.

The global superior characteristic of the antineutrino scenario is also witnessed by the sensitivity features illustrated in Fig 3, where the 95% sensitivity contour covers the entire 95% joint gallium-reactor region. Therefore the internal antineutrino source test appears to be very conclusive, being able to disprove or confirm convincingly the sterile neutrino hypothesis.

It should be pointed out that also in Fig. 99 (right) both the rate only and the rate + waves analysis are reported, highlighting the zone where the powerful tool of the waves detection across the detector is effective to enhance the experimental sensitivity. This region is located at higher  $\Delta m^2$  with respect to the similar wave region in the Fig. 99 (left), as consequence of the different (higher) energy range of the antineutrino source, and this is an advantage to better cover the gallium-reactor zone.

In both the preliminary calculations whose results are illustrated in Fig. 99, the two main errors affecting the test are considered, *e.g.* the uncertainty on the intensity of the source and the error on

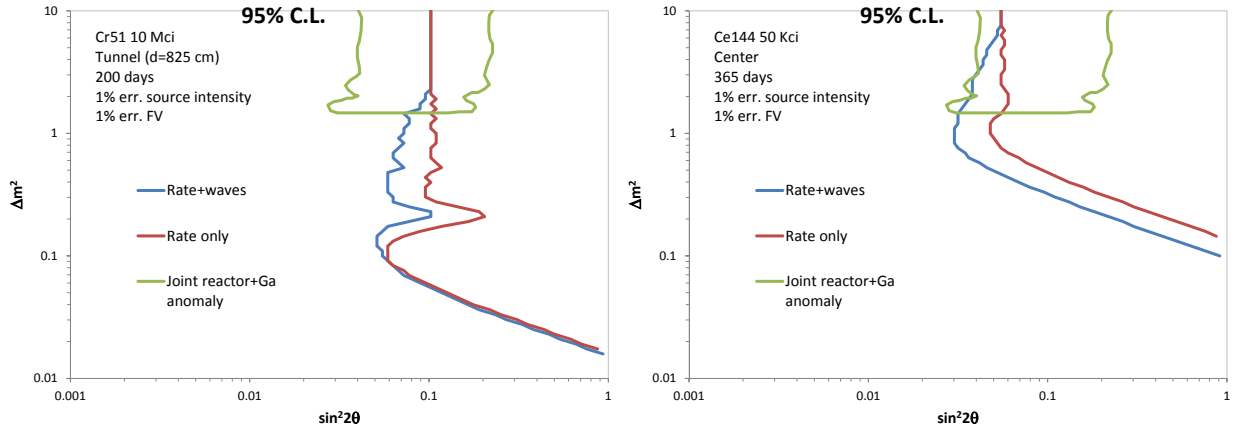


Figure 99. Exclusion plots (both rate only and rate+waves) at the 95% C.L. illustrating the sensitivity reach of the experiment performed with (left) a  $^{51}\text{Cr}$  external source of intensity equal to 10 MCi and (right) a  $^{144}\text{Ce}$  source deployed in the center of Borexino. The green contour represents the joint Gallium-reactor anomaly. The significant reach of  $^{144}\text{Ce}$  experiment is clearly shown by the overlap of the sensitivity contours with practically the entire joint Gallium-reactor anomaly region.

the fiducial volume, both assumed to amount to 1%. For the fiducial volume such an uncertainty is well within the Borexino capability, as determined through numerous calibration efforts. On the other hand, the ambitious 1% error on the source intensity will require an important calibration effort to be carried out after its preparation through several complementary measurement methods. Anyhow, it should be stressed that in the region of the parameter space where the sensitivity relies mostly on the spatial distribution of the detected events the degree to which both errors affect the measure is drastically attenuated, since the shape of the waves does not depend on the precision of the source activity nor on the knowledge of the fiducial volume.

Moreover, in the antineutrino source scenario it can be conceived to exploit the full volume to perform the measurement, due to the positron-neutron correlated tag, and thus the fiducial volume error can be ignored, further increasing the sensitivity region of the test with respect to Fig. 99 (right).

From the general framework described so far it stems that our proposed experimental program contemplates the construction and deployment of two sources, a mono-chromatic  $^{51}\text{Cr}$  neutrino external source and an antineutrino internal source being the  $^{90}\text{Sr}$ - $^{90}\text{Y}$  “historical” option, cited in the Borexino proposal, likely replaced by the  $^{144}\text{Ce}$ - $^{144}\text{Pr}$  material, emerged recently as the most attractive and practical anti- $\nu$  solution.

For the former source the path was traced in the 90’s by the pioneering work of the Gallex/GNO collaboration, which calibrated the Gallium detector twice with a  $^{51}\text{Cr}$  neutrino source [649]. Another similar effort was successfully accomplished by the SAGE collaboration [418].

The  $^{51}\text{Cr}$  neutrino source decays by electron capture and emits monochromatic neutrinos of energy 746 keV, with a branching ratio of about 90%. The spectrum of the  $^{51}\text{Cr}$  events is shown in Fig. 100 together with the main expected background. All curves in Fig. 100 are normalized to 120 days of data taking. The  $^{51}\text{Cr}$  technology is known and the enriched  $^{50}\text{Cr}$  material is still available at CEA Saclay. Work is in progress to understand where a new irradiation could be done, and at which cost. The  $^{51}\text{Cr}$  life-time is 39.96 days, so a  $^{51}\text{Cr}$  run might be done with little impact on the Borexino solar neutrino program.

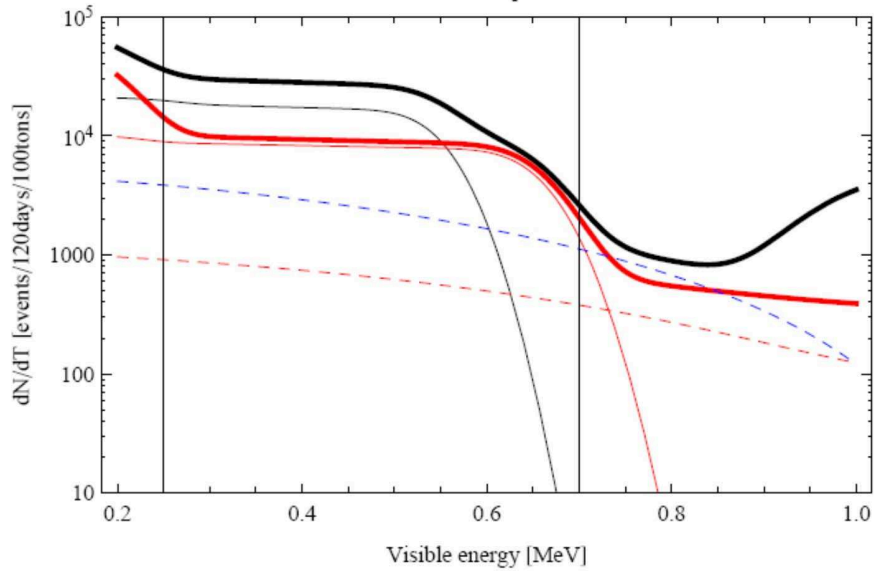


Figure 100. The expected spectra for:  ${}^7\text{Be}$  neutrinos (red-thin),  ${}^{51}\text{Cr}$  events (black-thin),  ${}^{210}\text{Bi}$  at the level of 20 cpd/100 t (blue-dashed), CNO neutrinos (red-dashed). The red thick line is the solar neutrino total, while the black thick line is the  ${}^{51}\text{Cr}$  signal + background. The rise above 0.8 MeV is due to cosmogenic  ${}^{11}\text{C}$  background. The  ${}^{51}\text{Cr}$  events are computed for a 5 MCi source (initial activity) with 120 days of data taking.

On the other hand, sizable quantities of both materials ( ${}^{90}\text{Sr}$ - ${}^{90}\text{Y}$  and  ${}^{144}\text{Ce}$ - ${}^{144}\text{Pr}$ ) being considered for the anti- $\nu$  test are available world-wide as fission products; we are currently investigating the possibility to procure in Russia the source whose strength would be of the order of 50 kCi.

The antineutrinos interact in the scintillator via the usual inverse beta decay on proton, yielding a prompt signal from the positron and a delayed coincidence from the neutron capture. Therefore, as mentioned before, the background is in this case virtually zero, though only the part of the neutrino spectrum above the 1.8 MeV kinematic threshold contributes to the signal. The end-point of the spectrum of the  ${}^{144}\text{Ce}$ - ${}^{144}\text{Pr}$  is about 3 MeV, higher than the 2.2 MeV featured by  ${}^{90}\text{Sr}$ - ${}^{90}\text{Y}$ , therefore the former originates more events, further strengthening the case of its superior features.

Contrary to the external neutrino source, the deployment of the anti- $\nu$  source in the center of the detector will require a major technical effort and also important hardware changes, therefore it is envisioned after the end of the Borexino solar phase.

## 5. Ce-LAND: A proposed search for a fourth neutrino with a PBq antineutrino source<sup>28</sup>

As reported in this white paper several observed anomalies in neutrino oscillation data can be explained by a hypothetical fourth neutrino separated from the three standard neutrinos by a squared mass difference of a few eV<sup>2</sup>.

We propose in the following an unambiguous search for this fourth neutrino by using a 1.85 PBq (50 kCi) <sup>144</sup>Ce or <sup>106</sup>Ru antineutrino  $\beta$ -source deployed at the center of a kilo-ton scale detector such as Borexino [650], KamLAND [651], or SNO+ [652].

Antineutrino detection will be made via the inverse beta-decay (IBD) reaction  $\bar{\nu}_e + p \rightarrow e^+ + n$ . The delayed coincidence between detection of the positron and the neutron capture gamma rays will allow for a nearly background free experiment. The small size ( $\sim 10$  g) of the source compared to the size a nuclear reactor core, may allow the observation of an energy-dependent oscillating pattern in event spatial distribution that would unambiguously determine neutrino mass differences and mixing angles.

This project is called Ce-LAND<sup>29</sup> for Cerium in a Liquid Antineutrino Detector [653].

### Experimental Concept

Large liquid scintillator (LS) detectors, called LLSD hereafter, share key features well suited to search for an eV-scale fourth  $\nu$  ( $\bar{\nu}$ ) state mixing with  $\nu_e$  ( $\bar{\nu}_e$ ). The active mass is composed of about thousand tons of ultra-pure LS contained in a nylon or acrylic vessel. The scintillation light is detected via thousands of photomultipliers uniformly distributed on a stainless steel spherical vessel. In Borexino and KamLAND the target is surrounded by mineral oil or scintillator contained in a stainless steel vessel. This buffer is enclosed in a water tank instrumented by photomultipliers detecting the Cherenkov light radiated by cosmic muons. In the following we study the deployment of a  $\nu$  source of energy spectrum  $\mathcal{S}(E_\nu)$ , mean lifetime  $\tau$ , and initial activity  $\mathcal{A}_0$ , encapsulated inside a thick tungsten (W) and copper (Cu) shielding sphere, at the center of a LLSD. We consider a running time  $t_e$  with a fully efficient detector. The theoretical expected number of interactions at a radius  $R$  and energy  $E_\nu$  can be written:

$$\frac{d^2 N(R, E_\nu)}{dR dE_\nu} = \mathcal{A}_0 \cdot n \cdot \sigma(E_\nu) \cdot \mathcal{S}(E_\nu) \cdot \mathcal{P}(R, E_\nu) \int_0^{t_e} e^{-t/\tau} dt, \quad (\text{A7})$$

where  $n$  is the density of free protons in the target for inverse beta decay,  $\sigma$  is the cross section.  $\mathcal{P}(R, E_\nu)$  is the  $2\nu$  oscillation survival probability, defined as:

$$\mathcal{P}(R, E_\nu) = 1 - \sin^2(2\theta_{new}) \cdot \sin^2\left(1.27 \frac{\Delta m_{new}^2 [\text{eV}^2] R [\text{m}]}{E_\nu [\text{MeV}]}\right), \quad (\text{A8})$$

where  $\Delta m_{new}^2$  and  $\theta_{new}$  are the new oscillation parameters relating  $\nu_e$  to the fourth  $\nu$ . In our simulations we assume a 15 cm vertex resolution and a 5% energy resolution. In the no-oscillation

<sup>28</sup> Proposed by M. Cribier, M. Fechner, Th. Lasserre, A. Letourneau, D. Lhuillier, G. Mention, D. Franco, V. Kornoukhov, S. Schoenert, M. Vivier

<sup>29</sup> [http://irfu.cea.fr/Phocea/Vie\\_des\\_labos/Ast/ast\\_sstechnique.php?id.ast=3139](http://irfu.cea.fr/Phocea/Vie_des_labos/Ast/ast_sstechnique.php?id.ast=3139)



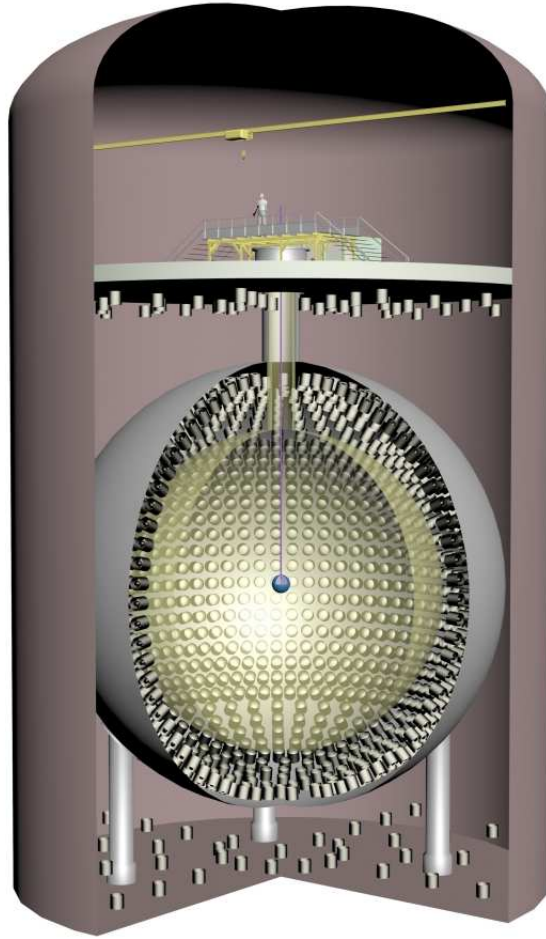


Figure 101. Sketch of the Ce-LAND experiment: a 15 g  $^{144}\text{Ce}$  antineutrino source and its 80 cm diameter shielding deployed at the center of a large liquid scintillator detector.

scenario we expect a constant  $\nu$  rate in concentric shells of equal thickness (see Eq. A7). At 2 MeV the oscillation length is 2.5 m for  $\Delta m_{new}^2 = 2 \text{ eV}^2$ , proportional to  $1/\Delta m_{new}^2$  (see Eq. A8). A definitive test of the reactor antineutrino anomaly, independent of the knowledge of the source activity, would be the observation of the oscillation pattern as a function of the  $\nu$  interaction radius and possibly the  $\nu$  energy.

### Limitations of $\nu_e$ Sources

Intense man-made  $\nu$  sources were used for the calibration of solar- $\nu$  experiments. In the nineties,  $^{51}\text{Cr}$  ( $\sim 750 \text{ keV}$ ,  $\mathcal{A}_0 \sim \text{MCi}$ ) and  $^{37}\text{Ar}$  (814 keV,  $\mathcal{A}_0=0.4 \text{ MCi}$ ) were used as a check of the radiochemical experiments Gallex and Sage [419, 420, 649]. There are two options for deploying  $\nu$  sources in LS: monochromatic  $\nu_e$  emitters, like  $^{51}\text{Cr}$  or  $^{37}\text{Ar}$ , or  $\bar{\nu}_e$  emitters with a continuous  $\beta$ -spectrum. In the first case, the signature is provided by  $\nu_e$  elastic scattering off electrons in the LS molecules. This signature can be mimicked by Compton scattering induced by radioactive and cosmogenic background, or by Solar- $\nu$  interactions. The constraints of an experiment with

$\nu_e$  impose the use of a very high activity source (5-10 MCi) outside of the detector target. In the second option,  $\bar{\nu}_e$  are detected via inverse beta decay. Its signature, provided by the  $e^+$ -n delayed coincidence, offers an efficient rejection of the mentioned background. For this reason, we focus our studies on  $\bar{\nu}_e$  sources.

### Choice and Production of $\bar{\nu}_e$ Sources

A suitable  $\bar{\nu}_e$  source must have  $Q_\beta > 1.8$  MeV (the IBD threshold) and a lifetime that is long enough ( $\geq 1$  month) to allow for production and transportation to the detector. For individual nuclei, these two requirements are contradictory so we expect candidate sources to involve a long-lived low- $Q$  nucleus that decays to a short-lived high- $Q$  nucleus. We identified four such pairs  $^{144}\text{Ce}$ - $^{144}\text{Pr}$  ( $Q_\beta(\text{Pr})=2.996$  MeV),  $^{106}\text{Ru}$ - $^{106}\text{Rh}$  ( $Q_\beta(\text{Rh})=3.54$  MeV),  $^{90}\text{Sr}$ - $^{90}\text{Y}$  ( $Q_\beta(\text{Y})=2.28$  MeV), and  $^{42}\text{Ar}$ - $^{42}\text{K}$  ( $Q_\beta(\text{K})=3.52$  MeV), some of them also reported in [654].

The first three are common fission products from nuclear reactors that can be extracted from spent fuel rods. While not minimizing the difficulty of doing this, the nuclear industry does have the technology to produce sources of the appropriate intensity, at the ppm purity level. In fact, 10 kCi  $^{90}\text{Sr}$  sources have been produced and used industrially for heat generation. Delays obtaining authorizations for transportation and deployment of the source into an underground laboratory should be addressed at the start of the project.

For this white paper, we concentrate on the  $^{144}\text{Ce}$  source (Fig. 102) because its  $Q_\beta$  is greater than that of  $^{90}\text{Sr}$  and because it is easier to extract chemically than  $^{106}\text{Ru}$ . We note also that it has a very low production rate of high-energy  $\gamma$  rays ( $> 1\text{MeV}$ ) from which the  $\bar{\nu}_e$  detector must be shielded to limit background events. Finally cerium is present in fission products of uranium and plutonium at the level of a few percent.

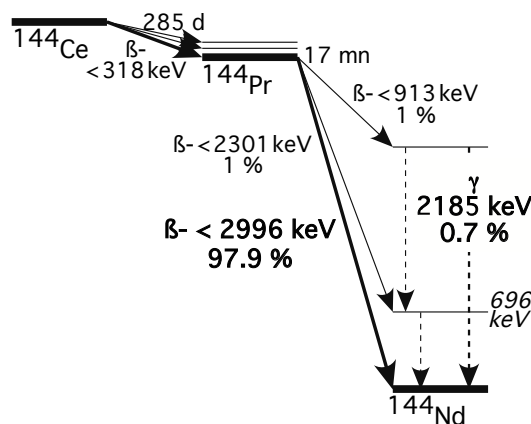


Figure 102. In this simplify decay scheme the relatively long lifetime  $^{144}\text{Ce}$  decay into the short life  $^{144}\text{Pr}$  decaying itself mainly through an energetic  $\beta$  extending up to 2996 keV.

Source	F.Y. $^{235}\text{U}/^{239}\text{Pu}$	$t_{1/2}$	$1^{st} \beta^-$ (keV)	$2^{nd} \beta^-$ (keV)	$I_{\gamma>1\text{MeV}}$	$I_{\gamma>2\text{MeV}}$	W/kCi	kCi/4 $10^4$ int./y
$^{144}\text{Ce}-^{144}\text{Pr}$	5.2%/3.7%	285 d	318 (76%) 184 (20%) 238 (4%)	2996 (99%) 810 (1%)	1380 (0.007%) 1489 (0.28%)	2185 (0.7%)	7.47	43.7
$^{106}\text{Ru}-^{106}\text{Rh}$	0.5%/4.3%	373 d	39.4 (100%)	3540 (78%) 3050 (8%) 2410 (10%) 2000 (2%)	1050 (1.6%) 1128-1194 (0.47 %) 1496-1562 (0.19 %) 1766-1988 (0.09 %)	2112 (0.04%) 2366 (0.03%) 3400 (0.016%)	8.40	23.0

Table XXXI. Features of  $^{144}\text{Ce}-^{144}\text{Pr}$  and  $^{106}\text{Ru}-^{106}\text{Rh}$  pairs, extracted from spent nuclear fuel. F.Y. are the fission yields of  $^{144}\text{Ce}$  and  $^{106}\text{Ru}$ ,  $t_{1/2}$ , their half-lives.  $\beta^-$ -end-points are given for  $1^{st}$  and  $2^{nd}$  nucleus of each pair. The  $I_\gamma$ 's are the branching ratio of gammas  $\gamma$  rays per beta-decay above 1 and 2 MeV. The two last columns are the heat produced/kCi and the activity required to get 40,000 events/year.

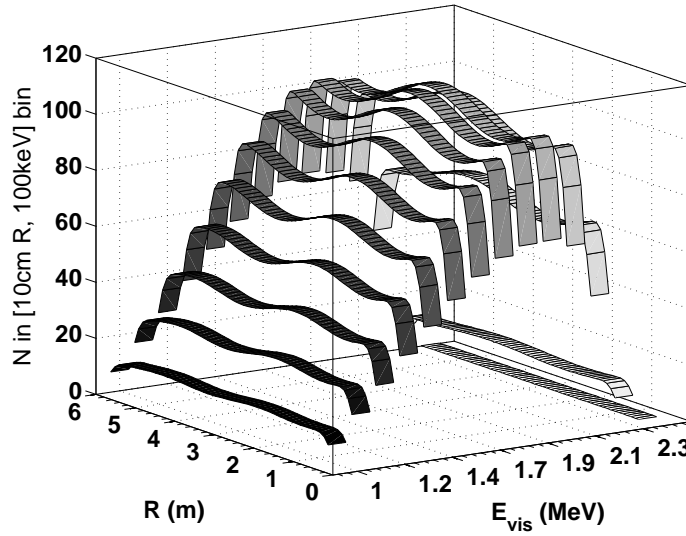


Figure 103. Advantage of  $\bar{\nu}_e$  sources providing both R and  $E_{vis}$  oscillation patterns. IBD rate for a 50 kCi  $^{144}\text{Ce}$  source deployed at a center of a LLSD, in 10 cm radius bins and 100 keV bins of visible energy,  $E_{vis}=E_e+2m_e$ . In one year, 38,000  $\bar{\nu}_e$  interact between 1.5 m and 6 m radius, for  $\Delta m_{new}^2 = 2 \text{ eV}^2$  and  $\sin^2(2\theta_{new}) = 0.1$ .

### The $\bar{\nu}_e$ source and its signal

We now focus on the unique oscillation signature induced by an eV-scale sterile  $\nu$  at the center of a LLSD. For  $^{144}\text{Ce}-^{144}\text{Pr}$ , 1.85 PBq (50 kCi) source is needed to reach 40,000 interactions in one year in a LLSD, between 1.5 and 6 m away from the source ( $n_H=5.3 \cdot 10^{28} \text{ m}^{-3}$ ). This is realized with 14 g of  $^{144}\text{Ce}$ , whereas the total mass of all cerium isotopes is  $\sim 1.5 \text{ kg}$ , for an extraction from selected fission products. The compactness of the source,  $<4 \text{ cm}$ , is small enough to be considered as a point-like source for  $\Delta m_{new}^2 \text{ eV}^2$  oscillation searches. This source initially releases  $\sim 300 \text{ W}$ , and it could be cooled either by convective exchanges with the LS, or via conduction through an ultrapure copper cold finger connecting the massive passive shield to a low temperature bath.  $\beta^-$ -decay induced  $\bar{\nu}_e$  are detected through IBD. The cross section is  $\sigma(E_e) = 0.956 \cdot 10^{-43} \times p_e E_e \text{ cm}^2$ , where  $p_e$  and  $E_e$  are the momentum and energy (MeV) of the detected  $e^+$ , neglecting recoil, weak

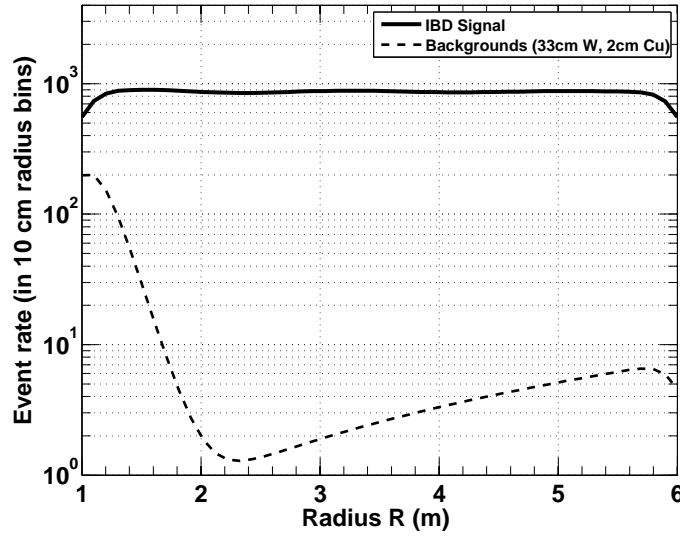


Figure 104. Signal rate of a 50 kCi  $^{144}\text{Ce}$  deployed for 1 year at a center of a LLSD (plain line), compared to the sum of all identified background rates (dashed line), as a function of the detector radius in 10 cm concentric bins. A shield made of 33 cm of W and 2 cm of Cu attenuates the backgrounds, dominated primarily by  $^{144}\text{Ce}$   $\gamma$  lines, then by external bremsstrahlung of the  $^{144}\text{Ce}$   $\beta$ -decay electrons slowing down in the Cerium material.

magnetism, and radiative corrections (%-level correction). The  $e^+$  promptly deposits its kinetic energy in the LS and annihilates emitting two 511 keV  $\gamma$ -rays, yielding a prompt event, with a visible energy of  $E_e = E_\nu - (m_n - m_p)$  MeV; the emitted keV neutron is captured on a free proton with a mean time of a few hundred microseconds, followed by the emission of a 2.2 MeV deexcitation  $\gamma$ -ray providing a delayed coincidence event. The expected oscillation signal for  $\Delta m_{\text{new}}^2 = 2 \text{ eV}^2$  and  $\sin^2(2\theta_{\text{new}}) = 0.1$ , is shown on Fig. 103. LLSD are thus well suited to search for an eV-scale fourth  $\nu$  state. Note that a study of signals of a  $^{90}\text{Sr}$  MCi source external of a LLSD was done in [655].

## Backgrounds

The space-time coincidence signature of IBD events ensure an almost background-free detection. Backgrounds are of two types, those induced by the environment or detector, and those due to the source and its shielding.

The main concern is accidental coincidences between a prompt ( $E > 0.9 \text{ MeV}$ ) and a delayed energy depositions ( $E > 2.0 \text{ MeV}$ ) occurring within a time window taken as three neutron capture lifetimes on hydrogen (equivalent to about  $772 \mu\text{sec}$ ), and within a volume of  $10 \text{ m}^3$  (both positions are reconstructed, this last cut leading to a background rejection of a factor 100). The main source of detector backgrounds originates from accidental coincidences, fast neutrons, and the long-lived muon induced isotopes  $^9\text{Li}/^8\text{He}$  and scales with  $R^2$  when using concentric  $R$ -bins. These components have been measured in-situ for the Borexino geo- $\nu$  searches [647], at  $0.14 \pm 0.02$  counts/day/100 tons. Being conservative we increase it to 10 counts/day/100 tons in our simulation.

Geologic  $\bar{\nu}_e$  arising from the decay of radioactive isotopes of Uranium/Thorium in the Earth have been measured at a rate of a few events/(100 ton.year) in KamLAND [656] and Borexino [647]. Reactor  $\bar{\nu}_e$  emitted by the  $\beta$ -decays of the fission products in the nuclear cores have been measured in KamLAND at a rate of  $\sim 10$  events/(100 ton.year) in the energy range of interest [656]. We use a rate of 20 events/(100 ton.year), which is negligible with respect to the  $\bar{\nu}_e$  rate from a kCi source.

The most dangerous source background originates from the energetic  $\gamma$  produced by the decay through excited states of  $^{144}\text{Pr}$  (Table XXXI). We approximate  $\gamma$  ray attenuation in a shield of 33 cm of W and 2 cm of Cu with an exponential attenuation law accounting for Compton scattering and photoelectric effect. The intensity of 2185 keV  $\gamma$  rays is decreased by a factor  $< 10^{-12}$  ( $\lambda_W \sim 1.2$  cm) [657], to reach a tolerable rate.

The energy spectrum of external bremsstrahlung photons in the cerium is estimated with a simulation using the cross section of [658]. Results were confirmed with a GEANT4 [659] simulation. The number of photons above a prompt signal threshold of 0.9 MeV is  $6.5 \cdot 10^{-3}$  photons per  $\beta$  decay, and  $10^{-4}$  photon per  $\beta$  decay  $> 2.0$  MeV.

An important remaining background source could be the W shield itself. Activities at the level of ten to hundreds mBq/kg have been reported. We anticipate the need of an external layer of ultrapure copper, set to 2 cm in our simulation. It allows one to achieve the radiopurity and material compatibility requirements. Assuming a  $\sim 4$  tons shield we consider a prompt and delayed event rates of 50 Hz and 25 Hz, respectively. The escaping  $\gamma$  are attenuated in the LS, assuming a 20 cm attenuation length [657]. Beyond a distance of 1.5 m from the source the backgrounds become negligible. Any of the bremsstrahlung photons or shielding backgrounds can account for either the prompt or delayed event, depending on their energy. The sum of the backgrounds integrated over their energy spectrum is shown on Fig. 104, supporting the case of kCi  $\bar{\nu}_e$  source versus MCi  $\nu_e$  source for which solar- $\nu$ 's become an irreducible background. A light doping of the LS with gadolinium or an oil buffer surrounding the shielding would further suppress backgrounds; finally, non-source backgrounds could be measured in-situ during a blank run with an empty shielding.

## Sensitivity

We now assess the sensitivity of an experiment with a 50 kCi  $^{144}\text{Ce}$  source running for 1 year. With the shield described above and using events between 1.5 m and 6 m, the background is negligible. With  $\Delta m_{new}^2 = 2 \text{ eV}^2$  and  $\sin^2(2\theta_{new}) = 0.1$ , the interaction rate decreases from 40,000 to 38,000 per year. The 95% C.L. sensitivity is extracted through the following function:

$$\chi^2 = \sum_i \sum_j \frac{(N_{obs}^{i,j} - (1 + \alpha)N_{exp}^{i,j})^2}{N_{exp}^{i,j}(1 + \sigma_b^2 N_{exp}^{i,j})} + \left(\frac{\alpha}{\sigma_N}\right)^2, \quad (\text{A9})$$

where  $N_{obs}^{i,j}$  are the simulated data in the no-oscillation case and  $N_{exp}^{i,j}$  the expectations for a given oscillation scenario, in each energy  $E_i$  and radius  $R_j$  bin.  $\sigma_b$  is a 2% fully uncorrelated systematic error, accounting for a fiducial volume uncertainty of 1% in a calibrated detector, as well as for ( $e^+$ , n) space-time coincidence detection efficiencies uncertainties at the sub-percent level.  $\sigma_N$  is a normalization error of 1%, describing for the source activity uncertainty (from calorimetric measurement, see [660]), and  $\alpha$  is the associated nuisance parameter. Fig. 105 clearly shows that 50 kCi of  $^{144}\text{Ce}$  allows us to probe most of the reactor antineutrino anomaly parameter space [118] at 95% C.L. An analysis assuming no knowledge on the source activity shows that the oscillatory

behavior can be established for  $\Delta m_{new}^2 < 10 \text{ eV}^2$ . Fig. 106 provides the same analysis as described before, but the confidence level is now  $5\sigma$ . This illustrates the potential of the Ce-LAND project to definitively test the reactor and gallium neutrino anomalies [118]. We note that a 5 kCi source would be enough to test the anomaly at 90% C.L. This is illustrated on Fig. 107 To conclude we simulate an oscillation signal induced by a fourth neutrino state mixing with the electron antineutrino, assuming  $\Delta m_{new}^2 = 2.35 \text{ eV}^2$  and  $\sin^2(2\theta_{new}) = 0.1$ . Results are displayed in Fig. 108. A

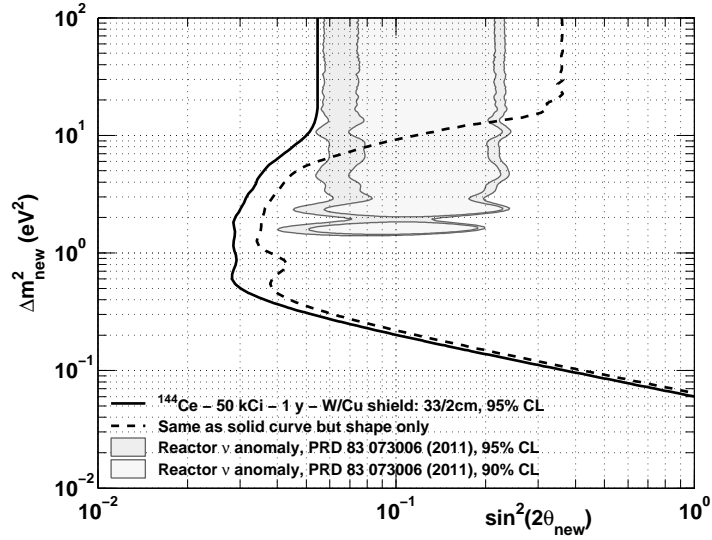


Figure 105. 95% C.L. exclusion limits of the 50 kCi.y  $^{144}\text{Ce}$  experiment obtained in the  $\Delta m_{new}^2$  and  $\sin^2(2\theta_{new})$  plane (2 dof). Our result (plain and dashed lines with and w/o knowledge of source activity) is compared to the 90% and 95% C.L. inclusion domains given by the combination of reactor neutrino experiments, Gallex and Sage calibration sources experiments, as described in Fig. 8 of [118] (gray areas).

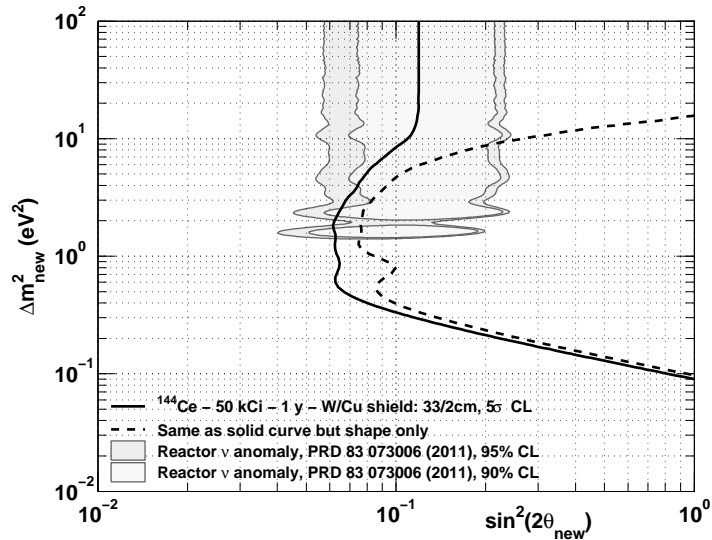


Figure 106.  $5\sigma$  exclusion limits of the 50 kCi.y  $^{144}\text{Ce}$  experiment obtained in the  $\Delta m_{new}^2$  and  $\sin^2(2\theta_{new})$  plane (2 dof).

precise measurement of the mixing parameters is obtained at the  $3\sigma$  level.

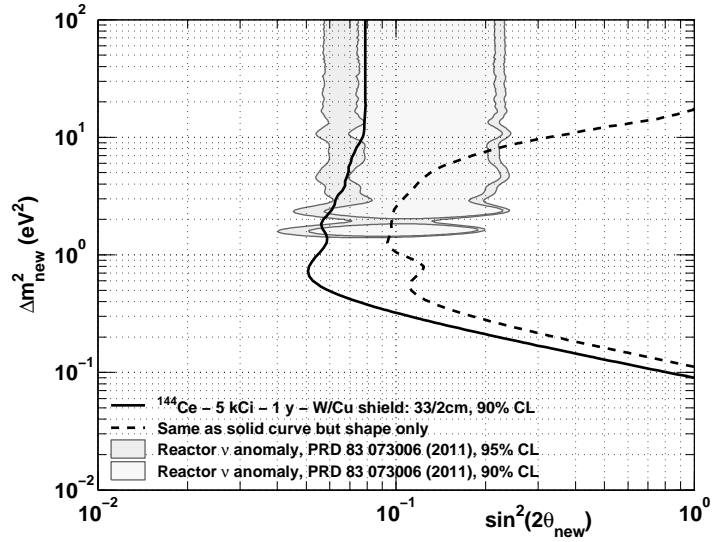


Figure 107. 90% C.L. exclusion limits of the 5 kCi.y  $^{144}\text{Ce}$  experiment obtained in the  $\Delta m_{new}^2$  and  $\sin^2(2\theta_{new})$  plane (2 dof). The reactor antineutrino anomaly can be tested, but it requires the knowledge of the source activity at the percent level. The low statistics does not allow a powerful shape-only analysis at low mixing angle values.

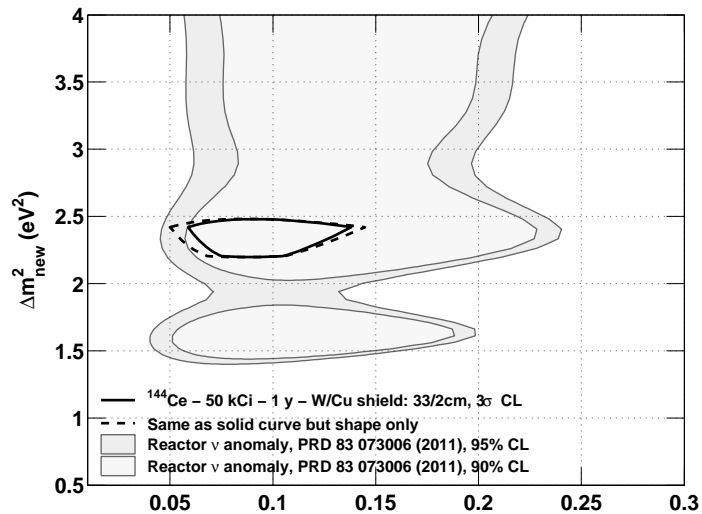


Figure 108.  $3\sigma$  contours obtained with a 50 kCi.y  $^{144}\text{Ce}$  experiment in the  $\Delta m_{new}^2$  and  $\sin^2(2\theta_{new})$  plane (2 dof). The true oscillation parameters simulated are as follows:  $\Delta m_{new}^2 = 2.35 \text{ eV}^2$  and  $\sin^2(2\theta_{new}) = 0.1$ .

## 6. Search for Sterile Neutrinos with a Radioactive Source at Daya Bay<sup>30</sup>

Data from a variety of short-baseline experiments as well as astrophysical observations and cosmology favor the existence of additional neutrino mass states beyond the 3 active species in the standard model. Most recently, a re-analysis of short-baseline reactor neutrino experiments found a 3% deficit between the predicted antineutrino flux and observations [118]. This has been interpreted as indication for the existence of at least one sterile neutrino, with a mass splitting of  $\sim 1\text{eV}^2$  [498]. The possible implications of additional sterile neutrino states would be profound and change the paradigm of the standard model of Particle Physics. As a result, great interest has developed in testing the hypothesis of sterile neutrinos and providing a definitive resolution to the question if sterile neutrinos exist [661, 662].

We propose to use the far site detector complex of the Daya Bay reactor experiment together with a compact PBq  $\bar{\nu}_e$  source as a location to search for sterile neutrinos with  $\geq \text{eV}$  mass [663]. The Daya Bay reactor experiment is located at the Daya Bay Nuclear Power Plant near Shenzhen, China and designed to make a high-precision measurement of the neutrino mixing angle  $\theta_{13}$  using antineutrinos from the Daya Bay reactor complex [457]. The experiment has three underground sites, two at short distances from the reactors ( $\sim 400$  m) with two  $\bar{\nu}_e$  detectors each, and one at a further baseline ( $\sim 1.7$  km) with four  $\bar{\nu}_e$  detectors. The far site detector complex of the Daya Bay reactor experiment houses four 20-ton antineutrino detectors with a separation of 6 m.

When combined with a compact radioactive  $\bar{\nu}_e$  source the Daya Bay far detectors provide a unique setup for the study of neutrino oscillation with multiple detectors over baselines ranging from 1.5-8 m. The geometric arrangement of the four identical Daya Bay detectors and the flexibility to place the  $\bar{\nu}_e$  source at multiple locations outside the antineutrino detectors and inside the water pool allows for additional control of experimental systematics. Daya Bay's unique feature of being able to use multiple detectors and multiple possible source positions will allow us to cross-check any results. In addition, the water pool surrounding the four far-site Daya Bay detectors provides natural shielding and source cooling minimizing technical complications resulting from a hot, radioactive source. As a source we propose to use a heavily shielded, 18.5 PBq  $^{144}\text{Ce}$  source approximately 16 cm in diameter ( $\Delta Q = 2.996$  MeV).

This experimental setup can probe sterile neutrino oscillations most powerfully by measuring spectral distortions of the energy and baseline spectrum. If the source's  $\bar{\nu}_e$  rate normalization is well-measured, further information can be provided by measuring total rate deficits. The dominant background of this experiment, reactor  $\bar{\nu}_e$ , will be measured to less than 1% in rate and spectra by the near-site detectors. In addition, the detector systematics of all detectors will be well-understood after 3 years of dedicated  $\theta_{13}$  running, minimizing expected detector-related systematics.

The proposed Daya Bay sterile neutrino experiment can probe the 0.3-10  $\text{eV}^2$  mass splitting range to a sensitivity of as low as  $\sin^2 2\theta_{\text{new}} < 0.04$  at 95% CL. The experiment will be sensitive at 95% CL to most of the 95% CL allowed sterile neutrino parameter space suggested by the reactor neutrino anomaly, MiniBooNE, LSND, and the Gallium experiments. In one year, the 3+1 sterile neutrino hypothesis can be tested at essentially the full suggested range of the parameters  $\Delta m_{\text{new}}^2$  and  $\sin^2 2\theta_{\text{new}}$  (90% C.L.).

In order to realize such an experiment, R&D towards the development of a PBq  $\bar{\nu}_e$  source is necessary. The process of selectively harvesting fission products from spent nuclear fuel has been

---

<sup>30</sup>Proposed by: D.A. Dwyer, P. Vogel (Caltech), K. M. Heeger, B.R. Littlejohn (University of Wisconsin)



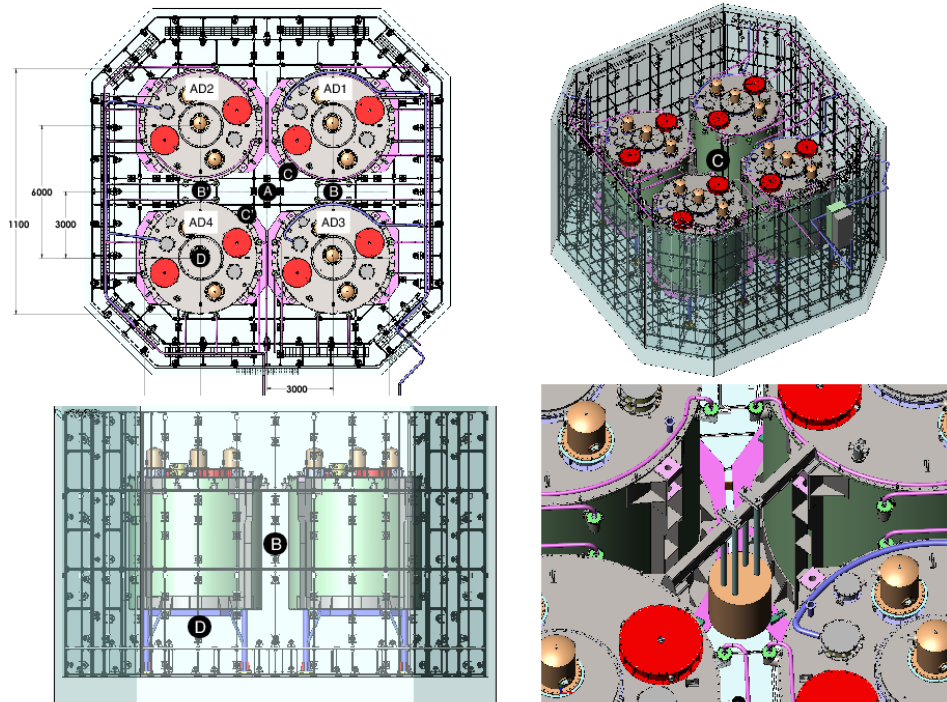


Figure 109. Model of the four antineutrino detectors (AD1-4) in the Daya Bay Far Hall. Left: Top and side view of the Far Hall with water pool (octagonal frame), four antineutrino detectors (grey cylinders) on their support stands (pink), and water cosmic ray veto photomultipliers and support structure (small black features). *A*, *B*, *C*, and *D* mark possible antineutrino source locations. Positions *B'* and *C'* are symmetric to *B* and *C* and can be used as cross-checks and for systematic studies. Detector dimensions are given in mm. Right: ISO view of the Far Hall. *A*, *B*, *C* are all at half-height of the antineutrino detectors, *D* is directly below it. Right bottom: Illustration of suspending a source between the detectors in the water pool. Figures adapted from Ref. [457, 664].

developed in the nuclear reprocessing industry, and will need to be tailored to remove  $^{144}\text{Ce}$  with high efficiency and purity from a small number of spent fuel assemblies. The necessary R&D and development work can be conducted in the years ahead during the  $\theta_{13}$  measurement at Daya Bay.

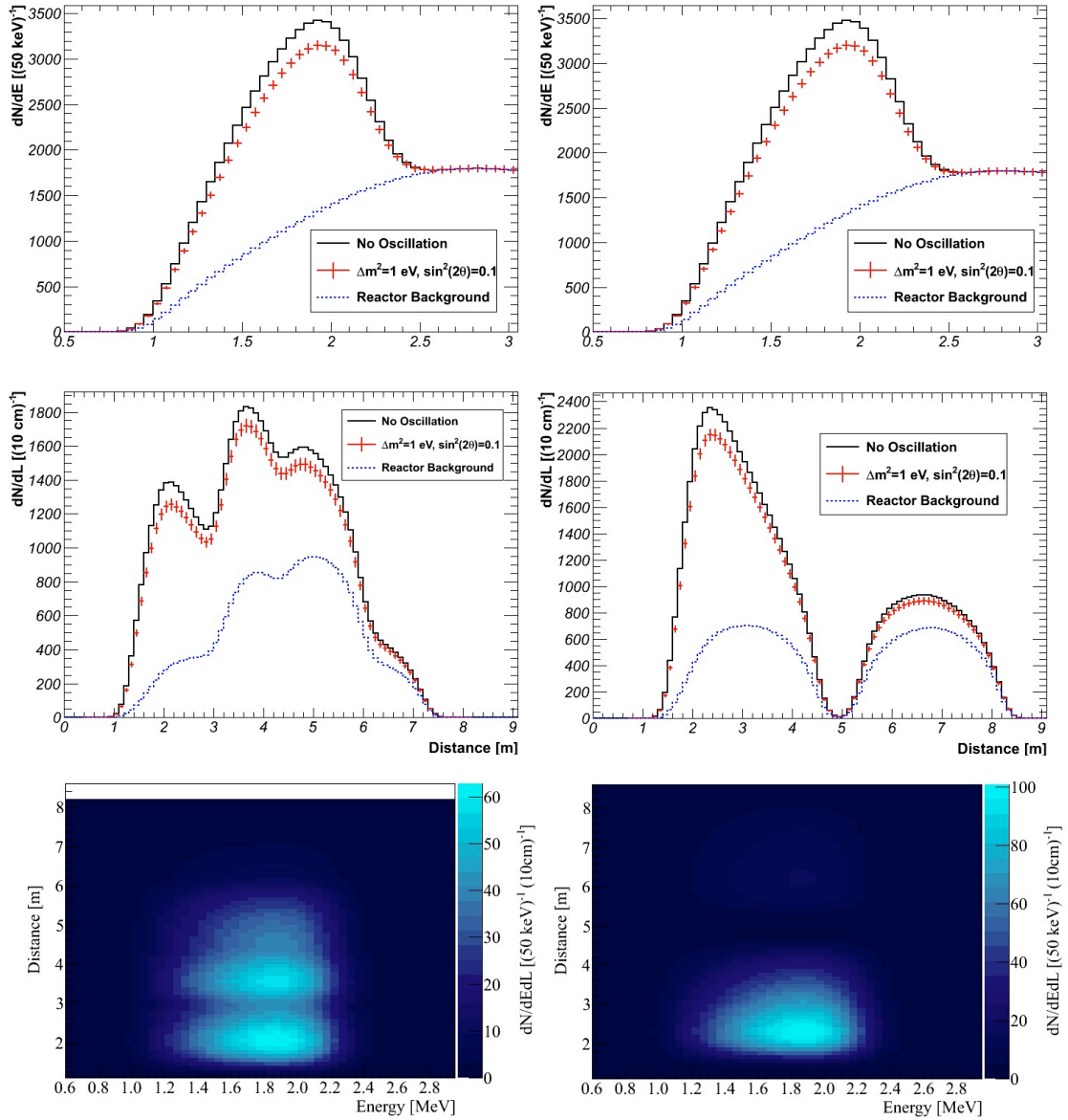


Figure 110. Energy and position dependence of the event rates in the antineutrino detectors. The bottom row shows the 2-dimensional distributions of event rate versus energy and distance from source. Top and middle rows are the 1-dimensions projections of expected events versus energy (top) and distance from source (middle) for the case of no oscillation (black histogram), the observed event rate in case of  $\bar{\nu}_e \rightarrow \nu_s$  oscillation (red points), and the reactor  $\bar{\nu}_e$  background (blue dots). Left panels correspond to source position *C* while right panels are for source position *B*.

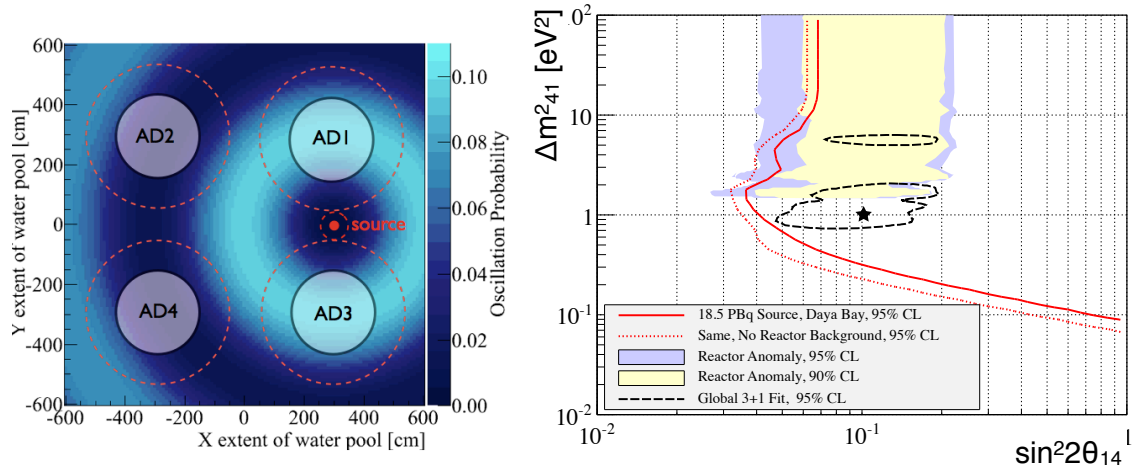


Figure 111. Left: Illustration of sterile neutrino oscillation in the Daya Bay Far Hall and top view of the geometric arrangement of the antineutrino detectors and the  $\bar{\nu}_e$  source. Source at position  $B$ . Figure shows an overlay of the positions of the active regions of the antineutrino detectors with the disappearance probability for  $\bar{\nu}_e \rightarrow \nu_s$  oscillation with  $\Delta m_{41}^2 = 1 \text{ eV}^2$  and  $\sin^2 2\theta_{14} = 0.1$  into sterile species. Active regions of the source and detectors are shown in solid red and grey color respectively, while the physical outer dimensions of the source and detectors are indicated by the dashed lines. Right: Sensitivity of a  $\bar{\nu}_e$  search at Daya Bay to the oscillation parameters  $\Delta m_{41}^2$  and  $\sin^2 2\theta_{14}$  assuming a 500 kCi  $^{144}\text{Ce}$  source at position  $B$  in the Daya Bay Far Hall. We show the 95% C.L. sensitivity of the Daya Bay source experiment with reactor background (red solid) and without (red dashed), the 90% and 95% C.L. preferred regions of the reactor anomaly (shaded yellow and blue) [118], and the 95% best-fit region from a 3+1 global fit to all neutrino data (dashed black) [498]. The parameter space to the left and above the Daya Bay sensitivity curve will be excluded at 95% C.L.

## 7. SNO+Cr<sup>31</sup>

As was noted in Section A 1, combining a low-energy solar neutrino detector sensitive with an electron capture neutrino source like <sup>51</sup>Cr, can result in an experiment for sensitive sterile neutrino search. There are currently three detectors in operation or under construction that are designed to study solar neutrinos down around the 861 MeV <sup>7</sup>Be neutrino peaks – which is only a little more energetic than the 751 KeV <sup>51</sup>Cr neutrino. They are Borexino [665], KamLAND [651], and SNO+ [652]. The best way to use a radioactive neutrino source is to put it in the middle of the detector, which will typically result in a factor of 3 or more neutrino interactions than for a source placed outside the detector. Of the thee active solar neutrino detectors, only SNO+ has a neck wide enough accommodate an appropriately shielded neutrino source. Hence this concept shall be referred to as SNO+Cr.

Unlike the LENS-Sterile proposal discussed in Section A 1, where the neutrinos are detected through a pure charged current process, when a <sup>51</sup>Cr source is used with an undoped liquid scintillator (LS) detector the reaction channel is neutrino-electron elastic scattering. While on the positive side, the elastic scattering interaction rate in LS is two orders of magnitude larger than the <sup>115</sup>In interaction rate in LENS, on the negative side, there is no coincidence tag to eliminate backgrounds. So care must be taken in preparing detector and source materials to reduce radioactive backgrounds inside the detector.

The source is modeled as a 4.5 cm diameter by 4.5 cm tall bundle of Cr rods embedded in the center of a 16 cm radius sphere of tungsten alloy. The tungsten shield reduces the rate of gamma-rays from <sup>51</sup>Cr decay to a few Hz at its surface. In this analysis it is assumed that impurities, that have lead to MeV gamma-rays in past sources, have been eliminated prior to source irradiation. Shielding of only 5 cm is sufficient to reduce the rate of 320 keV gammas, present in 10% of all <sup>51</sup>Cr decays, to the Hz level. Instead the gamma rate at the surface of a 16 cm shielded is dominated by the internal bremsstrahlung (IB) gammas which are present in about a part in 2000 decays [666]. Only a tiny fraction of gammas in the high energy tail of the IB spectrum pass through the shielded, but they, nonetheless, drive the shield design.

It should be noted that solar neutrinos interactions may constitute a significant fraction of the

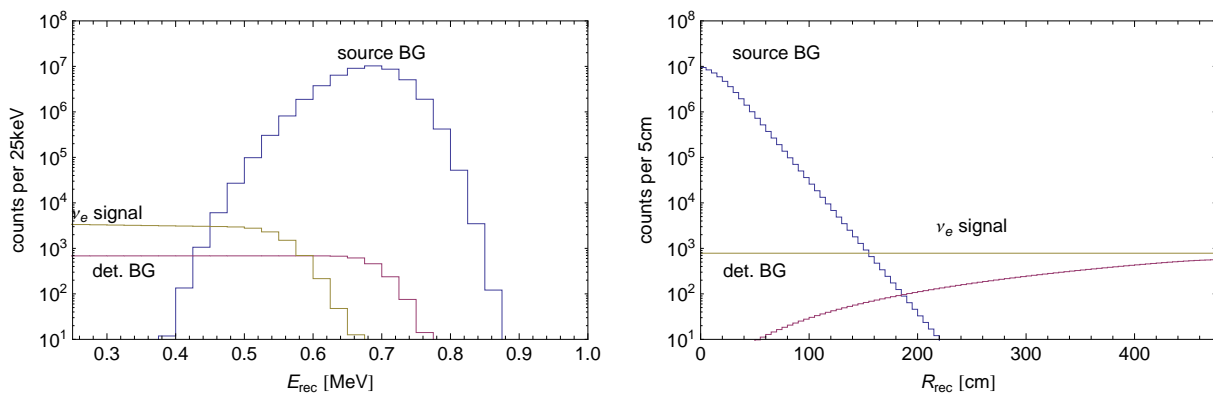


Figure 112. Plots of signal events, source background and detector background as a function of energy (left) and radius (right).

<sup>31</sup>Proposed by P. Huber and J.M. Link(Virginia Tech)

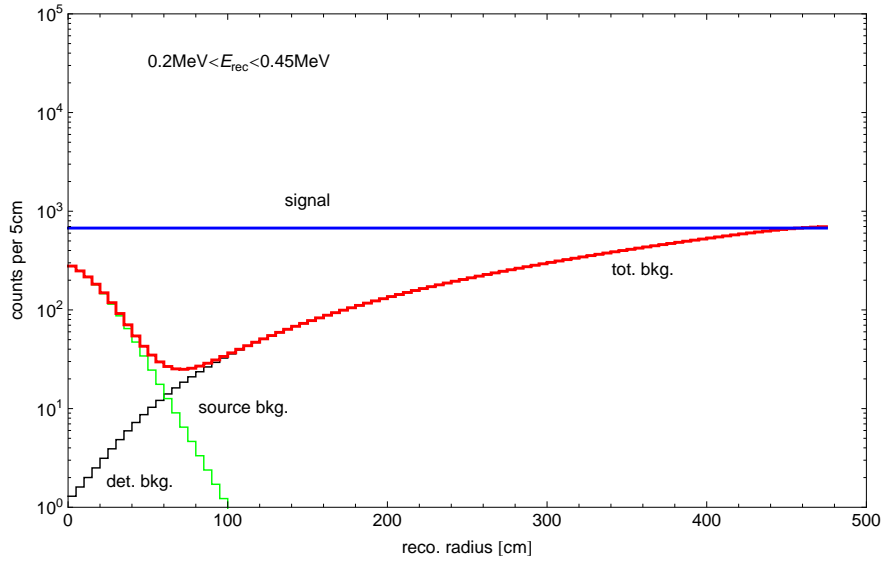


Figure 113. Signal, source background and detector background event rates after a reconstructed energy cut and plotted as a function of radius in the detector.

detector background. Fortunately, the detector background, which is present during source-free running will be measured directly to high precision. On the other hand, the source background is only present when the source is active, and, assuming that it is dominated by gamma-rays from  $^{51}\text{Cr}$  decay, it decays away at the same rate as the Cr neutrino flux.

The left side of figure 112 shows the resolution smeared energy spectrum of the elastic scattering signal events, the source gamma-ray background and the projected detector background for SNO+<sup>32</sup>. It shows that the the source background is only significant at energies above 450 keV and therefore can be eliminated with an energy cut.. The right side of figure 112 shows the event rates as a function of detector radius. Without oscillations the signal rate is flat as a function of radius. The detector background, which is distributed uniformly through the detector fiducial volume, grows as  $R^3$ , while the source background falls off rapidly as the product of  $R^2$  and an exponential for attenuation. Figure 113 shows the rates as a function of detector radius with an energy cut applied ( $200 \text{ keV} < E_{rec} < 450 \text{ keV}$ ). With the energy cut, signal events outnumber background events through out the entire fiducial volume.

The experiment's sensitivity is calculated using GLOBES [546]. A single 75 day run is assumed. In the baseline scenario the source strength is 2 MCi, the source strength normalization uncertainty is 2%, and the detector spatial resolution is 10 cm at 1 MeV. Figure 114 shows the sensitivity of the baseline scenario and with a series of variations on the baseline including, changes to the background rate (Fig 114a), the source strength normalization (Fig 114b), the source strength (Fig 114c), and the detector spatial resolution (Fig 114d). The background variation shows that the sensitivity does not have a strong dependence on the background rate. Even increasing backgrounds by a factor of 10, only lowers the sensitivity by a half. With the baseline spatial resolution, the signal strength normalization uncertainty primarily effects sensitivity for  $\Delta m^2$  greater than  $2 \text{ eV}^2$ . For larger  $\Delta m^2$  the oscillation length is too short to be resolved and sensitivity comes from the ability to resolve a deficit in the total rate. The sensitivity is strongly dependent on the source strength showing that the experiment is statistically limited. Therefore, the reach in  $\sin^2 2\theta$

<sup>32</sup>Personal communication with Gabriel Orebi Gann

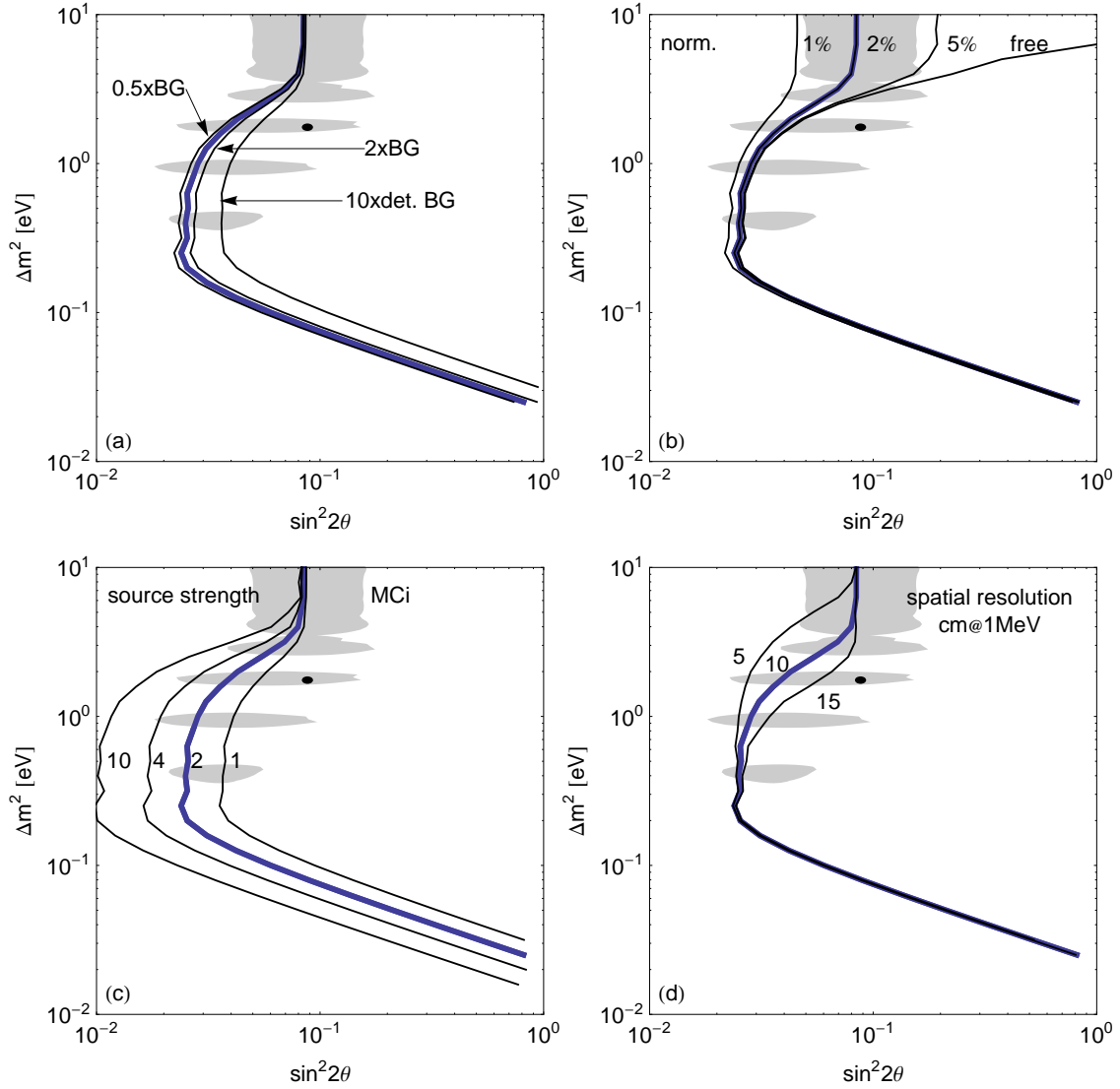


Figure 114. The 90%CL sensitivity of SNO+ to sterile neutrinos as a function of  $\sin^2 2\theta$  and  $\Delta m^2$ . The heavy curve corresponds to the default assumptions. Plot (a) Shows the sensitivity as the background from radioactivity in the scintillator is varied; in (b) the uncertainty on the source normalization is varied; in (c) the source strength is varied; and in (d) the detector spatial resolution is varied. The gray region is the 90% CL sterile allowed region from Ref. [112].

can be improved by either increasing the source strength or by adding additional runs. Finally, we see that the detector spatial resolution determines the dividing point in  $\Delta m^2$  between the sensitivity from the resolved rate variation in radius or from a total rate deficit. Better spatial resolution would allow a direct observation of oscillometry over a greater range in  $\Delta m^2$ .

## 8. Reactors with a small core<sup>33</sup>

In Refs. [667, 668] the sensitivity to the mixing angle of sterile neutrino oscillations at very short baseline reactor oscillation experiments is examined by a spectrum analysis.<sup>34</sup> The assumptions are that the experiment has two identical detectors whose size and efficiency are exactly the same as those used at the Bugey experiment [391] and  $\chi^2$  is optimized with respect to the baseline lengths of the two detectors. In the case of a commercial reactor, the sensitivity is lost above  $1\text{eV}^2$  due to the smearing of the finite core size. In the case of a research reactor with a small core (such as Joyo [674] with MK-III upgrade [675], ILL [676], Osiris [677], PIK [678]), on the other hand, one obtains the sensitivity as good as a several  $\times 10^{-2}$  for  $1\text{eV}^2 \lesssim \Delta m_{41}^2 \lesssim 10\text{eV}^2$  if the detectors are located at  $L_N = 4\text{m}$  and  $L_F = 8\text{m}$  (See Fig. 115). To turn this idea into reality, one has to put detectors at a location very near to a research reactor and has to veto potentially huge backgrounds from the reactor.

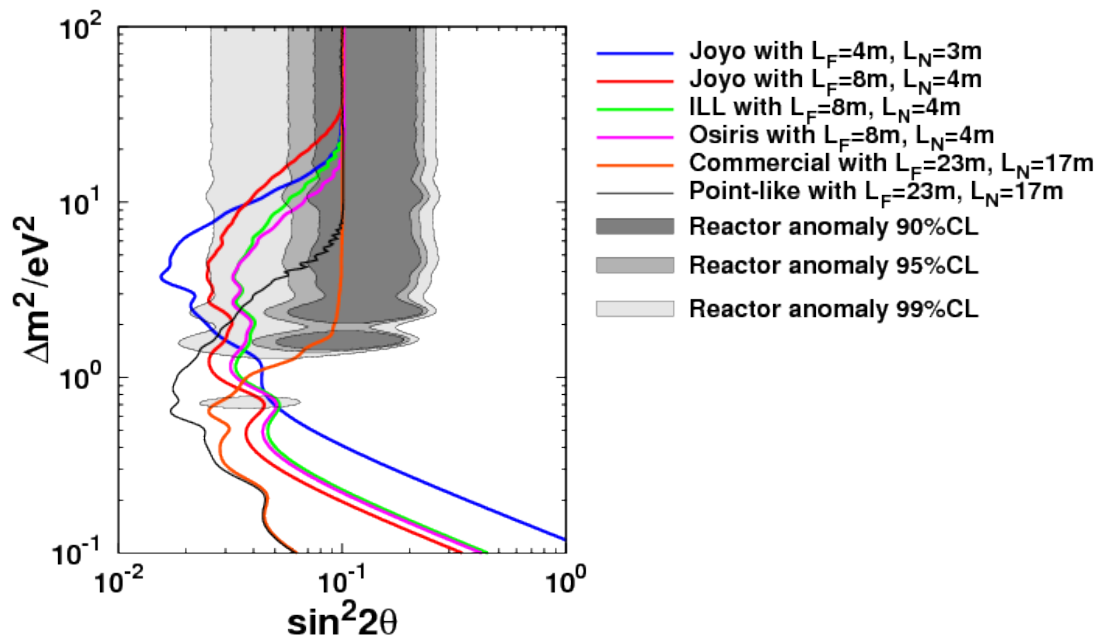


Figure 115. The sensitivity to  $\sin^2 2\theta$  of each reactor with the two detectors at its optimum baseline lengths. The region given in Ref. [118] from the combination of the reactor neutrino experiments, Gallex and Sage calibration sources experiments, the MiniBooNE reanalysis of Ref. [439], and the ILL-energy spectrum distortion is also shown as a shaded area for comparison.

<sup>33</sup> Contributed by Osamu Yasuda (Tokyo Metropolitan University)

<sup>34</sup> See, *e.g.*, Refs. [669, 670] which discuss the same issue from other points of view, and Refs. [671] (the published version), [672, 673] for earlier works on search for sterile neutrinos at a reactor.

## 9. SCRAAM: A reactor experiment to rapidly probe the Reactor Antineutrino Anomaly

Here we describe the proposed Southern California Reactor Antineutrino Anomaly Monitor (SCRAAM) experiment. The primary objective of SCRAAM is to experimentally probe the existence of sterile neutrinos in the  $\Delta m_{14}^2 \approx 1 \text{ eV}^2$  region allowed by the Reactor Antineutrino Anomaly (RAA) [118] using carefully chosen reactor antineutrino sources. The project would begin by performing a rapid experiment at a large Pressurized Water Reactor (PWR) (the San Onofre Nuclear Generating Station (SONGS) in Southern California). A follow-up effort at a compact research reactor (most likely the Advanced Test Reactor (ATR) at the Idaho National Laboratory) would broaden the  $\Delta m_{14}^2$  sensitivity of SCRAAM, while also allowing verification of the SONGS measurement at one or more different baselines. The secondary objective of the project is to use the high precision reactor antineutrino spectrum measurement central to the sterile oscillation search to also improve reactor antineutrino flux predictions [472].

Notably, much of the reactor-sector contribution to the RAA excluded phase space arises from comparison of rate measurements with flux and background predictions, as is also true of the Mini-BOONE and radiochemical experiments. Any experiment seeking to test these anomalies and have the potential to unequivocally prove the existence of a sterile neutrino must use a more conclusive experimental technique. The oscillation phenomena at the heart of the problem provides such a probe: a sterile oscillation should have a distinctive pattern that varies with both neutrino energy and baseline. A direct oscillation pattern measurement can be rapidly and inexpensively provided by well sited reactor antineutrino measurements at short (10-25m) baselines. This experimental approach has several advantages: the high antineutrino flux close to a reactor allows a rapid measurement using a small, inexpensive detector, and the broad energy range spanned by the reactor antineutrino emissions (2-10 MeV) allows a sterile oscillation search directly via spectral distortion. Finally, a high precision reactor spectrum measurement is a natural outcome of such an effort, which could help constraint the magnitude of corrections to flux predictions.

The spread in both  $E$ , *e.g.* from detector energy resolution, and  $L$ , due to the spatial extent of the reactor core and detector, must be considered when planning such a measurement. Relevant parameters are summarized in Table XXXII for the SONGS and ATR reactors and for the Bugey3 measurement conducted at 15 m [391]. The relative baseline distribution for these three reactor sites is shown in Fig. 116. The effect the baseline spread has upon the ability to resolve an oscillation pattern is demonstrated in Fig. 117. Here, the electron antineutrino survival probability is displayed as a function of both baseline and energy for the RAA best fit sterile oscillation parameter values for each reactor site. It is apparent that the large baseline spread of the Bugey3 experiment substantially reduces the oscillation pattern contrast compared to that accessible at the SONGS and ATR sites.

Reactor	Baseline	Core	$\Delta L/L$	Power	Antineutrino Flux
Bugey3	15 m	$\varnothing 2.5 \text{ m} \times 2.5 \text{ m}$	$\approx 30\%$	$2800 \text{ MW}_{th}$	$\approx 2 \times 10^{17} \text{ m}^{-2}\text{s}^{-1}$
SONGS	24 m	$\varnothing 3.0 \text{ m} \times 3.8 \text{ m}$	$\approx 10\%$	$3400 \text{ MW}_{th}$	$\approx 1 \times 10^{17} \text{ m}^{-2}\text{s}^{-1}$
ATR	12 m	$\varnothing 1.2 \text{ m} \times 1.2 \text{ m}$	$\approx 10\%$	$150 \text{ MW}_{th}$	$\approx 2 \times 10^{16} \text{ m}^{-2}\text{s}^{-1}$

Table XXXII. Reactor parameters of the two appropriate sites identified, as well as those for the 15 m Bugey3 measurement.



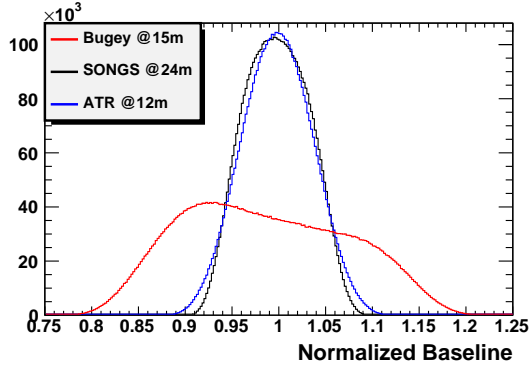


Figure 116. Normalized baseline distributions for the proposed reactor deployment sites and that of the Bugey3 experiment. The wide Bugey3 distribution, where the baseline is only a few times the size of the reactor, is marked asymmetric, largely due to the difference in solid angle from the front to back of the core.

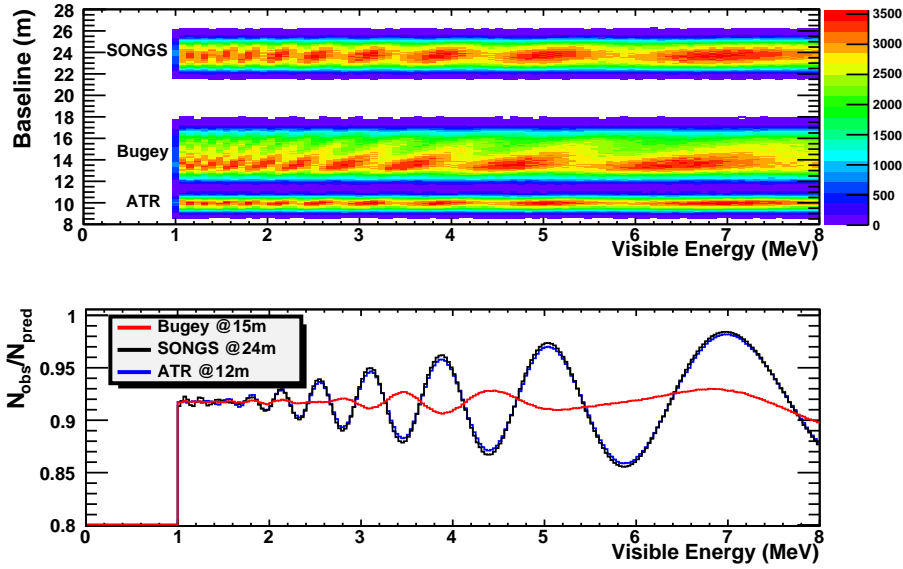


Figure 117. The predicted pattern of a sterile oscillation with  $\sin^2(2\theta_{14}) = 0.15$  and  $\Delta m_{14}^2/\bar{L} = 0.1 \text{ eV}^2\text{m}^{-1}$  (i.e.  $\Delta m_{14}^2 = 2.4 \text{ eV}^2$  for the SONGS baseline of 24 m) for each of the three reactor sites considered. The top panel shows the variation of the  $\bar{\nu}_e$  survival probability with  $E$  and  $L$ , while the bottom panel shows the projection onto the energy axis - the experimentally accessible quantity. For clarity, the ATR pattern in the top panel is displaced to  $\bar{L} = 10$ .

Besides providing sensitivity to the physics of interest, the two identified reactor sites have many other desirable features. In the case of SONGS, our group has almost a decade of operational experience at this site to draw on, including many antineutrino detector deployments and measurements [679–681]. We maintain an excellent relationship with the operator and are confident of being able to obtain ready access to the site for this effort. Finally, the below-ground “tendon gallery” deployment location provides a convenient 30 m.w.e. overburden. A preliminary survey of the ATR site has yielded potential deployment sites with 10 – 20 m.w.e. overburden at  $\approx 12$  m baseline, as well as the possibility to vary that baseline. Also, the 150 MW<sub>th</sub> power of the ATR is relatively high for a research reactor, the core is primarily  $^{235}\text{U}$ , and its 60 day on, 30 day off cycle provide ample opportunity for background measurement.

Drawing upon our own recent experience, and that of the wider neutrino oscillation physics community, we believe that a relatively compact, inexpensive, and high precision liquid scintillator antineutrino detector could be rapidly designed and built for this experiment. The key features required are: high detection efficiency;  $\approx 4\%$  precision on the absolute value of that efficiency, including reactor power uncertainties; and good energy resolution. Reactor antineutrinos would be detected via the inverse beta decay interaction:  $(p(\bar{\nu}_e, e^+)n)$ . Due to the kinematics of the interaction, the final state positron energy is closely related to the antineutrino energy. Near-coincident detection of the final state neutron, typically via Gd-doping, provides powerful background rejection. An efficiency of 50% for a 1.5 ton active mass would yield a detection rate of  $\approx 4,500/\text{day}$  at SONGS and provide a high statistics spectrum measurement within  $\approx 6$  months of running. Given the width of the baseline distributions of the proposed sites, a readily achievable resolution of  $10\%/\sqrt{E}$  ( $E$  in MeV) will not limit sensitivity. We estimate the component costs of such a device to be  $< \$1\text{M}$ .

To achieve these performance goals, we envisage a cylindrical detector with PMTs at either end. Application of a Teflon coating to the detector walls will provide a highly diffuse reflective surface. This configuration will provide excellent light collection performance and uniformity across the entire detector volume, while fitting inside the relatively narrow confines of a tendon gallery. We have performed preliminary Monte Carlo simulations of this design which indicate encouraging performance. Detector calibration will be a critical part of this experiment, because knowledge of the absolute energy scale and its stability will be central to an oscillation analysis and a high precision spectrum measurement. This will be achieved via regular calibrations with small sealed gamma ray and neutron sources deployed via guide tubes within the detector volume.

Using simulated data, we have estimated the sensitivity of SCRAAM to the oscillation parameters of a sterile neutrino flavor using shape information only. For SONGS, we assume 150 days of reactor on operation, 45 days of reactor off operation, a flat background spectrum with signal to background of 8/1 (a reasonable factor 2 improvement over SONGS1), and an energy scale uncertainty of 1.5%. The expected spectral distortion that would be observed for the RAA best fit parameters and the 99% exclusion region in the oscillation parameter space are shown in Fig. 118. For the ATR deployment we assume 300 days of reactor on operation, 150 days of reactor off operation, and a similar signal to background as SONGS. It can be seen that SONGS alone excludes much of the RAA phase space around  $1\text{eV}^2$ , including the best fit region. It is notable that this measurement alone covers the RAA phase space that is consistent with astrophysical indications of a sterile neutrino with mass  $< 1\text{ eV}$ . The ATR deployment extends the range of  $\Delta m^2$  covered by approximately a factor of 2, which is to be expected given that it is placed at half the baseline. Combined, these two measurements cover a broad portion of the RAA phase space and provide a crosscheck of the Bugey3 result that provides much of the RAA exclusion at low  $\Delta m^2$  values. Finally, we note that additional sensitivity could probably be gained by performing a combined analysis of the SONGS and ATR results, by performing the ATR measurement at two baselines, or by using position resolution in the detector at the ATR to probe multiple baselines. Recent work [667] suggests that sensitivity to lower  $\sin^2(2\theta_{14})$  values could be achieved in this way, so long as relative detector normalization is well controlled.

In summary, SCRAAM can provide a direct sterile neutrino exclusion measurement at the source of one of the hints of their existence: nuclear reactors. Deployment of a compact antineutrino detector at the locations identified will probe a large fraction the sterile oscillation parameter phase space allowed by the Reactor Antineutrino Anomaly. Because of the advantageous features of the reactor sites we have identified, this experiment can proceed rapidly and at relatively modest cost.

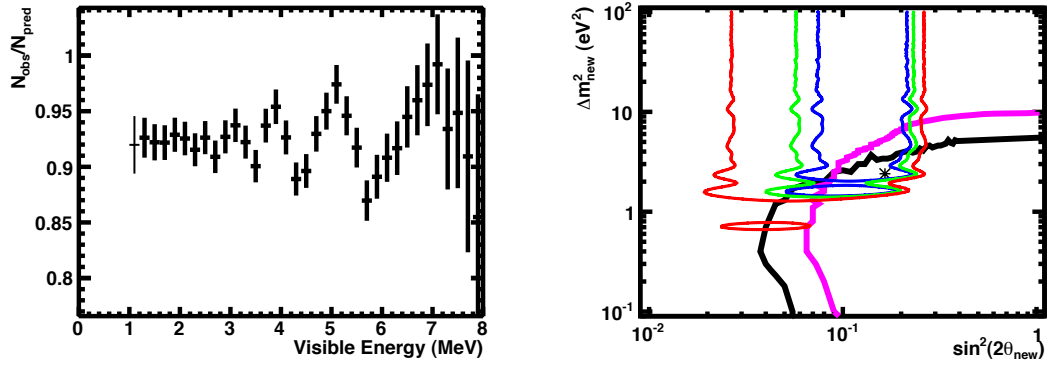


Figure 118. LEFT: Simulated spectral data for the RAA best fit parameters after 150 days at SONGS. The error bars shown include both statistical and systematic errors. RIGHT: 99% C.L. SCRAAM shape-only sensitivity at SONGS (solid black) and the ATR (solid purple). Also shown are the 90%, 95% and 99% allowed contours of the RAA (dashed). The RAA best-fit point is indicated with a star.

This work performed under the auspices of the U.S. Department of Energy by Lawrence Livermore National Laboratory under Contract DE-AC52-07NA27344. LLNL-PROC-520315

## 10. Nucifer: a Small Detector for Short-Distance Reactor Electron Antineutrino Studies<sup>35</sup>

### Introduction

The Nucifer [682] project firstly aims at testing a small electron-antineutrino detector in order to apply this technology to non proliferation. Installing such a detector a few 10 meters from a reactor core allows to monitor its thermal power and to estimate its plutonium content. The design of the detector emphasizes compactness and simplicity, while keeping efficient background rejection.

As reported in Section III H, recent work on reactor neutrino spectra [462] has led to the surprising re-evaluation of the expected neutrino counting rate by an amount of 3 %. This has triggered the re-analysis of previous short-distance reactor neutrino experiments [118], showing a significant discrepancy (about  $3\sigma$ , see III) between measured and expected neutrino counting rates. Among various hypotheses such as experimental bias, a new oscillation to a sterile neutrino state, invisible to detectors has been proposed.

The Nucifer experiment is going to take data at the Osiris research reactor in 2012/13, at only 7 meters from the core. This unique configuration, short distance and the compactness of Osiris core reduces the dispersion of neutrino paths. If an  $eV^2$  sterile neutrino exists (as discussed in Section I), the measured energy spectrum could appear distorted according to the neutrino oscillation hypothesis. The shape-only analysis of the Nucifer data will be the first unambiguous test of the existence of a sterile neutrino, although the complete area of the reactor anomaly contour can not be covered by this experiment alone.

The installation of the detector is now completed and 1 year of data taking is foreseen at the French Osiris research reactor.

### Description

The Nucifer [682] detector target is a stainless steel vessel of 1.8 m in height, and 1.2 m in diameter (see Figure 119) filled with about  $0.85\text{ m}^3$  of Gd-doped liquid scintillator (EJ335 from Eljen technology). The internal surface of the vessel is coated with Teflon to ensure the compatibility with the liquid scintillator and to increase the light diffusionthe light reflections (diffusive and specular). All mechanical parts, in particular welding materials, are low radioactive materials and their radiopurity was controlled with a High purity Germanium in our low background laboratory [683]. The photodetection system is based on 16 large (8 inches in diameter, R5912) photomultipliers (PMTs) from Hamamatsu, providing a large dynamic of light detection from the single photoelectron to few hundreds of photoelectrons and ensuring an efficient light collection.

PMTs are coupled to a 250 mm thick acrylic vessel placed at the top of the target vessel. This so-called acrylic buffer aims at ensuring the uniformity of the response in the whole target volume while reducing the light generated by the intrinsic PMT radioactivity in the scintillator. 80 liters of mineral oil are used to ensure the optical coupling between the PMTs and the acrylic.

---

<sup>35</sup> Proposed by J. Gaffiot, D. Lhuillier, Th. Lasserre, A. Cucoanes, A. Letourneau, G. Mention, M. Fallot, A. Porta, R. Granelli, L. Giot, F. Yermia, M. Cribier, J. L. Sida, M. Fechner, M. Vivier

The Data Acquisition system (DAQ) is based on the VMEbus and the LabView software, and allows a dead time below 1% at 1.5 kHz trigger rate and a remote control of the DAQ. The physic trigger is basically a threshold on an analogic summation of all PMTs' signals. The time and the charge of each PMT are recorded with commercial CAEN Time to Digital Converter (TDC) and Charge to Digital Converter (QDC) modules. The collection of the total and late charges of the pulse is used off line for the Pulse Shape Discrimination analysis.

During operation, a set of 5 LEDs injects light in the detector. One of them is a low intensity diode to monitor the gain of PMTs at the level of the single photoelectron and the rest are high intensity diodes with light Teflon diffuser to monitor the liquid stability and the linearity of the response of the detector.

Four sources are used for the absolute calibration of the detector:  $^{137}\text{Cs}$ ,  $^{22}\text{Na}$ ,  $^{60}\text{Co}$  and Am-Be, providing an energy deposition in the range 0.7-5.5 MeV. A vertical calibration tube located at the center of the target volume allows the introduction of the sources along the target central axis. Moreover the Am-Be source provides tagged neutrons with a 4.4 MeV gamma-ray that is used to calibrate the neutron detection efficiency.

## Background

The experimental challenge is to operate such a small detector in a high background environment. Due to the proximity to the reactor, Nucifer will operate under a high flux of gamma-rays, including high energy gamma-rays from neutron capture on metals. A remnant flux of thermal neutrons has also been measured on site. Osiris is a pool reactor, and only 7.0 meters separate the core center from the detector center, which means only 2.9 meters of water and 2.0 meters of concrete as shielding. To reduce the accidental background in the detector due to random coincidences of external gamma-rays and neutrons, the detector is enclosed within a shielding composed of one layer of 10 cm of lead and one layer of 14 cm of boron-doped polyethylene. As part of the gamma-rays come directly from the core, a lead wall of 10 cm is added between the concrete wall of the reactor pool and the detector. Using this shielding, the accidental background rate is estimated to be of the same level than the neutrino signal. It will be measured online using the reverse and shifted coincidence windows between the prompt and the delayed signal.

Moreover, the detector is close to the surface, with only 5 meters equivalent water above, so the muon flux is only divided by a factor 2.7 compared to surface and significant rapid neutron flux is expected, leading to a correlated event rate few times above the expected neutrino rate. To reduce this background, a 5-sided muon veto will allow us to veto the acquisition during 200  $\mu\text{s}$  after each muon, with few percent dead time. Since muon-induced rapid neutron could be produced outside of the muon veto, we will use Pulse Shape Discrimination (PSD) to reject remaining correlated background.

Our PSD analysis is based on the comparison of the total charge of the event and the charge of its tail, given by our two QDCs. Test on a small 10 cm<sup>3</sup> cell filled with the final EJ335 liquid from Eljen Technology shows a great power of separation between rapid neutron induced proton recoil and gamma induced electron recoil. To preserve the final liquid, tests in lab were performed with Nucifer filled by a homemade liquid, non loaded, based on linear alkyl-benzene (LAB). It was shown that loss of separation power in a large diffusive tank are limited, thanks to our good light collection. We finally expect a rejection of correlated background higher than a factor 10, leading to a signal over correlated background ratio higher than 4.

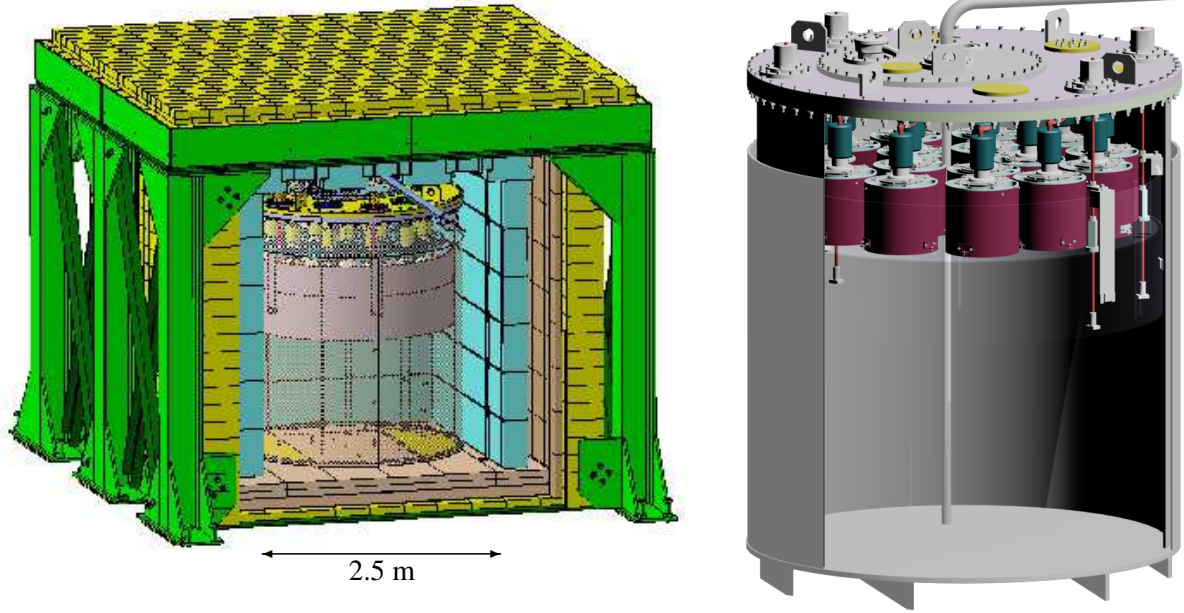


Figure 119. Left: Nucifer with shieldings, including 10 cm of lead, 14 cm of boron doped plastic and  $\mu$  veto Right: Nucifer tank topped by the acrylic buffer and the 16 PMTs

### Short baseline oscillation study

In the scheme of a new oscillation at short distance, we calculated the performances of Nucifer to measure a spectral distortion of the signal.

The Osiris reactor has a thermal power of 70 MW, with a compact core of  $57 \times 57 \times 60 \text{ cm}^3$ , and an enrichment in  $^{235}\text{U}$  of almost 20%. With preliminary plans, we estimate the core center to detector center distance to 7.0 meter. A Monte-Carlo simulation allows us to calculate the solid angle and propagate neutrinos from core to detector. The neutrino energy is drawn in the neutrino spectra of uranium and plutonium, and the Nucifer GEANT4 energy resolution is used to draw the visible energy. We add also a 5% uncertainty on the whole energy scale. The neutron efficiency is largely dependent of background, and according to our simulation it could be from 12% with a neutron energy cut at 6 MeV to 60% with a cut at 4 MeV. We use here an efficiency of 40% corresponding to a cut at 5 MeV. So 400 neutrino interactions are expected in the tank with only 330 above threshold on visible energy at 2 MeV. Since our PSD measurement shown a great power of correlated background rejection, we suppose that the dominant background is accidental, with an expected signal over background ratio of 1. We use here an exponential shape at low energy, below 3 MeV, and a flat shape at high energy.

Figure 120) shows the result for 100 days of running (corresponding to  $\sim 6$  months with reactor off periods) with  $\Delta m_{new}^2$  and  $\theta_{new}$  best fit values taken in Ref [118]. We see a distortion, but its significance will be decreased by accounting for the full set of systematic errors. Figure 121 shows the expected contour with 300 days of data, corresponding to about 1 year on site.

To go further, precise power history, controlled at the percent level, will be used, and dedicated simulation of the Osiris core is under development to control the variations of the fissions barycenter. The measurement of the detector position in respect with the core will allow an uncertainty on the neutrino propagation length at the five centimeters level. The tank will be weighted after and before filling with weigh sensors, allowing a precision in liquid mass below one percent.

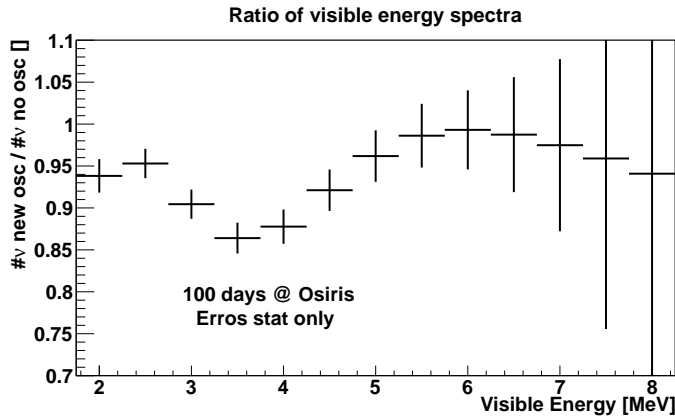


Figure 120. Expected distortion of neutrino spectrum in Nucifer with a new oscillation controlled by  $\Delta m_{new}^2 = 2.3$  and  $\theta_{new} = 0.17$

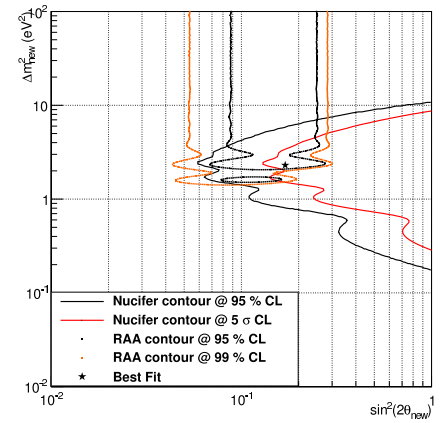


Figure 121. Discovery potential of Nucifer compared to Reactor Antineutrino Anomaly

The hydrogen fraction in the liquid scintillator has been measured by a BASF laboratory, which finally provides a proton number at the percent level. The proton number in the tank will thus be controlled at the percent level.

## Conclusions

The Nucifer detector will take data in 2012/2013, and due to its closeness with the compact Osiris research reactor core, it will be the first reactor experiment testing the  $eV^2$  sterile neutrino hypothesis at reactors. The sensitivity contour shows interesting prospects for the test of the best fit parameters pointed out by the combination of the gallium and reactor anomaly (Ref [118]). Detection efficiency and background rejection will dominate the final systematics and thus performances.

## 11. Stereo Experiment<sup>36</sup>

### Principle

The combination of the reactor anomaly with the neutrino deficit already observed in Gallium experiments favors the hypothesis of a sterile neutrino at the  $3.6 \sigma$  level (see section III H). The most probable values of the new oscillation parameters are

$$|\Delta m_{new}^2| = 2.3 \pm 0.1 \text{ eV}^2 \quad \sin^2(2\theta_{new}) = 0.17 \pm 0.04 (1\sigma) \quad (\text{A10})$$

So far the sterile neutrino hypothesis relies mainly on a missing contribution in the integrated observed rate. An unambiguous signal of a new neutrino must show an oscillation pattern related to the quite large  $\Delta m_{new}^2$ . At the typical few MeV energy scale of reactor antineutrinos, the expected oscillation length is of the order 1 m. Hence to avoid a complete smearing of the oscillation signal the uncertainty of the event-by-event baseline should be below 1 m. On the source side the compact core of a research reactor can meet this specification. On the detector side, standard vertex resolutions are well below 1 m.

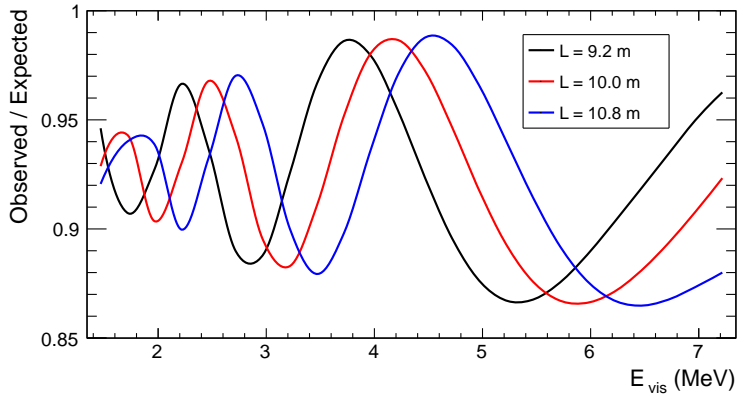


Figure 122. Ratio of expected/observed neutrino spectra for three of the 5 baseline bins of the Stereo detector. Each bin is 40 cm wide.

The proposed experiment is an antineutrino spectrum measurement at short distance from a research reactor, using the standard beta-inverse process in a liquid scintillator (LS) doped with Gd



The prompt positron signal gives the antineutrino energy. The emitted neutron is captured mainly on Gd with a capture time  $\simeq 30 \mu\text{s}$ . This delayed signal is used to reject backgrounds. Along the axis pointing toward the core, the detector is built long enough to see the phase of the new oscillation in the energy spectrum changing along this axis. To prove the existence of a sterile neutrino, emphasis is put on the shape-only analysis, looking for the relative deformation of the

<sup>36</sup>Proposed by D. Lhuillier, A. Collin, M. Cribier, Th. Lasserre, A. Letourneau, G. Mention, J. Gaffiot (CEA-Saclay, DSM/Irfu), A. Cucoanes, F. Yermia (CNRS-IN2P3, Subatech), D. Duchesneau, H. Pessard (LAPP, Universit de Savoie, CNRS/IN2P3).



spectrum along the detector with as little as possible normalization input. Figure 122 illustrates the expected oscillation pattern of the antineutrino energy spectrum in three baseline bins of the Stereo detector. All detection effects presented in the Inner Detector Section are included and the best fit parameters of Eq.(A10) are used. The oscillation patterns and their phase variation are clearly measurable.

### Inner Detector

The proposed setup, based on experience from the Double Chooz [456] and Nucifer experiments, is illustrated in figure 123. The target liquid scintillator, doped with Gd, is contained in a 8 mm thick acrylic vessel. The section of the target is about  $1\text{ m} \times 1\text{ m}$  and the length is  $2\text{ m}$ . The target vessel is immersed in another LS, not doped with Gd, contained in a second acrylic vessel. This 15 cm thick outer layer collects part of the energy of  $\gamma$ -rays escaping from the target, reducing the low energy tail of the detector response. In the current version, 64 PMTs of 8 inches diameter are distributed across the lateral surfaces of the outer acrylic box. The roof and bottom planes are covered with diffusive white Teflon. Fixed optical coupling of the photomultipliers with thick lateral acrylic walls can be used to provide mechanical support and serve as a buffer layer for a more uniform detector response.

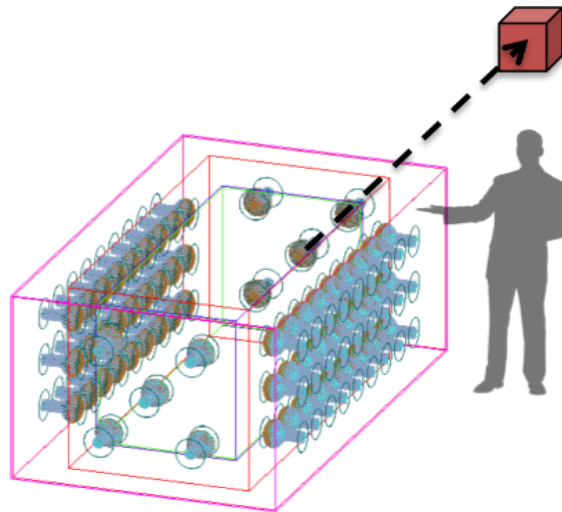


Figure 123. Illustration of the proposed setup (shielding not represented). The longest detector axis points toward the core of the reactor.

### Backgrounds

At the shallow depths considered here, the main source of background is induced by the cosmic rays. When interacting in the surrounding material, they can generate fast neutrons. In the liquid scintillator these fast neutrons will induce recoils of protons. Despite a typical quenching factor of about 5, these protons can mimic a prompt signal above the detection threshold. Then the neutron will keep losing energy and will be captured, generating the same delayed signal than in the case of an antineutrino interaction. The production of multiple neutrons induced by cosmic rays

contributes to the same effect. This correlated background can be efficiently suppressed by the use of the pulse shape discrimination (PSD) properties of liquid scintillators to separate proton recoils from the sought positron signals. Measurements performed in the  $1\text{ m}^3$  target of Nucifer has shown that the volume effects do not reduce significantly the PSD. Muons interacting in the detector can also produce long-lived  $\beta$ -n emitters like  ${}^9\text{Li}$  which mimic the  $e^+, n$  emission of the IBD process. This signal passes all the antineutrino selection cuts and it can't be rejected by a long veto after every muon because of dead time issue. Still the final contribution of muon-induced background is accurately measured during reactor off periods, comparable in length to on periods at research reactors. The expected muon rate in Stereo is few 100 Hz, leading to an acceptable few percent deadtime with a  $100\ \mu\text{s}$  veto (3 times the neutron capture time in Gd doped LS).

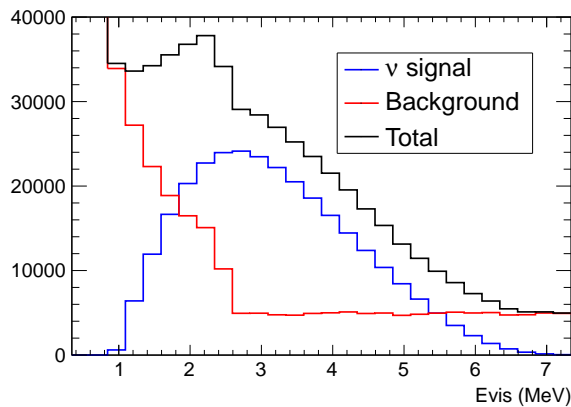


Figure 124. Example of expected spectra for S/B=2 in the range of visible energy [2-7] MeV.

Accidental background is induced by the ambient radioactivity. This source is limited by the use of radiopure materials. At very short baseline, thermal neutrons and high energy  $\gamma$ s emitted by the core itself can also reach the casemate of the detector. By definition this background is correlated with the operation of the reactor and can't be measured during the reactor off periods. It must be suppressed by heavy shieldings isolating the inner detector from the outside. The final geometry has to be optimized depending on the background measured on site. The default shielding structure considered here is based on the Nucifer study at the Osiris site:

- The first layer around the target is an active muon veto made of plastic scintillator or water for Cerenkov light detection.
- If thick enough the muon veto can thermalize and absorb most neutrons. An extra polyethylene layer doped with Boron can be added.
- An external layer of  $\approx 10$  cm of lead suppresses the  $\gamma$  background.

The mass of the setup is dominated by the lead shielding, estimated at about 45 tons for the Stereo experiment. The total mass is about 60 tons for a foot print of  $4.5\text{ m} \times 3.5\text{ m}$  and a total height of  $2\text{ m}$ .

The ILL experiment performed in the eighties [448] has shown that the particle flux from the reactor did not induce correlated background in the detector and that the accidental background was efficiently rejected by the shieldings. The remaining contribution of accidentals can always

be measured online using shifted coincidence windows. The Nucifer experiment will provide valuable inputs on background rejection in the next few months for the Osiris site. Meanwhile, for the following studies we assume a background level similar to the published ILL data [448]. The figure 124 illustrates the crude model of prompt background spectrum, with a fast decrease at low energy and an almost flat behavior at high energy. With a detection threshold set at 2 MeV (visible energy) the ratio of the total expected antineutrino signal over the total background is about 1.5.

### Performances

The Stereo setup is simulated with a GEANT4 software adapted from the simulation of the Double Chooz experiment [456]. It includes a detailed optical model of light emission by the liquid scintillator as well as its propagation to the PMT's. The response to each photo-electron (p.e.) is simulated according to the measured response of the 8" PMTs. The analogic total pulse of each PMT is then built from the sum of all single p.e. The arrival time of each PMT pulse is determined via a simulated constant fraction discriminator. The total charge is integrated in a 150 ns gate.

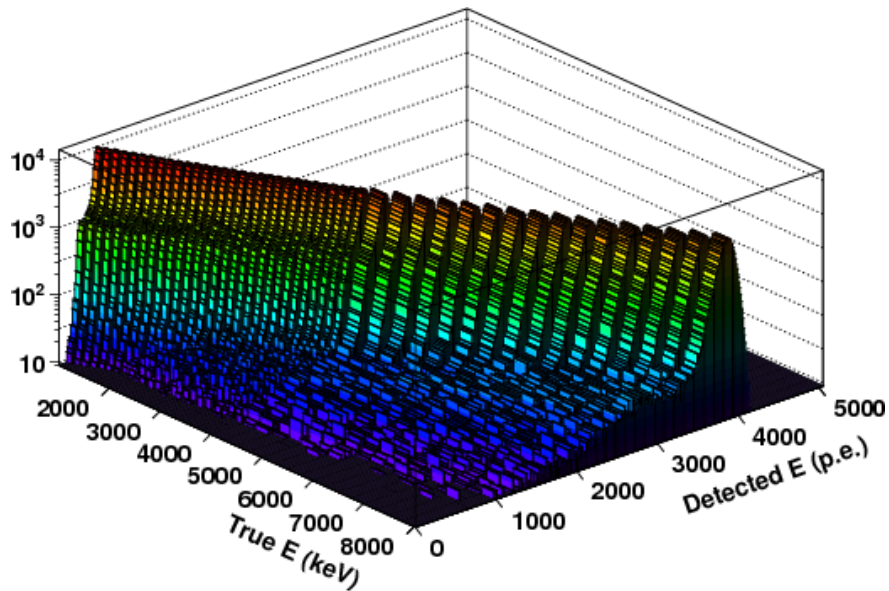


Figure 125. Transition matrix describing the energy response of the detector.

A vertex resolution of 15 cm is assumed, based on the arrival time of the first photons on the PMT's of opposite sides of the detector. This parameter is not critical since the extension of the reactor core itself already generate a smearing of the antineutrino baseline of about 30 cm ( $1\sigma$ ). For the oscillation analysis the antineutrino events are collected in bins of  $\approx 40$  cm width along the detector-core axis.

The energy response is described by a transition matrix connecting any incident antineutrino energy with a reconstructed energy projected in bins (fig.125). The more important energy loss of events close to the edges of the target induces some spectral distortion along the detector axis. To account for this effect a specific transition matrix is computed for each detector slice considered in the oscillation analysis (see the Sensitivity Section). A symmetry with respect to the middle vertical plane of the detector is assumed.

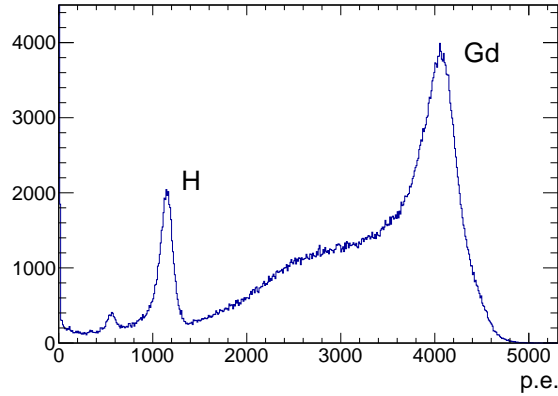


Figure 126. Visible energy spectrum for neutron capture with initial vertex uniformly distributed in the target volume. The energy scale is about 500 p.e. per MeV.

The signal of the neutron capture is the emission of  $\gamma$  rays. About 3  $\gamma$ s and a total energy of  $\simeq 8$  MeV for the capture on Gadolinium, a single 2.2 MeV  $\gamma$  for the capture on hydrogen. Figure 126 shows the simulated response to neutron capture. Assuming a cut of 6 MeV for neutron capture candidates, the predicted detection efficiency is 58%.

### Sensitivity

The contours expected from the Stereo experiment are computed using the full simulated detector response described above. Two candidate sites are tested: the ILL research reactor in Grenoble, France and the Osiris research reactor in Saclay, France. The relevant parameters of each site are summarized in table XXXIII. The detection threshold is set at 2 MeV on the visible energy, equiv-

	ILL	Osiris
Power	58 MW	70 MW
Core size	$\phi = 28\text{cm}, h = 80\text{cm}$	$61 \times 61 \times 63\text{cm}$
Nuclear fuel	93% U5 enriched	20% U5 enriched
Det-Core distance	8 m	10 m
Overburden	$\simeq 5$ m.w.e.	$\simeq 5$ m.w.e.
Expected $\bar{\nu}_e/\text{day}$	708	1043

Table XXXIII. Characteristics of the ILL and Osiris sites.

alent to a 2.78 MeV threshold on the antineutrino energy. The background model of figure 124 is used with an signal/background ratio of 1.5. The exposure time is 300 full days, corresponding to about 2 years running at the reactor when accounting for the commissioning and the reactor off periods.

To evaluate the sensitivity to the new oscillation we introduce the following  $\chi^2$ , built according

to annex A of [684]

$$\chi^2(\Delta m_{new}^2, \theta_{new}) = \sum_{l,i} \left( \frac{O_{l,i}(\Delta m^2, \sin^2 \theta) - T_{l,i}}{\sigma^2(O_{l,i})} \right)^2 + \sum_l \left( \frac{\beta_l}{\sigma_\beta} \right)^2 + \sum_i \left( \frac{\alpha_i}{\sigma_{\alpha_i}} \right)^2 + \left( \frac{\alpha_{WM}}{\sigma_{WM}} \right)^2 \quad (\text{A12})$$

with

$$T_{l,i} = [1 + \alpha_l + \alpha_i + \alpha_{WM} * (E_i - 1)] N_{l,i} + \beta_l \left. \frac{dN_{l,i}}{d\beta_l} \right|_{\beta_l=0} \quad (\text{A13})$$

$O_{l,i}(\Delta m^2, \sin^2 \theta)$  is the expected event rate for the mass square splitting  $\Delta m_{new}^2$  and the mixing angle  $\theta_{new}$ .  $T_{l,i}$  is the theoretical prediction without oscillation and  $N_{l,i}$  the expected number of events in the  $i^{th}$  energy bin (250 keV bin width) and  $l^{th}$  baseline bin in the detector. The default energy binning is 250 keV, adapted to the simulated detector resolution. Similar sensitivity is achieved with 500 keV bins. With a 2 m long target 5 baseline bins of  $\simeq 40$  cm are used in the analysis. These detector slices are perpendicular to the detector-reactor axis which can differ significantly from the detector axis, depending on the site.

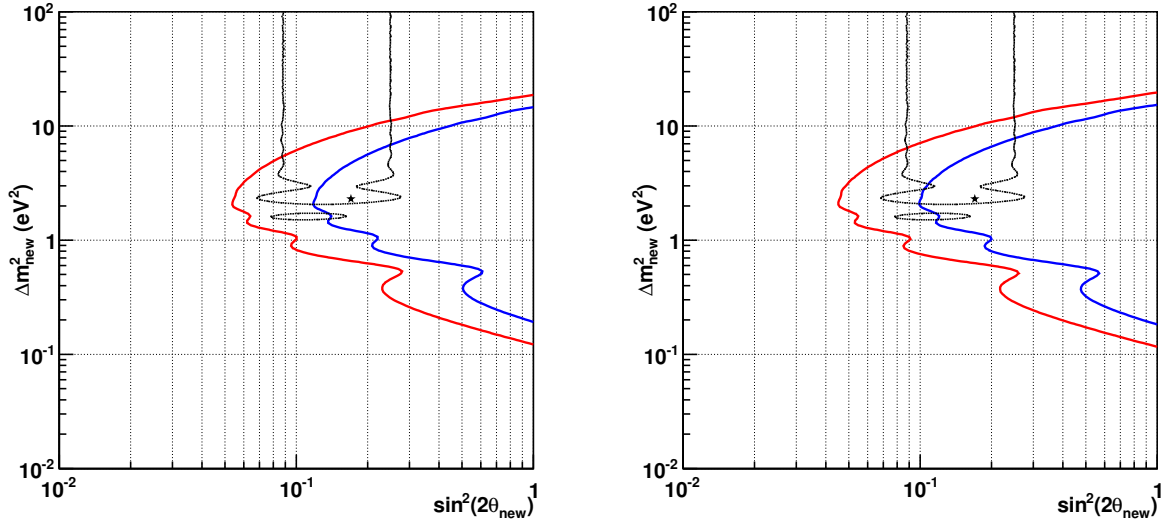


Figure 127. Contours of the Stereo experiment for the ILL site (left) and Osiris site (right). The contours are obtained for 300 full days of data, 58% detection efficiency, 2 MeV visible energy threshold and signal/background=1.5

For each set of oscillation parameters, the  $\chi^2$ -function has to be minimized with respect to the parameters  $\alpha_l$ ,  $\alpha_i$ ,  $\alpha_{WM}$ , and  $\beta_l$  modeling the systematical errors.  $\alpha_l$  are free normalization parameters for the  $L$  baseline bins. The absence of associated pull term provides a shape-only analysis. Their minimization absorbs the variation of rate with  $L^2$ , as well as any mean effect of the oscillation. The parameters  $\alpha_i$  refer to bin-to-bin uncorrelated error uncertainty on the shape of the expected energy spectrum. They are dominated by the electron to antineutrino conversion error

and the statistical error. The  $\alpha_i$  are taken from [472]. The uncertainty on the weak magnetism correction is another independent source of shape uncertainty, correlated between energy bins but not equivalent to a simple normalisation error. It is described by a linear correction with  $\alpha_{WM}$  a slope parameter. The size of the uncertainty used here,  $\sigma(\alpha_{WM})=1\%$ , corresponds to a  $\sim 3\%$  change of the total predicted rate. This is the dominant theoretical error beyond normalization for the predicted neutrino spectra. The energy scale uncertainty in the two detectors is taken into account by the parameter  $\beta_l$  with  $\sigma_\beta = 2\%$  and

$$\left. \frac{dN_{l,i}}{d\beta_l} \right|_{\beta_l=0} = \frac{E_i^+(N_{l,i} + N_{l,i}^+) - E_i^-(N_{l,i}^- + N_{l,i})}{2 * (E_i^+ - E_i^-)} \quad (\text{A14})$$

The  $+(-)$  exponents refer to the values at the upper (lower) edge of the energy bin.

Finally  $\sigma(O_{l,i}) = \sqrt{N_{l,i} + b_i + b_i}$ , taking into account the subtracted background contribution  $b_i$  and assuming comparable time dedicated to background measurement and data. The same background model (rate and spectrum shape) is used in all baseline bins.

This formalism provides a quite complete treatment of all experimental systematics. The contours are illustrated in figure 127. The 99% contour of the experiment covers the 99% contour of the reactor anomaly in the  $\Delta^2 m_{new}$  area of interest. The key points of the experiment are to insure a good background rejection and to minimize the energy losses outside the target volume. This study uses background conditions already achieved by previous experiments. With a 15 cm  $\gamma$ -catcher layer, the simulation shows that the edge effects in the first and last baseline bins are not critical. For instance, we checked that using the central transition matrix for all baseline bins doesn't modify significantly the contours in the reactor anomaly area. We also checked numerically that the impact of the other parameters (bin size, bin-to bin uncorrelated errors of the prediction, weak magnetism correction, energy scale) was not dominant.

This experiment proposes a powerful test of the reactor anomaly using a well known technology. The best fit of the reactor anomaly is tested well beyond the 5 sigma level.

## 12. A Very Short-Baseline Study of Reactor Antineutrinos at the National Institute of Standards and Technology Center for Neutron Research<sup>37</sup>

Data from a variety of short-baseline experiments, astrophysical observations, and evidence from cosmology are beginning to favor the existence of additional neutrino mass states beyond the three active species in the standard model of Particle Physics (SM). Most recently, a re-analysis of short-baseline reactor neutrino experiments has revealed a discrepancy between observations and the predicted antineutrino flux of about 3% [118]. This can be interpreted as an indication of the existence of at least one sterile neutrino with a mass splitting of  $\sim 1\text{eV}^2$  relative to the SM neutrinos [498]. The possible implications of additional sterile neutrino states would be profound. This would be the first direct observation of a particle beyond the SM, and have a significant impact on our understanding of the Universe. As a result, great interest has developed in carrying out a definitive test of the sterile neutrino hypothesis with the suggested mass splitting [661, 662] as well as in making a precision determination of the absolute reactor neutrino flux.

Various approaches have been proposed to address this situation [662, 663]. One possibility is to measure the reactor antineutrino flux from compact research reactors at distances comparable to the expected oscillation length of sterile neutrinos ( $\sim 2\text{-}3\text{ m}$ ). A measurement of the rate and shape of the antineutrino spectrum as a function of distance will reveal the signature of sterile neutrinos in the form of both an overall rate deficit and a spectral distortion. Though the finite dimensions of the reactor core as well as the spread in the position reconstruction of events inside the detector will smear the spectral and rate signatures of sterile neutrinos, compact cores with dimensions of  $\sim 1\text{ m}$  and demonstrated detector technology will allow a direct observation of a spatial deviation from  $1/r^2$ . Furthermore, Highly Enriched Uranium (HEU) research reactors may allow a more accurate absolute prediction of the reactor neutrino flux from thermal power data and fuel simulations compared to commercial reactors. This in turn should result in a better comparison of the absolute measured antineutrino flux with the flux prediction from the reactor. In this context the major challenge of antineutrino measurements near research reactors is expected to come from the lack of overburden and the need to operate the detectors close to the core. (Overburden and underground locations typically help reduce environmental and cosmogenic backgrounds in low-energy neutrino measurements.) In addition, fast neutron backgrounds associated with the reactor and adjacent experiments will contribute significantly to the ambient backgrounds near the reactor. In spite of these challenges, recent development of antineutrino detectors in the context of non-proliferation and nuclear verification efforts have demonstrated the feasibility of antineutrino detection in such a situation.

Measurement of the reactor antineutrinos in a typical detector utilizes the inverse beta decay reaction yielding a prompt signal followed by a neutron capture tens of microseconds later. This detection principle has been used for decades in many reactor neutrino experiments and a variety of methods are available (*e.g.* choice of scintillator and doping isotope) for optimization of the detector design in a specific background environment and detector geometry. The delayed coincidence allows for a significant reduction in accidental backgrounds from natural radioactivity and neutron capture gamma backgrounds.

The National Institute of Standards and Technology (NIST) [657] operates a 20 MW D<sub>2</sub>O-moderated research reactor at the NIST Center for Neutron Research (NCNR) [685]. The National Bureau of Standards Reactor (NBSR) is a split core geometry with 18 cm vertical separation

---

<sup>37</sup>Proposed by H. P. Mumm (National Institute of Standards and Technology) and K. M. Heeger (University of Wisconsin)

between fuel segments and overall dimensions of roughly 1 m diameter by 74 cm in height. See Figure 128. The primary purpose of the reactor is to produce neutrons for a broad program of fundamental and applied neutron science at NIST [686]. The reactor operates in 38-day cycles with approximately 10-day refueling periods which provide an ideal opportunity for detailed studies of natural backgrounds. During every refueling 4 of the 30 fuel elements are replaced while others are repositioned. Overall operating time at 20 MW averages 250 days per year. Furthermore, an engineering model-based MCNP simulation package has been developed and validated at NIST to quantitatively predict fast neutron fluxes at instruments inside the facility. Finally, detailed information on the operation of the reactor is expected to be available to an experiment at the NIST facility.

The reactor is inside a confinement building (Figure 128) that houses seven thermal neutron beams supporting a variety of applied and fundamental neutron experiments. Space and infrastructure include a full suite of standard utilities, an overhead crane, truck access, and floor loading capacity are suitable to support the installation and operation of an antineutrino detector of several tons. The space next to the biological shield indicated in Fig. 128 is designated the “thermal column”. This experimental area is designed to produce a high flux of thermal neutrons through successive moderation in a heavy water tank (currently filled with light water) and graphite blocks. It is consequently the area of the confinement building that has the lowest fast neutron flux. Fast neutron backgrounds in this area are expected to be dominated by scattering from adjacent instruments. A volume measuring 10 m long by 1.57 m wide by 2.5 m tall centered at roughly core height and at a minimum baseline of 3.6 m from the reactor core is potentially available, though floor level access to rear areas of the confinement building must be maintained. In practice this suggests a smaller detector that is moved through the region indicated by grey in Fig. 128.

reactor type	D <sub>2</sub> O, HEU
power	20 MW <sub>th</sub>
fuel cycle	38 days
number of fuel elements	30 (load 4 fresh fuel elements in every cycle)
fuel composition	93% <sup>235</sup> U <sub>3</sub> O <sub>8</sub> + Al
average operating days per year	250
core geometry	split core, hexagonal
core dimensions	overall height: 74 cm (including 18 cm central gap) hexagonal sides: 52.8 cm overall diameter: ~1 m

Table XXXIV. Characteristics of the NIST research reactor, NBSR.

A variety of existing neutron spectrometers and the expertise of the NIST group would allow a thorough characterization of the fast neutron background in the vicinity of the thermal column and a validation of the shielding design for a potential detector package. Along with these measurements this background can be simulated once additional support is available. The NIST reactor is currently undergoing an upgrade and precise data will become available once the reactor is operational again in mid-2012. Measurements of the neutron background taken for health physics surveys can be used to estimate backgrounds in the near term. It is clear that substantial shielding will be required for the envisioned surface detector. However, based on initial estimates, cost, and structural requirements would not be expected to be prohibitive.



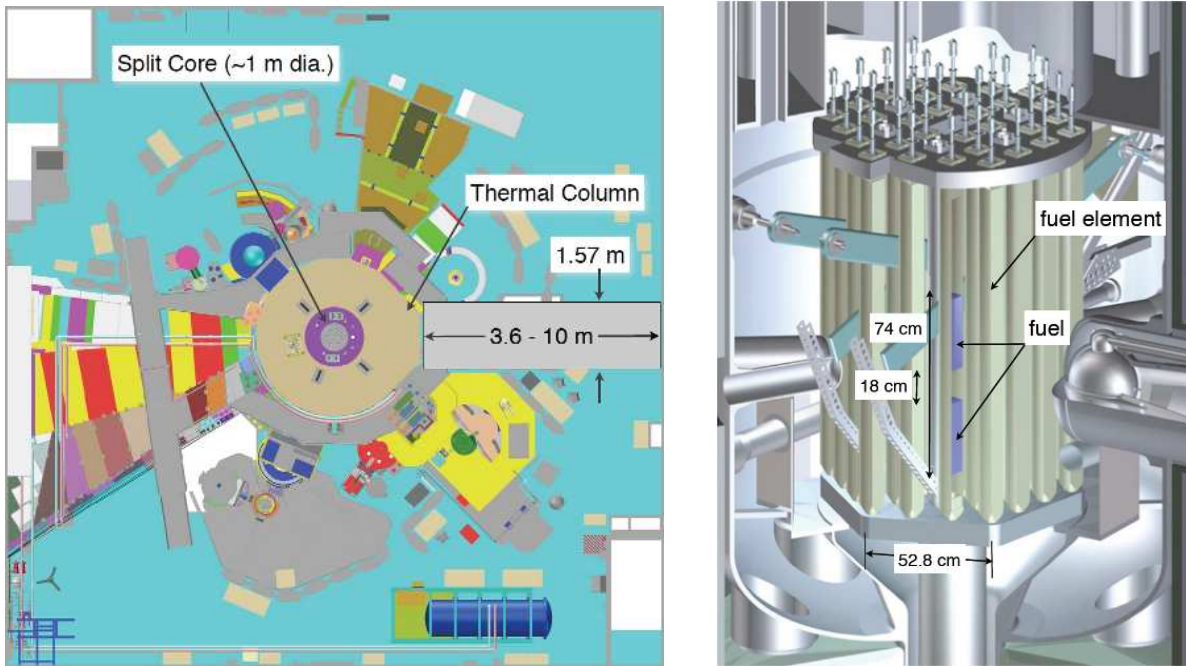


Figure 128. Left: The layout the NBSR confinement building with the reactor and adjacent instruments [657]. The confinement building allows the placement of a detector at distances of 3.6 to 10 m from the reactor core. A several-ton antineutrino detector can be located in and moved through the region indicated in grey. Right: Model of the NIST reactor core [657]. The purple region indicates location of fuel within an element.

The NIST Center for Neutron Research appears to be an attractive location for a possible short baseline reactor antineutrino experiment. A more detailed study of the sensitivity and shielding requirements of a several ton liquid-scintillator experiment is currently underway.

### 13. OscSNS: A Precision Neutrino Oscillation Experiment at the SNS<sup>38</sup>

The issue of whether or not light sterile neutrinos ( $m_{\nu_s} \sim 1 \text{ eV}/c^2$ ) exist has received very considerable attention recently. Such exotic particles, first invoked to explain the  $\bar{\nu}_\mu \rightarrow \bar{\nu}_e$  appearance signal observed by LSND, require a neutrino mass of  $\sim 1 \text{ eV}/c^2$ , which is far above the mass scale associated with the active neutrinos. This unexpected appearance is ascribed a process that proceeds through a sterile neutrino. More recently, lower than expected neutrino event rates from calibrated radioactive sources and nuclear reactors can also be explained by the existence of a sterile neutrino with mass  $\sim 1 \text{ eV}/c^2$ . No experiment directly contradicts the existence of such a sterile neutrino, though there is tension between limits on  $\nu_\mu$  disappearance and the LSND observation. Fits to the world neutrino and antineutrino data are consistent with one or two light sterile neutrinos at this  $\sim 1 \text{ eV}/c^2$  mass scale. It is crucial to establish if such totally unexpected light sterile neutrinos exist. The Spallation Neutron Source (SNS), located at Oak Ridge National Laboratory and built to herald a new era in neutron research, provides the opportunity to make that critical determination. The SNS with 1MW beam power is a prodigious source of neutrinos from  $\pi^+$  and  $\mu^+$  decay at rest and has a duty factor more than 100 times shorter than that of LAMPF. This much smaller duty factor not only reduces backgrounds, it also allows the  $\nu_\mu$  induced events from  $\pi^+$  decay to be separated from the  $\nu_e$  and  $\bar{\nu}_\mu$  events from  $\mu^+$  decay. The monoenergetic 29.8 MeV  $\nu_\mu$  can be used to investigate the existence of light sterile neutrinos via the neutral-current reaction  $\nu_\mu C \rightarrow \nu_\mu C^*(15.11 \text{ MeV})$ , which has the same cross section for all active neutrinos but is zero for sterile neutrinos. An oscillation or suppression of this reaction would be direct evidence for sterile neutrinos. OscSNS can obviously carry out a unique and decisive test of the LSND appearance  $\bar{\nu}_\mu \rightarrow \bar{\nu}_e$  signal that has not been executed to date. The existence and properties of light sterile neutrino is central to understanding the creation of the heaviest elements and verifying our understanding of the nuclear reactions involved in nuclear reactors. An OscSNS detector is based on the LSND and MiniBooNE detectors and can be built for  $\sim \$12\text{M}$  (or  $\sim \$8\text{M}$  if the MiniBooNE oil and phototubes are reused and  $\sim \$5\text{M}$  if the tank size is reduced).

Observations of neutrino oscillations, and therefore neutrino mass, have been made by solar-neutrino experiments at a  $\Delta m^2 \sim 8 \times 10^{-5} \text{ eV}^2$ , and by atmospheric-neutrino experiments at a  $\Delta m^2 \sim 3 \times 10^{-3} \text{ eV}^2$ , where  $\Delta m^2$  is the difference in squared mass of the two mass eigenstates contributing to the oscillations. In addition to these observations, the LSND experiment, which took data at Los Alamos National Laboratory (LANSCE) for six years from 1993 to 1998, obtained evidence for  $\bar{\nu}_\mu \rightarrow \bar{\nu}_e$  oscillations at a  $\Delta m^2 \sim 1 \text{ eV}^2$ . Oscillations at the mass splittings seen by LSND do not fit with well-established oscillation observations from solar and atmospheric experiments. The standard model, with only three flavors of neutrinos, cannot accommodate all three observations. Confirmation of LSND-style oscillations would require further non-trivial extensions to the standard model.

The MiniBooNE experiment at Fermilab, designed to search for  $\nu_\mu \rightarrow \nu_e$  and  $\bar{\nu}_\mu \rightarrow \bar{\nu}_e$  oscillations and to further explore the LSND neutrino oscillation evidence, has presented neutrino and antineutrino oscillation results. Combining these results, MiniBooNE observes a  $3.7\sigma$  excess of events in the 200-1250 MeV oscillation energy range. Many of the beyond the standard model explanations of this excess involve sterile neutrinos, which would have a huge impact on astro-

<sup>38</sup> Proposed by: S. Habib, I. Stancu (University of Alabama), M. Yeh (Brookhaven National Laboratory), R. Svoboda (University of California, Davis), B. Osmanov, H. Ray (University of Florida, Gainesville), R. Tayloe (Indiana University, Bloomington), G. T. Garvey, W. Huelsnitz, W. C. Louis, G. B. Mills, Z. Pavlovic, R. Van de Water, D. H. White (Los Alamos National Laboratory), R. Imlay (Louisiana State University), B. P. Roe (University of Michigan), M. Chen, (Oak Ridge National Laboratory), Y. Efremenko (University of Tennessee), F. T. Avignone (University of South Carolina), J. M. Link (Virginia Tech).

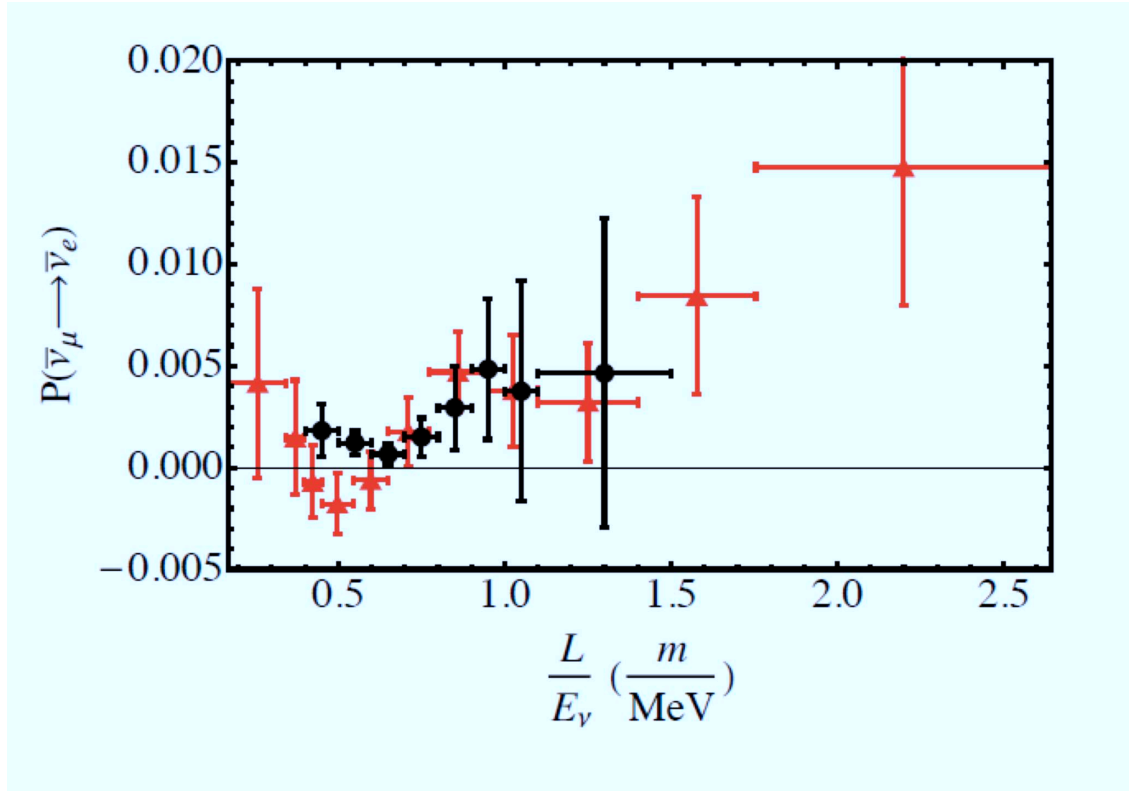


Figure 129. The probability of  $\bar{\nu}_e$  appearing in a  $\bar{\nu}_\mu$  beam as a function of the neutrino proper time.

physics, supernovae neutrino bursts, and the creation of the heaviest elements. Figure 129 shows the  $L/E$  (neutrino proper time) dependence of  $\bar{\nu}_\mu \rightarrow \bar{\nu}_e$  from LSND and MiniBooNE. The correspondence between the two experiments is striking. Furthermore, Figure 130 shows fits to the world neutrino plus antineutrino data that indicate that the world data fit reasonably well to a 3+2 model with three active neutrinos plus two sterile neutrinos.

The SNS offers many advantages for neutrino oscillation physics, including known neutrino spectra, well understood neutrino cross sections (uncertainties less than a few percent), low duty cycle for cosmic ray background rejection, low beam-induced neutrino background, and a very high neutrino rate of  $> 10^{15}/s$  from the decay of stopped pions and muons in the Hg beam dump. Stopped pions produce 29.8 MeV monoenergetic  $\nu_\mu$  from  $\pi^+ \rightarrow \mu^+ \nu_\mu$  decay, while stopped muons produce  $\bar{\nu}_\mu$  and  $\nu_e$  up to the 52.8 MeV endpoint from  $\mu^+ \rightarrow e^+ \nu_e \bar{\nu}_\mu$  decay. Note that  $\pi^-$  and  $\mu^-$  mostly capture in Hg before they have a chance to decay, so that hardly any neutrinos are produced from either  $\pi^- \rightarrow \mu^- \bar{\nu}_\mu$  or  $\mu^- \rightarrow e^- \bar{\nu}_e \nu_\mu$  decay. The rapid capture of the negatively charged meson in the Hg environment is an advantage over the LSND experiment, where the production target was more open with greater possibility of  $\pi^-$  decay in flight and the resulting  $\mu^-$  decaying to  $e^- \bar{\nu}_e \nu_\mu$ .

The SNS neutrino flux is ideal for probing  $\bar{\nu}_\mu \rightarrow \bar{\nu}_e$  and  $\nu_\mu \rightarrow \nu_e$  appearance, as well as  $\nu_\mu$  disappearance into sterile neutrinos. The appearance searches both have a two-fold coincidence for the rejection of background. For  $\bar{\nu}_\mu \rightarrow \bar{\nu}_e$  appearance, the signal is an  $e^+$  in coincidence with a 2.2 MeV  $\gamma$ :  $\bar{\nu}_e p \rightarrow e^+ n$ , followed by  $np \rightarrow D\gamma$ . For  $\nu_\mu \rightarrow \nu_e$  appearance, the signal is an  $e^-$  in coincidence with an  $e^+$  from the  $\beta$  decay of the ground state of  $^{12}N$ :  $\nu_e ^{12}C \rightarrow e^- ^{12}N_{gs}$ , followed by  $^{12}N_{gs} \rightarrow ^{12}C e^+ \nu_e$ . The disappearance search will detect the prompt 15.11 MeV  $\gamma$  from the neutral-current reaction  $\nu_\mu C \rightarrow \nu_\mu C^*(15.11)$ . This reaction has been measured by the KARMEN experiment, which has determined a cross section that is consistent with theoretical expectations.

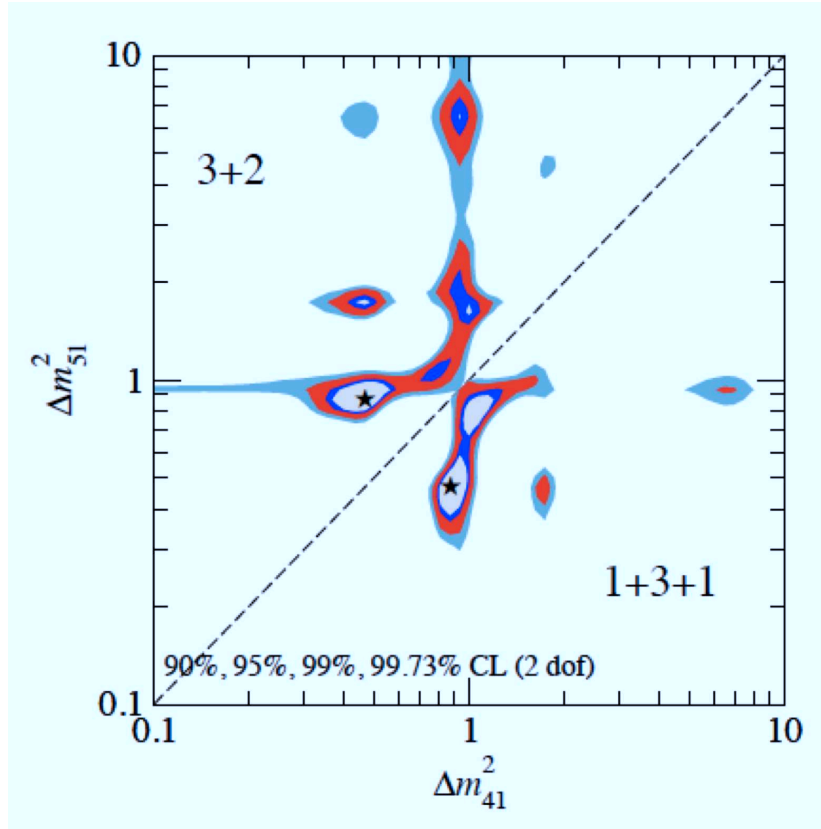


Figure 130. A global fit to the world neutrino plus antineutrino data indicates that the world data fit reasonably well to a 3+2 model with three active neutrinos plus two sterile neutrinos.

However, the KARMEN result was measured in a sample of 86 events, and carries a 20% total error. OscSNS will be able to greatly improve upon the statistical and systematic uncertainties of this measurement. If OscSNS observes an event rate from this neutral-current reaction that is less than expected, or if the event rate displays a sinusoidal dependence with distance, then this will be evidence for  $\nu_\mu$  oscillations into sterile neutrinos.

In addition to the neutrino oscillation searches, OscSNS will also make precision cross section measurements of  $\nu_e C \rightarrow e^- N$  scattering and  $\nu e^- \rightarrow \nu e^-$  elastic scattering. The former reaction has a well-understood cross section and can be used to normalize the total neutrino flux, while the latter reaction, involving  $\nu_\mu$ ,  $\nu_e$ , and  $\bar{\nu}_\mu$ , will allow a precision measurement of  $\sin^2 \theta_W$ . We have simulated many of the processes mentioned above, and in Figures 131 and 132 we present some of the most relevant results.

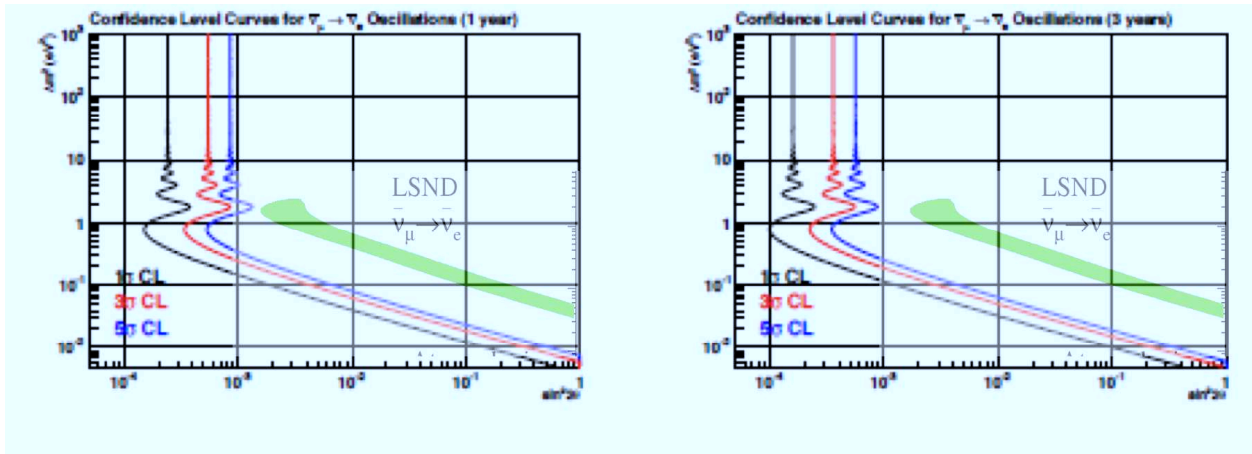


Figure 131. The OscSNS sensitivity curves for the simulated sensitivity to  $\bar{\nu}_\mu \rightarrow \bar{\nu}_e$  oscillations after one (left) and three (right) years of operation. Note that it has more than  $5\sigma$  sensitivity to the LSND result in 1 year.

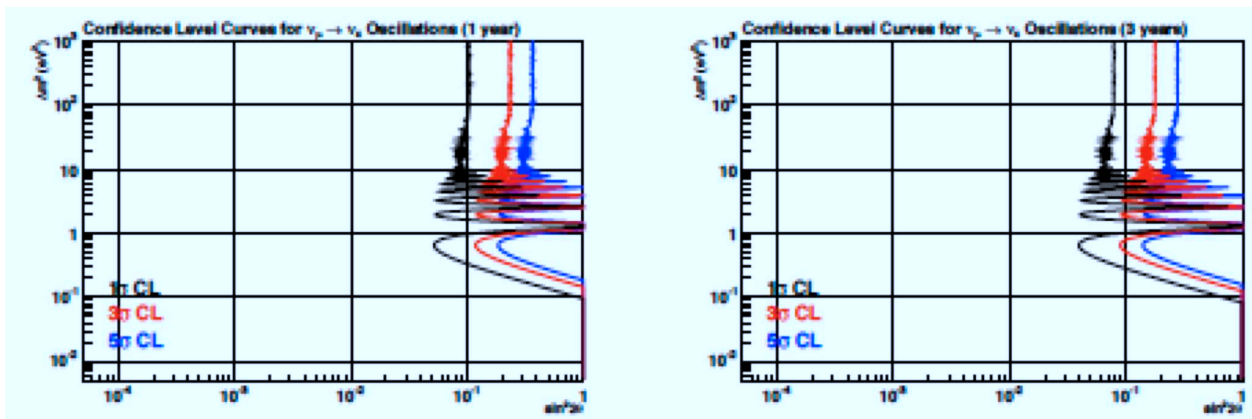


Figure 132. The OscSNS sensitivity curves for  $\nu_\mu$  disappearance for 1 and 3 years, respectively.

## 14. LSND Reloaded<sup>39</sup>

This note is based on Ref. [687] and more details can be found in there. The basic proposal is to repeat LSND [114, 688, 689] using a stopped pion neutrino source and Super-Kamiokande doped with Gadolinium [690–692] as detector. In this configuration both neutrino production and detection employ the same mechanism as LSND did. The crucial difference is that the cosmogenic background rate in Super-Kamiokande is negligible and the enormous size of the detector allows to map out the  $L/E$ -dependence of the effect over the range of  $0.3 - 2.2 \text{ m MeV}^{-1}$ . The  $\bar{\nu}_e$  signal for a typical choice of oscillation parameters is shown as red line in figure 133. At the same time any beam related background scales as  $L^3/L^{-2} = L$  shown as black dashed line in figure 133, which is quite distinct from the signal.

Super-Kamiokande has a fiducial mass of 22.5 kt compared to around 120 t in LSND and thus a relatively modest beam power can yield significant event rates, for details of the proton source, see [645, 693]. If we assume 300 kW beam power we obtain the following event rates per year of operation are, whereas the background event rate due to beam contamination is 765. Secondly,

$\Delta m^2$ [eV <sup>2</sup> ]	0.1	1	10	100
signal	29	1605	1232	1314

Table XXXV. Number of signal events after one year for  $\sin^2 2\theta = 10^{-3}$  including efficiency and energy resolution. Table and caption taken from [687].

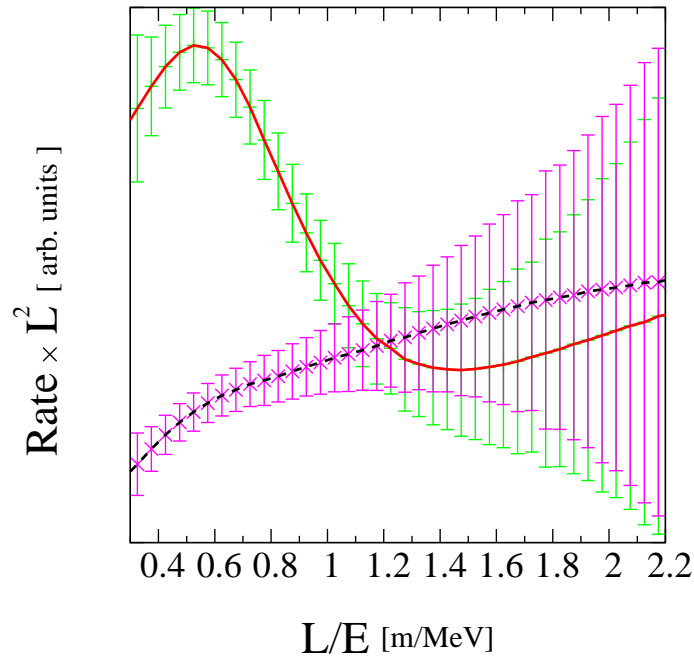


Figure 133. The signal event rate after one year weighted with  $L^2$  as function of the reconstructed baseline divided by reconstructed neutrino energy  $L/E$ , shown as solid line. The dashed line shows the background weighted with  $L^2$ . The error bars show the statistical errors only. The oscillation signal is computed for  $\sin^2 2\theta = 10^{-3}$  and  $\Delta m^2 = 2 \text{ eV}^2$ . Figure and caption taken from [687].

<sup>39</sup>Proposed by Sanjib K. Agarwalla and Patrick Huber (Virginia Tech).

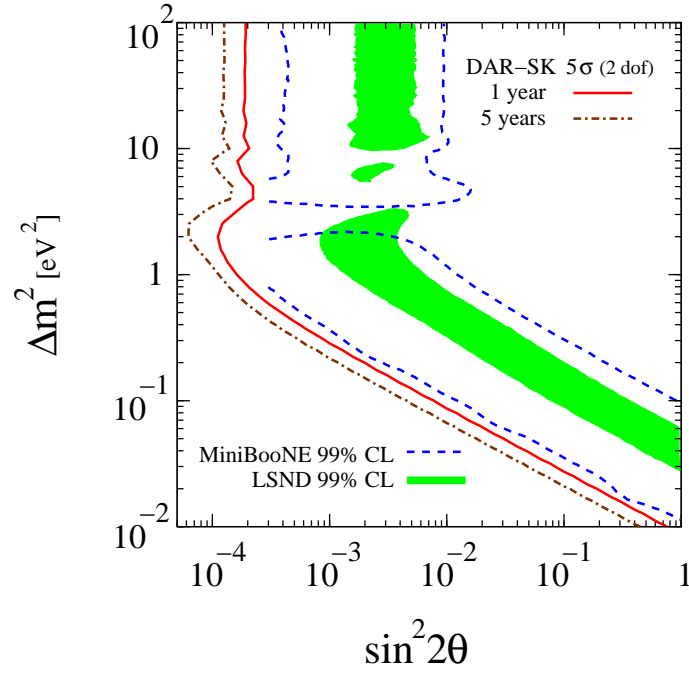


Figure 134. Sensitivity limit to sterile neutrino oscillation at the  $5\sigma$  confidence level, shown as red, solid line, labeled DAR-SK. This limit corresponds to a one year run. The green/gray shaded region is the LSND allowed region at 99% confidence level, whereas the dashed line is the MiniBooNE antineutrino run allowed region at 99% confidence level [117]. Figure and caption taken from [687].

the large rock overburden of approximately 2,700 mwe, compared to 120 mwe in LSND, reduces cosmic ray induced backgrounds to negligible levels [645, 693].

A detailed  $\chi^2$  analysis is presented in Ref. [687] which does include a 5% systematic error. The resulting  $5\sigma$  sensitivity in comparison to the allowed regions from LSND and MiniBooNE is shown in figure 134. A one year run at 300 kW beam power provides a significant test of LSND and MiniBooNE, or equivalently a 5 year run at 60 kW beam power. Spreading out the luminosity over several years is possible because cosmogenic backgrounds are very small compared to beam backgrounds.

In summary, the experiment proposed in Ref. [687] will allow to conclusively test the LSND and MiniBooNE claims for  $\bar{\nu}_\mu \rightarrow \bar{\nu}_e$  oscillations with more than  $5\sigma$  significance. Due to the ability to observe a wide range of  $L/E$  it will be straightforward to disentangle backgrounds and the signal as well as to identify the underlying physical mechanism for flavor transitions. Since both the production and detection mechanism as well as the energy and baseline are identical to the ones used in LSND, this will be the final test of LSND.

## 15. Kaon Decay-at-Rest for a Sterile Neutrino Search <sup>40</sup>

Monoenergetic muon neutrinos from positive charged kaon decay-at-rest can be used as a source for an electron neutrino appearance search in probing the neutrino oscillation parameter space near  $\Delta m^2 \sim 1 \text{ eV}^2$  [694]. The charged kaon decays to a muon and a 235.5 MeV muon neutrino ( $K^+ \rightarrow \mu^+ \nu_\mu$ ) about 64% of the time. Electron neutrinos, originating from these muon neutrinos ( $\nu_\mu \rightarrow \nu_e$ ), can be searched for in a narrow reconstructed energy window around 235.5 MeV. The signature of an electron neutrino event is the charged current, quasi-elastic interaction  $\nu_e n \rightarrow e^- p$ . The analogous muon neutrino charged current interaction as well as electron neutrino events, coming from the three body kaon decays  $K^+ \rightarrow \pi^0 e^+ \nu_e$  (BR=5.1%) and  $K_L^0 \rightarrow \pi^\pm e^\mp \nu_e$  (BR=40.6%), are the background for this appearance search. However, these event classes can also be used to perform the flux, cross section, and *in-situ* background measurements necessary to extract the oscillation probability from an observed electron neutrino signal.

### Experimental description

This experimental design calls for an intense source of charged kaon decays. A large copper block is placed just downstream of a powerful  $\gtrsim 3 \text{ GeV}$  kinetic energy proton beam. Kaons created in primary proton-copper and secondary interactions quickly come to rest and subsequently decay. A LArTPC-based detector is envisioned opposite the primary proton beam's direction at a baseline of 160 m from the isotopic neutrino source in order to search for electron neutrino appearance events near a reconstructed energy of 235.5 MeV. A schematic of the experimental design can be seen in Fig. 135. The baseline is chosen in consideration of sensitivity to LSND and the  $1/r^2$  dependence of the flux. The oscillation maximum at the LSND best fit  $\Delta m^2 = 1.2 \text{ eV}^2$  occurs at about 240 m for 235.5 MeV neutrinos.

The Booster Neutrino Beam (BNB) at Fermilab, currently featuring an 8 GeV kinetic energy beam providing  $\sim 3 \times 10^{20}$  protons on target (POT) every year, has been considered as a source for such an experiment—although many proton beam facilities around the world can be used. The precise calorimetric reconstruction, background identification, and three dimensional imaging capabilities of LArTPCs make the technology optimal for this design [695].

### Flux, nuclear effects, background and detector resolution

The signal-inducing monoenergetic muon neutrino and all-energy background electron neutrino flux are determined using the Geant4 simulation package [659]. Both decay-at-rest and decay-in-flight kaons (charged and neutral) are studied. The simulation predicts a monoenergetic  $\nu_\mu$ /proton yield of 0.038.

Nuclear effects and detector resolution act to significantly smear the reconstructed energy of signal and background events, making the nominally distinctive monoenergetic signal more difficult to identify. The NuWro neutrino event generator and its argon spectral function implementation are employed for simulating neutrino events on an argon nucleus [696, 697]. Intra-nuclear interactions, often resulting in multiple ejected nucleons, are simulated as well.

---

<sup>40</sup>Proposed by J. Spitz (MIT)



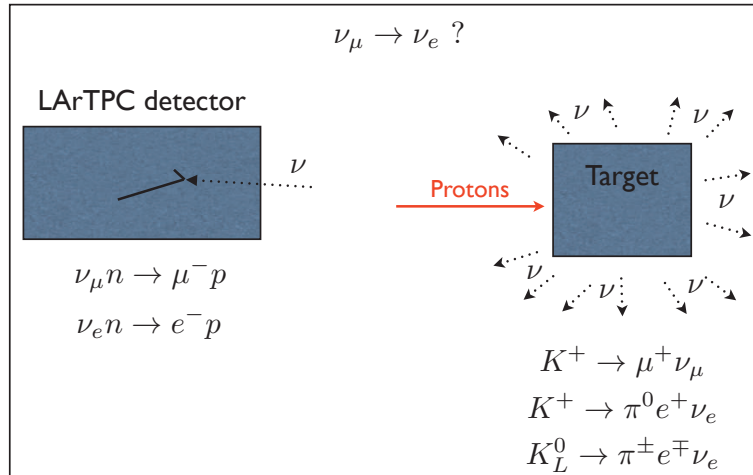


Figure 135. A kaon decay-at-rest based experimental design for probing the sterile neutrino parameter space. The relevant kaon decay modes and neutrino interactions are shown on the right and left, respectively.

The dominant background contribution to the electron neutrino appearance search comes from three body charged kaon decay at rest ( $K^+ \rightarrow \pi^0 e^+ \nu_e$ ) which produces electron neutrinos with maximum  $\sim 226$  MeV energy. The concept described here can be thought of as similar to that of a neutrinoless double beta decay search with a signal sought near the endpoint of a well predicted and measured background spectrum. There are also background contributions from three body kaon decay-in-flight with neutrino energies up to and exceeding 235.5 MeV.

The background-free identification and precise calorimetric reconstruction of electron neutrino events is vital to this experimental concept. Along with differentiating muon and electron events, calorimetrically reconstructing the outgoing proton(s) and electron-induced electromagnetic shower are important for distinguishing the monoenergetic signal from background. The reconstruction resolution assumptions employed for the sensitivity estimates discussed later are consistent with currently available LArTPC-based measurements [698, 699].

A “signal region”, around a reconstructed energy of 235.5 MeV, is defined in consideration of optimizing signal-to-background and having enough events left over to recognize a signal. The expected signal and background rates, after accounting for nuclear and detector resolution effects, are shown in Fig. 136. The signal region requirement, visible in the figure, leaves approximately 45% of signal events. Although the chosen size and location of this region is largely based on the neutrino event generation nuclear models employed in this study as well as assumptions about the detector’s calorimetric resolution, the actual signal region can be tuned once more information is available. Furthermore, the background prediction can be refined with *in-situ* measurements below the signal region, most relevant for understanding the three body decay-at-rest spectrum ( $K^+ \rightarrow \pi^0 e^+ \nu_e$ ), and above the signal region, most relevant for understanding the charged and neutral kaon decay-in-flight induced background. The relationship between true neutrino energy and reconstructed energy, as well as relevant cross section measurements, can be obtained with these electron neutrinos along with the thousands of monoenergetic muon neutrinos expected.

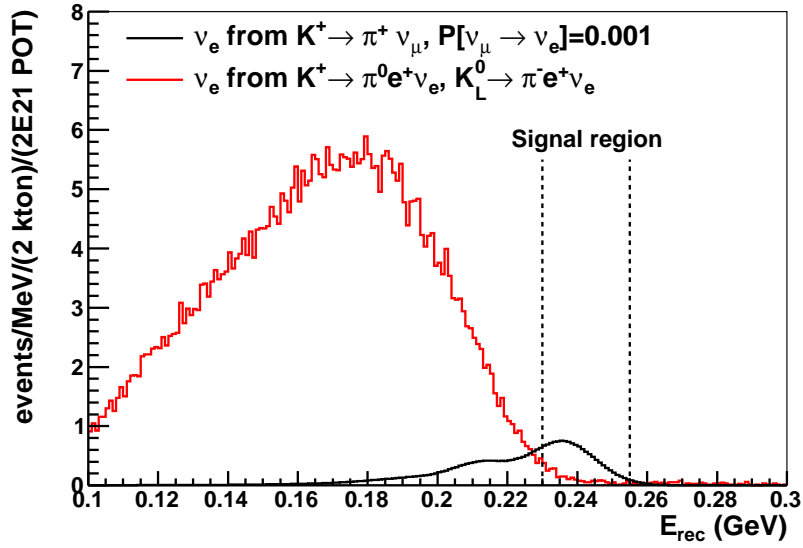


Figure 136. The expected background rate alongside an injected electron neutrino appearance signal [ $P(\nu_\mu \rightarrow \nu_e) = 0.001$ ]. Note that the signal originates from oscillated monoenergetic muon neutrinos at 235.5 MeV. The reconstructed energy signal region is denoted by the vertical lines.

### Sensitivity

A simple single bin, counting experiment is employed in an attempt to discern a potential oscillation signal from background inside the region of interest. Along with signal region fine tuning, a more sophisticated analysis beyond the counting only experiment can be employed in the future for oscillation sensitivity improvement.

A 2 kton detector and  $2 \times 10^{21}$  POT exposure are considered for oscillation sensitivity studies. These values have been chosen in order to provide  $\geq 5\sigma$  sensitivity to most of the LSND allowed region. As an example, approximately 16  $\nu_e$ -like (signal+background) events above a background of 3 events are expected with an oscillation probability of  $P(\nu_\mu \rightarrow \nu_e) = 0.001$ . The most relevant experimental parameters and assumptions can be seen in Table XXXVI.

The sensitivity of the experiment to the parameter space near  $\Delta m^2 \sim 1 \text{ eV}^2$ , using a two neutrino oscillation probability, is shown in Fig. 137. The curves have been arrived at using fully frequent confidence intervals via the profile log-likelihood method [700, 701]. Sensitivity is defined based on the median upper limit that would be obtained by a set of experiments measuring just background, in the absence of a true signal [394]. A 2 kton detector and  $2 \times 10^{21}$  POT exposure provides  $> 5\sigma$  sensitivity to most of the 90% CL LSND allowed region. Although this mass and exposure can be considered optimistic, the idea of utilizing the monoenergetic muon neutrino from kaon decay-at-rest as a source for an electron neutrino appearance search is one that can be employed at a number of current and future proton facilities around the world.

Proton target	Copper
$\frac{\nu_\mu(235.5 \text{ MeV})}{\text{proton}}$ yield at $T_p = 8 \text{ GeV}$	0.038
Exposure	$2 \times 10^{21}$ protons on target
Baseline	160 m
Neutrino target	$^{40}\text{Ar}$ (22 neutrons)
Neutrino target mass	2 kton
Detection efficiency	100%
$\nu_e \sigma_{\text{CC}}$ at 235.5 MeV	$1.9 \times 10^{-43} \text{ m}^2/\text{neutron}$
$\nu_\mu \sigma_{\text{CC}}$ at 235.5 MeV	$1.3 \times 10^{-43} \text{ m}^2/\text{neutron}$
$\frac{\Delta E}{E}$ for $e^-$ reconstruction	$0.33/\sqrt{E(\text{MeV})} + 0.012$
$\frac{\Delta T}{T}$ for proton reconstruction	0.10
Background syst. uncertainty	25%
Neutrino baseline spread	$\pm 10 \text{ m}$

Table XXXVI. The relevant parameters and assumptions employed in this study.

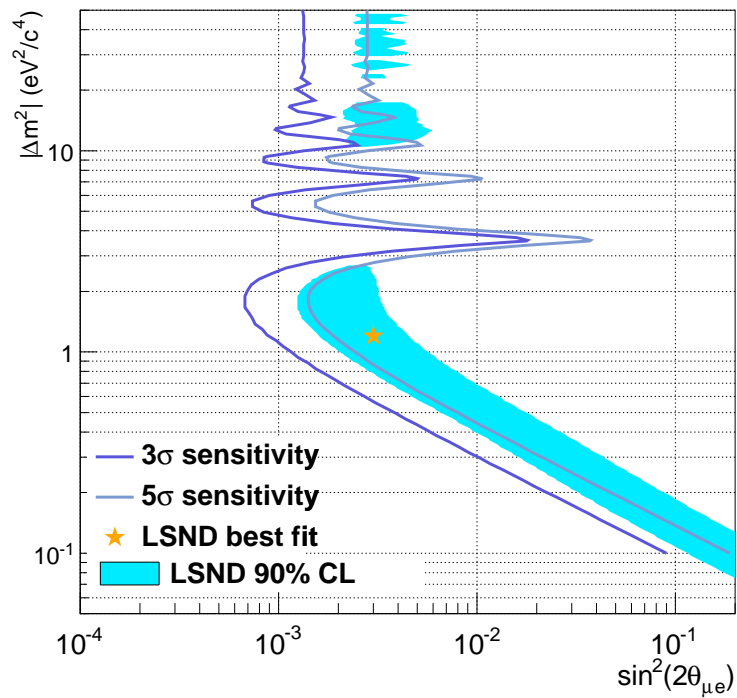


Figure 137. The sensitivity of a kaon decay-at-rest based electron neutrino appearance experiment to the LSND allowed region.

## 16. The MINOS+ Project<sup>41</sup>

The MINOS contributions to the body of knowledge on sterile neutrino searches will be continued and improved upon by the proposed MINOS+ project [702]. In MINOS+, both MINOS detectors will continue operation during the NO $\nu$ A era (starting in 2013), using the NuMI beam upgraded to 700 kW of beam power. MINOS+ is expected to run for at least two years in neutrino and one year in antineutrino mode. The expected sensitivities to  $\theta_{24}$  are shown in Fig. 138 for neutrino and antineutrino running. The 3+1 sterile neutrino oscillation model employed in producing these sensitivities includes the effects of oscillations at the Near Detector short baseline in the Far Detector predicted spectrum and waive the restrictions on the value of  $\Delta m_{43}^2$  applied in the MINOS analysis described in Section III J. The MINOS+ sensitivities to neutrino disappearance show roughly a factor of 2 improvement over the current exclusion limits from MINOS. Compared to other experiments that study neutrino disappearance over short baselines, MINOS+ will place the most stringent limit on neutrino disappearance for  $\Delta m_{43}^2 \lesssim 2\text{eV}^2$  and on antineutrino disappearance for  $\Delta m_{43}^2 \lesssim 20\text{eV}^2$ .

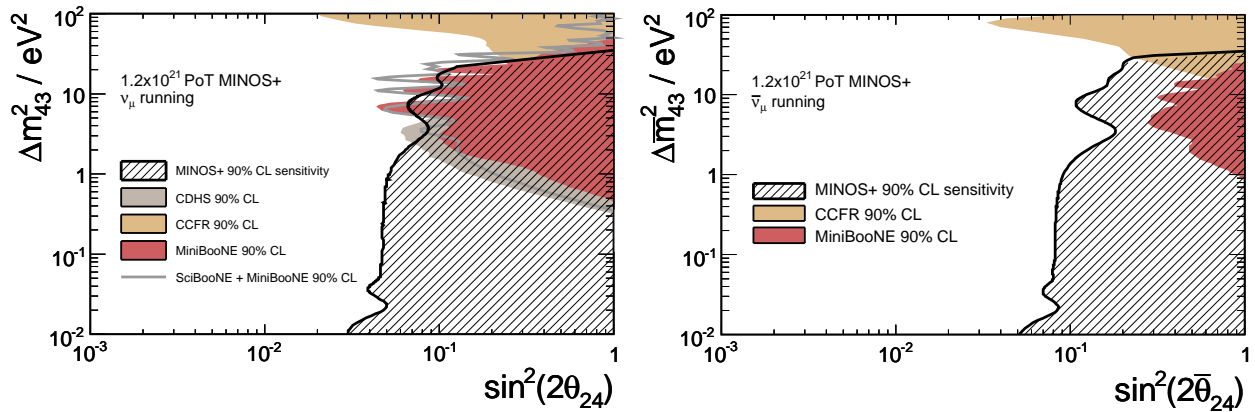


Figure 138. Expected MINOS+ 90% C.L. exclusion regions for the  $\theta_{24}$  mixing angle compared to other disappearance measurements for neutrino(left) and antineutrino (right) running.

<sup>41</sup>Proposed by the MINOS Collaboration  
(<http://www-numi.fnal.gov/>)

## 17. The BooNE Proposal<sup>42</sup>

The MiniBooNE detector began to take data on September 1, 2002. The experiment was designed to search for the appearance of excess electron (anti) neutrinos in a primarily muon (anti) neutrino beam. While resources were not available to construct both a near and far detector at the time, it was envisioned that a second detector would be constructed at a location appropriate to the observed signal if MiniBooNE should see a signal. The second detector would be able to differentiate between a true neutrino oscillation effect and an unforeseen new process or background. A number of scientists now believe that a significant signal has been observed at MiniBooNE, and a collaboration of scientists is forming in order to upgrade MiniBooNE to a twodetector experiment: BooNE.

MiniBooNE has enjoyed a remarkable 9 years of smooth operation, during which an astounding  $6 \times 10^{20}$  protons on target (POT) have been delivered in neutrino mode, and an even more astounding  $1 \times 10^{21}$  POT have been delivered in antineutrino mode. The neutrino mode data has yielded a low-energy excess of  $129 \pm 20(stat) \pm 38(sys)$  events at reconstructed neutrino energies below 475 MeV. That low-energy excess is not described well by a simple two-neutrino model, but can be accommodated by an extended 3 active + 2 sterile neutrino model, fit to the worlds relevant neutrino data. While the statistical significance of the low-energy excess is  $6\sigma$ , the overall significance is limited to  $3\sigma$  by the systematic error in the estimation of the background, either in the low energy range of 200-475 MeV or in the full range 200-1250 MeV. That systematic error is related to the error in the detector acceptance or efficiency for  $\pi^0$  background events, and to a lesser extent, the flux of neutrinos, and the neutrino-nucleus cross sections. Similarly, an excess of is observed in antineutrino mode of  $54.9 \pm 17.4(stat) \pm 16.3(sys)$  events events, consistent with the neutrino-mode data. The antineutrino-mode excess is limited in statistical power to  $3\sigma$  and appears to have a higher energy component of 500-600 MeV.

We now believe we have explored all the possible avenues for explaining the excess events by conventional processes and have exhausted the possible ways to reduce the systematic errors via further analysis. We believe the construction of a near detector, BooNE[703], at 200 meters from the Booster Neutrino Beam proton target to be the most expedient way understand whether or not the excess events observed by MiniBooNE are caused by an oscillation process or some other process that scales more conventionally by  $L^{-2}$ . The primary motivation for building a near detector, rather than a detector further away, is that the neutrino interaction rate will be over 7 times larger, and the measurement will precisely determine the neutrino-related backgrounds within 6 months of running. A far-detector would take much longer to accumulate sufficient statistics. The combination of the present MiniBooNE neutrino-mode data, plus a 4-month ( $1 \times 10^{20}$  POT or 700,000 neutrino events) neutrino-mode run with a near detector, would result in a  $5\sigma$  sensitivity to whether or not the low energy excess is an oscillation effect. With MiniBooNEs anticipated  $1.5 \times 10^{21}$  POT in antineutrino-mode, BooNE will provide a unique measurement of antineutrino appearance and disappearance with an 8 month run ( $2 \times 10^{20}$  POT or 140,000 events) required for comparable statistics.

Furthermore, a two-detector BooNE experiment, in conjunction with the ultra-fine-grained MicroBooNE liquid argon TPC, would be a tremendously powerful, oscillation-hunting combination. While MicroBooNE does not anticipate any antineutrino-mode operation, the operation of BooNE during the MicroBooNE neutrino-mode run would double the statistics of the present MiniBooNE

---

<sup>42</sup>Proposed by the BooNE Collaboration

neutrino data to  $1.2 \times 10^{21}$  POT. That powerful trio of detectors would yield precise measurements of both electron-neutrino appearance and muon neutrino disappearance, which are tightly coupled in nearly all sterile-neutrino oscillation models

## 18. Search for anomalies with muon spectrometers and large LArTPC imaging detectors at CERN<sup>43</sup>

An experimental search for sterile neutrinos at new CERN-SPS neutrino beam has been recently proposed [704]. The experiment is based on two identical LAr-TPCs [705, 706] followed by magnetized spectrometers [707], observing the electron and muon neutrino events at the Far and Near positions 1600 and 300 m from the proton target, respectively (Figure 139). The project will exploit the ICARUS T600 detector, the largest LAr-TPC ever built with a size of about 600 t of imaging mass, now running in the LNGS underground laboratory exposed to the CNGS beam, moved to the CERN Far position. An additional 1/4 of the T600 detector (T150) will be constructed and located in the “Near” position. Two spectrometers will be placed downstream of the two LAr-TPC detectors to greatly complement the physics capabilities. Spectrometers will exploit a classical dipole magnetic field with iron slabs, and a new concept air-magnet, to perform charge identification and muon momentum measurements from low energy ( $< 1$  GeV) in a wide energy range over a large transverse area ( $> 50$  m<sup>2</sup>).



Figure 139. The new SPS North Area neutrino beam layout. Main parameters are: primary beam: 100 GeV; fast extracted from SPS; target station next to TCC2,  $\sim 11$  m underground; decay pipe: 100 m, 3 m diameter; beam dump: 15 m of Fe with graphite core, followed by muon stations; neutrino beam angle: pointing upwards; at  $\sim 3$  m in the far detector  $\sim 5$  mrad slope.

In the two positions, the shapes of the radial and energy spectra of the  $\nu_e$  beam component are practically identical. Comparing the two detectors, in absence of oscillations, all cross sections and experimental biases cancel out, and the two experimentally observed event distributions must be identical. Any difference of the event distributions at the locations of the two detectors might be attributed to the possible existence of  $\nu$ -oscillations, presumably due to additional neutrinos with a mixing angle  $\sin^2(2\theta)$  and a larger mass difference  $\Delta m^2$ .

The superior quality of the LAr imaging TPC, now widely experimentally demonstrated, and in particular its unique *electron* -  $\pi^0$  discrimination allows full rejection of backgrounds and offers

<sup>43</sup>Proposed by the ICARUS + NESSiE Collaborations [704].

a lossless  $\nu_e$  detection capability. The determination of the muon charge with the spectrometers allows the full separation of  $\nu_\mu$  from  $\bar{\nu}_\mu$  and therefore controlling systematics from muon misidentification largely at high momenta.

Two main anomalies will be explored with both neutrino and antineutrino focused beams. According to the first anomaly, emerged in radioactive sources and reactor neutrino experiments (see Sections III G and III H, some of the  $\nu_e$  ( $\bar{\nu}_e$ ) and/or of the  $\nu_\mu$  ( $\bar{\nu}_\mu$ ) events might be converted into invisible (sterile) components, leading to observation of oscillatory, distance dependent disappearance rates. In a second anomaly (following LSND and MiniBooNE observations [114, 116, 117, 532]) some distance dependent  $\nu_\mu \rightarrow \nu_e$  oscillations may be observed as  $\nu_e$  excess, especially in the antineutrino channel. The disentangling of  $\nu_\mu$  from  $\bar{\nu}_\mu$  will allow to exploit the interplay of the different possible oscillation scenario, as well as the interplay between disappearance and appearance of different neutrino states and flavors. Moreover the NC/CC ratio will provide a sterile neutrino oscillation signal by itself and it will beautifully complement the normalization and the systematics studies. This experiment will offer remarkable discovery potentialities, collecting a very large number of unbiased events both in the neutrino and antineutrino channels, largely adequate to definitely settle the origin of the  $\nu$ -related anomalies.

### The new SPS neutrino facility

To explore the interesting neutrino  $\Delta m^2 \sim 1 \text{ eV}^2$  region the Far distance has been chosen at 1.6 km with a central value of the onaxis neutrino beam energy spectrum around  $E_\nu \sim 2 \text{ GeV}$  (Figure 140). A proton beam intensity of  $4.5 \times 10^{19}$  pot/year at 100 GeV energy has been assumed as a conservative reference in order to produce high intensity  $\nu$  beam and to minimize the beam related background expected at the Near Detector located at 300 m. A fast proton extraction from SPS is also required for the LAr-TPC operation at surface in order to time tag the beam related events among the cosmic ray background.

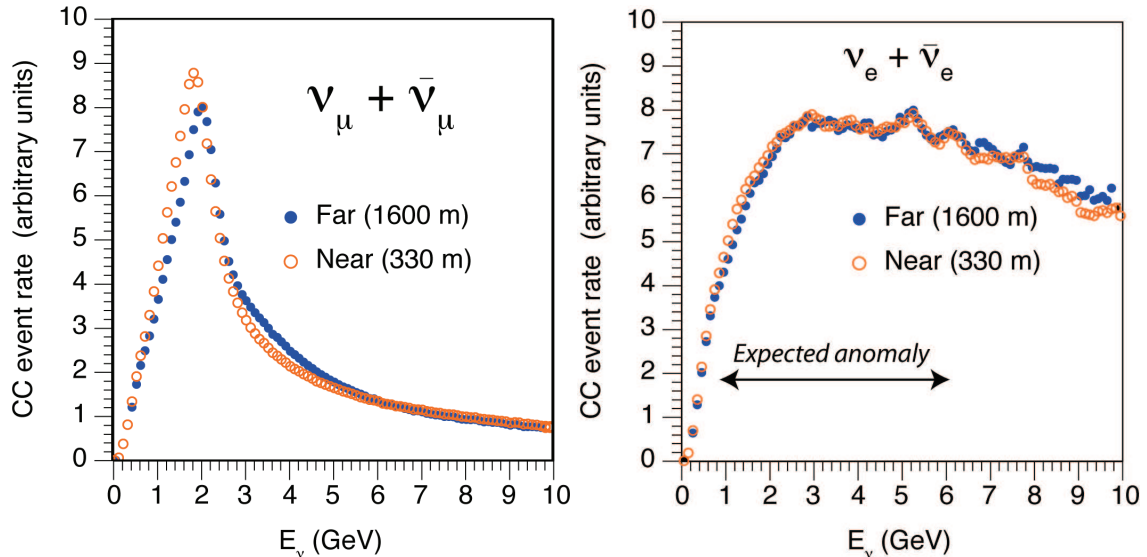


Figure 140. Muon (left) and electron (right) neutrino CC interaction spectra, at Near and Far positions.



## Expected sensitivities to neutrino oscillations

A complete discussion of  $\nu_\mu \rightarrow \nu_e$  oscillation search both in appearance and disappearance modes has been presented in the SPSC-P345 document [705, 706], that includes the genuine event selection and background rejection in the LAr-TPC. In particular, due to the excellent  $\pi^0$  to electron separation, a  $\pi^0$  rejection at  $10^3$  level is obtained when requiring at least 90% electron recognition efficiency. The effects of the high-energy event tail in the event selection has been carefully studied: the resulting background is negligible, of the same order of the residual NC background.

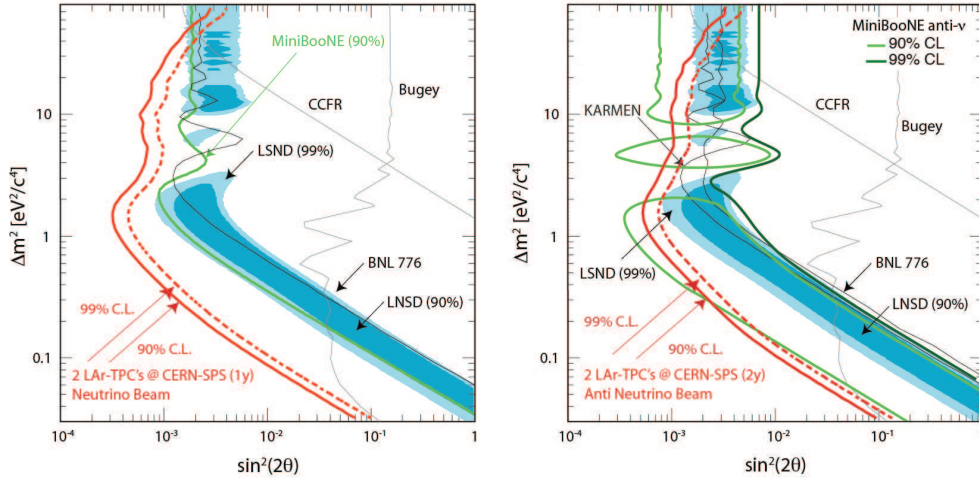


Figure 141. Expected sensitivity for the proposed experiment exposed at the CERN-SPS neutrino beam (left) and antineutrino (right) for  $4.5 \times 10^{19}$  pot (1 year) and  $9.0 \times 10^{19}$  pot (2 years), respectively. The LSND allowed region is fully explored in both cases.

In addition to the  $\nu_\mu \rightarrow \nu_e$  oscillation studies mentioned above,  $\nu_\mu$  oscillation in disappearance mode was discussed at length in [707], by using large mass spectrometers with high capabilities in charge identification and muon momentum measurement. It is important to note that all sterile models predict large  $\nu_\mu$  disappearance effects together with  $\nu_e$  appearance/disappearance. To fully constrain the oscillation searches, the  $\nu_\mu$  disappearance studies have to be addressed. Much higher disappearance probabilities are expected than in appearance mode, where relative amplitudes as large as 10% are possible. The spectrometers will be able to correctly identify about 40% of all the CC events produced in, and escaped from, the LAr-TPCs, both in the near and far sites. That will greatly increase the fraction of CC events with charge identification and momentum measurement. Therefore complete measurement of the CC event spectra will be possible, along with the NC/CC event ratio (in synergy with the LAr-TPC), and the relative background systematics.

The large mass of the magnets will also allow an internal check of the NC/CC ratio in an extended energy range, and an independent measure of the CC oscillated events.

A sensitivity of  $\sin^2(2\theta) > 3 \times 10^{-4}$  (for  $|\Delta m^2| > 1.5 \text{ eV}^2$ ) and  $|\Delta m^2| > 0.01 \text{ eV}^2$  (for  $\sin^2(2\theta) = 1$ ) at 90% C.L. is expected for the  $\nu_\mu \rightarrow \nu_e$  transition with one year exposure ( $4.5 \times 10^{19}$  pot) at the CERN-SPS  $\nu_\mu$  beam (Figure 141 left). The parameter space region allowed by the LSND experiment is fully covered, except for the highest  $\Delta m^2$  region. The sensitivity has been computed according to the above described particle identification efficiency and assuming a 3% systematic uncertainty in the prediction of Far to Near  $\nu_e$  ratio. A further control of the overall systematics

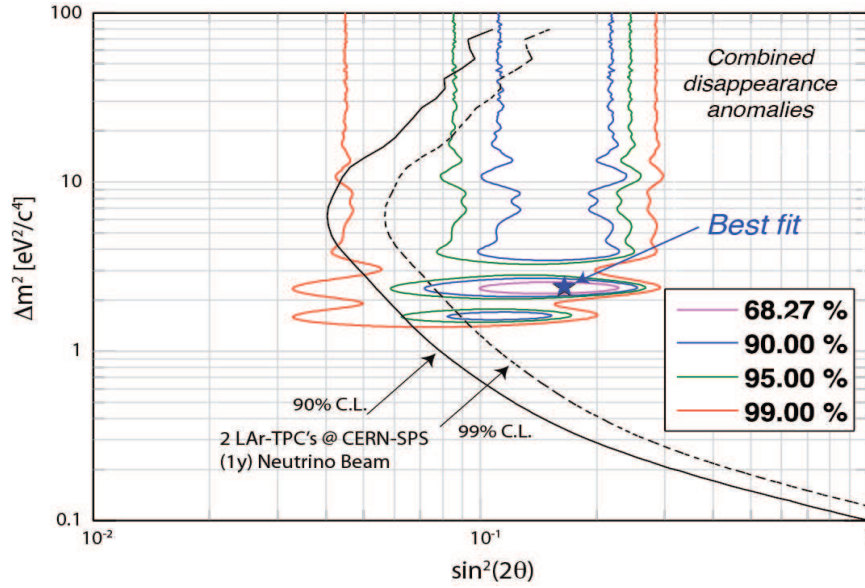


Figure 142. Oscillation sensitivity in  $\sin^2(2\theta)$  vs  $\Delta m^2$  distribution for 1 year data taking. A 3% systematic uncertainty on energy spectrum is included. Combined anomalies from reactor neutrino, Gallex and Sage experiments are also shown.

will be provided by the LAr and spectrometer combined measurement of CC spectra in the Near site and over the full energy range.

	NEAR (Negative foc.)	NEAR (Positive foc.)	FAR (Negative foc.)	FAR (Positive foc.)
$\nu_e + \bar{\nu}_e$ (LAr)	35 K	54 K	4.2 K	6.4 K
$\nu_\mu + \bar{\nu}_\mu$ (LAr)	2000 K	5200 K	270 K	670 K
Appearance Test Point	590	1900	360	910
$\nu_\mu$ CC (NESSiE+LAr)	230 K	1200 K	21 K	110 K
$\nu_\mu$ CC (NESSiE alone)	1150 K	3600 K	94 K	280 K
$\bar{\nu}_\mu$ CC (NESSiE+LAr)	370 K	56 K	33 K	6.9 K
$\bar{\nu}_\mu$ CC (NESSiE alone)	1100 K	300 K	89 K	22 K
Disappearance Test Point	1800	4700	1700	5000

Table XXXVII. The expected rates of interaction (LAr) and reconstructed (NESSiE) events 1 year of operation. Values for  $\Delta m^2$  around  $2 \text{ eV}^2$  are reported as example.

In antineutrino focusing, twice as much exposure ( $0.9 \times 10^{20}$  pot) allows to cover both the LSND region and the new MiniBooNE results (Figure 141 right) [114, 116, 117, 532]. Both favored MiniBooNE parameter sets, corresponding to two different energy regions in the MiniBooNE antineutrino analysis, fall well within the reach of this proposal. In Figure 142 the sensitivity for  $\nu_e$  disappearance search in the  $\sin^2(2\theta)$ ,  $\Delta m^2$  plane is shown for one year data taking. The oscillation parameter region related to the anomalies from the combination of the published reactor neutrino experiments, Gallex and Sage calibration sources experiments is completely explored.

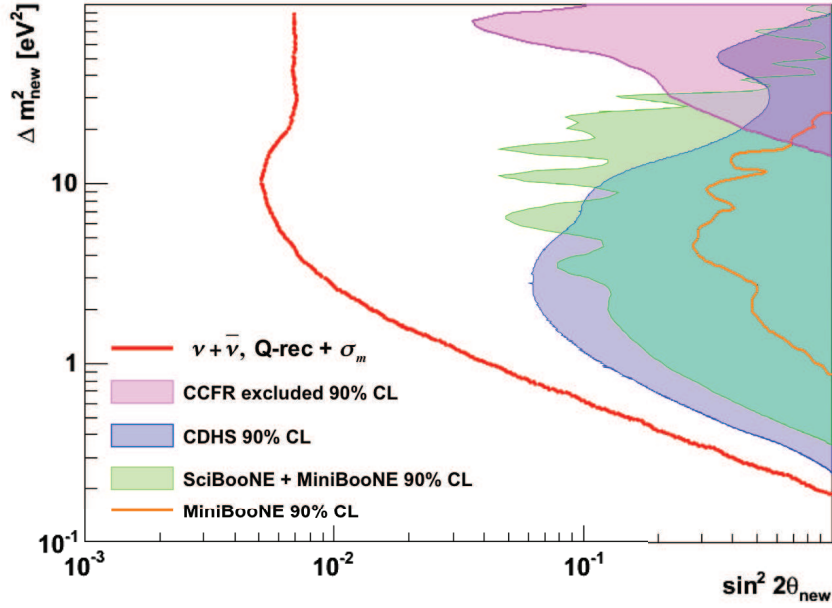


Figure 143. Sensitivity plot (at 90% C.L.) considering 3 years of the CERN-SPS beam (2 years in antineutrino and 1 year in neutrino mode) from CC events fully reconstructed in NESSiE+LAr. Red line:  $\nu_\mu$  exclusion limit. The three filled areas correspond to the present exclusion limits on the  $\nu_\mu$  from CCFR, CDHS and SciBooNE+MiniBooNE experiments (at 90% C.L.). Orange line: recent exclusion limits on  $\nu_\mu$  from MiniBooNE alone measurement.

Osc. type	Neutrinos	Experiments
$\theta_{12}$	$\nu_e$ (solar, reactors)	SNO, SK, Borexino, Kamland
$\theta_{23}$	$\nu_\mu$ (atmospheric, accelerators)	SK, Minos, T2K
$\theta_{13}$	$\nu_e$ (reactors)	Daya Bay, Reno, Double Chooz
$\theta_{14}$	$\nu_e$ (reactors, radioactive sources)	SBL Reactors, Gallex, Sage. <b>This Proposal</b>
$\theta_{24}$	$\nu_\mu$ (accelerators)	CDHS, MiniBooNE. <b>This Proposal</b>

Table XXXVIII. Measurements of the mixing angle as provided by different experiments.

The  $\nu_\mu$  disappearance signal is well studied by the spectrometers, with a very large statistics and disentangling of  $\nu_\mu$  and  $\bar{\nu}_\mu$  interplay [112, 113]. As an example, Figure 143 shows the sensitivity plot (at 90% C.L.) for two years negative-focusing plus one year positive-focusing. A large extension of the present limits for  $\nu_\mu$  by CDHS and the recent SciBooNE+MiniBooNE will be achievable in  $\sin^2(2\theta)$ ,  $\Delta m^2$ .

For 1 year of operation, either with negative or positive polarity beam, Table XXXVII reports the expected interaction rates in the LAr-TPCs at the Near (effective 119 t) and Far locations (effective 476 t), and the expected rates of fully reconstructed events in the NESSiE spectrometers at the Near (effective 241 t) and Far locations (effective 661 t), with and without LAr contribution. Both  $\nu_e$  and  $\nu_\mu$  disappearance modes will be used to add conclusive information on the sterile mixing angles as shown in the Table XXXVIII.

## 19. Liquid Argon Time Projection Chambers<sup>44</sup>

Liquid Argon Time Projection Chambers (LArTPCs) use a recently developed technology for neutrino detection. These detectors, in addition to offering good neutrino efficiency, allow for excellent background rejection. Their good calorimetric reconstruction, their high resolution and their good particle ID, demonstrated both in simulations and measurements (*e.g.* ref [708]), make these detectors a very attractive choice for high precision neutrino physics.

### MicroBooNE

MicroBooNE is a new experiment currently under construction. The MicroBooNE detector is a 170 ton LArTPC (61.4 tons fiducial volume). The  $2.5\text{m} \times 2.3\text{m} \times 10.4\text{m}$  TPC, shown in Figure 144, will be located 470m downstream of the Booster Neutrino Beam (BNB) at Fermilab, and consequently be exposed to the same  $\nu_\mu$ -dominated beam as MiniBooNE. MicroBooNE will start taking data in 2013. More details on the MicroBooNE experiment can be found here [709–711].

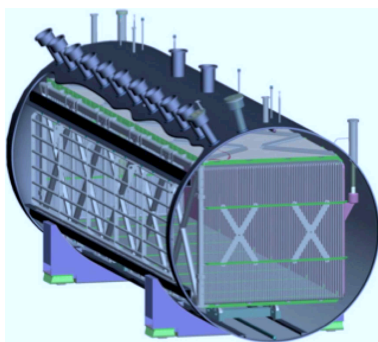


Figure 144. The MicroBooNE detector. The  $2.5\text{m} \times 2.3\text{m} \times 10.4\text{m}$  TPC is inserted into the cryostat.

The main physics goal for the MicroBooNE experiment is to address the MiniBooNE low-energy excess [117]. During its neutrino-mode run, the MiniBooNE experiment observed a  $3\sigma$  excess of events in the 200-475 MeV range. The excess events are electron-like, which could be either electrons or photons. Water Cherenkov detectors do not have the capability to distinguish between electrons and photons, since both produce electromagnetic showers.

In order to address the excess, the MicroBooNE detector will be located close to MiniBooNE, so that the L/E conditions are nearly identical. The MicroBooNE detector will offer a better  $\nu_e$  efficiency, being about two times that of MiniBooNE. In addition, using the ability of LArTPCs to differentiate between electrons and photons, by examining the  $dE/dx$  along the first few centimeters of the electromagnetic shower, MicroBooNE will be able to tell if the MiniBooNE excess comes from electron or photon events. MicroBooNE will have a  $>5\sigma$  sensitivity (statistical) if the events are due to electrons and a  $4\sigma$  sensitivity (statistical) if the events are due to photons. Finally, MicroBooNE's low energy threshold (tens of MeV) will allow to study how the excess varies at lower energy.

<sup>44</sup>Proposed by the MicroBooNE Collaboration  
(<http://www-microboone.fnal.gov/public/collaboration.html>).

MicroBooNE is approved to run in neutrino mode for 3 years, accumulating  $6.6 \times 10^{20}$  Protons On Target (POTs). With this amount of data, MicroBooNE will offer sensitivity to a sterile neutrino search considering a 3+1 neutrino model, which will be comparable to the MiniBooNE's neutrino-mode sensitivity. The left plot in Figure 145 shows the sensitivity to a 3+1 neutrino model (statistical errors only), for  $6.6 \times 10^{20}$  POTs in neutrino mode, for MicroBooNE (61.4 tons fiducial volume).

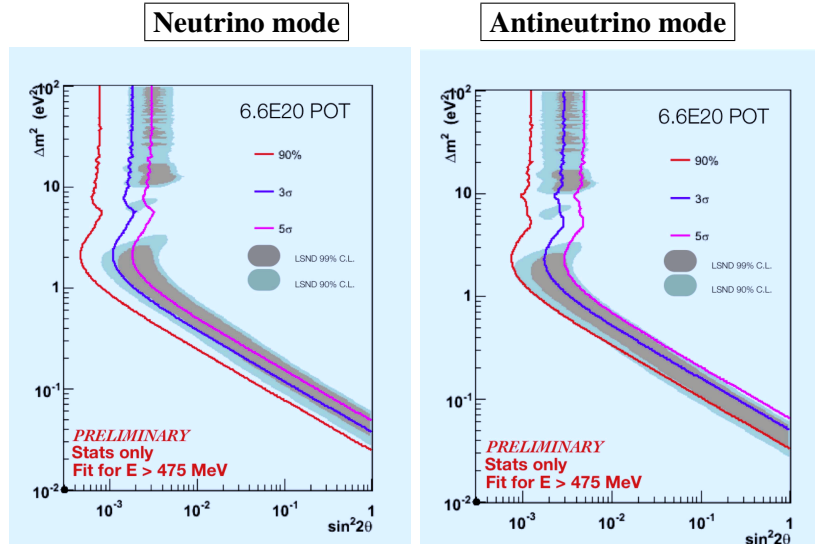


Figure 145. Sensitivity curves (statistical errors only) for the MicroBooNE detector (61.4 tons fiducial volume, 470m from the BNB) to a 3+1 neutrino model in the  $(\Delta m^2, \sin^2 2\theta)$  parameter space, for  $6.6 \times 10^{20}$  POTs. The left plot is for neutrino mode and the right plot is for the antineutrino mode. The fits are done for energies above 475 MeV only.

It could, however, be possible to run the MicroBooNE experiment in antineutrino mode as well, as a phase 2 for MicroBooNE. Motivation for antineutrino running could be justified by LSND's antineutrino result and MiniBooNE's (final) antineutrino results. The right plot in Figure 145 shows the sensitivity to a 3+1 neutrino model (statistical errors only), for  $6.6 \times 10^{20}$  POTs in antineutrino mode.

MicroBooNE will have a definitive answer ( $5\sigma$  level) to the MiniBooNE's low-energy excess, if the excess events are due to  $\nu_e$ . When looking at the simple 3+1 neutrino model to search for sterile neutrinos, MicroBooNE will offer good sensitivity in the region allowed by LSND. MicroBooNE, using a statistical error only analysis, will be able to exclude the allowed LSND region at almost  $3\sigma$  level in neutrino mode and at 90% C.L. in antineutrino mode. However, MicroBooNE will not have the sensitivity to exclude the LSND allowed region at the  $5\sigma$  level.

## Two LAr-detector experiment at FNAL

An interesting and powerful way to probe the MiniBooNE/LSND anomalies would be to combine the MicroBooNE detector, described in the previous section, to another, larger, LArTPC (LarLAr) in a near/far configuration. A near/far configuration would considerably reduce the systematic errors, while the size of the second detector would increase statistics significantly, which are expected to be the limiting factor for a MicroBooNE-only search.

The LBNE collaboration is currently designing a 1kt LArTPC as an engineering prototype [712]. It has been pointed out that this detector could be instrumented and placed in the BNB at Fermilab to study short-baseline oscillations [713, 714].

Several configurations have been considered for this experiment. The MicroBooNE detector, used as the near detector, could be located either at 200m or 470m from the BNB. The far detector, LarLAr, could be placed either at 470m or 700m. Note that no further optimization has been done on the chosen detector locations, which leaves room for improvement.

In the sensitivity studies presented here, the fiducial volumes assumed for MicroBooNE and LarLAr are 61.4t and 347.5t respectively. A flat 80%  $\nu_e$  efficiency was assumed. All results shown below are for statistical errors only, which are assumed to be the dominant source of uncertainty.

Figure 146 shows sensitivity curves to a 3+1 neutrino model, for different configurations with both MicroBooNE and LarLAr detectors combined in neutrino and antineutrino modes, for a total of  $6.6 \times 10^{20}$  POT in each mode.

It is clear from these studies that combining two LAr detectors is a very powerful way to probe short-baseline oscillations. If systematic uncertainties can be reasonably mitigated, this two LAr-detector experiment would offer definitive measurements (at the  $5\sigma$  level) of the Mini-BooNE/LSND anomalies in both neutrino and antineutrino modes. Note that in the antineutrino case, more than  $6.6 \times 10^{20}$  POTs would be required to reach the  $5\sigma$  level for the whole allowed parameter space.

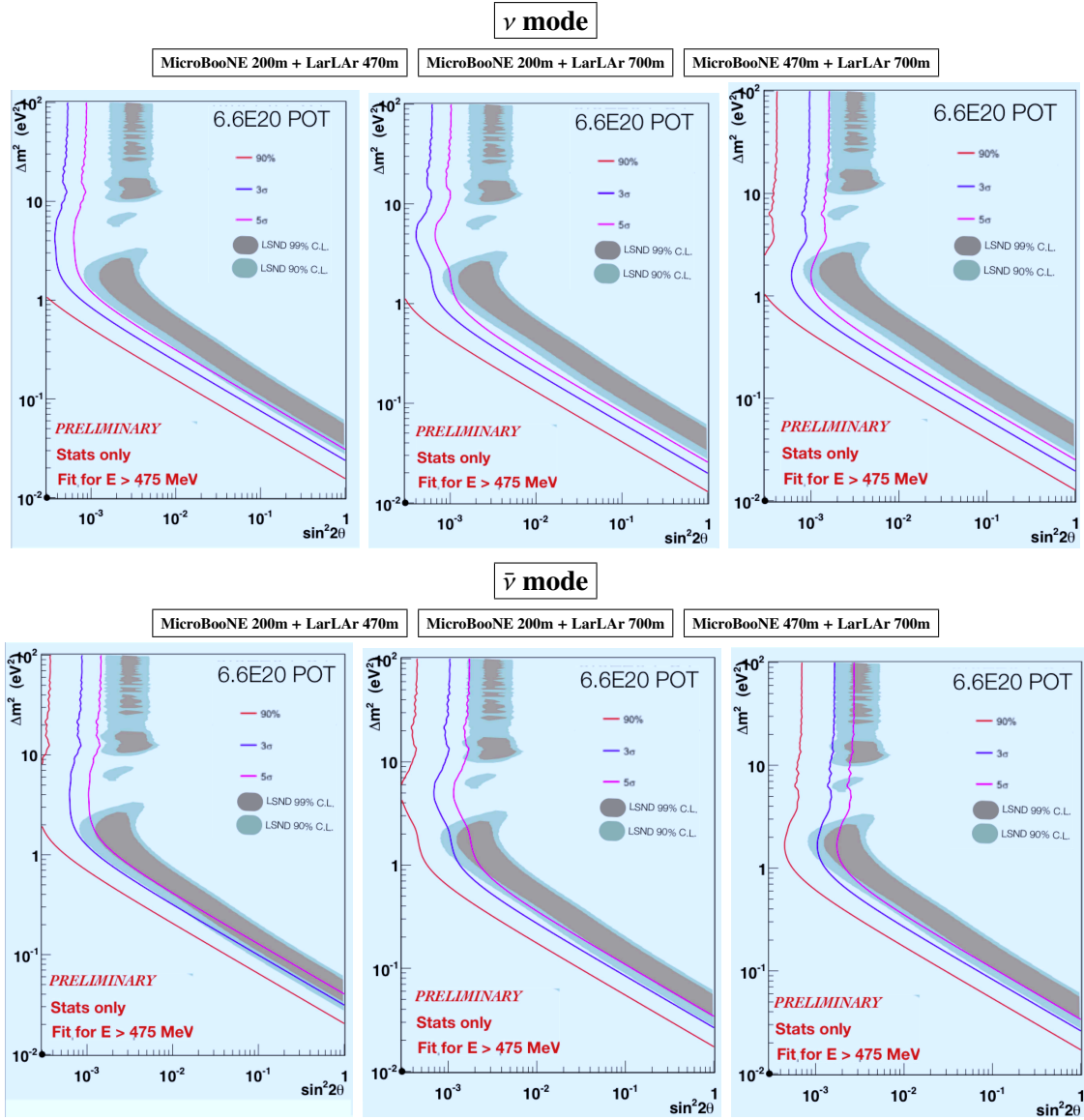


Figure 146. Sensitivity curves for a combined configuration with the MicroBooNE detector (as the near detector) and the LarLAr one (as the far detector) to a 2-neutrino model in the  $\Delta m^2/\sin^2 2\theta$  parameter space. The top plots show the sensitivities for neutrino mode and the bottom plots show the antineutrino mode. The left plots are for a configuration where the MicroBooNE detector is located at 200m and LarLAr at 470m. The middle plots are for a configuration with MicroBooNE at 200m and LarLAr at 700m. And finally the right plots are for a configuration with the MicroBooNE detector at 470m and LarLAr at 700m.

## 20. Very-Low Energy Neutrino Factory (VLENF)<sup>45</sup>

The idea of using a muon storage ring to produce a high-energy ( $\approx 50$  GeV) neutrino beam for experiments was first discussed by Koshkarev [715]. However, a detailed description of the concept for neutrino oscillation experiments was first produced by Neuffer [716] in 1980. The Very-Low Energy Neutrino Factory (VLENF) is essentially the same facility proposed in 1980 and would utilize a 2-3 GeV/c muon storage ring to study eV-scale oscillation physics and, in addition, could add significantly to our understanding of  $\nu_e$  and  $\nu_\mu$  cross sections. In particular the facility can:

1. Address the large  $\Delta m^2$  oscillation regime and add significantly to the study of sterile neutrinos.
2. Make precision  $\nu_e$  and  $\bar{\nu}_e$  cross-section measurements.
3. Provide a technology ( $\mu$  decay ring) test demonstration and  $\mu$  beam diagnostics test bed.
4. Provide a precisely understood  $\nu$  beam for detector studies

Pions are collected from a target, then transported to and injected into a storage ring where they decay to muons. The muons then subsequently decay into electrons and neutrinos. We are starting with a storage ring design that is optimized for 2 GeV/c muon momentum. In this case, the energy is optimized for the needs of both the oscillation and the cross section physics. See Fig. 147 for a schematic of the facility.

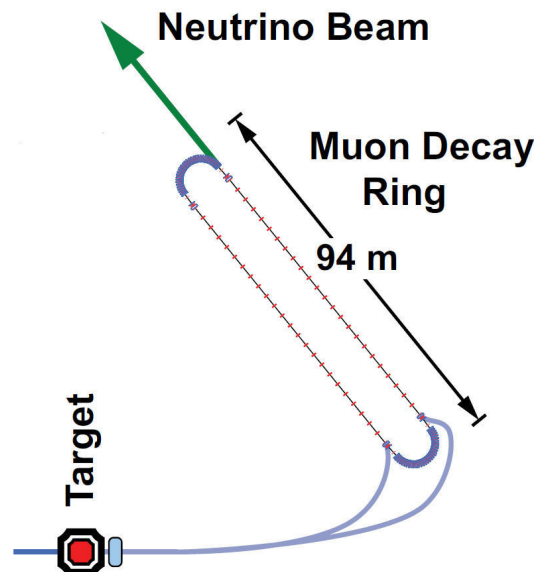


Figure 147. Schematic of Very-Low Energy Neutrino Factory

<sup>45</sup>Proposed by M. Ellis, P. Kyberd (Brunel University), C. M. Ankenbrandt, S. J. Brice, A. D. Bross, L. Coney, S. Geer, J. Kopp, N. V. Mokhov, J. G. Morfin, D. Neuffer, M. Popovic, T. Roberts, S. Striganov, G. P. Zeller (Fermi National Accelerator Laboratory), A. Blondel, A. Bravar (University of Geneva), R. Bayes, F. J. P. Soler (University of Glasgow), A. Dobbs, K. R. Long, J. Pasternak, E. Santos, M. O. Wascko (Imperial College, London), S. A. Bogacz (Jefferson Laboratory), J. B. Lagrange, Y. Mori (Kyoto University) A. P. T. Palounek (Los Alamos National Laboratory), A. de Gouvea (Northwestern University), Y. Kuno, A. Sato (Osaka University), C. D. Tunnell (University of Oxford), K. T. McDonald (Princeton University), S. K. Agarwalla (Universitat de València), P. Huber, J. M. Link (Virginia Tech), and W. Winter (Universität Würzburg) 236



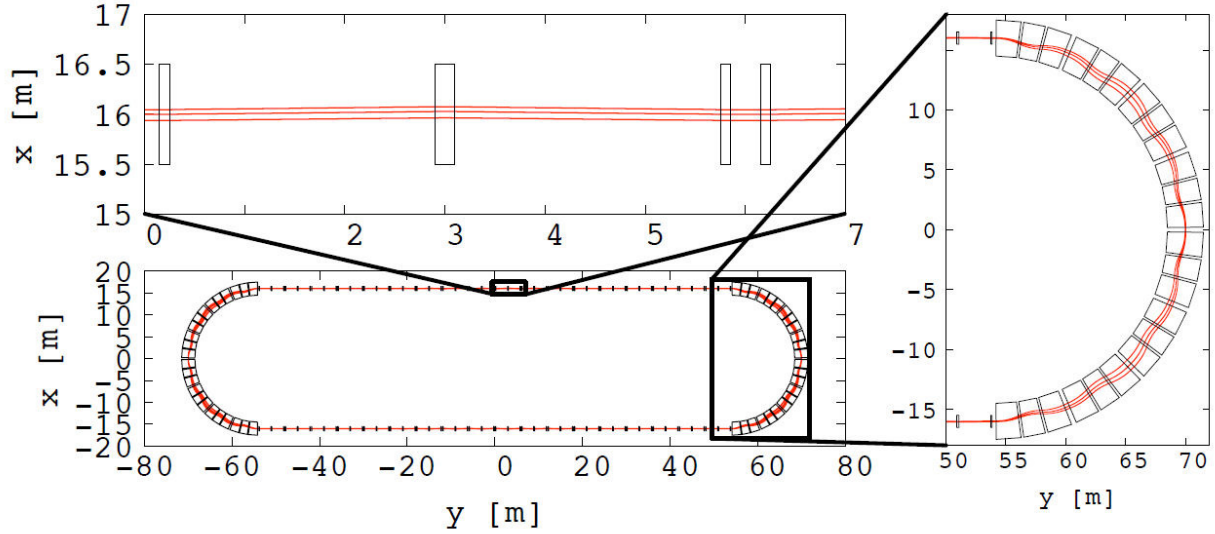


Figure 148. Top view of the racetrack FFAG lattice (bottom left scheme). The top left scheme shows a zoom on the straight section and the right scheme a zoom on the arc section.

For positive muons, the decay,  $\mu^+ \rightarrow e^+ + \bar{\nu}_\mu + \nu_e$ , yields a neutrino beam of precisely known flavor content. In addition, if the circulating muon flux in the ring is measured accurately (with beam-current transformers, for example) then the neutrino beam flavor content and flux are precisely known. Near and far detectors are placed along one of the straight sections of the racetrack decay ring. The near detector can be placed at 20-50 meters from the end of the straight and will measure neutrino-nucleon cross sections that are potentially important for future long-baseline experiments. This would include the first precision measurements of  $\nu_e$  and  $\bar{\nu}_e$  cross sections. A far detector at 800-1000 m would study neutrino oscillation physics and would be capable of performing searches in both appearance and disappearance channels (see Ref. [717] for a recent disappearance proof of principle). The experiment will take advantage of the “golden channel” of oscillation appearance  $\nu_e \rightarrow \nu_\mu$ , where the resulting final state has a muon of the wrong-sign from interactions of the  $\nu_\mu$  in the beam. In the case of  $\mu^+$ s stored in the ring, this would mean the observation of an event with a  $\mu^-$ . This detector would need to be magnetized for the wrong-sign muon appearance channel, as is the case for the baseline Neutrino Factory detector [718]. A number of possibilities for the far detector exist. However, a magnetized iron detector similar to that used in MINOS is likely to be the most straightforward approach for the far detector design. For the purposes of the VLENF oscillation physics, a detector inspired by MINOS, but with thinner plates and much larger excitation current (larger B field) is assumed.

Both conventional (FODO) and fixed field alternating gradient (FFAG) lattices are being investigated. The racetrack FFAG [719] is a very promising possibility for this application due to its large momentum acceptance ( $\simeq 20\%$ ). A schematic of the current racetrack FFAG concept is shown in Fig. 148. Both the FODO design implemented in our simulation (see below) and the FFAG referenced above would require only normal conducting magnets which would simplify construction, commissioning, and operations.

$\bar{\nu}$ -mode with stored $\mu^-$		$\nu$ -mode with stored $\mu^+$	
Channel name	Number Events	Channel name	Number Events
$\bar{\nu}_e \rightarrow \bar{\nu}_\mu$ CC	23	$\nu_e \rightarrow \nu_\mu$ CC	60
$\bar{\nu}_e \rightarrow \bar{\nu}_e$ CC	24824	$\nu_e \rightarrow \nu_e$ CC	61448
$\nu_\mu \rightarrow \nu_\mu$ NC	26657	$\bar{\nu}_\mu \rightarrow \bar{\nu}_\mu$ NC	12456
$\nu_\mu \rightarrow \nu_\mu$ CC	72539	$\bar{\nu}_\mu \rightarrow \bar{\nu}_\mu$ CC	30596

Table XXXIX. VLENF raw event rates for  $10^{21}$  POT.

## Physics Reach

At present, the VLENF has been simulated using G4Beamline [720] only for a conventional (FODO) ring lattice with a central  $\mu$  momentum of 3.0 GeV/c. The design input to this simulation included:

1. 8 GeV protons on a  $2 \lambda_l$  Be target.
2. Decay ring tuned for muons with kinetic energy of 3.0 GeV.
3. Decay ring acceptance of  $\frac{\delta p}{p} = 2\%$  rms.

The flux of the circulating muon beam (after 10 turns to allow all pions to decay) determined by this simulation was  $1.1 \times 10^8$  muons per  $10^{12}$  protons on target. This yields a figure of merit of  $1.1 \times 10^{-4}$  stored  $\mu$  per proton on target. However, the simulation does not yet include pion capture, transport and injection into the decay ring. For this analysis, it was assumed all pions (within a 100 mrad forward cone from the target) make it into the ring. Although a conceptual scheme for capture, transport and injection exists, a full design and its simulation will be part of future work.

In the sensitivity calculations that follow, we have assumed the racetrack FFAG decay ring performance described in [719]: a center momentum of 2 GeV and a momentum acceptance of 16% (full width). We also have assumed a total exposure of  $10^{21}$  protons on target, which yields  $\sim 10^{18}$  muons. Finally, a detector fiducial mass of 1kT is assumed. Background levels are based on extrapolations from the MIND analysis [718] (see detector considerations below). The background rejection for the wrong-sign muons is assumed to be  $10^{-4}$  in neutral current (NC) events and  $10^{-5}$  for  $\mu$  charge misidentified charged current (CC) events. The backgrounds from  $\nu_e \rightarrow \nu_e$  CC and NC are negligible. Sensitivities have been calculated for both  $\nu$  and  $\bar{\nu}$  running. Finally, a 35% background normalization error has been assumed as well as a 2% signal systematic error.

Tables of the raw event rates are given below. The first row corresponds to the “golden channel” appearance signal. The other rows are potential backgrounds to the signal. The backgrounds that drive the analyses are charged-current  $\bar{\nu}_\mu \rightarrow \bar{\nu}_\mu$  and  $\nu_\mu \rightarrow \nu_\mu$ , for neutrinos and antineutrinos, respectively.

The oscillation sensitivities have been computed using the GLOBES software (version 3.1.10) [546, 547]. Since GLOBES, by default, only allows for a  $3 \times 3$  mixing matrix, the SNU (version 1.1) add-on [721, 722] is used to extend computations in GLOBES to  $4 \times 4$  mixing matrices. See [723] for details regarding the analysis. Fig. 149 shows the appearance sensitivity for this facility under the above assumptions.

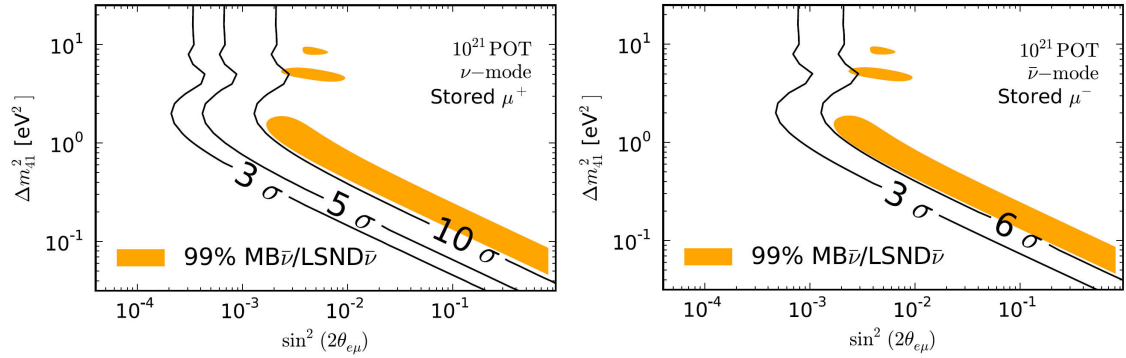


Figure 149. Appearance channel sensitivity plots. Left for  $\nu$  running, right for  $\bar{\nu}$  running.

### Detector Considerations

The concept for the far detector for the VLENF that we are exploring is basically a modified MINOS near detector [724]. However, in our case we have reduced the plate thickness to 1 cm (from the 1" used in MINOS), are using two layers of scintillator between Fe plates (X and Y measurement) and will increase the excitation current to roughly 270 kA-turns by using multiple turns of the superconducting transmission line [725]. A preliminary ANSYS analysis indicates that for a 6 m diameter plate, the magnetic field is  $\geq 1.8\text{T}$  throughout the entire plate volume. In addition, a very preliminary Geant4 simulation indicates that the  $\mu$  charge mis-ID rate is at or below  $10^{-4}$  for  $p_\mu \geq 250 \text{ MeV}/c$ . See Fig. 150. This gives us confidence that with a full Geant4 simulation with an optimized tracking algorithm, we will reach the  $10^{-5}$  specification given above.

### Conclusions

As can be seen from Fig. 149, this facility has the potential to give unprecedented performance in the large  $\Delta m^2$  oscillation regime providing the opportunity to explore physics beyond the  $\nu\text{SM}$ . If new physics exists, the VLENF will allow for a detailed study of these processes. In addition, the  $\mu$  storage ring presents the only way to obtain large samples of  $\nu_e$  events for cross-section measurements and offers the only experiment that can measure both  $\nu_e$  and  $\nu_\mu$  cross-sections with high precision. The next generation of long-baseline oscillation experiments will face a significant challenge in order to get their systematic errors to the 1% level. Gaining a better understanding of these cross sections will be essential for them to meet this goal.

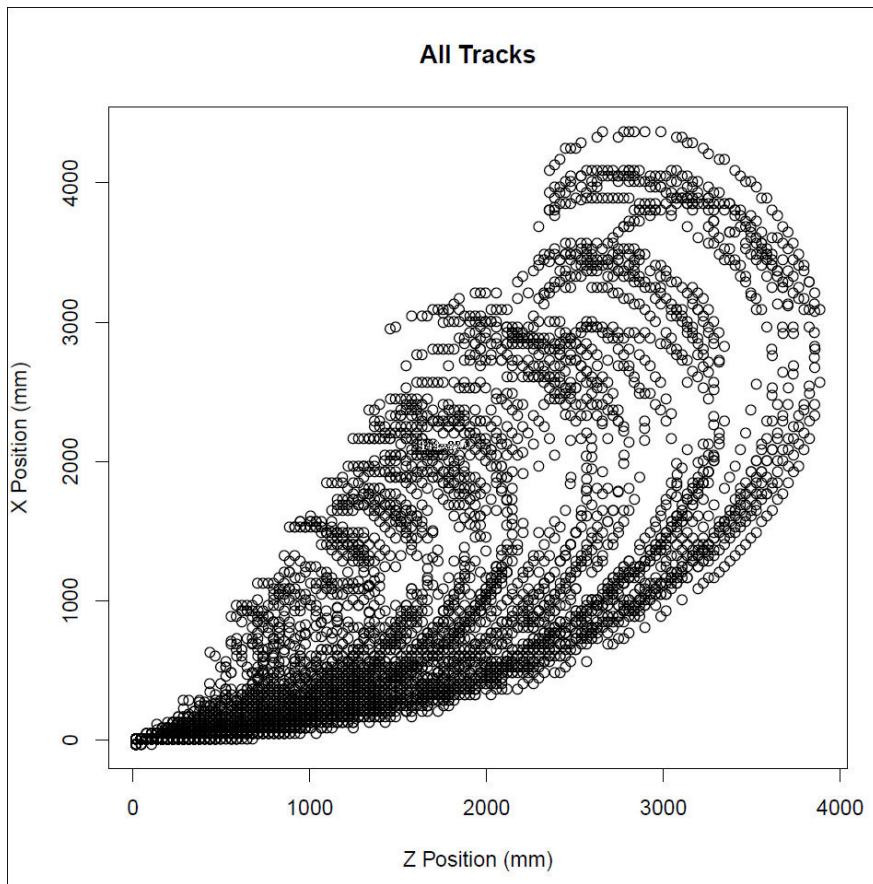


Figure 150. Plot of muon events (XY projection) for 10 muons in each momentum bin where the momentum range is from 0.1 GeV/c to 3.0 GeV/c.

## 21. Probing active-sterile oscillations with the atmospheric neutrino signal in large iron/liquid argon detectors<sup>46</sup>

The down-going atmospheric  $\nu_\mu$  and  $\bar{\nu}_\mu$  fluxes can be significantly altered due to the presence of eV<sup>2</sup>-scale active-sterile oscillations. We study the sensitivity of a large Liquid Argon detector and a large magnetized iron detector like the proposed ICAL at INO to these oscillations. Using the allowed sterile parameter ranges in a 3+1 mixing framework, we perform a fit assuming active-sterile oscillations in both the muon neutrino and antineutrino sectors, and compute oscillation exclusion limits using atmospheric down-going muon neutrino and antineutrino events. We find that (for both  $\nu_\mu$  and  $\bar{\nu}_\mu$ ) a Liquid Argon detector, an ICAL-like detector or a combined analysis of both detectors with an exposure of 1 Mt yr provides significant sensitivity to regions of parameter space in the range  $0.5 < \Delta m^2 < 5 \text{ eV}^2$  for  $\sin^2 2\theta_{\mu\mu} \geq 0.07$ . Thus atmospheric neutrino experiments can provide complementary coverage in these regions, improving sensitivity limits in combination with bounds from other experiments on these parameters.

We perform our statistical analysis using two kinds of proposed detectors:

- A large Liquid Argon detector[695, 726, 727], which can detect charged particles with very good resolution over the energy range of MeV to multi GeV, with magnetization over a 100 kT volume with a magnetic field of about 1 tesla [728]. For the down-going events, with a baseline range of 15 to 130 Kms, and energies upto 20 GeV (above which the flux is very small), the L/E range is exactly the one relevant to sterile-parameter induced oscillations. We assume the following energy resolutions over the ranges relevant to our calculations [726]:  $\sigma_{E_e} = 0.01$ ,  $\sigma_{E_\mu} = 0.01$ ,  $\sigma_{E_{had}} = \sqrt{(0.15)^2/E_{had} + (0.03)^2}$ ,  $\sigma_{\theta_e} = 0.03 \text{ radians} = 1.72^\circ$ ,  $\sigma_{\theta_\mu} = 0.04 \text{ radians} = 2.29^\circ$ ,  $\sigma_{\theta_{had}} = 0.04 \text{ radians} = 2.29^\circ$ . Here  $E_{had}$  is the hadron energy in GeV,  $\sigma_E$  are the energy resolutions and  $\sigma_\theta$  are the angular resolutions of electrons, muons and hadrons as indicated. The energy and angular resolution of the detector in terms of the neutrino energy and zenith angle can be derived from the above. In our computation, we take the average rapidity in the GeV energy region to be 0.45 for neutrinos and 0.3 for antineutrinos [729]. The energy threshold and ranges in which charge identification is feasible are  $E_{threshold} = 800 \text{ MeV}$  for muons and  $E_{electron} = 1 - 5 \text{ GeV}$  for electrons. Charged lepton detection and separation (e vs  $\mu$ ) without charge identification is possible for  $E_{lepton} > \text{few MeV}$ .
- An iron calorimeter detector like ICAL [730], which, like the above detector, offers the advantage of muon charge discrimination using magnetization with a field of 1.3 tesla, allowing a separate observation of atmospheric muon neutrino and antineutrino events. For this detector, standard resolutions of  $10^\circ$  in angle and 15% in energy are assumed.

The muon event rates are a function of both  $P_{\mu\mu}$  and  $P_{e\mu}$ , but  $P_{e\mu}$  is highly suppressed due to the smallness of the parameter  $\sin^2 2\theta_{e\mu}$ . Thus it is reasonable to anticipate that the downgoing muon event spectrum should reflect the behaviour of  $P_{\mu\mu}$ , and hence show signatures of oscillations due to the sterile parameters  $\theta_{\mu\mu}$  and  $\Delta m^2$  defined above.

A 1 Mt yr exposure is assumed for both types of detectors, and flux uncertainties and systematic errors are incorporated by the pull method [731]. The values of uncertainties are chosen as in

<sup>46</sup>Contributed by Pomita Ghoshal and Raj Gandhi.

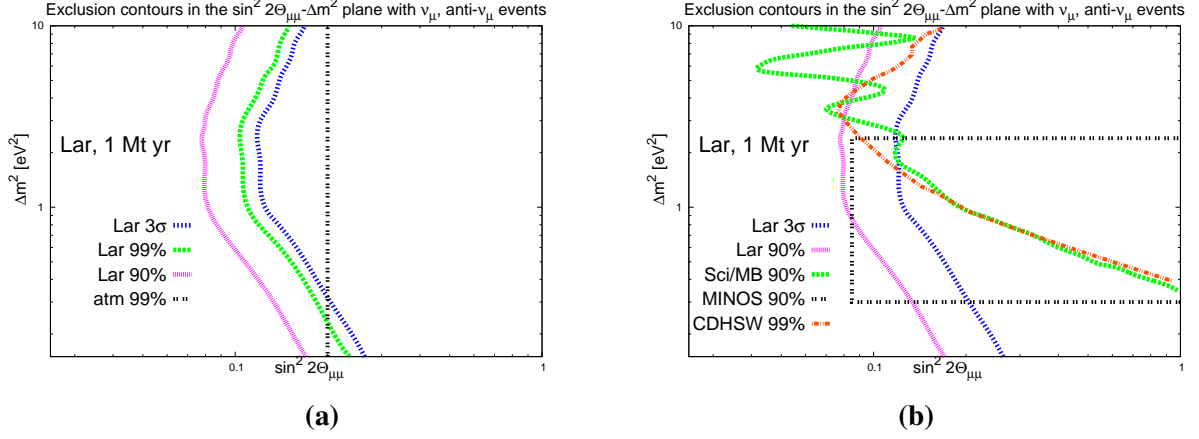


Figure 151. Exclusion curves in the  $\sin^2 2\theta_{\mu\mu} - \Delta m^2$  plane using Liquid Argon (1 Mt yr) downgoing muon and anti-muon events with sterile oscillations - (a) Comparison with 99% c.l. limit from atmospheric analysis [113, 516], (b) Comparison with 90% limits from SciBooNE/MiniBooNE [409] and MINOS [410], 99% c.l. limit from CDHSW [113, 408].

[732]. We take a double binning in energy and zenith angle, with 20 energy bins in the range 1-20 GeV and 18  $\cos \theta_z$  bins in the range 0.1 to 1.0. The atmospheric fluxes are taken from the 3-dimensional calculation in [733]. The earth matter profile defined in [734] is used to take into account matter effects on the oscillation probabilities.

One can extract the statistical sensitivity with which experimental-set ups like the ones described above may be able to exclude sterile-scale oscillations and constrain sterile parameters using the downgoing muon and anti-muon event spectra as the signal. We perform this study in two stages:

a) The best exclusion limits possible from this analysis are determined using simultaneously the downgoing muon neutrino and antineutrino event spectra for both kinds of detectors and doing a combined fit.

b) In order to test the MiniBooNE/LSND antineutrino results, the atmospheric downgoing muon antineutrino event spectra with sterile oscillations for both kinds of detectors are analysed to determine the bounds for the sterile parameters, and compared with the bounds from MiniBooNE.

### Exclusion limits with a combined $\nu_\mu, \bar{\nu}_\mu$ analysis

For this study, the sterile oscillation exclusion limits are computed by combining both the atmospheric downgoing muon and antimuon event spectra with sterile-scale oscillations. This involves taking i) the 'expected' spectrum  $N_{th}$ , in which sterile oscillations are included and the test values of the sterile parameters are varied, and ii) the 'observed' spectrum  $N_{ex}(\text{no} - \text{osc})$ , where 'no-osc' indicates no sterile-scale oscillations. Since homogeneity is expected between the  $\nu$  and  $\bar{\nu}$  sectors in the 3+1 scenario, we assume identical sterile-scale oscillations in both sectors. The exclusion limits are presented in Figure 1 and 2 for a Liquid Argon detector and an ICAL detector respectively, with an exposure of 1 Mt yr for both. Figure 3 shows the results obtained with a combined analysis of ICAL (1 Mt yr) + Liquid Argon (1 Mt yr). In each case, the left panel gives a comparison of the bounds obtained from our analysis with the 99% c.l. exclusion region from atmospheric neutrino data [113, 516], and the right panel compares our results with the 90% limits from SciBooNE/MiniBooNE [409] and MINOS [410] and the 99% limit from the CDHSW disappearance

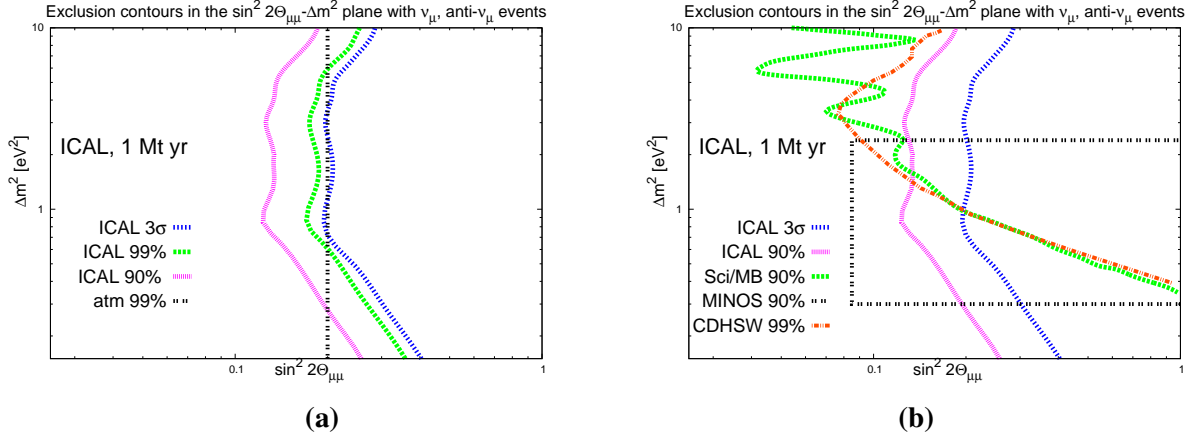


Figure 152. Same as Figure 1 using ICAL (1 Mt yr) downgoing muon and antimuon events.

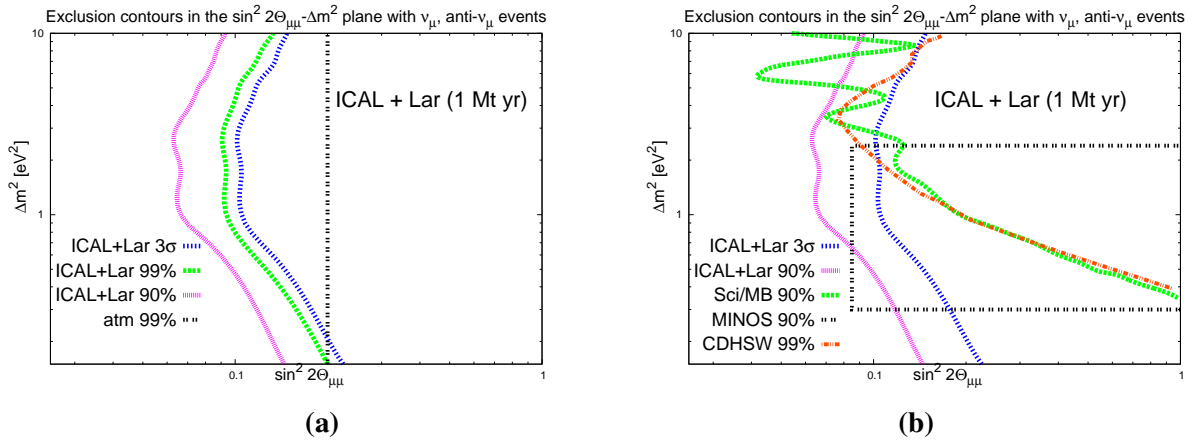


Figure 153. Same as Figure 1 using ICAL (1 Mt yr) + Liquid Argon (1 Mt yr) downgoing muon and antimuon events.

analysis [113, 408]. Figure 4 compares the 90% c.l. bounds from our Liquid Argon and combined Liquid Argon/ICAL studies with the allowed regions at 90% c.l. from the most recent global analysis in [515].

With a Liquid Argon detector and an exposure of 1 Mt yr, regions greater than  $\sin^2 2\theta_{\mu\mu} \sim 0.08$  can be excluded at 90% c.l. with a combination of muon and anti-muon events over most of the allowed  $\Delta m^2$  range. An ICAL-like detector with a similar exposure gives a weaker 90% c.l. exclusion bound at  $\sin^2 2\theta_{\mu\mu} \sim 0.12$  with this combination. A combined analysis of the two experiments gives a  $3\sigma$  exclusion bound for  $\sin^2 2\theta_{\mu\mu} \geq 0.1$ , and a 90% c.l. limit for  $\sin^2 2\theta_{\mu\mu} \geq 0.07$ , which is seen to be an improvement over the earlier bounds obtained from atmospheric neutrinos, as well as those from CDHSW, SciBooNE/MiniBooNE and MINOS, over significant regions of the parameter space. Also, Figure 4 shows that the exclusion limits given by Liquid Argon or a Liquid Argon/ICAL combination can significantly affect the fits and allowed regions given by the current global analysis.

### Testing LSND and Miniboone results with sterile oscillations in the $\bar{\nu}$ sector

Here we compute the sterile oscillation exclusion limits using the downgoing antimuon event spectrum with sterile-scale oscillations, for comparison with the results from MiniBooNE/LSND an-

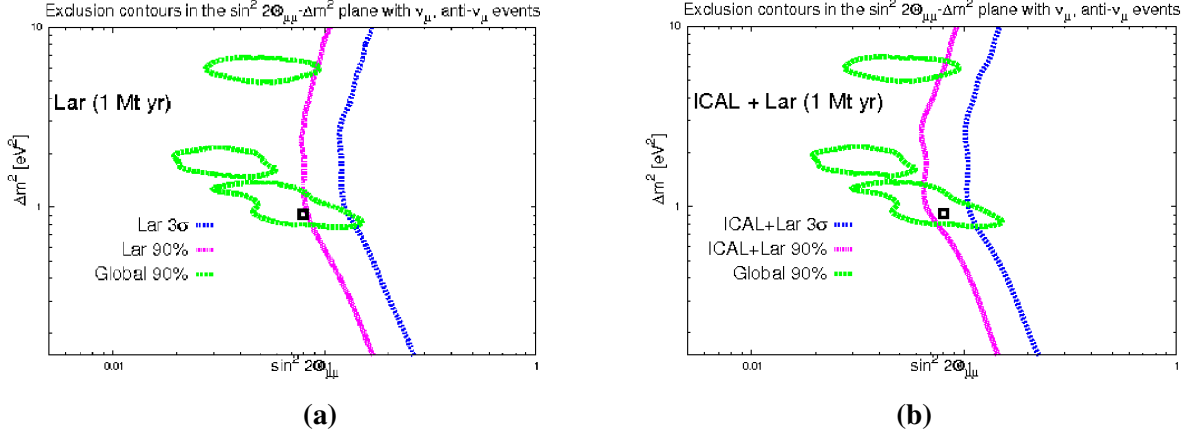


Figure 154. Exclusion curves in the  $\sin^2 2\theta_{\mu\mu} - \Delta m^2$  plane using (a) Liquid Argon (1 Mt yr) and (b) ICAL (1 Mt yr) + Liquid Argon (1 Mt yr) downgoing muon and anti-muon events. Comparison with 90% c.l. allowed regions from the GLO-LOW global analysis in [515]. The small squares denote the best-fit point from the global analysis.

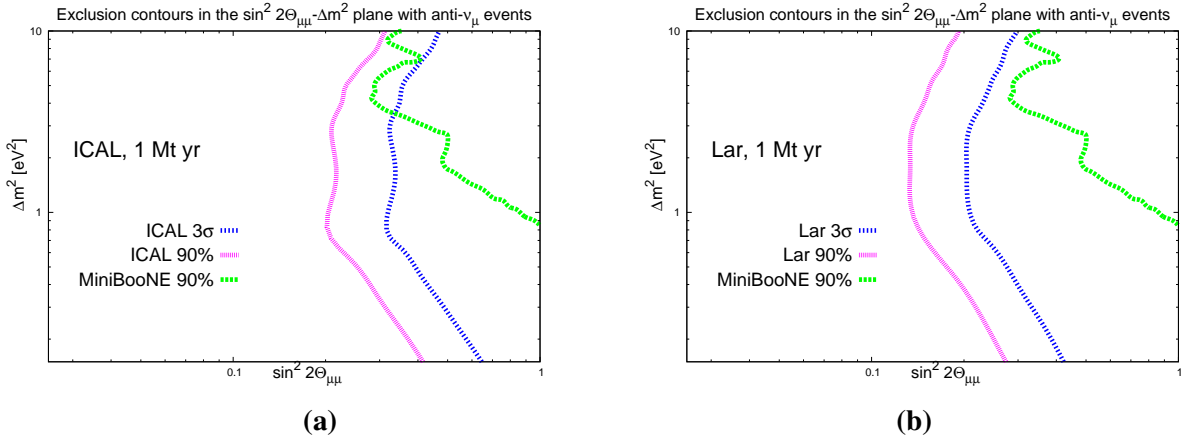


Figure 155. Exclusion curves in the  $\sin^2 2\theta_{\mu\mu} - \Delta m^2$  plane using (a) ICAL (1 Mt yr) downgoing anti-muon events and (b) Liquid Argon (1 Mt yr) downgoing anti-muon events with sterile oscillations. The limits at 90% c.l. and  $3\sigma$  are indicated. The 90% exclusion limit from the MiniBooNE [402] antineutrino analysis is also shown.

antineutrino data. The bounds obtained from this analysis are presented in Figure 5. The left and right panels correspond to the exclusion bounds for the parameters  $\Delta m^2$  and  $\sin^2 2\theta_{\mu\mu}$  with the downgoing  $\bar{\nu}_{\mu}$  spectrum for an ICAL detector and a Liquid Argon detector respectively, both with an exposure of 1 Mt yr. The 90% exclusion limit from MiniBooNE [402] is superimposed on the figure in both cases. It can be seen that this set-up provides a 90% c.l. exclusion capacity with an ICAL-like detector with an exposure of 1 Mt yr for about  $\sin^2 2\theta_{\mu\mu} > 0.2$  for a range  $0.5 < \Delta m^2 < 5$  eV<sup>2</sup>, and for a Liquid Argon detector with an exposure of 1 Mt yr for about  $\sin^2 2\theta_{\mu\mu} > 0.15$  for a range  $0.5 < \Delta m^2 < 5$  eV<sup>2</sup>. These are stronger bounds than those from the MiniBooNE antineutrino analysis.

## Summary

We have studied the possible sensitivity of atmospheric neutrino data in a large magnetized iron calorimeter detector like the proposed ICAL at INO and a large Liquid Argon detector, to eV<sup>2</sup>-



scale active-sterile neutrino and antineutrino oscillations. With the present sterile parameter ranges in a 3+1 mixing framework, down-going atmospheric  $\nu_\mu$  and  $\bar{\nu}_\mu$  events can show signatures of eV<sup>2</sup>-scale oscillations, due to their suitable energy and baseline range (neutrinos with multi-GeV energies and baselines ranging from about 10 to 100 Kms). The results of our analysis are as follows:

- **Active-sterile oscillation exclusion limits using both  $\nu_\mu$  and  $\bar{\nu}_\mu$  events:**

- a) With a Liquid Argon detector and an exposure of 1 Mt yr, regions greater than  $\sin^2 2\theta_{\mu\mu} \sim 0.08$  can be excluded at 90% c.l. with a combination of muon and anti-muon events, over most of the  $\Delta m^2$  range. A  $3\sigma$  exclusion bound is possible for  $\sin^2 2\theta_{\mu\mu} \sim 0.15$ .
- b) With an ICAL-like detector and an exposure of 1 Mt yr, a weaker 90 % c.l. exclusion bound is obtained at  $\sin^2 2\theta_{\mu\mu} \sim 0.12$  with a combination of muon and anti-muon events.
- c) With a combined analysis of ICAL (1 Mt yr) and Liquid Argon (1 Mt yr), a 90% c.l. exclusion limit is obtained for  $\sin^2 2\theta_{\mu\mu} \geq 0.07$  and a  $3\sigma$  bound for  $\sin^2 2\theta_{\mu\mu} \geq 0.1$ , which compares favorably with present limits from CDHSW, MINOS, MiniBooNE and atmospheric neutrinos (Figure 3), and is able to exclude a significant part of the allowed region from the most recent global analysis (Figure 4).

- **Fit with active-sterile oscillations in the muon antineutrino sector for comparison with MiniBooNE:**

Such oscillations can be excluded by this set-up at 90% c.l. with

- a) an ICAL-like detector with an exposure of 1 Mt yr for about  $\sin^2 2\theta_{\mu\mu} > 0.2$  for a range  $0.5 < \Delta m^2 < 5 \text{ eV}^2$ ,
- b) A Liquid Argon detector with an exposure of 1 Mt yr for about  $\sin^2 2\theta_{\mu\mu} > 0.15$  for a range  $0.5 < \Delta m^2 < 5 \text{ eV}^2$ .

The limits for both detectors from an exposure of 1 Mt yr may be accessible in a time-frame of about 10-15 years.

In conclusion, a down-going event analysis using large future atmospheric detectors may be helpful in providing significant complementary constraints on the sterile parameters, which can strengthen existing bounds when combined with other experimental signatures of sterile-scale oscillations. Evidence (or the lack of it) from such detectors has the advantage of originating in a sector which is different from those currently providing clues pointing to the existence of sterile neutrinos (i.e short-baseline experiments). Additionally, it permits access to a wide-band of  $L/E$ , which is important if oscillatory behaviour is to be unambiguously tested.

- 
- [1] P. Minkowski, Phys. Lett. **B67**, 421 (1977).
- [2] M. Gell-Mann, P. Ramond, and R. Slansky, *Supergravity* (North Holland, Amsterdam, 1979) p. van Nieuwenhuizen and D.Z. Freedman (eds.).
- [3] R. N. Mohapatra and G. Senjanovic, Phys. Rev. Lett. **44**, 912 (1980).
- [4] T. Yanagida, Conf.Proc. **C7902131**, 95 (1979).
- [5] J. Schechter and J. W. F. Valle, Phys. Rev. **D22**, 2227 (1980).
- [6] M. Fukugita and T. Yanagida, Phys.Lett. **B174**, 45 (1986).
- [7] S. Davidson, E. Nardi, and Y. Nir, Phys. Rept. **466**, 105 (2008), arXiv:0802.2962 [hep-ph].
- [8] P. Langacker, *The standard model and beyond* (Taylor and Francis, Boca Raton, FL, 2010).
- [9] P. Langacker, Phys.Rev. **D58**, 093017 (1998), arXiv:hep-ph/9805281 [hep-ph].
- [10] N. Arkani-Hamed, L. J. Hall, H. Murayama, D. Tucker-Smith, and N. Weiner, Phys.Rev. **D64**, 115011 (2001), arXiv:hep-ph/0006312 [hep-ph].
- [11] M. Cvetič and P. Langacker, Phys. Rev. **D78**, 066012 (2008), arXiv:0803.2876 [hep-th].
- [12] R. Blumenhagen, M. Cvetič, S. Kachru, and T. Weigand, Ann.Rev.Nucl.Part.Sci. **59**, 269 (2009), arXiv:0902.3251 [hep-th].
- [13] K. R. Dienes, E. Dudas, and T. Gherghetta, Nucl.Phys. **B557**, 25 (1999), arXiv:hep-ph/9811428 [hep-ph].
- [14] N. Arkani-Hamed, S. Dimopoulos, G. Dvali, and J. March-Russell, Phys.Rev. **D65**, 024032 (2002), arXiv:hep-ph/9811448 [hep-ph].
- [15] S. Weinberg, Phys. Rev. **D22**, 1694 (1980).
- [16] T. Hambye, E. Ma, and U. Sarkar, Nucl.Phys. **B602**, 23 (2001), arXiv:hep-ph/0011192 [hep-ph].
- [17] R. Foot, H. Lew, X. He, and G. C. Joshi, Z.Phys. **C44**, 441 (1989).
- [18] P. Langacker, “Neutrino Masses from the Top Down,” (2011), submitted to Annual Reviews of Nuclear and Particle Science, arXiv:1112.5992 [hep-ph].
- [19] B. Pontecorvo, Sov. Phys. JETP **26**, 984 (1968).
- [20] Z. Maki, M. Nakagawa, and S. Sakata, Prog. Theor. Phys. **28**, 870 (1962).
- [21] A. de Gouvêa, W.-C. Huang, and J. Jenkins, Phys.Rev. **D80**, 073007 (2009), arXiv:0906.1611 [hep-ph].
- [22] J. F. Beacom, N. F. Bell, D. Hooper, J. G. Learned, S. Pakvasa, *et al.*, Phys.Rev.Lett. **92**, 011101 (2004), arXiv:hep-ph/0307151 [hep-ph].
- [23] M. Kobayashi and C. Lim, Phys.Rev. **D64**, 013003 (2001), 17 pages, LaTeX file Report-no: KEK-TH-733, KOBE-TH-00-10, arXiv:hep-ph/0012266 [hep-ph].
- [24] H. Davoudiasl, P. Langacker, and M. Perelstein, Phys.Rev. **D65**, 105015 (2002), arXiv:hep-ph/0201128 [hep-ph].
- [25] K. Nakamura *et al.* (Particle Data Group), J.Phys.G **G37**, 075021 (2010).
- [26] A. de Gouvêa and J. Jenkins, Phys.Rev. **D78**, 053003 (2008), arXiv:0804.3627 [hep-ph].
- [27] A. de Gouvêa, W.-C. Huang, and S. Shalgar, Phys.Rev. **D84**, 035011 (2011), arXiv:1007.3664 [hep-ph].
- [28] T. Asaka, S. Eijima, and H. Ishida, JHEP **1104**, 011 (2011), arXiv:1101.1382 [hep-ph].
- [29] M. Blennow and E. Fernandez-Martinez, Phys.Lett. **B704**, 223 (2011), arXiv:1107.3992 [hep-ph].
- [30] A. de Gouvêa, Phys.Rev. **D72**, 033005 (2005), arXiv:hep-ph/0501039 [hep-ph].
- [31] B. W. Lee and R. E. Shrock, Phys.Rev. **D16**, 1444 (1977).
- [32] A. Y. Smirnov and R. Zukanovich Funchal, Phys.Rev. **D74**, 013001 (2006), arXiv:hep-ph/0603009 [hep-ph].

- [33] A. Kusenko, F. Takahashi, and T. T. Yanagida, Phys. Lett. **B693**, 144 (2010), arXiv:1006.1731 [hep-ph].
- [34] A. Adulpravitchai and R. Takahashi, JHEP **09**, 127 (2011), arXiv:1107.3829 [hep-ph].
- [35] T. Asaka, S. Blanchet, and M. Shaposhnikov, Phys. Lett. **B631**, 151 (2005), arXiv:hep-ph/0503065.
- [36] A. Boyarsky, O. Ruchayskiy, and M. Shaposhnikov, Ann.Rev.Nucl.Part.Sci. **59**, 191 (2009), arXiv:0901.0011 [hep-ph].
- [37] S. Dodelson and L. M. Widrow, Phys. Rev. Lett. **72**, 17 (1994), arXiv:hep-ph/9303287.
- [38] X.-D. Shi and G. M. Fuller, Phys. Rev. Lett. **82**, 2832 (1999), arXiv:astro-ph/9810076.
- [39] M. Laine and M. Shaposhnikov, JCAP **0806**, 031 (2008), arXiv:0804.4543 [hep-ph].
- [40] A. Kusenko, Phys. Rev. Lett. **97**, 241301 (2006), arXiv:hep-ph/0609081.
- [41] S. Petcov, Phys.Lett. **B110**, 245 (1982).
- [42] M. Shaposhnikov, Nucl. Phys. **B763**, 49 (2007), arXiv:hep-ph/0605047.
- [43] M. Lindner, A. Merle, and V. Niro, JCAP **1101**, 034 (2011), arXiv:1011.4950 [hep-ph].
- [44] T. Schwetz, M. Tortola, and J. W. F. Valle, New J. Phys. **13**, 109401 (2011), arXiv:1108.1376 [hep-ph].
- [45] S. Petcov and W. Rodejohann, Phys.Rev. **D71**, 073002 (2005), arXiv:hep-ph/0409135 [hep-ph].
- [46] J. Ahn *et al.* (RENO collaboration), (2012), arXiv:1204.0626 [hep-ex].
- [47] Y. Abe *et al.* (DOUBLE-CHOOZ Collaboration), “Indication for the disappearance of reactor electron antineutrinos in the Double Chooz experiment,” (2011), arXiv:1112.6353 [hep-ex].
- [48] F. An *et al.* (Daya BaryCollaboration), “Observation of electron-antineutrino disappearance at Daya Bay,” (2012), arXiv:1203.1669 [hep-ex].
- [49] A. Merle and V. Niro, JCAP **1107**, 023 (2011), arXiv:1105.5136 [hep-ph].
- [50] R. Mohapatra, Phys.Rev. **D64**, 091301 (2001), arXiv:hep-ph/0107264 [hep-ph].
- [51] S. L. Glashow, Phys.Lett. **B256**, 255 (1991).
- [52] E. Chun, C. Kim, and U. Lee, Phys.Rev. **D58**, 093003 (1998), arXiv:hep-ph/9802209 [hep-ph].
- [53] Y. Chikira, N. Haba, and Y. Mimura, Eur.Phys.J. **C16**, 701 (2000), arXiv:hep-ph/9808254 [hep-ph].
- [54] C. Liu and J.-H. Song, Phys.Rev. **D60**, 036002 (1999), arXiv:hep-ph/9812381 [hep-ph].
- [55] B. McKellar, J. Stephenson, G.J., J. Goldman, and M. Garbutt, “A Seesaw mechanism with light sterile neutrinos,” (2001), arXiv:hep-ph/0106121 [hep-ph].
- [56] K. L. McDonald, B. McKellar, and A. Mastrano, Phys.Rev. **D70**, 053012 (2004), arXiv:hep-ph/0401241 [hep-ph].
- [57] K. L. McDonald and B. McKellar, Int.J.Mod.Phys. **A22**, 2211 (2007), arXiv:hep-ph/0401073 [hep-ph].
- [58] T. Araki and Y. Li, “Q6 flavor symmetry model for the extension of the minimal standard model by three right-handed sterile neutrinos,” (2011), arXiv:1112.5819 [hep-ph].
- [59] C. Froggatt and H. B. Nielsen, Nucl.Phys. **B147**, 277 (1979).
- [60] N. E. Mavromatos, “Neutrinos and the Universe,” (2011), arXiv:1110.3729 [hep-ph].
- [61] J. Barry, W. Rodejohann, and H. Zhang, JHEP **07**, 091 (2011), arXiv:1105.3911 [hep-ph].
- [62] J. Barry, W. Rodejohann, and H. Zhang, “Sterile Neutrinos for Warm Dark Matter and the Reactor Anomaly in Flavor Symmetry Models,” (2011), arXiv:1110.6382 [hep-ph].
- [63] W. Grimus and L. Lavoura, JHEP **0011**, 042 (2000), arXiv:hep-ph/0008179 [hep-ph].
- [64] H. Hettmansperger, M. Lindner, and W. Rodejohann, JHEP **1104**, 123 (2011), arXiv:1102.3432 [hep-ph].
- [65] F. Bezrukov, H. Hettmansperger, and M. Lindner, Phys.Rev. **D81**, 085032 (2010), arXiv:0912.4415 [hep-ph].
- [66] R. Mohapatra, S. Nasri, and H.-B. Yu, Phys.Rev. **D72**, 033007 (2005), arXiv:hep-ph/0505021 [hep-ph].

- ph].
- [67] R. Mohapatra, Phys.Rev.Lett. **56**, 561 (1986).
  - [68] R. N. Mohapatra and J. W. F. Valle, Phys. Rev. **D34**, 1642 (1986).
  - [69] C. S. Fong, R. N. Mohapatra, and I. Sung, Phys.Lett. **B704**, 171 (2011), arXiv:1107.4086 [hep-ph].
  - [70] E. J. Chun, A. S. Joshipura, and A. Y. Smirnov, Phys.Rev. **D54**, 4654 (1996), arXiv:hep-ph/9507371 [hep-ph].
  - [71] H. Zhang, “Light Sterile Neutrino in the Minimal Extended Seesaw,” (2011), arXiv:1110.6838 [hep-ph].
  - [72] G. Altarelli and F. Feruglio, Rev.Mod.Phys. **82**, 2701 (2010), arXiv:1002.0211 [hep-ph].
  - [73] H. Ishimori, T. Kobayashi, H. Ohki, Y. Shimizu, H. Okada, *et al.*, Prog.Theor.Phys.Suppl. **183**, 1 (2010), arXiv:1003.3552 [hep-th].
  - [74] Z. G. Berezhiani and R. N. Mohapatra, Phys.Rev. **D52**, 6607 (1995), arXiv:hep-ph/9505385 [hep-ph].
  - [75] E. Ma, Phys.Lett. **B380**, 286 (1996), arXiv:hep-ph/9507348 [hep-ph].
  - [76] M. Bando and K. Yoshioka, Prog.Theor.Phys. **100**, 1239 (1998), arXiv:hep-ph/9806400 [hep-ph].
  - [77] N. Arkani-Hamed and Y. Grossman, Phys.Lett. **B459**, 179 (1999), arXiv:hep-ph/9806223 [hep-ph].
  - [78] Q. Shafi and Z. Tavartkiladze, Phys.Lett. **B451**, 129 (1999), arXiv:hep-ph/9901243 [hep-ph].
  - [79] K. Babu and G. Seidl, Phys.Rev. **D70**, 113014 (2004), arXiv:hep-ph/0405197 [hep-ph].
  - [80] J. Sayre, S. Wiesenfeldt, and S. Willenbrock, Phys.Rev. **D72**, 015001 (2005), arXiv:hep-ph/0504198 [hep-ph].
  - [81] M.-C. Chen, A. de Gouvea, and B. A. Dobrescu, Phys.Rev. **D75**, 055009 (2007), arXiv:hep-ph/0612017 [hep-ph].
  - [82] V. Barger, P. Fileviez Perez, and S. Spinner, Phys.Lett. **B696**, 509 (2011), arXiv:1010.4023 [hep-ph].
  - [83] D. K. Ghosh, G. Senjanovic, and Y. Zhang, Phys.Lett. **B698**, 420 (2011), arXiv:1010.3968 [hep-ph].
  - [84] K. L. McDonald, Phys.Lett. **B696**, 266 (2011), arXiv:1010.2659 [hep-ph].
  - [85] C.-S. Chen and R. Takahashi, “Hierarchically Acting Sterile Neutrinos,” (2011), arXiv:1112.2102 [hep-ph].
  - [86] C.-Q. Geng and R. Takahashi, Phys.Lett. **B710**, 324 (2012), arXiv:1201.1534 [hep-ph].
  - [87] T. Lee and C.-N. Yang, Phys.Rev. **104**, 254 (1956).
  - [88] I. Kobzarev, L. Okun, and I. Pomeranchuk, Sov.J.Nucl.Phys. **3**, 837 (1966).
  - [89] L. Okun and C. Rubbia, Conf.Proc. **C670920**, 301 (1967).
  - [90] M. Pavsic, Int.J.Theor.Phys. **9**, 229 (1974), arXiv:hep-ph/0105344 [hep-ph].
  - [91] S. Blinnikov and M. Khlopov, Sov.J.Nucl.Phys. **36**, 472 (1982).
  - [92] R. Foot, H. Lew, and R. Volkas, Phys.Lett. **B272**, 67 (1991).
  - [93] R. Foot, H. Lew, and R. Volkas, Mod.Phys.Lett. **A7**, 2567 (1992).
  - [94] Z. Silagadze, Phys.Atom.Nucl. **60**, 272 (1997), arXiv:hep-ph/9503481 [hep-ph].
  - [95] L. Okun, Phys.Usp. **50**, 380 (2007), arXiv:hep-ph/0606202 [hep-ph].
  - [96] R. Foot and R. Volkas, Phys.Rev. **D52**, 6595 (1995), arXiv:hep-ph/9505359 [hep-ph].
  - [97] V. Berezhinsky, M. Narayan, and F. Vissani, Nucl.Phys. **B658**, 254 (2003), arXiv:hep-ph/0210204 [hep-ph].
  - [98] J. E. Kim and G. Carosi, Rev.Mod.Phys. **82**, 557 (2010), arXiv:0807.3125 [hep-ph].
  - [99] E. J. Chun, Phys.Lett. **B454**, 304 (1999), arXiv:hep-ph/9901220 [hep-ph].
  - [100] K. Choi, E. J. Chun, and K. Hwang, Phys.Rev. **D64**, 033006 (2001), arXiv:hep-ph/0101026 [hep-ph].
  - [101] J. E. Kim and H. P. Nilles, Phys.Lett. **B138**, 150 (1984).
  - [102] E. Chun, J. E. Kim, and H. P. Nilles, Nucl.Phys. **B370**, 105 (1992).
  - [103] E. Chun, J. E. Kim, and H. P. Nilles, Phys.Lett. **B287**, 123 (1992), arXiv:hep-ph/9205229 [hep-ph].
  - [104] E. Chun and A. Lukas, Phys.Lett. **B357**, 43 (1995), arXiv:hep-ph/9503233 [hep-ph].

- [105] G. Giudice and R. Rattazzi, *Phys.Rept.* **322**, 419 (1999), arXiv:hep-ph/9801271 [hep-ph].
- [106] K. Choi, K. Hwang, and E. J. Chun, *Phys.Rev.* **D60**, 031301 (1999), arXiv:hep-ph/9811363 [hep-ph].
- [107] A. Donini, P. Hernandez, J. Lopez-Pavon, and M. Maltoni, *JHEP* **1107**, 105 (2011), arXiv:1106.0064 [hep-ph].
- [108] F. Maltoni, J. Niczyporuk, and S. Willenbrock, *Phys.Rev.Lett.* **86**, 212 (2001), arXiv:hep-ph/0006358 [hep-ph].
- [109] J. Casas, J. Espinosa, and I. Hidalgo, *JHEP* **0411**, 057 (2004), arXiv:hep-ph/0410298 [hep-ph].
- [110] A. de Gouvêa, “GeV seesaw, accidentally small neutrino masses, and Higgs decays to neutrinos,” (2007), arXiv:0706.1732 [hep-ph].
- [111] A. de Gouvêa and W.-C. Huang, “Constraining the (Low-Energy) Type-I Seesaw,” (2011), arXiv:1110.6122 [hep-ph].
- [112] J. Kopp, M. Maltoni, and T. Schwetz, *Phys.Rev.Lett.* **107**, 091801 (2011), arXiv:1103.4570 [hep-ph].
- [113] C. Giunti and M. Laveder, *Phys.Rev.* **D84**, 073008 (2011), arXiv:1107.1452 [hep-ph].
- [114] A. Aguilar *et al.* (LSND Collaboration), *Phys.Rev.* **D64**, 112007 (2001), arXiv:hep-ex/0104049 [hep-ex].
- [115] A. Aguilar-Arevalo *et al.* (The MiniBooNE Collaboration), *Phys.Rev.Lett.* **98**, 231801 (2007), arXiv:0704.1500 [hep-ex].
- [116] A. Aguilar-Arevalo *et al.* (MiniBooNE Collaboration), *Phys.Rev.Lett.* **102**, 101802 (2009), arXiv:0812.2243 [hep-ex].
- [117] A. Aguilar-Arevalo *et al.* (The MiniBooNE Collaboration), *Phys.Rev.Lett.* **105**, 181801 (2010), arXiv:1007.1150 [hep-ex].
- [118] G. Mention, M. Fechner, T. Lasserre, T. Mueller, D. Lhuillier, *et al.*, *Phys.Rev.* **D83**, 073006 (2011), arXiv:1101.2755 [hep-ex].
- [119] A. de Gouvea, J. Jenkins, and N. Vasudevan, *Phys.Rev.* **D75**, 013003 (2007), arXiv:hep-ph/0608147 [hep-ph].
- [120] J. Barrett and J. Formaggio, *Phys.Lett.* **B706**, 68 (2011), arXiv:1105.1326 [nucl-ex].
- [121] J. Hamann, S. Hannestad, G. G. Raffelt, I. Tamborra, and Y. Y. Wong, *Phys.Rev.Lett.* **105**, 181301 (2010), arXiv:1006.5276 [hep-ph].
- [122] J. Hamann, S. Hannestad, G. G. Raffelt, and Y. Y. Wong, *JCAP* **1109**, 034 (2011), arXiv:1108.4136 [astro-ph.CO].
- [123] M. Mitra, G. Senjanovic, and F. Vissani, *Nucl.Phys.* **B856**, 26 (2012), arXiv:1108.0004 [hep-ph].
- [124] W. Rodejohann, *Int.J.Mod.Phys.* **E20**, 1833 (2011), arXiv:1106.1334 [hep-ph].
- [125] J. Fan and P. Langacker, “Light Sterile Neutrinos and Short Baseline Neutrino Oscillation Anomalies,” (2012), arXiv:1201.6662 [hep-ph].
- [126] M. Sorel, J. M. Conrad, and M. Shaevitz, *Phys. Rev.* **D70**, 073004 (2004), arXiv:hep-ph/0305255.
- [127] E. Akhmedov and T. Schwetz, *JHEP* **10**, 115 (2010), arXiv:1007.4171 [hep-ph].
- [128] C. Giunti and M. Laveder, *Phys. Rev.* **D82**, 093016 (2010), arXiv:arXiv:1010.1395 [hep-ph].
- [129] J. Casas and A. Ibarra, *Nucl.Phys.* **B618**, 171 (2001), arXiv:hep-ph/0103065 [hep-ph].
- [130] T. Asaka and M. Shaposhnikov, *Phys. Lett.* **B620**, 17 (2005), hep-ph/0505013.
- [131] F. Bezrukov and M. Shaposhnikov, *Phys.Lett.* **B659**, 703 (2008), arXiv:0710.3755 [hep-th].
- [132] M. Shaposhnikov and D. Zenhausern, *Phys.Lett.* **B671**, 187 (2009), arXiv:0809.3395 [hep-th].
- [133] M. Shaposhnikov and D. Zenhausern, *Phys.Lett.* **B671**, 162 (2009), arXiv:0809.3406 [hep-th].
- [134] M. Shaposhnikov, “Is there a new physics between electroweak and Planck scales?” (2007), arXiv:0708.3550 [hep-th].
- [135] F. Bezrukov, *Phys.Rev.* **D72**, 071303 (2005), arXiv:hep-ph/0505247 [hep-ph].
- [136] D. Gorbunov and M. Shaposhnikov, *JHEP* **0710**, 015 (2007), arXiv:0705.1729 [hep-ph].

- [137] T. Akiri *et al.* (LBNE Collaboration), (2011), arXiv:1110.6249 [hep-ex].
- [138] A. Boyarsky, A. Neronov, O. Ruchayskiy, M. Shaposhnikov, and I. Tkachev, Phys.Rev.Lett. **97**, 261302 (2006), arXiv:astro-ph/0603660 [astro-ph].
- [139] K. N. Abazajian, “Detection of Dark Matter Decay in the X-ray,” (2009), arXiv:0903.2040 [astro-ph.CO].
- [140] J. den Herder, A. Boyarsky, O. Ruchayskiy, K. Abazajian, C. Frenk, *et al.*, “The Search for decaying Dark Matter,” (2009), arXiv:0906.1788 [astro-ph.CO].
- [141] A. Dolgov, S. Hansen, G. Raffelt, and D. Semikoz, Nucl.Phys. **B580**, 331 (2000), arXiv:hep-ph/0002223 [hep-ph].
- [142] A. Dolgov, S. Hansen, G. Raffelt, and D. Semikoz, Nucl.Phys. **B590**, 562 (2000), arXiv:hep-ph/0008138 [hep-ph].
- [143] O. Ruchayskiy and A. Ivashko, “Experimental bounds on sterile neutrino mixing angles,” (2011), arXiv:1112.3319 [hep-ph].
- [144] M. Davis, G. Efstathiou, C. S. Frenk, and S. D. White, Astrophys.J. **292**, 371 (1985).
- [145] S. Tremaine and J. E. Gunn, Phys. Rev. Lett. **42**, 407 (1979).
- [146] A. Boyarsky, O. Ruchayskiy, and D. Iakubovskiy, JCAP **0903**, 005 (2009), arXiv:0808.3902 [hep-ph].
- [147] D. Gorbunov, A. Khmelnitsky, and V. Rubakov, JCAP **0810**, 041 (2008), arXiv:0808.3910 [hep-ph].
- [148] P. B. Pal and L. Wolfenstein, Phys.Rev. **D25**, 766 (1982), revised Version.
- [149] K. Abazajian, G. M. Fuller, and W. H. Tucker, Astrophys. J. **562**, 593 (2001), arXiv:astro-ph/0106002.
- [150] A. D. Dolgov and S. H. Hansen, Astropart. Phys. **16**, 339 (2002), arXiv:hep-ph/0009083.
- [151] A. Boyarsky, J. W. den Herder, A. Neronov, and O. Ruchayskiy, Astropart.Phys. **28**, 303 (2007), arXiv:astro-ph/0612219 [astro-ph].
- [152] A. Boyarsky, O. Ruchayskiy, D. Iakubovskiy, A. V. Maccio’, and D. Malyshev, “New evidence for dark matter,” (2009), arXiv:0911.1774 [astro-ph.CO].
- [153] P. Bode, J. P. Ostriker, and N. Turok, Astrophys. J. **556**, 93 (2001), astro-ph/0010389.
- [154] K. N. Abazajian and G. M. Fuller, Phys. Rev. **D66**, 023526 (2002), arXiv:astro-ph/0204293.
- [155] K. Abazajian, Phys. Rev. **D73**, 063506 (2006), arXiv:astro-ph/0511630.
- [156] T. Asaka, M. Laine, and M. Shaposhnikov, JHEP **0606**, 053 (2006), arXiv:hep-ph/0605209 [hep-ph].
- [157] T. Asaka, M. Laine, and M. Shaposhnikov, JHEP **01**, 091 (2007), arXiv:hep-ph/0612182.
- [158] M. Shaposhnikov, JHEP **0808**, 008 (2008), arXiv:0804.4542 [hep-ph].
- [159] K. Abazajian, G. M. Fuller, and M. Patel, Phys.Rev. **D64**, 023501 (2001), arXiv:astro-ph/0101524 [astro-ph].
- [160] A. Boyarsky, J. Lesgourgues, O. Ruchayskiy, and M. Viel, JCAP **0905**, 012 (2009), arXiv:0812.0010 [astro-ph].
- [161] J. Wang and S. D. White, “Discreteness effects in simulations of Hot/Warm dark matter,” (2007), submitted to Mon.Not.Roy.Astron.Soc., arXiv:astro-ph/0702575 [ASTRO-PH].
- [162] E. Polisensky and M. Ricotti, Phys.Rev. **D83**, 043506 (2011), arXiv:1004.1459 [astro-ph.CO].
- [163] M. R. Lovell, V. Eke, C. S. Frenk, L. Gao, A. Jenkins, *et al.*, Mon.Not.Roy.Astron.Soc. **420**, 2318 (2012), arXiv:1104.2929 [astro-ph.CO].
- [164] E. Semboloni, H. Hoekstra, J. Schaye, M. P. van Daalen, and I. J. McCarthy, “Quantifying the effect of baryon physics on weak lensing tomography,” (2011), arXiv:1105.1075 [astro-ph.CO].
- [165] S. H. Hansen, J. Lesgourgues, S. Pastor, and J. Silk, Mon.Not.Roy.Astron.Soc. **333**, 544 (2002), arXiv:astro-ph/0106108 [astro-ph].
- [166] M. Viel and M. G. Haehnelt, Mon. Not. Roy. Astron. Soc. **365**, 231 (2006), arXiv:astro-ph/0508177

- [astro-ph].
- [167] K. Abazajian, *Phys.Rev.* **D73**, 063513 (2006), arXiv:astro-ph/0512631 [astro-ph].
- [168] U. Seljak, A. Makarov, P. McDonald, and H. Trac, *Phys. Rev. Lett.* **97**, 191303 (2006), arXiv:astro-ph/0602430.
- [169] M. Viel, J. Lesgourgues, M. G. Haehnelt, S. Matarrese, and A. Riotto, *Phys. Rev. Lett.* **97**, 071301 (2006), arXiv:astro-ph/0605706.
- [170] M. Viel, G. D. Becker, J. S. Bolton, M. G. Haehnelt, M. Rauch, *et al.*, *Phys.Rev.Lett.* **100**, 041304 (2008), arXiv:0709.0131 [astro-ph].
- [171] L. E. Strigari, J. S. Bullock, M. Kaplinghat, A. V. Kravtsov, O. Y. Gnedin, *et al.*, *Astrophys.J.* **652**, 306 (2006), arXiv:astro-ph/0603775 [astro-ph].
- [172] R. K. de Naray, G. D. Martinez, J. S. Bullock, and M. Kaplinghat, “The Case Against Warm or Self-Interacting Dark Matter as Explanations for Cores in Low Surface Brightness Galaxies,” (2009), arXiv:0912.3518 [astro-ph.CO].
- [173] A. V. Maccio’ and F. Fontanot, “How cold is Dark Matter? Constraints from Milky Way Satellites,” (2009), arXiv:0910.2460 [astro-ph.CO].
- [174] A. Schneider, R. E. Smith, A. V. Maccio, and B. Moore, “Nonlinear Evolution of Cosmological Structures in Warm Dark Matter Models,” (2011), arXiv:1112.0330 [astro-ph.CO].
- [175] A. Boyarsky, J. Lesgourgues, O. Ruchayskiy, and M. Viel, *Phys. Rev. Lett.* **102**, 201304 (2009), arXiv:0812.3256 [hep-ph].
- [176] A. A. Klypin, A. V. Kravtsov, O. Valenzuela, and F. Prada, *Astrophys. J.* **522**, 82 (1999), arXiv:astro-ph/9901240.
- [177] B. Moore *et al.*, *Astrophys. J.* **524**, L19 (1999), arXiv:astro-ph/9907411.
- [178] J. S. Bullock, A. V. Kravtsov, and D. H. Weinberg, *Astrophys. J.* **539**, 517 (2000), arXiv:astro-ph/0002214.
- [179] A. J. Benson, C. S. Frenk, C. G. Lacey, C. M. Baugh, and S. Cole, *Mon. Not. Roy. Astron. Soc.* **333**, 177 (2002), arXiv:astro-ph/0108218.
- [180] L. E. Strigari, C. S. Frenk, and S. D. White, *Mon.Not.Roy.Astron.Soc.* **408**, 2364 (2010), arXiv:1003.4268 [astro-ph.CO].
- [181] M. Boylan-Kolchin, J. S. Bullock, and M. Kaplinghat, *Mon.Not.Roy.Astron.Soc.* **415**, L40 (2011), arXiv:1103.0007 [astro-ph.CO].
- [182] K. Markovic, S. Bridle, A. Slosar, and J. Weller, *JCAP* **1101**, 022 (2011), arXiv:1009.0218 [astro-ph.CO].
- [183] R. E. Smith and K. Markovic, *Phys.Rev.* **D84**, 063507 (2011), arXiv:1103.2134 [astro-ph.CO].
- [184] M. P. van Daalen, J. Schaye, C. Booth, and C. D. Vecchia, *Mon.Not.Roy.Astron.Soc.* **415**, 3649 (2011), arXiv:1104.1174 [astro-ph.CO].
- [185] A. Boyarsky, A. Neronov, O. Ruchayskiy, and M. Shaposhnikov, *Mon.Not.Roy.Astron.Soc.* **370**, 213 (2006), arXiv:astro-ph/0512509 [astro-ph].
- [186] A. Boyarsky, J. Nevalainen, and O. Ruchayskiy, *Astron.Astrophys.* **471**, 51 (2007), arXiv:astro-ph/0610961 [astro-ph].
- [187] C. R. Watson, J. F. Beacom, H. Yuksel, and T. P. Walker, *Phys. Rev.* **D74**, 033009 (2006), arXiv:astro-ph/0605424.
- [188] K. Abazajian and S. M. Koushiappas, *Phys.Rev.* **D74**, 023527 (2006), arXiv:astro-ph/0605271 [astro-ph].
- [189] A. Boyarsky, D. Iakubovskiy, O. Ruchayskiy, and V. Savchenko, *Mon.Not.Roy.Astron.Soc.* **387**, 1361 (2008), arXiv:0709.2301 [astro-ph].
- [190] K. N. Abazajian, M. Markevitch, S. M. Koushiappas, and R. C. Hickox, *Phys.Rev.* **D75**, 063511

- (2007), arXiv:astro-ph/0611144 [astro-ph].
- [191] S. Riemer-Sorensen, S. H. Hansen, and K. Pedersen, *Astrophys. J.* **644**, L33 (2006), arXiv:astro-ph/0603661.
- [192] A. Boyarsky, D. Malyshev, A. Neronov, and O. Ruchayskiy, *Mon. Not. Roy. Astron. Soc.* **387**, 1345 (2008), arXiv:0710.4922 [astro-ph].
- [193] M. Loewenstein, A. Kusenko, and P. L. Biermann, *Astrophys.J.* **700**, 426 (2009), arXiv:0812.2710 [astro-ph].
- [194] M. Loewenstein and A. Kusenko, *Astrophys.J.* **714**, 652 (2010), arXiv:0912.0552 [astro-ph.HE].
- [195] A. Boyarsky, A. Neronov, O. Ruchayskiy, and M. Shaposhnikov, *JETP Lett.* **83**, 133 (2006), arXiv:hep-ph/0601098 [hep-ph].
- [196] P.-H. Gu, *Phys.Rev.* **D82**, 093009 (2010), arXiv:1005.1632 [hep-ph].
- [197] R. J. Scherrer and M. S. Turner, *Phys. Rev.* **D31**, 681 (1985).
- [198] M. Shaposhnikov and I. Tkachev, *Phys. Lett.* **B639**, 414 (2006), arXiv:hep-ph/0604236.
- [199] A. Anisimov, Y. Bartocci, and F. L. Bezrukov, *Phys. Lett.* **B671**, 211 (2009), arXiv:0809.1097 [hep-ph].
- [200] F. Bezrukov and D. Gorbunov, *JHEP* **1005**, 010 (2010), arXiv:0912.0390 [hep-ph].
- [201] S. Das and K. Sigurdson, *Phys.Rev.* **D85**, 063510 (2012), 8 pages, 6 figures, 1 table/ References added, Eq. 16 corrected, and appendix with surface of allowed dark-matter abundance added, arXiv:1012.4458 [astro-ph.CO].
- [202] K. Petraki and A. Kusenko, *Phys.Rev.* **D77**, 065014 (2008), arXiv:0711.4646 [hep-ph].
- [203] I. M. Shoemaker, K. Petraki, and A. Kusenko, *JHEP* **1009**, 060 (2010), arXiv:1006.5458 [hep-ph].
- [204] F. Bezrukov, D. Gorbunov, and M. Shaposhnikov, *JCAP* **1110**, 001 (2011), arXiv:1106.5019 [hep-ph].
- [205] F. Bezrukov, D. Gorbunov, and M. Shaposhnikov, *JCAP* **0906**, 029 (2009), arXiv:0812.3622 [hep-ph].
- [206] D. Gorbunov and A. Panin, *Phys.Lett.* **B700**, 157 (2011), arXiv:1009.2448 [hep-ph].
- [207] X.-G. He, T. Li, and W. Liao, *Phys.Rev.* **D81**, 033006 (2010), arXiv:0911.1598 [hep-ph].
- [208] H.-S. Lee, “Long-range interaction effects on neutrino oscillation,” (2011), arXiv:1110.1335 [hep-ph].
- [209] J. Heeck and W. Rodejohann, *J.Phys.G* **G38**, 085005 (2011), arXiv:1007.2655 [hep-ph].
- [210] P. Langacker and D. London, *Phys.Rev.* **D38**, 907 (1988).
- [211] G. Karagiorgi, M. Shaevitz, and J. Conrad, “Confronting the short-baseline oscillation anomalies with a single sterile neutrino and non-standard matter effects,” (2012), arXiv:1202.1024 [hep-ph].
- [212] A. E. Nelson and J. Walsh, *Phys.Rev.* **D77**, 033001 (2008), arXiv:0711.1363 [hep-ph].
- [213] N. Engelhardt, A. E. Nelson, and J. R. Walsh, *Phys.Rev.* **D81**, 113001 (2010), arXiv:1002.4452 [hep-ph].
- [214] G. Barenboim and J. D. Lykken, *Phys.Rev.* **D80**, 113008 (2009), arXiv:0908.2993 [hep-ph].
- [215] G. Barenboim and J. D. Lykken, *Phys.Lett.* **B554**, 73 (2003), arXiv:hep-ph/0210411 [hep-ph].
- [216] L. Wolfenstein, *Phys. Rev.* **D17**, 2369 (1978).
- [217] S. P. Mikheyev and A. Y. Smirnov, *Sov. J. Nucl. Phys.* **42**, 913 (1985).
- [218] C. Biggio, M. Blennow, and E. Fernandez-Martinez, *JHEP* **08**, 090 (2009), arXiv:0907.0097 [hep-ph].
- [219] S. Davidson, C. Peña-Garay, N. Rius, and A. Santamaria, *JHEP* **03**, 011 (2003), hep-ph/0302093.
- [220] J. Barranco, O. G. Miranda, C. A. Moura, and J. W. F. Valle, *Phys. Rev.* **D73**, 113001 (2006), hep-ph/0512195.
- [221] J. Barranco, O. G. Miranda, C. A. Moura, and J. W. F. Valle, *Phys. Rev.* **D77**, 093014 (2008),



- arXiv:0711.0698 [hep-ph].
- [222] A. Bolanos *et al.*, Phys. Rev. **D79**, 113012 (2009), arXiv:0812.4417 [hep-ph].
  - [223] C. Biggio, M. Blennow, and E. Fernandez-Martinez, JHEP **03**, 139 (2009), arXiv:0902.0607 [hep-ph].
  - [224] S. Antusch, J. P. Baumann, and E. Fernandez-Martinez, Nucl. Phys. **B810**, 369 (2009), arXiv:0807.1003 [hep-ph].
  - [225] M. B. Gavela, D. Hernandez, T. Ota, and W. Winter, Phys. Rev. **D79**, 013007 (2009), arXiv:0809.3451 [hep-ph].
  - [226] M. S. Bilenky and A. Santamaria, Nucl. Phys. **B420**, 47 (1994), arXiv:hep-ph/9310302.
  - [227] S. Bergmann, Y. Grossman, and D. M. Pierce, Phys. Rev. **D61**, 053005 (2000), hep-ph/9909390.
  - [228] F. Cuyppers and S. Davidson, Eur. Phys. J. **C2**, 503 (1998), arXiv:hep-ph/9609487.
  - [229] A. De Gouvea, G. F. Giudice, A. Strumia, and K. Tobe, Nucl. Phys. **B623**, 395 (2002), arXiv:hep-ph/0107156.
  - [230] A. Broncano, M. B. Gavela, and E. E. Jenkins, Phys. Lett. **B552**, 177 (2003), arXiv:hep-ph/0210271.
  - [231] S. Antusch, C. Biggio, E. Fernandez-Martinez, M. B. Gavela, and J. Lopez-Pavon, JHEP **10**, 084 (2006), arXiv:hep-ph/0607020.
  - [232] A. Abada, C. Biggio, F. Bonnet, M. B. Gavela, and T. Hambye, JHEP **12**, 061 (2007), arXiv:0707.4058 [hep-ph].
  - [233] D. Tommasini, G. Barenboim, J. Bernabeu, and C. Jarlskog, Nucl. Phys. **B444**, 451 (1995), arXiv:hep-ph/9503228.
  - [234] S. Davidson and V. Sanz, Phys.Rev. **D84**, 113011 (2011), arXiv:1108.5320 [hep-ph].
  - [235] B. Bellazzini, Y. Grossman, I. Nachshon, and P. Paradisi, JHEP **1106**, 104 (2011), arXiv:1012.3759 [hep-ph].
  - [236] R. Alonso *et al.*, “Summary report of MINSIS workshop in Madrid,” (2010), arXiv:1009.0476 [hep-ph].
  - [237] S. Antusch, M. Blennow, E. Fernandez-Martinez, and T. Ota, JHEP **06**, 068 (2010), arXiv:1005.0756 [hep-ph].
  - [238] E. Fernandez-Martinez, M. B. Gavela, J. Lopez-Pavon, and O. Yasuda, Phys. Lett. **B649**, 427 (2007), arXiv:hep-ph/0703098.
  - [239] S. Goswami and T. Ota, Phys. Rev. **D78**, 033012 (2008), arXiv:0802.1434 [hep-ph].
  - [240] J. Kopp, T. Ota, and W. Winter, Phys. Rev. **D78**, 053007 (2008), arXiv:0804.2261 [hep-ph].
  - [241] S. Antusch, M. Blennow, E. Fernandez-Martinez, and J. Lopez-Pavon, Phys. Rev. **D80**, 033002 (2009), arXiv:0903.3986 [hep-ph].
  - [242] A. Gago, H. Minakata, H. Nunokawa, S. Uchinami, and R. Zukanovich Funchal, JHEP **1001**, 049 (2010), arXiv:0904.3360 [hep-ph].
  - [243] P. Coloma, A. Donini, J. Lopez-Pavon, and H. Minakata, JHEP **1108**, 036 (2011), arXiv:1105.5936 [hep-ph].
  - [244] M. Carpentier and S. Davidson, Eur.Phys.J. **C70**, 1071 (2010), arXiv:1008.0280 [hep-ph].
  - [245] A. Dolgov, Phys.Rept. **370**, 333 (2002), arXiv:hep-ph/0202122 [hep-ph].
  - [246] N. Weiner and K. M. Zurek, Phys.Rev. **D74**, 023517 (2006), arXiv:hep-ph/0509201 [hep-ph].
  - [247] S. Das and N. Weiner, Phys.Rev. **D84**, 123511 (2011), 14 pages, 2 figures, arXiv:astro-ph/0611353 [astro-ph].
  - [248] R. Fardon, A. E. Nelson, and N. Weiner, JCAP **0410**, 005 (2004), arXiv:astro-ph/0309800 [astro-ph].
  - [249] R. Fardon, A. E. Nelson, and N. Weiner, JHEP **0603**, 042 (2006), arXiv:hep-ph/0507235 [hep-ph].
  - [250] A. E. Nelson, Phys.Rev. **D84**, 053001 (2011), arXiv:1010.3970 [hep-ph].
  - [251] D. B. Kaplan, A. E. Nelson, and N. Weiner, Phys.Rev.Lett. **93**, 091801 (2004), arXiv:hep-

- ph/0401099 [hep-ph].
- [252] K. M. Zurek, *JHEP* **0410**, 058 (2004), arXiv:hep-ph/0405141 [hep-ph].
- [253] V. Kostelecky and J. Tasson, *Phys.Rev.Lett.* **102**, 010402 (2009), arXiv:0810.1459 [gr-qc].
- [254] D. Colladay and V. Kostelecky, *Phys.Rev.* **D55**, 6760 (1997), arXiv:hep-ph/9703464 [hep-ph].
- [255] V. Kostelecky and S. Samuel, *Phys.Rev.* **D39**, 683 (1989).
- [256] V. Kostelecky and R. Potting, *Nucl.Phys.* **B359**, 545 (1991), dedicated to the memory of John Stewart Bell.
- [257] D. Colladay and V. Kostelecky, *Phys.Rev.* **D58**, 116002 (1998), arXiv:hep-ph/9809521 [hep-ph].
- [258] O. Greenberg, *Phys.Rev.Lett.* **89**, 231602 (2002), arXiv:hep-ph/0201258 [hep-ph].
- [259] S. R. Coleman and S. L. Glashow, *Phys.Rev.* **D59**, 116008 (1999), arXiv:hep-ph/9812418 [hep-ph].
- [260] G. Barenboim, L. Borissov, J. D. Lykken, and A. Smirnov, *JHEP* **0210**, 001 (2002), arXiv:hep-ph/0108199 [hep-ph].
- [261] N. E. Mavromatos, *J.Phys.Conf.Ser.* **171**, 012007 (2009), arXiv:0904.0606 [hep-ph].
- [262] V. Kostelecky and N. Russell, *Rev.Mod.Phys.* **83**, 11 (2011), arXiv:0801.0287 [hep-ph].
- [263] R. Bluhm, *Lect.Notes Phys.* **702**, 191 (2006), arXiv:hep-ph/0506054 [hep-ph].
- [264] J. S. Diaz, “Overview of Lorentz Violation in Neutrinos,” (2011), arXiv:1109.4620 [hep-ph].
- [265] V. Kostelecky and M. Mewes, *Phys.Rev.* **D69**, 016005 (2004), arXiv:hep-ph/0309025 [hep-ph].
- [266] V. Kostelecky and M. Mewes, *Phys.Rev.* **D70**, 076002 (2004), arXiv:hep-ph/0406255 [hep-ph].
- [267] J. S. Diaz, V. Kostelecky, and M. Mewes, *Phys.Rev.* **D80**, 076007 (2009), arXiv:0908.1401 [hep-ph].
- [268] L. Auerbach *et al.* (LSND Collaboration), *Phys.Rev.* **D72**, 076004 (2005), arXiv:hep-ex/0506067 [hep-ex].
- [269] P. Adamson *et al.* (MINOS Collaboration), *Phys.Rev.Lett.* **101**, 151601 (2008), arXiv:0806.4945 [hep-ex].
- [270] P. Adamson *et al.* (MINOS Collaboration), *Phys.Rev.Lett.* **105**, 151601 (2010), arXiv:1007.2791 [hep-ex].
- [271] P. Adamson *et al.* (The MINOS Collaboration), *Phys.Rev.* **D85**, 031101 (2012), 6 pages, 2 figures, 4 tables, arXiv:1201.2631 [hep-ex].
- [272] R. Abbasi *et al.* (IceCube Collaboration), *Phys.Rev.* **D82**, 112003 (2010), arXiv:1010.4096 [astro-ph.HE].
- [273] A. Aguilar-Arevalo *et al.* (MiniBooNE Collaboration), “Test of Lorentz and CPT violation with Short Baseline Neutrino Oscillation Excesses,” (2011), arXiv:1109.3480 [hep-ex].
- [274] V. Kostelecky and M. Mewes, *Phys.Rev.* **D70**, 031902 (2004), arXiv:hep-ph/0308300 [hep-ph].
- [275] Y. Ashie *et al.* (Super-Kamiokande), *Phys. Rev. Lett.* **93**, 101801 (2004), hep-ex/0404034.
- [276] V. Barger, D. Marfatia, and K. Whisnant, *Phys.Lett.* **B653**, 267 (2007), arXiv:0706.1085 [hep-ph].
- [277] V. Barger, J. Liao, D. Marfatia, and K. Whisnant, *Phys.Rev.* **D84**, 056014 (2011), arXiv:1106.6023 [hep-ph].
- [278] T. Katori, V. Kostelecky, and R. Tayloe, *Phys.Rev.* **D74**, 105009 (2006), arXiv:hep-ph/0606154 [hep-ph].
- [279] J. S. Diaz and V. Kostelecky, *Phys.Lett.* **B700**, 25 (2011), arXiv:1012.5985 [hep-ph].
- [280] J. S. Diaz and A. Kostelecky, *Phys.Rev.* **D85**, 016013 (2012), 17 pages two-column REVTeX, arXiv:1108.1799 [hep-ph].
- [281] A. Kostelecky and M. Mewes, “Neutrinos with Lorentz-violating operators of arbitrary dimension,” (2011), arXiv:1112.6395 [hep-ph].
- [282] V. Kostelecky and M. Mewes, *Phys.Rev.* **D80**, 015020 (2009), arXiv:0905.0031 [hep-ph].
- [283] V. Kostelecky and M. Mewes, *Astrophys.J.* **689**, L1 (2008), arXiv:0809.2846 [astro-ph].
- [284] T. Araki *et al.* (KamLAND), *Phys. Rev. Lett.* **94**, 081801 (2005), hep-ex/0406035.

- [285] S. Abe *et al.* (KamLAND Collaboration), Phys.Rev.Lett. **100**, 221803 (2008), arXiv:0801.4589 [hep-ex].
- [286] N. C. Ribeiro *et al.*, Phys. Rev. **D77**, 073007 (2008), arXiv:0712.4314 [hep-ph].
- [287] A. E. Bernardini and O. Bertolami, Phys.Rev. **D77**, 085032 (2008), arXiv:0802.2199 [hep-ph].
- [288] B. Altschul, J.Phys.Conf.Ser. **173**, 012003 (2009).
- [289] S. Ando, M. Kamionkowski, and I. Mocioiu, Phys.Rev. **D80**, 123522 (2009), arXiv:0910.4391 [hep-ph].
- [290] M. Bustamante, A. Gago, and C. Pena-Garay, JHEP **1004**, 066 (2010), arXiv:1001.4878 [hep-ph].
- [291] S. Yang and B.-Q. Ma, Int.J.Mod.Phys. **A24**, 5861 (2009), arXiv:0910.0897 [hep-ph].
- [292] P. Arias and J. Gamboa, Mod.Phys.Lett. **A25**, 277 (2010), arXiv:0907.2078 [hep-ph].
- [293] A. Bhattacharya, S. Choubey, R. Gandhi, and A. Watanabe, JCAP **1009**, 009 (2010), arXiv:1006.3082 [hep-ph].
- [294] C. Liu, J.-t. Tian, and Z.-h. Zhao, Phys.Lett. **B702**, 154 (2011), arXiv:1106.5927 [hep-ph].
- [295] Y. Grossman, Phys. Lett. **B359**, 141 (1995), arXiv:hep-ph/9507344.
- [296] S. Hollenberg, O. Micu, and H. Pas, Phys.Rev. **D80**, 053010 (2009), arXiv:0906.5072 [hep-ph].
- [297] J. Christenson, J. Cronin, V. Fitch, and R. Turlay, Phys.Rev.Lett. **13**, 138 (1964).
- [298] A. Sakharov, Pisma Zh.Eksp.Teor.Fiz. **5**, 32 (1967), reprinted in \*Kolb, E.W. (ed.), Turner, M.S. (ed.): The early universe\* 371-373, and in \*Lindley, D. (ed.) et al.: Cosmology and particle physics\* 106-109, and in Sov. Phys. Usp. 34 (1991) 392-393 [Usp. Fiz. Nauk 161 (1991) No. 5 61-64].
- [299] G. Gamow, Phys.Rev. **70**, 572 (1946).
- [300] V. Kuzmin, V. Rubakov, and M. Shaposhnikov, Phys.Lett. **B155**, 36 (1985).
- [301] O. Bertolami, D. Colladay, V. Kostelecky, and R. Potting, Phys.Lett. **B395**, 178 (1997), arXiv:hep-ph/9612437 [hep-ph].
- [302] A. Dolgov, Phys.Atom.Nucl. **73**, 588 (2010), arXiv:0903.4318 [hep-ph].
- [303] G. Barenboim and N. E. Mavromatos, Phys.Rev. **D70**, 093015 (2004), arXiv:hep-ph/0406035 [hep-ph].
- [304] G. Barenboim and N. E. Mavromatos, JHEP **0501**, 034 (2005), arXiv:hep-ph/0404014 [hep-ph].
- [305] R. M. Wald, Phys.Rev. **D21**, 2742 (1980).
- [306] J. R. Ellis, N. E. Mavromatos, and M. Westmuckett, Phys.Rev. **D71**, 106006 (2005), arXiv:gr-qc/0501060 [gr-qc].
- [307] J. R. Ellis, N. E. Mavromatos, and M. Westmuckett, Phys.Rev. **D70**, 044036 (2004), arXiv:gr-qc/0405066 [gr-qc].
- [308] J. Bernabeu, N. E. Mavromatos, and S. Sarkar, Phys.Rev. **D74**, 045014 (2006), arXiv:hep-th/0606137 [hep-th].
- [309] G. Lindblad, Commun.Math.Phys. **48**, 119 (1976).
- [310] J. R. Ellis, J. Hagelin, D. V. Nanopoulos, and M. Srednicki, Nucl.Phys. **B241**, 381 (1984).
- [311] J. R. Ellis, J. L. Lopez, N. Mavromatos, and D. V. Nanopoulos, Phys.Rev. **D53**, 3846 (1996), arXiv:hep-ph/9505340 [hep-ph].
- [312] F. Benatti and R. Floreanini, Phys.Rev. **D64**, 085015 (2001), arXiv:hep-ph/0105303 [hep-ph].
- [313] G. Fogli, E. Lisi, A. Marrone, D. Montanino, and A. Palazzo, Phys.Rev. **D76**, 033006 (2007), arXiv:0704.2568 [hep-ph].
- [314] E. Lisi, A. Marrone, and D. Montanino, Phys.Rev.Lett. **85**, 1166 (2000), arXiv:hep-ph/0002053 [hep-ph].
- [315] G. Barenboim, N. E. Mavromatos, S. Sarkar, and A. Waldron-Lauda, Nucl.Phys. **B758**, 90 (2006), arXiv:hep-ph/0603028 [hep-ph].
- [316] U. Debnath, B. Mukhopadhyay, and N. Dadhich, Mod.Phys.Lett. **A21**, 399 (2006), arXiv:hep-

- ph/0510351 [hep-ph].
- [317] B. Mukhopadhyay, *Mod.Phys.Lett.* **A20**, 2145 (2005), arXiv:astro-ph/0505460 [astro-ph].
  - [318] B. Mukhopadhyay, *Class.Quant.Grav.* **24**, 1433 (2007), arXiv:gr-qc/0702062 [GR-QC].
  - [319] M. Sinha and B. Mukhopadhyay, *Phys.Rev.* **D77**, 025003 (2008), arXiv:0704.2593 [hep-ph].
  - [320] G. Mangano *et al.*, *Nucl.Phys.* **B729**, 221 (2005), arXiv:hep-ph/0506164 [hep-ph].
  - [321] P. Langacker, *On the Cosmological Production of Light Sterile-Neutrinos*, Tech. Rep. (University of Pennsylvania, 1989).
  - [322] P. Di Bari, *Phys.Rev.* **D65**, 043509 (2002), arXiv:hep-ph/0108182 [hep-ph].
  - [323] K. N. Abazajian, *Astropart.Phys.* **19**, 303 (2003), arXiv:astro-ph/0205238 [astro-ph].
  - [324] M. Cirelli, G. Marandella, A. Strumia, and F. Vissani, *Nucl.Phys.* **B708**, 215 (2005), arXiv:hep-ph/0403158 [hep-ph].
  - [325] A. Melchiorri, O. Mena, S. Palomares-Ruiz, S. Pascoli, A. Slosar, *et al.*, *JCAP* **0901**, 036 (2009), arXiv:0810.5133 [hep-ph].
  - [326] K. Abazajian, N. F. Bell, G. M. Fuller, and Y. Y. Wong, *Phys.Rev.* **D72**, 063004 (2005), arXiv:astro-ph/0410175 [astro-ph].
  - [327] R. Foot and R. Volkas, *Phys.Rev.Lett.* **75**, 4350 (1995), arXiv:hep-ph/9508275 [hep-ph].
  - [328] R. Foot, M. J. Thomson, and R. Volkas, *Phys.Rev.* **D53**, 5349 (1996), arXiv:hep-ph/9509327 [hep-ph].
  - [329] E. Aver, K. A. Olive, and E. D. Skillman, “An MCMC determination of the primordial helium abundance,” (2011), arXiv:1112.3713 [astro-ph.CO].
  - [330] M. Pettini, B. J. Zych, M. T. Murphy, A. Lewis, and C. C. Steidel, “Deuterium Abundance in the Most Metal-Poor Damped Lyman alpha System: Converging on Omega baryons,” (2008), arXiv:0805.0594 [astro-ph].
  - [331] Y. Izotov and T. Thuan, *Astrophys.J.* **710**, L67 (2010), arXiv:1001.4440 [astro-ph.CO].
  - [332] G. Mangano and P. D. Serpico, *Phys.Lett.* **B701**, 296 (2011), arXiv:1103.1261 [astro-ph.CO].
  - [333] K. M. Nollett and G. P. Holder, “An analysis of constraints on relativistic species from primordial nucleosynthesis and the cosmic microwave background,” (2011), arXiv:1112.2683 [astro-ph.CO].
  - [334] A. Dolgov, S. Hansen, S. Pastor, S. Petcov, G. Raffelt, *et al.*, *Nucl.Phys.* **B632**, 363 (2002), arXiv:hep-ph/0201287 [hep-ph].
  - [335] S. Pastor, T. Pinto, and G. G. Raffelt, *Phys.Rev.Lett.* **102**, 241302 (2009), arXiv:0808.3137 [astro-ph].
  - [336] A. Cuoco, J. Lesgourgues, G. Mangano, and S. Pastor, *Phys.Rev.* **D71**, 123501 (2005), arXiv:astro-ph/0502465 [astro-ph].
  - [337] M. Shiraishi, K. Ichikawa, K. Ichiki, N. Sugiyama, and M. Yamaguchi, *JCAP* **0907**, 005 (2009), arXiv:0904.4396 [astro-ph.CO].
  - [338] E. Komatsu *et al.* (WMAP Collaboration), *Astrophys.J.Suppl.* **192**, 18 (2011), arXiv:1001.4538 [astro-ph.CO].
  - [339] W. Hu, D. J. Eisenstein, M. Tegmark, and M. J. White, *Phys.Rev.* **D59**, 023512 (1999), arXiv:astro-ph/9806362 [astro-ph].
  - [340] S. Bashinsky and U. Seljak, *Phys.Rev.* **D69**, 083002 (2004), arXiv:astro-ph/0310198 [astro-ph].
  - [341] J. Dunkley *et al.* (WMAP Collaboration), *Astrophys.J.Suppl.* **180**, 306 (2009), arXiv:0803.0586 [astro-ph].
  - [342] Z. Hou, R. Keisler, L. Knox, M. Millea, and C. Reichardt, “How Additional Massless Neutrinos Affect the Cosmic Microwave Background Damping Tail,” (2011), arXiv:1104.2333 [astro-ph.CO].
  - [343] J. Dunkley, R. Hlozek, J. Sievers, V. Acquaviva, P. Ade, *et al.*, *Astrophys.J.* **739**, 52 (2011), arXiv:1009.0866 [astro-ph.CO].

- [344] R. Keisler, C. Reichardt, K. Aird, B. Benson, L. Bleem, *et al.*, *Astrophys.J.* **743**, 28 (2011), arXiv:1105.3182 [astro-ph.CO].
- [345] J. Hamann, J. Lesgourgues, and G. Mangano, *JCAP* **0803**, 004 (2008), arXiv:0712.2826 [astro-ph].
- [346] B. A. Reid, L. Verde, R. Jimenez, and O. Mena, *JCAP* **1001**, 003 (2010), arXiv:0910.0008 [astro-ph.CO].
- [347] A. G. Riess *et al.*, *Astrophys.J.* **699**, 539 (2009), arXiv:0905.0695 [astro-ph.CO].
- [348] B. A. Reid *et al.*, *Mon.Not.Roy.Astron.Soc.* **404**, 60 (2010), arXiv:0907.1659 [astro-ph.CO].
- [349] A. Mantz, S. W. Allen, and D. Rapetti, *Mon.Not.Roy.Astron.Soc.* **406**, 1805 (2010), arXiv:0911.1788 [astro-ph.CO].
- [350] M. Archidiacono, E. Calabrese, and A. Melchiorri, *Phys.Rev.* **D84**, 123008 (2011), arXiv:1109.2767 [astro-ph.CO].
- [351] A. Smith, M. Archidiacono, A. Cooray, F. De Bernardis, A. Melchiorri, *et al.*, “The Impact of Assuming Flatness in the Determination of Neutrino Properties from Cosmological Data,” (2011), arXiv:1112.3006 [astro-ph.CO].
- [352] J. Hamann, S. Hannestad, J. Lesgourgues, C. Rampf, and Y. Y. Wong, *JCAP* **1007**, 022 (2010), arXiv:1003.3999 [astro-ph.CO].
- [353] M. C. Gonzalez-Garcia, M. Maltoni, and J. Salvado, *JHEP* **08**, 117 (2010), arXiv:arXiv:1006.3795 [hep-ph].
- [354] A. X. Gonzalez-Morales, R. Poltis, B. D. Sherwin, and L. Verde, “Are priors responsible for cosmology favoring additional neutrino species?” (2011), arXiv:1106.5052 [astro-ph.CO].
- [355] J. Hamann, *JCAP* **1203**, 021 (2012), arXiv:1110.4271 [astro-ph.CO].
- [356] J. Hamann, S. Hannestad, G. Raffelt, and Y. Y. Wong, *JCAP* **0708**, 021 (2007), arXiv:0705.0440 [astro-ph].
- [357] E. Giusarma, M. Archidiacono, R. de Putter, A. Melchiorri, and O. Mena, “Constraints on massive sterile plus active neutrino species in non minimal cosmologies,” (2011), arXiv:1112.4661 [astro-ph.CO].
- [358] J. R. Kristiansen and Ø. Elgarøy, “Reactor sterile neutrinos, dark energy and the age of the universe,” (2011), arXiv:1104.0704 [astro-ph.CO].
- [359] S. Hannestad, H. Tu, and Y. Y. Wong, *JCAP* **0606**, 025 (2006), arXiv:astro-ph/0603019 [astro-ph].
- [360] S. Galli, M. Martinelli, A. Melchiorri, L. Pagano, B. D. Sherwin, *et al.*, *Phys.Rev.* **D82**, 123504 (2010), arXiv:1005.3808 [astro-ph.CO].
- [361] S. Wang, Z. Haiman, W. Hu, J. Khoury, and M. May, *Phys.Rev.Lett.* **95**, 011302 (2005), arXiv:astro-ph/0505390 [astro-ph].
- [362] J. M. Blondin and A. Mezzacappa, *Nature* (2006), arXiv:astro-ph/0611680 [astro-ph].
- [363] M. Arnould, S. Goriely, and K. Takahashi, *Phys.Rept.* **450**, 97 (2007), arXiv:0705.4512 [astro-ph].
- [364] H. Duan, G. M. Fuller, and Y.-Z. Qian, *Ann.Rev.Nucl.Part.Sci.* **60**, 569 (2010), arXiv:1001.2799 [hep-ph].
- [365] A. Balantekin and H. Yuksel, *New J.Phys.* **7**, 51 (2005), arXiv:astro-ph/0411159 [astro-ph].
- [366] H. Duan, A. Friedland, G. C. McLaughlin, and R. Surman, *J.Phys.G* **G38**, 035201 (2011), arXiv:1012.0532 [astro-ph.SR].
- [367] G. Sigl and G. Raffelt, *Nucl.Phys.* **B406**, 423 (1993).
- [368] G. C. McLaughlin, G. M. Fuller, and J. R. Wilson, *Astrophys.J.* **472**, 440 (1996), arXiv:astro-ph/9701114 [astro-ph].
- [369] J. Beun, G. McLaughlin, R. Surman, and W. Hix, *Phys.Rev.* **D73**, 093007 (2006), 11 pages, 7 figures, Corrected Typos, arXiv:hep-ph/0602012 [hep-ph].
- [370] P. Keranen, J. Maalampi, M. Myrskylainen, and J. Riittinen, *Phys.Rev.* **D76**, 125026 (2007),

- arXiv:0708.3337 [hep-ph].
- [371] J. Fetter, G. McLaughlin, A. Balantekin, and G. Fuller, *Astropart.Phys.* **18**, 433 (2003), arXiv:hep-ph/0205029 [hep-ph].
- [372] J. M. Fetter, *Resonant active sterile neutrino conversion and r process nucleosynthesis in neutrino heated supernova ejecta*, Ph.D. thesis, University of Wisconsin (2000).
- [373] G. McLaughlin, J. Fetter, A. Balantekin, and G. Fuller, *Phys.Rev.* **C59**, 2873 (1999), arXiv:astro-ph/9902106 [astro-ph].
- [374] J. Hidaka and G. M. Fuller, *Phys.Rev.* **D76**, 083516 (2007), arXiv:0706.3886 [astro-ph].
- [375] H. Nunokawa, J. Peltoniemi, A. Rossi, and J. Valle, *Phys.Rev.* **D56**, 1704 (1997), arXiv:hep-ph/9702372 [hep-ph].
- [376] I. Tamborra, G. G. Raffelt, L. Hudepohl, and H.-T. Janka, *JCAP* **1201**, 013 (2012), arXiv:1110.2104 [astro-ph.SR].
- [377] J. Hidaka and G. M. Fuller, *Phys.Rev.* **D74**, 125015 (2006), arXiv:astro-ph/0609425 [astro-ph].
- [378] A. Kusenko and G. Segre, *Phys.Rev.* **D59**, 061302 (1999), arXiv:astro-ph/9811144 [astro-ph].
- [379] G. M. Fuller, A. Kusenko, I. Mocioiu, and S. Pascoli, *Phys.Rev.* **D68**, 103002 (2003), arXiv:astro-ph/0307267 [astro-ph].
- [380] C. L. Fryer and A. Kusenko, *Astrophys.J.Suppl.* **163**, 335 (2006), arXiv:astro-ph/0512033 [astro-ph].
- [381] G. M. Fuller, A. Kusenko, and K. Petraki, *Phys.Lett.* **B670**, 281 (2009), arXiv:0806.4273 [astro-ph].
- [382] A. Kusenko, S. Pascoli, and D. Semikoz, *JHEP* **0511**, 028 (2005), arXiv:hep-ph/0405198 [hep-ph].
- [383] A. Kusenko, *Phys. Rept.* **481**, 1 (2009), arXiv:0906.2968 [hep-ph].
- [384] G. M. Fuller, C. T. Kishimoto, and A. Kusenko, (2011), arXiv:1110.6479 [astro-ph.CO].
- [385] G. Raffelt and G. Sigl, *Astropart.Phys.* **1**, 165 (1993), arXiv:astro-ph/9209005 [astro-ph].
- [386] E. Church, K. Eitel, G. B. Mills, and M. Steidl, *Phys.Rev.* **D66**, 013001 (2002), arXiv:hep-ex/0203023 [hep-ex].
- [387] C. Athanassopoulos *et al.* (LSND Collaboration), *Nucl.Instrum.Meth.* **A388**, 149 (1997), arXiv:nucl-ex/9605002 [nucl-ex].
- [388] R. Burman, *Nucl.Instrum.Meth.* **A368**, 416 (1996).
- [389] R. Reeder, B. Dieterle, C. Gregory, F. Schaefer, K. Schum, *et al.*, *Nucl.Instrum.Meth.* **A334**, 353 (1993).
- [390] J. Napolitano *et al.*, *Nucl.Instrum.Meth.* **A274**, 152 (1989).
- [391] Y. Declais *et al.*, *Nucl. Phys.* **B434**, 503 (1995).
- [392] B. Armbruster *et al.* (KARMEN Collaboration), *Phys.Rev.* **D65**, 112001 (2002), arXiv:hep-ex/0203021 [hep-ex].
- [393] H. Gemmeke *et al.*, *Nucl.Instrum.Meth.* **A289**, 490 (1990).
- [394] G. J. Feldman and R. D. Cousins, *Phys. Rev.* **D57**, 3873 (1998), arXiv:physics/9711021.
- [395] S. Nakayama *et al.* (K2K Collaboration), *Phys.Lett.* **B619**, 255 (2005), arXiv:hep-ex/0408134 [hep-ex].
- [396] Y. Ashie *et al.* (Super-Kamiokande Collaboration), *Phys.Rev.* **D71**, 112005 (2005), arXiv:hep-ex/0501064 [hep-ex].
- [397] A. Dziewonski and D. Anderson, *Physics Earth and Planet. Inter.* **25**, 297 (1981).
- [398] V. D. Barger, K. Whisnant, S. Pakvasa, and R. Phillips, *Phys.Rev.* **D22**, 2718 (1980).
- [399] G. L. Fogli, E. Lisi, and A. Marrone, *Phys.Rev.* **D63**, 053008 (2001), arXiv:hep-ph/0009299 [hep-ph].
- [400] A. Aguilar-Arevalo *et al.* (MiniBooNE Collaboration), *Phys.Rev.* **D79**, 072002 (2009), arXiv:0806.1449 [hep-ex].
- [401] A. Aguilar-Arevalo *et al.* (MiniBooNE Collaboration), *Nucl.Instrum.Meth.* **A599**, 28 (2009),

- arXiv:0806.4201 [hep-ex].
- [402] A. A. Aguilar-Arevalo *et al.* (MiniBooNE Collaboration), *Phys.Rev.Lett.* **103**, 061802 (2009), arXiv:0903.2465 [hep-ex].
- [403] A. Aguilar-Arevalo *et al.* (SciBooNE Collaboration), “Bringing the SciBar detector to the booster neutrino beam,” (2006), spokespersons: T. Nakaya, M.O. Wascko, arXiv:hep-ex/0601022 [hep-ex].
- [404] K. Nitta, E. Aliu, S. Andringa, S. Aoki, S. Choi, *et al.*, *Nucl.Instrum.Meth.* **A535**, 147 (2004), arXiv:hep-ex/0406023 [hep-ex].
- [405] Y. Nakajima *et al.* (SciBooNE Collaboration), *Phys.Rev.* **D83**, 012005 (2011), arXiv:1011.2131 [hep-ex].
- [406] I. Stockdale *et al.* (CCFR Collaboration), *Phys.Rev.Lett.* **52**, 1384 (1984).
- [407] I. Stockdale *et al.* (CCFR Collaboration), *Z.Phys.* **C27**, 53 (1985).
- [408] F. Dydak *et al.*, *Phys. Lett.* **B134**, 281 (1984).
- [409] K. Mahn *et al.* (SciBooNE and MiniBooNE Collaborations), *Phys.Rev.* **D85**, 032007 (2012), 10 pages, 9 figures. Re-submitted to *Phys. Rev. D*, arXiv:1106.5685 [hep-ex].
- [410] P. Adamson *et al.* (MINOS Collaboration), *Phys.Rev.Lett.* **107**, 011802 (2011), arXiv:1104.3922 [hep-ex].
- [411] A. Aguilar-Arevalo *et al.* (MiniBooNE Collaboration), *Phys.Rev.* **D81**, 092005 (2010), arXiv:1002.2680 [hep-ex].
- [412] A. Aguilar-Arevalo *et al.* (MiniBooNE Collaboration), *Phys.Rev.* **D84**, 072005 (2011), arXiv:1102.1964 [hep-ex].
- [413] J. Grange (MiniBooNE Collaboration), *AIP Conf.Proc.* **1405**, 83 (2011), arXiv:1107.5327 [hep-ex].
- [414] G. Cheng *et al.* (SciBooNE Collaboration), *Phys.Rev.* **D84**, 012009 (2011), arXiv:1105.2871 [hep-ex].
- [415] P. Anselmann *et al.* (GALLEX Collaboration.), *Phys.Lett.* **B342**, 440 (1995).
- [416] W. Hampel *et al.* (GALLEX Collaboration), *Phys.Lett.* **B420**, 114 (1998).
- [417] F. Kaether, W. Hampel, G. Heusser, J. Kiko, and T. Kirsten, *Phys.Lett.* **B685**, 47 (2010), arXiv:1001.2731 [hep-ex].
- [418] D. Abdurashitov, V. Gavrin, S. Girin, V. Gorbachev, T. V. Ibragimova, *et al.*, *Phys.Rev.Lett.* **77**, 4708 (1996).
- [419] J. Abdurashitov *et al.* (SAGE Collaboration), *Phys.Rev.* **C59**, 2246 (1999), arXiv:hep-ph/9803418 [hep-ph].
- [420] J. Abdurashitov, V. Gavrin, S. Girin, V. Gorbachev, P. Gurkina, *et al.*, *Phys.Rev.* **C73**, 045805 (2006), arXiv:nucl-ex/0512041 [nucl-ex].
- [421] J. Abdurashitov *et al.* (SAGE Collaboration), *Phys.Rev.* **C80**, 015807 (2009), arXiv:0901.2200 [nucl-ex].
- [422] S. M. Bilenky and B. Pontecorvo, *Phys.Rept.* **41**, 225 (1978).
- [423] S. M. Bilenky and S. Petcov, *Rev.Mod.Phys.* **59**, 671 (1987).
- [424] S. M. Bilenky, C. Giunti, and W. Grimus, *Prog.Part.Nucl.Phys.* **43**, 1 (1999), arXiv:hep-ph/9812360 [hep-ph].
- [425] M. Gonzalez-Garcia and Y. Nir, *Rev.Mod.Phys.* **75**, 345 (2003), arXiv:hep-ph/0202058 [hep-ph].
- [426] C. Giunti and M. Laveder, “Neutrino mixing,” (2003), to be published in ‘Progress in Quantum Physics Research’, edited by V. Krasnoholovets, Nova Science Publishers, Inc., arXiv:hep-ph/0310238 [hep-ph].
- [427] M. Maltoni, T. Schwetz, M. Tortola, and J. Valle, *New J.Phys.* **6**, 122 (2004), arXiv:hep-ph/0405172 [hep-ph].
- [428] G. Fogli, E. Lisi, A. Marrone, and A. Palazzo, *Prog.Part.Nucl.Phys.* **57**, 742 (2006), arXiv:hep-

- ph/0506083 [hep-ph].
- [429] A. Strumia and F. Vissani, (2006), arXiv:hep-ph/0606054.
- [430] C. Giunti and C. W. Kim, *Fundamentals of Neutrino Physics and Astrophysics* (Oxford University Press, Oxford, UK, 2007) pp. 1–728.
- [431] V. A. Kuzmin, Sov. Phys. JETP **22**, 1051 (1966).
- [432] J. N. Bahcall, Phys.Rev. **C56**, 3391 (1997), arXiv:hep-ph/9710491 [hep-ph].
- [433] J. N. Bahcall, P. Krastev, and E. Lisi, Phys.Lett. **B348**, 121 (1995), arXiv:hep-ph/9411414 [hep-ph].
- [434] M. Laveder, Nucl.Phys.Proc.Suppl. **168**, 344 (2007).
- [435] C. Giunti and M. Laveder, Mod.Phys.Lett. **A22**, 2499 (2007), arXiv:hep-ph/0610352 [hep-ph].
- [436] C. Giunti and M. Laveder, Phys.Rev. **D77**, 093002 (2008), arXiv:0707.4593 [hep-ph].
- [437] M. A. Acero, C. Giunti, and M. Laveder, Phys.Rev. **D78**, 073009 (2008), arXiv:0711.4222 [hep-ph].
- [438] C. Giunti and M. Laveder, Phys.Rev. **D80**, 013005 (2009), arXiv:0902.1992 [hep-ph].
- [439] C. Giunti and M. Laveder, Phys.Rev. **D82**, 053005 (2010), arXiv:1005.4599 [hep-ph].
- [440] V. Gavrin, V. Gorbachev, E. Veretenkin, and B. Cleveland, “Gallium experiments with artificial neutrino sources as a tool for investigation of transition to sterile states,” (2010), arXiv:1006.2103 [nucl-ex].
- [441] C. Giunti and M. Laveder, Phys.Rev. **C83**, 065504 (2011), arXiv:1006.3244 [hep-ph].
- [442] N. Hata and W. Haxton, Phys.Lett. **B353**, 422 (1995), arXiv:nucl-th/9503017 [nucl-th].
- [443] W. Haxton, Phys.Lett. **B431**, 110 (1998), arXiv:nucl-th/9804011 [nucl-th].
- [444] D. Krofcheck, E. Sugarbaker, J. Rapaport, D. Wang, R. Byrd, *et al.*, Phys.Rev.Lett. **55**, 1051 (1985).
- [445] G. Fogli, E. Lisi, A. Marrone, and A. Palazzo, “Solar neutrinos: With a tribute to John. N. Bahcall,” (2006), arXiv:hep-ph/0605186 [hep-ph].
- [446] Y. Farzan, T. Schwetz, and A. Y. Smirnov, JHEP **0807**, 067 (2008), arXiv:0805.2098 [hep-ph].
- [447] M. Gonzalez-Garcia and M. Maltoni, Phys.Rept. **460**, 1 (2008), arXiv:0704.1800 [hep-ph].
- [448] H. Kwon, F. Boehm, A. Hahn, H. Henrikson, J. Vuilleumier, *et al.*, Phys.Rev. **D24**, 1097 (1981).
- [449] G. Zacek *et al.* (CALTECH-SIN-TUM COLLABORATION), Phys.Rev. **D34**, 2621 (1986).
- [450] Y. Declais, H. de Kerret, B. Lefievre, M. Obolensky, A. Etenko, *et al.*, Phys.Lett. **B338**, 383 (1994).
- [451] A. Afonin *et al.*, JETP Lett. **93**, 1 (1988).
- [452] V. Kuvshinnikov *et al.*, JETP Lett. **59**, 390 (1994).
- [453] G. Vidyakin, V. Vyrodov, Y. Kozlov, A. Martemyanov, V. Martemyanov, *et al.*, JETP Lett. **93**, 424 (1987).
- [454] G. Vidyakin, V. Vyrodov, Y. Kozlov, A. Martemyanov, V. Martemyanov, *et al.*, JETP Lett. **59**, 390 (1994).
- [455] Z. Greenwood, W. Kropp, M. Mandelkern, S. Nakamura, E. Pasierb-Love, *et al.*, Phys.Rev. **D53**, 6054 (1996).
- [456] F. Ardellier *et al.* (Double Chooz), (2006), hep-ex/0606025.
- [457] X. Guo (Daya Bay), “A precision measurement of the neutrino mixing angle  $\theta_{13}$  using reactor antineutrinos at daya bay,” (2007), hep-ex/0701029.
- [458] J. Ahn *et al.* (RENO Collaboration), “RENO: An Experiment for Neutrino Oscillation Parameter  $\theta_{13}$  Using Reactor Neutrinos at Yonggwang,” (2010), arXiv:1003.1391 [hep-ex].
- [459] K. Schreckenbach, G. Colvin, W. Gelletly, and F. Von Feilitzsch, Phys.Lett. **B160**, 325 (1985).
- [460] F. Von Feilitzsch, A. Hahn, and K. Schreckenbach, Phys.Lett. **B118**, 162 (1982).
- [461] A. Hahn, K. Schreckenbach, G. Colvin, B. Krusche, W. Gelletly, *et al.*, Phys.Lett. **B218**, 365 (1989).
- [462] T. Mueller, D. Lhuillier, M. Fallot, A. Letourneau, S. Cormon, *et al.*, Phys.Rev. **C83**, 054615 (2011), arXiv:1101.2663 [hep-ex].
- [463] W. M. et al, Nucl.Instrum.Meth **154**, 127 (1978).



- [464] A. Sirlin, Phys.Rev. **164**, 1767 (1967).
- [465] P. Vogel, Phys.Rev. **D29**, 1918 (1984).
- [466] J. Hardy, B. Jonson, and P. Hansen, Phys.Lett. **B136**, 331 (1984).
- [467] <http://www.nndc.bnl.gov/ensdf>.
- [468] O. Tengblad, G. Nyman, K. Aleklett, E. Lund, G. Rudstam, *et al.*, Nucl.Phys. **A503**, 136 (1989).
- [469] R. Greenwood *et al.*, Nucl.Instrum.Meth. **A314**, 514 (1992).
- [470] O. Meplan *et al.*, “MURE: MCNP Utility for Reactor Evolution - Description of the methods, first applications and results,” Proceeding of the European Nuclear Conference. Nuclear Power for the XXIst Century: From basic research to high-tech industry, France. (2005).
- [471] P. Vogel, Phys.Rev. **C76**, 025504 (2007).
- [472] P. Huber, Phys.Rev. **C84**, 024617 (2011), arXiv:1106.0687 [hep-ph].
- [473] D. Lhuillier, “Recent re-evaluation of reactor neutrino fluxes,” (2011), slides of a talk given at Sterile Neutrinos At the Crossroads, Sept. 25-28 2011, Blacksburg, VA, USA.
- [474] <http://www.fusion.org.uk/techdocs/ukaea-fus-534.pdf>.
- [475] N. H. Haag and K. Schreckenbach, (2004), private communication.
- [476] J. Katakura, T. Yoshida, K. Oyamatsu, and T. Tachibana, *JENDL Fission Product Decay Data File*, Tech. Rep. (2000).
- [477] K. Takahashi, Prog.Theor.Phys. **45**, 1466 (1971).
- [478] P. Vogel, G. Schenter, F. Mann, and R. Schenter, Phys.Rev. **C24**, 1543 (1981).
- [479] V. Kopeikin, L. Mikaelyan, and V. Sinev, Phys.Atom.Nucl. **67**, 1892 (2004), arXiv:hep-ph/0410100 [hep-ph].
- [480] C. Jones, A. Bernstein, J. Conrad, Z. Djurcic, M. Fallot, *et al.*, (2011), arXiv:1109.5379 [nucl-ex].
- [481] A. Hoummada *et al.*, Appl. Rad. Isot. **46**, 449 (1995).
- [482] B. Armbruster *et al.*, Phys.Rev. **C57**, 3414 (1998), 20 pages including 13 figures, submitted to Phys.Rev.C, arXiv:hep-ex/9801007 [hep-ex].
- [483] B. Bodmann *et al.* (KARMEN Collaboration.), Phys.Lett. **B332**, 251 (1994).
- [484] L. Auerbach *et al.* (LSND Collaboration), Phys.Rev. **C64**, 065501 (2001), arXiv:hep-ex/0105068 [hep-ex].
- [485] J. Conrad and M. Shaevitz, Phys.Rev. **D85**, 013017 (2012), published version, arXiv:1106.5552 [hep-ex].
- [486] R. Burman, M. Potter, and E. Smith, Nucl.Instrum.Meth. **A291**, 621 (1990).
- [487] D. Krakauer, R. Talaga, R. Allen, H. Chen, R. Hausammann, *et al.*, Phys.Rev. **C45**, 2450 (1992).
- [488] M. Fukugita, Y. Kohyama, and K. Kubodera, Phys.Lett. **B212**, 139 (1988).
- [489] E. Kolbe, K. Langanke, and P. Vogel, Nucl.Phys. **A652**, 91 (1999), arXiv:nucl-th/9903022 [nucl-th].
- [490] T. Donnelly and R. Peccei, Phys.Rept. **50**, 1 (1979).
- [491] S. Mintz and M. Pourkaviani, Phys.Rev. **C37**, 2249 (1988).
- [492] E. Kolbe, K. Langanke, and P. Vogel, Nucl.Phys. **A613**, 382 (1997).
- [493] D. Michael *et al.* (MINOS Collaboration), Nucl.Instrum.Meth. **A596**, 190 (2008), arXiv:0805.3170 [physics.ins-det].
- [494] P. Adamson *et al.*, Phys. Rev. Lett. **106**, 181801 (2011), arXiv:arXiv:1103.0340 [hep-ex].
- [495] P. Adamson *et al.* (The MINOS Collaboration), Phys.Rev. **D82**, 051102 (2010), arXiv:1006.0996 [hep-ex].
- [496] P. Adamson *et al.* (The MINOS Collaboration), Phys.Rev. **D81**, 052004 (2010), arXiv:1001.0336 [hep-ex].
- [497] D. Hernandez and A. Smirnov, Phys.Lett. **B706**, 360 (2012), arXiv:1105.5946 [hep-ph].
- [498] C. Giunti and M. Laveder, Phys.Rev. **D84**, 093006 (2011), arXiv:1109.4033 [hep-ph].

- [499] S. Goswami, Phys.Rev. **D55**, 2931 (1997), arXiv:hep-ph/9507212 [hep-ph].
- [500] J. Gomez-Cadenas and M. Gonzalez-Garcia, Z.Phys. **C71**, 443 (1996), arXiv:hep-ph/9504246 [hep-ph].
- [501] S. M. Bilenky, C. Giunti, and W. Grimus, Eur.Phys.J. **C1**, 247 (1998), arXiv:hep-ph/9607372 [hep-ph].
- [502] N. Okada and O. Yasuda, Int.J.Mod.Phys. **A12**, 3669 (1997), arXiv:hep-ph/9606411 [hep-ph].
- [503] V. D. Barger, T. J. Weiler, and K. Whisnant, Phys.Lett. **B427**, 97 (1998), arXiv:hep-ph/9712495 [hep-ph].
- [504] V. D. Barger, S. Pakvasa, T. J. Weiler, and K. Whisnant, Phys.Rev. **D58**, 093016 (1998), arXiv:hep-ph/9806328 [hep-ph].
- [505] S. M. Bilenky, C. Giunti, W. Grimus, and T. Schwetz, Astropart.Phys. **11**, 413 (1999), arXiv:hep-ph/9804421 [hep-ph].
- [506] S. M. Bilenky, C. Giunti, W. Grimus, and T. Schwetz, Phys. Rev. **D60**, 073007 (1999), arXiv:hep-ph/9903454.
- [507] V. D. Barger, B. Kayser, J. Learned, T. J. Weiler, and K. Whisnant, Phys.Lett. **B489**, 345 (2000), arXiv:hep-ph/0008019 [hep-ph].
- [508] O. Peres and A. Smirnov, Nucl.Phys. **B599**, 3 (2001), arXiv:hep-ph/0011054 [hep-ph].
- [509] W. Grimus and T. Schwetz, Eur. Phys. J. **C20**, 1 (2001), arXiv:hep-ph/0102252.
- [510] M. Gonzalez-Garcia, M. Maltoni, and C. Pena-Garay, Phys.Rev. **D64**, 093001 (2001), arXiv:hep-ph/0105269 [hep-ph].
- [511] M. Maltoni, T. Schwetz, and J. Valle, Phys.Lett. **B518**, 252 (2001), arXiv:hep-ph/0107150 [hep-ph].
- [512] M. Maltoni, T. Schwetz, and J. Valle, Phys.Rev. **D65**, 093004 (2002), arXiv:hep-ph/0112103 [hep-ph].
- [513] M. Maltoni, T. Schwetz, M. Tortola, and J. Valle, Nucl.Phys. **B643**, 321 (2002), arXiv:hep-ph/0207157 [hep-ph].
- [514] A. Strumia, Phys.Lett. **B539**, 91 (2002), arXiv:hep-ph/0201134 [hep-ph].
- [515] C. Giunti and M. Laveder, Phys.Lett. **B706**, 200 (2011), arXiv:1111.1069 [hep-ph].
- [516] M. Maltoni and T. Schwetz, Phys. Rev. **D76**, 093005 (2007), arXiv:0705.0107 [hep-ph].
- [517] G. Karagiorgi *et al.*, Phys.Rev. **D75**, 013011 (2007), arXiv:hep-ph/0609177 [hep-ph].
- [518] G. Karagiorgi *et al.*, Phys.Rev. **D80**, 073001 (2009), arXiv:0906.1997 [hep-ph].
- [519] G. Karagiorgi, “Confronting Recent Neutrino Oscillation Data with Sterile Neutrinos,” (2011), arXiv:1110.3735 [hep-ph].
- [520] K. Abe *et al.* (Super-Kamiokande Collaboration), Phys.Rev. **D83**, 052010 (2011), arXiv:1010.0118 [hep-ex].
- [521] C. Giunti and Y. Li, Phys.Rev. **D80**, 113007 (2009), arXiv:0910.5856 [hep-ph].
- [522] A. Palazzo, Phys.Rev. **D83**, 113013 (2011), arXiv:1105.1705 [hep-ph].
- [523] S. Choubey, JHEP **0712**, 014 (2007), arXiv:0709.1937 [hep-ph].
- [524] S. Razzaque and A. Smirnov, JHEP **1107**, 084 (2011), arXiv:1104.1390 [hep-ph].
- [525] R. Gandhi and P. Ghoshal, “Atmospheric neutrinos as a probe of  $eV^2$ -scale active-sterile oscillations,” (2011), arXiv:1108.4360 [hep-ph].
- [526] V. Barger, Y. Gao, and D. Marfatia, Phys.Rev. **D85**, 011302 (2012), 4 pages, 4 figures, 2 tables, arXiv:1109.5748 [hep-ph].
- [527] G. Fogli, E. Lisi, A. Marrone, A. Melchiorri, A. Palazzo, *et al.*, Phys.Rev. **D78**, 033010 (2008), arXiv:0805.2517 [hep-ph].
- [528] S. A. Thomas, F. B. Abdalla, and O. Lahav, Phys.Rev.Lett. **105**, 031301 (2010), arXiv:0911.5291 [astro-ph.CO].

- [529] E. Giusarma *et al.*, Phys.Rev. **D83**, 115023 (2011), arXiv:1102.4774 [astro-ph.CO].
- [530] R. H. Cyburt, B. D. Fields, K. A. Olive, and E. Skillman, Astropart.Phys. **23**, 313 (2005), arXiv:astro-ph/0408033 [astro-ph].
- [531] P. Astier *et al.* (NOMAD), Phys. Lett. **B570**, 19 (2003), arXiv:hep-ex/0306037.
- [532] E. Zimmerman (MiniBooNE), (2011), PANIC 2011.
- [533] Z. Djurcic (MiniBooNE), (2011), Nufact 2011.
- [534] A. Kuvshinnikov *et al.*, JETP Lett. **54**, 253 (1991).
- [535] A. Hoummada, S. Lazrak Mikou, G. Bagieu, J. Cavaignac, and D. Holm Koang, Applied Radiation and Isotopes **46**, 449 (1995).
- [536] G. Vidyakin *et al.*, Sov.Phys.JETP **71**, 424 (1990).
- [537] S. Abe *et al.* (KamLAND Collaboration), Phys.Rev.Lett. **100**, 221803 (2008), arXiv:0801.4589 [hep-ex].
- [538] C. Giunti and M. Laveder, Phys.Rev. **D83**, 053006 (2011), arXiv:1012.0267 [hep-ph].
- [539] M. Maltoni and T. Schwetz, Phys. Rev. **D68**, 033020 (2003), arXiv:hep-ph/0304176.
- [540] G. Vidyakin *et al.*, Sov.Phys.JETP **66**, 243 (1987).
- [541] M. Apollonio *et al.* (CHOOZ), Eur. Phys. J. **C27**, 331 (2003), hep-ex/0301017.
- [542] F. Boehm *et al.*, Phys.Rev. **D64**, 112001 (2001), arXiv:hep-ex/0107009 [hep-ex].
- [543] T. Schwetz, M. Tortola, and J. Valle, New J.Phys. **13**, 063004 (2011), arXiv:1103.0734 [hep-ph].
- [544] Zarko Pavlovic (MiniBooNE Collaboration), “Short baseline neutrino oscillations,” (2011), talk given at DPF 2011.
- [545] P. Astier *et al.* (NOMAD), Nucl. Phys. **B611**, 3 (2001), arXiv:hep-ex/0106102.
- [546] P. Huber, M. Lindner, and W. Winter, Comput. Phys. Commun. **167**, 195 (2005), hep-ph/0407333.
- [547] P. Huber, J. Kopp, M. Lindner, M. Rolinec, and W. Winter, Comput. Phys. Commun. **177**, 432 (2007), hep-ph/0701187.
- [548] B. Bhattacharya, A. M. Thalapillil, and C. E. Wagner, “Implications of sterile neutrinos for medium/long-baseline neutrino experiments and the determination of  $\theta_{13}$ ,” (2011), arXiv:1111.4225 [hep-ph].
- [549] R. J. Hill, Phys.Rev. **D84**, 017501 (2011), arXiv:1002.4215 [hep-ph].
- [550] S. Goswami and W. Rodejohann, JHEP **10**, 073 (2007), arXiv:0706.1462 [hep-ph].
- [551] M. C. Gonzalez-Garcia, M. Maltoni, and J. Salvado, JHEP **04**, 056 (2010), arXiv:arXiv:1001.4524 [hep-ph].
- [552] J. Kopp, M. Maltoni, and T. Schwetz, Work in progress.
- [553] L. Bento and Z. Berezhiani, Phys.Rev. **D64**, 115015 (2001), arXiv:hep-ph/0108064 [hep-ph].
- [554] A. Dolgov and F. Takahashi, Nucl.Phys. **B688**, 189 (2004), arXiv:hep-ph/0402066 [hep-ph].
- [555] C. Athanassopoulos *et al.* (LSND Collaboration), Phys.Rev.Lett. **77**, 3082 (1996), arXiv:nucl-ex/9605003 [nucl-ex].
- [556] C. Athanassopoulos *et al.* (LSND Collaboration), Phys.Rev.Lett. **81**, 1774 (1998), arXiv:nucl-ex/9709006 [nucl-ex].
- [557] S. Hollenberg, O. Micu, and H. Pas, Prog.Part.Nucl.Phys. **64**, 193 (2010), arXiv:0911.1018 [hep-ph].
- [558] S. Hollenberg, O. Micu, H. Pas, and T. J. Weiler, Phys.Rev. **D80**, 093005 (2009), arXiv:0906.0150 [hep-ph].
- [559] E. Akhmedov and T. Schwetz, AIP Conf.Proc. **1382**, 94 (2011).
- [560] J. A. Harvey, C. T. Hill, and R. J. Hill, Phys.Rev.Lett. **99**, 261601 (2007), arXiv:0708.1281 [hep-ph].
- [561] S. Gninenko, (2011), arXiv:1101.4004 [hep-ex].
- [562] S. Gninenko and D. Gorbunov, Phys.Rev. **D81**, 075013 (2010), arXiv:0907.4666 [hep-ph].
- [563] S. N. Gninenko, Phys.Rev. **D83**, 015015 (2011), arXiv:1009.5536 [hep-ph].

- [564] S. Gninenko, Phys.Rev.Lett. **103**, 241802 (2009), arXiv:0902.3802 [hep-ph].
- [565] S. Gninenko, (2011), arXiv:1107.0279 [hep-ph].
- [566] C. Dib, J. C. Helo, S. Kovalenko, and I. Schmidt, Phys.Rev. **D84**, 071301 (2011), arXiv:1105.4664 [hep-ph].
- [567] E. Zimmerman (for the MiniBooNE Collaboration), (2011), arXiv:1111.1375 [hep-ex].
- [568] L. Everett, PDF2011 proceedings.
- [569] R. Shrock, Phys.Lett. **B96**, 159 (1980).
- [570] B. H. J. McKellar, Phys. Lett. **B97**, 93 (1980).
- [571] I. Y. Kobzarev, B. V. Martemyanov, L. B. Okun, and M. G. Shchepkin, Sov. J. Nucl. Phys. **32**, 823 (1980).
- [572] F. Vissani, Nucl.Phys.Proc.Suppl. **100**, 273 (2001), arXiv:hep-ph/0012018 [hep-ph].
- [573] Y. Farzan, O. Peres, and A. Smirnov, Nucl.Phys. **B612**, 59 (2001), arXiv:hep-ph/0105105 [hep-ph].
- [574] J. Studnik and M. Zralek, (2001), arXiv:hep-ph/0110232 [hep-ph].
- [575] Y. Farzan and A. Smirnov, Phys.Lett. **B557**, 224 (2003), arXiv:hep-ph/0211341 [hep-ph].
- [576] C. Kraus *et al.*, Eur. Phys. J. **C40**, 447 (2005), arXiv:hep-ex/0412056.
- [577] V. M. Lobashev, Nucl. Phys. **A719**, C153 (2003), 17th International Nuclear Physics Divisional Conference: Europhysics Conference on Nuclear Physics in Astrophysics (NPDC 17), Debrecen, Hungary, 30 Sep – 3 Oct 2002.
- [578] F. Fraenkle, (2011), arXiv:1110.0087 [physics.ins-det].
- [579] C. Weinheimer, (2009), arXiv:0912.1619 [hep-ex].
- [580] S. R. Elliott and P. Vogel, Ann.Rev.Nucl.Part.Sci. **52**, 115 (2002), arXiv:hep-ph/0202264 [hep-ph].
- [581] S. Bilenky, C. Giunti, J. Grifols, and E. Masso, Phys.Rept. **379**, 69 (2003), arXiv:hep-ph/0211462 [hep-ph].
- [582] S. R. Elliott and J. Engel, J.Phys.G **G30**, R183 (2004), arXiv:hep-ph/0405078 [hep-ph].
- [583] I. Avignone, Frank T., S. R. Elliott, and J. Engel, Rev.Mod.Phys. **80**, 481 (2008), arXiv:0708.1033 [nucl-ex].
- [584] C. Giunti, Phys.Rev. **D61**, 036002 (2000), arXiv:hep-ph/9906275 [hep-ph].
- [585] S. Goswami and W. Rodejohann, Phys.Rev. **D73**, 113003 (2006), arXiv:hep-ph/0512234 [hep-ph].
- [586] Y. Li and S.-s. Liu, Phys.Lett. **B706**, 406 (2012), arXiv:1110.5795 [hep-ph].
- [587] J. Gomez-Cadenas, J. Martin-Albo, M. Mezzetto, F. Monrabal, and M. Sorel, Riv.Nuovo Cim. (2011), arXiv:1109.5515 [hep-ex].
- [588] W. Rodejohann and J. Valle, Phys.Rev. **D84**, 073011 (2011), arXiv:1108.3484 [hep-ph].
- [589] F. Halzen and S. R. Klein, Rev.Sci.Instrum. **81**, 081101 (2010), arXiv:1007.1247 [astro-ph.HE].
- [590] H. Nunokawa, O. Peres, and R. Zukanovich Funchal, Phys.Lett. **B562**, 279 (2003), arXiv:hep-ph/0302039 [hep-ph].
- [591] R. Abbasi *et al.* (IceCube Collaboration), Phys.Rev. **D84**, 082001 (2011), arXiv:1104.5187 [astro-ph.HE].
- [592] R. Abbasi *et al.* (IceCube Collaboration), Phys.Rev. **D83**, 012001 (2011), arXiv:1010.3980 [astro-ph.HE].
- [593] R. Abbasi *et al.* (IceCube Collaboration), Astrophys.J. **732**, 18 (2011), arXiv:1012.2137 [astro-ph.HE].
- [594] K. Daum *et al.* (Frejus Collaboration.), Z.Phys. **C66**, 417 (1995).
- [595] M. Gonzalez-Garcia, M. Maltoni, and J. Rojo, JHEP **0610**, 075 (2006), arXiv:hep-ph/0607324 [hep-ph].
- [596] R. Abbasi *et al.* (IceCube Collaboration), Phys.Rev. **D79**, 102005 (2009), arXiv:0902.0675 [astro-ph.HE].

- [597] R. Abbasi *et al.* (IceCube Collaboration), *Astropart.Phys.* **34**, 48 (2010), arXiv:1004.2357 [astro-ph.HE].
- [598] G. Barr, T. Gaisser, P. Lipari, S. Robbins, and T. Stanev, *Phys.Rev.* **D70**, 023006 (2004), arXiv:astro-ph/0403630 [astro-ph].
- [599] R. Enberg, M. H. Reno, and I. Sarcevic, *Phys.Rev.* **D78**, 043005 (2008), arXiv:0806.0418 [hep-ph].
- [600] A. Esmaili and O. L. Peres, “Indirect Dark Matter Detection in the Light of Sterile Neutrinos,” (2012), arXiv:1202.2869 [hep-ph].
- [601] C. A. Argüelles and J. Kopp, “Sterile neutrinos and indirect dark matter searches in IceCube,” (2012), arXiv:1202.3431 [hep-ph].
- [602] M. Pospelov, *Phys.Rev.* **D84**, 085008 (2011), arXiv:1103.3261 [hep-ph].
- [603] R. Harnik, J. Kopp, and P. A. Machado, “Exploring nu signals in dark matter detectors,” (2012), arXiv:1202.6073 [hep-ph].
- [604] M. Pospelov and J. Pradler, “Elastic scattering signals of solar neutrinos with enhanced baryonic currents,” (2012), arXiv:1203.0545 [hep-ph].
- [605] A. Gould, *Astrophys.J.* **388**, 338 (1992).
- [606] M. Cirelli *et al.*, *Nucl. Phys.* **B727**, 99 (2005), arXiv:hep-ph/0506298.
- [607] M. Blennow, J. Edsjo, and T. Ohlsson, *JCAP* **0801**, 021 (2008), arXiv:0709.3898 [hep-ph].
- [608] R. Abbasi *et al.* (ICECUBE), *Phys. Rev. Lett.* **102**, 201302 (2009), arXiv:0902.2460 [astro-ph.CO].
- [609] R. Abbasi *et al.* (IceCube Collaboration), *Phys.Rev.* **D85**, 042002 (2012), arXiv:1112.1840 [astro-ph.HE].
- [610] S. Desai *et al.* (Super-Kamiokande), *Phys. Rev.* **D70**, 083523 (2004), arXiv:hep-ex/0404025.
- [611] R. Abbasi *et al.* (The IceCube Collaboration), “The IceCube Neutrino Observatory IV: Searches for Dark Matter and Exotic Particles,” (2011), arXiv:1111.2738 [astro-ph.HE].
- [612] H. S. Lee *et al.* (KIMS), *Phys. Rev. Lett.* **99**, 091301 (2007), arXiv:0704.0423 [astro-ph].
- [613] E. Behnke *et al.*, *Phys.Rev.Lett.* **106**, 021303 (2011), arXiv:1008.3518 [astro-ph.CO].
- [614] M. Felizardo *et al.*, “Final Analysis and Results of the Phase II SIMPLE Dark Matter Search,” (2011), arXiv:1106.3014 [astro-ph.CO].
- [615] A. Esmaili and Y. Farzan, *Phys.Rev.* **D81**, 113010 (2010), arXiv:0912.4033 [hep-ph].
- [616] A. Esmaili and Y. Farzan, *JCAP* **1104**, 007 (2011), arXiv:1011.0500 [hep-ph].
- [617] A. Gutlein *et al.*, *Astropart.Phys.* **34**, 90 (2010), arXiv:1003.5530 [hep-ph].
- [618] E. Aprile *et al.*, *Phys.Rev.* **D83**, 082001 (2011), arXiv:1101.3866 [astro-ph.IM].
- [619] G. Bellini, J. Benziger, D. Bick, S. Bonetti, G. Bonfini, *et al.*, *Phys.Rev.Lett.* **107**, 141302 (2011), arXiv:1104.1816 [hep-ex].
- [620] C. Aalseth, P. Barbeau, J. Colaresi, J. Collar, J. Diaz Leon, *et al.*, *Phys.Rev.Lett.* **107**, 141301 (2011), arXiv:1106.0650 [astro-ph.CO].
- [621] R. Bernabei *et al.* (DAMA Collaboration), *Eur.Phys.J.* **C56**, 333 (2008), arXiv:0804.2741 [astro-ph].
- [622] K. Freese, J. A. Frieman, and A. Gould, *Phys.Rev.* **D37**, 3388 (1988).
- [623] R. Bernabei, P. Belli, F. Cappella, R. Cerulli, C. Dai, *et al.*, *Eur.Phys.J.* **C67**, 39 (2010), arXiv:1002.1028 [astro-ph.GA].
- [624] V. Kudryavtsev, M. Robinson, and N. Spooner, *J.Phys.Conf.Ser.* **203**, 012039 (2010).
- [625] J. P. Ralston, “One Model Explains DAMA/LIBRA, CoGENT, CDMS, and XENON,” (2010), arXiv:1006.5255 [hep-ph].
- [626] D. Nygren, “A testable conventional hypothesis for the DAMA-LIBRA annual modulation,” (2011), arXiv:1102.0815 [astro-ph.IM].
- [627] K. Blum, “DAMA vs. the annually modulated muon background,” (2011), arXiv:1110.0857 [astro-ph.HE].

- [628] R. Bernabei, P. Belli, F. Cappella, V. Caracciolo, R. Cerulli, *et al.*, “No role for muons in the DAMA annual modulation results,” (2012), arXiv:1202.4179 [astro-ph.GA].
- [629] C. Grieb, J. Link, and R. S. Raghavan, *Phys. Rev.* **D75**, 093006 (2007), arXiv:hep-ph/0611178.
- [630] L. W. Alvarez, *A Signal Generator for Ray Davis’ Neutrino Detector*, Tech. Rep. Physics Notes, Memo No. 767 (Lawrence Radiation Laboratory, 1973) available online at <http://alvarezphysicsmemos.lbl.gov>.
- [631] R. S. Raghavan, in *Proceedings on the Informal Conference on Status and Future of Solar Neutrinos Research*, Brookhaven National Laboratory Report No. 50879, Vol. 2 (1978) p. 270.
- [632] M. Cribier and M. Spiro, Tech. Rep. Saclay-Gallex Note 87-01 (CEA, Saclay, 1987).
- [633] W. Haxton, *Phys.Rev.* **C38**, 2474 (1988).
- [634] G. E. Popov *et al.*, *Nucl. Instrum. Meth.* **A362**, 532 (1995).
- [635] D. Z. Freedman, D. N. Schramm, and D. L. Tubbs, *Ann.Rev.Nucl.Part.Sci.* **27**, 167 (1977).
- [636] V. Barsanov, A. Dzhanlidze, S. Zlokazov, N. Kotelnikov, S. Markov, *et al.*, *Phys.Atom.Nucl.* **70**, 300 (2007).
- [637] K. Irwin, *Appl.Phys.Lett.* **66**, 1998 (1995).
- [638] S. R. Bandler, R. P. Brekosky, A. D. Brown, J. A. Chervenak, E. Figueroa-Feliciano, F. M. Finkbeiner, N. Iyomoto, R. L. Kelley, C. A. Kilbourne, F. S. Porter, J. Sadleir, and S. J. Smith, *J. Low Temp. Phys.* **151**, 400 (2008).
- [639] E. Figueroa-Feliciano, *J. Appl. Phys.* **99**, 4513 (2006).
- [640] C. D. Reintsema *et al.*, in *The Thirteenth International Workshop on Low Temperature Detectors – LTD13* (AIP Conference Proceedings, 2009) pp. 237–240.
- [641] D. Bintley *et al.*, *Proc.SPIE Int.Soc.Opt.Eng.* **7741**, 774106 (2010).
- [642] M. D. Niemack *et al.*, *Appl. Phys. Lett.* **96**, 163509 (2010).
- [643] A. Anderson, J. Conrad, E. Figueroa-Feliciano, K. Scholberg, and J. Spitz, *Phys.Rev.* **D84**, 013008 (2011), arXiv:1103.4894 [hep-ph].
- [644] A. Anderson, J. Conrad, E. Figueroa-Feliciano, C. Ignarra, G. Karagiorgi, *et al.*, “Measuring Active-to-Sterile Neutrino Oscillations with Neutral Current Coherent Neutrino-Nucleus Scattering,” (2012), 10 pages, 7 figures, arXiv:1201.3805 [hep-ph].
- [645] J. M. Conrad and M. H. Shaevitz, *Phys. Rev. Lett.* **104**, 141802 (2010), arXiv:0912.4079 [hep-ex].
- [646] D. Frekers, H. Ejiri, H. Akimune, T. Adachi, B. Bilgier, *et al.*, *Phys.Lett.* **B706**, 134 (2011).
- [647] G. Bellini, J. Benziger, S. Bonetti, M. Avanzini, B. Caccianiga, *et al.*, *Phys.Lett.* **B687**, 299 (2010), arXiv:1003.0284 [hep-ex].
- [648] G. Bellini, R. Raghavan, *et al.* (Borexino Collaboration), (1991), <http://borex.lngs.infn.it/papers/1991-08%20BorexYellowBook.pdf>.
- [649] M. Cribier, L. Gosset, P. Lamare, J. Languillat, P. Perrin, *et al.*, *Nucl.Instrum.Meth.* **A378**, 233 (1996).
- [650] G. Alimonti *et al.* (Borexino Collaboration), *Astropart.Phys.* **16**, 205 (2002), arXiv:hep-ex/0012030 [hep-ex].
- [651] M. Decowski (KamLand Collaboration), *J.Phys.Conf.Ser.* **136**, 022005 (2008).
- [652] M. Chen, *Nucl.Phys.Proc.Suppl.* **145**, 65 (2005).
- [653] M. Cribier, M. Fechner, T. Lasserre, A. Letourneau, D. Lhuillier, *et al.*, *Phys.Rev.Lett.* **107**, 201801 (2011), arXiv:1107.2335 [hep-ex].
- [654] V. Kornoukhov, *Some aspects of the creation and application of anti-neutrino artificial sources*, Tech. Rep. ITEP-90-94 (Institute of Theoretical and Experimental Physics, Moscow, 1994).
- [655] A. Ianni, D. Montanino, and G. Scioscia, *Eur.Phys.J.* **C8**, 609 (1999), arXiv:hep-ex/9901012 [hep-ex].
- [656] K. Inoue, Neutrino 2010 Conference (2010).

- [657] National Institute of Standard and Technology, NIST, <http://www.nist.gov/>.
- [658] H. Koch and J. Motz, *Rev.Mod.Phys.* **31**, 920 (1959).
- [659] S. Agostinelli *et al.* (GEANT4), *Nucl.Instrum.Meth.* **A506**, 250 (2003).
- [660] V. Kornoukhov, *Phys.Atom.Nucl.* **60**, 558 (1997).
- [661] SNAC 2011 Conference, Blacksburg, VA, USA, Sep. 24-29, 2001  
<http://www.cpe.vt.edu/snac/program.html>.
- [662] Short-Baseline Neutrino Workshop, Chicago, IL, USA, May 12-14, 2011  
<http://www.aps.org/units/dpb/news/shortbaseline.cfm>.
- [663] D. Dwyer, K. Heeger, B. Littlejohn, and P. Vogel, (2011), arXiv:1109.6036 [hep-ex].
- [664] K. Heeger *et al.* (Daya Bay Collaboration), “First data with the daya bay antineutrino detectors,” TAUP2011, Munich, Germany, September 2011.
- [665] C. Arpesella *et al.* (Borexino), *Phys.Rev.Lett.* **101**, 0913202 (2008), arXiv:0805.3843 [astro-ph].
- [666] M. Mitterer, *Phys.Rev.* **C8**, 1370 (1973).
- [667] O. Yasuda, *JHEP* **09**, 036 (2011), arXiv:1107.4766 [hep-ph].
- [668] O. Yasuda, “Search for sterile neutrinos at reactors with a small core,” (2011), arXiv:1110.2579 [hep-ph].
- [669] T. Lasserre (Nucifer Collaboration),  
<http://www.e15.physik.tu-muenchen.de/fileadmin/downloads/seminars/1011/SterileNeutrinosWorkshop/lasserre-tumE15-feb2011-nucifer.pdf>.
- [670] S. Oguri, [http://www.awa.tohoku.ac.jp/AAP2010/2ndDay/AAP2010\\_panda.pdf](http://www.awa.tohoku.ac.jp/AAP2010/2ndDay/AAP2010_panda.pdf).
- [671] H. Sugiyama and O. Yasuda, *Int.J.Mod.Phys.* **A22**, 3407 (2007), arXiv:hep-ph/0508090 [hep-ph].
- [672] D. Latimer, J. Escamilla, and D. Ernst, *Phys.Rev.* **C75**, 042501 (2007), arXiv:hep-ex/0701004 [hep-ex].
- [673] A. de Gouvêa and T. Wytock, *Phys.Rev.* **D79**, 073005 (2009), arXiv:0809.5076 [hep-ph].
- [674] The experimental fast reactor Joyo, <http://www.jaea.go.jp/04/o-arai/joyo/english/index.html>.
- [675] T. Aoyama, T. Sekine, S. Maeda, A. Yoshida, Y. Maeda, S. Suzuki, and T. Takeda, *Nuclear Engineering and Design* **237**, 353 (2007).
- [676] The ILL research reactor, <http://www.ill.eu/>.
- [677] The Osiris research reactor,  
[http://nucleaire-saclay.cea.fr/en/Phoce/Vie\\_des\\_labos/Ast/ast\\_sstheme.php?id\\_ast=66](http://nucleaire-saclay.cea.fr/en/Phoce/Vie_des_labos/Ast/ast_sstheme.php?id_ast=66).
- [678] A. Derbin, A. Kayunov, and V. Muratova, “Search for neutrino oscillations at a research reactor,” (2012), arXiv:1204.2449 [hep-ph].
- [679] N. S. Bowden *et al.*, *Nucl. Instrum. Meth.* **A572**, 985 (2007), arXiv:physics/0612152.
- [680] A. Bernstein, N. S. Bowden, A. Misner, and T. Palmer, *J. Appl. Phys.* **103**, 074905 (2008), arXiv:0804.4723 [nucl-ex].
- [681] N. S. Bowden *et al.*, “Observation of the Isotopic Evolution of PWR Fuel Using an Antineutrino Detector,” (2008), arXiv:0808.0698 [nucl-ex].
- [682] A. Porta *et al.*, *IEEE Transactions on Nuclear Science* **57**, 2732 (2010).
- [683] M. Fechner, C. Henson, J. Gaffiot, T. Lasserre, A. Letourneau, *et al.*, *Applied Radiation and Isotopes* **69**, 1033 (2011), arXiv:1101.4000 [physics.ins-det].
- [684] P. Huber, M. Lindner, T. Schwetz, and W. Winter, *Nucl.Phys.* **B665**, 487 (2003), arXiv:hep-ph/0303232 [hep-ph].
- [685] (), nIST Center for Neutron Research, <http://www.ncnr.nist.gov/>.
- [686] (), nCNR Expansion Initiative, <http://www.ncnr.nist.gov/expansion2/>.
- [687] S. K. Agarwalla and P. Huber, *Phys. Lett.* **B696**, 359 (2011), arXiv:1007.3228 [hep-ph].

- [688] C. Athanassopoulos *et al.* (LSND), Phys. Rev. Lett. **75**, 2650 (1995), arXiv:nucl-ex/9504002.
- [689] C. Athanassopoulos *et al.* (LSND), Phys. Rev. **C58**, 2489 (1998), arXiv:nucl-ex/9706006.
- [690] J. F. Beacom and M. R. Vagins, Phys. Rev. Lett. **93**, 171101 (2004), arXiv:hep-ph/0309300.
- [691] H. Watanabe *et al.* (Super-Kamiokande Collaboration), Astropart.Phys. **31**, 320 (2009), 17 pages, 11 figures, arXiv:0811.0735 [hep-ex].
- [692] S. Dazeley, A. Bernstein, N. S. Bowden, and R. Svoboda, Nucl. Instrum. Meth. **A607**, 616 (2009), arXiv:0808.0219 [nucl-ex].
- [693] J. Alonso *et al.*, “Expression of Interest for a Novel Search for CP Violation in the Neutrino Sector: DAEdALUS,” (2010), arXiv:1006.0260 [physics.ins-det].
- [694] J. Spitz, “A Sterile Neutrino Search with Kaon Decay-at-rest,” (2012), arXiv:1203.6050 [hep-ph].
- [695] A. Rubbia, “Experiments for CP-violation: A giant liquid argon scintillation, Cerenkov and charge imaging experiment?” (2004), arXiv:hep-ph/0402110.
- [696] C. Juszczak, Acta Phys.Polon. **B40**, 2507 (2009), arXiv:0909.1492 [hep-ex].
- [697] T. Golan, C. Juszczak, and J. T. Sobczyk, “Final State Interactions Effects in Neutrino-Nucleus Interactions,” (2012), arXiv:1202.4197 [nucl-th].
- [698] A. Ankowski *et al.* (ICARUS Collaboration), Acta Phys.Polon. **B41**, 103 (2010), 24 pages, 16 figures, arXiv:0812.2373 [hep-ex].
- [699] F. Arneodo *et al.* (ICARUS-Milano Collaboration), Phys.Rev. **D74**, 112001 (2006), arXiv:physics/0609205 [physics].
- [700] W. A. Rolke, A. M. Lopez, and J. Conrad, Nucl.Instrum.Meth. **A551**, 493 (2005), arXiv:physics/0403059 [physics].
- [701] J. Lundberg, J. Conrad, W. Rolke, and A. Lopez, Comput.Phys.Commun. **181**, 683 (2010), arXiv:0907.3450 [physics.data-an].
- [702] G. Tzanakos *et al.* (MINOS+ Collaboration), *MINOS+ : a Proposal to FNAL to run MINOS with the medium energy NuMI beam*, Tech. Rep. (2011) spokespersons R. Plunkett and J. Thomas.
- [703] I. Stancu *et al.*, “A Proposal to Build a MiniBooNE Near Detector: BooNE,” (2011).
- [704] M. Antonello, D. Bagliani, B. Baibussinov, H. Bilokon, F. Boffelli, *et al.*, (2012), arXiv:1203.3432 [physics.ins-det].
- [705] C. Rubbia *et al.*, *A comprehensive search for ‘anomalies’ from neutrino and anti-neutrino oscillations at large mass differences ( $\Delta m^2 \sim 1 \text{ eV}^2$ ) with two LArDTPC imaging detectors at different distances from the CERN-PS*, Tech. Rep. (2011).
- [706] C. Rubbia *et al.* (ICARUS/CNGS2 Collaboration), *Physics Programme for ICARUS after 2012*, Tech. Rep. (2011).
- [707] P. Bernardini *et al.*, *Prospect for Charge Current Neutrino Interactions Measurements at the CERN-PS*, Tech. Rep. (2011).
- [708] C. Anderson *et al.* (ArgoNeuT Collaboration), “First Measurements of Inclusive Muon Neutrino Charged Current Differential Cross Sections on Argon,” (2011), arXiv:1111.0103 [hep-ex].
- [709] T. Katori (MicroBooNE), Proceedings of Crimea-11 (2011).
- [710] B. J. P. Jones, “The Status of the MicroBooNE Experiment,” (2011), arXiv:1110.1678 [physics.ins-det].
- [711] H. Chen *et al.* (MicroBooNE Collaboration), “Proposal for a New Experiment Using the Booster and NuMI Neutrino Beamlines: MicroBooNE,” (2007).
- [712] B. Baller, Proceedings of GLA2011 (2011).
- [713] R. Guenette, Proceedings of GLA2011 (2011).
- [714] G. Karagiorgi, Proceedings of TIPP2011 (2011).
- [715] D. G. Koshkarev, *Proposal for a Decay Ring to Produce Intense Secondary Particle Beams at the*



- SPS, Tech. Rep. (1974).
- [716] D. Neuffer, “Design Considerations for a Muon Storage Ring,” (1980), Telmark Conference on Neutrino Mass, Barger and Cline eds., Telmark, Wisconsin.
  - [717] W. Winter, “Optimization of a Very Low Energy Neutrino Factory for the Disappearance Into Sterile Neutrinos,” (2012), arXiv:1204.2671 [hep-ph].
  - [718] S. Choubey *et al.* (IDS-NF Collaboration), “International Design Study for the Neutrino Factory, Interim Design Report,” (2011), arXiv:1112.2853 [hep-ex].
  - [719] J. Lagrange and Y. Mori, “Advanced Scaling FFAG Muon decay ring for Very Low Energy Neutrino Factory,” (2011), acc-kurri- 1119-01-2011.
  - [720] T. J. Roberts and D. M. Kaplan, Conf.Proc. **C070625**, 3468 (2007).
  - [721] J. Kopp, Int.J.Mod.Phys. **C19**, 523 (2008), arXiv:physics/0610206 [physics].
  - [722] J. Kopp, M. Lindner, T. Ota, and J. Sato, Phys. Rev. **D77**, 013007 (2008), arXiv:0708.0152 [hep-ph].
  - [723] C. D. Tunnell, J. H. Cobb, and A. D. Bross, “Sensitivity to eV-scale Neutrinos of Experiments at a Very Low Energy Neutrino Factory,” (2011), arXiv:1111.6550 [hep-ph].
  - [724] J. Nelson, Int.J.Mod.Phys. **A16S1C**, 1181 (2001).
  - [725] G. Ambrosio *et al.* (VLHC Design Study Group), *Design study for a staged very large hadron collider*, Tech. Rep. SLAC-R-591, FERMILAB-TM-2149 (2001).
  - [726] A. Bueno *et al.*, JHEP **04**, 041 (2007), arXiv:hep-ph/0701101.
  - [727] D. B. Cline, F. Raffaelli, and F. Sergiampietri, JINST **1**, T09001 (2006), arXiv:astro-ph/0604548.
  - [728] A. Ereditato and A. Rubbia, Nucl. Phys. Proc. Suppl. **155**, 233 (2006), arXiv:hep-ph/0510131.
  - [729] R. Gandhi, C. Quigg, M. H. Reno, and I. Sarcevic, Astropart. Phys. **5**, 81 (1996), arXiv:hep-ph/9512364.
  - [730] INO Collaboration, <http://www.imsc.res.in/~ino/OpenReports/INOReport.pdf>.
  - [731] M. C. Gonzalez-Garcia and M. Maltoni, Phys. Rev. **D70**, 033010 (2004), arXiv:hep-ph/0404085.
  - [732] R. Gandhi *et al.*, Phys. Rev. **D76**, 073012 (2007), arXiv:0707.1723 [hep-ph].
  - [733] M. Honda, T. Kajita, K. Kasahara, and S. Midorikawa, Phys. Rev. **D70**, 043008 (2004), arXiv:astro-ph/0404457.
  - [734] A. M. Dziewonski and D. L. Anderson, Phys. Earth Planet. Interiors **25**, 297 (1981).